United States
Environmental Protection
Agency

Industrial Environmental Research
Laboratory
Research Triangle Park NC 27711

EPA-600 9-82-005b
July 1982

Research and Development

EPA

Third Symposium on the Transfer and Utilization of Particulate Control Technology:

Volume II. Electrostatic Precipitators

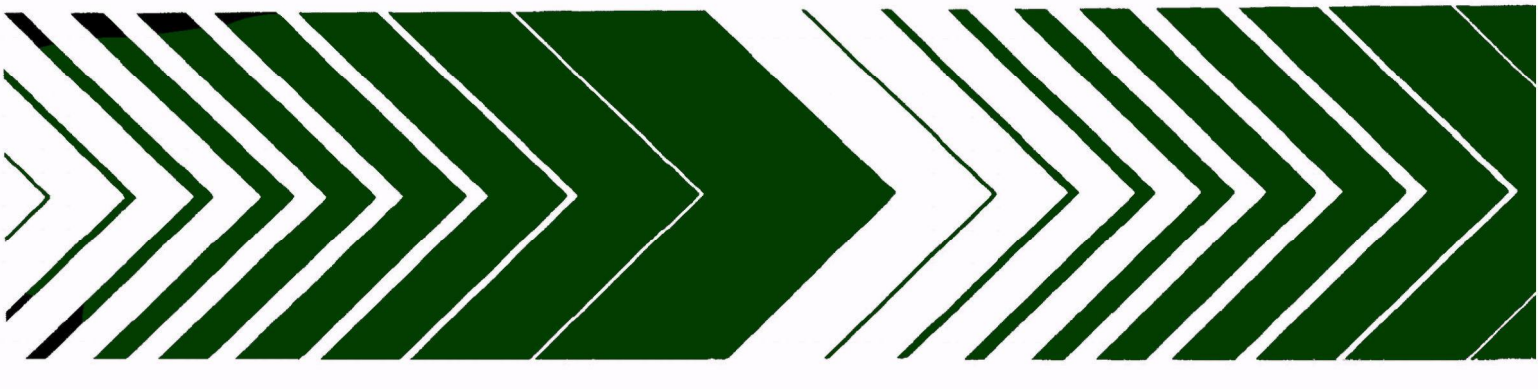

EPA-600/9-82-005b

THIRD SYMPOSIUM ON THE TRANSFER AND UTILIZATION OF PARTICULATE CONTROL TECHNOLOGY VOLUME II. ELECTROSTATIC PRECIPITATORS

Compiled by:

F.P. Venditti, J.A. Armstrong, and M. Durham

Denver Research Institute
P.O. Box 10127
Denver, Colorado 80208

Grant Number: R805725

Project Officer

Dale L. Harmon
Office of Environmental Engineering and Technology
Industrial Environmental Research Laboratory
Research Triangle Park, NC 27711

Prepared for:

INDUSTRIAL ENVIRONMENTAL RESEARCH LABORATORY
OFFICE OF RESEARCH AND DEVELOPMENT
U.S. ENVIRONMENTAL PROTECTION AGENCY
RESEARCH TRIANGLE PARK, NC 27711

DISCLAIMER

This report has been reviewed by the Industrial Environmental Research Laboratory-Research Triangle Park, North Carolina, Office of Research and Development, U.S. Environmental Protection Agency, and approved for publication. Approval does not signify that the contents necessarily reflect the views and policies of the U.S. Environmental Protection Agency, nor does mention of trade names or commercial products constitute endorsement or recommendation for use.

ABSTRACT

The papers in these four volumes of Proceedings were presented at the Third Symposium on the Transfer and Utilization of Particulate Control Technology held in Orlando, Florida during 9 March through 13 March 1981, sponsored by the Particulate Technology Branch of the Industrial Environmental Research Laboratory of the Environmental Protection Agency and coordinated by the Denver Research Institute of the University of Denver.

The purpose of the symposium was to bring together researchers, manufacturers, users, government agencies, educators and students to discuss new technology and to provide an effective means for the transfer of this technology out of the laboratories and into the hands of the users.

The three major categories of control technologies -- electrostatic precipitators, scrubbers, and fabric filters -- were the major concern of the symposium. These technologies were discussed from the perspectives of economics; new technical advancements in science and engineering; and applications. Several papers dealt with combinations of devices and technologies, leading to a concept of using a systems approach to particulate control rather than device control. Additional topic areas included novel control devices, high temperature/high pressure applications, fugitive emissions, and measurement techniques.

These proceedings are divided into four volumes, each volume containing a set of related session topics to provide easy access to a unified technology area.

VOLUME II

Page

VOLUME I. COAL FIRED BOILERS--CONTENTS ix
VOLUME III. PARTICULATE CONTROL DEVICES--CONTENTS . . . xiii
VOLUME IV. ATYPICAL APPLICATIONS--CONTENTS. xviii

Section A - Fundamentals

MATHEMATICAL MODELING OF IONIC CONDUCTION IN FLY ASH LAYERS 1
R.B. Mosley, J.R. McDonald and L.E. Sparks

MEASUREMENTS OF ELECTRICAL PROPERTIES OF FLY ASH LAYERS 13
R.B. Mosley, P.R. Cavanaugh, J.R. McDonald and L.E. Sparks

LASER DOPPLER ANEMOMETER MEASUREMENTS OF PARTICLE VELOCITY IN A LABORATORY PRECIPITATOR 25
P.A. Lawless, A.S. Damle, A.S. Viner, E.J. Shaughnessy and L.E. Sparks

PROGRESS IN MODELING BACK CORONA. 35
P.A. Lawless

A COMPUTER MODEL FOR ESP PERFORMANCE 44
P.A. Lawless, J.W. Dunn and L.E. Sparks

MEASUREMENT AND INTERPRETATION OF CURRENT DENSITY DISTRIBUTION AND CHARGE/MASS DATA 54
M. Durham, G. Rinard, D. Rugg and L.E. Sparks

THE RELATIONSHIP BETWEEN GAS STREAM TURBULENCE AND COLLECTION EFFICIENCY IN A LAB-SCALED ELECTROSTATIC PRECIPITATOR 66
B.E. Pyle, J.R. McDonald, W.B. Smith

PARTICLE DEPOSITION PROFILES AND REENTRAINMENT IN A WIRE-PLATE ELECTROSTATIC PRECIPITATOR 76
E. Arce-Medina and R.M. Felder

PARTICLE TRANSPORT IN THE EHD FIELD 87
T. Yamamoto

SURFACE REENTRAINMENT OF COLLECTED FLY ASH IN ELECTROSTATIC PRECIPITATORS 97
M. Mitchner, M.J. Fisher, D.S. Gere, R.N. Leach and S.A. Self

VOLUME II CONTENTS (cont.)

Page

ELECTROMECHANICS OF PRECIPITATED ASH LAYERS 109
G.B. Moslehi and S.A. Self

EXPERIMENTAL MEASUREMENTS OF THE EFFECT OF TURBULENT DIFFUSION ON PRECIPITATOR EFFICIENCY 120
G.L. Leonard, M. Mitchner and S.A. Self

CAN REENTRAINMENT BE EXPLAINED USING A NEW PRECIPITATOR FORMULA? 130
S. Maartmann

A LABORATORY FURNACE FOR THE PRODUCTION OF SYNTHETIC FLY ASH FROM SMALL COAL SAMPLES 141
K.M. Sullivan

COMPUTER SIMULATION OF THE WIDE PLATE SPACING EFFECT 149
E.A. Samuel

SIMULTANEOUS MEASUREMENTS OF AERODYNAMIC SIZE AND ELECTRIC CHARGE OF AEROSOL PARTICLES IN REAL TIME ON A SINGLE PARTICLE BASIS 160
M.K. Mazumder, R.G. Renninger, T.H. Chang, R.W. Raible, W.G. Hood, R.E. Ware and R.A. Sims

APPLICATION OF LASER DOPPLER INSTRUMENTATION TO PARTICLE TRANSPORT MEASUREMENTS IN AN ELECTROSTATIC PRECIPITATOR 169
M.K. Mazumder, W.T. Clark III, R.E. Ware, P.C. McLeod, W.G. Hood, J.E. Straub and S. Wanchoo

THE APPLICATION OF MEASUREMENTS OF AEROSOL CHARGE ACQUISITION BY BIPOLAR IONS TO THE PROBLEM OF BACK CORONA 179
R.A. Fjeld, R.O. Gauntt, G.J. Laughlin and A.R. McFarland

IDENTIFICATION OF BACK DISCHARGE SEVERITY 189
S. Masuda and Y. Nonogaki

Section B - Operations and Maintenance

MODELING OF ELECTROSTATIC PRECIPITATORS WITH RESPECT TO RAPPING REENTRAINMENT AND OUTLET OPACITY 199
M.G. Faulkner, W.E. Farthing, J.R. McDonald and L.E. Sparks

NEW PRECIPITATOR TECHNOLOGY FOR PARTICULATE CONTROL 208
J.R. Zarfoss

VOLUME II CONTENTS (cont.)

Page

AN APPLICATION SUMMARY OF HIGH ENERGY SONIC CLEANING APPLIED TO ELECTROSTATIC PRECIPITATORS 218
M.J. Berlant

THE IMPACT OF INTELLIGENT PRECIPITATOR CONTROLS 230
N.Z. Shilling, R.O. Reese and J.A. Fackler

AN ENERGY MANAGEMENT SYSTEM FOR ELECTROSTATIC PRECIPITATORS 242
R.R. Crynack and M.P. Downey

RELATIONSHIP BETWEEN ELECTROSTATIC PRECIPITATOR PERFORMANCE AND RECORDKEEPING PRACTICES 252
S.P. Schliesser

AN OPERATION AND MAINTENANCE PROGRAM FOR A PHOSPHATE ROCK ELECTROSTATIC PRECIPITATOR 262
D.B. Rimberg

Section C - Advanced Design

ELECTROSTATIC PRECIPITATOR PERFORMANCE WITH PULSE EXCITATION. 273
D. Rugg, M. Durham, G. Rinard and L.E. Sparks

DEVELOPMENT OF A CHARGING DEVICE FOR HIGH-RESISTIVITY DUST USING HEATED AND COOLED ELECTRODES. 283
G. Rinard, M. Durham, D. Rugg and L.E. Sparks

THE EVALUATION OF NOVEL ELECTROSTATIC PRECIPITATOR SYSTEMS USING A TRANSPORTABLE PROTOTYPE 295
G. Rinard, M. Durham, D. Rugg, J. Armstrong, L.E. Sparks and J.H. Abbott

ANALYSIS OF THE ELECTRICAL AND CHARGING CHARACTERISTICS OF A THREE ELECTRODE PRECHARGER 304
K.J. McLean

PARTICLE CHARGING IN AN ELECTROSTATIC PRECIPITATOR BY PULSE AND DC VOLTAGES. 314
L.E. Sparks, G.H. Ramsey, R.E. Valentine and J.H. Abbott

PARTICLE COLLECTION IN A TWO STAGE ELECTROSTATIC PRECIPITATOR WITH VARIOUS COLLECTOR STAGES. 326
L.E. Sparks, G.H. Ramsey, R.E. Valentine and J.H. Abbott

HIGH INTENSITY IONIZER DEVELOPMENT 334
M.H. Anderson, J.R. McDonald, J.P. Gooch and D.V. Giovanni

VOLUME II CONTENTS (cont.)

Page

DEMONSTRATION OF AIR POLLUTION SYSTEMS HIGH INTENSITY IONIZER/ELECTROSTATIC PRECIPITATOR ON AN OIL-FIRED BOILER 349
G.A. Raemhild, A. Prem and F. Weisz

PRIMARY AND SECONDARY IONIZATION IN AN ELECTRON BEAM PRECIPITATOR SYSTEM 358
W.C. Finney, L.C. Thanh, J.S. Clements and R.H. Davis

INFLUENCE ON PARTICLE CHARGING OF ELECTRICAL PARAMETERS AT DC AND PULSE VOLTAGES 370
H.J. Joergensen, J.T. Kristiansen and P. Lausen

BOXER-CHARGER MARK III AND ITS APPLICATION IN ESP'S 380
S. Masuda, H. Nakatani and A. Mizuno

THE PERFORMANCE OF AN EXPERIMENTAL PRECIPITATOR WITH AN ALL-PLATE ZONE 390
J. Dalmon

THE PHYSICS OF PULSE ENERGIZATION OF ELECTROSTATIC PRECIPITATORS 404
L. Menegozzi and P.L. Feldman

ADVANCED ELECTRODE DESIGN FOR ELECTROSTATIC PRECIPITATORS 405
S. Bernstein, K. Ushimaru and E.W. Geller

Section D - Industrial Applications

PROBLEMS IN APPLYING AN ELECTROSTATIC PRECIPITATOR TO A SALVAGE FUEL-FIRED BOILER. 415
C.R. Thompson

THE APPLICATION OF ELECTROSTATIC PRECIPITATORS TO BOILERS FIRING MULTIPLE FUELS 425
R.L. Bump

AUTHOR INDEX 435

VOLUME I

COAL FIRED BOILERS

Section A - Fabric Filters

Page

COAL PROPERTIES AND FLY ASH FILTERABILITY 1
R. Dennis, J.A. Dirgo and L.S. Hovis

PULSE-JET FILTRATION WITH ELECTRICALLY CHARGED FLYASH 11
R.P. Donovan, L.S. Hovis, G.H. Ramsey and J.H. Abbott

ELECTRICALLY CHARGED FLYASH EXPERIMENTS IN A LABORATORY SHAKER BAGHOUSE 23
L.S. Hovis, J.H. Abbott, R.P. Donovan and C.A. Pareja

ELECTROSTATIC AUGMENTATION OF FABRIC FILTRATION 35
D.W. VanOsdell, G.P. Greiner, G.E.R. Lamb and L.S. Hovis

FABRIC WEAR STUDIES AT HARRINGTON STATION 45
R. Chambers, K. Ladd, S. Kunka and D. Harmon

SPS PILOT BAGHOUSE OPERATION 55
K. Ladd, W. Hooks, S. Kunka and D. Harmon

REVIEW OF SPS INVESTIGATION OF HARRINGTON STATION UNIT 2 FABRIC FILTER SYSTEM 65
K. Ladd, S. Kunka

A SUMMARY OF PERFORMANCE TESTING OF THE APITRON ELECTROSTATICALLY AUGMENTED FABRIC FILTER 75
D. Helfritch and L. Kirsten

FABRIC FILTER OPERATING EXPERIENCE FROM SEVERAL MAJOR UTILITY UNITS 82
O.F. Fortune, R.L. Miller and E.A. Samuel

EVALUATION OF THE 25 MW KRAMER STATION BAGHOUSE: TRACE ELEMENT EMISSION CONTROL. 94
M.W. McElroy and R.C. Carr

CHARACTERIZATION OF A 10 MW FABRIC FILTER PILOT PLANT 96
W.B. Smith, K.M. Cushing and R.C. Carr

SPECIFYING A FABRIC FILTER SYSTEM 107
R.L. Ostop and D.A. Single

VOLUME I CONTENTS (cont.)

Page

EVALUATION OF THE 25 MW KRAMER STATION BAGHOUSE: OPERATIONAL FACTORS IN PARTICULATE MATTER EMISSION CONTROL 118
R.C. Carr and M.W. McElroy

PULSE-JET TYPE FABRIC FILTER EXPERIENCE AT AIR TO CLOTH RATIOS OF 5 TO 1 ON A BOILER FIRING PULVERIZED COAL 120
G.L. Pearson

SELECTION AND OPERATION OF BAGHOUSES AT R.D. NIXON STATION, UNIT #1 129
R.C. Hyde, J. Arello and D.J. Huber

POTENTIAL FOR IMPROVEMENT IN BAGHOUSE DESIGN 138
R.M. Jensen

REVIEW OF OPERATING AND MAINTENANCE EXPERIENCES WITH HIGH TEMPERATURE FILTER MEDIA ON COAL-FIRED BOILERS . . . 148
L.K. Crippen

Section B - Electrostatic Precipitators

PILOT DEMONSTRATION OF THE PRECHARGER-COLLECTOR SYSTEM. 157
P. Vann Bush, Duane H. Pontius

REMEDIAL TREATMENTS FOR DETERIORATED HOT SIDE PRECIPITATOR PERFORMANCE 165
R.E. Bickelhaupt

EVALUATION OF THE UNITED McGILL ELECTROSTATIC PRECIPITATOR 176
D.S. Ensor, P.A. Lawless, A.S. Damle

PREDICTING THE EFFECT OF PROPRIETARY CONDITIONING AGENTS ON FLY ASH RESISTIVITY. 185
R.J. Jaworowski and J.J. Lavin

SO_3 CONDITIONING TO ENABLE ELECTROSTATIC PRECIPITATORS TO MEET DESIGN EFFICIENCIES 197
J.J. Ferrigan, III

ENHANCED PRECIPITATOR COLLECTION EFFICIENCIES THROUGH RESISTIVITY MODIFICATION 206
D.F. Mahoney

Page

DEVELOPMENT OF A NEW SULFUR TYPE ASH CONDITIONING 216
R.H. Gaunt

OPERATING EXPERIENCE WITH FLUE GAS CONDITIONING SYSTEMS AT COMMONWEALTH EDISON COMPANY 226
L.L. Weyers and R.E. Cook

THE APPLICATION OF A TUBULAR WET ELECTROSTATIC PRECIPITATOR FOR FINE PARTICULATE CONTROL AND DEMISTING IN AN INTEGRATED FLY ASH AND SO_2 REMOVAL SYSTEM ON COAL-FIRED BOILERS 236
E. Bakke and H.P. Willett

FIELD EVALUATIONS OF AMMONIUM SULFATE CONDITIONING FOR IMPROVEMENT OF COLD SIDE ELECTROSTATIC PRECIPITATOR PERFORMANCE 237
E.C. Landham, Jr., G.H. Marchant, Jr., J.P. Gooch and R.F. Altman

EVALUATION OF PERFORMANCE ENHANCEMENT OBTAINED WITH PULSE ENERGIZATION SYSTEMS ON A HOT SIDE ELECTROSTATIC PRECIPITATOR 253
W. Piulle, L.E. Sparks, G.H. Marchant, Jr. and J.P. Gooch

A NEW MICROCOMPUTER AND STRATEGY FOR THE CONTROL OF ELECTROSTATIC PRECIPITATORS 265
K.J. McLean, T.S. Ng, Z. Herceg and Z. Rana

ASSESSMENT OF THE COMMERCIAL POTENTIAL FOR THE HIGH INTENSITY IONIZER IN THE ELECTRIC UTILITY INDUSTRY 272
J.S. Lagarias, J.R. McDonald and D.V. Giovanni

APPLICATION OF ENERGY CONSERVING PULSE ENERGIZATION FOR PRECIPITATORS--PRACTICAL AND ECONOMIC ASPECTS 291
H. H. Petersen and P. Lausen

Section C - Dry SO_2 Scrubbers

SO_2 REMOVAL BY DRY INJECTION AND SPRAY ABSORPTION TECHNIQUES 303
E.L. Parsons, Jr., V. Boscak, T.G. Brna and R.L. Ostop

DRY SCRUBBING SO_2 AND PARTICULATE CONTROL 313
N.J. Stevens, G.B. Manavizadeh, G.W. Taylor and M.J. Widico

FIBER AND FABRIC ASPECTS FOR SO_2 DRY SCRUBBING BAGHOUSE SYSTEMS 323
L. Bergmann

VOLUME I CONTENTS (cont.)

Page

TWO-STAGE DRY FLUE GAS CLEANING USING CALCIUM ALKALIS 333
D.C. Gehri, D.F. Dustin and S.J. Stachura

CONTROL OF SULFUR DIOXIDE, CHLORINE, AND TRACE ELEMENT EMISSIONS FROM COAL-FIRED BOILERS BY FABRIC FILTRATION 341
R.J. Demski, J.T. Yeh and J.I. Joubert

Section D - Scrubbers

FLYASH COLLECTION USING A VENTURI SCRUBBER--MINNESOTA POWER'S COMMERCIAL OPERATING EXPERIENCE 352
C.A. Johnson

AUTHOR INDEX 361

VOLUME III

PARTICULATE CONTROL DEVICES

Section A - Scrubbers

Page

THE CALVERT SCRUBBER 1
S. Calvert, R.G. Patterson and S. Yung

FLUX FORCE/CONDENSATION SCRUBBER SYSTEM FOR COLLECTION OF FINE PARTICULATE EMISSIONS FROM AN IRON MELTING CUPOLA 10
S. Calvert and D.L. Harmon

DEMONSTRATION OF HIGH-INTENSITY-IONIZER-ENHANCED VENTURI SCRUBBER ON A MAGNESIUM RECOVERY FURNACE FUME EMISSIONS 21
A. Prem, M.T. Kearns and D.L. Harmon

A NEW ENTRY IN THE HIGH EFFICIENCY SCRUBBER FIELD 33
L.C. Hardison and F. Ekman

PERFORMANCE OF PARTICULATE SCRUBBERS AS INFLUENCED BY GAS-LIQUID CONTACTOR DESIGN AND BY DUST FLOCCULATION 43
K.T. Semrau and R.J. Lunn

INVESTIGATION OF VENTURI SCRUBBER EFFICIENCY AND PRESSURE DROP 51
R. Parker, T. Le and S. Calvert

SCRUBBER TECHNOLOGY AND THE INTERACTION OF A UNIQUE STRUCTURE AS MIST ELIMINATOR 60
G.C. Pedersen

NOVEL ANNULAR VENTURI SCRUBBER DESIGN REDUCES WASTE DISCHARGE PROBLEMS 71
H.P. Beutner

CONSIDERATION OF THE PERTINENT DESIGN AND OPERATING CHARACTERISTICS ESSENTIAL FOR OPTIMIZATION OF VENTURI SCRUBBER PERFORMANCE 80
H.S. Oglesby

APPLICATION OF SCRUBBERS FOR PARTICULATE CONTROL OF INDUSTRIAL BOILERS 90
M. Borenstein

VOLUME III CONTENTS (cont.)

Page

APPLICATION OF HIGH ENERGY VENTURI SCRUBBERS TO SEWAGE INCINERATION 102
F.X. Reardon

AN INCINERATOR SCRUBBER THAT WORKS: A CASE STUDY 111
C. Menoher

EVALUATION OF ENTRAINED LIQUOR CONTRIBUTION TO TOTAL MASS EMISSIONS DOWNSTREAM OF A WET SCRUBBER . . . 119
W. David Balfour, L.O. Edwards and H.J. Williamson

Section B - Fabric Filters

A DUAL-BEAM BACKSCATTER BETA-PARTICLE GAUGE FOR MEASURING THE DUST CAKE THICKNESS ON OPERATING BAG FILTERS INDEPENDENT OF POSITION 128
R.P. Gardner, R.P. Donovan and L.S. Hovis

DIAGNOSING FILTER FABRIC CAPABILITIES WITH LIGHT SCATTERING AND NUCLEI DETECTING INSTRUMENTATION 140
R. Dennis, D.V. Bubenick and L.S. Hovis

ACID DEWPOINT CORROSION IN PARTICULATE CONTROL EQUIPMENT 150
T.E. Mappes, R.D. Tems and K.E. Foster

SECOND GENERATION OF EMISSIONS CONTROL SYSTEM FOR COKE OVENS 160
J.D. Patton

EFFECTS OF FLYASH SIZE DISTRIBUTION ON THE PERFORMANCE OF A FIBERGLASS FILTER 171
W.F. Frazier and W.T. Davis

FUNDAMENTAL STUDY OF A FABRIC FILTER WITH A CORONA PRECHARGER 181
K. Iinoya and Y. Mori

ECONOMIC EVALUATION FACTORS IN BID EVALUATIONS--A SENSITIVITY ANALYSIS 193
J.G. Musgrove and J.E. Shellabarger

FLY ASH RE-ENTRAINMENT IN A BAGHOUSE-- WHAT DOES IT COST? 201
J.G. Musgrove

VOLUME III CONTENTS (cont.)

Page

WHY PERFORM MODEL STUDY OF FABRIC FILTER COLLECTOR? 211
W.T. Langan, N.Z. Shilling, W.A. Van Kleunen and O.F. Fortune

EXPERIENCES OF A SMALL INSULATION MANUFACTURER IN MAINTAINING COMPLIANCE WITH AIR POLLUTION CONTROL REGULATIONS 221
R.L. Hawks

ADVANCED FABRIC FILTER TECHNOLOGY FOR DIFFICULT PARTICULATE EMISSIONS 228
H.P. Beutner

DEVELOPMENT OF GUIDELINES FOR OPTIMUM BAGHOUSE FLUID DYNAMIC SYSTEM DESIGN 238
D. Eskinazi, G.B. Gilbert and R.C. Carr

THEORETICAL ASPECTS OF PRESSURE DROP REDUCTION IN A FABRIC FILTER WITH CHARGED PARTICLES 250
T. Chiang, E.A. Samuel and K.E. Wolpert

EXPERIMENTAL CORRELATION OF DUST CAKE POROSITY, AIR-TO-CLOTH RATIO AND PARTICLE-SIZE DISTRIBUTIONS 261
T. Chiang and R.L. Ostop

MODEL FOR DUST PENETRATION THROUGH A PULSE-JET FABRIC FILTER 270
D. Leith and M.J. Ellenbecker

PERFORMANCES OF DUST LOADED AIR FILTERS 280
C. Kanaoka, H. Emi and M. Ohta

ELECTROSTATICALLY ENHANCED FABRIC FILTRATION OF PARTICULATES 290
T. Ariman and S.T. McComas

A STAGGERED ARRAY MODEL OF A FIBROUS FILTER WITH ELECTRICAL ENHANCEMENT 301
F. Henry and T. Ariman

Section C - Granular Beds

AEROSOL FILTRATION BY A COCURRENT MOVING GRANULAR BED: PENETRATION THEORY 311
T.W. Kalinowski and D. Leith

FUNDAMENTAL EXPERIMENTS ON A GRANULAR BED FILTER 321
K. Iinoya and Y. Mori

VOLUME III CONTENTS (cont.)

Page

DRY DUST COLLECTION OF BLAST FURNACE EXHAUST GAS BY MOVING GRANULAR BED FILTER 332
A. Wakabayashi, T. Sugawara and S. Watanabe

Section D - Novel Devices

IRON AND STEEL AIR POLLUTION CONTROL USING MAGNETIC SEPARATION 341
D.C. Drehmel, C.E. Ball and C.H. Gooding

TECHNICAL AND ECONOMIC EVALUATION OF TWO NOVEL PARTICULATE CONTROL DEVICES 353
R.R. Boericke, J.T. Kuo and K.R. Murphy

THE ELECTROSCRUBBER™ FILTER--APPLICATIONS AND PARTICULATE COLLECTION PERFORMANCE 363
D. Parquet

HIGH EFFICIENCY PARTICULATE REMOVAL WITH SINTERED METAL FILTERS 373
B.E. Kirstein, W.J. Paplawsky, D.T. Pence and T.G. Hedahl

APPLICATION OF ELECTROSTATIC TECHNIQUES TO THE REMOVAL OF DUST AND FUME FROM THE INDUSTRIAL ENVIRONMENT 382
S.A. Hoenig

THE DRY VENTURI 393
A.J. Teller and D.R.J. Roy

FIBER BED FILTER SYSTEM CONTROL OF WELDING PARTICULATES 398
J.A. Bamberger and W.K. Winegardner

THE USE OF GLASS CAPILLARY FILTERS TO CLASSIFY ACTINOLITE FIBERS 406
J.W. Gentry, T.C. Chen, S.W. Lin and P.Y. Yu

ULTRA-HIGH EFFICIENCY FILTRATION SYSTEMS (AIR RECIRCULATION) 417
R.W. Potokar

THE WET WALL ELECTROSTATIC PRECIPITATOR 428
J. Starke, J. Kautz and K-R. Hegemann

VOLUME III CONTENTS (cont.)

Page

Section E - Mechanical Collectors

TROUBLESHOOTING MULTIPLE CYCLONES ON FUEL-OIL-FIRED BOILERS 438
F. Crowson and R.L. Gibbs

COLLECTION EFFICIENCIES OF CYCLONE SEPARATORS 449
P.W. Dietz

ELECTROSTATICALLY AUGMENTED COLLECTION IN VORTICAL FLOWS 459
P.W. Dietz

HIGH PERFORMANCE CYCLONE DEVELOPMENT 468
W.G. Giles

AUTHOR INDEX 481

VOLUME IV

ATYPICAL APPLICATIONS

Section A - Advanced Energy Applications

Page

HIGH TEMPERATURE PARTICLE COLLECTION WITH A.P.T. EPxP DRY SCRUBBER 1
S. Yung, T. Lee, R.C. Patterson, S. Calvert and D.C. Drehmel

PARTICLE COLLECTION IN CYCLONES AT HIGH TEMPERATURE AND HIGH PRESSURE 2
R. Parker, R. Jain, S. Calvert, D.C. Drehmel and J. Abbott

OPERATING RESULTS OF ELECTROSTATIC PRECIPITATORS AT HIGH TEMPERATURE AND HIGH PRESSURES 3
P.L. Feldman and K.S. Kumar

CONTROL OF PARTICULATES IN PROCESS AREA 12, SOLVENT REFINED COAL PROCESS 15
W.H. Wilks, P.D. Wilkinson and J.A. Schlosberg

NON-PLUGGING RETAINING STRUCTURE FOR GRANULAR BED FILTER FOR HTHP APPLICATION 26
A.M. Presser and J.C. Alexander

PARTICULATE EMISSIONS CONTROL FROM A COAL-FIRED OPEN-CYCLE MAGNETOHYDRODYNAMICS/STEAM POWER PLANT . . . 36
H.H. Wang and T.E. Dowdy

REAL TIME COARSE PARTICLE MASS MEASUREMENTS IN A HIGH TEMPERATURE AND PRESSURE COAL GASIFIER PROCESS TREATMENT 46
J. Wegrzyn, J. Saunders and W. Marlow

THE DESIGN, ENGINEERING, AND STARTUP OF A VENTURI SCRUBBER SYSTEM ON AN OIL SHALE OFF-GAS INCINERATOR . . . 55
P.A. Czuchra and J.S. Sterrett

FLUIDIZED-BED COMBUSTION HOT FLUE GAS CLEANUP PERSPECTIVE ON CYCLONES AND OTHER DEVICES 63
R.F. Henry and W.F. Podolski

PRESSURIZED AND NON-PRESSURIZED ACOUSTIC AGGLOMERATORS FOR HOT-GAS CLEANUP APPLICATIONS. 73
K.H. Chou and D.T. Shaw

VOLUME IV CONTENTS (cont.)

Page

ALKALIS AND THEIR CONTRIBUTIONS TO CORONA CURRENT AT HIGH TEMPERATURE AND HIGH PRESSURE 74
R.W.L. Snaddon

HOT GAS CLEANUP IN PRESSURIZED FLUIDIZED BED COMBUSTION 83
L.N. Rubow and M.G. Klett

VENTURI SCRUBBING FOR CONTROL OF PARTICULATE EMISSIONS FROM OIL SHALE RETORTING 95
G.M. Rinaldi and R.C. Thurnau

OVERVIEW OF THE DEPARTMENT OF ENERGY'S PRESSURIZED FLUIDIZED-BED COMBUSTOR CLEANUP TECHNOLOGY PROGRAM . . . 105
W.E. Moore

THE CYCLOCENTRIFUGE^{TM}--AN ADVANCED GAS/SOLIDS SEPARATOR FOR COAL CONVERSION PROCESSES 116
P.R. Albrecht, J.T. McCabe and W. Fedarko

Section B - Fugitive Emissions

DEMONSTRATION OF THE USE OF CHARGED FOG IN CONTROLLING FUGITIVE DUST FROM LARGE-SCALE INDUSTRIAL SOURCES 125
E.T. Brookman, R.C. McCrillis and D.C. Drehmel

THE CONTROL OF FUGITIVE EMISSIONS USING WINDSCREENS . . . 135
D. Carnes and D.C. Drehmel

THE INFLUENCE OF AGGREGATE PILE SHAPE AND ORIENTATION ON PARTICULATE FUGITIVE EMISSIONS 145
D. Martin

SPRAY CHARGING AND TRAPPING SCRUBBER FOR FUGITIVE PARTICLE EMISSION CONTROL 155
S. Yung, S. Calvert and D.C. Drehmel

IMPROVED STREET SWEEPER FOR CONTROLLING URBAN INHALABLE PARTICULATE MATTER 156
S. Calvert, H. Brattin, S. Bhutra, R. Parker and D.C. Drehmel

A WIND TUNNEL FOR DUST ENTRAINMENT STUDIES 168
A.S. Viner, M.B. Ranade, E.J. Shaughnessy, D.C. Drehmel and B.E. Daniels

VOLUME IV CONTENTS (cont.)

Page

TECHNIQUES AND EQUIPMENT FOR MEASURING INHALABLE PARTICULATE FUGITIVE EMISSIONS 179
H.J. Kolnsberg

BALLOON SAMPLING TO CHARACTERIZE PARTICLE EMISSIONS FROM FUGITIVE SOURCES. 188
J.A. Armstrong and D.C. Drehmel

AN ELECTROSTATICALLY CHARGED FOG GENERATOR FOR THE CONTROL OF INHALABLE PARTICLES 200
C.V. Mathai, L.A. Rathbun and D.C. Drehmel

RELATIVE EFFECTIVENESS OF CHEMICAL ADDITIVES AND WIND SCREENS FOR FUGITIVE DUST CONTROL. 210
D.C. Drehmel and B.E. Daniel

PARTICULATE IMPACT COMPARISON BETWEEN CONTROLLED STACK EMISSIONS FOR A 2000 MW ELECTRICAL GENERATING STATION 222
H.E. Hesketh and F.L. Cross

OPERATING EXPERIENCE AND THE TECHNIQUES IN THE CONTROL OF COAL DUST EMISSIONS FROM LARGE STORAGE PILE AT NANTICOKE TGS 232
N. Krishnamurthy, W. Whitman and Y.V. Nguyen

Section C - Opacity

MODELING SMOKE PLUME OPACITY FROM PARTICULATE CONTROL EQUIPMENT 242
D.S. Ensor, P.A. Lawless, S.J. Cowen

TETHERED BALLOON PLUME SAMPLING OF A PORTLAND CEMENT PLANT 252
J.A. Armstrong, P.A. Russell, M.N. Plooster

THE RELATIONSHIP OF FLY ASH LIGHT ABSORPTION TO SMOKE PLUME OPACITY 264
S.J. Cowen, D.S. Ensor

Section D - Measurements

A SPECIAL METHOD FOR THE ANALYSIS OF SULFURIC ACID MISTS 275
P. Urone, R.B. Mitchell, J.E. Rusnak, R.A. Lucas and J.F. Griffiths

VOLUME IV CONTENTS (cont.)

Page

A MICROCOMPUTER-BASED CASCADE-IMPACTOR DATA-REDUCTION SYSTEM 285
M. Durham, S. Tegtmeyer, K. Wasmundt and L.E. Sparks

DEVELOPMENT OF A SAMPLING TRAIN FOR STACK MEASUREMENT OF INHALABLE PARTICULATE 297
A.D. Williamson, W.B. Smith

INHALABLE PARTICULATE MATTER SAMPLING PROGRAM FOR IRON AND STEEL: AN OVERVIEW PROGRESS REPORT 306
R.C. McCrillis

DEVELOPMENT OF IP EMISSION FACTORS 317
D.L. Harmon

INHALABLE PARTICULATE EMISSION FACTOR PROGRAM PURPOSE AND DEVELOPMENT 326
F.M. Noonan and J.H. Southerland

INHALABLE PARTICULATE EMISSION FACTORS FOR BLAST FURNACE CASTHOUSES IN THE IRON AND STEEL INDUSTRY 335
P.D. Spawn, S. Piper and S. Gronberg

INHALABLE PARTICULATE EMISSIONS FROM VEHICLES TRAVELING ON PAVED ROADS 344
R. Bohn

QUALITY ASSURANCE FOR PARTICLE-SIZING MEASUREMENTS . . . 353
C.E. Tatsch

PARTICULATE EMISSIONS CHARACTERIZATION FOR OIL-FIRED BOILERS 363
D. Mormile, S. Hersh, B.F. Piper and M. McElroy

A CONTINUOUS REAL-TIME PARTICULATE MASS MONITOR FOR STACK EMISSION APPLICATIONS 373
J.C.F. Wang, H. Patashnick and G. Rupprecht

Section E - Mobile Sources

STUDIES OF PARTICULATE REMOVAL FROM DIESEL EXHAUSTS WITH ELECTROSTATIC AND ELECTROSTATICALLY-AUGMENTED TECHNIQUES 383
J.L. DuBard, M.G. Faulkner, J.R. McDonald, D.C. Drehmel and J.H. Abbott

VOLUME IV CONTENTS (cont.)

Page

STUDIES OF PARTICULATE REMOVAL FROM DIESEL EXHAUSTS WITH MECHANICAL TECHNIQUES 395
M.G. Faulkner, J.L. DuBard, J.R. McDonald, D.C. Drehmel and J.H. Abbott

UPDATE ON STATUS OF CONNECTICUT'S CONTROL PROGRAM FOR TRANSPORTATION-RELATED PARTICULATE EMISSIONS 406
H.L. Chamberlain and J.H. Gastler

AUTHOR INDEX 413

MATHEMATICAL MODELING OF IONIC CONDUCTION IN FLY ASH LAYERS

by: Ronald B. Mosley and Jack R. McDonald
Southern Research Institute
2000 Ninth Avenue, South
Birmingham, Alabama 35255

Leslie E. Sparks
Industrial Environmental Research Laboratory
U.S. Environmental Protection Agency
Research Triangle Park, N.C. 27711

ABSTRACT

Charge transport through the bulk of fly ash layers is discussed in terms of both mobile and non-mobile ions. It is proposed that charge profiles in the bulk of the layer may be due to charges which are trapped as a result of discontinuities in the conduction paths through the layer. Comparisons of the theoretical potential and electric field profiles with laboratory measurements show good agreement. The potentials and electric fields generated in the boundary layers near the electrodes are discussed. Mathematical solutions appropriate for perfectly blocking electrodes are presented. Mathematical solutions in the sodium depleted layer near the negative electrode are also discussed.

INTRODUCTION

With the increasing use of coals which produce high resistivity fly ashes, there is increasing interest in studying the electrical conduction properties of fly ash layers. The ability to conduct current through a collected layer of high resistivity fly ash often plays an important role in limiting the performance of an electrostatic precipitator. In order to develop more effective ways to improve the conduction properties of fly ash layers, a better understanding of the conduction mechanisms is needed.

For instance, in the literature, there seems to be little agreement as to whether the primary charge carriers are electronic or ionic in nature. The most convincing evidence on this point is given by Bickelhaupt[1,2] who demonstrated through transference tests that for a large number of representative fly ashes the current is carried by alkali metal ions (primarily sodium). At present, it is also uncertain whether the critical value of electric field which leads to electrical breakdown in the layer develops as a result of the difficulty in transporting charge through the layer, or as a result of the difficulty in neutralizing the charges which accumulate near the electrode interfaces. Although limited theoretical studies[3-7] of the electrical processes in fly ash layers have been performed, there is presently no comprehensive model to describe the conduction processes in fly ash.

The present paper attempts to describe recently measured[8] potential and electric field profiles in fly ash layers in the temperature range 260°C to 400°C. It also speculates as to the nature of the field profiles in thin layers very near the electrodes.

CONDUCTION IN THE BULK OF THE LAYER

Recent measurements[8] of electric field profiles in fly ash layers indicate that appreciable variations of charge density extend into the bulk of the fly ash layer. Figure 1 schematically represents the observed phenomena. Under a negative applied potential, the indicated charge separation occurs. The charge on the electrodes results from the externally applied potential while the charge separation in the layer can be considered a response to the field produced by the surface charge.

In order to present a model for qualitative comparison with measured field and potential profiles, the layer will be treated as a homogeneous layer of semi-insulating material whose conductivity is proportional to the product of an effective mobility and charge carrier density. For simplicity, the charge carriers will be assumed to be sodium ions. Thermal diffusion will be assumed to make a negligible contribution to the current in the bulk of the layer.

As sodium ions migrate toward the negative electrode, they may tend to produce a concentration of positive charge near that electrode. The excess positive charge density may extend an appreciable distance into the bulk of the layer. The migrating positive ions leave excess negative ions near the positive electrode. The excess negative charge may also extend a considerable distance into the bulk of the layer.

There is a tendency for the loss of positive ions in the bulk to be compensated by other ions which migrate to take their place. This would suggest that no space charge would occur in the middle of the layer and, consequently, the electric field would be small and nearly uniform in that part of the layer. However, measurements indicate that space charge exists in essentially all parts of the layer.

A possible explanation for the existence of space charge in the center of the layer lies in the fact that fly ash is not a homogeneous material, but consists of randomly packed fly ash particles. Within the randomly packed layer of particles, there are numerous regions which are isolated on one side from paths of continuity spanning the distance to the electrode on that side of the region. Such regions, forming small peninsulas of particles, would be distributed throughout the layer. If positive ions migrate away from these peninsulas, there are no conducting paths for other positive ions to move in to replace the ones that were lost. Such isolated regions act somewhat like localized traps for negative charge. In a similar manner, if small regions near the negative electrode are isolated from that electrode, then migrating positive ions could be trapped in these dead-end paths. Much of the charge-density profiles indicated by the potential measurements mentioned earlier may be due to such localized charge traps. These apparent charge traps result from discontinuties in some of the conducting paths through the layer. The saturation value of charge-density which would occur in one of these localized traps would be approximately proportional to the macroscopic electric field in the vicinity of the trap.

The processes described above can be incorporated into a mathematical model by dividing the layer into region 1 and region 2 as illustrated in Figure 1. The charge density is negative in region 1 and positive in region 2. First, consider region 1. The current density is given by

$$j = ebE(x)C(x) \quad , \tag{1}$$

where

j = current density (A/m^2),
e = electronic charge (C),
b = effective mobility of sodium ions (m^2/Vs),
$E(x)$ = electric field at position x (V/m),
$C(x)$ = concentration of mobile sodium ions at x (m^{-3}), and
x = position in the layer.

Poisson's equation is

$$\frac{dE}{dx} = \frac{e}{\varepsilon} [C(x) - C_0] + \frac{Q_t}{\varepsilon} \quad , \tag{2}$$

with

$\frac{dE}{dx}$ = derivative of the electric field (V/m^2),

ε = permittivity of the layer (As/Vm),

C_0 = equilibrium concentration of mobile sodium ions (m^{-3}), and

Q_t = density of trapped charge (C/m^3).

Recall that

$$Q_t = - \alpha E \quad , \tag{3}$$

where α is a constant which is determined by the number and size of local traps. Equations (1), (2), and (3) can be combined to yield

$$j = \varepsilon bE \frac{dE}{dx} + ebC_0E + \alpha bE^2 \quad . \tag{4}$$

After separating the variables, equation (4) can be integrated to yield

$$x = - \frac{\varepsilon}{2\alpha} \ln \left\{\frac{\alpha bE^2 + ebC_0E - j}{\alpha bE_0^2 + ebC_0E_0 - j}\right\}$$

$$+ \left(\frac{\varepsilon}{2\alpha}\right)\left(\frac{ebC_0}{A}\right) \ln \left\{\frac{2\alpha bE + ebC_0 - A}{2\alpha bE_0 + ebC_0 - A}\right\}$$

$$+ \left(\frac{\varepsilon}{2\alpha}\right)\left(\frac{ebC_0}{A}\right) \ln \left\{\frac{2\alpha bE_0 + ebC_0 + A}{2\alpha bE + ebC_0 + A}\right\} \quad , \tag{5}$$

where

$$A = [(ebC_0)^2 + 4j\alpha b]^{\frac{1}{2}} \quad .$$

Equation (5) expresses position within the layer as a function of the electric field. This equation is not easily inverted algebraically to express the electric field as an explicit function of position. The electric field profile associated with equation (5) can be evaluated directly by varying the electric field over the appropriate range of values.

Next consider region 2 in which the net charge is positive. The current equation in region 2 has the same form as equation (1). Poisson's equation in region 2 becomes

$$\frac{dE}{dx} = \frac{e}{\varepsilon}\,[C(x) - C_0] + \frac{Q_t}{\varepsilon} \quad , \tag{6}$$

with

$$Q_t = \beta E \quad , \tag{7}$$

where Q_t is the density of trapped charge and β is a constant which depends on the number and size of charge traps. Equation (6) and (7) can be combined with equation (1) to yield

$$j = \varepsilon bE\,\frac{dE}{dx} + ebC_0E - \beta bE^2 \quad . \tag{8}$$

When the variables are separated, equation (8) can be integrated in region 2 to yield

$$x-\delta = \frac{\varepsilon}{2\beta}\,\ln\left\{\frac{\beta bE^2 - ebC_0E + j}{\beta bE_\delta^{\,2} - ebC_0E_\delta + j}\right\}$$

$$+ \left(\frac{\varepsilon}{2\beta}\right)\left(\frac{ebC_0}{B}\right)\,\ln\left\{\frac{2\beta bE - ebC_0 - B}{2\beta bE_\delta - ebC_0 - B}\right\}$$

$$+ \left(\frac{\varepsilon}{2\beta}\right)\left(\frac{ebC_0}{B}\right)\,\ln\left\{\frac{2\beta bE_\delta - ebC_0 + B}{2\beta bE - ebC_0 + B}\right\} \quad , \tag{9}$$

where δ represents the separation of region 1 and region 2, E_δ is the field at δ, and

$$B = [(ebC_0)^2 - 4j\beta b]^{\frac{1}{2}} \quad . \tag{10}$$

Once again position is found expressed as an explicit function of electric field. Field profiles in region 2 can be computed in the same manner as in region 1. Analytic expressions for the potential profiles are not readily available in either region 1 or region 2. However, numerical values for the potential profiles are easily computed from the integral of the field profiles. Both the electric field and the potential must be continuous at $x = \delta$.

Figure 2 shows a comparison of the measured and computed potential profiles for an applied potential of 3 kV. The average deviation from the experimental measurements is about 4 percent. The corresponding comparison of measured and predicted electric field profiles is shown in Figure 3. Note that the electric field profiles have been extrapolated to the electrodes. Agreement of the predictions with the measurements is quite good. The values of the parameters used in the predicted curves are shown in the figures. These parameters are expressed in SI units. The values of b and C_0 in Figures 2 and 3 correspond to an initial resistivity of 9×10^9 ohm-cm. The given value of α would require less than 1 percent of the particles to participate in the trapping process.

Figure 4 shows a comparison of potential profiles for the same sample with an applied potential of 20 volts. The predicted potential profiles for small applied potentials give much poorer agreement with measurements than do those for the higher applied potentials. A comparison of the electric field profiles for an applied potential of 20 volts is given in Figure 5. The reason that equations (5) and (9) give much better agreement with measurements for the higher applied potentials is not known. It is possible that the space charge distributions in the layer are influenced more strongly by the electrode interfaces for low applied potentials than for the higher potentials.

CONDUCTION IN THE BOUNDARY LAYER NEAR THE NEGATIVE ELECTRODE

Electrical transport through fly ash layers is commonly described in terms of partially blocking electrodes. This terminology refers to situations in which the charge carriers are not readily transferred from the sample (the fly ash layers) to the attached electrodes used to impress a potential difference across the sample. If the electrodes were perfectly blocking, no charge would be transferred between the sample and the electrodes. For the case of perfectly blocking electrodes, a condition of steady state conduction could never be established. In this case charge would continue to build up at the interfaces until the current was totally suppressed.

In the case of partially blocking electrodes, a sufficient density of charge accumulates near the interface for some charge to be transferred to the electrode as a result of the strong fields associated with the space charge layer. For ionic conduction in fly ash layers, charge carriers are not supplied by the electrodes. It is believed that the current is carried in most of the layer by alkali-metal ions (primarily sodium ions). These ions are extracted from the structure of the fly ash particles and transported to the surface of the layer at the negative electrode. By chemically reacting with the surrounding environment, the charge on the sodium ions is neutralized and the resulting molecule of reactant precipitates either on the surface of the ash layer or on the surface of the electrode.

Perhaps some insight into the processes could be gained by considering the limiting case of perfectly blocking electrodes. Since a steady current is not possible, the current flowing as the result of a certain applied potential would decrease until it approached zero. The system would then be in a state of thermo-dynamic equilibrium. Suppose the law for electrical

transport is adequately represented by the linear diffusion equation

$$j = -eD \frac{dC}{dx} + ebE(x)C(x) \quad , \tag{11}$$

where D is the diffusion coefficient, and the other quantities are as previously defined. The electric field and the ion density are coupled through Poisson's equation

$$\frac{dE}{dx} = eC(x)/\varepsilon \quad . \tag{12}$$

Suppose the dust layer is quite thick. There are two possible situations that can occur in the layer. If the field goes to zero in the layer, we have the case in which the surface charge field is perfectly screened from the interior of the dust layer by the layer of space charge which develops. This case will be called "perfect screening." If the field is reduced to some non-zero value, this case will be called "imperfect screening."

The space charge layer near the negative electrode in Figure 1 is of interest. For perfect screening, the electric field near this electrode can be written as[9]

$$E(x) = E(L)/(1 + \frac{b}{2D} E(L)(L - x)) \tag{13}$$

$$= E(L)/(1 + (L - x)/x_s)$$

where L is the thickness of the layer. Perfect screening requires that

$$E^2(L) = \frac{2De}{b\varepsilon} C(L) \quad . \tag{14}$$

It is natural to define a screening length

$$x_s = \frac{2D}{bE(L)} = [\frac{2D\varepsilon}{ebC(L)}]^{\frac{1}{2}} \quad , \tag{15}$$

where x_s indicates the distance required for the field to decrease to half its maximum value. It should be pointed out that this screening length is related to the classical Debye length x_D by

$$x_s = x_D \sqrt{2} \quad . \tag{16}$$

From equation (13), it can be noted that the field will decrease by two orders of magnitude in about 100 multiples of x_s.

From measurements[8] of charge in the layer, a field of about 2×10^8 V/m was calculated in a temperature of 340°C. Using this field and the Einstein relation in equation (15), the screening length is found to be about

5×10^{-10}m. It follows that a field of 2×10^{8} V/m at the negative electrode would be screened to a value of 2×10^{6} V/m at a distance of 5×10^{-8}m from the electrode. Even though the value of 2×10^{8} V/m represents a rather large electric field, it would only exist over a distance of less than 0.05 μm. Breakdown in air over such a short path would not occur. Consequently, the large charge measured[8] in the layer seems compatible with the observation that electrical breakdown did not occur.

The situation which actually occurs is more similar to imperfect screening. In this case, the electric field near the negative electrode is given by[9]

$$E(x) = E_{\delta} \left\{ \frac{E(L)\cosh\left[\alpha_{\delta}(L-x)\right] + E_{\delta}\sinh\left[\alpha_{\delta}(L-x)\right]}{E(L)\sinh\left[\alpha_{\delta}(L-x)\right] + E_{\delta}\cosh\left[\alpha_{\delta}(L-x)\right]} \right\} , \tag{17}$$

the corresponding potential is

$$V(x) = V(x_2) + \frac{2D}{b} \ln\left\{ \frac{E(L)\sinh\left[\alpha_{\delta}(L-x)\right] + E_{\delta}\cosh\left[\alpha_{\delta}(L-x)\right]}{E(L)\sinh\left[\alpha_{\delta}(L-x_2)\right] + E_{\delta}\cosh\left[\alpha_{\delta}(L-x_2)\right]} \right\} , \tag{18}$$

where

$$\alpha_{\delta} = \frac{b}{2D} E_{\delta} , \tag{19}$$

and

$$E_{\delta}^{2} = E^{2}(L) - \frac{2D}{b} \frac{e}{\varepsilon} C(L) . \tag{20}$$

Figure 6 illustrates the predictions of equations (13) and (17) for conditions similar to those present when the charge measurements mentioned in reference 8 were performed. Since equilibrium is being discussed, the chemical potential[9]

$$V(L) - V(x_2) = \frac{D}{b} \ln\left(\frac{C(x_2)}{C(L)}\right) , \tag{21}$$

can be used to estimate the total change in ion concentration upon moving a distance x_2 from the negative electrode. Note that a potential difference of 0.5 volts at a temperature of 352°C corresponds to the ion concentration decreasing by a factor of 10^{4}. For perfect screening, a potential difference of 0.5 volts corresponds to a value for x_2 of about 5×10^{-8}m. This illustrates how very large electric fields can exist in very thin layers near the electrodes and not be apparent in measurements with potential probes. Although equations (11) and (12) can be solved in closed form for finite currents, the solution is somewhat more cumbersome than the equilibrium approximations and would add little to this qualitative description. The method of solution and the result are very similar to those used to describe two ionic species near the positive electrode.

CONDUCTION IN THE BOUNDARY LAYER NEAR THE POSITIVE ELECTRODE

Sodium ions move away from the region of the positive electrode, leaving behind a net negative charge due to the uncompensated oxygen ions which were associated with the sodium ions in the glassy structure of the fly ash particles. In the case of sodium silicate glasses, the mobility of the oxygen ions is several orders of magnitude smaller than that of sodium ions. It seems reasonable to assume that a similar relation between the mobilities of oxygen and sodium ions would exist in the fly ash. As a result of the relatively small value of the oxygen ion mobility, a rather large concentration of oxygen ions might be expected to accumulate near the positive electrode. In order for a steady state to exist it will be necessary for negative charge to escape at the positive electrode at the same rate at which positive charge escapes at the negative electrode. Because of the high density of charge which would result in significant screening of the surface charge field near the positive electrode, the region which is highly depleted of sodium ions is expected to be confined to a layer very near the positive electrode. In this thin layer both negative and positive ions will contribute to the current. When a steady state exists, both positive and negative ions must be removed at the same rate. This requires that the average charge currents be equal. When two ionic species of opposite sign are mobile, an equation analogous to (11) can be written for each species. These equations would be coupled through Poisson's equation. It can be shown[10] that the three equations mentioned can be combined to yield

$$E''(x) - 1/2\ (\frac{e}{kT})^2 E^3(x) + 1/2\ (\frac{e}{kT})^2 [E^2(o) - E_s^{\,2} - \frac{2}{\varepsilon}(\frac{j_1}{b_1} - \frac{j_2}{b_2})x]E(x)$$

$$+ \frac{e}{\varepsilon kT}\ (\frac{j_1}{b_1} + \frac{j_2}{b_2}) = 0 \quad , \tag{22}$$

where

$E''(x)$ = the second derivative of the electric field (V/m^3),

e = the electronic charge (C),

k = Boltzmann's constant (Joules/K),

T = absolute temperature (K),

$E(x)$ = the electric field at x (V/m),

$E(o)$ = the electric field at x=o (V/m),

$E_s^{\,2} = \frac{2kT}{\varepsilon}\ [C_1(o)+C_2(o)]$ (V^2/m^2),

ε = the permittivity of the fly ash (A sec/Vm),

$C_1(o)$ = the concentration of negative ions at x=o (m^{-3}),

$C_2(o)$ = the concentration of positive ions at x=o (m^{-3}),

b_1 = the mobility of the negative ions (m^2/Vsec),

b_2 = the mobility of the positive ions (m^2/Vsec),

x = position within the layer (m),

j_1 = the current density of negative ions (A/m^2), and

j_2 = the current density of positive ions (A/m^2).

If a quasi steady state exists in the region in which both ions contribute to the current, $j_1 \simeq j_2$. Now suppose that $|b_1| << |b_2|$. With these assumptions, equation (22) reduces to

$$E''(x) - 1/2(\frac{e}{kT})^2E^3(x)+1/2(\frac{e}{kT})^2\{E^2(o)-E_s^2-\frac{2j_1}{\varepsilon b_1}x\}E(x)+\frac{ej_1}{\varepsilon kTb_1} = 0. \quad (23)$$

It can be shown by differentiation that equation (23) has the same solution as

$$E'(x)+1/2\,\frac{e}{kT}\,E^2(x)-1/2\,(\frac{e}{kT})\,\{E^2(o)-E_s^2-\frac{2j_1}{\varepsilon b_1}x\} = 0. \quad (24)$$

This is a first order, non-linear, differential equation whose solution yields the electric field. This is the same equation that would have resulted if only the negative ions had been considered. Equation (23) can be linearized by the transformation

$$E(x) = \frac{2kT}{e}\,\frac{1}{y(x)}\,\frac{dy}{dx}\ , \quad (25)$$

where, y(x) is an arbitrary function. Following the procedure outlined in reference 9, the solution of equation (24) yields an electric field

$$E(x) = -(\frac{4kTj_1}{e\varepsilon b_1})^{1/3}\{\frac{Ai'(\xi)+K_1Bi'(\xi)}{Ai(\xi)+K_1Bi(\xi)}\}\ , \quad (26)$$

where $Ai(\xi)$ and $Bi(\xi)$ are Airy functions and $Ai'(\xi)$ and $Bi'(\xi)$ are the first derivatives of $Ai(\xi)$ and $Bi(\xi)$, respectively. The argument in the Airy functions is given by

$$\xi = (\frac{e\varepsilon b_1}{4kTj_1})^{2/3}[E^2(o)-E_s^2-\frac{2j_1}{\varepsilon b_1}x]\ . \quad (27)$$

The constant K_1 is to be determined by the boundary conditions. The potential within the boundary layer is given by

$$V(x)=V(o)-\frac{2kT}{e}\ln\{\frac{Ai(\xi)+K_1Bi(\xi)}{Ai(\xi_0)+K_1Bi(\xi_0)}\}\ , \quad (28)$$

where

$V(o)$ = the potential at x=o, and

$$\xi_0 = \xi\Big|_{x=o} = \left(\frac{e\varepsilon b_1}{4kTj_1}\right)^{2/3}[E^2(o)-E_s^2] \quad . \tag{29}$$

Notice that, for the case corresponding to perfect screening at the positive electrode, $\xi_0 = 0$. The value of the argument ξ in equation (27) depends very sensitively on the value of b_1 which is not known for fly ash. Both the electric field and the potential in equations (26) and (28), respectively, depend on ξ. Since b_1 is unknown, it may be more instructive at the present time to discuss a thin boundary layer solution to equation (22).

For moderate currents and small x, the solution to equation (22) can be written as

$$E(x) = E_\delta \coth\left(\frac{eE_\delta}{2kT}x + \beta\right) \quad , \tag{30}$$

where

$$\beta = \text{Arc coth}\left(\frac{E(o)}{E_\delta}\right) \quad , \tag{31}$$

and

$$E_\delta = [E^2(o) - \frac{2kT}{\varepsilon}C_1(o)]^{\frac{1}{2}} \quad . \tag{32}$$

The electric field in equation (32) decays from $E(o)$ to E_δ for relatively small values of x. Note from equation (32) that E_δ is significantly less than $E(o)$ only when $C_1(o)$ has a value near that associated with electrostatic screening.

The maximum value of $C_1(o)$ is determined by the processes which are involved in neutralizing the negative charge at the positive electrode. The value of $E(o)$ increases with applied potential. As $E(o)$ increases with the applied potential, $C_1(o)$ also increases in such a manner as to screen the surface charge field from the interior of the layer. When the maximum value of $C_1(o)$ is reached, the increasing surface charge field is no longer effectively screened from the interior of the layer. As the applied potential is further increased, the field in the layer may become sufficiently large to produce electrical breakdown in some of the enclosed pockets of gas.

ENDNOTES

1. R. E. Bickelhaupt, "Electrical Volume Conduction in Fly Ash", APCA Journal 24:251, 1974.

2. R. E. Bickelhaupt, "Surface Resistivity and the Chemical Composition of the Fly Ash", APCA Journal 25(2):148, 1975.

3. J. R. McDonald, R. B. Mosley, and L. E. Sparks, "An Approach for Describing Electrical Characteristics of Precipitated Dust Layers", APCA Journal, 30(4):372, 1980.

4. J. K. McLean, "Factors Affecting the Resistivity of a Particulate Layer in Electrostatic Precipitators", APCA Journal, 26(9):866-870, 1976.

5. S. Masuda and A. Mizuno, "Flashover Measurements of Back Discharge", J. Electrostatics, 4:215, 1978.

6. L. C. Thanh, "Back Corona. Part I: Its Formation", J. Electrostatics 6: 139-160, 1979.

7. L. C. Thanh, "A Model for Dielectric Breakdown in Porous Dielectrics", Third International Symposium on High Voltage Engineering, Milan (1979).

8. R. B. Mosley, P. R. Cavanaugh, J. R. McDonald, and L. E. Sparks, "Measurements of Electrical Properties of Fly Ash Layers", The Third Symposium on the Transfer and Utilization of Particulate Control Technology, Orlando, Florida, 1981.

9. R. B. Mosley and A. T. Fromhold, Jr., "Kinetics of Oxide Film Growth on Metal Crystals: Space-Charge-Modified Thermal Electron Emission and Ionic Diffusion. Part 1. Pertinent Equations", Oxidation of Metals 8:19, 1974.

10. G. G. Roberts and R. H. Tredgold, "Double Injection Including Diffusion Effects", Physics Letters 14(2):94-95, 1965.

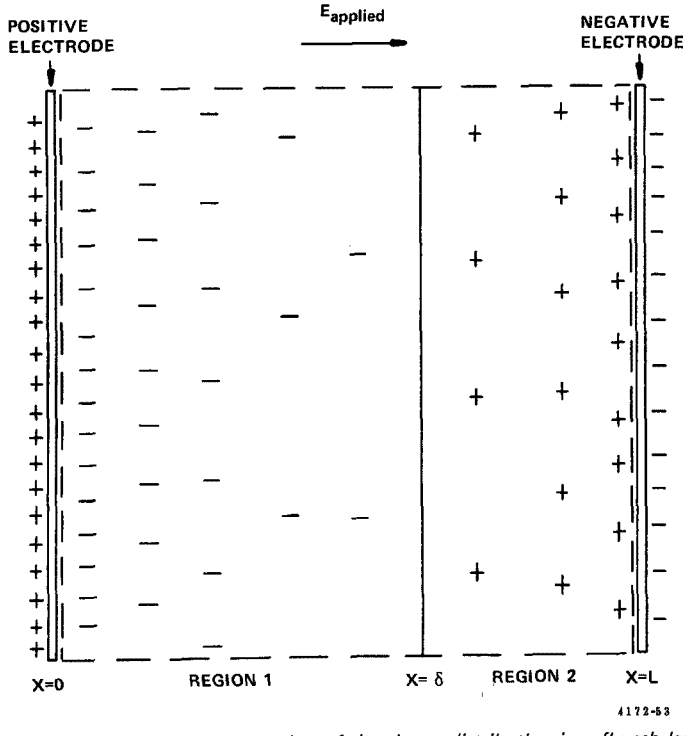

Figure 1. Schematic representation of the charge distribution in a fly ash layer.

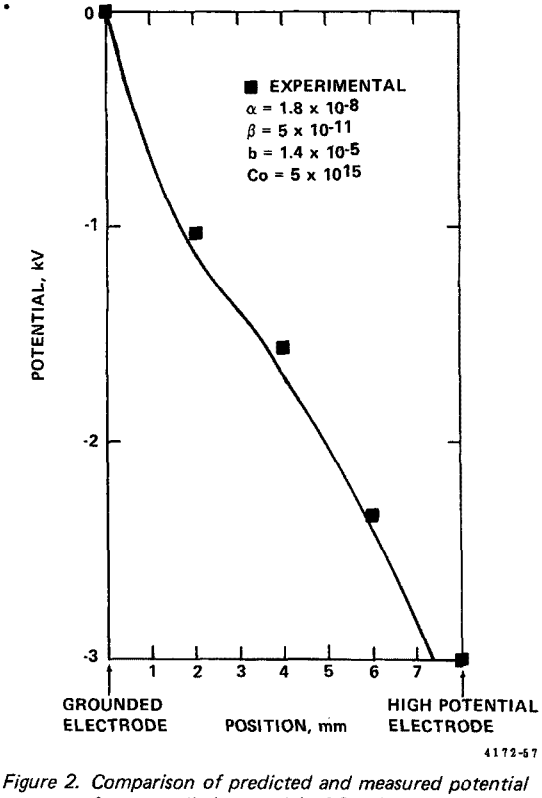

Figure 2. Comparison of predicted and measured potential for an applied potential of 3 kV at a temperature of 371°C.

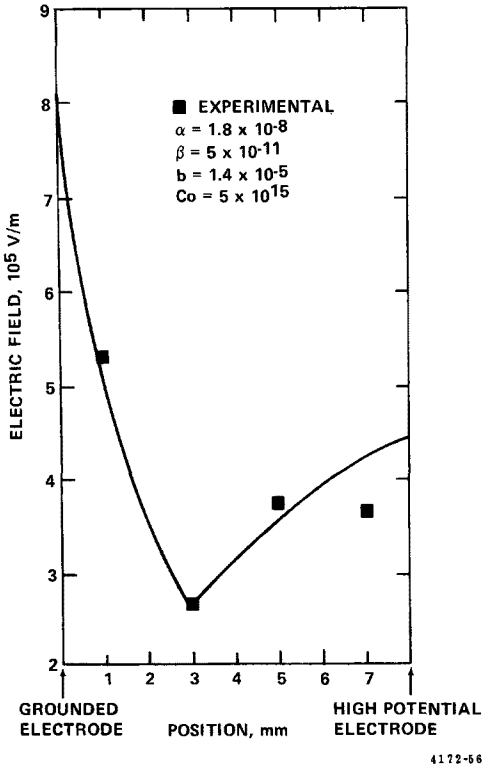

Figure 3. Comparison of predicted and measured electric field profile for an applied potential of 3 kV at a temperature of 371°C.

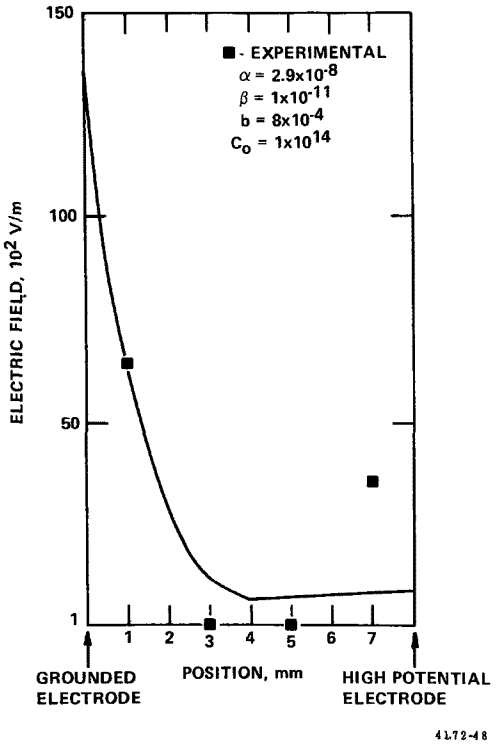

Figure 5. Comparison of predicted and measured electric field profile for an applied potential of 20 volts at a temperature of 371°C.

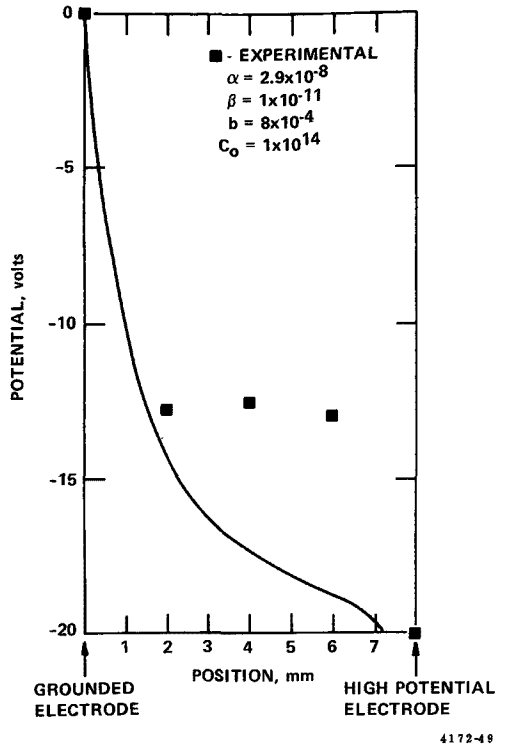

Figure 4. Comparision of predicted and measured potential profile for an applied potential of 20 volts at a temperature of 371°C.

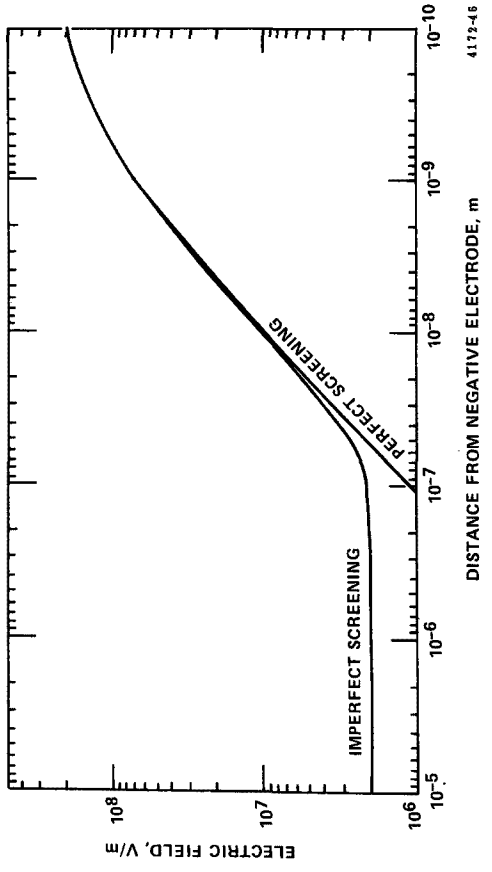

Figure 6. Screened electric field near the negative electrode corresponding to a surface charge field of $2x10^8$ V/m.

MEASUREMENTS OF ELECTRICAL PROPERTIES OF FLY ASH LAYERS

By: Ronald B. Mosley, Paul R. Cavanaugh, Jack R. McDonald
Southern Research Institute
2000 Ninth Avenue, South
Birmingham, Alabama 35255

Leslie E. Sparks
Industrial Environmental Research Laboratory
U.S. Environmental Protection Agency
Research Triangle Park, N.C. 27711

ABSTRACT

Measured electric potential and resistivity profiles demonstrate that the electric field and the charge-carrier densities are nonuniform within the fly ash layer. An activation energy of 0.88 eV associated with the migration of alkali metal ions was obtained. A charge as large as 1.8×10^{-5} C was found to accumulate in the layer as the result of an applied potential. An average diffusion coefficient of 1.2×10^{-13} m^2/s was measured for sodium ions in a fly ash layer. Electrical breakdown voltages of fly ash layers are displayed as a function of pressure, thickness, and temperature.

INTRODUCTION

Difficulty in transporting charge through a high resistivity layer collected on the plates often limits the performance of an electrostatic precipitator (ESP). The limits on performance usually manifest themselves in limits on the electrical operating conditions of the ESP. It is necessary not to exceed a certain operating voltage in order to avoid back corona which is believed to be initiated by electrical breakdown in the dust layer. In order to understand why back corona occurs and whether remedial technology can prevent it, it is necessary to understand the processes involved in electrical breakdown of the dust layer. This in turn requires an understanding of the conduction mechanisms in the dust layer.

Due to limited space, it is not possible to provide a comprehensive list of references on experimental studies of the electrical properties of fly ash layers. However, a considerable number of these studies are referred to in the references which are listed here. The present paper will show the results of some measurements of (a) potential, electric field, and resistivity profiles within the fly ash layer, (b) activation energies for current transport, (c) the field dependence of resistivity, (d) current-voltage curves, (e) thermal diffusion coefficient, (f) breakdown properties, and (g) charge buildup in the layer.

ELECTRICAL CONDUCTION PROPERTIES

In order to study the electrical conduction properties of fly ash layers, a standard resistivity cell has been modified by inserting potential measuring

probes into the layer. The probes consist of fine (No. 36 gauge) platinum wires stretched across the sample cup at different depths. The wires are insulated except in the region directly beneath the measuring electrode. A variety of probe arrangements and spacings have been used. The results of these different configurations are generally in good agreement. The probes divide the sample into a number of layers. By measuring the potential drop across each of these layers, the average field and resistivity in each layer is easily computed. Any graph which shows the electric potential, the electric field, or the resistivity as a function of position within the fly ash layer will be referred to as a profile. Potential profiles for applied potential up to 100 volts are illustrated in Figure 1. The first observation pertaining to these profiles is their nonlinear character. Linear potential profiles would be associated with a uniform electric field. A uniform field would be expected if no space charge were generated in the layer. A second observation is the lack of symmetry in the shape of the potential profiles. The shape of the potential curve suggests that an inflection point exists somewhere in the layer. An inflection point implies a change in sign of the space charge density. If the deviation from linearity of the potential profiles is caused by space charge associated with migrating ions, then the skewed shape of the profiles suggests that ions of one sign are appreciably more mobile than those of the other sign.

The curve marked as initial in Figure 2 shows that the potential profile in the bulk of the layer is more nearly linear at high than at low values of applied potential. The other two curves in Figure 2, however, show that the potential profile in the bulk becomes less linear with passing time under an applied potential. The second two curves were taken 1 hour and 26 hours, respectively, after the initial profile.

Figures 1 and 2 show that the potential profiles in the bulk of the layer tend to become more linear with increasing voltage, but become less linear with the passage of time while the higher voltages are applied. These trends may indicate that two different processes are occurring.

One possible explanation of this behavior assumes that a quasi steady-state charge distribution occurs more quickly at the larger applied potentials. Suppose that both electrodes are partially blocking and that the positive ions (sodium) are much more mobile than the negative ones. By partially blocking, it is meant that neither species of mobile ion is supplied by the electrodes, but that the ions may be removed through chemical reactions with the surrounding gases at the surfaces of the layer. The electrodes are partially blocking because the rate of the chemical reactions would depend on the concentration of free ions near the surfaces of the layer. When a potential is applied, positive ions migrate toward the negative electrode. Since the electrode is partially blocking, the positive ions will pile up there until an equilibrium is established with the surrounding environment such that positive ions are removed by reacting with the surroundings at the same rate that they arrive at the surface. The motion of the positive ions will leave behind relatively immobile negative ions. While a steady state is being established, the distribution of excess negative ions may penetrate a considerable distance into the layer. Except near the positive electrode, the loss of positive ions tends to be compensated by other positive ions moving

in to replace the ones that were lost. Thus, near the positive electrode, the excess negative charge tends to increase with time. Eventually, the density of negative ions near the positive electrode will become sufficient that the negative ions will begin to react with the surrounding environment at that surface. In order for a steady state to exist, negative ions at the positive electrode must be removed at the same rate as positive ions at the negative electrode. A quasi steady state may occur when the positive and negative charge distributions move near the two electrodes, leaving the center of the layer nearly charge-neutral. Such a quasi steady state may be achieved more readily at higher applied potentials and therefore may explain the linear region of the potential profile in Figure 2. The changes in the profiles with time may indicate an approach to a true steady state.

Figure 3 shows the electric field profiles which correspond to the potential profiles in Figure 2. First note that the electric fields nearest the electrodes are considerably larger than those near the center of the layer. (The average field is indicated by the dashed line.) Also note that most of the changes with time occurred near the positive electrode. The decrease in the electric field near the center of the layer may result from the increased screening associated with the increased negative charge.

Figure 4 shows electric field profiles for applied potentials of 100, 200, and 400 volts. By comparing the curves in Figure 4 with those in Figure 3, it can be seen that the shapes of the field profiles change not only with time, but also with applied potential. At the lower applied potentials, the minimum in the magnitude of the electric field occurs closer to the negative electrode, while for higher potentials this minimum is closer to the positive electrode.

Figure 5 shows three potential profiles measured on the same sample under a reversed potential. The potential was reversed after 26 hours of continuously applied positive potential. The second two curves were taken 1 hour and 94 hours, respectively, after the first negative potential profile. The potential profile changes with time.

The corresponding electric field profiles are shown in Figure 6. The field in the bulk of the layer first increases and then decreases, while the fields near the electrodes behave in the opposite sequence. The increase in the field near the positive electrode is consistent with the assumption of a slow buildup of negative ions. Perhaps the most striking feature of these field profiles is the extent to which the variations penetrate into the center of the layer. These variations indicate that significant charge densities of both signs extend deep into the layer.

The resistivity profiles corresponding to the curves in Figures 5 and 6 are shown in Figure 7. Note that the only significant changes in the resistivity occurred in regions adjacent to the electrodes. In these two regions the resistivity first decreased and then increased. This behavior correlates relatively well with that of the electric field in the same regions.

Figure 8 shows some electric field profiles for three applied voltages and five different temperatures. The shape of the field profile, and

consequently the charge distribution in the layer, is surprisingly sensitive to the temperature. The profile is most sensitive to temperature in the range 260°C to 319°C. The reason for the sudden change in charge distribution with increasing temperature is uncertain. The observed changes would be consistent with either an increase in ion mobility or an increase in the rate at which charge is removed at the surfaces. If the charge distribution were characteristic of some types of localized charge traps in the layer, the changes with increasing temperature might indicate charge escaping from the traps due to increased thermal energy.

The sensitivity to temperature is further illustrated by the resistivity profiles displayed in Figure 9 for an applied voltage of 1 kV. These curves also illustrate how the shape of the charge distribution depends on the temperature. The sample was divided into five approximately equal layers by the measuring probes. The variation of the resistivity with electric field in each of these five layers is shown for two temperatures in Figure 10. Note that the resistivity in layer No. 5 which is adjacent to the positive electrode has the greatest value for both temperatures. It seems reasonable to assume that the current through the sample is primarily limited by layer No. 5. Figure 10 suggests that the resistivity in layer No. 5 decreases approximately exponentially with the electric field in the layer. This result is not easily explained in terms of barrier suppression by the electric field. The difficulty in explaining the exponential dependence of resistivity in terms of barrier suppression lies in the relatively small values of electric field. Such a description would be applicable only if the field were much larger than the measured values at some point in the layer very near the electrode. This would be plausible only if the large field existed in a layer so thin that it gave little contribution to the measured potential difference in that region.

The curves shown in Figures 11 and 12 provide strong evidence that the conduction mechanism involves an activated process. The activation energies are proportional to the slopes of these curves. In Figure 11, the average resistivity in the entire sample is plotted as a function of the reciprocal temperature; in Figure 12, the resistivity in the individual layers is displayed in the same manner. In both cases, the slopes of the curves decrease at the higher temperatures. For temperatures below 340°C, the average activation energy is 0.88 eV; for temperatures between 340°C and 385°C, the average activation energy is 0.46 eV. Although it may appear from Figure 11 that the slopes of the curves, and therefore the activation energies for temperatures less than 340°C, are independent of the applied voltage, careful analysis shows that the activation energy actually decreases with increasing voltage. For temperatures in the range 340°C to 385°C the activation energy increases with increasing applied potential. The reason for this increase in activation energy with applied potential is uncertain. Although it is not shown in Figure 11, it was found that for an applied potential of 3 kV the activation energy is about the same for the entire temperature range shown.

Figure 13 shows another set of electric field profiles which are of interest. The profiles are measured for higher applied potentials. In fact, the profile corresponding to a voltage of 6.5 kV was recorded immediately

before electrical breakdown at a slightly higher voltage. No dramatic differences are apparent in this profile. A maximum measured field of about 9.25 kV/cm occurs in layer No. 5. Such a small electric field cannot explain electrical breakdown of either the gas or the fly ash particles in the layer. In order to explain electrical breakdown it must be assumed either that the local field is much enhanced over the macroscopic value being measured, or that a large field exists somewhere near the electrode.

In consideration of the first assumption above, a model was recently presented[1] in which the local electric field between fly ash particles is enhanced by the dielectric polarization of the particles. The enhancement factor from this model is given by

$$h = 1 + 1.25\ (K-1) \tag{1}$$

where K is the dielectric constant of the particles. For K = 5, we obtain an enhancement factor of 6. This would predict a local field of at least 55 kV/cm. According to Paschen's law,[2,3,4] this field would be capable of explaining breakdown in air at 350°C only if the cavity of air were 10^{-4}m or larger in diameter. It does not seem likely that many cavities this large would exist in the layer. However, the macroscopic field could be extrapolated to a value somewhat larger than 9 kV/cm near the positive electrode. The possibility of even larger fields will be discussed later.

Typical current-voltage curves are shown in Figure 14. Although the current-voltage relationship cannot be accurately represented as a simple power law, it can be approximated in different ranges of applied potential by $j = \alpha V^n$, where α is a constant and n is a little greater than 1 for small V and is about 2 for larger V. Note that the case for n = 2 is indicative of space charge limited currents.

MEASUREMENT OF THE THERMAL DIFFUSION COEFFICIENT OF SODIUM IONS IN FLY ASH

The principal equation governing one-dimensional non-steady state diffusion in solids is Fick's second law. For a semi-infinite solid in which the concentration of diffusing species is maintained constant at one surface, the solution[5] to Fick's second law can be written:

$$C(x,t) = C(0,t)\ \mathrm{erfc}\ \left(\frac{x}{2\sqrt{Dt}}\right) , \tag{2}$$

where

C(x,t) = the concentration of diffusing species at position x and time t,
C(0,t) = the concentration at the surface which is held constant,
erfc = complementary error function,
x = position in the solid,
D = diffusion coefficient, and
t = time.

Equation 2 can be written as:

$$\eta = \text{erfc}^{-1}\left(\frac{C(x,t)}{C(0,t)}\right) = \frac{x}{2\sqrt{Dt}} \tag{3}$$

A plot of η versus x that yields a straight line implies that D is independent of the concentration and that its value can be computed from the slope of the line.

An experiment was performed by placing a layer of low sodium fly ash on top of a layer of higher sodium fly ash and thermally annealing the sample at about 538°C for many hours. The sample was then sectioned into layers about 0.2 mm thick and chemically analyzed for sodium content. In this manner, a sodium concentration profile was established in the layer and η was plotted as a function of x. Figure 15 illustrates the results for two such sets of measurements. The two ashes used in these experiments had sodium oxide concentrations of 1.7 and 8.2 percent by weight. The measured values of diffusion coefficient shown in Figure 15 are 1 to 2 orders of magnitude smaller than are commonly measured in sodium silicate glasses. It should be pointed out that in computing the diffusion coefficient it was assumed that all the sodium ions present in the fly ash participate in the migration process. If only a fraction of the ions migrate, the diffusion coefficient should be larger.

ELECTRICAL BREAKDOWN OF FLY ASH LAYERS

The phenomenon of back-corona constitutes a severe limit on the operation of ESPs collecting high resistivity fly ash. It is believed that the condition of back-corona develops as a result of initial electrical breakdown of the fly ash layer. The mechanisms of electrical breakdown of the ash layer are not presently understood. It has long been known that breakdown of the ash layer often occurs for average fields which are too small to produce breakdown either in gases or in solids. In order to explain the electrical breakdown we must explain how the field in the layer is larger than the average field.

The fly ash layer is a two-phase material consisting of solid dielectric fly ash particles and pockets of gas enclosed between the particles. It is important to establish which phase of the layer is breaking down electrically. In an effort to establish the phase in which it occurs, the breakdown voltage for several ash layers was studied as a function of the gas pressure. A vacuum system was used to control the pressure. The breakdown voltage-pressure relations for three layer thicknesses are shown in Figure 16.

The similarily of the curves in Figure 16 to the well known Paschen's law[4] for electrical breakdown of air should be noted. Although no quantitative attempt has been made to compare the curves in Figure 16 with Paschen's law, the general characteristics of gaseous breakdown are apparent. In the ranges of pressure indicated by the dashed curves, no measurements were obtained because glow discharges occurred from all exposed areas of the high-voltage side of the circuit. At pressures below about 2 mm Hg the glow discharge disappeared and the breakdown voltage increased with decreasing pressure. The present vacuum system could not achieve pressures below about 0.005 mm Hg.

Note that the low-pressure range of Figure 16 has an expanded scale.

One further indication that the gas in the layer breaks down is contained in Table 1. Table 1 shows a comparison of breakdown voltages at atmospheric pressure when the gas is helium to those when the gas is air. The same procedures were used for air and for helium. The chamber was evacuated to a pressure of about 0.01 mm Hg and then either helium or laboratory air was added to bring the chamber to atmospheric pressure. The fly ash layers containing helium broke down at about half the voltage of those containing air. These breakdown measurements were performed at room temperature.

TABLE 1. COMPARISON OF LAYER BREAKDOWN VOLTAGES IN HELIUM AND IN AIR

	Helium				Air			
Sample	1	2	3	4	5	6	7	8
Thickness (mm)	6	6	6	6	6	6	6	6
Breakdown Voltage (kV)	3.3	2.9	3.1	3.95	7.3	6.45	6.0	6.25
Average (kV)	3.31				6.50			

Figure 17 illustrates breakdown voltage as a function of layer thickness. The room temperature (22°C) set of curves illustrates breakdown for two different ashes under two different conditions of heat treatment. The unheated samples indicate ashes which had been in laboratory air for months. The heat-treated ashes were held at 260°C for several hours immediately before being tested. The tests were performed near room temperature. The intent of the heat treatment was to remove moisture from the surface of the particles. The measurements performed at the higher temperatures used ash No. 1 which had been held at 800°C overnight to volatilize any hydrocarbons present. Although these curves illustrate the decrease in the breakdown strength of air with increasing temperature, there seems to be an even greater effect of the temperature on the local field which leads to the breakdown. Figure 8 suggests that this reduction in the local field could be due to the reduced contribution from space charge in the layer.

MEASUREMENT OF THE CHARGE BUILDUP IN THE LAYER

The profiles illustrated in the first nine figures of this paper indicate that space charge distributions exist in the fly ash layer which has been stressed by an applied potential. If this space charge consists of ions of relatively low mobility, it may be possible to measure the charge in the layer

by removing the power source and measuring the charge which flows in an external circuit when the electrodes of the sample are shorted. Figure 18 shows the time dependence of the current measured by an electrometer connected between the electrodes of a sample which has experienced the application of 3 kV for different lengths of time. The currents have opposite signs to those when the potential was applied. The current is also about 3 orders of magnitude smaller than when the potential was applied. The background current or noise was somewhat smaller than the level indicated as noise in Figure 18. The areas under these curves represent the charge which flows through the electrometer. The implication is that at least this much charge was contained in the fly ash layer. These values of charge are indicated in Figure 18. From these curves, it is apparent that the charge in the layer builds up rather slowly. Although it is not evident in Figure 18, there were some indications that a saturation of charge is approached. For instance, it was found that about the same charge was accumulated in 16.5 hours at 3 kV as was accumulated in 64 hours at 2 kV.

In order to better appreciate the implications of the fly ash layer containing 1.8×10^{-5}C of charge, let's apply Poisson's equation:

$$E(\ell) - E(0) = \frac{Q}{\varepsilon A} = \frac{1.8 \times 10^{-5}\text{C}}{(4.4\text{x}10^{-11}\ \frac{\text{C}}{\text{Vm}})\ 2.03 \times 10^{-3}\text{m}^2} = 2.2 \times 10^{8}\ \text{V/m}, \quad (4)$$

where

$E(\ell) - E(0)$ = the total change in the electric field due to charge Q,

Q = total charge in the layer,

ε = permittivity, and

A = cross sectional area of the layer.

This value of electric field is very much greater than any that were measured by the potential probes. Such large fields could only exist in very thin layers near the electrodes. According to measurements[2,3] of breakdown field in air for very small electrode spacings, such large fields can only exist over distances of the order 1 μm or less without producing breakdown of the air. If we suppose that 1.8×10^{-5}C of charge is distributed uniformly in a layer 1 μm thick at the electrode, the charge carrier density in this layer would be 5.5×10^{22} ions/m^3. This number is quite small in comparison to the equilibrium density of sodium ions present in the fly ash.

SUMMARY

Potential profiles in the layer are found to be nonlinear indicating a buildup of space charge in the layer. The electric field profiles indicate charge distributions of opposite signs near the two electrodes. These charge distributions are sensitive to both temperature and applied voltage. The potential and field profiles are observed to change with time. The resistivity is found to vary somewhat exponentially with electric field.

Below 340°C the average activation energy is 0.88 eV. Above 340°C and below 3 kV the average activation energy is 0.46 eV and increases with applied potential. The electric field profile does not change dramatically as electrical breakdown is approached. An average diffusion coefficient of 1.2 x 10^{-13} m^2/s is measured for sodium ions in fly ash at 538°C. The breakdown voltage pressure relationship for fly ash layers in air at room temperature is very similar to Paschen's law. In a helium environment, fly ash layers break down at about half the voltage as in an air environment. Breakdown of the layer is found to depend on the temperature. The charge which builds up in the layer under the action of an applied voltage was found to reach values of 1.8 x 10^{-5}C.

ENDNOTES

1. J. R. McDonald, R. B. Mosley, and L. E. Sparks, "An Approach for Describing Electrical Characteristics of Precipitated Dust Layers," APCA Journal, 30, (4):372-376 (1980).

2. L. C. Thanh, "Back Corona, Part I: Its Formation," Journal of Electrostatics, 6:139-160 (1979).

3. M. Knoll, F. Ollendorff, and R. Rompe, Gasentladungstabellen. Springer Verlag, Berlin, 1935. p. 83.

4. L. B. Loeb, Fundamental Processes of Electrical Discharge in Gases. John Wiley and Sons, Inc., New York, NY, 1939. p. 410 ff.

5. T. Dosdale and A. P. Morris, "The Evaluation of Diffusion Coefficients from Concentration Profiles in Semi-infinite Solids," Philosophical Magazine A, 42(3):369-384 (1980).

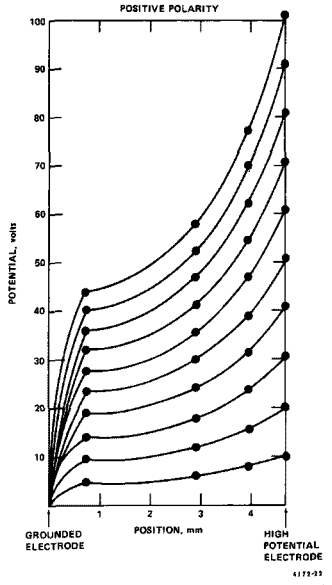

Figure 1. Potential profiles for positive applied potentials from 10 to 100 volts at 404°C.

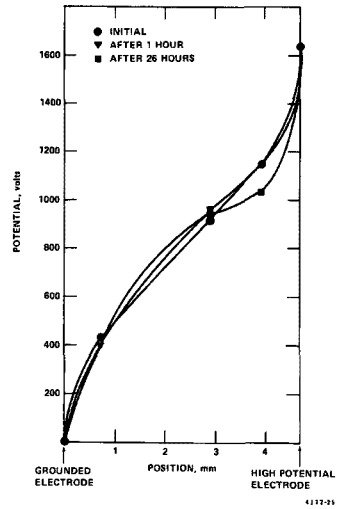

Figure 2. Potential profiles for positive applied potential of 1642 volts taken at three different times at 404°C.

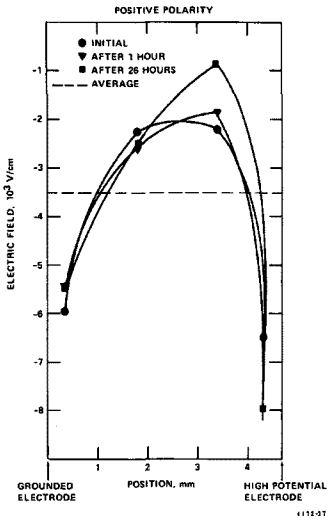

Figure 3. Electric field profiles for positive applied potential of 1642 volts taken at three different times at 404°C.

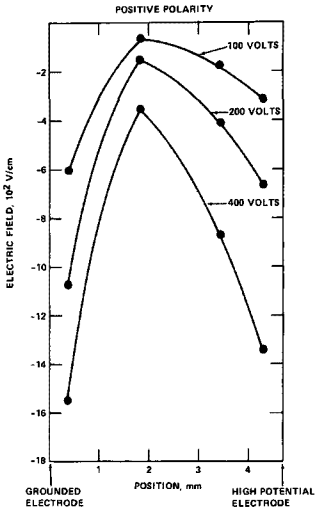

Figure 4. Electric field profiles for positive applied potentials of 100, 200, and 400 volts at 404°C.

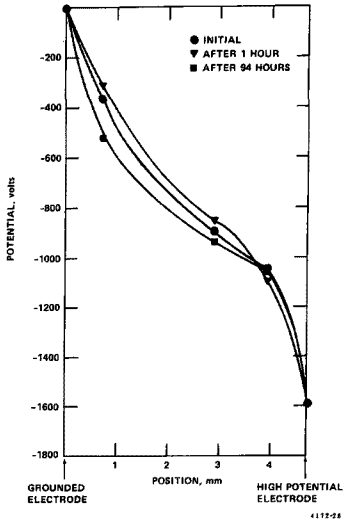

Figure 5. Potential profiles for negative applied potential of 1594 volts taken at three different times at 404°C.

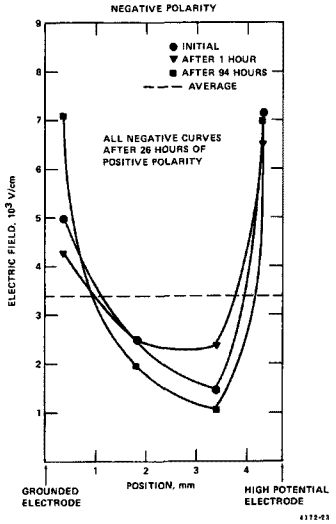

Figure 6. Electric field profiles for negative applied potential of 1594 volts taken at three different times at 404°C.

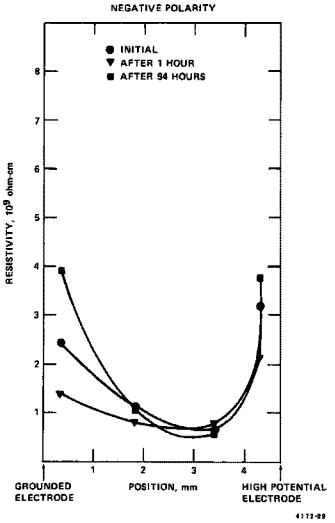

Figure 7. Resistivity profiles for negative applied potential of 1594 volts taken at three different times at 404°C.

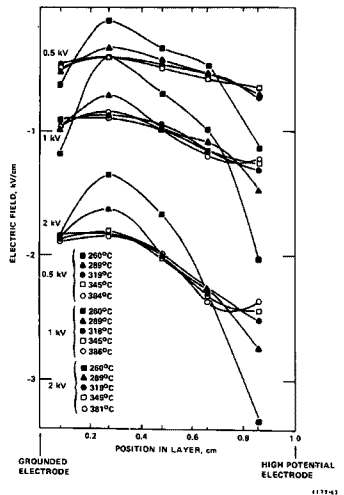

Figure 8. Electric field profiles for positive applied potentials of 0.5, 1.0, and 2.0 kV at five different temperatures.

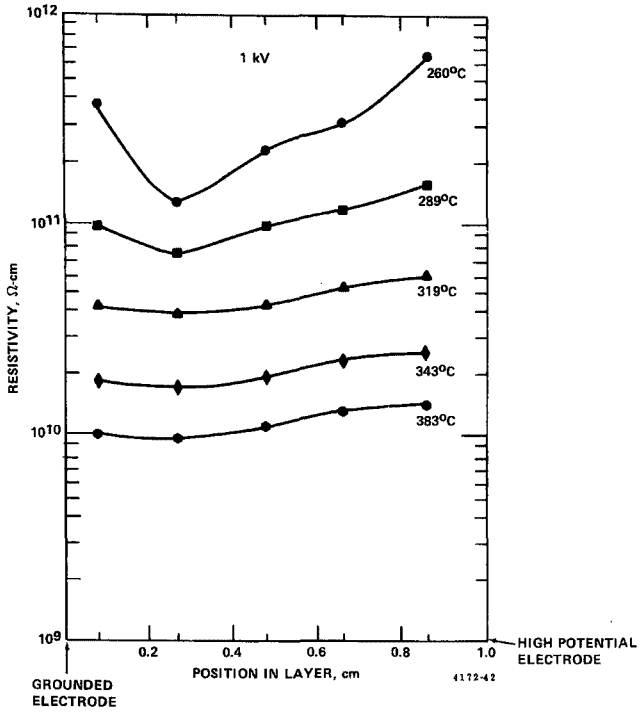

Figure 9. Resistivity profiles for positive potential of 1 kv and five temperatures.

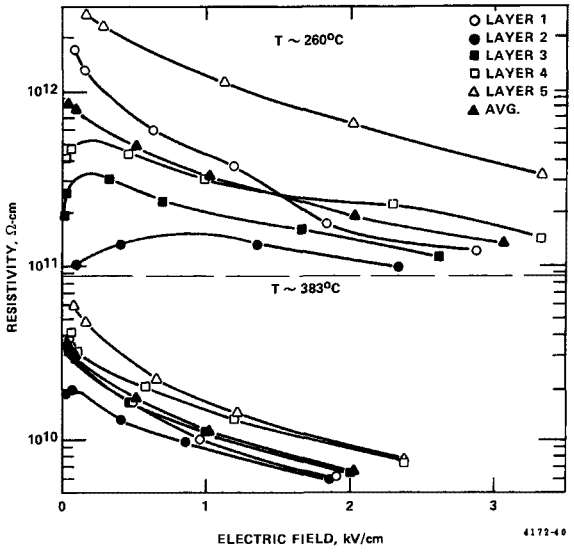

Figure 10. Field dependence of the resistivity.

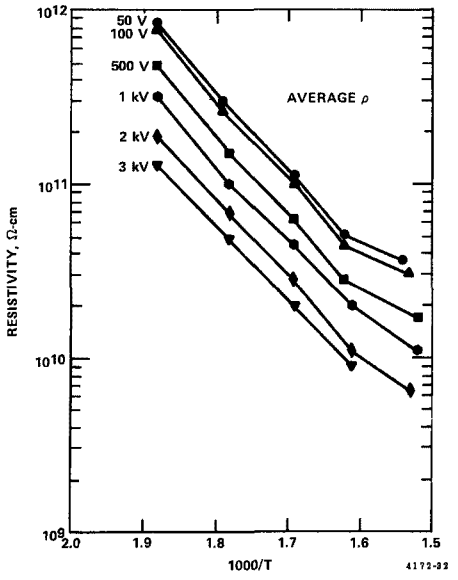

Figure 11. Average resistivity versus reciprocal temperature for several applied potentials.

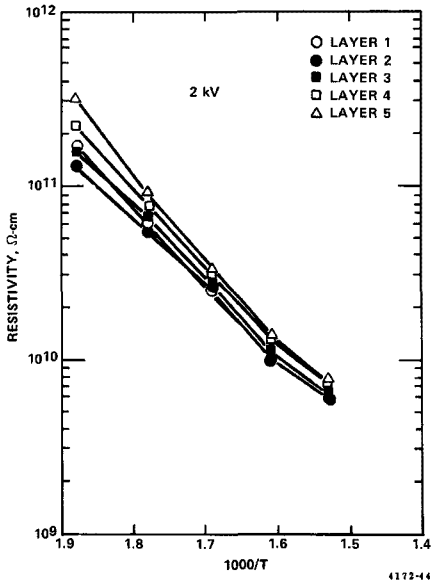

Figure 12. Resistivity versus reciprocal temperature in the individual layers.

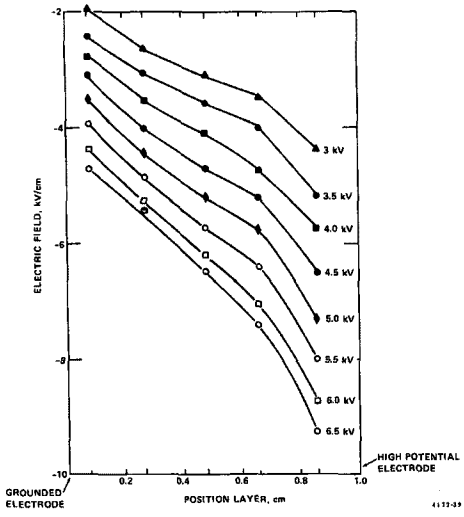

Figure 13. Field profiles for several applied potentials.

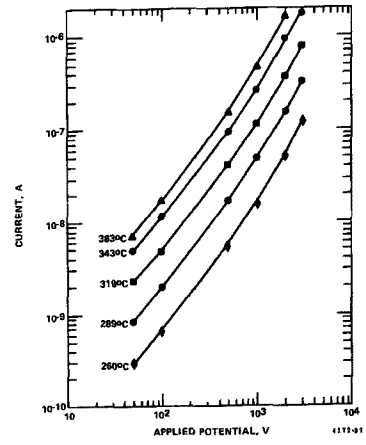

Figure 14. Current versus applied voltage.

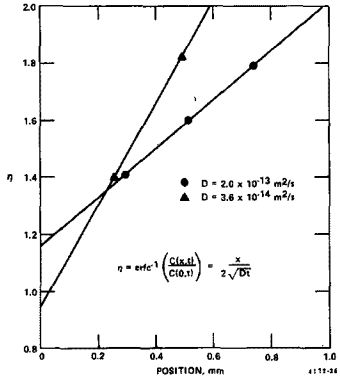

Figure 15. Plot of η versus position for the diffusion experiment.

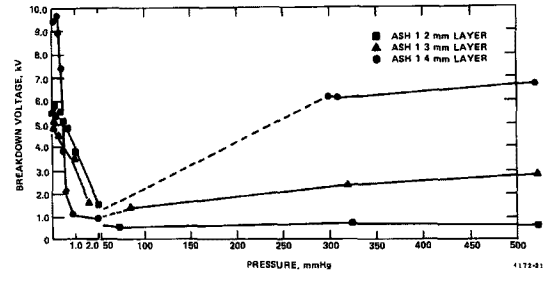

Figure 16. Paschen's law type plot for breakdown of dust layers.

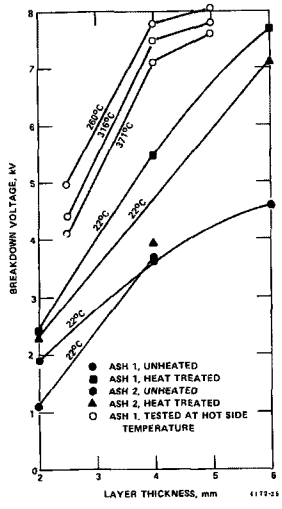

Figure 17. Breakdown voltage versus layer thickness for several temperatures.

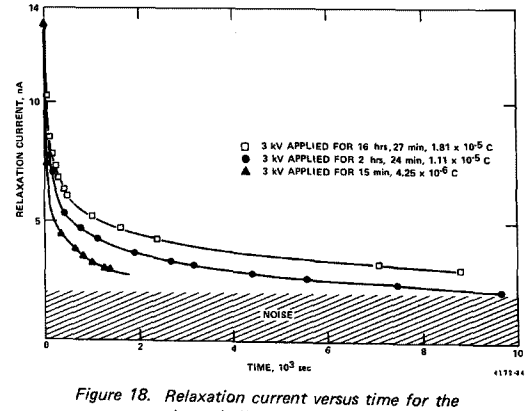

Figure 18. Relaxation current versus time for the charge built up in the layer at a temperature of 348°C.

LASER DOPPLER ANEMOMETER MEASUREMENTS OF PARTICLE VELOCITY IN A LABORATORY PRECIPITATOR

By: Phil A. Lawless, Ashok S. Damle, Andrew S. Viner
Research Triangle Institute
P. O. Box 12194
Research Triangle Park, North Carolina 27709

Edward J. Shaughnessy
School of Engineering
Duke University
Durham, North Carolina 27706

Leslie E. Sparks
Industrial Environmental Research Laboratory
U. S. Environmental Protection Agency
Research Triangle Park, North Carolina 27711

ABSTRACT

A laboratory electrostatic precipitator (ESP) was constructed to permit direct measurement of particle velocities by means of laser Doppler anemometry. Dimensions of the ESP were chosen to reflect realistic ESP designs, and the flow conditions were carefully established. Measurements of particle velocities were carried out for a variety of particle sizes and electrical conditions. These velocities were interpreted in light of current theories for electric field configuration and particle charging. The conclusions reached were: 1) particles of the same size acquire the same charge, 2) a suitable average electric field adequately describes the charging conditions, and 3) current theories significantly underpredict velocities of particles in the ESP.

INTRODUCTION

Laser Doppler anemometry is a technique admirably suited to particle velocity measurements in an ESP: it directly measures particle velocity and causes no distortion of the electric field at the point of measurement. The electrical conditions in a wire-duct precipitator can be adequately calculated from voltage and current measurements if certain symmetries are obeyed and the corona is uniformly distributed along the wire. If the electrical conditions are known, including the time of exposure to ions, and if particle size can be determined, fairly accurate charging theories can predict the level of charge on the particles. This allows for comparison of theoretical particle velocity with the measured value.

Measurement Techniques

The laser used was a Lexel Model 85-.5 argon ion laser. Typical power was 200 mW at 514.5 nm. The flow velocity components were measured directly, while the cross-flow velocity components were measured with a DISA frequency shifter. The detector was a solid state photo diode with preamplifier. Frequency measurement was primarily with a TSI tracker, but a Honeywell™ autocorrelator was also used. The voltage and current were measured with

standard voltage dividers and millivolt ammeters. The flow velocity profile and turbulence intensity were measured with a TSI linearized hot-wire anemometer.

The particles were a wax, stearic acid, formed in a condensation aerosol generator. Under most conditions, the particles formed were monodisperse with a geometric standard deviation of 1.06 to 1.10. The particles were sized with a Climet optical counter and multichannel analyzer which was calibrated for stearic acid with a TSI Berglund-Liu generator.

Particle velocities were measured at several physical locations and under four electrical conditions: current densities of 0.0, 7.3, 44, and 73 nA/cm^2, with corresponding voltages of 0.0, 36.2, 40.0, and 42.8 kV, respectively. Back corona was occasionally detected by abnormally low voltages and inconsistent velocity measurements; when this occurred, the ESP was throughly cleaned.

Methods of Analysis

Two methods of analyzing the velocity data have been used. The first is a way of calculating the particle charge by assuming that the particle experiences only a Stokes viscous drag force, which is equal to the Coulomb force on it. The equation is:

$$q = 6\pi \eta rv/EC, \qquad (1)$$

where q is the particle charge; η, the gas viscosity; r, the particle radius; v, the measured velocity; E, the electric field at the point of measurement; and C, the Cunningham correction factor.

The second method of analysis is to compare the measured velocity with the velocity calculated from the theoretical particle charge and the electric field at the point of measurement. The particle charge was calculated with the theory of Liu and Kapadia (1) by assuming a particle trajectory and evaluating the charge at increments along that path. To minimize errors in the comparison, trajectories were chosen for which the electric field did not vary rapidly and the measured velocities were nearly constant.

Wind Tunnel Design

A wind tunnel was chosen as the inlet to the ESP section in order to allow the turbulence to develop fully. The tunnel represents the effect of a long lane within the full-scale ESP. The width of the tunnel was 0.152 m (6 in.); the height, 0.610 m (24 in.); and the length, 6.1 m (20 ft). With the addition of several roughness elements at the inlet end, the velocity profile at the precipitator section was unaffected by room air currents. Particles from the condensation generator were introduced at the center of the duct just inside the tunnel inlet. The particle concentration was nearly uniform at the test section.

Velocity and turbulence intensity measurements taken just upstream of the precipitator are shown in Figure 1. The tunnel center-line velocity was 1.74 m/s (5.71 ft/s), and the central 75 percent of the flow was within

5 percent of this value, with the same velocity profile as shown in Figure 1. The Reynolds number for this flow was 19000. The average root mean square fluctuation velocity over the region where particle measurements were taken was 11.5 cm/s.

ESP Design

The ESP was designed as a three-wire unit, with measurements to be taken near the middle wire. The collector plates measured 0.61 m (24 in.) in the flow direction and 0.56 m (22 in.) parallel to the wires, for a total area of 0.68 m^2; their separation was 0.152 m (6 in.). The wires were smooth rods, 3.18 mm (1/8-in.) in diameter and were spaced 0.152 m apart. This geometry was chosen to facilitate calculations of the electric field. Positive corona was selected so that the corona glow would be most representative of the model used.(2)

Electrical Characteristics

Because the first and third wires tend to shield the second (middle) wire, it was expected that the middle wire would have a higher onset voltage than the others. This was confirmed by visual observation of the corona and can be seen in the V-I curve (Figure 2). The ESP model was adjusted to fit each part of the curve attributed to a given wire; the composite curve from this fitting procedure is also shown in Figure 2. For the voltages and currents used in these tests, the actual voltage applied has less effect on the electric field than the actual current driven by that voltage. For this reason, the measurements were always taken at constant current, with the voltage allowed to drift with temperature, amount of dust on the wires, and humidity. Except for back-corona conditions, the maximum amount of voltage drift was about 3 percent from the values used in the model fit. This would cause about a 1 percent change in the electric field at the higher current densities.

Laser Beam Path

The laser Doppler technique defines a plane by two intersecting beams in which the velocity component is measured. To allow for the best coverage of the ESP volume, glass plates were used to support the corona wires and allow the beams access to the active region.

The two beams emerging from the frequency shifter were parallel and 5 cm apart. They were passed through a lens of 50 cm nominal focal length that brought them to a common focus in the center of the precipitator. At the point of entry into the ESP, the beams were 3.5 cm apart, which limited the closest approach to the precipitator wall to 1.75 cm. The beam path geometry is shown in Figure 3.

Measured Velocities

Particle velocities were measured at three distances downstream of the middle wire: immediately downstream, one quarter of the distance to the next wire, and one half of the distance to the next wire. At each of these

stations, velocities were measured at 8 to 10 points across the flow stream.

The measured velocities were generally in proportion to the electric field: just downstream of the middle wire, the velocities were high close to the wire and decreased toward the wall. This is illustrated in Figure 4. Farther downstream, the velocities were low in the middle of the precipitator, increasing toward the wall.

The velocities measured at zero current were not always consistent with one another over long periods of time. However, the aims of this work were to elucidate the electrical components of particle motion; and so it was deemed proper to subtract the zero current velocity from the velocities under nonzero current.

Velocity Uncertainties

The measured velocity at a given position in the tunnel represents an average over an extended time interval (40 to 100 s). During this time, there are real fluctuations in velocity due to turbulence and to the distribution of particle sizes. In addition, there are inherent errors in measuring the frequency of a single particle because of the small number of cycles over which it can be determined. The measured rms velocity is about 7.6 cm/s, regardless of the mean value. The best estimate of the contribution due to particle size distribution is 0.5 cm/s, and that of the frequency uncertainty is 1 cm/s. Because these sources of variation add in quadrature, most of the velocity spread must be due to turbulence. This is consistent with the measured value of fluctuation velocity, 11.5 cm/s.

However, the measurements are highly repeatable: measurements repeated at one position had a standard deviation of the mean of 0.2 cm/s. Over the period of several hours, with traverses to different stations, the standard deviation was 0.5 cm/s.

Errors in Theory

The calculation of the electric field has been discussed in some detail. (2) The accuracy of the method for calculating the V-I curve is of the order of 1 percent. The accuracy in calculating the electric field depends upon the number of subdivisions in the calculation. We conservatively estimate the error in the field at 3 percent at any point where it was evaluated and 5 percent where interpolations between grid points were required.

The agreement between the charging theory of Liu and Kapadia (1) and published experimental data is of the order of 5 to 10 percent and is discussed in the original paper. Considering all sources of error, we estimate that the uncertainty in the charging calculation is 10 percent and dominates the error in the theoretical calculation of velocity.

Calculated Particle Charge

Using Equation 1, the average charge on the particles was calculated at each point where a velocity was measured, close to the walls or close to the

midline of the precipitator. The immediate impression given was that the charges were nearly independent of position. The charge, averaged over positions, as a function of particle size at 73 nA/cm^2 is shown in Figure 5. The standard deviations of the data are shown as the error bars to indicate how uniform the particle charges were.

The solid line is the Liu-Kapadia predicted charge for particles exposed in an electric field of 3.8×10^5 V/m. This field corresponds closely to the electric fields directly opposite the first corona wire, averaged over the outermost two thirds of the flow channel. The charge measurements for the 7.3 nA/cm^2 runs cannot be fit with a single electric field calculation. This indicates incomplete charging because of a low ion density.

Two conclusions may be drawn from these results. The first is that particles do not become highly charged near the corona wires. They move away before acquiring an unusually high charge. The second conclusion is that it is reasonable to assume that all particles of a given size have the same charge and that it is a charge characteristic of the field that the particles experience in the zone directly opposite the corona wires.

Comparison with Predicted Velocity

To compare measured velocities with calculated velocities, particle trajectories were started on a line 4.5 cm from the center of the ESP. Calculations were done incrementally, using values of field and ion density from the electric field model and exposure time from the velocity profile. The distance traversed toward the wall was accounted for and amounted to less than 2 cm for the largest particle (about 1 cm for the others). Thus, the particles remained within the experimentally measured area for their entire flight. It was assumed that eddy diffusivity would not cause any greater deviation. The comparison of predicted with measure velocities is shown in Figure 6, for the 73 nA/cm^2 data. The measured velocities exceed the calculated velocities substantially for data taken near the corona wire and 3.8 cm downstream. The data taken 7.6 cm downstream are in good agreement with the calculated velocities. A similar situation holds for the data taken at 44 nA/cm^2. The lowest current density data, at 7.3 nA/cm^2, show some excess velocity over the calculated values but not a statistically significant amount.

Corona Wind Hypothesis

On the assumption that the excess velocity is due to corona wind, a measure of its magnitude was calculated from the equation:

$$v_{cw} = k\, j^{\frac{1}{2}}, \qquad (2)$$

where v_{cw} is the corona wind velocity; k, a constant; and j, the local current density. A plot of the mean excess velocity as a function of local current density is shown in Figure 7. The value of k was computed by a least squares method and is shown in Table 1, along with equivalent values from References 3 and 4.

Table 1. Comparison of k Values

Source	k $[m/s/(A/m^2)^{\frac{1}{2}}]$
This work	1.9
Reference 3	12.5
Reference 4	20.0*

* At zero flow velocity; Reference 3 gives 24.2 at zero velocity.

The agreement here is not good, but the conditions under which the measurements were made are not quite the same either: these measurements were made fairly close to the wall of the ESP; those in Reference 3 were heavily weighted toward the region near the wires; while those in Reference 4 were made by allowing a portion of the gas to pass through the precipitator wall.

Conclusions

These experiments have confirmed several assumptions about ESPs that are commonly used: that particles of the same size have the same charge; that, with high enough current density, particle charging is very rapid; and that the appropriate charging field to use is an average field near the collecting plate opposite a corona wire. The experiments also show that current charging and electric field theories underpredict particle velocities. The excess velocity measured can be interpreted as due to corona wind, but the data do not directly support other corona wind measurements.

ENDNOTES

1. Liu, B. Y. H., and A. Kapadia. Combined Field and Diffusion Charging of Aerosol Particles in the Continuum Regime. J. Aerosol Sci. 9:227, 1978.

2. Lawless, P. A., and L. E. Sparks. A Mathematical Model for Calculating Effects of Back Corona in Wire-Duct Electrostatic Precipitators. J. Appl. Phys. 51:242, 1980.

3. Robinson, M. Effects of the Corona Discharge on Electric-Wind Convection and Eddy Diffusion in an Electrostatic Precipitator. HASL-301, Health and Safety Laboratory, U. S. Energy Research and Development Administration, 1976.

4. Isahaya, F. Electrostatic Precipitator Using Ionic Wind for Very Low Resistivity Dusts from High Temperature Flue Gas of Petroleum-Cokes Calcining Kiln. In: Symposium on the Transfer and Utilization of Particulate Control Technology, Volume I, EPA-600/7-79/044a (NTIS PB 295226). P. 453, February 1979.

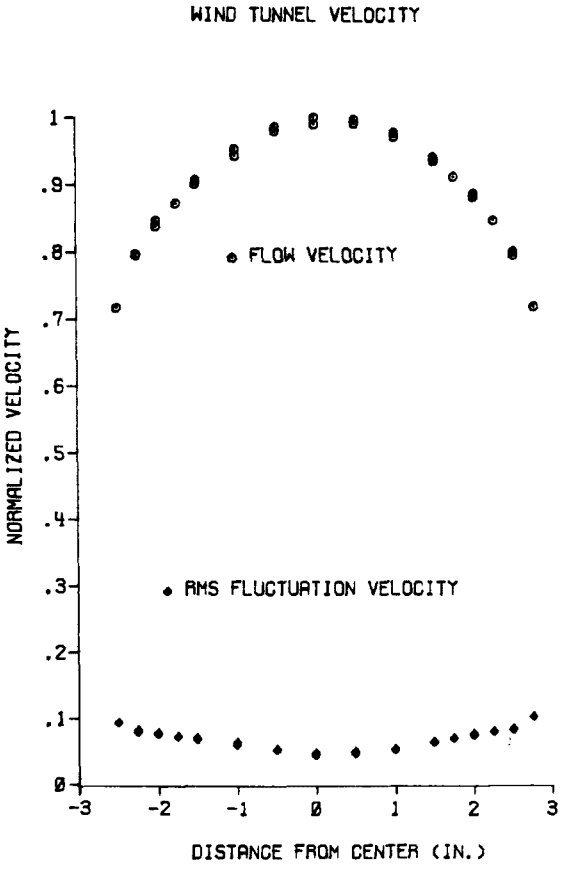

Figure 1. Normalized measurements of flow velocity profile and fluctuation velocity just upstream of ESP. (1.0 = 1.7 m/s)

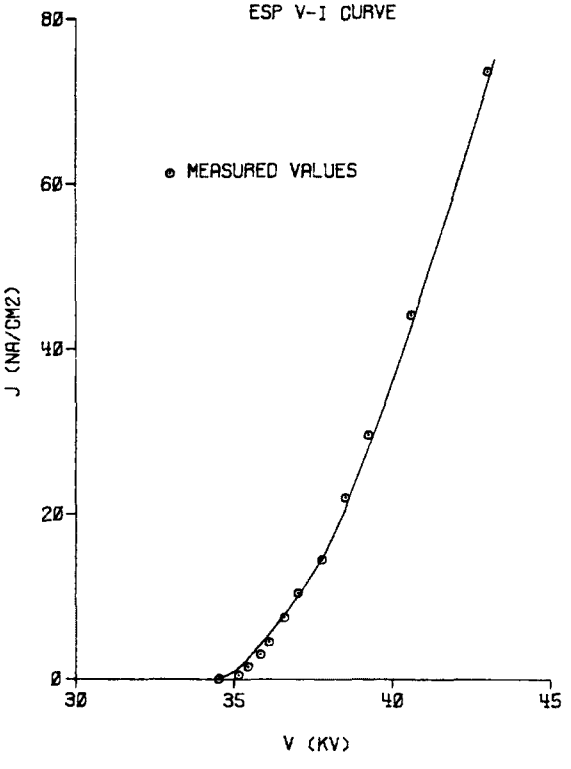

Figure 2. Fit of theoretical model to measured V-I characteristic of ESP.

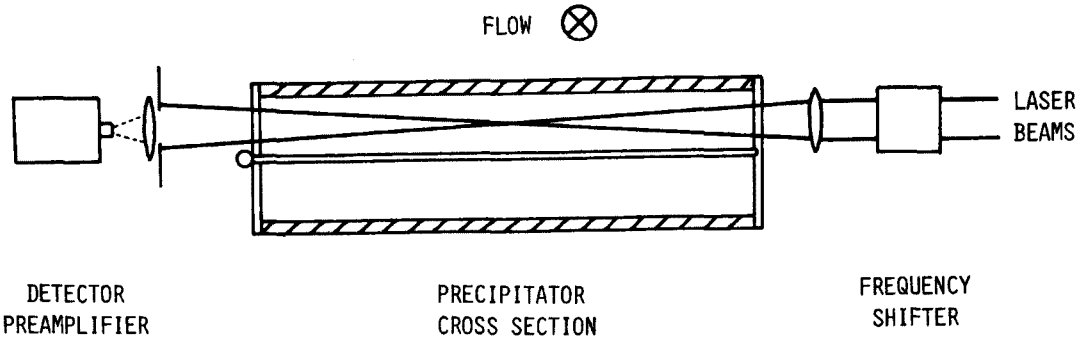

Figure 3. Laser anemometer beam path.

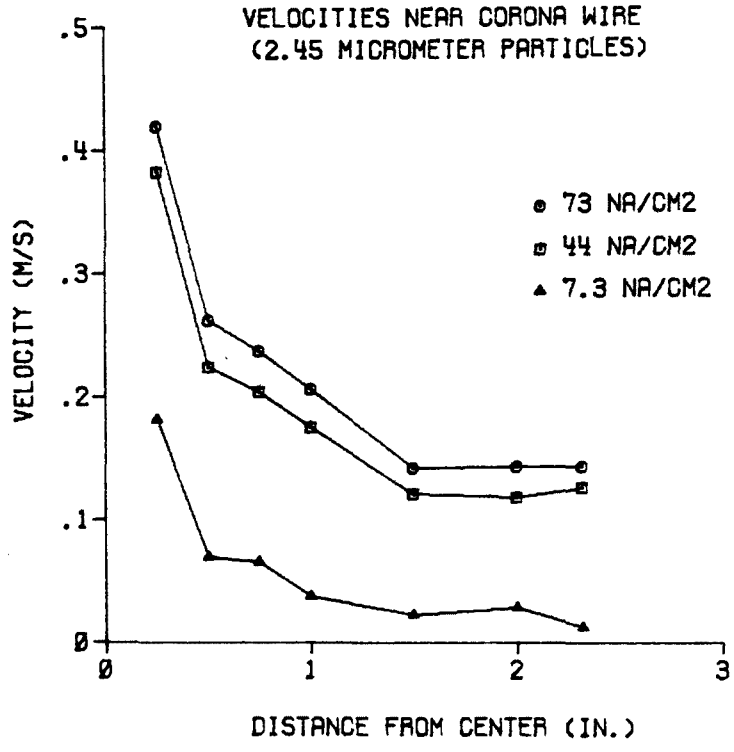

Figure 4. Measured particle velocities as a function of current density.

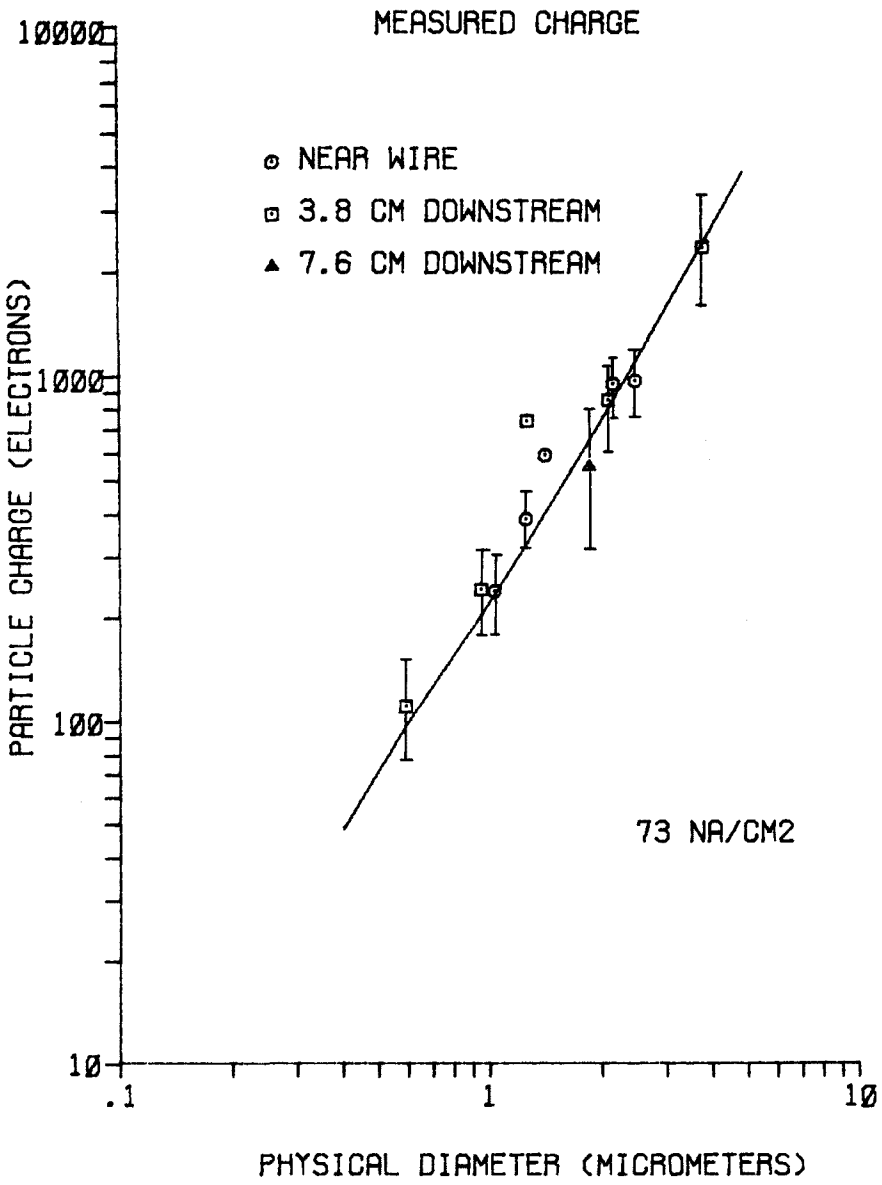

Figure 5. Comparison of charge calculated from measured velocities with theoretical charge calculation.

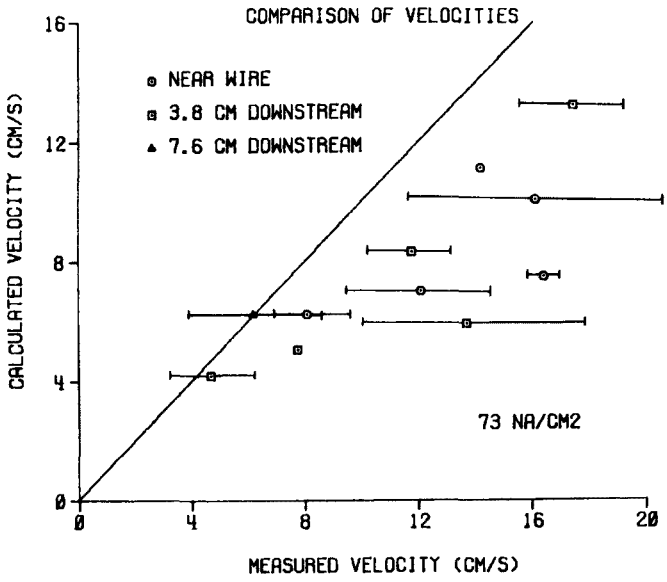

Figure 6. Comparison of measured particle velocities with calculated particle velocities. Line indicates perfect agreement.

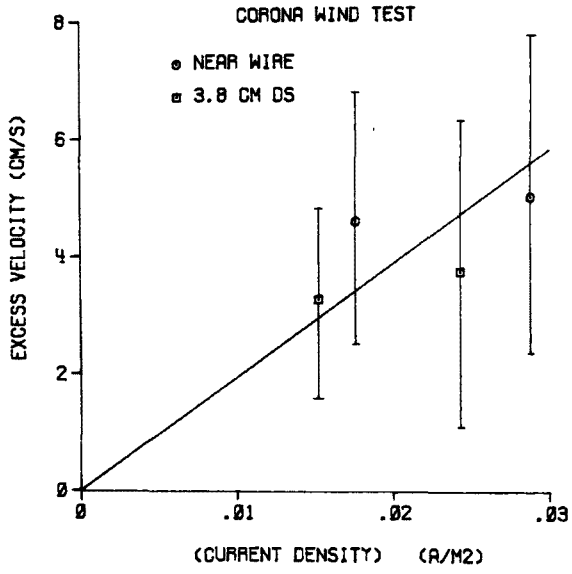

Figure 7. Fit of data to corona wind hypothesis. Line is least-squares determined.

PROGRESS IN MODELING BACK CORONA

By: Phil A. Lawless
Research Triangle Institute
P. O. Box 12194
Research Triangle Park, North Carolina 27709

ABSTRACT

Computer modeling of the electrical conditions in a wire-duct geometry under back corona conditions has been pursued. The model now includes differing positive and negative ion mobilities, ion-ion recombination, and dust layer effects on the current distribution. A simple avalanche breakdown model of the dust layer produces calculable quantities of positive ions over a wide range of parameters and can even be used to explain the V-I curve hysteresis so often observed.

INTRODUCTION

In attempting to model back corona, we aim at understanding the relevance of the phenomenon for particle collection. In particular, quantities relevant to particle charging by unequal bipolar currents are the relative and absolute magnitudes of the positive and negative current densities and the strength of the electric field where charging takes place.

Previous efforts along this line(1,2) were concerned with establishing a computational method and exploring various ad hoc assumptions to attempt to match the near vertical V-I curves and pronounced hysteresis typical of back corona. Where this could be done, the distribution of current along the collector plate was compared with experimental data(3) to test the validity. The initial work(1) was mainly concerned with method and exploration. Later refinements(2) added the effects of a resistive dust layer and resistivity-dependent back corona threshold current density.

In retrospect, the concern with the V-I curve hysteresis was misplaced. Two simple laboratory experiments illustrated this. These were comparisons of the clean plate V-I curves of a laboratory ESP with: 1) V-I curves of the same precipitator with a resistive layer on the plates, corona wire clean; and 2) V-I curves with a resistive layer on the wire, collection plates clean. The first case showed clearly the rapid current rise associated with back corona but no hysteresis. The second showed pronounced hysteresis on an otherwise ordinary V-I curve.

DUST LAYER MODEL

Numerous experiments in our laboratory have demonstrated that back corona occurs when an ion current flows through a porous resistive layer.

The layer must be both resistive and porous. Accordingly, the first element of the model is that back corona occurs because of ionization of the gas in the pores. The second element of the model is a mechanism to sustain the ionization since the production of ions is continuous [at least in some glow modes(4)]. This mechanism is the Townsend avalanche, which also governs the production of the corona at the wire. The avalanche is capable of sustained production of ions in a pore because the probability of photon-induced electron emission from the walls of the pore is high; almost all the photons are absorbed in the walls from the geometry.

The third element of the model is a method of sustaining the electric field in the pore so as to maintain the discharge. The generation of ions in the pore creates space charge clouds which tend to weaken the electric field producing ionization. This is opposed by the flow of negative ions into the dust layer surrounding the pore. The resistive material has an internal electric field due to current flow and its magnitude is maintained into the pore itself, as shown in Figure 1.

The last element of the model is a stabilizing influence, to prevent the discharge from forming arbitrarily large numbers of free ions. This element is the assumption that the positive space charge in the pore attracts most of the negative ions into the pore, leaving only enough to maintain the field in the dust layer. This is possible because the electrical impedance of the gas in the pore goes down as the number of ions goes up.

Combining all the elements in a calculation, the general results shown in Figures 2 and 3 are obtained. The electric field increases linearly with current density until the avalanche occurs, whereupon it remains almost constant. The positive ion current remains small until the avalanche occurs and then rises linearly with continued increases of negative ion current. This rise assumes no recombination of positive and negative ions within the pore, which preliminary calculations confirm. Over wide ranges of photoionization, electron generation, resistivity, and layer thickness parameters, these results hold; the only change is a slight variation of the field at which the avalanche occurs.

In order to illustrate the effect of layer thickness on the field required for breakdown, the field which produced an avalanche gain > 10^8 (ions produced/free electron) was calculated. The equations used were:

$$G = (\alpha/\beta)\exp(\beta d)/\{1 - \gamma(\alpha/\beta)[\exp(\beta d) - 1]\} \qquad (1)$$

where G is the gain, α is the Townsend avalanche coefficient, d is the layer thickness, γ is the feedback fraction, and β is the effective multiplication constant:

$$\beta = \alpha - \eta, \qquad (2)$$

where η is the electron attachment coefficient. Since both α and η are expressed as functions of E/P (electric field divided by temperature-reduced pressure), the breakdown field is also expressed as E/P_o. It is shown in Figure 4 for two values of feedback factor. Note that these results strictly apply only for air; a flue gas may have very different characteristics.

Three conclusions can be drawn from this calculation. One is that the frequency of plate rapping can have a significant effect on layer breakdown through the thickness relationship. Second, a high altitude hot-side ESP might have a layer breakdown field of 11 to 12 kV/cm (E/P = 46 V/cm-torr at a reduced pressure of 250 torr). Third, although the breakdown field corresponding to $\gamma = 0$ is required to initiate the avalanche, once feedback mechanisms (photoionization) are available to maintain the avalanche, the sustaining field is reduced by as much as 30 percent.

The last effect introduces a small but significant hysteresis into the model. Its principal effect is to increase the degree of lateral spreading of the back corona region by moving the electrical conditions in the region adjacent to the pore toward the breakdown values.

CONSEQUENCES OF PORE BREAKDOWN MODEL

In Reference 1, we postulated several models for generating positive ions at the collector plate. The pore model developed here identifies one particular model and quantifies a previously arbitrary constant. The model was formulated:

$$\rho_+ = \beta(j_x - j_{th})/E_o b, \qquad (3)$$

where ρ_+ is the positive ion density at the plate, j_x is the total current density at the plate (sum of positive and negative), j_{th} is the current density at breakdown, E_o is the electric field at the plate, and b is the positive ion mobility. There is assumed to be no generation of positive ions if $j_x < j_{th}$. The pore model sets the value of β at 0.5, and all previously calculated results for that value apply.

In particular, the vertical V-I curve associated with back corona is reproduced well. Figure 5 shows the results from Reference 1 for zero layer thickness. A more detailed calculation, which includes the effect of resistivity on the V-I curve, is shown in Figure 6.

The current directly under a corona wire may be high enough to cause layer breakdown without the threshold being exceeded at positions further away. Figure 7 shows experiment measurements of current density on the plate. These measurements were made with a small area electrode, moved relative to the corona wires in a small precipitator. The back corona was generated by a thin sheet of brown wrapping paper.

The back corona with the wire positive was distributed fairly uniformly under the corona wire; with a negative wire, it was found in patches under the wire and had a greater spread transverse to the direction of the wire. Both polarities showed continuous variation of current along the plates, with sharply defined boundaries, outside of which the current densities were less than the clean plate values. Based on values of the current density at the outer edge of the back corona zone, the resistivity of the layer is estimated as 10^{12} Ω-cm, which is a reasonable value.

Since the generation of positive ions does not commence until the threshold current density in the dust layer is exceeded, the formation of

back corona does not immediately result in severely degraded particle charging. Recent measurements(5,6) have shown that the parameter relevant to particle charging is the ratio of positive and negative current densities.

This ratio increases as the threshold current density is exceeded, approaching one as a limit. Since back corona also spreads to cover the space between wires, there is a range of ratios throughout the corona space. The ratio of current densities immediately adjacent to the plate is shown in Figure 8. These values are similar to those reported in Reference 7. Not shown in this figure is the result that the negative current density outside the back corona region increases only slightly above the prebreakdown values. All the signifcant current increase occurs in the back corona region.

The average electric field in the corona space follows the trend of the voltage: when the voltage stops increasing at breakdown, the field also stops increasing. Thus, the collection field can be assumed to remain at the value it had just prior to breakdown, without undue error.

CONCLUSIONS

A model for breakdown in a dust pore has been constructed, which permits a direct calculation of the V-I characteristics of a wire-plate precipitator. The model produces current distributions which agree qualitatively with experimental data and provides information suitable for use with a time-dependent bipolar charging theory. The overall model indicates that degradation of precipitator performance should be a function of the severity of back corona, as indicated by the level of current density compared to current density at breakdown.

ENDNOTES

1. Lawless, P. A. and L. E. Sparks. A Mathematical Model for Calculating Effects of Back Corona in Wire-Duct Electrostatic Precipitators. J. Appl. Phys. 51:242, 1980.

2. VanOsdell, D. W., P. A. Lawless, and L. E. Sparks. Theoretical Models of Back Corona and Laboratory Observations. In: Proceedings of the Second Symposium on the Transfer and Utilization of Particulate Control Technology. U. S. Environmental Protection Agency Report No. EPA-600/9-80-039b. p. 74.

3. Spencer, H. W., III. Electrostatic Precipitators: Relationship Between Resistivity, Particle Size and Sparkover. U. S. Environmental Protection Agency Report No. EPA-600/2-76-144, May 1976. (NTIS No. PB 257-130)

4. Masuda, S. Back Discharge Phenomena in Electrostatic Precipitators. In: Proceedings of the Symposium on the Transfer and Utilization of Particulate Control Technology. U. S. Environmental Protection Agency Report No. EPA-600/7-79-044a, 1979. p. 321.

5. Fjeld, R. A., E. O. Gauntt, G. J. Laughlin, and A. R. McFarland. Measurement of the Charge on Submicrometer Aerosol Exposed to Bipolar Ions. Proceedings of IEEE-IAS Annual Meeting, 1980. 2:1063, 1980.

6. Fjeld, R. A., R. O. Gauntt, G. J. Laughlin, and A. R. McFarland. The Application of Measurements of Aerosol Charge Acquisition by Bipolar Ions to the Problem of Back Corona. (Presented at the Third Symposium on the Transfer and Utilization of Particulate Control Technology, Orlando, Florida, March 9-12, 1981.)

7. Masuda, S. and Y. Nonogaki. Detection of Back Discharge in Electrostatic Precipitators. Proceedings of IEEE-IAS Annual Meeting, 1980. 2:912, 1980.

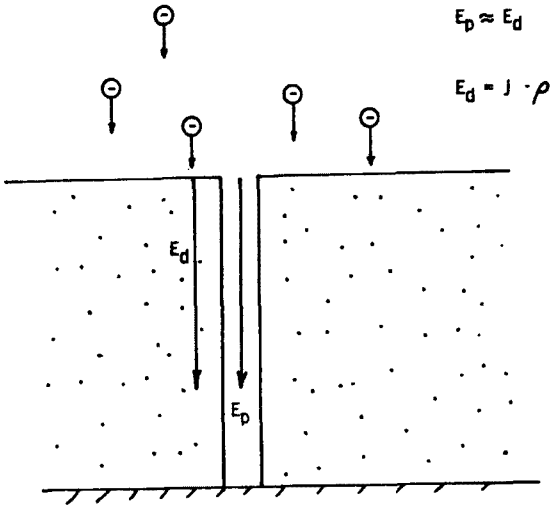

Figure 1. Electric field in pore due to field in dust.

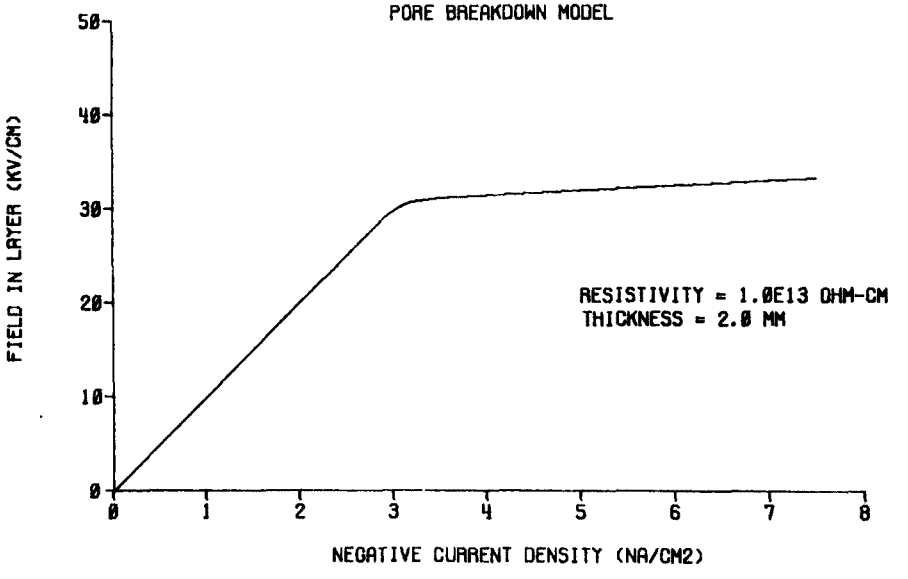

Figure 2. Electric field at breakdown.

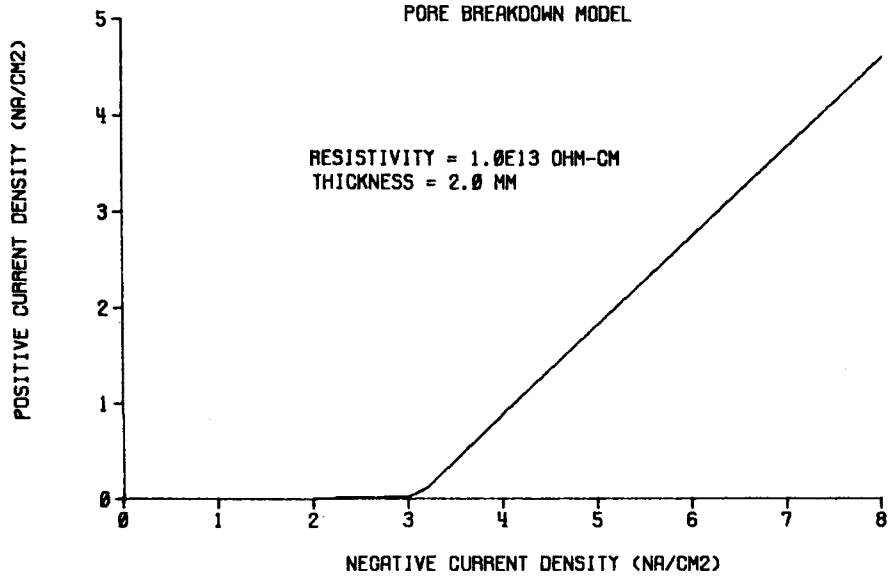

Figure 3. Positive ion generation at breakdown.

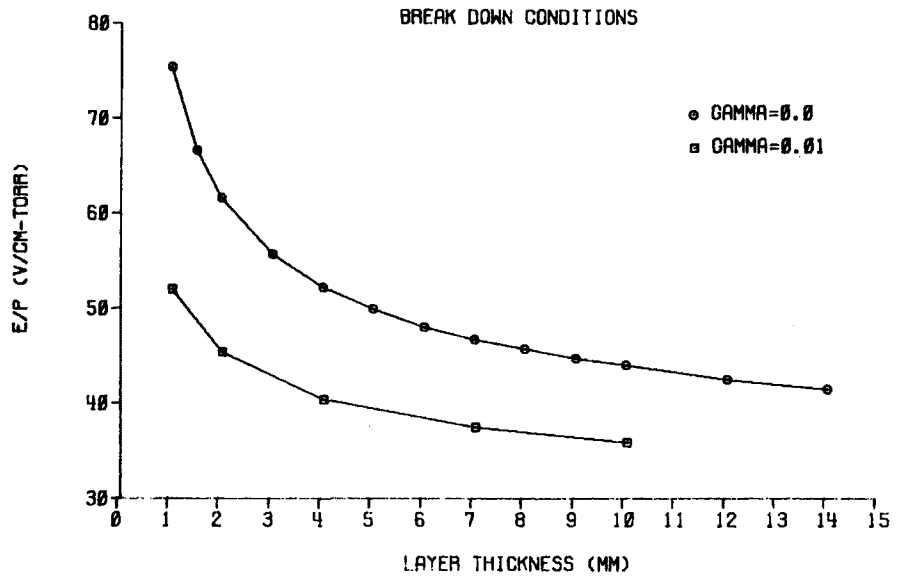

Figure 4. Breakdown field as a function of layer thickness.

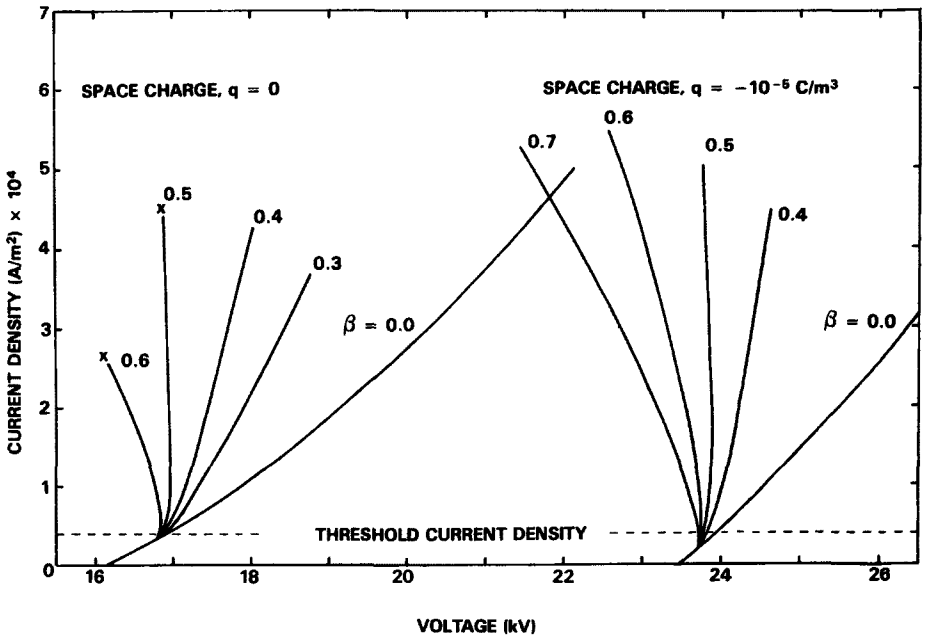

Figure 5. Theoretical V-I curves at zero layer thickness from Reference 1.

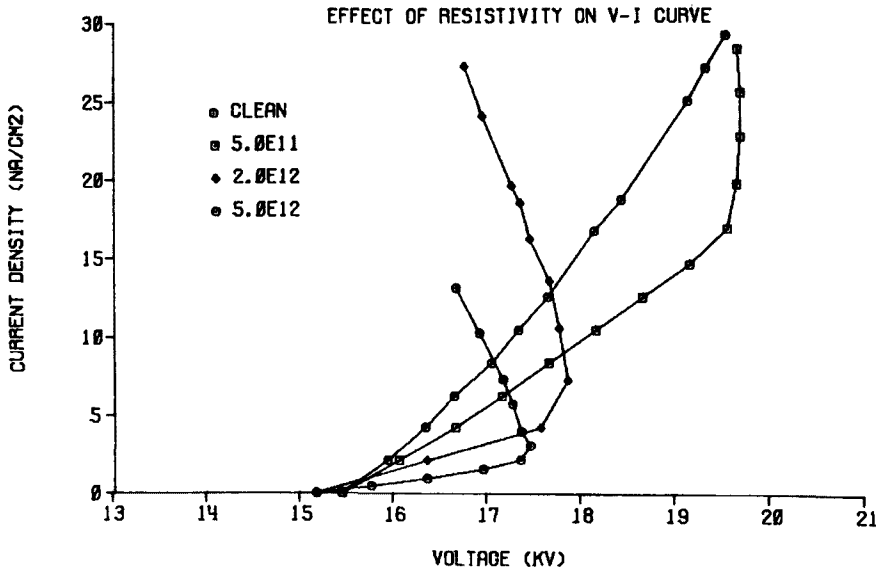

Figure 6. Theoretical V-I curves for $\beta = 0.5$ including resistivity.

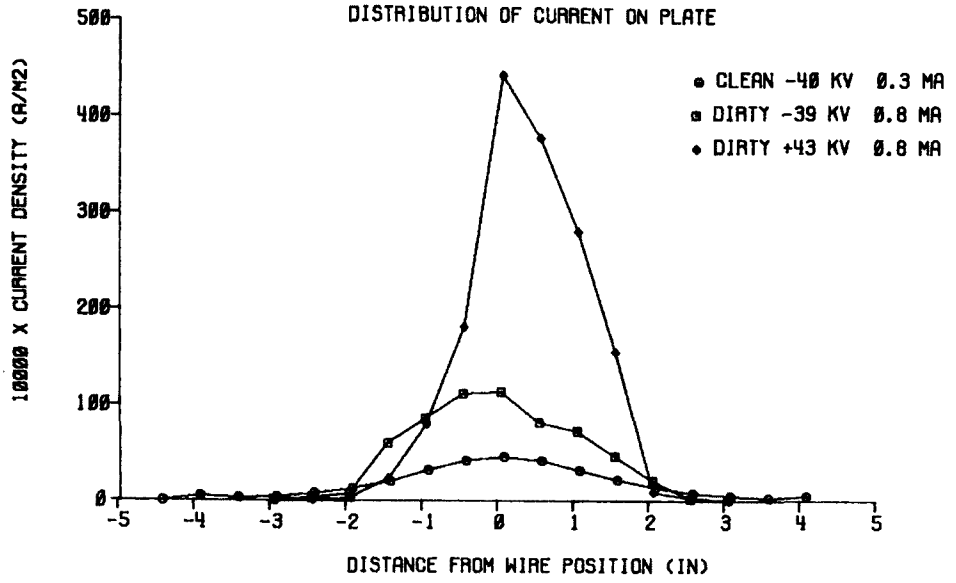

Figure 7. Experimental measurements of current density under a corona wire.

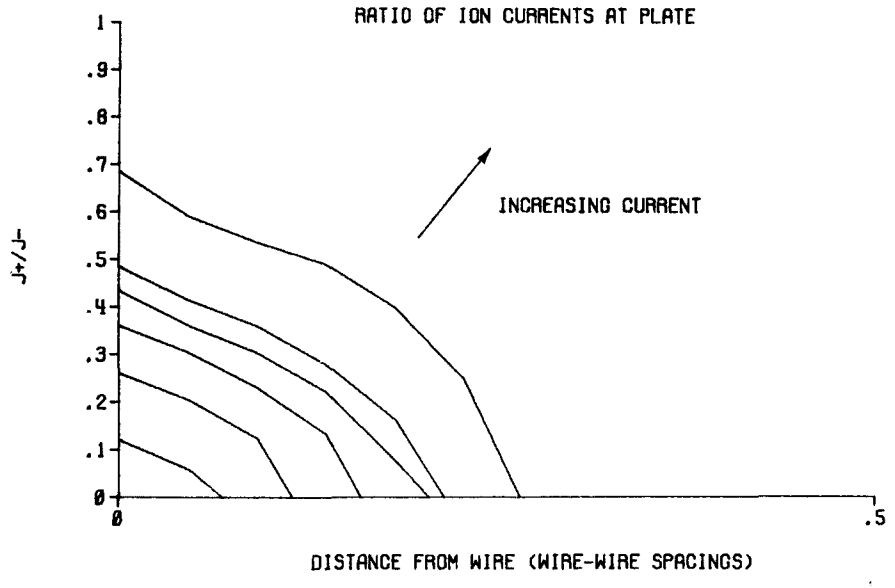

Figure 8. Calculated ratio of positive to negative current densities as a function of distance and total current.

A COMPUTER MODEL FOR ESP PERFORMANCE

By: Phil A. Lawless and J. W. Dunn
Research Triangle Insitute
P. O. Box 12194
Research Triangle Park, North Carolina 27709

Leslie E. Sparks
Industrial Environmental Research Laboratory
U. S. Environmental Protection Agency
Research Triangle Park, North Carolina 27711

ABSTRACT

A computer model has been developed for describing electrostatic precipitator (ESP) performance. It incorporates theoretical calculations of particle charge and electric field, but uses empirical expressions for turbulent diffusion and corona wind effects. Rapping re-entrainment and sneakage losses are accounted for. Using realistic estimates for unmeasured quantities, it can predict the performance of full scale ESPs quite well, if back-corona conditions are not severe. Examples of the performance are shown.

INTRODUCTION

The structure of the model owes a great deal to the work of Southern Research Institute.(1) However, in many instances alternative approaches, thought to possess advantages of accuracy and/or computing speed, have been pursued. Several generations of development separate this model from its predecessors.

Basic Elements of Model

An ESP performance model can be described in four main elements: particle charging, electrical conditions, particle collection, and collection degrading effects. Particle charging occurs generally under high electric field conditions with high ionic densities; a charging model suitable for those conditions is required. The electrical conditions include corona generation, operating electric fields, and ion densities--all of which are influenced by the particulate loading and composition of the flue gas. Particle collection must be realistically described in terms of combined diffusive and directed velocity components; the flow conditions found in most ESPs are neither laminar nor highly turbulent. The collection degrading effects include bypassing of sections (called sneakage), rapping re-entrainment, and velocity maldistribution. The occurrence of back-corona as a degrading effect is not considered in this model because it influences all four elements in various ways.

These elements are all interacting. Particle charging conditions are influenced by the electrical conditions, but the electrical conditions are a function of the particulate space charge, which is also influenced by the amount of material removed by the collection process. Insofar as the collection degrading mechanisms influence the amount of material in a given zone

of the ESP and its state of charge, then they too interact with the other elements. Without some simplifying assumptions, a computer model quickly becomes an exercise in bookkeeping.

An overview of the interaction of these elements is shown in Figures 1 and 2. Figure 1 identifies the relationship of two of the collection degrading effects to the overall operation of one electrical section. The first simplifying assumption made is that all the particulate of a given size going into the next section has the same charge. Figure 2 shows some of the detailed calculations that go on in the "electrical section" block of Figure 1. The electrical section is divided into subincrements of length. The second simplifying assumption is that for short enough increments, the particulate collection process does not seriously affect the electrical conditions for that increment and may be considered separately. The third assumption is that the particle charging conditions are adequately described by an average electric field and an average ion density in the subincrement.

PARTICLE CHARGING

The particle charging theory of Liu and Kapadia(2) has been adapted to this model by analytic approximations to their numerical results. The theory itself is a continuum theory in which the diffusion equation for ions in the presence of a polarized particle is solved numerically. There is no distinction between the classical "field" and "diffusion" charging. All particles charge continuously in the presence of ions, although the rate of charging becomes quite small for large particles. There are no arbitrary constants in the theory, yet it fits published experimental data quite well, 5 to 10 percent on the average.

The theory predicts that large conducting particles acquire up to 30 percent more charge than dielectric particles of the same size. The differences are much lower for smaller particles. The approximations used in our model produce particle charges intermediate between the two theoretical cases. Overall, it is thought that the approximations used do not seriously alter the estimates of accuracy of the theory.

Approximation to Theory

The equations describing the approximation are:

$$n = \gamma r k T (4\pi\varepsilon_o)/e^2, \tag{1}$$

where n is the number of elementary charges on a particle of radius r; γ, a dimensionless charge; k, Boltzmann's constant; T, absolute temperature; ε_o, the free space permittivity; and e, the electronic charge

$$w = eE_o r/kT, \tag{2}$$

where w is a dimensionless electric field; and E_o, the external electric field.

$$\tau = \pi\mu e N_o t/(4\pi\varepsilon_o), \tag{3}$$

where τ is a dimensionless time; μ, ion mobility; N_o, ion density; and t, exposure time.

The connecting equation is:

$$\gamma = \tau/(1 + \tau)[A + B\ln(0.1 + \tau)], \quad (4)$$

where A and B are functions of w, given by:

$$A = 4.642 + 1.770\ w, \quad (5)$$

$$\text{and } B = 1.059 + 0.238\ w. \quad (6)$$

The relationship of the approximation to the results of the theory is shown in Figure 3.

ELECTRICAL CONDITIONS

The electrical conditions are calculated by a finite difference approximation to Maxwell's equations.(3) The approximation is based on directly solving for electric field components, rather than solving for space potentials and differentiating to obtain the electric field components. The resulting algorithm is better suited to a computer model because it converges faster than a space potential calculation and the limits of error are better characterized.

Aside from the different method of computation, it should be noted that this model correctly accounts for the effect of particulate space charge on the corona current and electric fields. The charged particles are assumed to be immobile and do not, therefore, contribute to the collector plate current. Their presence does add to the electric field in the corona zone; if enough particulate is present, the corona current is severely reduced or quenched completely. The effect of particulate space on corona current is shown in Figure 4, calculated for the inlet section of one of the test cases. As the particulate space charge is removed by collection, the amount of current that flows increases dramatically.

PARTICULATE COLLECTION

Since Reynolds numbers calculated for the flow conditions in precipitators are less than 2×10^4 most of the time, the flow cannot be said to be "highly turbulent," and the assumption of a uniform concentration of particles across the flow cross section is unreasonable. A particle collection model was formulated based on the combined effects of turbulent diffusion and a wall-directed velocity.

The value used for the eddy diffusion coefficient is an average of experimental values.(4) The coefficient varies with position in the duct, approaching zero at the walls. The normalized variation with position is shown in Figure 5. The value of the midline coefficient is calculated from an analytic fit to the experimental results:

$$D = 6.37 \times 10^{-7}\ (N_{re} - 4000)^{2/3}, \quad (7)$$

where D is the eddy diffusion coefficient (m^2/s); and N_{re}, the Reynolds number in the duct. The values of D are only 10 to 20 times the values for molecular diffusion in air.

If we assume that the diffusion takes place in one dimension only, in a plane perpendicular to the walls and with a drift velocity toward the walls, then a line source of particles would spread accordingly to:

$$c(x,v,t) = \exp[-(x - vt)^2/4Dt]/\sqrt{4\pi Dt}, \quad (8)$$

where c is the relative concentration of particles; x, the distance from the flow streamline corresponding to the source; v, the velocity; and t, the time allowed for the substance to diffuse.(5) If, instead of a line source, a source of finite breadth is used, the concentration downstream of the source is given by:

$$c(x,v,t) = c_o/2 \left\{ \text{erf} \left\{ [x_1 - (x - vt)]/\sqrt{4Dt} \right\} - \text{erf} \left\{ [x_2 - (x - vt)]/\sqrt{4Dt} \right\} \right\} \quad (9)$$

where c_o is the initial concentration of particles located between positions x_1 and x_2 in the duct.

To use this one-dimensional collection process, the following conventions are used. Boundary pairs x_1 and x_2 are chosen so that five equal blocks span the distance from the midline of the duct to the wall. For a given particle radius, r, the velocity toward the wall is calculated by Stokes' law:

$$v = qEC/6\pi\eta r, \quad (10)$$

where q is particle charge; E, the local electric field; C, the Cunningham correction factor; and η, the gas viscosity. The diffusion constant calculated from Equation 7 and Figure 5 is assumed to apply for all particle sizes.

The amount of material crossing each boundary toward the wall and toward the center is calculated by integrating Equation 9 with respect to time, but the time interval is kept short enough that the average distance traveled by a particle in a given block is less than half the length of the block. At the end of the time interval, the amount of material in each block is totaled and assumed to be distributed uniformly throughout the block for the next time interval. Collection occurs at the wall because no particles are allowed to leave the wall.

Corona Wind Transport

Experimental measurements of corona wind transport (6) have indicated that it plays a significant role in ESP performance.

The velocity due to corona wind is assumed to provide a moving frame of reference in which the Stokes' law applies. The resulting velocity used in the collection process is the sum of the Stokes' velocity and the corona wind velocity, which is given by:

$$v_{cw} = k\sqrt{j}, \quad (11)$$

where k is an empirical constant; and j, the average current density. The experiments also show that corona wind increases the effective diffusivity of the gas stream; the diffusion constant is given by:

$$D_{cw} = 0.75\ kj/\bar{v}\ , \qquad (12)$$

where $\bar{v}$ is the average linear flow velocity. The constant, k, in Equations 11 and 12 is dependent on $\bar{v}$ and is given by:

$$k = 24.2 - 6.7\ \bar{v}\ , \qquad (13)$$

with $\bar{v}$ in SI units.

COLLECTION DEGRADING MECHANISMS

Sneakage

Sneakage, or bypassing of the collection stage, is assumed to occur for an entire electrical section. The particles bypassing the section are added to the outlet concentration at the end of each section. An important effect is that the gas flow through the section is also reduced by the sneakage fraction, resulting in improved collection of the fraction passing through. The net result is that the effect of sneakage is not very important if each electrical section is only moderately efficient.

Gas Velocity Maldistribution

In the model, particle treatment time is determined by $\bar{v}$, the mean flow velocity. By examining the effects on the performance of a single section as $\bar{v}$ was varied, empirical corrections for the performance were obtained. For relative standard deviations, σ_g, up to 0.5, the effect is not strong. The relative standard deviation is given by:

$$\sigma_g = (v_{rms}^2 - \bar{v}^2)^{\frac{1}{2}}/\bar{v}\ , \qquad (14)$$

where v_{rms} is the root mean square of all the velocities in the ESP; for $\sigma_g < 0.5$, $\bar{v}$ is replaced by v_{rms} in all the calculations. At $\sigma_g = 0.5$, this amounts to a 12 percent change in particle treatment time. At higher standard deviations, a stronger correction is applied, but these are not often encountered in practice.

Rapping Re-Entrainment

Rapping re-entrainment is based upon measurements performed for EPRI.(7) In the model, these measurements have been analyzed and expanded. Based on analysis of the results published, a different average rapping puff distribution was used for hot-side ESPs from that for cold-side ESPs. Also, the material re-entrained has been assumed to be proportional to that present on the plates for each section.

OPACITY CALCULATION

Using a light-scattering program, optical extinction cross sections were calculated for all the particle sizes in the model. The refractive index used was (1.525 - 0.05 i), which is generally in the range found for fly ash. These coefficients enable a rapid calculation of the total extinction cross section from the outlet particle concentrations and an estimation of opacity based upon various stack diameters.

TESTS OF MODEL

The data used to test the model have been published (7), with the exception of the United McGill ESP. The data for that unit are reported at this symposium.

The results of four fits are shown in Figures 6-9. The data were fit by assuming a sneakage fraction of 0.1 for all units, by using the wire roughness factors to fit the reported voltages and currents, and by choosing rapping re-entrainment fractions to give agreement with the measured penetrations. The rapping puff distributions derived from Reference 7 were used for the first three units, and a measured distribution was used for the last. The agreement with the measured values is generally good, but depends strongly on the actual rapping puff distribution.

CONCLUSIONS

This performance model is capable of good simulations of ESP operation. Although its predictive ability is limited by inclusion of empirical rapping distributions, its fundamental structure allows for inclusion of theoretical quantities as they become available.

ENDNOTES

1. McDonald, J. R. A Mathematical Model of Electrostatic Precipitation (Revision 1). Industrial Environmental Reserach Laboratory-Research Triangle Park, U. S. Environmental Protection Agency. EPA-600/7-78-111a and b (NTIS PB 284614 and 284615), 1978.

2. Liu, B. Y. H., and A. Kapadia. Combined Field and Diffusion Charging of Aerosol Particles in the Contiuum Regime. J. Aerosol Sci. 9:227, 1978.

3. Lawless, P. A., and L. E. Sparks. A Mathematical Model for Calculating Effects of Back Corona in Wire-Duct Electrostatic Precipitators. J. Appl. Phys. 51:242, 1980.

4. Page, F., Jr., W. G. Schlinger, D. K. Breaux, and B. H. Sage. Point Values of Eddy Conductivity and Viscosity in Uniform Flow Between Parallel Plates. Ind. and Eng. Chem. 44:424, 1952.

5. Jost, W. Diffusion in Solids, Liquids, Gases. New York, Academic Press, 1960.

6. Robinson, M. Effects of Corona Discharge on Electric-Wind Convection and Eddy Diffusion in an Electrostatic Precipitator. HASL-301, Health and Safety Laboratory, U. S. Energy Research and Development Administration, 1976.

7. Gooch, J. P., and G. H. Marchant. Electrostatic Precipitator Rapping Re-Entrainment and Computer Model Studies. Electric Power Research Institute Report No. EPRI FP-792, 1978.

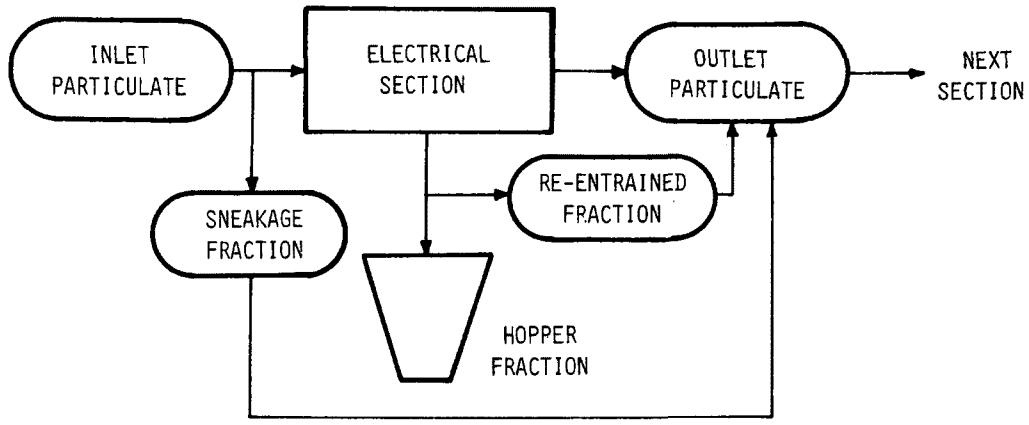

Figure 1. Schematic of model calculations for one precipitator section.

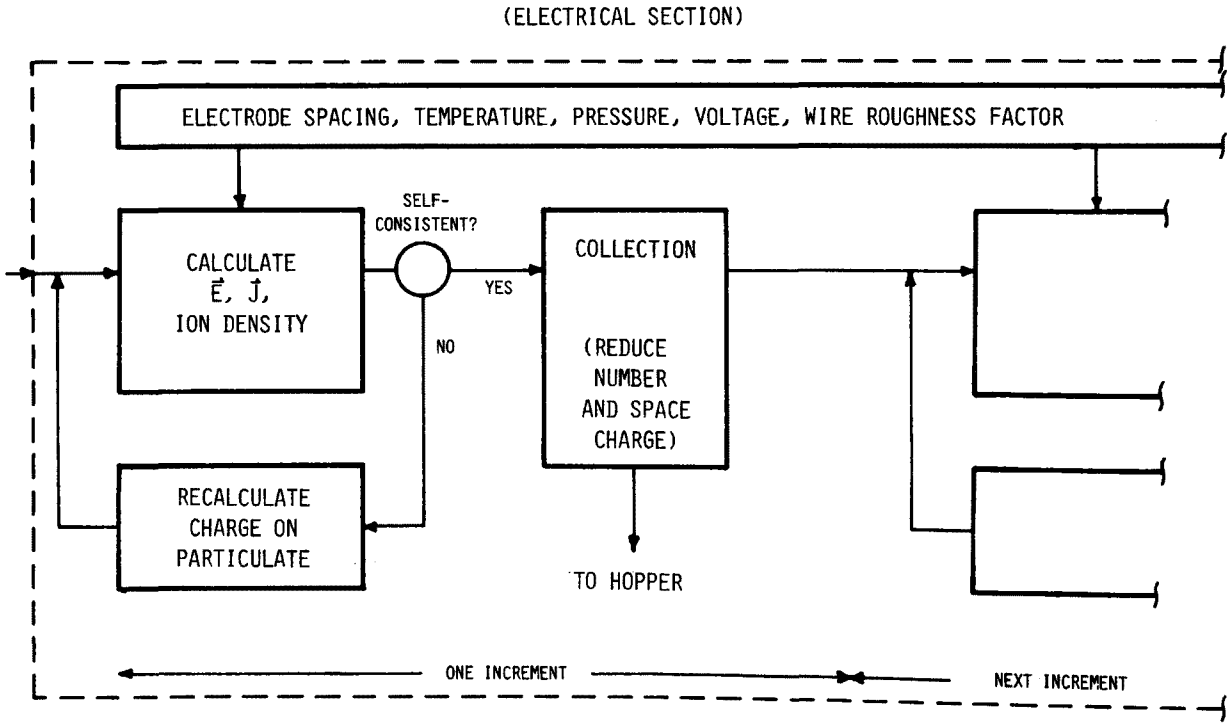

Figure 2. Schematic of model calculations within an electrical section.

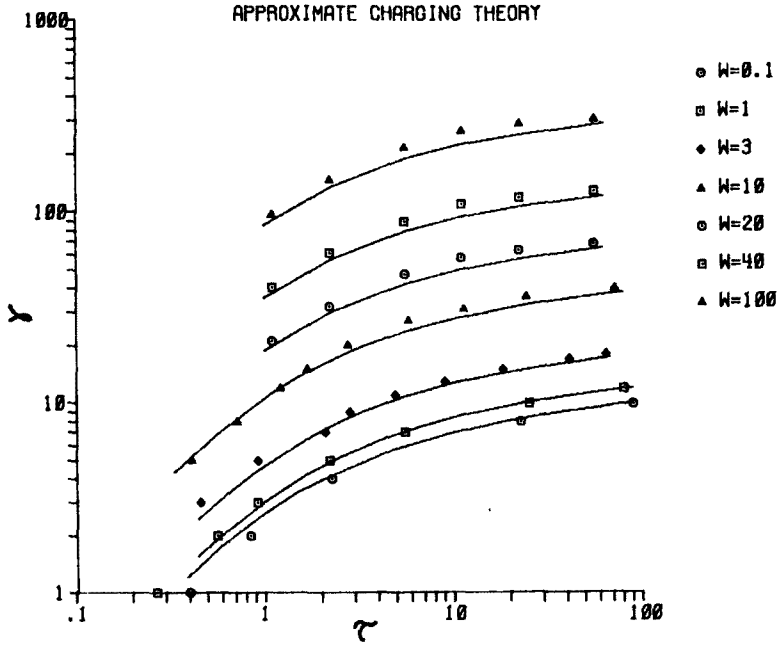

Figure 3. Comparison of the exact charging theory (symbols) for conducting particles with the approximations (lines).

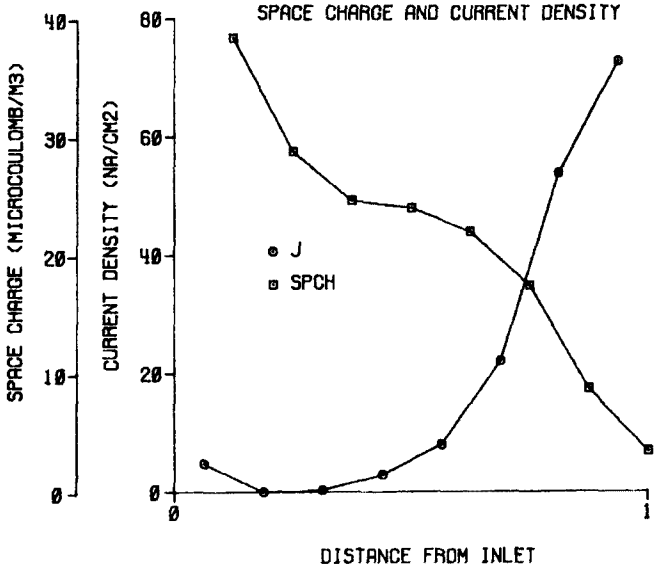

Figure 4. Model calculations of particulate space charge and current density for the inlet section of an ESP.

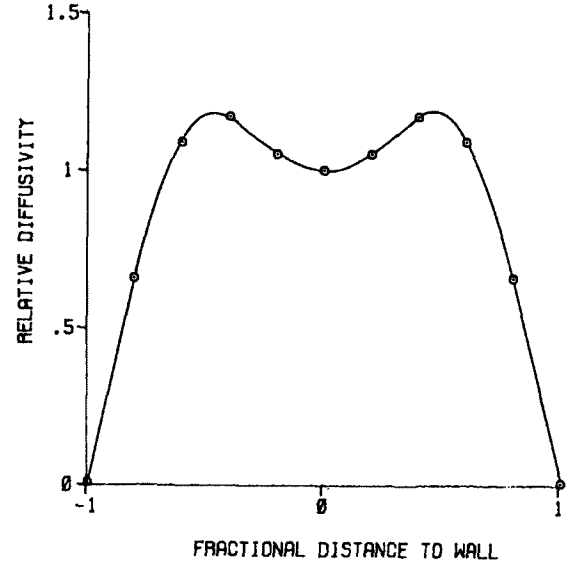

Figure 5. Averaged variation of experimental diffusivities with distance from the center of the flow lane.

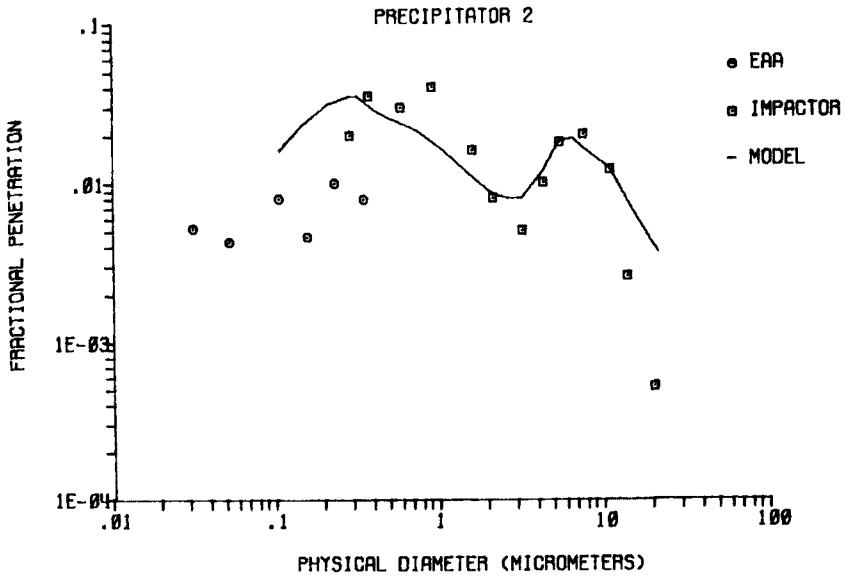

Figure 6. Cold-side precipitator. Rapping re-entrainment factor (RR) = 0.1/section. Calculated penetration = 0.0098; measured penetration = 0.0043. Calculated opacity (2m path) = 6%.

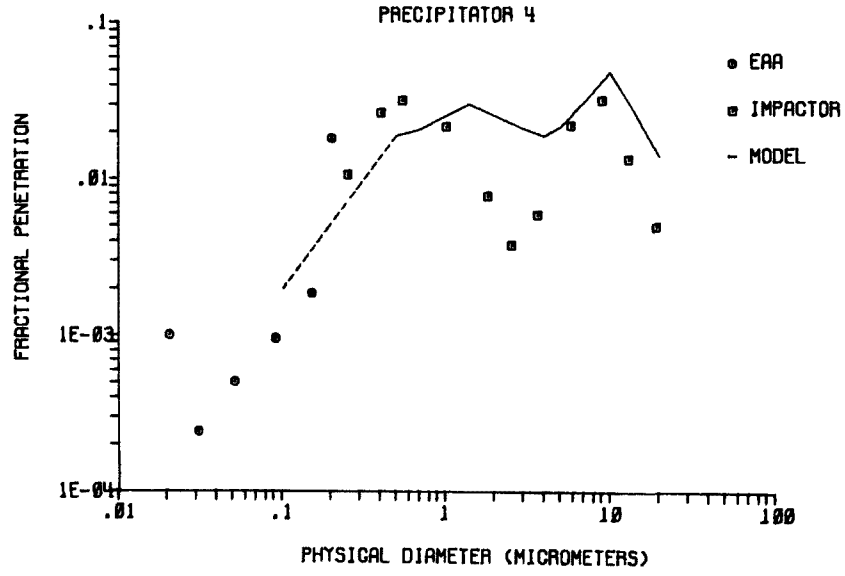

Figure 7. Hot-side precipitator. RR = 0.2/section. calculated penetration = 0.0061; measured penetration = 0.0077. Calculated opacity = 5%; measured opacity = 7%.

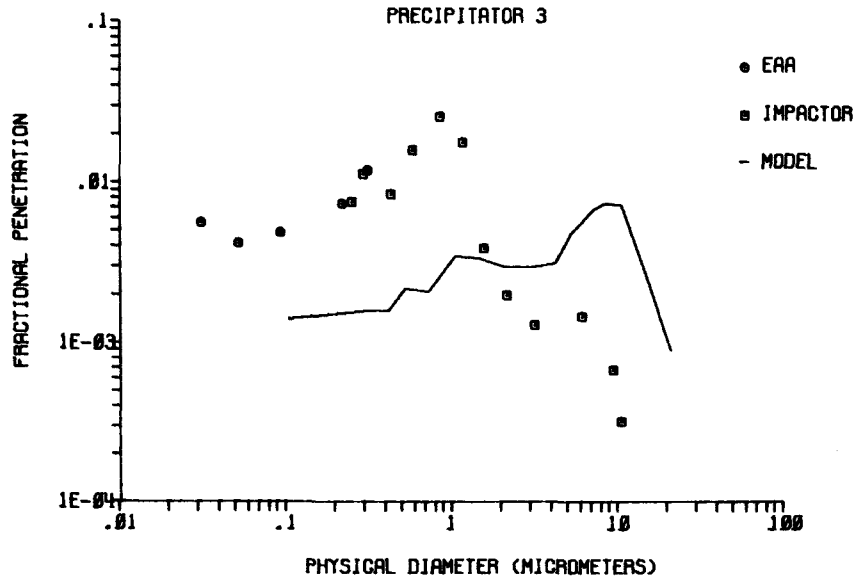

Figure 8. Cold-side precipitator. RR = 0.1/section. Calculated penetration = 0.0013; measured penetration = 0.0019. Calculated opacity = 0.8%; measured opacity $\leq$ 2.5%.

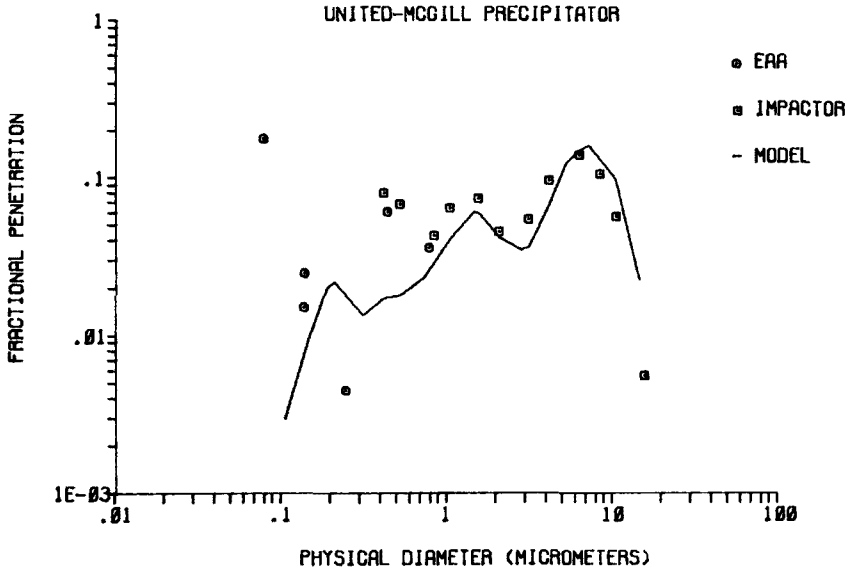

Figure 9. Cold-side precipitator with measured rapping puff. RR = 0.3/section. Calculated penetration = 0.038; measured penetration = 0.061. Calculated opacity = 6%; measured opacity = 7%. Calculated space charge = 2.9 x 10^{-7} C/m^3; measured space charge = 1.7 x 10^{-7} C/m^3.

MEASUREMENT AND INTERPRETATION OF CURRENT DENSITY DISTRIBUTION AND CHARGE/MASS DATA

By: Michael Durham
George Rinard
Don Rugg

Denver Research Institute
University of Denver
P.O. Box 10127
Denver, Colorado 80210

And

Leslie E. Sparks
U.S. Environmental Protection Agency
Industrial Environmental Research Laboratory
Research Triangle Park, N.C. 27711

ABSTRACT

Techniques have been developed for measuring current density distribution (CDD) and charge-to-mass ratios (Q/M) in electrostatic precipitators. These measurements have been used to analyze the operation of standard and novel precipitator concepts. Corona current density distribution is measured by a plate consisting of 96 isolated 5 cm squares. By means of a picoammeter and a switching box, the current from a single square or a combination of squares can be measured. This device has been used to analyze the performance of several corona geometries as well as the effect of pulsed excitation. Experimental data are presented and interpretation of results are described.

The measurement of Q/M is done by an in-stack faraday cage device. Details of the design of the probe are presented, and sampling precautions are described. The role of particle size distribution in interpreting Q/M data is also discussed.

INTRODUCTION

As part of an EPA funded research project, the Denver Research Institute evaluated several conventional and novel charging and collecting devices to determine their characteristics when used with high resistivity dusts. One of the symptoms of back ionization induced by high resistivity is the uneven distribution of corona current. To help understand the nature of this problem, a current density distribution (CDD) plate was designed and fabricated. This plate was installed in the EPA/IERL-RTP pilot precipitator and used to determine the characteristics of several corona electrodes under dc and pulsed excitation.

In order to evaluate and compare different precharging concepts in a two-stage electrostatic precipitator scheme, a charge/mass (Q/M) sampler was

designed, fabricated, and tested. Although, charge measurements had been made in the past, there was no reported research on whether the charge measured was actually carried by the particles or due to free ions entering the sampler. Therefore, a series of experiments was undertaken to determine the legitimacy of Q/M measurements.

CURRENT DENSITY DISTRIBUTION (CDD) MEASUREMENTS

The current density distribution (CDD) plate is a 1.2 m (4 ft) square collector plate containing a section located next to the downstream edge of the plate and midway up the plate and was subdivided so that current measurements could be made. There were 96 electrically isolated subdivisions each 5 cm (2 in.) square with 12 subdivisions in the direction of the flow and 8 subdivisions vertically. Each subdivision was connected by means of a switch matrix so that the current in an individual subsection could be measured while the rest of the subsections were connected to ground.

Current Density Measurements for DC Electrodes

Tests were run on several corona electrode configurations all with 22.9 cm (9 in.) plate to plate spacing. The corona electrode configurations were 0.32 cm (1/8-in.) wires spaced 22.9 cm (9 in.), 0.32 cm (1/8-in.) wires spaced 7.6 cm (3 in.), and a grid electrode consisting of a woven wire mesh with 0.16 cm (1/16-in.) wires on 2.5 cm (1 in.) centers. The data were taken with the precipitator operation at 149°C (300°F). Two levels of current density were used for the wire electrodes. The first was 0.15 mA corresponding to 5 nA/cm^2. The second was 1.5 mA corresponding to 50 nA/cm^2. The screen electrode was operated at 0.2 mA, which corresponds to 6.67 nA/cm^2.

Figure 1 gives the clean plate current distribution for 0.32 cm (1/8-in.) wires spaced 22.9 cm (9 in.) apart with an average current density of 5 nA/cm^2. As can be seen from this figure, the current density is zero over nearly half of the plate, and the peak current density measured in the sampling section is more than 20 times the average current density. Figure 2 gives the current density distribution for the same conditions when the plate was covered with dust having an electrical resistivity of approximately 2×10^{12} ohm cm. As can be seen from this figure, the current density over most of the plate is zero with current occurring at a very small portion near the left-hand side of the current sampling section. It should be noted that in this case most of the current is flowing in the unsampled portion of the plate. The operating voltage in Figure 1 for the clean plate was 28.3 kV while that when the plate was dirty was only 15 kV. Even at this low current density, the plate was operating in back corona when dust was present.

Figure 3 gives the current density distribution for 0.32 cm (1/8-in.) wires spaced 22.9 cm (9 in.) with an average current density of 50 nA/cm^2. From this figure it is clear that the current density is much more uniform at this higher average value. The peak current density under these conditions barely exceeds twice the average current density.

Figure 4 is for the same configuration but when operating with high resistivity dust. While the current under these conditions is considerably less uniform than when clean, the current density distribution for the 50 nA/cm^2 average density is considerably better than it was when the average current density was 5 nA/cm^2. There were regions in this case where the current density was essentially zero and the peak current density was about 8 times the average current density. The operating voltage under clean characteristics was 35 kV and that when the plate was dirty was 17.7 kV, indicating that the dirty plate was in back corona.

Figure 5 gives the results for 0.32 cm (1/8-in.) wires spaced 7.6 cm (3 in.) for average current density of 50 nA/cm^2. The peak current density is 3 to 4 times the average current density, and the current density is zero over approximately 20 percent of the plate. Figure 6 is the same configuration with the high resistivity dust layer. Under these conditions approximately 40 percent of the plate was at zero current density, and the peak current density was 20 times the average current density. The operating voltage for the clean plate with 7.6 cm (3 in.) wire spacings was 37.7 kV while that for the dirty case was 19.3 kV, indicating that the dirty plate was operating in back corona.

Comparisons of Figures 1 through 6 indicate that, while a slightly higher operating voltage can be obtained with 7.6 cm (3 in.) wire spacing over that for 22.9 cm (9 in.) wire spacing, there is considerable degradation in the current density distribution for the closer wire spacing for a given average current density. These figures also show that the effect of back ionization is to further deteriorate the uniformity of the current density distribution.

Figure 7 gives the current density distribution for a 0.16 cm (1/16-in.) woven wire electrode operating at an average current density of 6.7 nA/cm^2. No clean plate characteristics are given for this configuration, since in this case the current at all points over the current sampling section was zero for all values of average corona current density up to 150 nA/cm^2. Figure 7 indicates that the current is zero over 80 to 90 percent of the sampling plate area. The peak current density was 60 times the average current density.

After the above test the ESP was opened and the sampling plate examined. The area in the upper left corner of the current sampling plate exhibited pock marks evidently as a result of back ionization. There was correspondence between the number of marks on a current sampling subsection and the magnitude of current measured.

Figures 1 through 7 indicate that the best average current density distribution for both clean and dirty characteristics was obtained with 22.9 cm (9 in.) wire spacing. Attempts to obtain more uniform current density by utilization of closer wire spacing or grid electrodes would not be successful. Furthermore, in the presence of high resistivity dust, back corona greatly affects the uniformity of the current density distribution. This effect is least noticeable for wire spacings of 22.9 cm (9 in.).

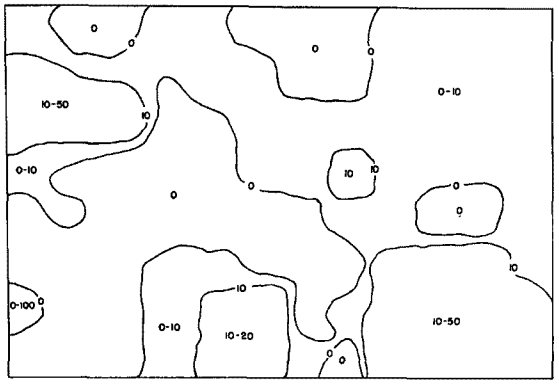

Figure 1. Average Current 5 nA/cm^2, Wires Spaced 22.9 cm (9 in.), Clean Conditions.

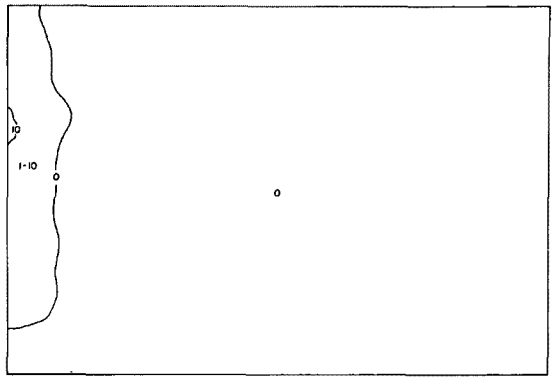

Figure 2. Average Current 5 nA/cm^2, Wires Spaced 22.9 cm (9 in.), Dirty Conditions.

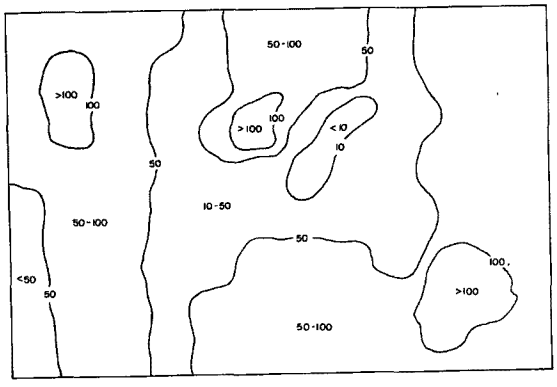

Figure 3. Average Current 50 nA/cm^2, Wires Spaced 22.9 cm (9 in.), Clean Conditions.

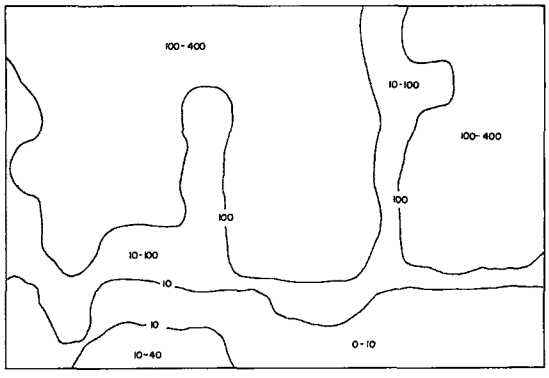

FIGURE 4.

Figure 4. Average Current 50 nA/cm^2, Wires Spaced 22.9 cm (9 in.), Dirty Conditions.

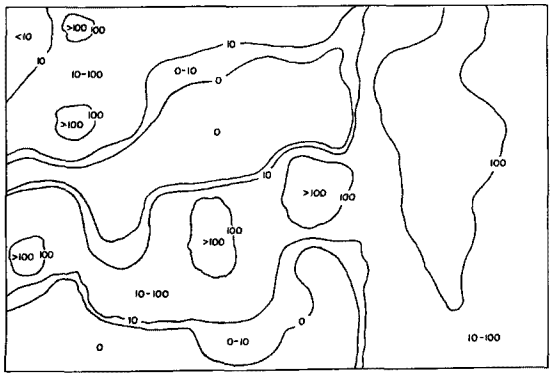

Figure 5. Average Current 50 nA/cm^2, Wires Spaced 7.6 cm (3 in.), Clean Conditions.

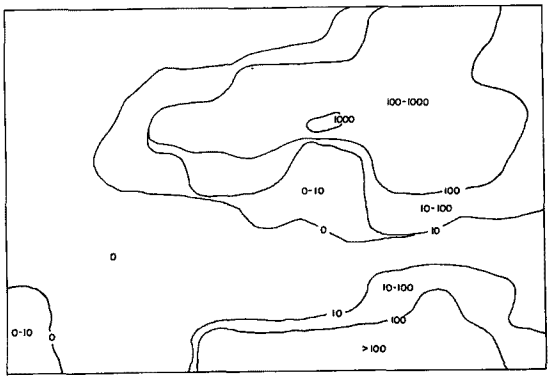

Figure 6. Average Current 50 nA/cm^2, Wires Spaced 7.6 cm (3 in.), Dirty Conditions.

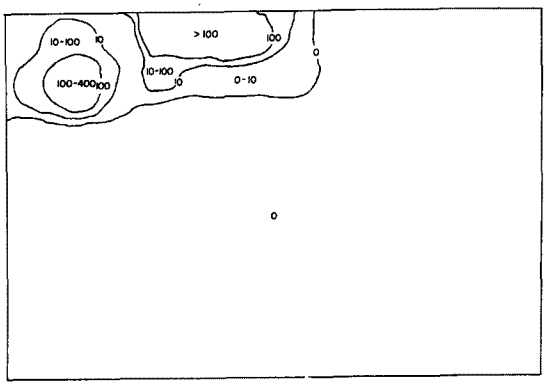

Figure 7. Average Current 6.7 nA/cm^2, Grid Electrode, Dirty Conditions.

Comparison of Current Density Distribution for dc and Pulsed Excitation

To determine the effectiveness of pulsed excitation in producing a more even current distribution, tests were run at ambient temperature and pressure on conventional wire electrodes and on a 0.63 cm (1/4-in.) rod electrode.

Corona current density distributions for the 0.16 cm (1/16-in.) wire electrodes were measured and the results appear in Figure 8. Figure 8(a) shows that the current distribution was quite uniform for dc excitation at an average current density of 50 nA/cm^2. Corona current was measured in all cells and the maximum cell current measured was only 1.6 to 1.8 times the average or less than 80 nA/cm^2.

The dc voltage was reduced from 38 kV to 27.5 kV, and the average current density decreased from 50 nA/cm^2 to 6.4 nA/cm^2 (see Figure 8(b)). The current distribution became more uneven as the current density was decreased. There was no current on 21 percent of the plate area. On one cell the current was 4 times the average value which corresponds to 25.6 nA/cm^2. Although the average current density was reduced by a factor of 8, localized current densities were reduced by only a factor of 3. This indicates that even under clean electrode conditions local current densities may be high when the average current density is low.

The current density distribution for pulse excitation of the 0.16 cm (1/16-in.) wire electrode is shown in Figure 8(c). Corona current was measured in all cells, and the maximum value was only 1.4 times the average. The current density distribution was essentially constant for an average current density of 6.7 nA/cm^2. These results show that for low average current densities the corona current is more uniformly distributed over the collector plates with pulse excitation than with dc excitation.

The characteristics of 0.63 cm (1/4-in.) rod electrodes with pulse excitation were also measured. Current distribution measurements showed that

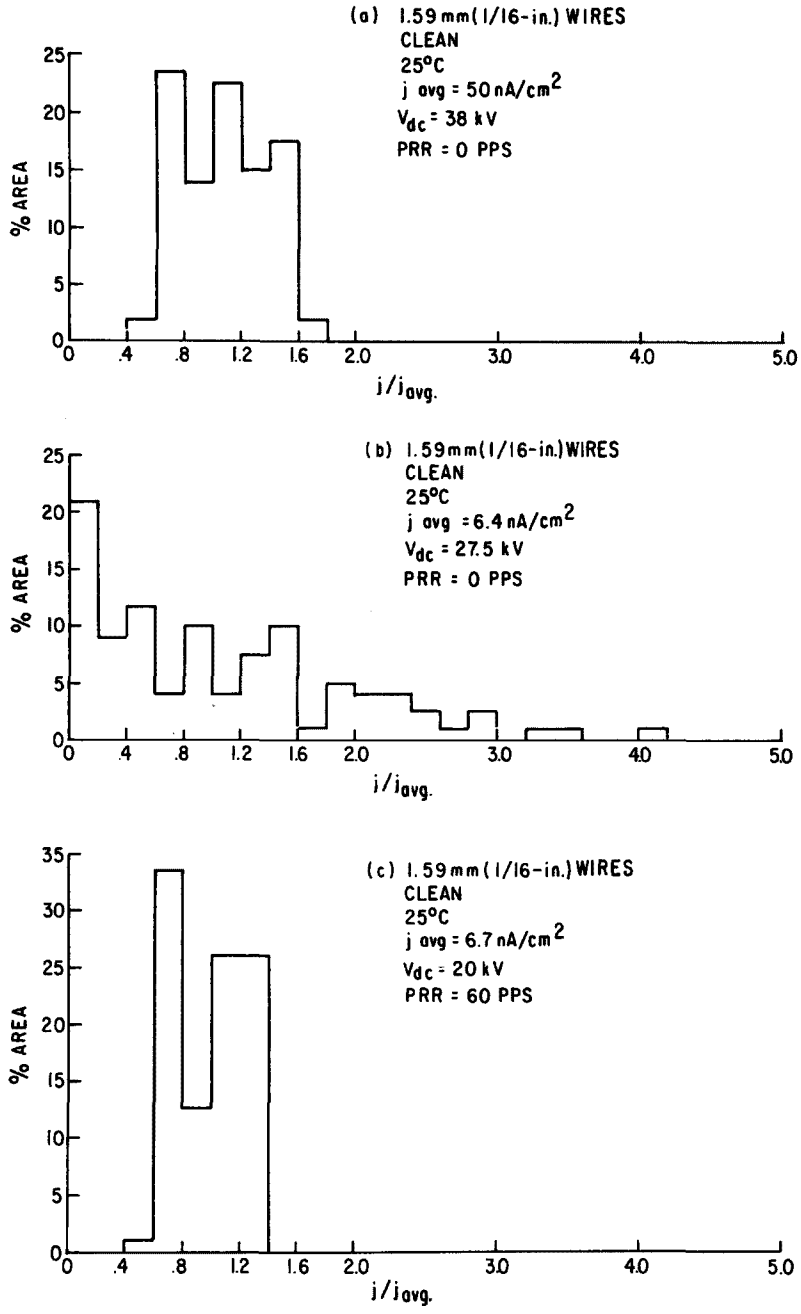

Figure 8. Current Density Distributions for 1.59 mm (1/16-in.) Wire Electrode.

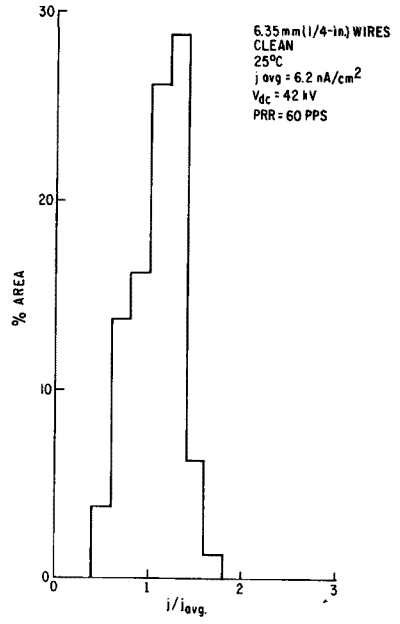

Figure 9. Current Density Distribution for 6.35 mm (1/4-in.) Wire Electrode with Pulse Excitation

for dc excitation at low current densities, 96 percent of the collector plate area had no current and the maximum current density was more than 40 times the average current density. For pulse excitation the 0.63 cm (1/4-in.) rod electrode characteristics were similar to the 0.16 cm (1/16-in.) wire electrode. The VI curve for a dc bias of 40 kV and a PRR of 60 pps shows the dc current density can be controlled at levels less than 10 nA/cm^2. Figure 9 shows that the current distribution is uniform for pulse excitation.

The current density measurements indicated that a high degree of control can be maintained over the current distribution using pulsed excitation. When these tests were repeated at 149°C with dirty conditions (Rugg et al., 1981), the distribution of current under dc excitation became more nonuniform while pulsing continued to produce an even distribution.

CHARGE/MASS MEASUREMENTS

In order to investigate the charging characteristics of different electrode configurations and various charging devices, it was necessary to develop a device for measuring the charge-to-mass ratio of the particles. The first model built consisted of a Gelman filter holder electrically isolated in a grounded stainless steel casing by means of two Teflon pipe nipples. The particles flowed through an electrically shielded probe to the filter holder where they were collected on a glass fiber filter. The charge on the particles was drained through a picocoulombmeter to ground and measured across an internal capacitor in the meter. To avoid the possibility

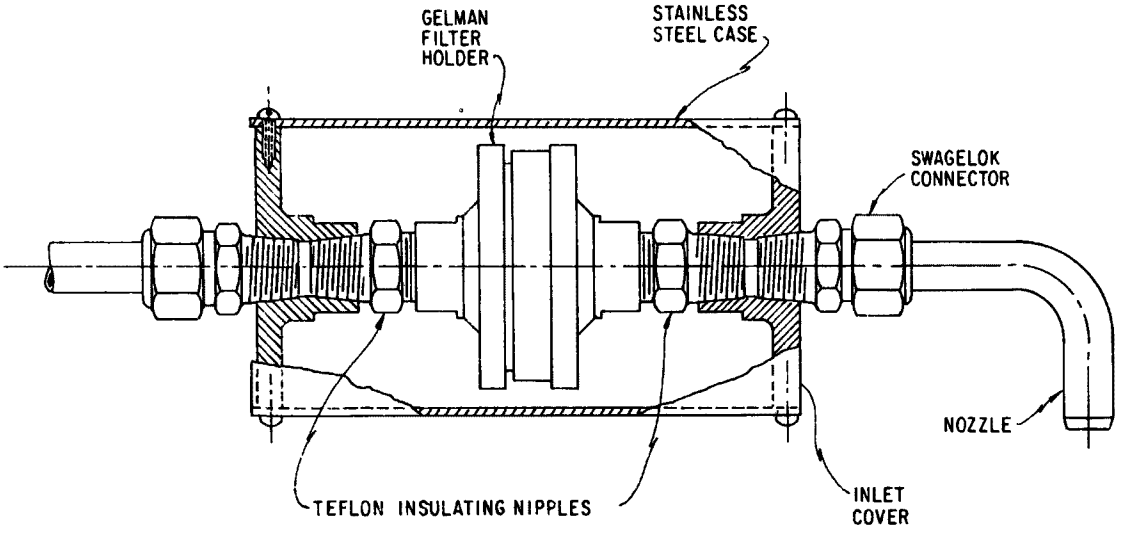

Figure 10. DRI Charge/Mass Sampler

of losing particles and charge in the probe, a special electrically shielded probe and nozzle were designed. The probe consisted of an inner stainless steel tube contained within a grounded stainless steel tube. The inner tube was electrically isolated from the grounded tube by sandwiching a Teflon tube between them. The charge would then be drained from the probe along with the charge on the filter, and the probe would be washed after each test so that the mass collected on the probe could be analyzed along with the filter weight. Thus the total charge-to-mass of all particles entering the nozzle could be analyzed.

Although this system produced useful information, several problems were encountered. The probe and filter casing were bulky and difficult to manage. Since the probe had to be cooled and washed after each test, the turnaround time between each test was long. In addition it was difficult to maintain a leak-tight system. Because of these problems the sampler was redesigned to look like that shown in Figure 10.

The current DRI in-stack charge/mass sampler consists of a Gelman filter holder electrically isolated by two Teflon nipples and contained in a stainless steel grounded housing. The housing prevents particles from impinging onto the outside of the filter holder and imparting a charge. Four nozzles, 0.32 cm, 0.635 cm, 0.95 cm, and 1.27 cm in diameter, are used for connection to the inlet cover so that isokinetic sampling can be maintained in a variety of flow conditions. A 1.3 cm diameter pipe is connected to the outlet cover which served as both a probe support and means of withdrawing a sample through the filter holder. The back of the probe support is connected by

means of a flexible tube to a condenser, dryer, pump, gas meter and orifice meter. The sampling system is leak-tight from the nozzle to the outlet of the sampling system.

When making a Q/M measurement in a stack, the velocity is measured and then an isokinetic flow rate is calculated. The stack gas is pulled through the nozzle to the glass fiber filter which removes all the particles. The charge on the particles drains through the filter holder to a picoammeter (Keithley Model 616) by means of a coaxial cable fastened to the rear of the filter holder and exiting through a hole in the outlet cover. A second coaxial cable is used to connect the picoammeter common to ground at the probe. This prevents currents on the outside of the probe and transient RF fields in the precipitator from causing errors in the charge measurements. After the test the accumulated charge across an internal capacitor in the meter and the volume of air sampled are recorded, and the mass collected on the filter is measured. This allows calculation of the charge to mass, charge to volume, mass loading, and percent isokinetic; all of which are important parameters in evaluating the data. The charge-to-volume measurement is useful in determining when there is a space charge limitation to the precharger. Mass loading can be used to determine how well the precharger collects.

One of the first concerns about making Q/M measurements in a cavity downstream of a precharger was the effect of the electric fields created by the charged particles. Theoretical analysis showed that, if the operating voltage and current of the precharger were high enough, the space charge produced by the particles would create electric fields sufficiently high to induce the nozzle to go into positive corona. Emission of positive ions at the tip of the nozzle would discharge the particles as they entered the nozzle thus producing false Q/M measurements.

To avoid this problem, a corona shield was designed to fit over the nozzle and inlet cover. This shield was made of 58 percent open perforated screen to allow minimal interference of the air flow. A hole was cut in the shield so that there was no obstruction directly in front of the nozzle. The shield creates an equipotential surface around the probe that prevents the sharp-tipped nozzle from going into corona. The shield was tested in the laboratory by placing it 11.5 cm from a high voltage plate. Without the shield the nozzle went into corona when the field strength was raised to 4.8 kV/cm. When the corona shield was placed over the probe, the field strength was raised to 8.3 kV/cm and sparking occurred, but the probe did not go into corona.

To determine the effect of the shield on the aspiration of particles into the nozzle, comparisons were made of the mass concentrations measured with and without the shield in the duct of a pilot precipitator. Results showed no difference between the mass concentration measured using the shield. Tests were then run after a precharger to compare Q/M results with and without the screen. Tests showed that although the amount of mass collected on the filter did not change, the measured charge was reduced by a factor of 5 when the screen was removed. This indicated that without the

screen the nozzle was going into corona and discharging the particles as they entered the nozzle.

Another concern about sampling in the close vicinity of a high voltage corona source was the possibility that some of the measured charge might be due to ions. If it were possible for ions to reach the filter, they would produce false measurement because, although they are charged, they contain no measurable mass. To investigate this possibility, experiments were performed in the laboratory.

The first experiment involved placing a high voltage across a needle placed inside the grounded nozzle producing corona. When the pump was turned on, a small amount of current (1-10 pA) was measured on the filter. This was less than 1 percent of that measured during a Q/M measurement. When smoke was blown into the area, the charge on the filter increased substantially, leading to a conclusion that particles were required to carry the charge to the filter. The small current measured, it was concluded, was probably due to the charging of the naturally occurring dust in the laboratory atmosphere.

To test this hypothesis under simulated conditions, a mockup of the APS High Intensity Ionizer was constructed to scale. Two 2.83 m^3/min (1000 cfm) blowers were connected to the ionizer to produce the appropriate velocity. Two large absolute filters were placed in series with the blowers to remove any particles existing in the laboratory. A voltage of 95 kV was applied to the ionizer producing 1.3 mA of current. The charge-to-mass probe was set up to sample at the outlet of the ionizer. The current measured at the filter was only 0.7 pA which was less than 0.1 percent of the current normally measured during a test. When one of the filters was removed, allowing unfiltered air through the ionizer, the current increased to 60 pA. When a smoke bomb was set off at the entrance to one of the blowers the current increased to 13 nA.

Another set of experiments was performed with a fine mesh brass screen cage placed in front of the ionizer, and the current to the cage was measured. When both filters were connected to the blowers, the current to the cage was 127 pA. However, when one filter was removed and a smoke bomb set off, the current increased to greater than 1 μA. These results verify that the ions not only don't reach the filter, but also they do not make it out of the ionizer unless transported by dust particles. This means that the charge-to-mass measurements are legitimate, and all the charge reaching the filter is due to charged particles. These experiments indicate that with reasonable care to eliminate corona from the probe, to sample isokinetically, and with good laboratory techinque, reliable Q/M data can be obtained. However, care must be exercised in interpreting the data since Q/M is dependent on particle size distribution.

Interpretation of Q/M Data

Figure 11 shows a comparison of the distribution of mass and charge for $\sigma = 2.0$ and $\sigma = 4.5$. The shift of the charge distribution to the left is due to the fact that the charge is proportional to d^2 while the mass is

proportional to d^3. The amount of the shift is proportional to the standard deviation of the distribution σ because σ determines the proportion of fine particles. It can be seen that although 50 percent of the mass is contained in particles larger than the mass mean diameter (i.e., $d/\bar{d}_m > 1$), less than 7 percent of the total charge is included in these particles.

Because of the sensitivity of the Q/M data to the particle size distribution, it is necessary to measure and report both the mass median diameter and the geometric standard deviation to give meaning to the value of Q/M. This also means that the Q/M measurement is sensitive to correct sampling technique, because an isokinetic sampling leads to non-representative amounts of the larger particles and inaccurate mass concentrations, while the charge remains relatively constant.

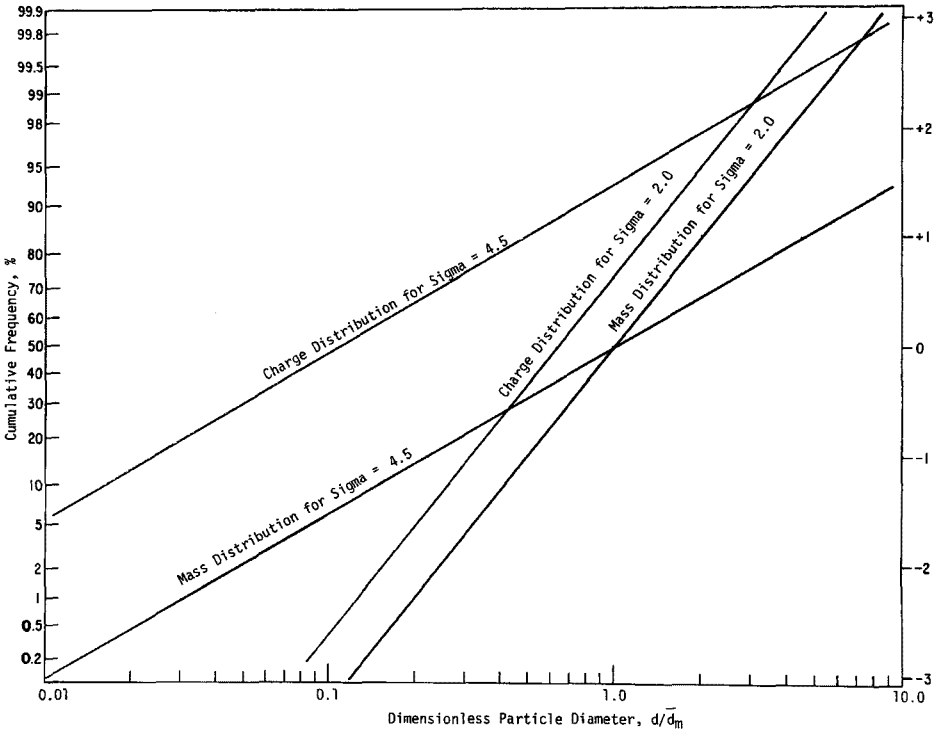

Figure 11. Comparison of the Distribution of Mass and Charge as a Function of Particle Size

CONCLUSIONS

The Current Density Distribution plate is a useful tool for evaluating the effect of back ionization on the current distribution in a collecting section. Current density values, obtained by dividing the total current by the total collecting area, are inaccurate and can be extremely misleading in the case with high resistivity dusts.

The Charge/Mass measurement is a relatively easy measurement to make if the proper precautions are taken to ensure isokinetic sampling and to shield the electrometer from sparking and RF. When making Q/M measurements, it is necessary to also make impactor measurements so that the Q/M data can be given meaning with particle size data.

REFERENCES

Rugg, D., Durham, M., and Rinard, G., (1981). Electrostatic Precipitator Performance with Pulse Excitation. Presented at the Third Symposium for the Transfer and Utilization of Particulate Control Technology, Orlando, Florida, March 9-12.

THE RELATIONSHIP BETWEEN GAS STREAM TURBULENCE AND COLLECTION EFFICIENCY IN A LAB-SCALED ELECTROSTATIC PRECIPITATOR

By: B. E. Pyle, J.R. McDonald, W.B. Smith
Southern Research Institute
2000 Ninth Avenue South
Birmingham, AL 35255

ABSTRACT

The interaction between the gas flow turbulence and the electric migration properties of charged particles in an electrostatic precipitator (ESP) has received considerable interest insofar as its effects upon collection efficiency have not been well understood. Toward this end, experimental measurements of the turbulence transport properties of micron sized particles have been carried out in a laboratory scale ESP of conventional wire/plate design. The results of these measurements are compared with the theoretical predictions of an ESP mathematical model based upon a turbulent mass-transport principle. The degree to which turbulent mechanisms influence collection efficiency is found to depend largely upon other operating parameters such as mean downstream gas velocity and the electrical migration velocity.

INTRODUCTION

Many of the mathematical models of electrostatic precipitation currently in use are based upon applications of the Deutsch equation(1). In this relation, the particle collection efficiency (η) can be expressed as

$$\eta = 1 - \exp(-wL/vb) \qquad (1)$$

where w is the electrical migration velocity, L is the active length of the precipitator, v is the average downstream gas velocity, and b is the separation distance between the corona electrode and the collection plate. Equation (1) implicitly assumes that the gas stream turbulence is sufficient to maintain a uniform particle concentration at any point in the precipitator. However, experimental evidence has shown that this is not always a realistic assumption(2).

Other models of precipitation have been developed by a number of authors(3,4,5). These models are based on solutions to a turbulent mass transport equation of one form or another. Applica-

tions of these models have been restricted in the past by computational difficulties, either with the solutions themselves or the limited availability of computer time and efficient algorithms. Practical results from these solutions have also been limited due to the lack of information available regarding the values of the turbulent diffusion coefficients of micron sized particles. We have carried out a series of investigations designed to correlate the predictions of turbulent diffusion model with the experimental results obtained using a laboratory scale electrostatic precipitator (ESP) illustrated in Figure 1.

THEORY

The theoretical predictions in this report were obtained from both the Deutsch relation, Equation (1), and a turbulent mass transport equation of the form(3)

$$D \frac{\partial^2 C}{\partial x^2} - w \frac{\partial C}{\partial x} = v \frac{\partial C}{\partial z} \qquad (2)$$

where C is the particle concentration at an arbitrary point(x,z). The variable z is measured from the ESP inlet and x from the plane of the corona electrodes toward the collecting plate. D is the coefficient of turbulent diffusion, w is the electric migration velocity, and v is the mean downstream gas velocity. These variables are illustrated in Figure 2 for a wire-plate geometry ESP.

In the inlet plane we have assumed the general condition that

$$C\ (x,o) = C_0(x) \qquad (3)$$

so that the effects of a nonuniform inlet loading could be investigated. Along the plane of the corona discharge electrode (corona wires for a wire dust geometry), the particle concentration must satisfy the condition

$$D \frac{\partial C}{\partial x} - wC = 0 \text{ at } x = 0 \text{ for all } z>0. \qquad (4)$$

This boundary condition simply requires that there be no net mass transfer across the plane of the corona electrodes. Because of the uncertainty of the exact nature of the particle concentration at the collector plates, the general condition

$$D \frac{\partial C}{\partial x} - fwC = 0 \text{ at } x = b \text{ for all } z>0 \qquad (5)$$

was assumed where b is the separation between the corona electrode and collecting plate, and f is a wall factor that governs the degree of particle reentrainment from the collector plate back into the gas stream(5). For all the conditions studied for this

paper we have assumed that no reentrainment occurs so that f = 0. This boundary condition (equation(5)) is discussed in detail by other authors(5,6).

Equations(2) through(5) were solved numerically using a second-order-correct Crank-Nicolson finite difference technique (7). For the case of the laboratory scale ESP shown in Figure 2, the duct was divided into six zones each centered on a corona wire. For each zone except the first, the inlet particle concentration profile was assumed to be that profile existing at the outlet of the previous zone. The set of finite difference equations were applied in each zone over a 21 x 21 rectangular mesh resulting in a system of 19 algebraic equations. The coefficient matrix for this set of equations is tridiagonal and the solutions were obtained using an algorithm developed by Thomas(7).

The collection efficiencies predicted by the turbulent diffusion model (equations(2)-(5)) are compared with those of the Deutsch relation (equation(1)) in Figure 3. For these calculations a uniform inlet loading was assumed. The ESP length was 91 cm with a wire to plate spacing of 10 cm and the mean gas was 193 cm/s. Figure 3 illustrates that at large values of D the predictions of the two models converge as expected. The influence of gas turbulence on collection efficiency is also seen to be greater at higher values of migration velocity. At small values of w there is essentially little difference in the predictions of either model.

EXPERIMENT

The apparatus used in this study was a laboratory scaled electrostatic precipitator of conventional design as illustrated in Figure 1. Typically the system has a volume flow rate of 3.5 x 10^5 cm^3/s at a mean gas velocity of approximately 190 cm/s. At the lowest level of gas flow turbulence, the velocity profile at the precipitator section is uniform with a standard deviation in velocity of 20 cm/s. The precipitator section has a total possible collection plate area of 2.5 x 10^4 cm^2 and a plate-to-plate separation of 20 cm. The air flow is self contained and passes through an absolute filter before being recirculated.

Aerosol particles can be isokinetically injected as a point source in the all plastic region, just upstream of the precipitator. To produce a uniform inlet loading, the particles are injected at the fan inlet where the turbulent actions of the fan and turning vanes are sufficient to randomize the spatial distribution of the particles. The concentration of particles at the precipitator outlet is mapped as a function of position by an isokinetic aspirating probe whose position is controlled by a minicomputer via an x-y traversing mechanism. Connected to the probe is a Climet optical particle analyzer operating at 118 cm^3/s.

The values of the coefficient of turbulent diffusion, D, were measured by injecting micron sized particles as a point source at the ESP inlet and then mapping their exit locations in the outlet plane. This resulting data was then reduced as outlined elsewhere(8) to yield values of D for various micron sized particles. Different levels of gas turbulence were produced by using a system of cylindrical obstructions and perforated plates upstream of the ESP section.

RESULTS

In the experiments to be described below an aerosol of monosized latex spheres was injected into the system to produce a concentration loading at the ESP inlet that was approximately uniform. The collection efficiency of the system was determined by measuring the particle concentrations downstream of the last turning vanes. The efficiencies were measured at various electrical operating points of the precipitator. For these tests only the wires in zones 1 through 4 were energized (wires 5 and 6 were removed). These measurements were repeated at several levels of gas stream turbulence, where the corresponding values of D were known from previous experiments. Any possible reentrainment of particles from the collector plates was prevented by coating the plates with grease.

The values of particle migration velocity toward the collector plates were calculated using the relation

$$w = \frac{qEc}{6\pi a\mu} \qquad (6)$$

where q is the average charge on a particle of radius a, μ is the gas viscosity, c is the Cunningham slip correction factor, and E is the average electrical field strength in the precipitator. The values of q were calculated from the experimental voltage and current values using a previously developed particle charging theory(9). To implement these calculations, the four active zones shown in Figure 2 were subdivided to form 16 segmented charging and collection regions. The predicted particle penetrations ($1-\eta$) at the outlet of each segment were calculated using both the Deutsch and turbulent diffusion models. These particle concentrations were then used as the inlet loadings of the next segment. The overall collection efficiencies were then calculated from the predicted penetrations of the last segment. The migration velocities calculated in each of the 16 segments using equation(6) were averaged to yield an overall value for each set of operating parameters.

The results of experimental measurements and theoretical predictions for 0.527 μm diameter styrene/butadiene latex spheres are shown in Figure 4. In this diagram values of predicted efficiency are plotted as a function of the average calculated migration

velocity for the turbulent diffusion (TDM) and Deutsch (D-A) models at two levels of gas stream turbulence. The two turbulent levels were characterized by values of D = 9.4 cm^2/s and D = 13.4 cm^2/s. Also shown are the experimentally measured efficiencies at the two gas stream conditions.

One interesting aspect of the results shown in Figure 4 is that the values of efficiency predicted by the turbulent model increases with the level of gas turbulence. This appears contradictory in view of the results shown in Figure 3. However, after examining the experimental conditions for which the calculations in Figure 4 were carried out, the apparent contradiction is easily resolved in the following manner. Because of the method used to increase the gas stream turbulence (a perforated plate followed by a plane of cylindrical rods) the mean gas velocity decreased from 193 cm/s (at D = 9.4 cm^2/s) to 149 cm/s (at D = 13.4 cm^2/s). Thus while the value of D increased by approximately 43% the mean gas velocity decreased by about 23%. Therefore, over the range of migration velocities and levels of turbulence considered here the mean downstream gas velocity is more effective in controlling collection efficiency than is the coefficient of turbulent diffusion. This is due to an increased average transit time across the four zones by approximately 30%, thus resulting in a significant increase in predicted efficiency values. This effect is observed in the experimental values in that the measured efficiencies are larger for the higher turbulent level.

Another important feature of the results shown in Figure 4 is the effects produced by a nonuniform distribution of the corona current along the length of the corona discharge wire. Both the Deutsch and the turbulent diffusion models rely upon the value of particle charge calculated from the measured values of voltage and total plate current in the ESP. However, at low values of voltage, just above the onset of corona, the current is very nonuniform and is localized to one or two corona tuffs per wire. Therefore, only a small fraction of the total number of particles pass through the region of gaseous ions where particle charging takes place. This is seen in Figure 4 where at low migration velocities the differences between either theoretical value and the measured values are quite large. At higher corona voltages, the current becomes more uniform along the length of the wire and the differences between theory and experimental values are much less. The corona current nonuniformities are particularly evident in this small ESP because of the limited number of corona wires. In a full scale system with a large number of wires these effects would be much less noticable because of the averaging effect of the particles passing many wires. The nonuniformities in corona discharge were clearly evident in our system by visual inspection. These irregularities have been quantitatively measured by at least one author (10). In all probability, the major portion of the effects of current irregularities could be eliminated through the use of a fine-barbed electrode.

The experiments above were repeated using an aerosol of 1.091 μm diameter polystyrene latex spheres. The results of these tests are shown in Figure 5. For these particles the turbulent diffusion coefficients were D = 8.0 cm^2/s and D = 13.6 cm^2/s at mean gas velocities of v = 193 cm/s and v = 149 cm/s respectively. These findings also show the effects of decreased gas velocity at the higher turbulent levels and their influence upon collection efficiency. Also seen in Figure 5 are the results due to nonuniform corona current distribution along the wire.

SUMMARY

From the results presented above it is evident that under certain operating conditions the effects of gas stream turbulence upon collection efficiency are less important than other parameters such as mean gas velocity. The effects of high turbulent diffusion also appear to be more detrimental to ESP efficiency at the higher values of electrical migration velocity. Although the range of gas stream turbulence levels covered in this report were somewhat narrow, it does represent a significant advancement in understanding the complex interaction between the competing mechanisms in an electrostatic precipitator.

ACKNOWLEDGEMENT

The authors wish to acknowledge the valuable comments and suggestions provided by Dr. Duane H. Pontius in the interpretation of many of the results of these experiments. The experimental data presented here was taken by Todd R. Snyder of SoRI. Portions of the work for this report were funded by the U.S. Environmental Protection Agency, IERL, Research Triangle Park, N.C. under Contract No. 68-02-2683 and Grant No. R806216010.

REFERENCES

1. Deutsch, W., Bewegung und Ladung der Elektrizitatstrager in Zylinderkundensotor, Ann. Phys. p. 350-352 (1922).

2. Yermilov, I.V. Determining the Concentration of Dust in the Field of Corona Discharge in an Electrostatic Precipitator. Electricheslvo, No. 7 (1974).

3. Williams, J.C. and R. Jackson, The Motion of Solid Particles in an Electrostatic Precipitator. Proc. Symposium on the Interaction between Fluids and Particles, Inst. Chem. E. London (1962).

4. Cooperman, P., A New Theory of Precipitator Efficiency, Atmospheric Environment, 5:541-551 (1971).

5. Feldman, P.L., K.S. Kamar, and G.D. Cooperman, Turbulent Diffusion in Electrostatic Precipitators, Paper presented at The Symposium on Electrostatic Precipitation. 60th Annual A.I.Ch.E. Meeting, November (1975) Los Angeles, CA.

6. Leonard, G., M. Mitchner, and S.A. Self, Particle Transport in Electrostatic Precipitators, Atmospheric Environment, 14:12890 1299 (1980).

7. Von Rosenberg, D.V., Methods for the Numerical Solution of Partial Differential Equations, American Elsevier Publishing Co., Inc. New York (1969).

8. Pyle, B.E., D.H. Pontius, T.R. Snyder, and L.E. Sparks, Particle Trajectory Studies in a Scale Model Electrostatic Precipitator Paper No. 80-49.2 presented at the 73rd Annual Meeting of the Air Pollution Control Association, Montreal, Quebec (1980).

9. Smith, W.B., and J.R. McDonald, Development of a Theory for the Charging of Particles by Unipolar Ions, J. Aerosol Sci., 7:151-166 (1976).

10. Tassicker, O.J., Aspects of Forces on Charged Particles in Electrostatic Precipitators, Dessertation, Wollongong. University College, University of New South Wales, Australia, (1972).

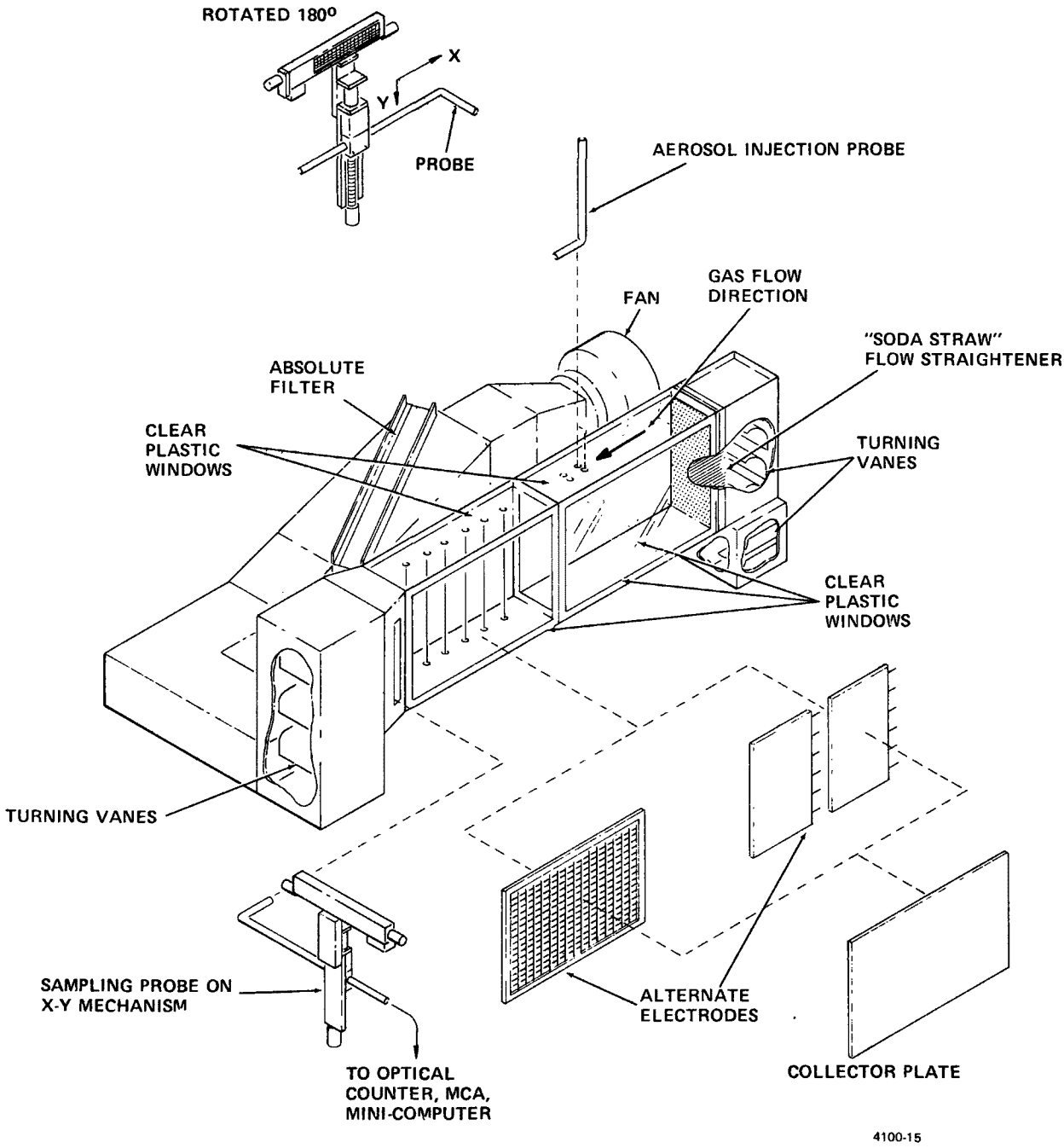

Figure 1. Perspective view of the laboratory scale electrostatic precipitator.

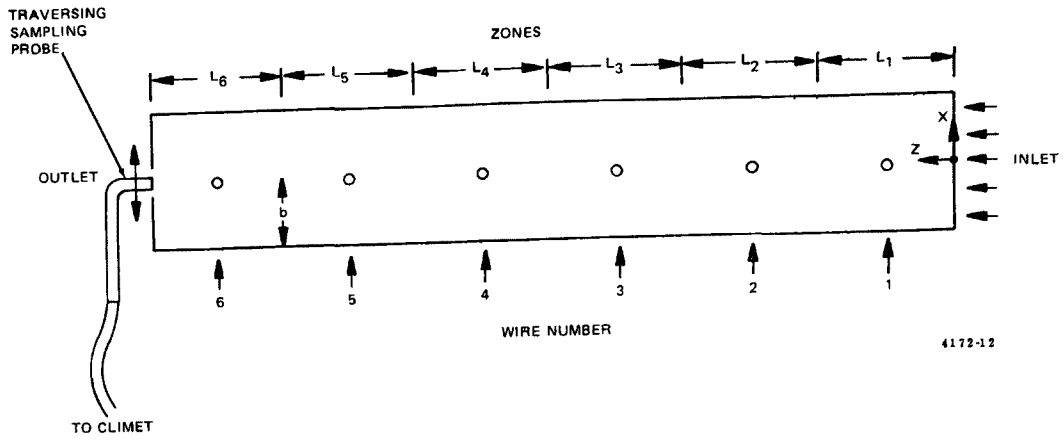

Figure 2. Zone divisions for the mathematical model of the laboratory scale electrostatic precipitator.

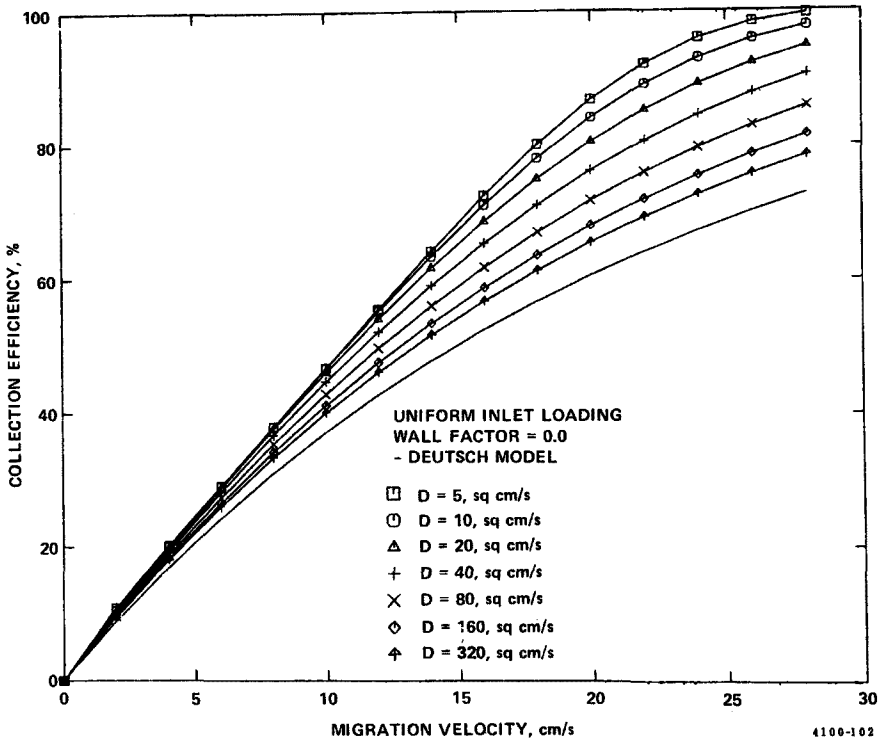

Figure 3. Comparison of predicted collection efficiencies for the Deutsch model to those of the Turbulent Diffusion model at various values of the diffusion coefficient.

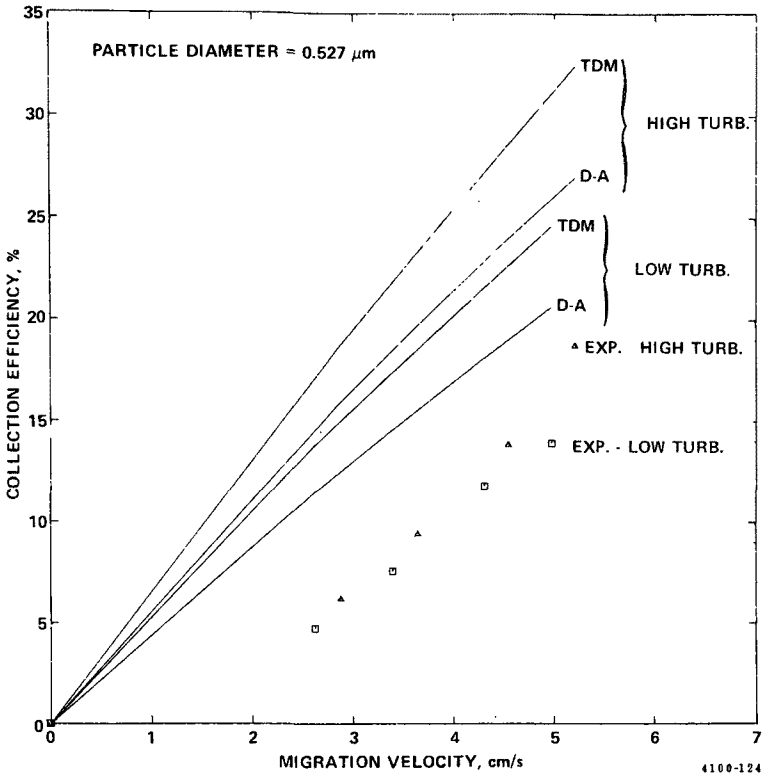

Figure 4. Comparison of predicted collection efficiencies to values measured using the laboratory scale ESP.

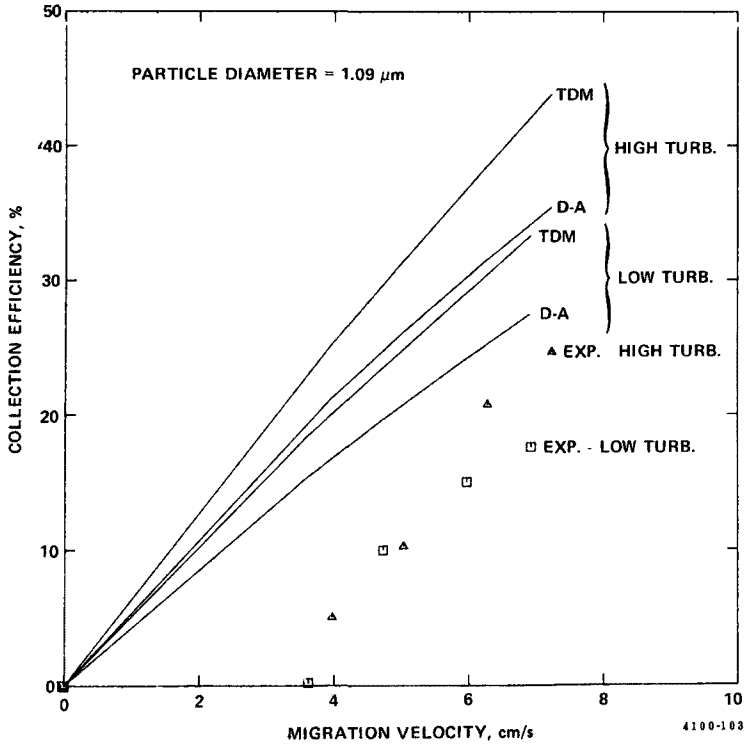

Figure 5. Comparison of predicted collection efficiencies to values measured using the laboratory scale ESP.

PARTICLE DEPOSITION PROFILES AND REENTRAINMENT IN A WIRE-PLATE ELECTROSTATIC PRECIPITATOR

By: E.Arce-Medina, R.M.Felder
Department of Chemical Engineering
North Carolina State University
Raleigh, NC 27650

ABSTRACT

A recently-devised radiotracer technique has been used to measure local particle deposition profiles and friction and impaction reentrainment in the NERC pilot-scale electrostatic precipitator, Research Triangle Park, North Carolina. Reentrainment rates are shown to vary with several experimental variables, including the temperature and humidity of the gas in the flow channel as well as the air velocity and inlet dust loading in the precipitator. The results suggest the magnitudes of these functional dependences, and show the necessity for careful monitoring of all four variables when performing precipitator measurements. Additional tests will be required to isolate the individual effects and to provide a data base for quantitative modeling studies.

INTRODUCTION

A recent paper described the development and testing of a radiotracer technique for measuring local particle deposition profiles and impaction reentrainment in an electrostatic precipitator (1). The technique has been used to perform eight runs on the NERC pilot-scale electrostatic precipitator. Labeled fly ash was injected into the ESP under varying experimental conditions (air velocity, inlet gas dust loading), with the collection plates either clean or coated with a previously deposited dust layer. The object was to obtain preliminary estimates of the effects of the variables cited on collection and reentrainment, as well as to assess the reproducibility of the experimental technique.

This report summarizes and discusses the results of these experiments, and outlines directions for further study. Details of the experimental and data analysis procedures may be found in the earlier work cited above (1).

EXPERIMENTS

The experimental conditions for the eight runs carried out in the most recent series of tests are summarized in Table 1. The temperatures shown are those prevalent in the laboratory during the runs, and should correspond reasonably closely to those in the precipitator. The humidities were obtained from the Weather Bureau on the run days, and are at best an approximation to laboratory conditions. The mean applied voltage in all runs was roughly -30.5 kV.

As Table 1 shows, three runs (12,14, and 16) were carried out with fly ash having been previously deposited on the collection plates, and the other five runs were begun with clean plates. In Runs 11-16, the voltage in the first stage of the precipitator was turned off, so that the dust feed to the second stage (where the tracer was injected) could be regulated. Two dust feed rates -- 30 g/min and 60 g/min -- were used under these conditions. In the last two experiments the voltage was turned on in the first stage, so that the feed to the second stage could only be roughly estimated.

The ash was a high resistivity coal combustion fly ash from a brewery power plant. A plot of resistivity versus temperature is shown in Figure 1. The tracer used in all runs was 0.5 g of this material, irradiated for 60 seconds in the North Carolina State University Pulstar Reactor at a power level of 1 MW and an approximate flux of 1.2×10^{13} n-cm^{-2}-s^{-1}. At the outset of each run, the labeled fly ash was injected at the inlet of the second stage of the precipitator at a point 1.25 cm. from the plate behind which the scintillation detector was mounted, and the injection device was then withdrawn to minimize background radiation. The air flow rate at the moment of injection was normally set at 85 m/min.

Following injection, the detector was moved back and forth, and the activity at several horizontal positions at the height of the injection was measured by recording the counts in one minute intervals. The detector was then fixed at the position of maximum activity, and the count rate was monitored for about 20 minutes. The dust feed was then switched on to its desired value, and monitoring continued for another 20-30 minutes. The air velocity was then increased to 140 m/min, and then to 220 m/min, with 20-30 minutes of monitoring following each change.

DEPOSITION PROFILES

Plots of activity following injection of the tracer versus axial position for the eight runs are shown in Figures 2, 3, and 4. A generally consistent pattern is observed, to the effect that the profile starts at a low level, increases to a maximum at a point roughly 30-40 cm. from the injection point, and decreases thereafter. The peak shape varies considerably from run to run. The variation could be due to the combined effects of variations in temperature, humidity, and the condition of the plate (clean or coated), and/or to normal experimental scatter. The latter effect may not be too great, however, since the curves for the two runs in which experimental conditions were most nearly identical (Runs 17 and 18,

Figure 4) show a considerable degree of correspondence.

IMPACTION REENTRAINMENT

Results

The tracer activity decay data were analyzed in terms of the first-order reentrainment model outlined by Felder and Arce-Medina(1). If n is the mass of dust deposited in some small region of the plate, then the loss due to impaction reentrainment is taken to be described by the differential equation

$$dn/dt = -kn$$

The reentrainment rate constant, k, provides a direct measure of the loss rate: half of the collected dust is reentrained, for example, in a time $t=0.693/k$.

The values of k measured for the eight runs performed are shown in Table 1. A considerable degree of scatter is evident. The few negative values of k, which indicate the physically impossible result of an activity increase with time, reflect extreme cases of this scatter.

Even apart from the scatter, however, the results shown in Table 1 at first appear to be inconsistent with each other in several ways. Increasing the air velocity, for example, sometimes increases the apparent reentrainment rate (as in Run 12), sometimes decreases it (Runs 13, 15, 16, and 18), and sometimes increases it initially and then decreases it (Runs 14 and 17). The magnitude of the reentrainment rate shows no obvious correlation with the dust loading at the precipitator inlet, and does not seem to depend on whether or not the plate was coated with a dust layer prior to injection of the tracer.

We believe, however, that these apparent contradictions in fact reflect the complexity of the precipitation process, and that they can be explained in terms of the fundamental phenomena underlying this process. Moreover, they provide a good indication of why precipitator models have not been notably successful in predicting actual performance. These points are elaborated on in the next section.

Discussion

Several experimental conditions and variables may have a significant effect on the collection efficiency of a precipitator and the likelihood of reentrainment of collected dust (2-5). Among these factors are the following:

1. Air velocity. Although the velocity is uniform across most of the flow channel, most of the resistance to mass transfer is concentrated in the laminar boundary layer adjacent to the plate, which has a thickness that varies inversely with velocity.

Moreover, the drag force on collected particles and the momentum of impacting particles both increase with increasing velocity. The net result is a tendency for reentrainment to increase with velocity.

2. Dust loading. The greater the dust loading at the inlet, the greater the frequency of impaction collisions, and hence the higher the reentrainment rate. On the other hand, a higher dust loading leads to a more rapid buildup of collected dust; this should not affect the rate of reentrainment in general, but by superimposing a layer over the deposited tracer it would decrease the tracer reentrainment rate, leading to errors in data interpretation.

3. Condition of the plate. The presence of a dust layer on the plate adds a layer of resistance between the electrodes, diminishing the effective field at the plate. This layer has two competing effects. On the one hand, it lowers the electrical adhesion force on collected particles at the layer surface, and therefore tends to increase the rate of reentrainment. On the other hand, the average momentum of impacting particles normal to the plate may be reduced (at least to the extent that their motion in this direction is imparted by the electrical potential driving force), which would tend to decrease reentrainment.

4. Temperature. The resistivity of a dust is invariably a strong function of temperature, particularly at the ambient temperatures of this study. This effect is clearly shown in Figure 1, wherein a temperature rise of $10^{o}C$ may be sufficient to change the resistivity by an order of magnitude. A small change in temperature from one run to another might therefore be expected to change the dust resistivity and hence the collection and reentrainment rates significantly, even if the applied corona voltage, inlet dust loading, and air velocity are all held constant.

5. Humidity. Figure 1 also shows the effect of moisture content on the fly ash resistivity. At $90^{o}C$, a change from 5% water to 10% water is seen to result in a resistivity decrease by a factor of 10, and the magnitude of the effect clearly increases dramatically as the temperature decreases. Similar results are given by Parker(1980). The curves shown do not extend to ambient temperatures, but it appears that there could be a difference of five orders of magnitude or more at such temperatures. A slight change in humidity from one run to another might therefore also be expected to cause pronounced changes in measured collection and reentrainment rates.

Another effect peculiar to the experimental setup used in these runs has to do with the method used to change air velocities. When the experiments were performed, the velocity could only be changed by changing an orifice plate in the flow line. The surge that occurred at subsequent restarting sometimes dislodged a considerable quantity of collected dust, including tracer. Following the completion of the experiments, a variable-speed fan controller was added to the system, so that this difficulty will not be

encountered in future runs.

The measured reentrainment rate constants shown in Table 1 can now be interpreted in the light of the above discussion.

Runs 11 and 12

These runs were carried out successively. The reentrainment rates are relatively low at the low temperature and high humidity prevalent during these runs. The lower reentrainment rate observed for the precoated plate in Run 12 suggests a "stickiness" associated with the dust at these conditions.

Runs 11 and 13

The difference in the initial reentrainment rates could be due to a combination of the differences between the air velocities, temperatures, and humidities during these runs. Both reentrainment rates were relatively low, however, so that the difference between them may not be significant. The decrease in reentrainment observed in successive stages of Run 13 is due to the buildup of dust over the tracer as the experiment progressed.

Runs 12 and 14

These runs were each carried out with precoated plates and the same air velocities and dust loadings. The pronounced differences in reentrainment rates thus provide a good indication of the strong influence of temperature and humidity on the precipitator performance, and in particular of the increased cohesiveness of the dust layer at lower temperatures and higher humidities.

Runs 13 and 14

The conditions of these runs were more or less the same, except that the injection in Run 14 was performed with a layer of dust already coating the plate. The reentrainment rate is significantly higher for the coated plate, probably reflecting the lower potential field at the surface caused by the dust layer resistivity. Increasing the air velocity from 85 to 140 m/min led to an increased reentrainment rate, suggesting that the greater friction and impaction momentum at the higher velocity more than compensated for the deposition of new dust over the tracer, while the opposite effect was observed for the step from 140 to 220 m/min.

Runs 13 and 15

Increasing the dust loading at a given velocity clearly has the effect of increasing the reentrainment rate. In both runs, the deposition of dust over the tracer decreased the reentrainment as the experiment proceeded.

Runs 15 and 16

Once again, the reentrainment rate was greater when the plate was coated with a dust layer. The magnitude of the effect is uncertain, since the temperature and humidity also varied from one run to the other.

Runs 17 and 18

In these runs, the voltage was turned on in the stage of the precipitator preceding that into which the tracer was injected. The dust loading could therefore only be roughly estimated. The effects of dust loading and air velocity are qualitatively similar to those found in the earlier experiments. We have no explanation for the anomalously high reentrainment rate observed in Run 18.

CONCLUSIONS

The radiotracer technique used in this preliminary study has been shown to provide a picture of the local deposition profile in an electrostatic precipitator, and to enable the measurement of local rates of impaction reentrainment. The technique may therefore be used to obtain correlations of these phenomena with precipitator operating conditions and with physical properties of the dust to be collected.

The rate of reentrainment is a function of the air velocity and inlet dust loading in the precipitator, but also depends to a great extent on the temperature and humidity of the gas in the flow channel. The present results suggest the magnitudes of these functional dependences, and show the necessity for careful control (or at least careful monitoring) of all four variables when performing precipitator measurements. Additional tests will be required to isolate the individual effects and to provide a data base for quantitative modeling studies.

ENDNOTES

1. Felder,R.M. and E.Arce-Medina, "Radiotracer Measurement of Particle Deposition and Reentrainment in an Electrostatic Precipitator," Int.J.Appl.Rad.Isotopes 31,761(1980).

2. Bassett,J.D., K.Akutsu and S.Masuda, "A Preliminary Study of Re-entrainment in an Electrostatic Precipitator," J.Electrostatics 3,311(1977).

3. Groves,J.F. and C.R.Smith, "Gas-Flow Distribution Effects in Electrostatic Precipitators," J.Electrostatics 8,343(1980).

4. Parker,K.R., "The Precipitation of Difficult Dust," J.Electrostatics 8, 355(1980).

5. Vincent,J.H. and A.S.M.MacLennan, "Aerodynamic Considerations in Electrostatic Precipitation," J.Electrostatics 8,325(1980).

TABLE 1. SUMMARY OF RUN CONDITIONS AND RESULTS

Run	T(^{o}F)	R.H.	Plate Condition	Dust feed rate(g/min)	Air velocity (m/min)	k x 10^{3} (min^{-1})*
11	47	100%	Clean	30	140	2.3
				60	140	1.6
12	46	95%	Coated	30	85	-1.6
					140	0.04
					220	2.5
13	60	50%	Clean	30	85	0.89
					140	0.22
					220	-5.0
14	56	40%	Coated	30	85	9.6
					140	14.0
					220	4.0
15	64	50%	Clean	60	85	4.9
					140	4.0
					220	-3.3
16	60	73%	Coated	60	85	6.6
					140	4.1
					220	3.1
17	58	65%	Clean	21**	85	6.0
					140	8.3
					220	2.0
18	59	53%	Clean	42**	85	25.0
					140	14.0
					220	-2.6

---

* k=reentrainment rate constant
** rough estimate

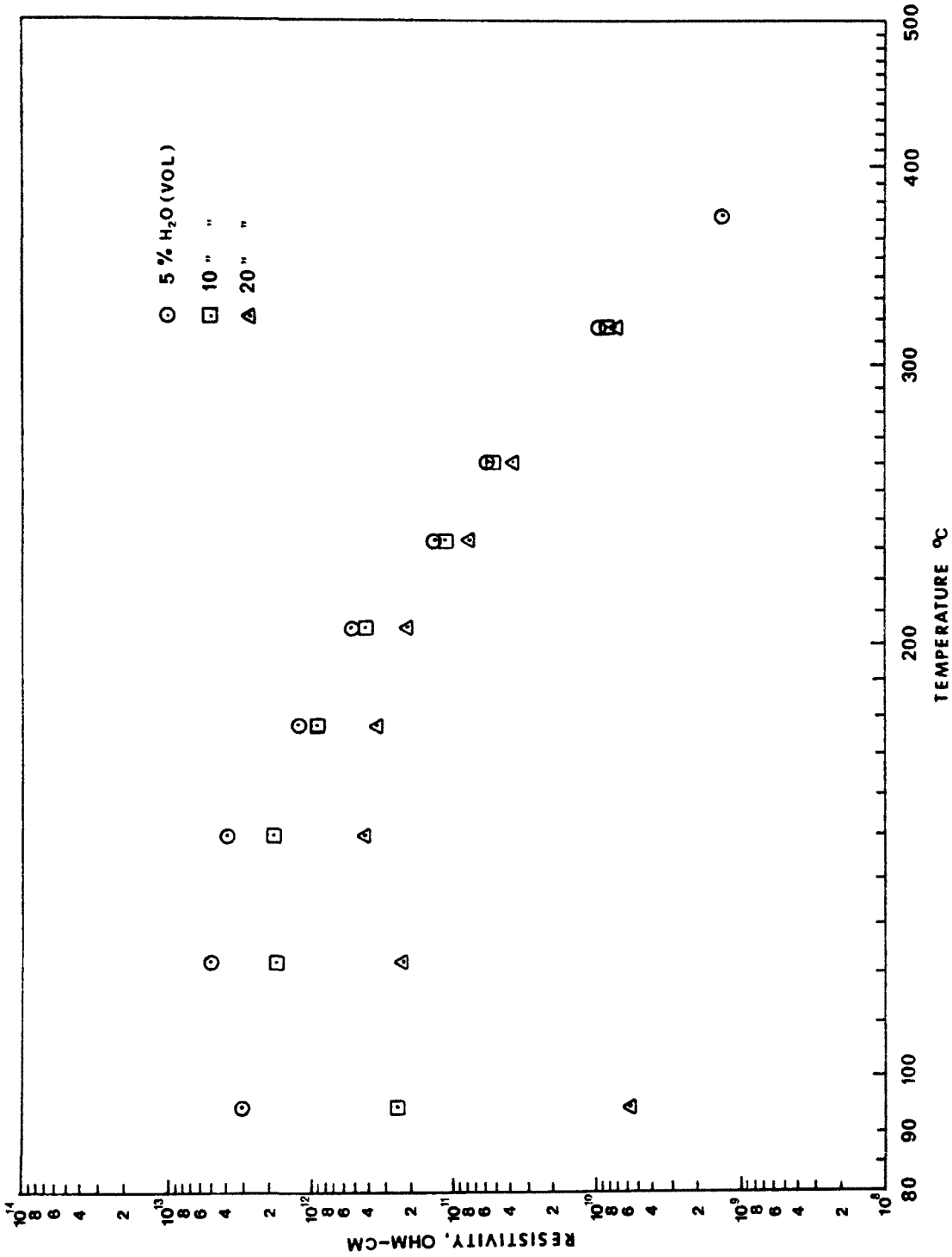

Figure 1. Dust resistivity versus temperature

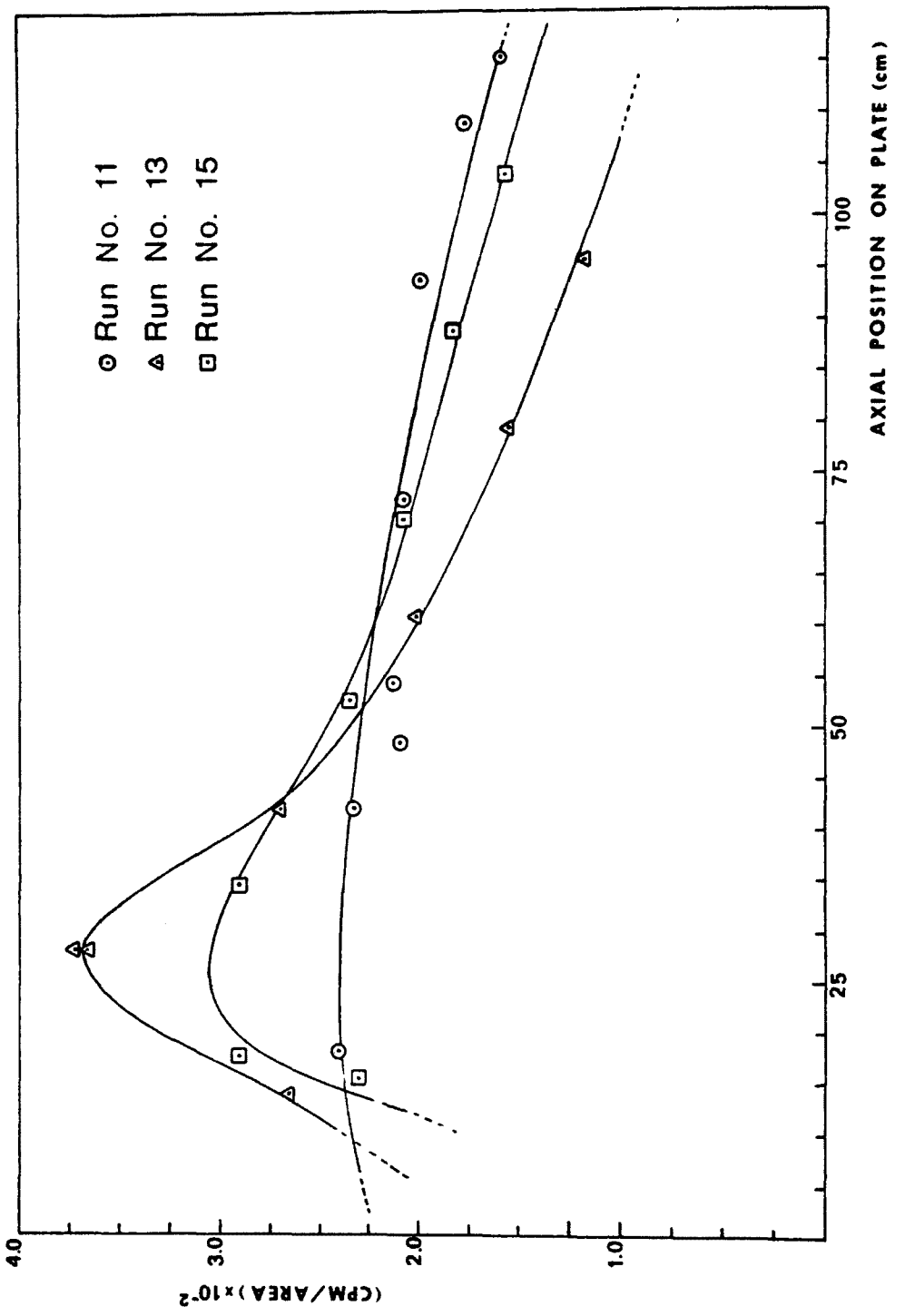

Figure 2. Deposition Profiles for Runs 11, 13, 15

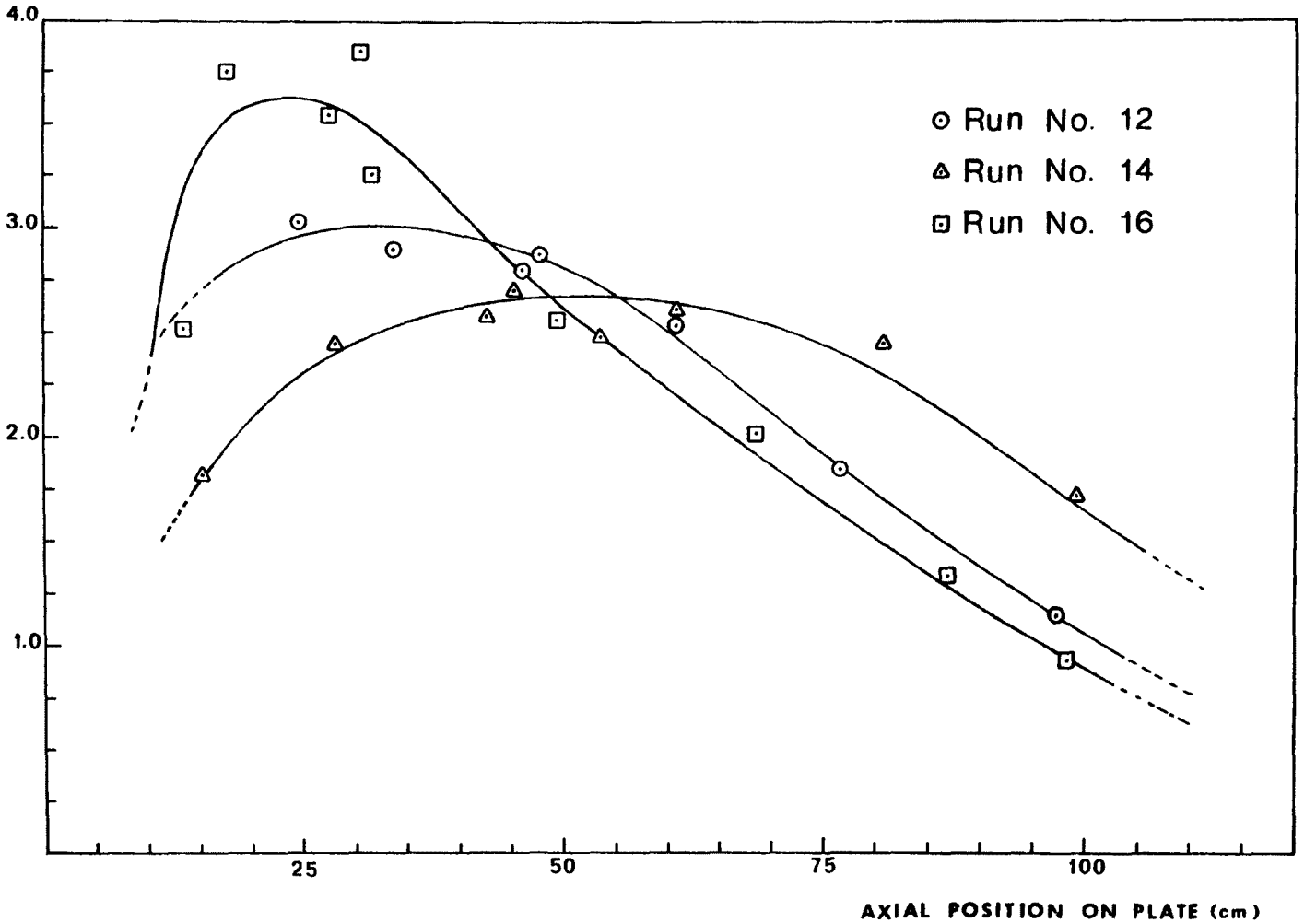

Figure 3. Deposition Profiles for Runs 12, 14, 16

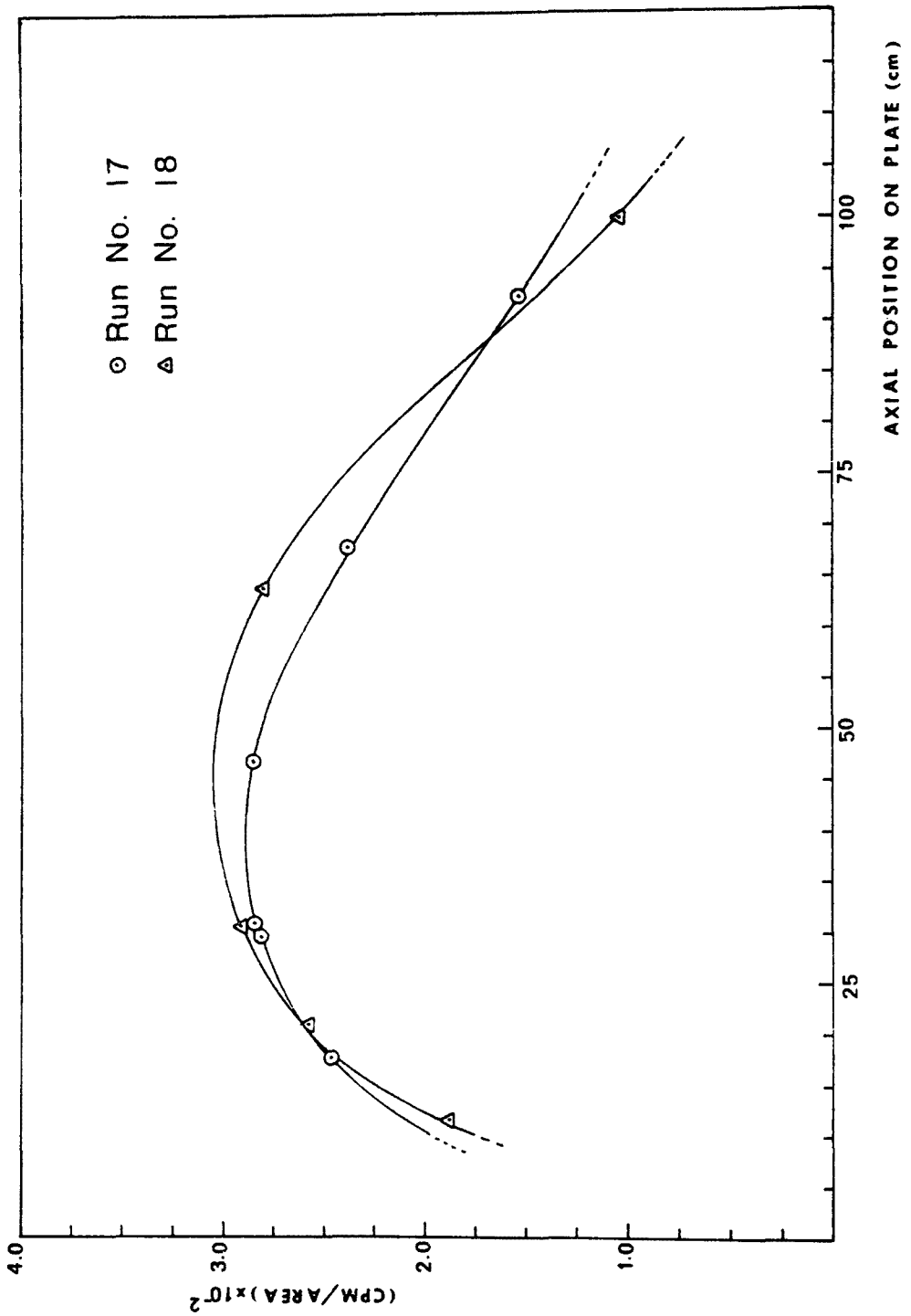

Figure 4. Deposition Profiles for Runs 17, 18

PARTICLE TRANSPOPT IN THE EHD FIELD

By Toshiaki Yamamoto

University of Denver
Denver Research Institute
Electronics Division
Denver, Colorado 80208

ABSTRACT

The study of the motion of fine particulate in the EHD (electrohydrodynamic) field has become important in not only the design of electrostatic precipitators but also electrostatic painting.

Experimental and theoretical studies have been conducted in the case of a two-dimensional, two-wire plate configuration precipitator. In the numerical study, the external force which consists of the electrostatic field and space charge density was first obtained. The second step was to solve the Navier-Stokes equations in the form of vorticity-stream function equations with appropriate boundary conditions. The particle trajectories were computed by integrating the equations of motion in the EHD field.

The implications of the results to precipitator performance are discussed by using the dimensionless EHD charge number. The calculated numerical results demonstrate close agreement with the experiment.

INTRODUCTION

In the process of particulate collection in an electrostatic precipitator, the motion of particulates is affected by both electrostatic field and fluid forces. The major limitations among all existing electrostatic precipitator theories have been the neglect of the use of simplified fluid dynamic models, and the weakness in the description of the fluid dynamic coupled with the electrostatic field, i.e., electrohydrodynamics. The previous investigations (1, 2, 3) have indicated that the interaction between the fluid and the electrostatic field was shown to have a significant role in altering the flow in the precipitator. The subject of the investigation presented in this paper is the analysis of particle motion in the EHD field, thereby establishing the roles of various operating parameters. The schematic diagram of the experimental set-up and the two-dimensional computational domains for the flow configuration with two wires are shown in Figure 1.

In the numerical study, the external force which consists of the electrostatic field and space charge density was obtained. The second step was to solve the Navier-Stokes equations in the form of vorticity-stream function equations with appropriate boundary conditions. The particle trajectories were computed by integrating the equation of motion in the EHD field. In the experimental study, current density distribution and

electrical potentials were measured and compared with the numerical results. The Schlieren optical technique is utilized to observe the flow interaction. The gross movement of particles in the EHD field is also observed by the introduction of mist particles in the primary flow gas stream.

In the analysis of the particle loci, the dimensionless EHD number, N_{EHD}, which is the ratio of the secondary flow velocity to the primary flow velocity is used as a parameter of flow interaction due to the secondary flow. Another dimensionless parameter, EHD charge number, N_{E-C}, which is the ratio of electrostatic force to the EHD viscous force to the particle is introduced as a parameter of controlling the motion of the particles. Finally, the effect of the particle migration in the EHD field and the implications of the results to precipitator performance are discussed.

EHD FLOW INTERACTION

Since the detailed study for the EHD interaction was previously reported (2, 3) only brief descriptions are given here. There are two fundamental assumptions in the theory: 1) In the EHD analysis, the effect of the space charge due to the particles on the secondary flow is assumed to be small. 2) The effect of adjacent particles' interaction is neglected in the analysis of the particle motion.

The governing equations for the electric potential and space charge density distributions are written as

$$\text{div grad } V = -\rho_c/\epsilon \tag{1}$$

$$\rho_c^2 - \epsilon \text{ grad } \rho_c \text{ grad } V = 0 \tag{2}$$

The electric field strength, E, and electric current density, J, are related to the potential, V, by $\tilde{E} = -$ grad V and $\tilde{J} = \rho_c (K \tilde{E} + \tilde{u}) \simeq \rho_c K \tilde{E}$. The boundary conditions for V in the computational domain shown in Figure 1 are $V = V_o$ measured electrical potential at the wire, $V = 0$ along the cathode plate, $\partial V/\partial n = 0$ along any symmetry lines.

The basic equations for the flow field are the Navier-Stokes equations expressed in terms of the vorticity-stream function form.

$$\bar{\omega}_t = -\bar{\psi}_y \bar{\omega}_x + \bar{\psi}_x \bar{\omega}_y + \frac{1}{R_{EHD}} (\bar{\omega}_{xx} + \bar{\omega}_{yy}) + \bar{\rho}_{c_x} \bar{V}_y - \bar{\rho}_{c_y} \bar{V}_x \tag{3}$$

$$\text{div grad } \bar{\psi} = \bar{\omega} \tag{4}$$

where all quantities are dimensionless with reference to d, U_e, V_o and the charge density at the wire ρ_{co}. The inlet flow boundary condition was set to a uniform flow based on the inlet configuration of the experimental set-up, $\bar{\psi} = \bar{U}_0 \bar{y}, \bar{\omega} = 0$. The less restrictive outlet boundary condition, $\bar{\psi}_x = 0, \bar{\omega}_x = 0$, implies that the parallel flow is established without specifying the flow velocity distribution. The nonslip boundary condition was applied along the channel wall by $\bar{\psi} = \bar{U}_0, \bar{\omega} = \bar{\psi}_{yy}$. Along the centerline of the channel, the symmetry boundary condition was given by $\bar{\psi} = 0, \bar{\omega} = 0$.

MOTION OF THE PARTICLE IN THE EHD FIELD

The equation of motion of a spherical fine particle in the EHD field is expressed as

$$m \frac{dV_p(\tilde{r})}{dt} + 6\pi\eta a (V_p(\tilde{r}) - V_f(\tilde{r})) = q E(\tilde{r}) \tag{5}$$

where m is the mass of the particle, $V_p(\tilde{r})$ and $V_f(\tilde{r})$ are the velocity vector of the particle and the fluid respectively, a is the radius of the particle, q is the particle charge and η is the viscosity coefficient. The particle motion is calculated by integrating the normalized equations under the given conditions. The dimensionless motion of the particle can be written as

$$\frac{d\bar{V}_p(\tilde{r})}{dt} + \zeta \bar{V}_p(\tilde{r}) = \zeta \bar{V}_f(\tilde{r}) + K\bar{E}(\tilde{r}) = \bar{F}_e(\tilde{r}) \tag{6}$$

where $\bar{V}_p(\tilde{r}) = V_p(\tilde{r})/U_e$, $\bar{t} = t/(d/U_e)$, $\zeta = 6\pi\eta a U_e/(mU_e^2/d)$, $K = qE_0/(mU_e^2/d)$, $U_e = (\rho_{co}V_o/\rho)^{1/2}$, $N_{EHD} = \frac{R_{EHD}}{R_d} = \frac{U_e}{2U_0}$

As seen in equation (6), ζ represents the effect of viscous drag force with respect to inertia force. Typical precipitator operation falls in the range of $\zeta \gg 1$. This implies that the viscous force is considerably greater than the inertia force, which corresponds to Stokes' flow hypothesis. On the other hand, K represents the effect of electrostatic force on the inertia force.

The EHD number, N_{EHD}, which is the ratio of the EHD Reynolds number to the ordinary Reynolds number is introduced as a parameter of flow interaction due to the secondary flow. It is also the ratio of the secondary flow velocity to the primary flow velocity. The detailed

treatments of the N_{EHD} parameter were discussed in the separate paper (2, 3). Using the N_{EHD}, ζ and K, the new parameter called the EHD charge number, N_{E-C}, is now defined as

$$N_{E-C} = 2 N_{EHD} \frac{K}{\zeta} = \frac{qE_0}{6\pi\eta a U_0} = C \frac{a\epsilon_s E_0 E_c}{\eta U_0} \tag{7}$$

The N_{E-C} is a ratio of average electrostatic force to average EHD drag force acting on the particle and a function of a, ϵ_s, E_o, E_c, U_o, and T. The dimensionless force, $\bar{F}_e(\tilde{r})$ can be rewritten in terms of N_{E-C} and K.

$$\bar{F}_e(\tilde{r}) = \frac{K}{N_{E-C}} \left(\bar{V}_f(\tilde{r}) + N_{E-C} \bar{E}(\tilde{r}) \right) \tag{8}$$

The value of N_{E-C} determines how close the particle moves along the EHD streamlines. For the condition $N_{E-C} \gg 1$, the particle motion is effectively controlled by the electrostatic field, while for $N_{E-C} \ll 1$, the particle motion is controlled by the EHD field. When $N_{E-C} \simeq 1.0$, the particle motion is controlled by both electrostatic and EHD field. The typical value for N_{E-C} in the industrial precipitator is much less than unity. Therefore, the particle loci is the EHD dominated pattern.

A particle is introduced from the left (the precipitator inlet) with the same speed as the fluid, whereas d at the flow inlet is divided into seventeen sections. The particle starting at Y = 2, 5, 8, 11, 14, 16 is secured during each time interval so that the particle velocity can be estimated at any location. This analysis is limited for the value of N_{E-C} between 0.01 and 1.0 because a typical value of N_{E-C} for industrial electrostatic precipitators falls in this range.

RESULTS AND DISCUSSION

The particle motion in the EHD field is analyzed by solving equation (6) in the dimensionless space under the given initial conditions. Figure 2 a-d and Figure 3 a-d illustrate the particle trajectories for the case of N_{EHD} = 2.69 and N_{EHD} = 1.34 respectively. The computed EHD streamline distributions are shown as a solid line in the succeeding Figures and demonstrate close agreement with experiments (3). It should be noted that the vertical scale shown in all successive Figures is twice as large as the horizontal scale.

When the N_{E-C} = 0.012 or less as shown in Figure 3-a, the loci of the particle motion is almost identical to the EHD streamlines. This implies that the particle collection is extremely difficult. As the N_{E-C} increases as shown in Figure 3-b for N_{E-C} = 0.024 and Figure 2-a for N_{E-C} = 0.048, the particle still moves very close to the EHD streamlines, in which the particle motion is largely controlled by the EHD force. A

small fraction of the particle introduced near the wall is collected. It is also shown from the histogram of the particle trajectory that the particle is accelerated as it is approaching the corona wire and decelerated as it is leaving the wire. The particle velocity which passes through the channel is 21 to 27 percent faster than the average fluid velocity, which implies that actual retention time is considerably shorter. As the N_{E-C} increases further as shown in Figure 3-c for N_{E-C} = 0.120 and Figure 2-b for the N_{E-C} = 0.241, the particle introduced about one third from the channel wall is effectively collected within two corona wires and the remaining particle is collected within the several successive corona wires. Because the particle tends to disperse towards the collection plate, the particle density distribution can be calculated at the channel outlet for given particle distribution at the channel inlet. At the N_{E-C} = 0.483 as shown in Figure 2-c and Figure 3-d, the effect of the electrostatic force remarkably increases. Most of the particles introduced are collected within two corona wires. It is rather astonishing to observe that the particle motion near the wall is extremely slow. Therefore, the particle collection will be interfered with by even trivially small flow disturbances. Because the particle motion is slower near the wall, one can observe the particles rotating by the combined electrostatic and EHD force. When the N_{E-C} = 0.966 as shown in Figure 2-d, the electrostatic and EHD viscous drag forces are equal in magnitude. This implies that the large particles are collected fairly rapidly, while fine particles remain suspended in the gas stream. It is also observed that the particle introduced at the centerline of the channel reduces speed rather quickly as it approaches the corona wire and stagnates at the wire. This is one of the possible mechanisms that the dust particle will build up on the corona wire.

Table 1 shows the migration velocity obtained by the classical theory against the maximum and minimum migration velocity obtained for various values of N_{E-C} an N_{EHD}. It is obvious from this table that the migration velocity is not constant but dependent upon the position of the particle. Let us consider the case for E_o = 5.0 kV/cm, E_c = 3.0 kV/cm, $q = 0.73\, q_s$ (4), $\rho_s = 0.6 \times 10^3$ kg/m^3, and T = 20 ^oC. Then, the first row represents particle radius a = 0.25 micron meter, the second a = 0.5 micron, and 2.5, 5.0 and 10.0 microns successively. This calculated migration velocity agrees well with experimentally determined values (5). All the units shown in this table are meter/sec except a.

Table 1 THEORETICAL MIGRATION VELOCITY VERSUS MAXIMUM AND MINIMUM MIGRATION VELOCITY AS A FUNCTION OF N_{E-C} AND N_{EHD}

		N_{EHD} = 2.69			N_{EHD} = 1.34		
a	V_{th}	N_{E-C}	V_{max}	V_{min}	N_{E-C}	V_{max}	V_{min}
0.25	0.015	0.024	0.318	-0.256	0.012	0.175	-0.241
0.5	0.029	0.048	0.327	-0.247	0.024	0.185	-0.240
2.5	0.147	0.241	0.398	-0.168	0.120	0.319	-0.233
5.0	0.294	0.483	0.487	-0.117	0.241	0.546	-0.226
10.0	0.588	0.966	0.698	-0.102	0.483	0.711	-0.209

The roles of various operating physical parameters in terms of their influence on the collection efficiency are established and thereby, general attempts are made to increase the N_{E-C} for given N_{EHD}; that is: to increase ϵ_s , a, E_o, E_c and decrease U_o, T or the change of particle characteristics such as enhancement of surface area and particle agglomeration.

It can also be deduced from the EHD study that the shear stress along the wall is altered significantly by the presence of the EHD action as compared to the non-EHD case. The results for the case of laminar flow are shown in Figure 4. As the Reynolds number is greater than approximately 3600 with an average field of 5.0 kV/sec (or $N_{EHD} < 2.0$), the shear stress is reduced from that of the non-EHD case, while as the Reynolds number decreases further, regions of significantly higher shear stress occur near the corona wire. This conclusion contradicts the past legend that the electric wind enhances the reentrainment of the dust. It is also noted that in laminar flow, small surface roughness due to the dust build-up has no effect on the flow properties. In turbulent flow, however, the roughness of the boundary surface will affect the physical properties of the fluid motion and the effect of the roughness is dependent upon the relative size of roughness and the thickness of the laminar film which is associated with the energy loss by rough surface.

Figure 5 illustrates the motion of the mist particle as obtained with injection of the mineral oil mist. The calculated streamlines are superimposed. The particle sizes for the mist particle used are 0.5 to 50 micron and therefore, this corresponds to approximately $N_{E-C} = 0.6$ with $N_{EHD} = 4.0$. It can be seen that the path of the mist particles has fair agreement with the calculated particle trajectory although the direct comparison can not be made. It also shows that the particles introduced near the centerline of the channel are more difficult to collect on the plate because both electrostatic and EHD forces are small.

CONCLUSIONS

Experimental and theoretical studies have been conducted to analyze the particle motion coupled with the EHD field with the focus on the two-wire electrostatic precipitator. Although all the calculations of the particle motion were made for a set of two dimensionless parameters such as N_{E-C} and N_{EHD}, the results can be extended to other sets of parameters having the same N_{E-C} and N_{EHD}. The results obtained can be summarized as follows:

1) The dimensionless EHD charge number, N_{E-C} is introduced as a parameter of the electrostatic force to the EHD viscous drag force and also shows how closely the particle moves to the EHD streamlines. As the N_{E-C} is smaller, the particle motion is controlled by the EHD force, resulting in difficulty of particle collection. The general attempt is to obtain higher N_{E-C} for higher efficiency.
2) The particle motion near the wall is extremely slow. Therefore, the

particle collection will be interfered with by very small flow disturbances.
3) A particle migration is not constant but dependent upon the position of the particle. It is also non-linear to the physical parameters.
4) The shear stress is reduced from that of the non-EHD case when the Reynolds number exceeds 3600 with an average field of 5.0 kV/cm (or N_{EHD}< 2.0).
5) In laminar flow, small surface roughness due to the dust build-up has no effect on the flow properties such as shear stress, whereas in turbulent flow, it will affect the flow properties.

REFERENCES

1. Noll, C. G., and Yamamoto, T. Towards a Microscopic Theory of Electrostatic Precipitation. Symposium on the Transfer and Utilization of Particulate Control Technology. 2: 374-390, July, 1979.

2. Yamamoto, T., Nakamura, S. and Velkoff, H. R. Numerical Study of Secondary Flow Interaction in an Electrostatic Precipitator. Innovative Numerical Analysis for the Applied Engineering Sciences, University Press of Virginia, 1980, p.3-12.

3. Yamamoto, T. and Velkoff, H. R. Electrohydrodynamics in an Electrostatic Precipitator. (Presented for Journal of Fluid Mechanics).

4. Nichols, G. B. and Oglesby, S. The significance of the Particle Charging Time in Electrostatic Precipitation. Second International Clean Air Congress of the International Union of Air Pollution Prevention Association, EN-41D, Dec. 1970.

5. Masuda, S., Akutsu, K. and Ko, M. Motion of Small Charged Particles inside an Electrostatic Precipitator. IEEE-IAS Annual Meeting, 139-145, Sept. 1979.

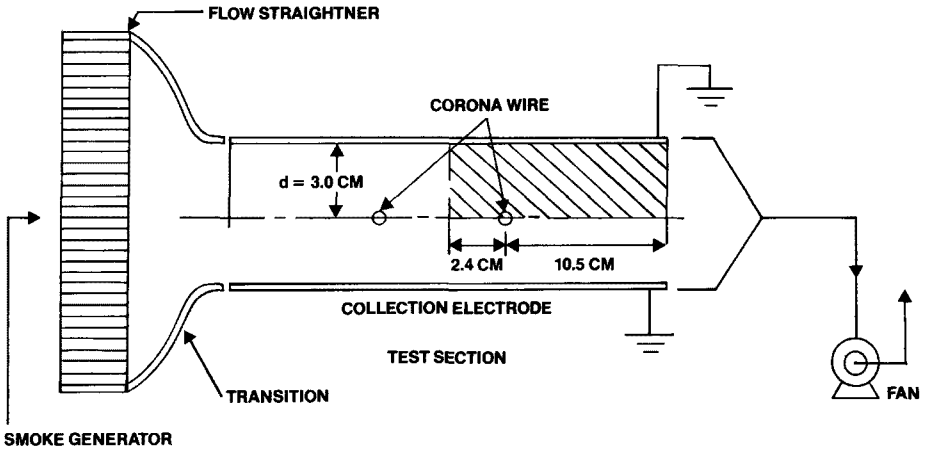

Figure 1. Schematic Diagram of the Experimental Set-up and the Two-Dimensional Computational Domains.

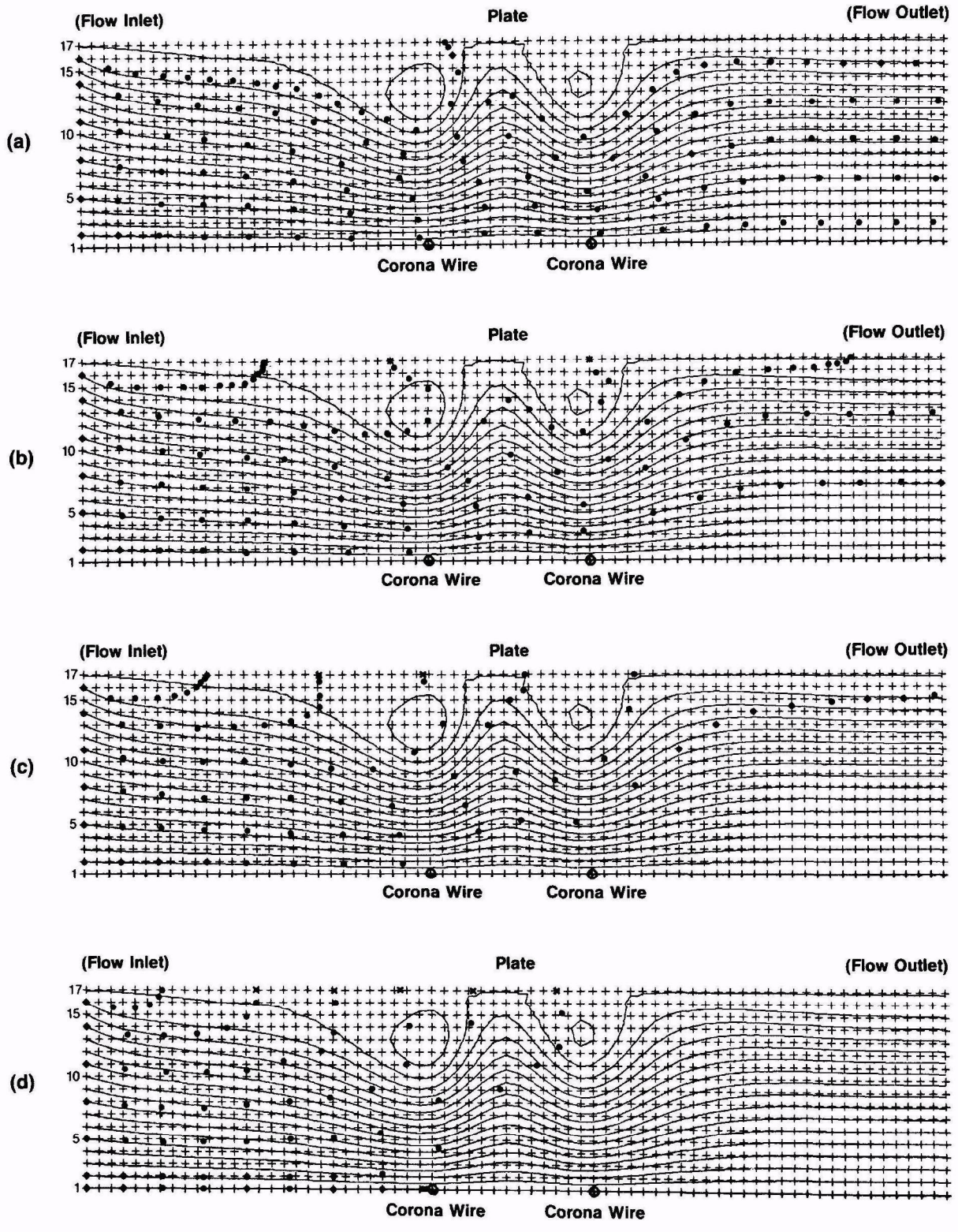

Figure 2. Particle Trajectories in the EHD Field for N_{EHD} = 2.69 (U_o = 0.61 m/sec, R = 2400, E_o = 5.0 kV/cm): (a) $N_{E\text{-}C}$ = 0.048, (b) $N_{E\text{-}C}$ = 0.241, (c) $N_{E\text{-}C}$ = 0.483, (d) $N_{E\text{-}C}$ = 0.966.

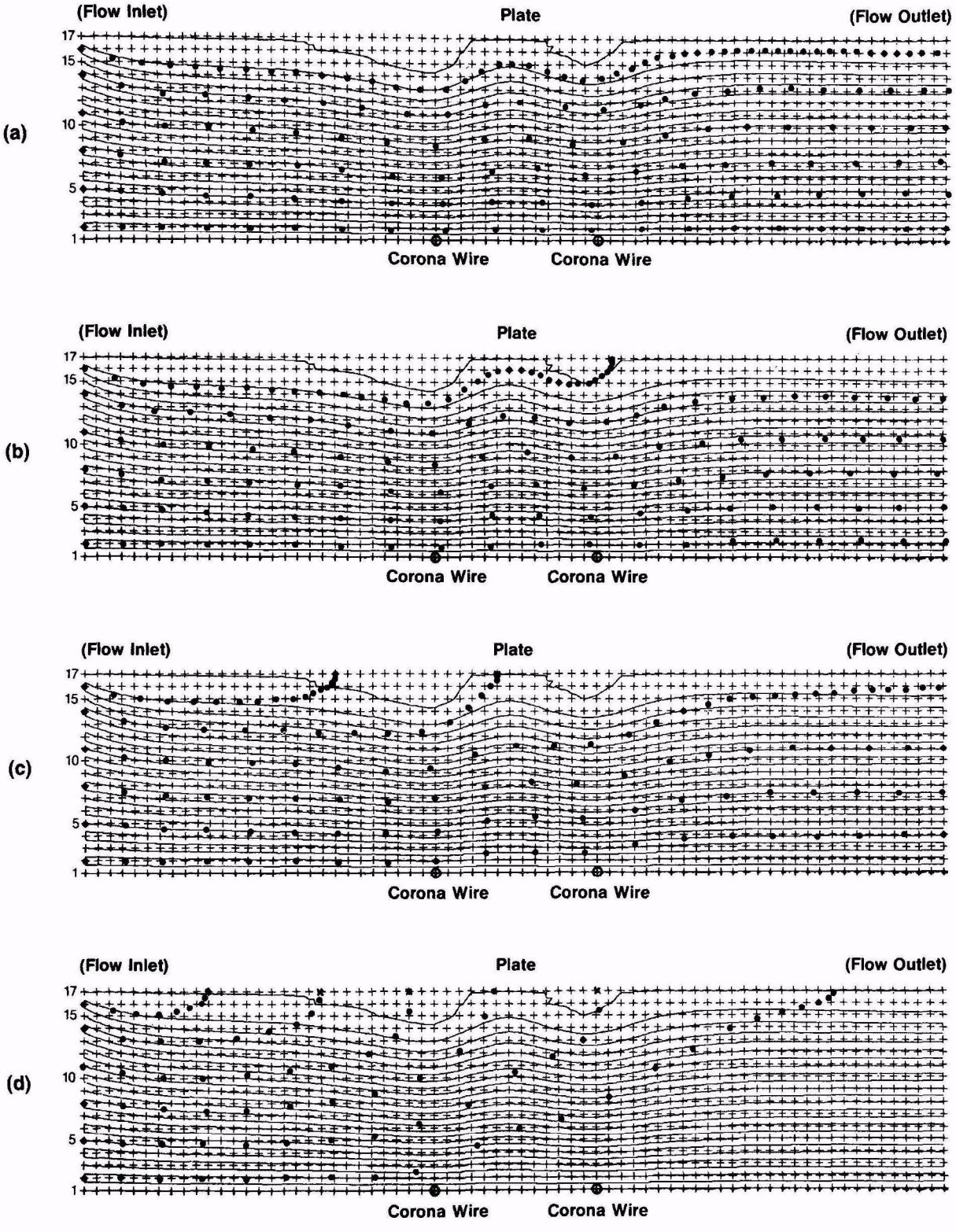

Figure 3. Particle Trajectories in the EHD Field for N_{EHD} = 1.34 (U_o = 1.22 m/sec, R = 4800, E_o = 5.0 kV/cm): (a) $N_{E\text{-}C}$ = 0.012, (b) $N_{E\text{-}C}$ = 0.024, (c) $N_{E\text{-}C}$ = 0.120, (d) $N_{E\text{-}C}$ = 0.483.

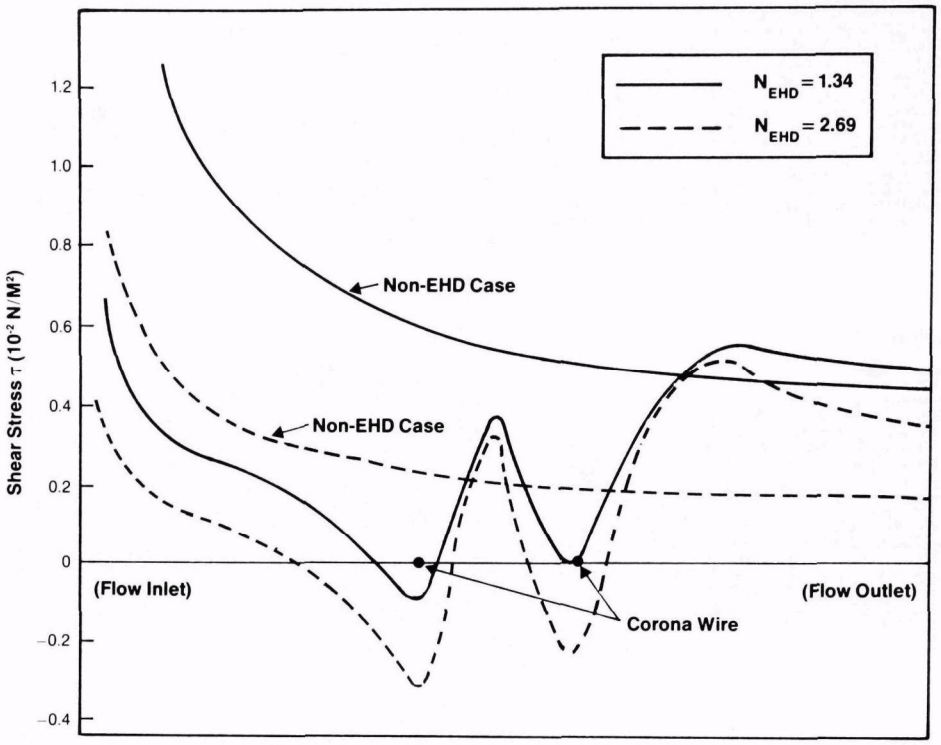

Figure 4. Shear Stress Distribution for EHD and Non-EHD Laminar Flow Case.

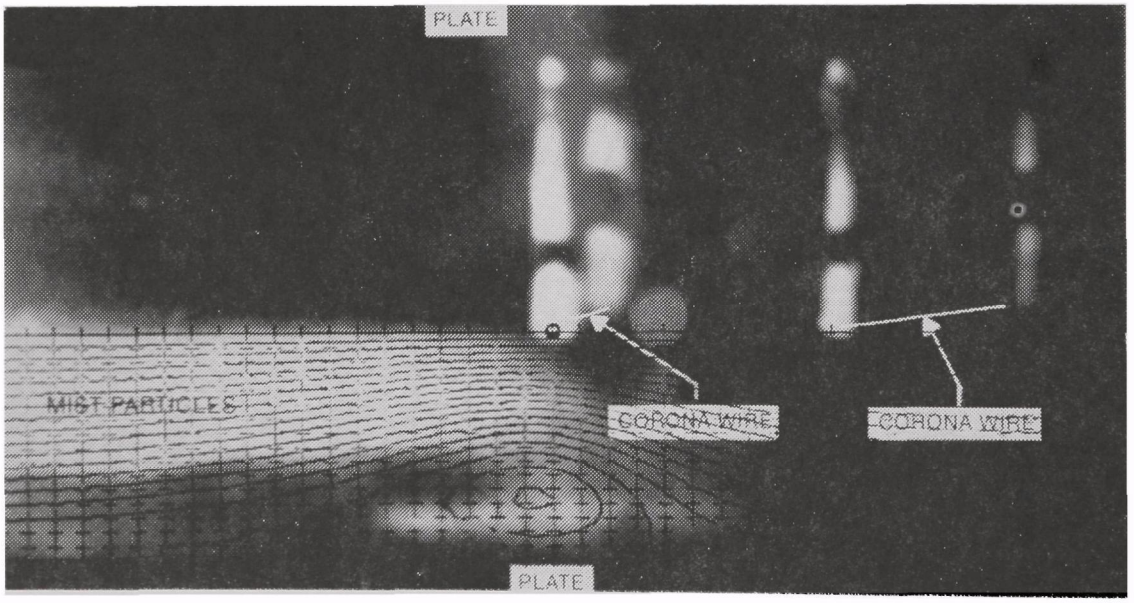

Figure 5. The Motion of the Mist Particle for N_{EHD} = 4.0 and N_{E-C} = 0.6.

SURFACE REENTRAINMENT OF COLLECTED FLY ASH IN ELECTROSTATIC PRECIPITATORS

By: M. Mitchner, M. J. Fisher, D. S. Gere, R. N. Leach, and S. A. Self
Dept. of Mechanical Engineering, Stanford University
Stanford, CA 94305, U.S.A.

ABSTRACT

Experiments have been performed in a horizontal flow wire-and-plate electrostatic precipitator (plate-to-plate spacing, 0.25 m) to study the effects of flow speed (from 3 to 22 ft/sec) and corona-type on the reentrainment of collected fly ash. The deposited dust layer is observed to exhibit a well-defined structure, with regions of highly-compacted dust separated by regions of loosely-packed dust. At lower flow speeds the loosely-packed areas are considerably deeper than the surrounding regions, whereas at higher speeds the reverse is the case. Surface reentrainment is observed to take place primarily from regions corresponding to locations of loosely-packed dust. Two modes of reentrainment are observed; a continuous erosion process which becomes more pronounced at higher speeds, and a relatively infrequent large scale fall-off process which tends to occur at lower speeds. It is shown that the dust layer structure results from the variation of corona current density J on the collector surface, with the compacted regions occurring where J is large, and with the loosely-packed areas occurring where J is zero (or small, in a time-average sense).

INTRODUCTION

Studies of particle transport through the gas to the collecting surfaces of an electrostatic precipitator indicate that in the absence of non-ideal effects precipitators should perform much better than they actually do. One reason for this reduced performance may be the reentrainment of fly ash from the collecting electrodes. In his book White [1] states "Particle loss by reentrainment is one of the most severe and oft recurring limitations present in the electrostatic precipitation of dry particles."

On the basis mostly of indirect measurements of quantities such as efficiency, the exit particle size distribution, or net particle charge, it is inferred that erosion tends to set in rather suddenly as gas velocity is increased. White states that values of the critical erosion velocity may range between 3 ft/sec for light, fluffy particles to 15 ft/sec for particles which form dense, compact layers. Other relevant factors include quality of gas flow, ash resistivity, corona current, the nature of the particles, and configuration of the collecting electrodes. White states that smooth flat, plates are unsatisfactory for dry-particle collection and that "great improvement is effected by providing shielded collection zones protected from the direct blast of the gas stream." Workers in the United kingdom [2] do not appear to agree with this conclusion.

Despite the importance of reentrainment there have been very few studies of the basic nature of the phenomenon and few systematic, quantitative studies of how reentrainment is affected by different conditions. The goal of the work reported here was to make direct observations of the ash layer in an operating electrostatic precipitator to obtain primarily a better qualitative understanding of the manner in which reentrainment takes place. To aid in the interpretation of our observations it was helpful to work with both positive and negative corona, and with both wire and point corona. In this study we have focused primarily on the effect of flow velocity, and have attempted to maintain other possibly relevant parameters constant.

The major finding of this work is that ash layers exhibit a well-defined pattern controlled by the pattern of the corona current density on the collector, and that reentrainment is initiated in regions of the ash layer where the corona current density is very small. The experimental apparatus and procedures used are described next, followed by a discussion of the observations and measurements.

EXPERIMENTAL APPARATUS AND PROCEDURES

The Electrostatic Precipitator Test Facility used for these experiments is basically a low speed, open circuit wind tunnel with provisions for injecting and removing particles, and for heating and humidifying the airstream. Air flow is generated by a 4000 cfm centrifugal blower at the exhaust end of the tunnel. The facility can operate with air flow velocities up to 10 m/s in a test section where length is variable up to 9 m.

For the experiments reported here, the test section used is representive of one unit of a conventional horizontal flow wire and plate electrostatic precipitator. The precipitator section is 24.7 cm wide, 75.5 cm high, and 175 cm long (10 in. x 30 in. x 6 ft.), and has seven corona wires 3 mm in diameter and 24.5 cm apart. For some of the experiments the corona wires were replaced with 5/8 in. diameter copper tubes which are of a large enough diameter that no corona discharges occur at the voltages applied. Sharp pointed electrodes were soldered onto four of the tubes to give a fixed corona pattern. The first, last, and middle tubes were left without points but were energized and contributed to the overall electric field.

The top of the test section is made of tempered safety glass to permit viewing of the interior of the precipitator. One side wall of the test section is hinged at the bottom so that it can be opened for detailed examination and measurements of the deposition pattern at the completion of a data run and to facilitate cleaning of the section.

The fly ash used in these experiments was a mixture of ash "B" and "C" taken from the Arapahoe Power Station in Colorado. This fly ash is normally in the medium-high resistivity range of $10^9 - 10^{10}$ Ωm and consists of particles having a mass median diameter of approximately 4 μm.

The majority of the experiments were performed at a nominal velocity of 1.7 m/s with a nominal particle loading of 3.9 grams/m^3. Runs were also made at velocities of 0.84, 3.3, and 6.7 m/s. Experiments were performed under ambient conditions using outside air.

Of primary interest in this study were the surface textures and patterns and the depth and density of the ash deposits as these features relate to reentrainment. Surface textures were observed and photographed with Polaroid and 35 mm cameras. Most of these photographs were taken at the completion of a data run by opening the hinged wall and photographing both the hinged wall and the fixed wall. To record the formation of the ash layer during precipitator operation, 8 mm time-lapse moving pictures were taken during some of the runs through the overhead mirror and window system at a rate of 2 frames/sec.

In addition to the visual observation of the dust patterns, isokinetic collectors located upstream and downstream of the precipitator section were used to determine the precipitator efficiency and to provide information on dust loading. Measured efficiencies ranged from 99.9% to about 70%, decreasing with increasing velocity, as would be expected from both the decreasing residence time in the precipitator and increasing surface re-entrainment.

Density measurements of the deposited ash were made by pressing a 1 cm diameter open-ended tube through the collected dust to seal against the metal surface, vacuuming the enclosed ash into a thimble collector, and then weighing the thimble. The depth of the ash immediately surrounding the collected area was measured with a specially-built micrometer depth gauge. Thus both the area density and the bulk density were obtained at points within selected areas of deposition.

For the experiments employing wire electrodes, the current was maintained at a constant nominal value of 2 mA, corresponding to an average current density at the collector plates of 0.75 mA/m^2. Actual current values are reduced owing to some degree of external corona leakage. To maintain this value, it was necessary to vary the corona voltage between 56 and 65 kV. At times it was necessary to reduce the current slightly below this value to prevent excessive sparkover.

While attempts were made to hold conditions constant during a run and for subsequent repeat runs, several parameters were difficult to control precisely. In addition to the corona current and the ash loading discussed above, other conditions such as relative humidity of the air and moisture in the ash varied (although the ash supply was kept dry by constant heating). When the hinged door was opened to gain access after a data run some fall-off would occasionally occur. Fall-off occuring as a result of opening the door would leave a clean metal surface, whereas fall-off occurring during a run was distinguished by the secondary dust that was precipitated on the metal surface subsequent to the initial fall-off.

OBSERVATIONS, MEASUREMENTS, AND DISCUSSION

This section is divided into two parts. The first part deals with the results of the lower velocity tests, in which no observable erosion took place. The second section describes the higher velocity test results in which erosion was observed to take place during precipitator operation.

Low Velocity Experiments (0.84 and 1.7 m/s)

Positive Corona

As shown in Figs. 1 and 2, the ash deposited at low velocities with a positive corona discharge forms a relatively smooth, uniform surface except for narrow ridges of ash which form straight vertical lines midway between the wire electrodes. The surface texture of these raised ridges is grainier than the surrounding ash. Measurements show that the bulk density of the ash in the ridges (0.25 g/cm^3) is approximately half that of the surrounding ash (0.45 to 0.50 g/cm^3), but it is deposited twice as deep. Therefore, the surface density of the ash on the ridge is equal to that of the surrounding ash, indicating no preferential collection of ash. Other secondary regularities in structure that may be observed are horizontal straight lines spaced approximately 1 cm. apart, and occasional gentle S-shaped elevations.

At these lower velocities, the ash layer periodically falls off the wall in an avalanche-like process as the weight of the ash overcomes the forces holding it to the wall. This large-scale fall-off process always begins in one of the loosely packed vertical areas between the electrodes, but fans out into the surrounding ash. The ash from this fall-off piles up on the floor of the precipitator where it remains for the duration of the run (i.e., it is not blown down the tunnel at velocities of 0.84 m/s and 1.7 m/s). The measured efficiencies were around 99% and 90% for the lower and higher velocities, respectively.

Negative Corona

The ash deposited with a negative corona discharge at low velocities forms a pattern of vertical lines and parabolic curves, as illustrated in Fig. 3. The vertical lines are similar to the lines seen with the positive corona, in that they consist of loosely-packed ash located midway between the wire electrodes, but with negative corona these lines are not straight. The loosely packed ash forms a series of straight line segments, joined together at slight angles to one another, which close off the parabolic forms. These parabolic shapes appear to occur at random spacings, and face either up or down stream. The ash within the parabolas is tightly packed and has a bulk density of approximately 0.5 g/cm^3, while the ash which forms the outline of the parabola consists of loosely packed ash. These parabolic lines rarely cross over one another and when they do, it is clear that both parabolas had not been formed at the same time (i. e., the parabolas occasionally move around with time). The parabolic shapes can be

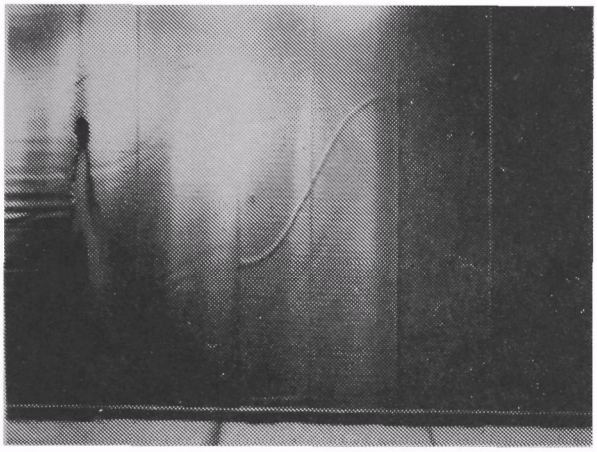

Fig. 1 Fly ash deposition pattern on vertical collector near upstream end of precipitator. Flow is from left to right in all figures. Flow velocity 1.7 m/s, positive corona, and 30 minutes run time. The lower left part of the large-scale fall-off region with its apex on the first ridge occurred during tunnel operation; the upper right part with the clean undersurface occurred when the door forming the opposite collector was opened.

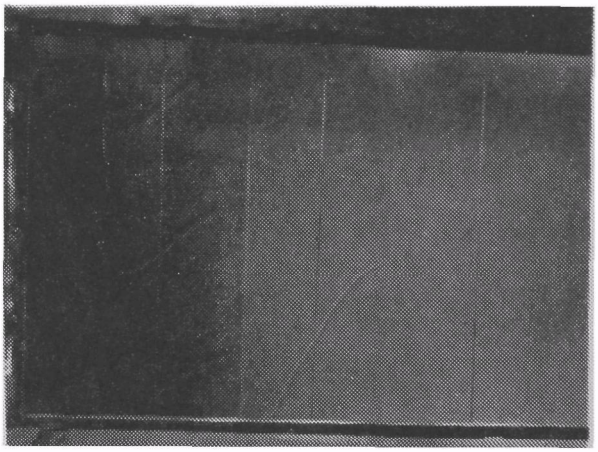

Fig. 2 Fly ash deposition pattern on vertical collector near upstream end of precipitator. Flow velocity 0.84 m/s, positive corona, and 60 minutes run time.

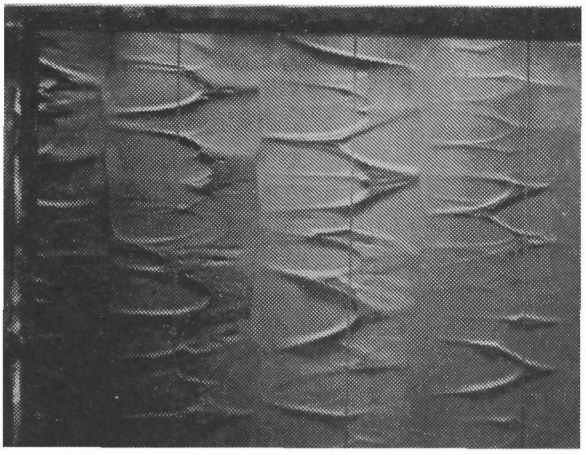

Fig. 3 Fly ash deposition pattern on vertical collector near upstream end of precipitator. Flow velocity 1.7 m/s, negative corona, and 30 minutes run time.

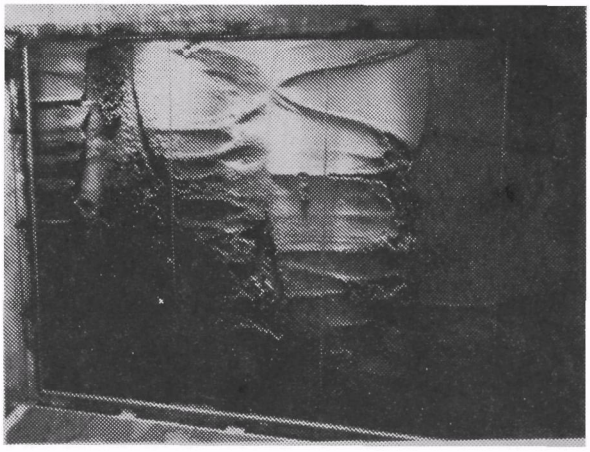

Fig. 4 Large-scale fall-off with negative corona. Flow velocity 1.7 m/s and 10 minutes run time.

faint or pronounced, large or small.

Large-scale avalanche-like fall-off was occasionally apparent with negative corona as it was with positive corona, as shown in Fig. 4. Fall-off would originate in a loosely packed region, and would then cause the ash to avalanche to the precipitator floor. With negative corona, this type of fall-off seemed to occur less frequently and to result in smaller fall-off regions than with positive corona. (In these respects, Fig. 4 is somewhat atypical). The precipitator efficiencies for these runs were approximately the same as obtained with positive corona.

Comparing the observations of positive and negative corona, it seemed as if the differences in deposition patterns could be explained in terms of the different current density distributions that would occur on the collector surface for these two modes of operation. With positive corona, current is usually emitted from the wires uniformally along the length of the wire. With negative corona, however, current is discharged from so-called "corona tufts" located at various points on the wire. To test this hypothesis, copper tubes with attached points were installed in place of the wire electrodes used in the previous runs. In all cases, the deposition patterns were quite striking in their regularity, as described next.

Point Electrodes

With the discharge points facing toward the wall oval patterns of very tightly packed ash surrounded by elevated loosely-packed ash were produced, as shown in Fig. 5. In Fig. 6, the upstream and downstream facing points from the upstream copper tube are seen to produce parabolic-shaped tightly packed regions with open ends facing upstream and downstream respectively and with a loosely packed region located directly opposite the tube; the dowstream copper tube with points facing the wall produces tightly packed oval shapes. With alternating streamwise-facing and wall-facing points placed on each tube, a deposition pattern such as illustrated in Fig. 7 is obtained. In all cases, there was one tightly packed region for each discharge point, and each tightly packed region was separated from the others by loosely packed ash. Furthermore, vertical lines midway between the tubes closed off the parabolic regions, and provided limits to the size of the oval sections.

As illustrated in Fig. 8, large-scale fall-off with point electrodes came only from loosely packed areas, even though there were tightly packed areas in the path of the avalanche. Also evident in this figure is the recapture of the avalanching ash as it falls past a tightly packed region. This behavior indicates that the adhesive forces are much larger in the tightly-packed regions than in the loosely-packed areas.

With point electrodes and at flow speeds of 1.7 m/s, the precipitator efficiency was approximately 90% for a corona current of 2 mA at 60 kV. The efficiency was increased to 95% for a corona current of 4 mA at 70 kV. The results of other measurements may be summarized as follows: (a) The ash surface density had approximately the same value in both the rough

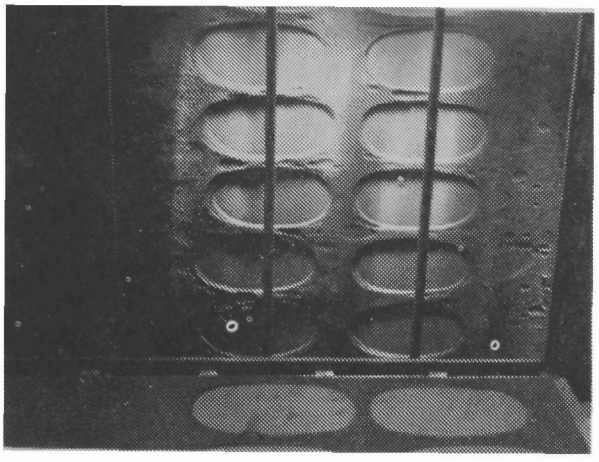

Fig. 5 Deposition pattern obtained with points facing collector surface. Flow velocity 1.7 m/s, negative corona, and 30 minutes run time. Ovals depressed. (Lighting from above.)

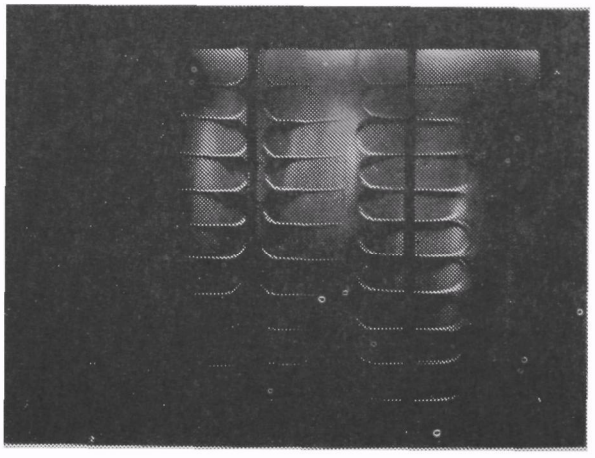

Fig. 6 Deposition pattern obtained with point electrodes. Upstream tube has points facing upstream and downstream; downstream tube has points facing toward collector surfaces. Velocity 1.7 m/s, negative corona, and 30 minutes run time. (Lighting from above.)

Fig. 7 Deposition pattern obtained with point electrodes. Alternating streamwise-facing and wall-facing points placed on each tube. The vertical ridge appears midway between 2nd and 3rd tubes. Velocity 1.7 m/s, positive corona, and 30 minutes run time. (Lighting from left.)

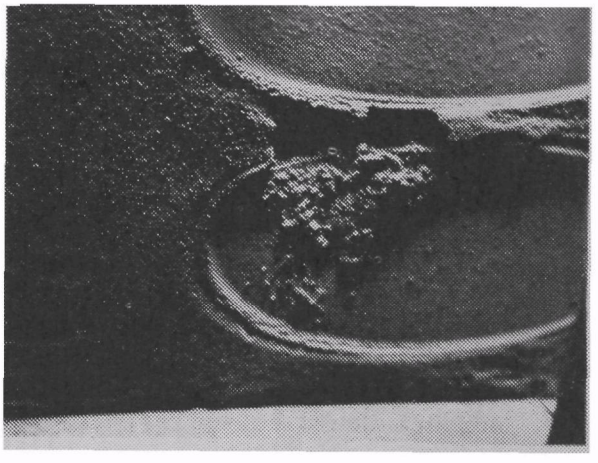

Fig. 8 Large-scale fall-off with point electrodes. Velocity 1.7 m/s, negative corona, and 30 minutes run time.

(i.e., loosely packed) and smooth (i.e., tightly packed) regions indicating no preferential deposition in these areas, except in the downstream precipitator sections where the rough areas consistently collected approximately 10% more ash than the smooth regions. (b) The bulk densities of ash were 0.9 g/cm^3 and 0.5 g/cm^3 in the smooth and rough regions, respectively, and were the same for both positive and negative corona to within ±15%. (c) The bulk density at the center of the ovals was approximately 10% higher than at the outer edge. (d) The ratio of rough ash height to smooth ash height was approximately 2:1. This ratio was slightly lower at the front of the precipitator and slightly higher at the rear. (e) The particle size distributions as determined using a Coulter Counter were the same for both the rough and smooth areas, just as they were with the wire electrodes.

Discussion

(a) The desposition patterns obtained with negative wire coronas appear to consist of a "random" superposition, in space and time, of the same kinds of patterns produced by point electrodes. These observations support the interpretation that the main differences in the deposition patterns between negative and positive wire coronas occur as a result of the "tuft-like" structure of negative corona discharges, in contrast to the more uniform structure of positive corona discharges.

(b) The tightly packed regions of ash appear to occur at locations on the collector plate where the corona current density is large, and result from the known large electrical "clamping forces" that accompany the presence of current flow through a highly resistant ash layer.

(c) The ion current beams originating from different wires, either uniformly or in the form of tufts, do not merge into one another because they are separated by electrical field lines from the wire which carry no ion current. Since electric field lines cannot cross, these non-current-carrying electric field lines always separate regions of ion current. The ion current beams can, however, squeeze the non-current carrying electric field lines into narrow regions and it is this mechanism which produces the lines of loosely packed ash on the collector.

(d) As shown by the measurements of Tassicker [3], although the corona current density at the collector surface is highly nonuniform, the electric field intensity is relatively uniform. (The transverse component of the Maxwell stress associated with the electric field would be expected to adjust the field distribution so that any forces parallel to the collector surface would be small). Thus the ash deposition rate will be approximately uniform and will produce a uniform ash surface density, as observed in the experiments.

High Velocity Experiments (3.3 and 6.7 m/sec)

Positive Corona - Flow Velocity 3.3 m/sec

At this velocity the entire ash pattern appears to be shifted slightly downstream with respect to the wire electrodes. As shown in Fig. 9, the

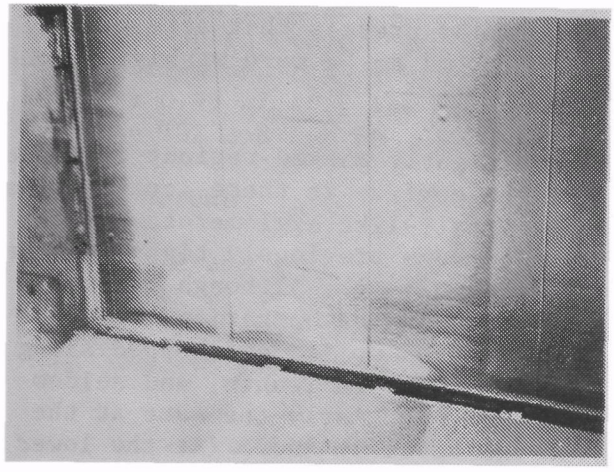

Fig. 9 Deposition pattern at higher gas velocities for positive corona showing effects of surface re-entrainment. Flow velocity 6.7 m/s, 30 minutes run time.

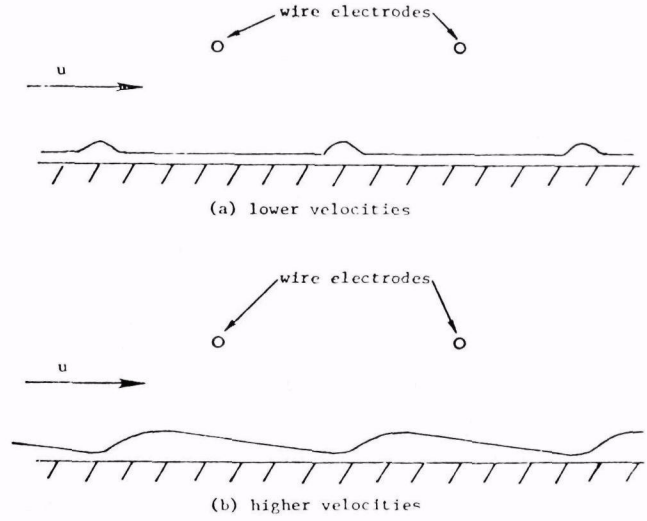

Fig. 10 Sketch showing the effect of surface re-entrainment at higher flow velocities on the thickness profile of the collected fly ash, for positive corona.

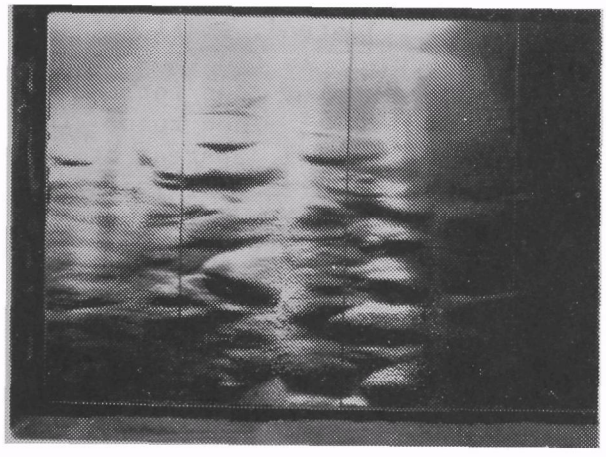

Fig. 11 Deposition pattern at higher gas velocities for negative corona showing effects of re-entrainment. Flow velocity 6.7 m/s, 30 minutes run time.

Fig. 12 Conditions as in Fig. 5 but flow velocity 6.7 m/s. Ovals elevated. (Lighting from above.)

locations on the collecting surface, where narrow elevated vertical ridges of ash occurred for lower velocities, are now occupied by broadened vertical depressions. The sketch in Fig. 10 of the variation of ash height in the flow direction illustrates that the downstream sides of the valleys are steeper than the upstream sides. The large-scale fall-off observed at lower velocities was much less apparent at 3.3 m/sec, and tended to occur, if at all, after very long periods of ash accumulation. These features are certainly indicative of a surface reentrainment process that acts preferentially on regions where the ash particles tend to be more weakly attached to each other.

Whereas the surface of the ash in the tightly packed regions is quite smooth at lower velocities, at 3.3 m/sec the surface at these locations is more grainy and appears to consist of small ball-like agglomerates of ash separated by air gaps. (The ash density in these previously tightly packed regions was now measured to be as low as 0.12 g/cm^2). Although it was difficult to see clearly into the precipitator during operation, it appeared that these ball-like agglomerates of ash rolled and hopped along the ash surface. The hops were usually about 6 cm in length, and seldom any longer. The average thickness of the ash was nearly the same at the downstream end of the precipitator as at the upstream end. (At the lower speeds, the ash thickness dropped off approximately exponentially with length). The average precipitator efficiency for the 3.3 m/sec runs was approximately 86%.

Positive Corona - Flow Velocity 6.7 m/sec

The hopping and rolling of ball-like agglomerates on the ash surface was no longer visible at this higher flow speed. Instead, small bits of ash seemed to jump off the ash layer and disintegrate in the flow stream. The surface texture of the ash deposit (although rougher than for the lower velocity runs) appeared to be smoother than for the 3.3 m/sec runs. The valley-like depressions observed at 3.3 m/sec were still apparent at locations previously occupied at lower speeds by elevations of loosely packed ash although shifted somewhat downstream. Occasionally the ash layer would exhibit secondary smaller depressions opposite the wire electrodes. The average thickness of the deposited ash was highest at either the middle or the downstream end of the precipitator. The ash bulk density was uniform over the length of the precipitator for these high speed runs, and was approximately 0.55 g/cm^3. No large-scale fall-off was ever observed, even when the precipitator was operated for long periods of time. The precipitator efficiency was approximately 70%.

Negative Corona - Flow Velocities 3.3 m/sec and 6.7 m/sec

The deposition patterns with negative corona at flow velocities of 3.3 m/sec and at 6.7 m/sec are very similar in appearance. As shown in Fig. 11, the ash surface has a quite "hilly" character. Locations which were occupied by elevated regions of loosely packed dust at low velocities are now regions in which the ash thickness is depressed. The regions from which the ash has been eroded correspond to regions of low corona current density.

The surface texture is slightly grainy, but much less so than for corresponding velocities with positive corona.

Visual observations during precipitator operation indicated that the reentrainment process consisted of a "hopping" of the ash from loosely-held areas to tightly packed regions. Large-scale fall-off was not observed for these velocities and it was possible to build up relatively deep thicknesses of ash (up to about 1 cm). The ash density in the tightly-packed regions (as determined from just one run at 6.7 m/sec) was quite high - approximately 0.95 g/cm^3. The measured precipitator efficiencies were approximately 90% and 66% at 3.3 m/sec and 6.7 m/sec respectively.

Point Corona

An example of the deposition pattern obtained at higher velocities with a regular array of point corona discharges is shown in Fig. 18. In comparison with the corresponding pattern at lower velocities, as shown in Fig. 5, the ash regions which were previously elevated are now depressed.

CONCLUSIONS

It has been shown by direct visual observation of the interior of an operating wire-and-plate electrostatic precipitator, that the onset of significant surface reentrainment for both positive and negative corona occurs at a flow velocity between 1.7 and 3.3 m/sec (i.e., between 5.5 and 11 ft/sec). Prior to the onset of reentrainment the ash layer exhibits a well-defined pattern on the collector surface, consisting of tightly packed regions and elevated loosely-packed regions. These regions correspond respectively to areas on the collector surface where the corona current density is high, and areas where the corona current density is zero (or the time-averaged current very small). Experiments with point electrodes have been used to explain the marked differences in deposition patterns between positive and negative corona as resulting from the uniform vs. "tuft-like" discharge structures respectively that characterize these two kinds of corona. Large-scale regions of ash were occasionally observed to fall from the ash layer in an avalanche-like process that is initiated in a loosely packed region.

At flow velocities where reentrainment occurs the deposition patterns remain well-defined, but at locations on the collector where the dust was previously elevated and loosely-packed, the ash layer is now depressed. Visual observations confirm that surface reentrainment appears to be initiated from ash located on the collector where the corona current density is very small. Large-scale fall-off at higher gas velocities was observed infrequently, or not at all. As a function of increasing flow velocity after the onset of reentrainment, the character of the reentrainment process for positive corona appeared to change significantly between 3.3 m/sec and 6.7 m/sec. The change in reentrainment behavior between these velocities was less evident for negative corona. At the highest velocities studied, the bulk density of the collected ash in the tightly packed regions was larger for negative than for positive corona. Although not examined

systematically in this study, it appeared that the bulk density of the collected ash increased with increasing current density to the collector.

It is clear from these experiments that the electrical "clamping" force associated with the flow of corona current through a resistive ash layer plays an essential role in the surface reentrainment process. Methods designed to improve the distribution of current density over the collector surface should lead to a reduction in the deleterious effects resulting from surface reentrainment at higher gas velocities.

ACKNOWLEDGEMENTS

This work was supported by the Electric Power Research Institute under Contract RP 533-1.

REFERENCES

1. White, H. J., "Industrial Electrostatic Precipitation." Addison-Wesley (1963).

2. Lowe, H. J. "Recent Advances in Electrostatic Precipitation for Dust Removal." Phil. Trans. Roy. Soc. Lond. A., 265, 301 (1969). See also: Dalmon, J. and H. J. Lowe, "Experimental Investigations into the Performance of Electrostatic Precipitators for P. F. Power Stations." Proc. Int. Symp. on Physics of Electrostatic Forces and Their Applications, Grenoble (1960).

3. Tassicker, O. J., "Aspects of Forces on Charged Particles in Electrostatic Precipitators." Ph.D. Thesis, University of New South Wales (1972). See also EPRI Reprint (1977).

ELECTROMECHANICS OF PRECIPITATED ASH LAYERS

By: G. B. Moslehi and S. A. Self
Dept. of Mechanical Engineering, Stanford University
Stanford, CA 94305, U.S.A.

ABSTRACT

A comprehensive analysis is given of the electromechanics of a precipitated ash layer, modeled as a regular array of resistive spheres, which allows for both volume and surface conduction and takes account of self-compression of the layer. Formulae are derived for the contact radius, the electric field distribution, the compressive stress in the layer and the apparent electrical resistivity. For typical precipitator conditions the electrical clamping force is found to be remarkably large (10 - 100 gm-wt/cm^2) and the layer resistivity is found to decrease with increasing current and field as found experimentally. The theory is extended to predict conditions for the onset of back discharge, in the form of intermittent microsparks in the contact regions. Preliminary measurements using glass beads in a resistivity cell show general agreement with the theoretical results.

INTRODUCTION

The electromechanics of the precipitated particulate layer is a most important aspect of the precipitation process which has attracted relatively little attention and is poorly understood. A comprehensive treatment of this subject should provide quantitative answers, in terms of fundamental quantities, to such matters as: (i) the cohesive stress which attaches the layer to the collector against reentrainment and must be overcome for successful dislodgement during rapping; (ii) prediction of the resistivity-current characteristic of particulate layers measured in-situ or in a standard resistivity cell; (iii) prediction of the average electric field for onset of back discharge in the layer.

In setting up a physical model for analysis, it is clear that the problem should be treated as one of resistive current flow (of the corona ion current) through a leaky dielectric. However, it is inadequate to treat the layer as a homogeneous leaky dielectric with cohesive stress $P = \varepsilon_o \varepsilon_A E_A^2/2$ (where ε_A and E_A are the average permittivity and field) since the calculated stress is insignificantly small - e.g. for $\varepsilon_A \sim 2$, $E_A \sim 10^6$ V/m, we find $P \lesssim 10$ N/m^2 ($\lesssim 0.1$ gm/cm^2). Moreover, unless the layer resistivity ρ_A is roughly greater than ρ_c, the resistivity of the corona medium (typically $\sim 10^{11}\Omega$.cm), the net force on the layer is found to be detaching [1].

The essential feature of the precipitated layer which must be included in the model is its particulate nature, as recognized by McLean [2] who modelled the layer as a regular cubical array of resistive spheres. The concentration of current in the region of contact between spheres implies a great enhancement of the field in the gap surrounding the contact area, above the average value E_A in the layer. The attractive force between

spheres, associated with this field, produces an average compressive stress in the layer which is much larger than that calculated for a homogeneous dielectric. Basically this is because in a highly inhomogeneous field $\langle E^2 \rangle$ is much greater than $\langle E \rangle^2$. For conditions typical of coal-fired power plant precipitators, the compressive stress may thus be $\gtrsim 10$ gm/cm^2, and it is clear that this plays an essential role in retaining the layer against aerodynamic and gravitational forces tending to detach it. Moreover, since there is no significant current concentration at the surface; where the ion current enters the layer (see Fig. 1), the net force on the layer is an attaching one even down to relatively low values of ash resistivity.

In this paper we outline the main features and results of a comprehensive theory of the electromechanics of a precipitated ash layer, which has been developed in the past year [3]. The layer is modeled as a regular cubical array of smooth spheres having volume resistivity ρ and surface resistivity s. (The theory can be extended to the case of a close-packed rhombohedral array without difficulty).

The first step is to solve for the potential distribution in a single sphere having current entering and leaving at point contacts at opposite poles. This solution is then adapted to find an approximate solution for the potential in the neighborhood of the contact between two spheres having a specified (non-zero) contact radius. From this potential, the electric field distribution in the gap surrounding the contact is found and thence attractive force between the two spheres is determined.

By treating the spheres as elastically deformable, use is made of the Hertz formula, relating contact radius and compressive force, to solve for the contact radius as a function of the current and material properties. This leads directly to self-consistent expressions for the contact radius, the field distribution, the average layer compressive stress and the average layer resistivity as a function of average layer current density (or field) and the material properties.

The apparent layer resistivity ρ_A is found to be a decreasing function of the average current density J_A or field E_A which is basically due to self compression of the layer which increases the contact radius. Its form depends on the relative contributions of surface and volume conduction, and is shown to correlate with preliminary measurements of the apparent resistivity of layers of glass beads in a standard resistivity cell.

Finally, the electric field distribution in the gaps is used, together with results from the literature for gas-discharge and vacuum breakdown in small gaps to predict the conditions for onset of back discharge in the form of intermittent microsparks between the spheres in the contact region.

FIELD BETWEEN CONTACTING RESISTIVE SPHERES

Potential Distribution for Single Sphere with Point Contacts

For a single sphere of radius a, having volume resistivity ρ, surface resistivity s, and with current I entering and leaving at the poles $\theta = 0, \pi$

(see Fig. 2) the potential distribution can be shown to be

$$V = \frac{I}{2\pi} \sum_{n=o}^{\infty} \left(\frac{4n+3}{2n+1}\right) \left[\frac{1}{\left(\frac{2n+2}{s}\right) + \frac{a}{\rho}}\right] \left(\frac{r}{a}\right)^{2n+1} P_{2n+1}(\mu) \quad . \qquad (1)$$

Here $\mu \equiv \cos\theta$ and P is the Legendre function of the first kind. The expression (1) has the expected form of two resistors in parallel and goes over to the known solutions [4] for the separate cases of volume and surface conduction. The diametral plane is the equipotential $V = 0$, and $V \to \pm\infty$ at the poles. In the latter regions alternative expressions can be given for V [3] which converge more rapidly and show that the equipotentials approximate spherical surfaces centered on the poles.

For points on the surface $r = a$, it is convenient to write

$$V(\sigma,\theta) = \frac{\rho I}{4\pi a} F(\sigma,\mu) = \frac{sI}{4\pi} \left[\frac{1}{\sigma} F(\sigma,\mu)\right] \qquad (2)$$

where $\sigma \equiv s\ a/\rho$ is a dimensionless measure of the relative contributions of volume and surface conduction, and F is a function calculable from explicit formulae [3]. For the case of volume conduction ($\sigma \to \infty$), and for small angles, $F \to F_V \to 2/\theta$, so that V has a simple pole at the contact point. On the other hand, for the case of surface conduction ($\sigma \to 0$), $(F_s/\sigma) \to 2 \ln(2/\theta)$, so that V has a logarithmic pole at the contact points.

Field in the Gap between Spheres with Non-Zero Contact Radius

The contact region is modeled as shown in Fig. 3. In the solution for a point contact, the region surrounding the contact point can be replaced by a perfect conductor whose potential V_o (say) and surface matches the equipotential which intersects the sphere at polar angle θ_o, without perturbing the potential in the rest of the sphere. Moreover the spherical cap of this conductor can be removed to leave a flat surface of contact angle θ_o, again without perturbing the rest of the potential solution. The contact between two spheres is then modeled by contacting the flat surfaces of two such bodies.

The field in the gap for a contact radius $\delta = a\,\theta_o$ is then found by dividing the potential difference across the gap by the gap height $2h$, which is a good approximation for small θ. Thus

$$E(\theta,\theta_o) = \frac{V(\sigma,\theta_o) - V(\sigma,\theta)}{h} = \frac{\rho I}{4\pi a^2} \left[\frac{F(\sigma,\mu_o) - F(\sigma,\mu)}{\mu_o - \mu}\right] \quad . \qquad (3)$$

Although the potential difference and gap height both tend to zero as $\theta \to \theta_o$, the field tends to a finite limit which is a maximum

$$E_{max} = \lim_{\mu \to \mu_o} [E(\theta,\theta_o)] = \left(\frac{\rho I}{4\pi a^2}\right) F'(\sigma,\mu_o) , \quad (4)$$

where $F' = dF/d\mu$.

Now the average field across the layer is just

$$E_A = (V_o/a) = (\rho I/4\pi a^2) F(\sigma,\mu_o) , \quad (5)$$

so the field enhancement factor in the gap can be written

$$(FEF) \equiv (E_{max}/E_A) = F'(\sigma,\mu_o)/F(\sigma,\mu_o) . \quad (6)$$

It is convenient to write the field in the gap as

$$E(\theta,\theta_o) \equiv E_{max} G(x) , \quad (7)$$

where $G = 1$ in the contact region itself and for $x \equiv (\theta/\theta_o) > 1$,

$$G(x) \equiv [F(\sigma,\mu_o) - F(\sigma,\mu)]/[(\mu_o-\mu) F'(\sigma,\mu_o)] . \quad (8)$$

The form of $G(x)$ is shown in Figure 4 for the limits of volume and surface conduction.

Average Resistivity of a Particulate Layer

The average resistivity of the layer is given by

$$\rho_A = 4aV_o/I = (\rho/\pi) F(\sigma,\mu_o) \quad (9)$$

CONTACT RADIUS AND FORCE BETWEEN SPHERES

Attractive Electrical Force Between Spheres for Given Contact Angle

The attractive force between spheres arises from the tension in the field lines in the gap which are highly concentrated around the contact area. The electrical force F_E can be evaluated as the area integral of the electric stress $\varepsilon_o E^2/2$, thus:

$$F_E = 4\pi\varepsilon_o a^2\theta_o^2 E_{max}^2 A(\sigma,\theta_o) , \quad (10)$$

where

$$A(\sigma,\theta_o) \equiv \frac{1}{4}\left[(1/2) + \frac{1}{\theta_o^2}\int_{\theta_o}^{\pi/2} [G(x)]^2 \sin\theta \cos\theta \, d\theta\right] . \quad (11)$$

The first term (1/2) comes from the contact region while the second comes from the gap surrounding the contact. The function A is a very weak function of θ_o and can be taken as constant with $A_v \sim 0.32$ and $A_s \sim 0.95$ in the volume and surface conduction limits respectively. One can also evaluate the average compressive stress in the layer P_E, as:

$$P_E = (F_E/4a^2) = \pi\varepsilon_o E_{max}^2 \theta_o^2 A(\sigma,\theta_o) \quad . \tag{12}$$

Contact Angle for a Given Compressive Force

The contact angle θ_o between elastically deformable spheres under a compressive force F_E is given by the Hertz formula [5]

$$F_E = a^2\theta_o^3/B \quad , \tag{13}$$

where

$$B \equiv 3(1-\nu^2)/4Y \quad . \tag{14}$$

Here Y is Young's modulus and ν is Poisson's ratio.

Contact Angle as a Function of Average Layer Field

By eliminating F_E between Eqs. (10) and (13) we can find the self-consistent contact angle for a given average layer field $E_A \equiv \rho_A J_A$ as

$$\theta_o = [4\pi\varepsilon_o C E_{sv}^2]^{1/5} \quad . \tag{15}$$

Here $C \equiv AB$ is a function of the material properties (σ, ν and Y) and $E_{sv} \equiv \theta_o^2 E_{max}$ is a characteristic field which is related to the average field by

$$E_A = K_{sv} E_{sv} \quad , \tag{16}$$

where

$$K_{sv}(\sigma,\theta_o) \equiv F(\sigma,\mu_o)/[\theta_o^2 F'(\sigma,\mu_o)] \quad . \tag{17}$$

SELF-CONSISTENT RESULTS

In general, given the explicit formulae for calculating F and F', and for specified values of the material properties $\sigma \equiv (s\ a/\rho)$ and B, then, for specified values of the average field E_A, Eqs. (15), (16) and (17) can be solved together to find the self-consistent values of E_{sv} and θ_o which take account of self-compression of the layer.

Then, using these values of E_{sv} and θ_o, one can calculate, as functions of J_A or E_A, self-consistent values of: (i) $E_{max} \equiv E_{sv}/\theta_o^2$; (ii) the field enhancement factor from Eq. (6); (iii) the average compressive stress in the layer P_E from Eq. (12) and (iv) the dimensionless average resistivity (ρ_A/ρ) from Eq. (9).

Volume Resistivity Case

In this case ($\sigma \equiv (s\ a/\rho) \to \infty$), which applies for high temperature and low humidity, we have $K_{sv} \to K_v = 1$, so that $E_{sv} = E_A$ and we obtain the explicit results:

$$\theta_o = (2/\pi)^{2/7} D_v^{1/7} (\rho J_A)^{2/7} = D_v^{1/5} E_A^{2/5} , \quad (18)$$

$$E_{max} = (2/\pi)^{1/7} D_v^{-3/7} (\rho J_A)^{1/7} = D_v^{-2/5} E_A^{1/5} , \quad (19)$$

$$P_E = 2(\pi/2)^{1/7} A_v \varepsilon_o D_v^{-4/7} (\rho J_A)^{6/7} = \pi A_v \varepsilon_o D_v^{-2/5} E_A^{6/5} , \quad (20)$$

$$(\rho_A/\rho) = (2/\pi)^{5/7} D_v^{-1/7} (\rho J_A)^{-2/7} = (2/\pi) D_v^{-1/5} E_A^{-2/5} , \quad (21)$$

where $D_v \equiv 4\pi\varepsilon_o C_v$.

Note that θ_o and E_{max} increase rather slowly with ρ, J_A and E_A, that P_E increases approximately linearly with ρ, J_A and E_A (rather than as the square, as simple considerations would suggest) and that (ρ_A/ρ) decreases slowly with ρ, J_A and E_A due to the self-compression.

These results can be illustrated by the following numerical estimates. For a typical glassy fly ash we take $Y \sim 7.5 \times 10^{10}$ N/m^2, $\nu \sim 0.25$, so that $B \sim 10^{-11}$ m^2/N and with $A_v \sim 0.32$ we have $C_v \sim 3 \times 10^{-12}$ m^2/N and $D_v \sim 3.3 \times 10^{-22}$ (V/m)$^{-2}$. We may also take $E_A \sim 3 \times 10^5$ V/m as a typical maximum average field below the onset of back discharge. Then we find $\theta_o \sim 8 \times 10^{-3}$ radian, and $E_{max} \sim 4.8 \times 10^9$ V/m corresponding to a field enhancement factor of 1.6×10^4. Although this value of E_{max} is very large, it is slightly less than the value (6.5×10^9 V/m) quoted [6] as the local field for vacuum breakdown in small gaps. The cohesive stress is calculated to be $P_E \sim 1.3 \times 10^4$ N/m^2 (≈ 130 gm/cm^2), which is much larger than calculated on the basis of a homogeneous dielectric and, in fact, is much larger than the weight per unit area of a typical ash layer. Finally, we find $(\rho_A/\rho) \sim 80$ which shows that the layer resistivity is much larger than the material resistivity as a result of the current concentration at the contacts.

Surface Resistivity Case

In this case ($\sigma \equiv (s\ a/\rho) \to 0$), which applies for low temperature and high humidity, the quantity $K_{sv} \to K_s$ is not a universal constant but is weakly dependent on E_A and on the material properties; and is given by

$$K_s \equiv (1/5) \ln [32 D_s^{-1} E_s^{-2}] , \quad (22)$$

where $D_s \equiv 4\pi\varepsilon_o C_s \equiv 4\pi\varepsilon_o A_s B \sim 1.0 \times 10^{-21}(V/m)^{-2}$ for $B \sim 10^{-11}$ m^2/N

With this value, K_s is calculated from Eqs. (22) and (16) to decrease from 7.5 to 5.5 as E_A increases from 10^4 to 10^6 V/m.

We can then write the explicit results:

$$\theta_o = (2/\pi)^{2/5} D_s^{1/5} (saJ_A)^{2/5} = D_s^{1/5} (E_A/K_s)^{2/5} , \quad (23)$$

$$E_{max} = (2/\pi)^{1/5} D_s^{-2/5} (saJ_A)^{1/5} = D_s^{-2/5} (E_A/K_s)^{1/5} , \quad (24)$$

$$P_E = 2(2/\pi)^{1/5} A_s \varepsilon_o D_s^{-2/5} (saJ_A)^{6/5} = \pi A_s \varepsilon_o D_s^{-2/5} (E_A/K_s)^{6/5} , \quad (25)$$

$$(\rho_A/s\,a) = (2/5\pi) \ln[8\pi^2 D_s^{-1} (sa\,J_A)^{-2}] = (2/5\pi) \ln [32\, D_s^{-1} (E_A/K_s)^{-2}] \quad (26)$$

Comparing these results with the case of volume conduction, it is seen that the dependence of θ_o, E_{max} and P_E on E_A is of similar form, apart from the weak dependence of K_s on E_A noted above. However the normalized layer resistance decreases more slowly with E_A because of the logarithm in Eq. (26).

Taking $D_s \sim 1.0 \times 10^{-21}$ $(V/m)^{-2}$ and $E_A \sim 3 \times 10^5$ V/m, for which $K_s \sim 6$, we find the following numerical values: $\theta_o \sim 4.8 \times 10^{-3}$ radian, about half that for the volume conductivity case; $E_{max} \sim 2.2 \times 10^9$ V/m, a factor ~ 2 lower than the volume case; $P_E \sim 2.9 \times 10^3$ N/m^2 a factor ~ 4 lower than the volume case; and $(\rho_A/sa) \sim 4$.

For the general case, when both volume and surface conductivity are significant, the results will be intermediate between those for the limiting cases $\sigma \to \infty$ and $\sigma \to 0$ discussed above, and can be computed by the method outlined at the beginning of this section.

ONSET OF BACK-DISCHARGE

Back-discharge is attributed to electrical breakdown in the contact area or the surrounding gap between particles, which is known to set in for average fields E_A of the order of 10^6 V/m. It is clear that the large field enhancement in the contact region is responsible for breakdown occurring at such low values of average field, because for small gaps, comparable with the mean free path λ of the gas, the breakdown field is typically $\gtrsim 10^8$ V/m. The discharge is expected to occur in the form of intermittent microsparks which discharge the gap, which then charges up slowly through the layer resistance. In fact the layer should act like a number of capacitative spark gaps in series, separated by high resistances, so that the discharge will propagate through the layer as a cascade of microsparks which discharges the layer locally. Moreover, as E_A exceeds some threshold value E_{AB} for breakdown, one would expect the frequency of sparking to increase so that the average layer current increases and its average resistivity decreases steadily rather than catastrophically.

The condition for back discharge onset can be found by using the field in the contact area and surrounding gap, given by Eq. (7), together with results from the literature for electrical breakdown of small gaps between electrodes in air. There are two mechanisms to consider, namely, gas discharge breakdown for gaps of height $d \gtrsim \lambda$ and "vacuum" breakdown for $d \lesssim \lambda$. Which mechanism occurs first with increasing E_A, and where it occurs, will be determined by which threshold field for breakdown is first exceeded.

Data for gas discharge breakdown [6,7,8] is usually presented in the form of a Paschen curve for the breakdown voltage V_B as a function of gap height d. This curve, for which piecewise curve fit formulae are available [8], exhibits a minimum which, for air at STP, occurrs for $V_B \sim 340$ V and $d \sim 8.6$ μm, corresponding to $E_B \sim 4 \times 10^7$ V/m. The curve of $E_B(d)$ is a monotonically decreasing function of d, as shown in Fig. 5. For the smallest gaps the appropriate curve-fit formula gives $E_B \sim 1.3 \times 10^9$ V/m at $d = 1.3$ μm and $E_B \sim 7.6 \times 10^{11}$ V/m at $d = 0.13$ μm. The latter E_B value is enormous and the curve-fit formula is probably inapplicable because d is approaching the mean free path $\lambda \sim 0.06$ μm.

For the regime $d \lesssim \lambda$ data from vacuum breakdown experiments shows that for gaps less than ~1mm the average field for breakdown is independent of d and is about 10^8 V/m. However, vacuum breakdown is believed to depend on field enhancement at microprojections on the electrodes and the local field initiating breakdown is quoted [6] as $E_B \sim 6.5 \times 10^9$ V/m. For the purpose in hand we take this value for gaps less than $d \sim 1$μm where the curve fit for gas breakdown yields the same value. Thus the composite breakdown curve E_B (d) shown in Fig. 5 is assumed to apply.

The method for determining the onset condition for back-discharge breakdown is best illustrated by the graphical proceedure shown in Fig. 5. For a given particle radius a and material properties, the field in the gap $E(\theta,\theta_o)$ can be calculated for given values of average field E_A using the formulae developed earlier. Three such curves are shown in Fig. 5 for the case of volume conduction ($\sigma \to \infty$), $a = 100$ μm, $B = 10^{-11}$ m^2/N and for $E_A = 1.0 \times 10^6$, 1.5×10^6 and 2.0×10^6 V/m. It is seen that the first curve does not intersect the E_B (d) curve, the second curve intersects E_B (d) in the vacuum breakdown regime, while the third curve additionally intersects E_B (d) in the gas discharge breakdown region. Interpolation from these curves shows that for these conditions breakdown occurs first in the contact region ($d \sim 0$) at an average field for breakdown $E_{AB} \sim 1.3 \times 10^6$ V/m followed by breakdown in the surrounding gap (at a position where the gap height is ~10μm) at an average field of $E_{AB} \sim 1.8 \times 10^6$ V/m.

Further analysis of the dependence of the breakdown condition on particle radius shows, for the case of volume conduction, with $B \sim 10^{-11}$ m^2/N, and for air at STP, that for $a < 140$ μm, breakdown always occurs first as vacuum breakdown in the contact region ($d \sim 0$) at $E_{AB} \sim 1.3 \times 10^6$ V/m. For larger particles however, breakdown occurs first as gas discharge breakdown in the surrounding gap where the gap height is ~ 10 μm and at a field which decreases roughly inversely with radius. Thus for particle sizes relevant to fly ash the analysis indicates that in the case of volume conduction back-discharge occurs in the contact region itself at an average field of ~ 1.3×10^6 V/m, which value is comparable with measured values. Results for the case of surface conduction (and the combined case) have not yet been fully evaluated, but appear to show results of similar form except that the breakdown field is higher.

PRELIMINARY MEASUREMENTS ON GLASS BEADS

Measurements of the current-voltage characteristics of layer of glass beads of diameter $2a \sim 450$μm in a standard resistivity cell (ASME Power Test Code 28) have been made under ambient air conditions (RH = 65%, T = 23°C) and at T = 160°C. The results are shown in normalized form in Figure 6, where

$\rho_A/(\rho_A)_{ref}$ is plotted versus E_A and the reference condition is taken as $E_A = 10^5$ V/m. Also shown are the characteristics calculated for the limiting cases of volume and surface conduction.

It is seen that the experimental curves consist of three parts. For $E_A \lesssim 3 \times 10^4$ V/m, ρ_A is approximately constant, which is attributed to the fact that the electrically induced compressive stress is small compared with the standard pressure ($\sim 10 g/cm^2$) due to the mechanical load on the top electrode. For larger E_A, the resistivity decreases linearly in this logarithmic plot with a dependence lying between $E_A^{-2/5}$ for the volume conduction case (Eq. 21) and the slower logarithmic dependence of Eq. 26. For the hot, dry condition, the experimental curve matches the volume conduction curve quite closely, whereas the curve for ambient conditions lies midway between the volume and surface conduction curves. This behavior is as should be expected. At high fields both curves show an increasing departure from the linearly reducing form which is attributed to the onset of intermittent backdischarge until at $E_A \sim 1.5 \times 10^6$ V/m gross breakdown of the layer occurs.

These preliminary results lead us to believe that the theory presented, though idealized, is basically capable of providing a quantitative explanation of the characteristics of fly ash resistivity data.

ACKNOWLEDGEMENT

This work was supported by the Electric Power Research Institute.

REFERENCES

1. O. J. Tassicker, "Aspects of Forces on Charged Particles in Electrostatic Precipitators," Ph. D. Thesis, University of New South Wales (1972).

2. K. J. McLean, "Cohesion of Precipitated Dust Layer in Electrostatic Precipitators," J. Air Pollution Control Association 27, 1100-1103, (1977).

3. HTGL Quarterly Reports on "Basic Studies to Reduce Electrostatic Precipitator Size and Cost," (1980.)

4. W. R. Smythe, Static and Dynamic Electricity, McGraw Hill, (1950), Ch. 6.

5. S. P. Timoshenko and J. N. Goodier, Theory of Elasticity, McGraw-Hill, New York, (1970.)

6. L. L. Alston, Editor, "High-voltage Technology," O.U.P. (1968), Ch. 4.

7. J. M. Meek, J. D. Craggs, Editors "Electrical Breakdown of Gases," John Wiley & Sons, Ltd. (1978), Chapters 2, 3 and 6.

8. H. L. Saums, W. W. Pendleton, "Materials for Electrical Insulating and Dielectric Function," Hayden Book Company, Inc., (1973), Chapter 2.

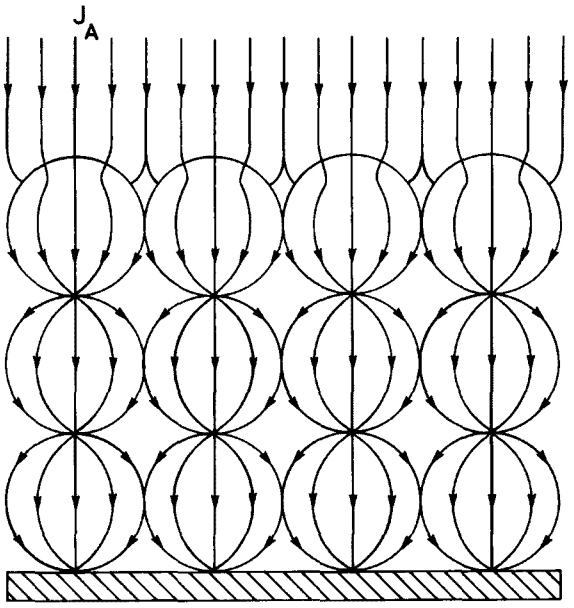

Fig. 1 Model for current flow through array of resistive spheres.

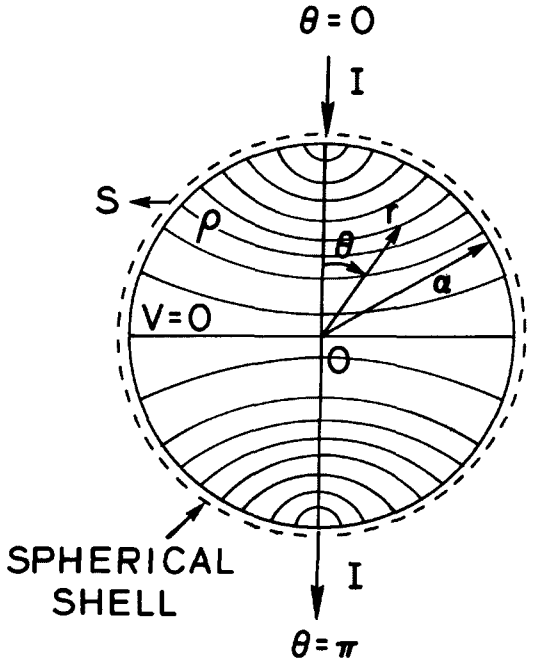

Fig. 2 Model for current flow through single sphere with point contacts.

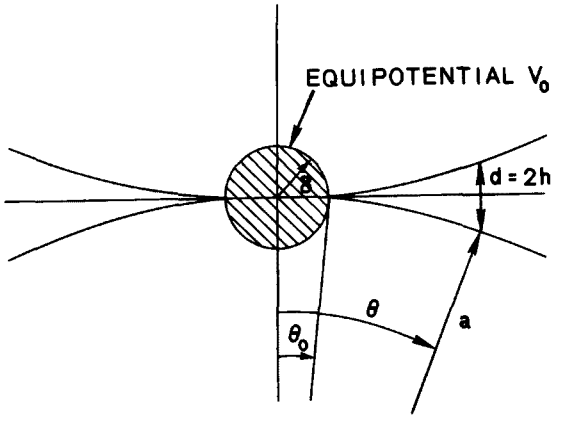

Fig. 3 Model for contact region between two spheres.

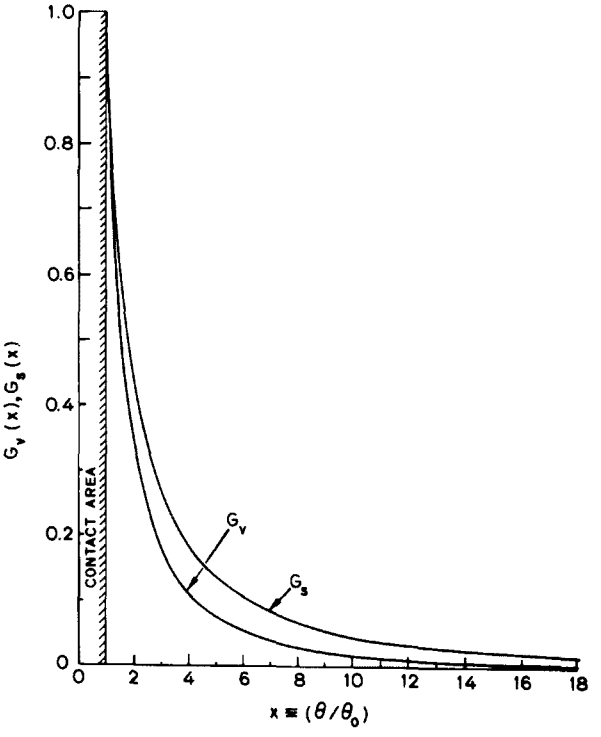

Fig. 4 Field distribution function G (x) in contact region.

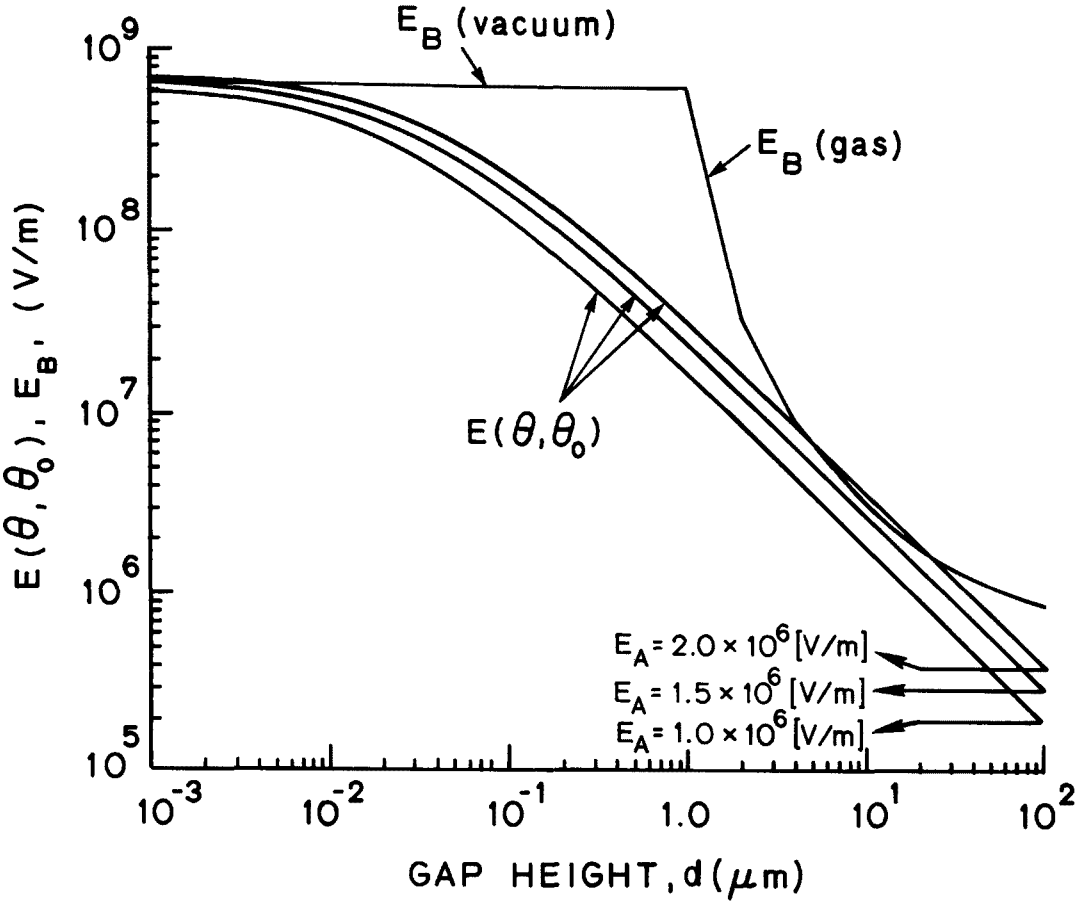

Fig. 5 Graphical proceedure for determining breakdown field $E_{\Delta R}$.

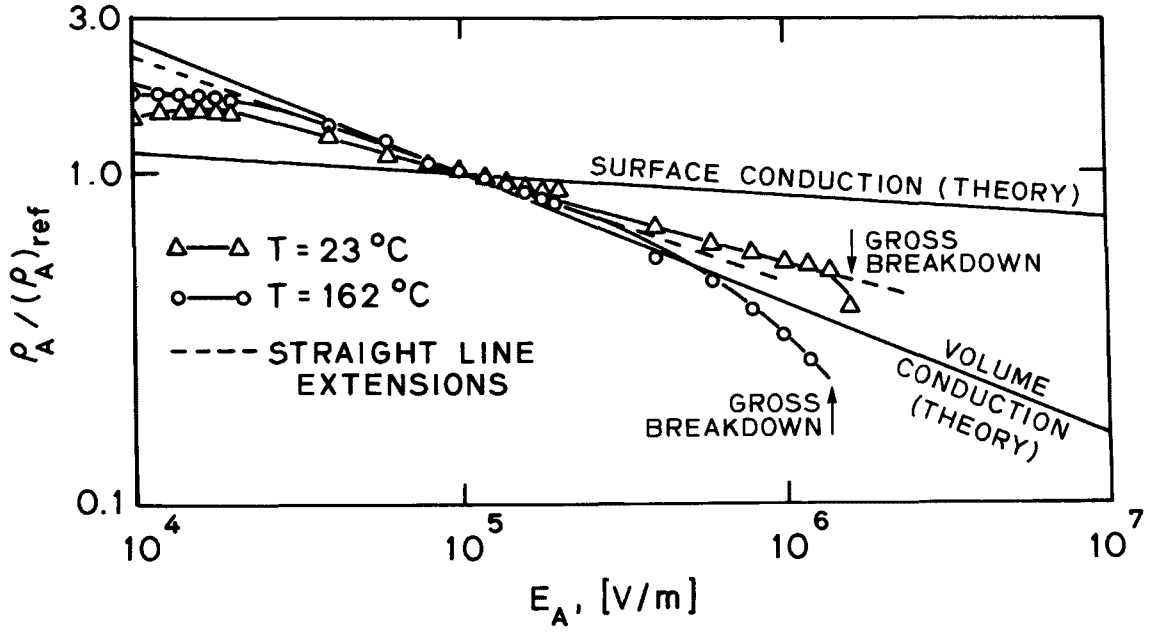

Fig. 6 Layer resistivity measurements for glass beads, D = 450 μm.

EXPERIMENTAL MEASUREMENTS OF THE EFFECT OF TURBULENT DIFFUSION ON PRECIPITATOR EFFICIENCY

by: G. L. Leonard, M. Mitchner and S. A. Self
Dept. of Mechanical Engineering, Stanford University
Stanford, CA 94305

ABSTRACT

The Deutsch model for predicting particle collection in an electrostatic precipitator assumes uniform particle concentration profiles and thus infinite mixing by the turbulent flow. Recent theories which treat the mixing as finite and thus allow for the formation of non-uniform particle concentration profiles predict efficiencies far in excess of Deutsch predictions. In this paper optically determined in-situ particle concentration profiles in a parallel plate precipitator are presented and compared with the predictions of these newer theories. Experiments were designed so as to permit separate control and precise measurement of the degree of turbulence and particle mobility of the precipitator. These measurements enable a critical assessment of these new theories to be made.

INTRODUCTION

Numerous investigators have used the convective diffusion equation in attempts to predict turbulent particle transport in electrostatic precipitators. Unfortunately there is almost a complete lack of suitable experimental data which can be used to test these predictions. In this paper we present measurements of average particle concentration profiles made in the second stage of a two-stage laboratory precipitator. The level of turbulence and particle migration velocity are independently controlled. The predictions of the convective diffusion equation are found to be in good agreement with the data.

EXPERIMENTAL FACILITY

Shown in Figure 1 is a schematic diagram of the test facility. Particles of oleic acid (3.5 microns in diameter) are generated with a spinning disk aerosol generator which has been modified so that the particles can be inductively charged at the point of their formation. The charged aerosol is then injected into the wind tunnel.

Just downstream of the tunnel nozzle a laser-Doppler-anemometer measures individual particle migration velocities w_y as a small sample of the particles is passed through a uniform electric field E. The charged aerosol then flows through a turbulence producing square grid before entering a parallel plate precipitator as shown in Figure 2.

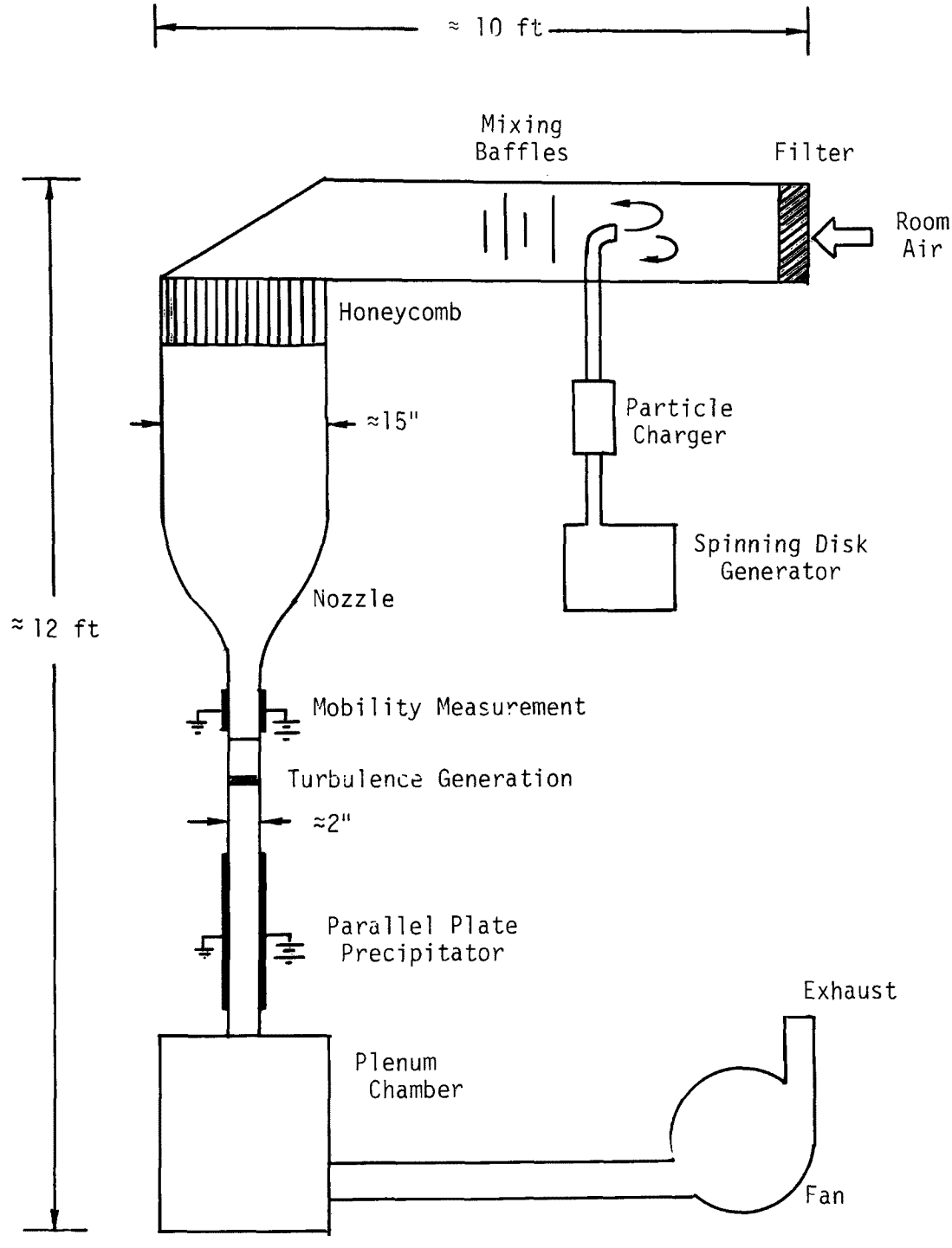

Figure 1. Flow Facility.

A laser beam is passed through the end walls of the precipitator. As particles travel through a localized region of this beam they scatter light which is detected with a photomultiplier. The number of particles passing through the localized region of the beam is counted for one minute with the precipitator's electric field on and then off. The ratio of these two counts gives the relative average particle concentration $n(x,y)/n_o$. Here $n(x,y)$ is the average particle concentration at (x,y) and n_o is the uniform inlet concentration.

EXPERIMENTAL RESULTS

Shown in Figure 3 are the results of a typical measurement of the distribution of migration velocities. The number of particles having a migration velocity within a 2 cm/s band centered at ω_y is shown plotted as a function of ω_y. The solid curve in Figure 3 is a Gaussian density function with a relative standard deviation, $\sigma/(\omega_y)_{ave}$, of .06. A total of 9000 particle migration velocities were determined in this one test.

Fluid velocity measurements in the precipitator made with a hot wire anemometer are shown in Figures 4a and 4b. The mean velocity profiles are flat to within ±2% over the core of the flow. Near the wall the mean velocity decreases in accordance with boundary layer behavior.

The turbulence producing square grid generates a turbulent core flow which decays slowly in the flow direction. (Two grids were used. The smaller mesh grid has a mesh length of .25" and a solidity of .34. The larger mesh grid has a mesh length of .40" and a solidity of .44.) The turbulence level increase near the walls is due to the presence of turbulent boundary layers.

Shown in Figure 5 are particle concentration profiles for the case of no turbulence generation. The freestream turbulence intensity of the tunnel was less than 0.3% for this case. Shown in Figure 6 are particle concentration profiles measured with the small mesh grid and with $u = 300$ cm/s, at the three downstream locations $x = 5$, 25 and 45 cm for $\omega_y = (\omega_y)_{ave} = 30$ cm/s. In figure 7 are shown particle concentration profiles measured with the small mesh grid and with $u = \pm 300$ cm/s at $x = 25$ cm for the four particle migration velocities, $\omega_y = 7.5$, 15.0, 30.0 and 45.0 cm/s. The data obtained with the large mesh grid was similar, except that the concentration gradient was somewhat reduced. (The large mesh data is plotted in self similar form in Figure 9.)

Shown in Figure 8 are particle concentration profiles for the case where the turbulence producing grid was replaced by wall baffle plates. The plates extended one centimeter from the tunnel side walls and were placed exactly opposite one-another at the location where the grid had been. It is seen that the turbulent flow generated by the baffle plates disperses the particles to a significantly greater extent than the grid-generated turbulence. Hot wire measurements made at $x = 30$ cm indicated that the turbulence intensity was a uniform 12% across the tunnel width for the flow with baffles.

COMPARISON WITH THEORY

The data of the previous section were compared with the predictions of the convective diffusion equation.

$$u \frac{\partial n}{\partial x} + \omega_y \frac{\partial n}{\partial y} = D \frac{\partial^2 n}{\partial y^2} \tag{1}$$

Here u is the mean gas velocity, ω_y is the particle migration velocity and D in the particle eddy diffusivity, all assumed constant. It can be shown that the exact solution to Eq. (1) subject to the proper initial and boundary conditions (1) can be expressed in terms of two dimensionless parameters, the Deutch exponent $\omega_y x/ud$, and the electric Peclet No. $P_E = \omega_y d/D$. (Here, d is the plate-to-plate spacing.) It can be shown that an approximate form of the solution is given by the equation

$$\frac{n(x, y; \omega_y)}{n_o} = P\left(\frac{y - \frac{\omega_y x}{u}}{\sqrt{\frac{2Dx}{u}}}\right) \tag{2}$$

when $P_E > 30$. Here $P(z)$ is the Gaussian probability distribution function (2).

To account for the effects of the non-uniform electric field at the precipitator inlet and the distribution in migration velocities (see Figure 3), Eq. (2) may be written in the modified form.

$$n(x,y) = P\left(\frac{y - \bar{\omega}_y \frac{(x + x_o)}{u}}{\sqrt{\frac{2D(x + x_o)}{u} + \left(\frac{\sigma}{\bar{\omega}_y}\right)^2 \left(\frac{\bar{\omega}_y}{u}\right)^2 (x + x_o)^2}}\right) \tag{3}$$

Here x_o (the effective increased length of the precipitator that accounts for the nonuniform inlet electric field) decreases approximately linearly with ω_y from a value of 6 cm at ω_y = 7.5 cm/s to 4 cm at ω_y = 45 cm/s. The quantity $\sigma/\bar{\omega}_y$ is the relative standard deviation of the migration velocity distribution and equals .06 for our test aerosol (see Figure 3).

The solid curves shown in Figures 5, 6 and 7 were generated using Eq. (3) The one free parameter of the model, D, was chosen as .6 cm^2/s for the small grid and as 1.2 cm^2/s for the large mesh grid. The shapes of the calculated curves are seen to agree well with the shapes of the data although the theoretical results sometimes appear shifted to either the left or right from the data. It is believed that this shift results from the innaccuracy in precisely locating the experimental y coordinate.

In Figure 9 the relative average particle concentration $n(x,y)/n_o$ is shown plotted as a function of

$$(y - \frac{\bar{\omega}_y (x + x_o)}{u}) / \sqrt{\frac{2D(x + x_o)}{u} + (\frac{\sigma}{\bar{\omega}_y})^2 (\frac{\bar{\omega}_y}{u})^2 (x + x_o)^2} \qquad (4)$$

for a number of different precipitation conditions. As predicted by Eq. (3) the data collapse upon a single curve. (The error introduced in locating the y coordinate origin was removed in obtaining Figure 9).

The solid curves in Figure 8 are the theoretical curves which fit the data of the grid - generated turbulence for the identical conditions of $\bar{\omega}_y$ and u. The baffles are seen to significantly degrade the precipitator performance. For example, the particle collection efficiency for the conditions of x = 45 cm and $\bar{\omega}_y$ = 30 cm/s has decreased from 94% for the grid-generated turbulent flow to 80% for the flow with the baffle plates.

The dotted curves in Figure 8 correspond to the solution to Equation (1) with the diffusion coefficient D equal to 30 cm^2/s. The theory is seen to agree with the data reasonable well in this case also.

CONCLUSIONS

Using the values 0.6 cm^2/s and 1.2 cm^2/s for the particle diffusivity (for the small and large mesh grids, resp.), the measured particle concentration profiles with grid-generated turbulence correspond to a range of electric Peclet Nos. between 30 and 350, and to Deutsch exponents between 0.05 and 1.0. In these conditions, the solution of the convective diffusion equation has been shown to agree well with the data.

When the grids were replaced by baffles the particle diffusivity increased by a factor of almost 50 (relative to the small mesh grid). Subsequently, as predicted by the convective diffusion equation the collections efficiency of the precipitator decreased from 94% to 80%. (It should be noted that the Deutsch equation gives a collection efficiency of 63%.)

In the absence of non-ideal affects such as re-entrainment, sneakage, back corona, rapping losses, and corona wind, the convective diffusion equation has been shown to provide a satisfactory quantitative description of turbulent particle transport. Future work will be directed toward a study of particle transport in turbulent flows generated by corona discharges, corresponding to conditions in a single-stage electrostatic precipitator.

ACKNOWLEDGEMENTS

This work was supported by the National Science Foundation under Grant No. CPE - 7926290 and in part by the Electric Power Research Institute under Contract RP 533-1.

REFERENCES

1. Leonard G. L., Mitchner M. and Self S. A. (1980) "Particle Transport in Electrostatic Precipitators", Atmospheric Environment, Vol. 14, No. 11, pp. 1289-1299.

2. Abramowitz M. and Stegun I. A. (Editors) "Handbook of Mathematical Functions", Dover Publications Inc., New York, pp. 966.

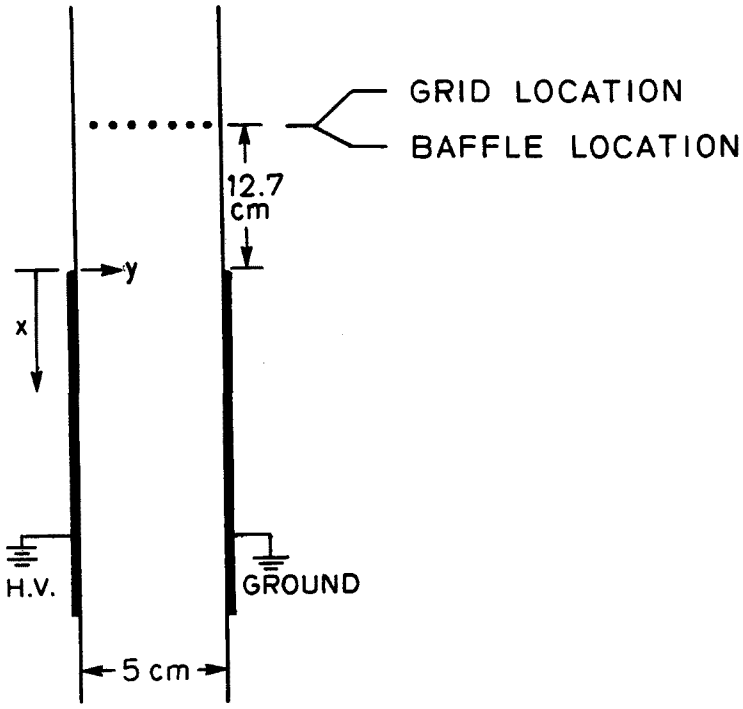

Figure 2. Parallel plate electrostatic precipitator.

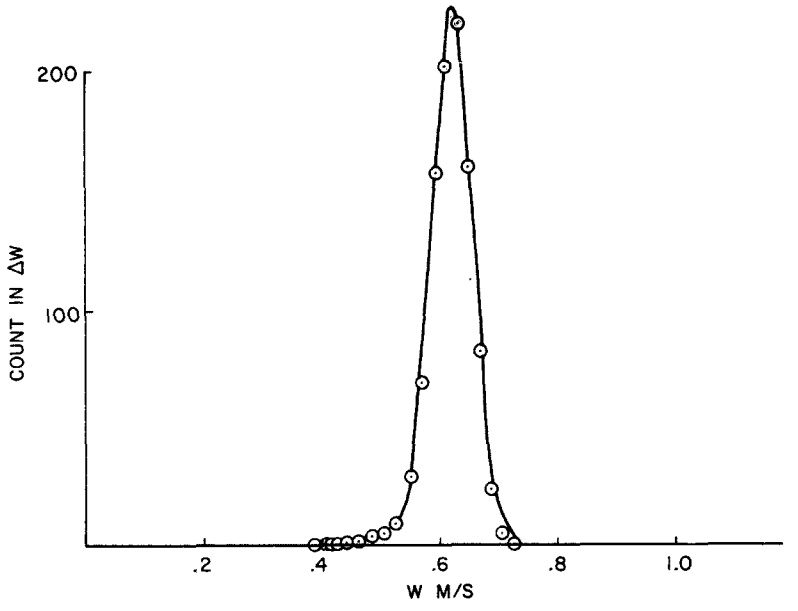

Figure 3. Migration velocity distribution function.

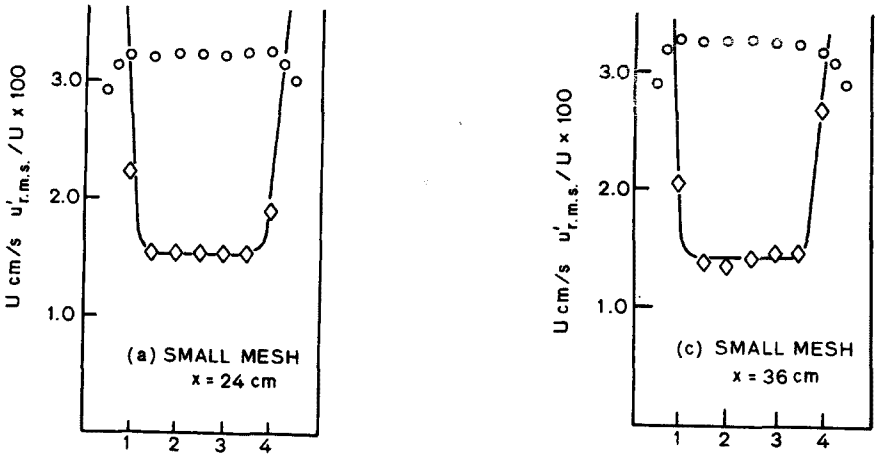

Figure 4. Mean velocity ○ and turbulence intensity ◇ profiles.

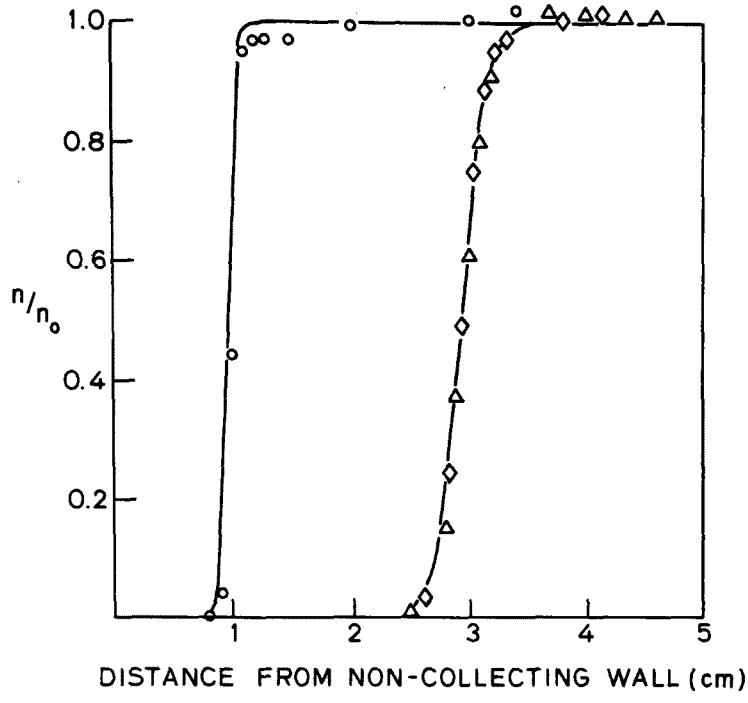

Figure 5. Particle concentration profiles; no grid; ○ $\overline{w}_y$ = 60 cm/s, u = 600 cm/s and x = 5 cm; △ $\overline{w}_y$ = 60 cm/s, u = 600 cm/s, and x = 25 cm; ◇ $\overline{w}_y$ = 30 cm/s, u = 300 cm/s and x = 25 cm.

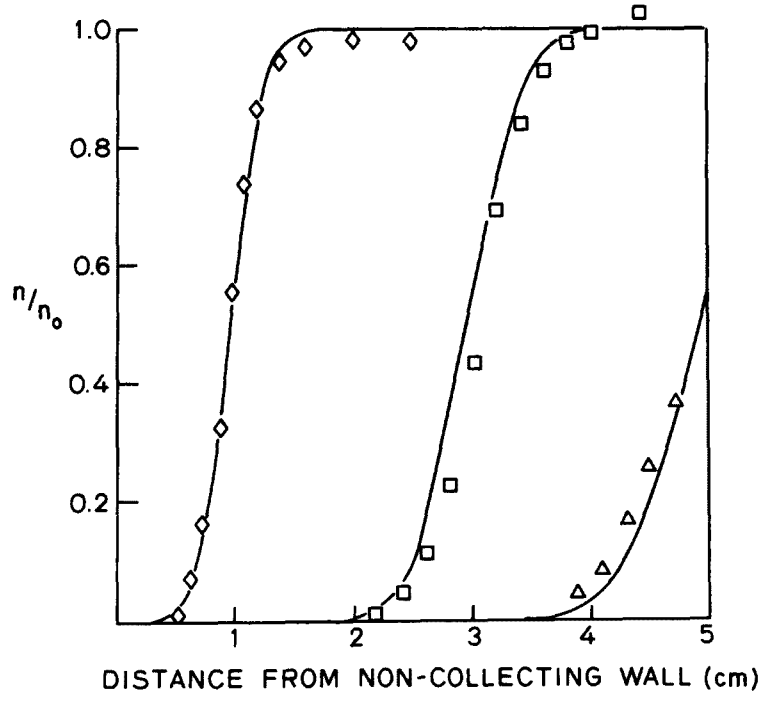

Figure 6. Particle concentration profiles; small mesh, u = 300 cm/s, $\overline{w}_y$ = 30 cm/s, ◇ x = 5 cm, □ x = 25 cm and △ x = 45 cm.

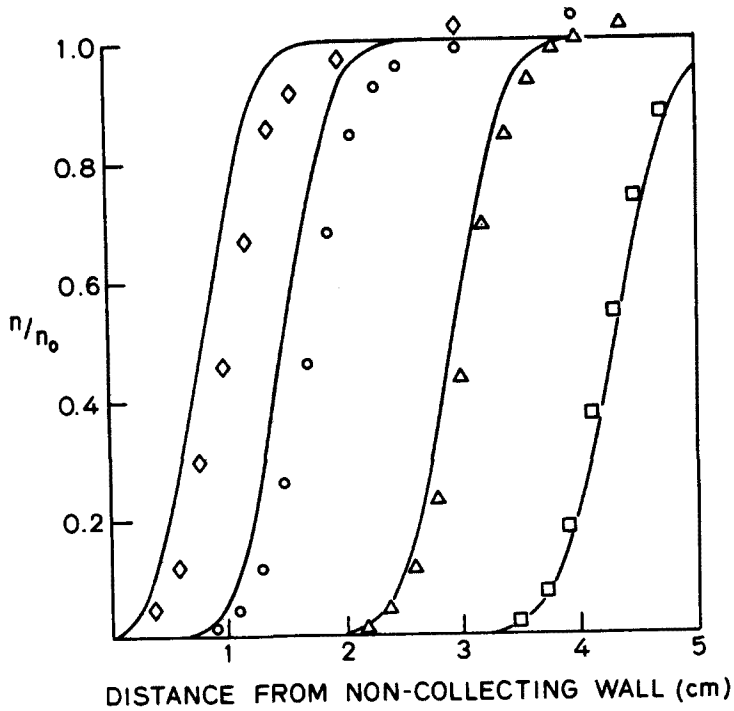

Figure 7. Particle concentration profiles; small mesh, u = 300 cm/s, x = 25 cm, ◇ $\overline{w}_y$ = 7.5 cm/s, ○ $\overline{w}_y$ = 15.0 cm/s, △ $\overline{w}_y$ = 30.0 cm/s and □ $\overline{w}_y$ = 45.0 cm/s.

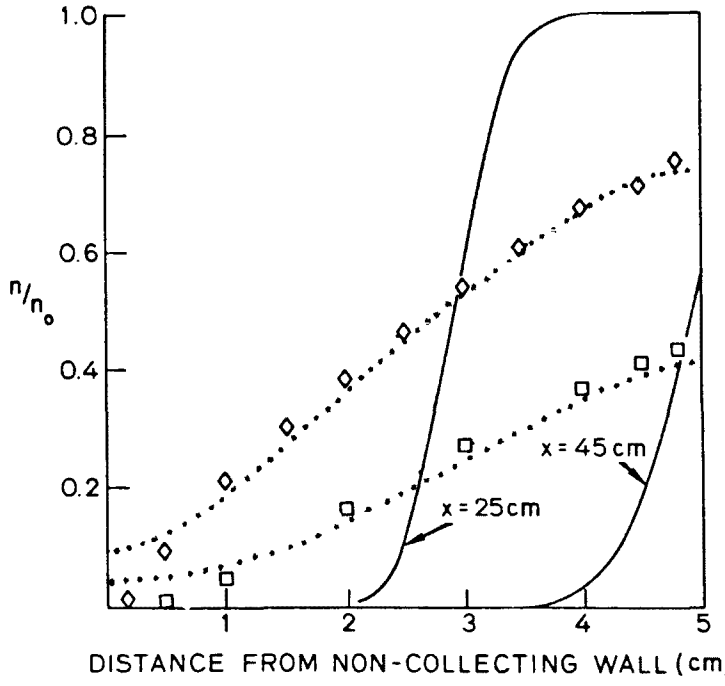

Figure 8. Non-dimensionalized particle concentration profiles for the case of wall baffles; $\overline{w}_y$ = 30 cm/s.

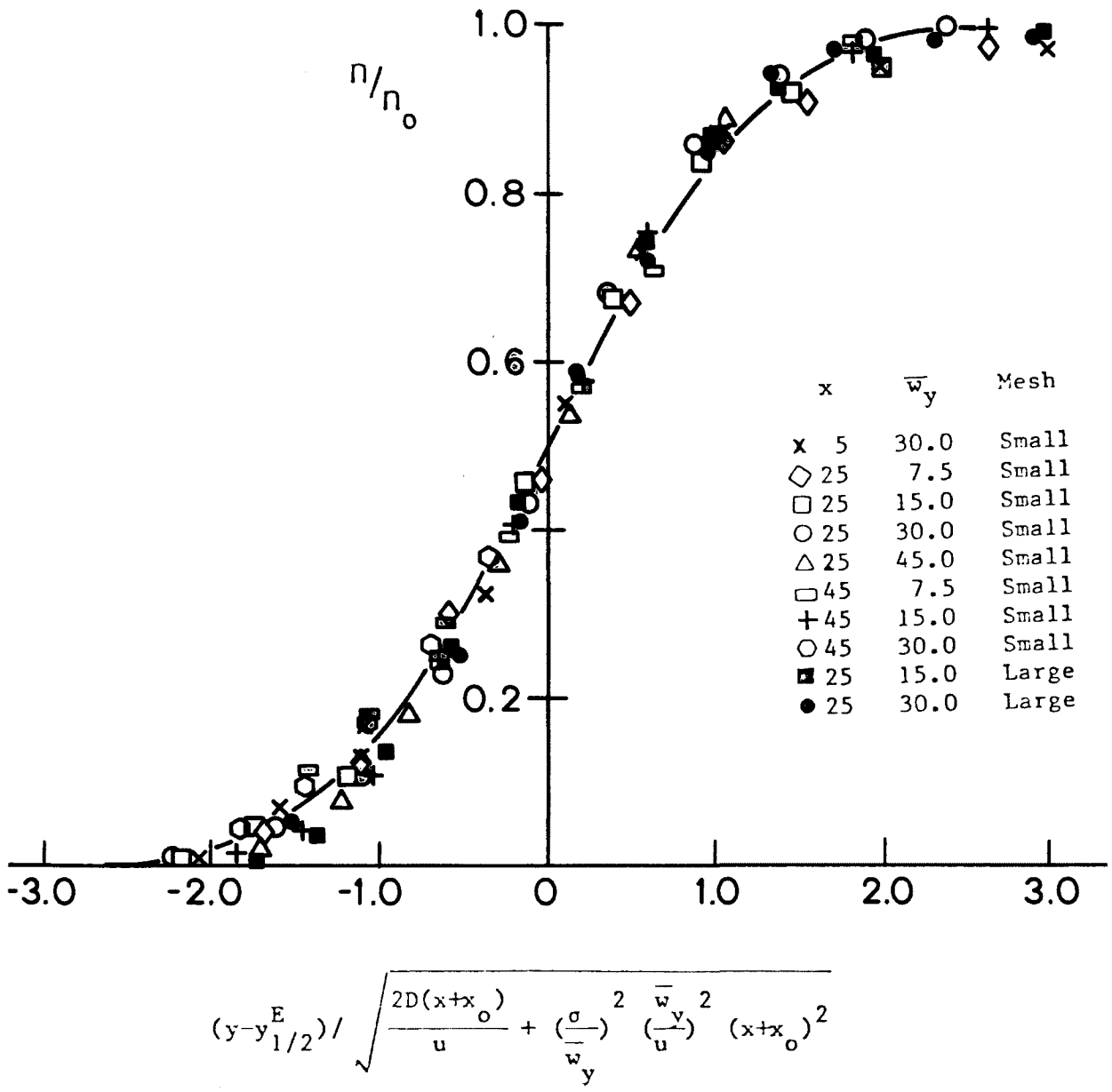

Figure 9. Non-dimensionalized particle concentration plotted in self similar form.

CAN REENTRAINMENT BE EXPLAINED USING A NEW PRECIPITATOR FORMULA?

By Sten Maartmann
Flakt Industri AB
Plant Engineering Division
S-351 87 Växjö, Sweden

ABSTRACT

According to precipitator literature reentrainment is defined as a decrease in migration velocity, calculated according to the Deutsch-Anderson formula, when gas velocity is increased above a certain limit.

Despite many efforts there is as yet no generally accepted formula which covers the variation of efficiency within the whole gas velocity or SCA range including that in which reentrainment takes place.

The paper describes how investigations of test results particularly from tests with pilot precipitator plants lead to the development of a new expression for efficiency. The possibility of using the expression as base for a new precipitator formula is being discussed as well as the possible general use of the new efficiency expression.

INTRODUCTION

Reentrainment is a word derived from entrain which according to Webster's dictionary means "To carry along or over as in precipitation or destillation". An alternative meaning is "To collect and transport (a substance) by the flow of another fluid moving at a high velocity".

In an electrostatic precipitator (ESP), both meanings are applicable to the fact that, particles which have been collected may reenter into the gas stream, for instance during rapping, be "carried along or over" and escape collection. Entrainment or reentrainment can be expected to be a property of an ESP already at a low gas velocity but increase in importance with gas velocity.

ESP literature reentrainment has occured particularly in cases where the design gas velocity has been high and/or the ESP has had a low length/height ratio. When efficiency tests were made at different gas velocities and the migration velocity (calculated according to the Deutsch-Anderson formula) studied against gas velocity, the following trend was found:

1. When the gas velocity was decreased below the design point, the migration velocity would increase up to a maximum and then decrease again.

2. At gas velocities above the design point, the migration velocity would decrease further the higher the gas velocity.

The result would be a bell shaped curve as in figure 1. This is based on a test series using a pilot ESP plant [1].

REENTRAINMENT CASES CITED IN LITERATURE

It is generally easier to test a pilot than a full scale ESP over a broad gas velocity range. Dalmon and Lowe show the relationship between overall effective migration velocity and gas velocity with the comment: "The deterioration of performance at the higher gas speeds is undoubtedly due to reentrainment caused by the scouring action of the gas-stream". They also show that "the various size fractions of the dust all behave in a similar manner". The fractions are 3.5, 11 and 51 micron, figure 1.

Robinson[2] shows results of an investigation involving a wet ESP collecting oil mist. The collection at various tube lengths was determined and the migration velocities calculated at gas velocities between about 1 and 7.5 m/s. In such an ESP without rapping gear, one would not expect reentrainment to occur. The results show however that above about 5 m/s it does.

SEARCH FOR MATHEMATICAL EXPRESSION WITH WHICH TO SIMULATE REENTRAINMENT

When Flakt started using the w_k formula (later called the modified Deutsch-Anderson formula) in the early sixties it was known that it could not be used in the reentrainment range with constant w_k value. Later when guarantees were requested on efficiency also at high velocity, for instance when only one of two ESP's was in operation, an investigation was initiated on trends in tests results when reentrainment had occured.

Flakt had detected reentrainment mainly during pilot plant testing in the early fifties using an ESP, 3.2 m long at gas velocities up to 2 m/s. Although the general trend agreed with that shown in figure 1, the tests had been run at different operating conditions. Therefore those published by Lau[3] were chosen for a closer study. The tests were run with gas velocities up to 10 m/s at four different duct widths (D), using the same dust, figure 2. The ESP had en effective length of 2 meters. The measured efficiencies (calculated using the migration velocities in figure 2 and the Deutsch-Anderson formula) are shown against gas velocity in figure 3.

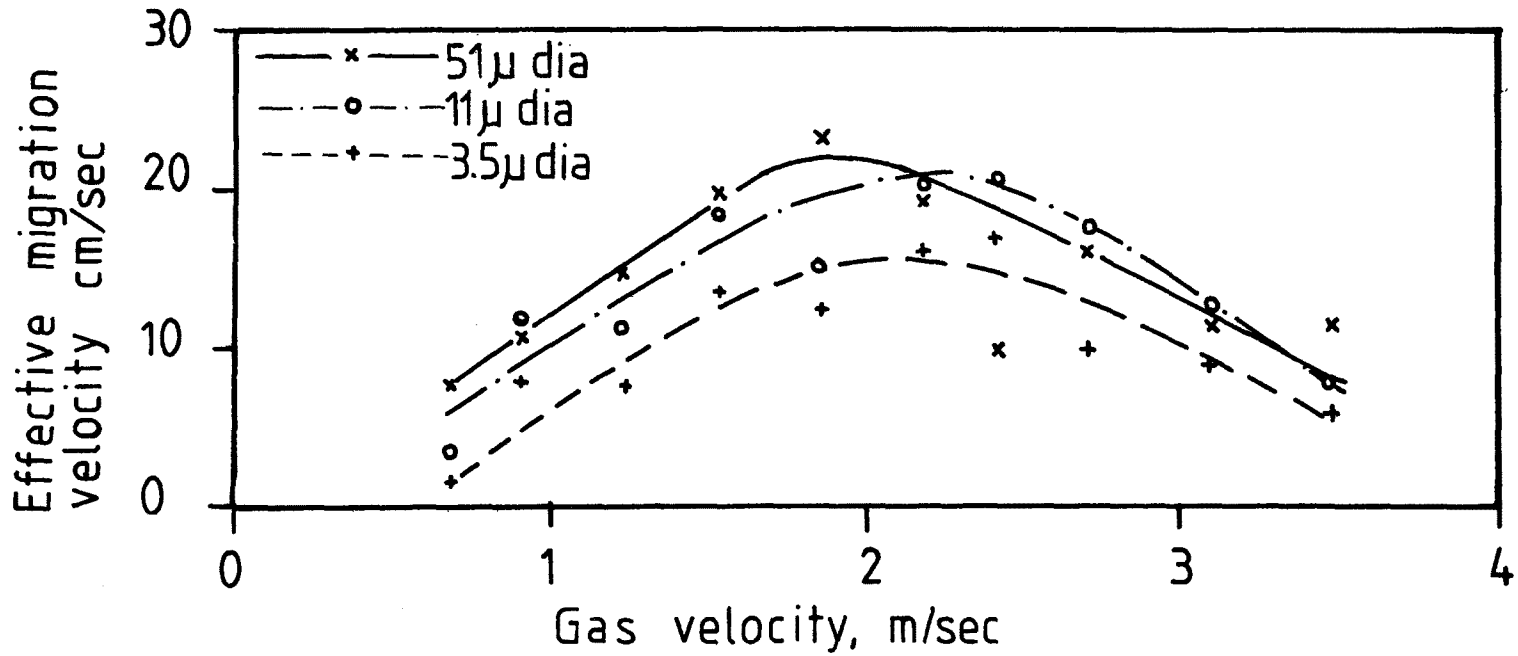

Figure 1. Variation of effective migration velocity for various particle sizes with gas velocity. According to Dalmon and Lowe.

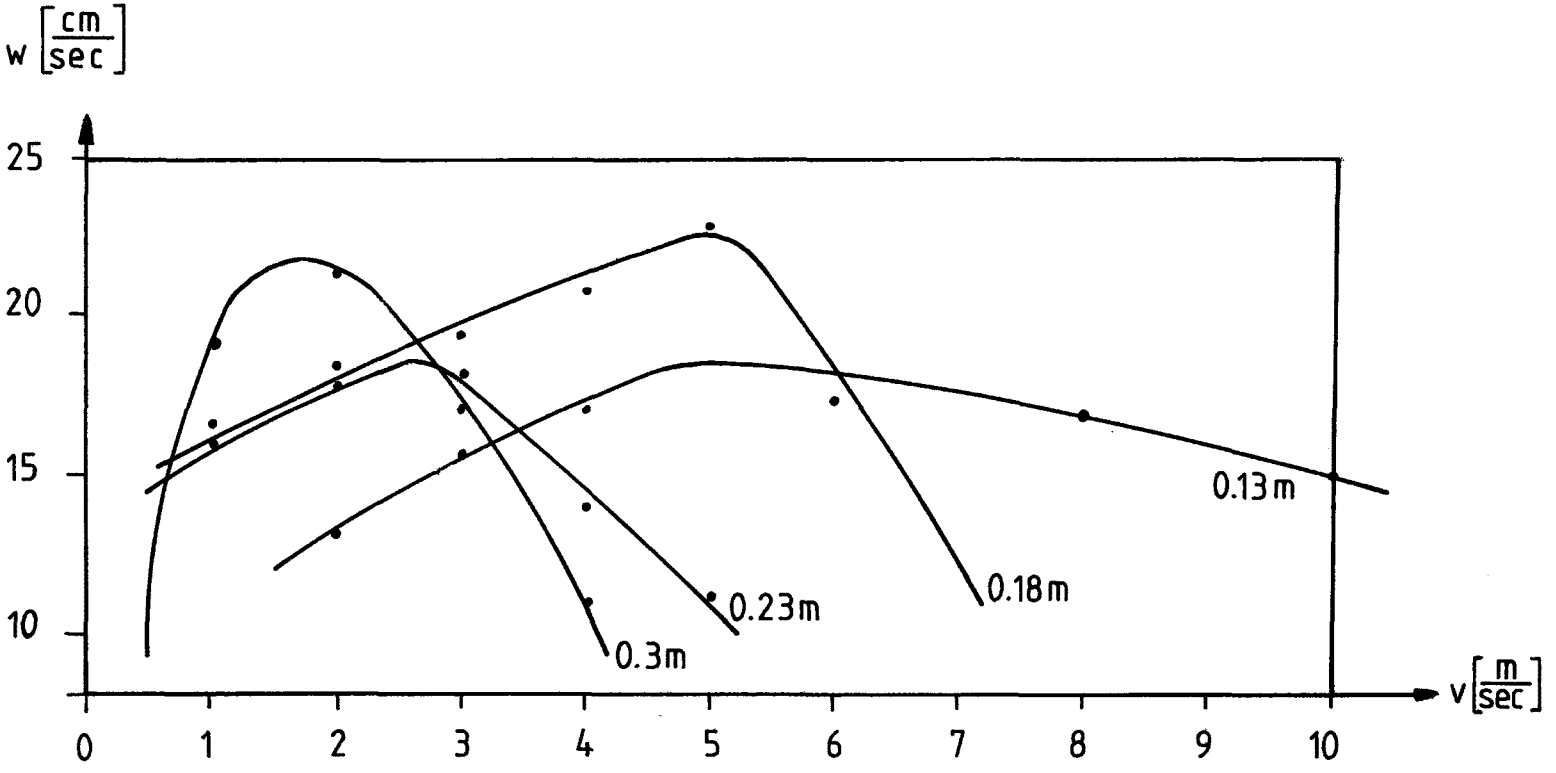

Figure 2. Variation of migration velocity with gas velocity at different duct widths. According to Lau.

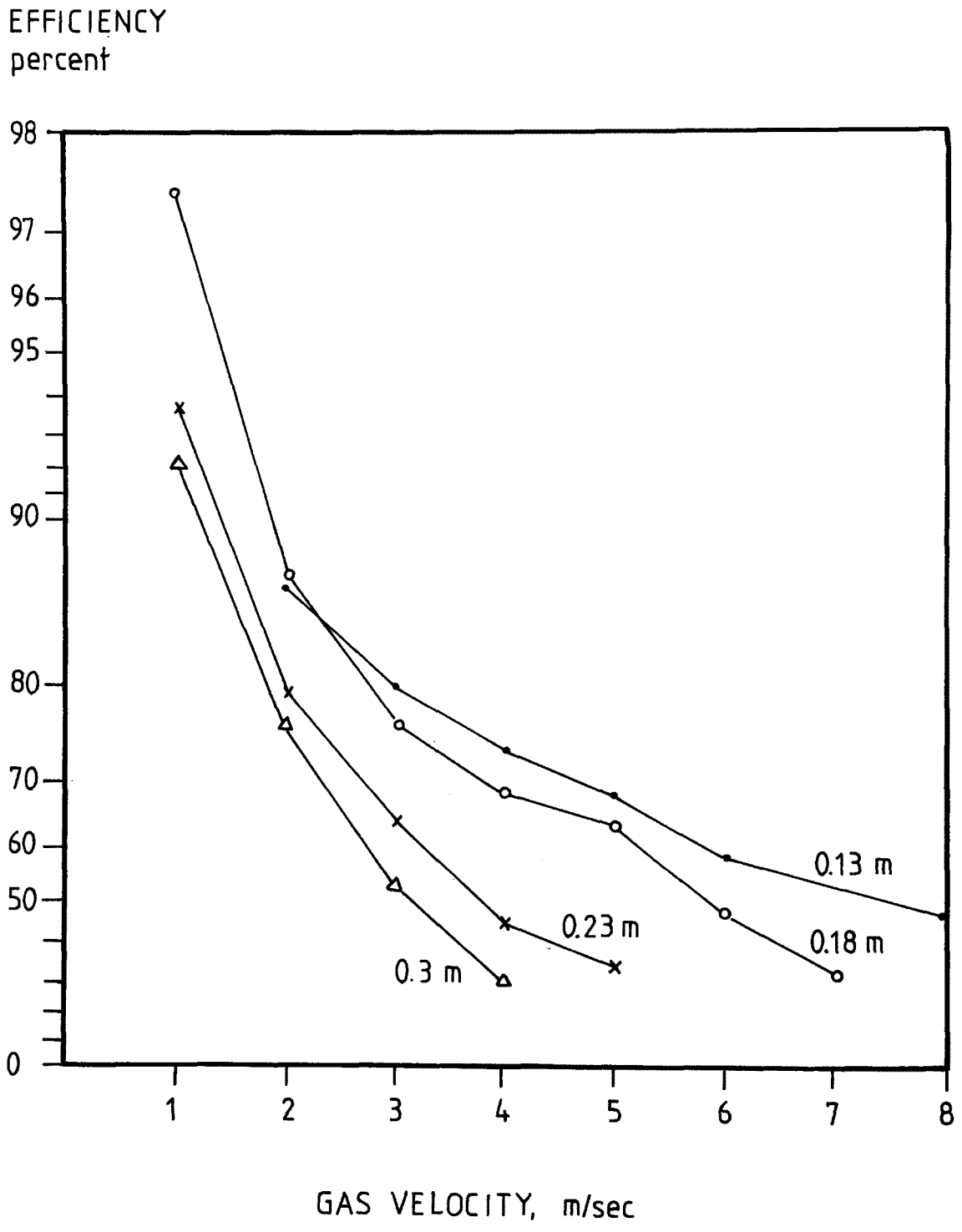

Figure 3. Variation of efficiencies calculated from figure 2 with gas velocity.

An approach is to recall that efficiency (E) can be expressed as

$$E = Dc/(Dc + Do) \quad (2)$$

where Dc = dust collected, Do = dust out.

Similarly loss (L) can be defined as

$$L = 1 - E = Do/(Dc + Do) \quad (3)$$

Then it is useful to form

$$E/(1 - E) = Dc/Do \quad (4)$$

and assume

$$E/(1 - E) = A_1 \times v^B \quad (5)$$

This equation can also be written as

$$E/(1 - E) = (A_2 \times v)^B \quad (6)$$

A regression analysis (curvefit) was performed on the data in figure 3. Of the six relationships an available computer program contained between $E/(1 - E)$ and v, three gave reasonable correlation coefficients, R^2, table 1.

TABLE 1. CORRELATION COEFFICIENTS R^2

Function	1	2	3
Duct width cm	$A \times e^{B \times v}$	$A \times v^B$	$A + B/v$
13	0.942	0.979	0.9986
18	0.6783	0.9894	0.9336
23	0.8950	0.9967	0.9774
30	0.9855	0.9710	0.9922
Average	0.8752	0.9840	0.9755

Although function 3 gives almost as good a fit as function 2, it is deemed impractical as $E/(1 - E)$ (and therefore also the efficiency) will be negative for v above B/A. (All B values are negative.) For this particular case the corresponding velocities are between 4 and 15 m/s.

The fit for function 2 is considerably better than for function 1. Furthermore the use of the latter appears limited as $E/(1-E) = A$ for $v=0$. The calculated efficiencies are, for the test data above, as low as between about 90 and 97 per cent. As a consequence function 2 was chosen for further discussion and investigation. Figure 4 shows the data in a suitable new type of diagram.

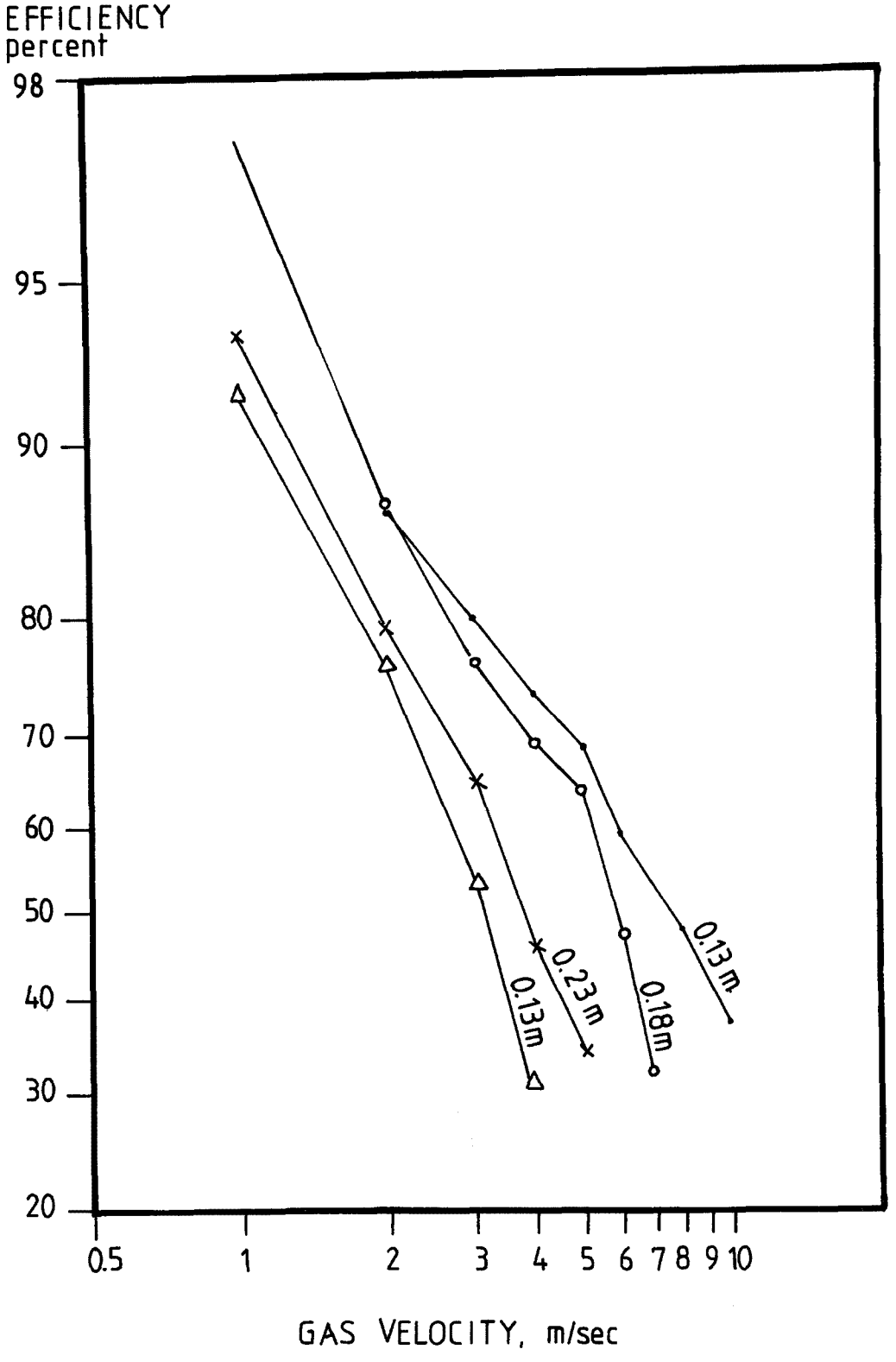

Figure 4. Variation of efficiencies calculated from figure 2 in E/(1-E) scale with gas velocity.

The original migration velocities (taken from figure 2), the corresponding efficiencies as well as the efficiencies and migration velocities calcualted using the "best fit" values for A and B (15.852 and -2.08648 respectively) are shown in table 2 for D = 23, i.e. the duct width for which the best fit was obtained.

TABLE 2. MEASURED AND CALCULATED MIGRATION VELOCITIES

Gas velocity m/s	1	2	3	4	5
Migration velocity cm/s	16	18	18	14	11
Efficiency %	93.8	79.1	64.8	45.6	34.2
Calculated efficiency %	94.1	78.9	61.6	46.8	35.6
Calculated migration velocity cm/s	16.2	17.9	16.5	14.5	12.6

The investigation had thus yielded the result that (6) can be used to simulate reentrainment conditions. It can also be used to predict the efficiency at high gas velocity (from an efficiency at lower velocity) provided that the value of B is known.

CAN THE E/(1-E) CONCEPT BE USED FOR A NEW ESP FORMULA?

Further study of the data from the regression analysis and of efficiency trends when using (6), resulted in that the following formula is proposed for further study:

$$E/(1-E) = (A_3 \times L/(v \times D))^{B \times f(wk) \times f(D)} \quad (7)$$

For a fixed value of D and exchanging $B \times f(w_k)$ with a new "migration velocity" we get

$$E/(1-E) = (A_4 \times SCA)^{w_n} \quad (8)$$

where w_n is the new "migration velocity" and B is positive.

Support for the form of the proposed formula

Duct width

Table 3 lists the values for A_1, A_2 and B obtained with the regression analysis.

TABLE 3. RESULT OF REGRESSION ANALYSIS

D cm	13	18	23	30
B	-1.499	-2.078	-2.086	-2.318
A_1	20.59	35.02	15.85	13.07
A_2	0.1329	0.1806	0.2659	0.3300

B decreases with increasing D. The best fit for this variation of D is

$$B = -2.932 + 17.89/D \quad (R^2 = 0.924) \tag{9}$$

A_1 and A_2 also vary with D. The curve fit for A_1 is very poor but the best fit for A_2 is

$$A_2 = 0.0248 + 0.012\ D \quad (R^2 = 0.985) \tag{10}$$

or approximately

$$A_2 = 0.013\ D \tag{11}$$

Thus Lau's results are best described by

$$E/(1-E) = (A \times v)^B \tag{12}$$

where $A = 0.013D$, $B = -2.93 + 17.9/D$

Length of the ESP

The Deutsch-Anderson formula was developed assuming that homogenous dust is collected with constant migration velocity lengthwise in an ESP. Many researchers have in the past proven that the assumption is reasonably correct.

Using (12) we get for D = 23 at a velocity of 1 m/s

$$E/(1-E) = (1.67 \times L)^{2.15} \tag{13}$$

For shorter L values than 2 m we get, table 4

TABLE 4. MIGRATION VELOCITIES LENGTHWISE

L m	0.4	0.8	1.2	1.6	2
Efficiency %	29.6	65.1	81.7	89.2	93.0
Migration velocity cm/s	10.0	15.1	16.3	16	15.3

Thus except for the first part, i.e. where the dust is being charged, the migration velocity is about constant.

Trend similarity with w_k

Using (12) for D = 23, efficiencies and migration velocities are calculated for gas velocities below the reentrainment range and w_k values added, table 5.

TABLE 5. TREND AT LOW GAS VELOCITY

Gas velocity m/s	0.4	0.5	0.6	0.8	1.0
Efficiency %	99.0	98.3	97.6	95.6	93.0
Migration velocity cm/s	10.5	11.8	12.8	14.3	15.3
w_k cm/s	48.1	48.3	44.7	44.7	40.8

The migration velocity decreases with gas velocity but w_k reaches a maximum for a velocity about 0.5 m/s and then starts to decrease. Within the gas velocity range 0.4 to 0.8 m/s (efficiencies between about 99 and 96 per cent) the difference between the w_k values is not more than about 8 per cent.

Why a function of w_k in the exponent?

As shown above, the trend of 6 agrees well with that of w_k for D = 23 at gas velocities below about 1 m/s. It has been found that the relationship between efficiency (in the above 95 percent range) and SCA for constant w_k, can be simulated with (6) resulting in high correlation coefficients. A_2 was reasonably constant whereas B increased with w_k. Therefore it is proposed that the influence of dust properties etc. covered by w_k shall be included in the exponent.

USE OF THE E/(1-E) CONCEPT IN OTHER AREAS, PARTICULARLY DUST COLLECTION AND GAS ABSORPTION

The E/(1-E) concept when used for ESP's appears to have a particular advantage in the low, i.e. below approximately 90 % efficiency range. Low efficiencies are usual for mechanical collectors but also for a newer technology, namely SO_2 absorption.

Flakt has performed extensive pilot plant test series at power plants in Denmark and the US using the dry scrubber method to collect SO_2[4]. When investigating trends between efficiency and stochiometric ratio the E/(1-E) concept was found to be a useful tool.

Initially the E/(1-E) concept was derived out of speculations on the use of the hyperbolic tangent equation. Later it was discovered that the same basic concept had been used elsewhere.

Economical forecasting

Fisher[5] has introduced the f/(1-f) concept (where f is called fraction) in order to describe how a new technology takes over from an old. It is now used for instance by IIASA for energy forecasting.

Fractional efficiencies for cyclones

Ghan[6] calls the use of the hyperbolic tangent equation "an emperical expression" and demonstrates how S-shaped fractional efficiency curves for cyclones can be simulated using a computer. Spilger[7] has done the same thing.

SUMMARY

It has been shown that by expressing efficiency as efficiency/loss, a mathematical expression can be derived emperically with which reentrainment in ESP's can be simulated mathematically. It has also been shown that the formula describes the relationship between efficiency and gas velocity in the higher efficiency range, about in the same way as the w_k formula. Therefore a new ESP formula is proposed for further study.

The E/(1-E) concept is already used in another dust collecting area (cyclones) and a study of efficiency data for dry SO_2 absorption systems shows that it appears to be useful also there. The fact that is is already in use in general forecasting on economies and energy, implies that the E/(1-E) or f/(1-f) concept could be used whenever the development of percentages is being studied.

ACKNOWLEDGEMENTS

The permission of Flakt Industri AB to publish this paper and the comments of P.O Alfredsson, K. Porle and S Matts are gratefully acknowledged.

REFERENCES

1. Dalmon, F. and H.I. Lowe. Experimental Investigations into the Performance of Electrostatic Precipitators for P.F. Power Stations. Colloques Internationaux du Centre National de la Recherche Scientifique. Grenoble, 1960,p 363-379.

2. Robinson, M. Electrostatic Precipitation. In: Air Pollution Control, Part, W. Strauss, ed. John Wiley & Sons, Inc., 1971, p 227-335.

3. Lau, H. Mit Wechselspannung betriebene Elektrofilter. Staub-Reinhalt. Luft, 8:311-314, 1969.

4. Åhman, S., J.F.Farrington, Jr. and T. Lillestolen, Flakt's Dry FGD Technology: Capability and Experience. Paper presented at the US EPA Symposium, Houston Oct. 1980.

5. Fisher, J.C. and R.H. Pry. A Simple Substitution Model of Technological Forecasting. Cetron, M.J. and C. Ralph, eds. John Wiley & Sons, Inc., 1971

6. Ghan, T. and M. Lippman. Particle Collection Efficiencies of Air Sampling Cyclones: An Emperical Theory, Env. Scie. & Tech., 4 (11): 377-382, 1977

7. Spilger, R. and H. Brauer. Computerberechnung von Zyklonen. In: VDI-Berichte 294, pp 77-84, 1978

A LABORATORY FURNACE FOR THE PRODUCTION OF SYNTHETIC FLY ASH FROM SMALL COAL SAMPLES

By: K. M. Sullivan
Australian Coal Industry Research Laboratories Ltd.
P. O. Box 83, North Ryde
N.S.W. 2113, Australia

ABSTRACT

A laboratory furnace was developed to produce a synthetic fly ash from a small coal sample.

Fly ash similarity was achieved by subjecting pulverised coal particles to a similar thermal and chemical history to that experienced in a full scale power station boiler.

The furnace was designed to accommodate small coal samples, whilst operating conditions were determined so as to produce similarity between the synthetic fly ash and isokinetically sampled fly ash obtained from power stations, in each instance when using the same coal.

Subsequent testing has confirmed that the furnaces produce synthetic fly ash that is similar to power station fly ash.

The furnaces are used as a means of assisting in the investigation of proposed coal mining areas which are intended for future use for power generation. The investigation involves the examination of a number of bore core coal samples and the production of synthetic fly ash samples which are tested electrically, physically, chemically and microscopically in order to rank and ascertain the variability of fly ash from the proposed mining area. In this way the furnaces are used as an early means of assisting future coal mining - power station development.

INTRODUCTION

Escalation in power requirements and power station size created a situation where power station development became integrated with the development of new coal mining operations. This resulted in previously unused and untested coal seams or blends of seams being proposed for use in major power station boilers, at a time when the need for compliance with air pollution requirements was becoming increasingly important.

Under these circumstances a programme was initiated to develop a laboratory furnace which would produce fly ash that was similar to the fly ash produced in a pulverised fuel fired power station boiler when using the same coal. A further requirement of the furnace was that it should be sized on the basis that only a portion (2 - 4 kg) of a 50 mm diameter coal borecore would be available for test firing. It was hoped that by producing a synthetic fly ash, subsequent examination would provide better information to assist with plant design than was available from analyses of the coal and its ash.

FURNACE DESCRIPTION

Design

A small vertical tube furnace was developed which was designed to provide each pulverised coal particle with a similar thermal and chemical path to that experienced in a pulverised fuel fired power station boiler.

The furnace assembly is shown schematically in Figure 1. The unit comprises a stirred pulverised coal bin, located above a screw feeder which is capable of controlled feeding within the range 10 - 0.5 g/h. A gas mixture of air, oxygen and propane is introduced into the coal feed at the discharge of the metering screw, after which the coal-gas mixture passes through a high speed impeller to reduce particle agglomeration. The mixture is then fired in the furnace through a tapered burner nozzle.

The furnace consists of a vertical, externally heated ceramic tube having a nominal bore of 38 mm, which provides a particle residence time of approximately 3 seconds. The tube is electrically heated in two zones and temperatures are controlled to provide a fixed profile which peaks in the centre zone at approximately 1450^{o}C.

Air, oxygen and propane gas rates are controlled and the gases are combined in a mixing bottle after which they pass through a flame arrestor prior to entering the feeder system.

Fly ash is collected in a heated mechanical collector, which is designed to maintain the fly ash above the dew point. A mechanical collector is used to prevent sample properties being effected by the method of collection.

Operation

Coal samples should represent the seam or blend of seams that are proposed to be fired in the power station boilers. The samples should be neither contaminated nor oxidised. Laboratory beneficiation of a sample must not result in chemical additions to the prepared coal, which would not be present in practice.

Each sample is milled to approximately 80% -76 micrometres, dried to approximately 3% moisture and stored under nitrogen prior to firing.

The pulverised coal feed rate is adjusted to produce a fly ash which usually contains less than 3% carbon. Depending on the nature of the coal some feeder pre-heating may be necessary to achieve this low carbon content.

Most steaming coals will produce satisfactory fly ash in the furnaces at production rates of up to a maximum of 0.15 g/h. Satisfactory firing and fly ash production may be determined by physical observation of the operation, supported by subsequent laboratory analyses. However some coals tested have caused operating difficulties resulting in poor combustion. In each case further examination of the coal and its resultant fly ash by optical microscopy and/or electron microscopy has indicated the cause of the problem, which

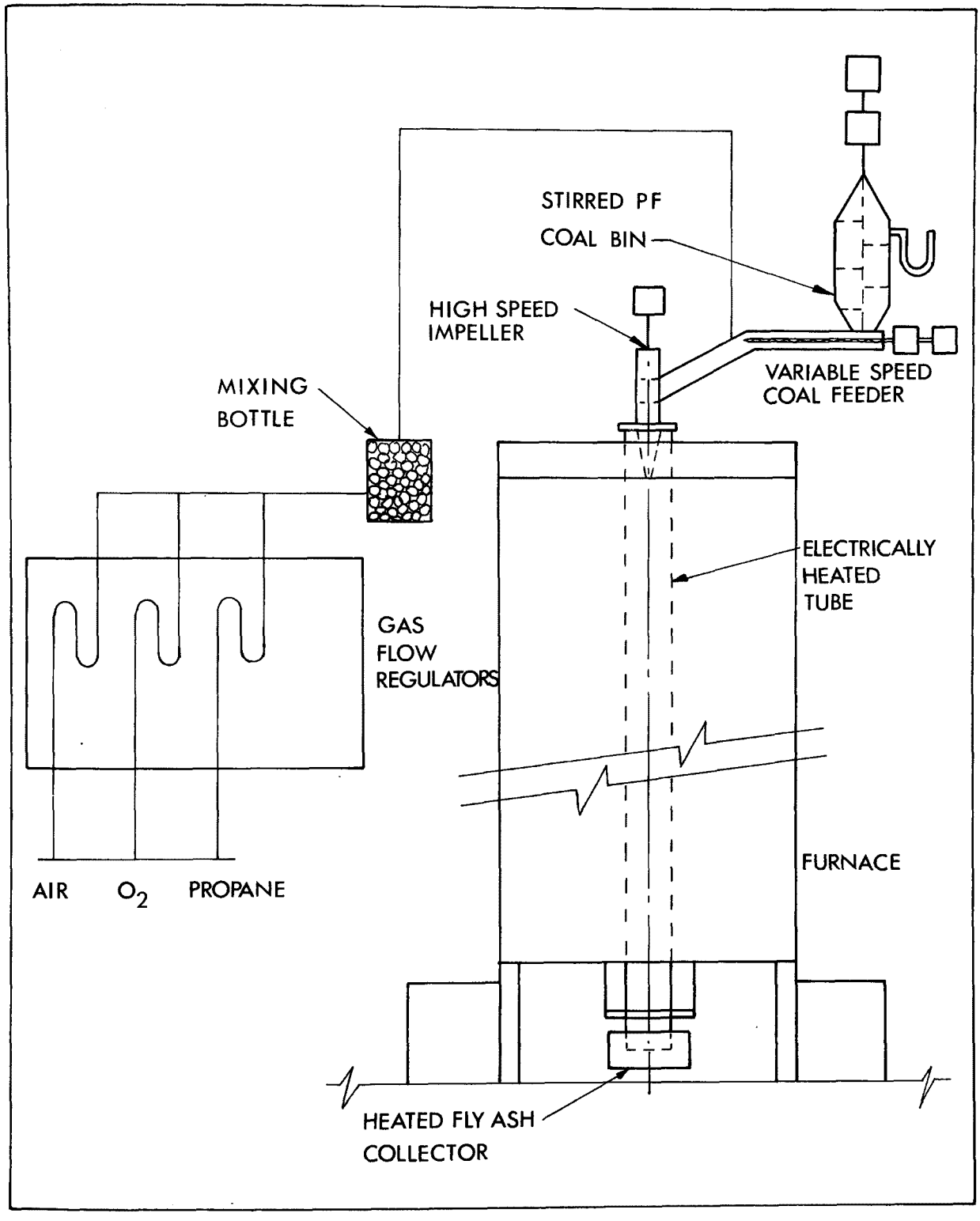

Figure 1. Schematic Arrangement of Furnace Assembly.

after analysis has permitted furnace operation to be adjusted to produce an acceptable fly ash.

Fly ash is collected in a simple mechanical separator which is heated to maintain the fly ash at approximately precipitator operating temperature. Clinker is removed from the fly ash and the ash is stored above dew point prior to testing.

Regular feeder and furnace maintenance is necessary to ensure the continuous production of a satisfactory fly ash. Agglomerated coal being fed to the nozzle, nozzle fouling and tube clinker build up will all result in a failure to produce fly ash.

Confirmative Testing

The furnaces were developed on the basis that each pulverised coal particle should experience a similar temperature and chemical path in the furnace to that experienced in a large pulverised fuel fired boiler.

Furnace conditions were established by comparing the fly ash produced in the test rig with power station fly ash generated from the same coal (1). Coal samples were obtained from boiler mill feeders at the same time as isokinetically collected fly ash samples were obtained from the boiler outlet. Operating conditions were adjusted until metallurgical similarity for iron components in both the model and associated power station fly ash were observed to approximately coincide. Once established, these furnace conditions were confirmed and more closely defined by producing fly ash and comparing it with its associated boiler fly ash taken from a number of power stations.

Since only a small quantity of coal was normally available from a 50 mm borecore sample, the University of Wollongong developed a micro-scale resistivity apparatus (2) for examining 10 g fly ash samples.

Following these developments further confirmative testing using resistivity determinations as a basis for comparison was undertaken on model fly ash and its associated power station fly ash (3, 4). The results confirmed the validity of the procedure and the ability of the laboratory furnaces to produce a model fly ash having similar collectability characteristics to its associated power station fly ash (5). The repeatability of electrical resistivity measurement was also demonstrated (6) and typical confirmative results are shown in Figure 2.

INVESTIGATION PROCEDURE

The furnaces were developed and are used as a means of producing synthetic fly ash. Operating experience has shown that characteristics related to slagging-fouling of the ash and carbon burn out of the fly ash will vary as in practice, but no correlation studies have been undertaken in these areas.

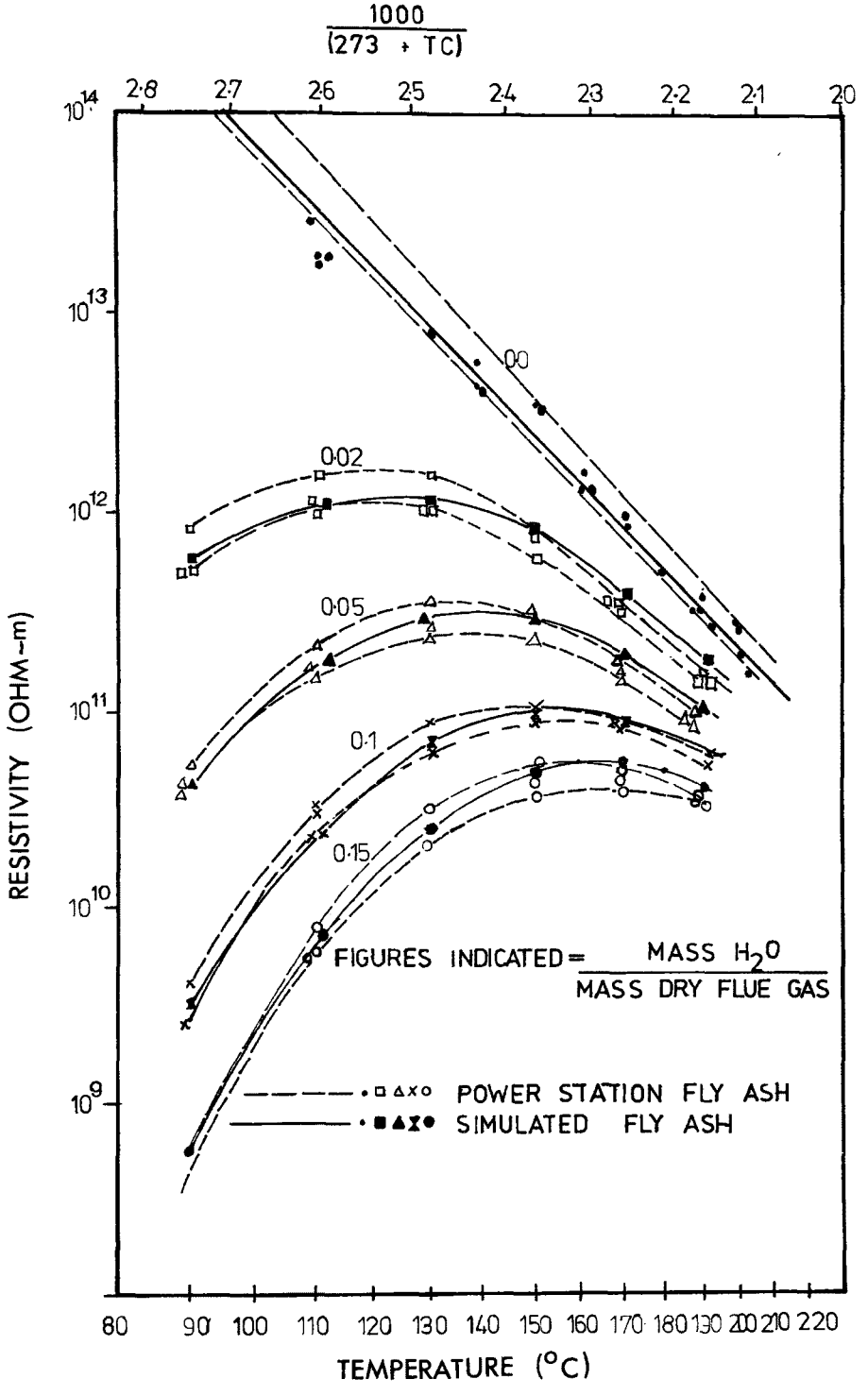

Figure 2. Resistivity curves comparing Synthetic and Power Station Fly Ash and also illustrating the repeatability of electrical measurement.

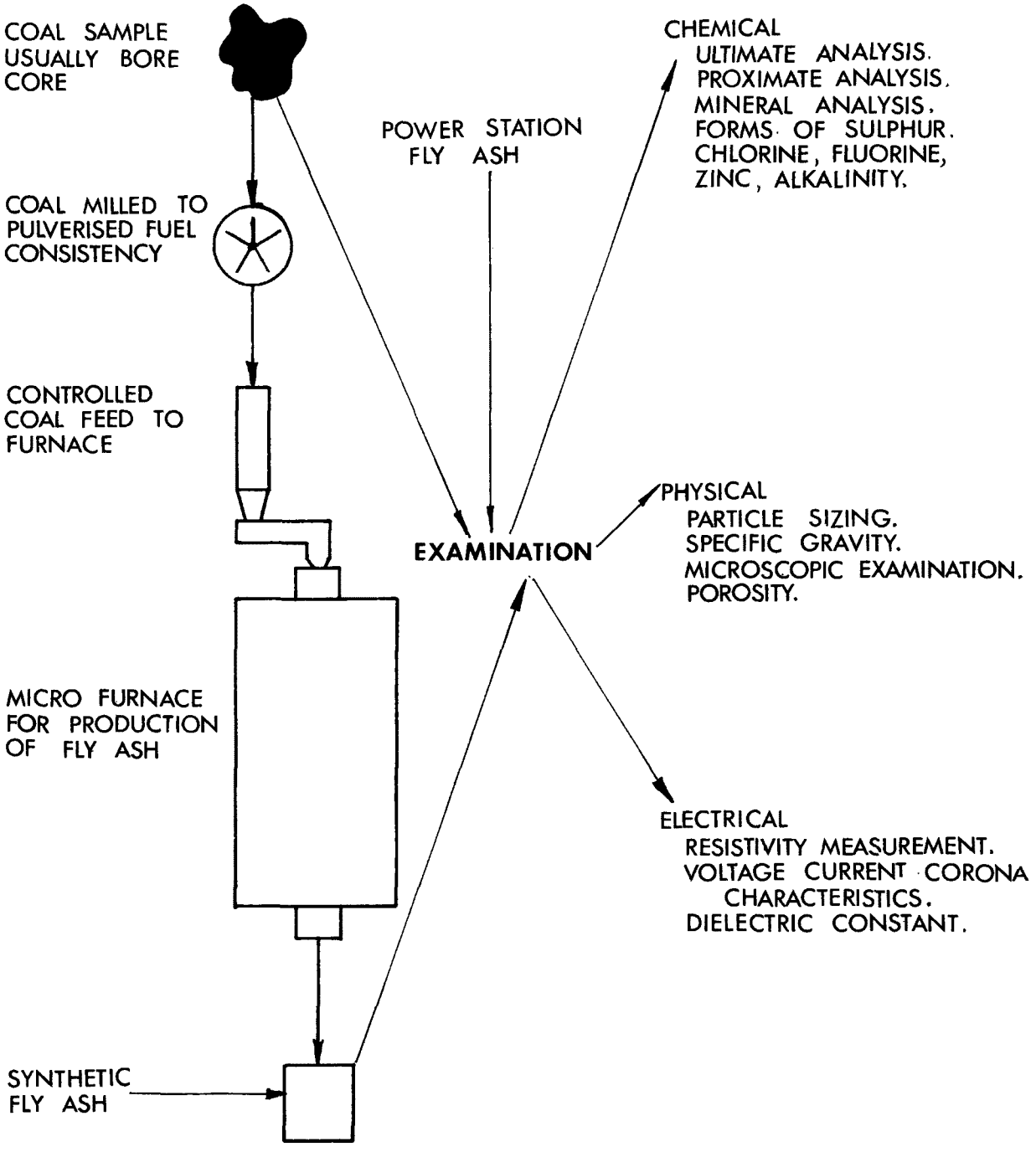

Figure 3. Procedure for examination of coal samples in order to estimate the fly ash collectability characteristics.

The synthetic fly ash that is obtained from the furnaces is used for estimating the likely collectability of fly ash that will result, when coal from a proposed mining development is fired in a pulverised fuel fired power station boiler.

The procedure used to examine a coal sample and to estimate the fly ash collectability characteristics (7, 8) is shown in Figure 3.

Once obtained from the furnace, the fly ash is chemically and physically examined for mineral analysis, carbon content, fluorine content, alkalinity, sizing, specific gravity, porosity and by using optical and/or electron microscopy techniques.

An electrical examination of the fly ash sample includes resistivity measurements obtained over a range of temperatures at various moisture contents in a flue gas environment at an electric stress of 400 kV/m. To complement this data, relative resistivity measurements are obtained over a range of temperature and moisture conditions at various voltages up to breakdown. Dielectric constant is determined for the bulk fly ash samples in the resistivity cell over a range of frequencies, temperatures and moisture conditions in a flue gas environment.

Voltage current corona characteristics are also determined for the fly ash over a range of temperatures and moisture contents in a flue gas environment. These results are then compared with the clean electrode characteristics.

The derived results on analysis are used to rank the coal area and to indicate variability that may occur over the coal seam. Resistivity variations of up to 150 : 1 have been observed to exist in a single coal seam, confirming the need for these examinations in order to be able to select an area from which to obtain a representative coal sample for large scale pilot plant testing.

CONCLUSION

Major coal fired power station developments coincide with new coal mining developments. In order to be able to predict the likely collectability and variability of fly ash resulting from the pulverised fuel combustion of coal taken from the proposed mining area it is necessary to produce and examine fly ash from a number of locations across the proposed mining area.

Small laboratory furnaces which can produce a synthetic fly ash from portion of a small borecore coal sample have been developed and shown to produce fly ash which is similar to power station fly ash generated from the same coal.

The furnaces have been used to examine bituminous, sub-bituminous and lignite coals from North America, Africa, New Zealand and Australia.

The data generated by examination of the synthetic fly ash has been used to assist with the selection and design of new power station particulate collectors.

ENDNOTES

References

1. Dugan, P., Guyot, R.E., and Moran, V.J. Laboratory Techniques for the Examination of the Combustion Characteristics of Coal - Part II - A Small Furnace Test. Australian Coal Industry Research Laboratories Ltd., P.R. 69-4, 1969.

2. Tassicker, O.J. and Sullivan, K.M. Estimation of Precipitator Performance for Collection of Fly Ash by Examination of Low Sulphur Bore Cores. Presented to 66th Annual Meeting of the Air Pollution Control Association, Chicago, Illinois, U.S.A., June, 1973.

3. Sullivan, K.M. A Comparative Study of Laboratory Fly Ash and Power Station Fly Ash. Australian Coal Industry Research Laboratories Ltd., P.R. 75-10, 1975.

4. Sullivan, K.M. A Comparative Study of Laboratory Fly Ash and Power Station Fly Ash - Part II. Australian Coal Industry Research Laboratories Ltd. P.R. 76-12, 1976.

5. Baker, J.W., Sullivan, K.M. and Tassicker, O.J. Assessment of a Laboratory Technique for Predicting the Precipitability of Fly Ash Derived from a Coal Bore Core. Proceedings of the Fourth International Clean Air Congress, Tokyo, Japan, May, 1977.

6. Baker, J.W. and Sullivan, K.M. Reproducibility of Ash Resistivity Determinations. Presented to Joint Power Generation Conference, Long Beach, California, U.S.A., September, 1977. I.E.E.E. Publication No. A78 303-0.

7. Baker, J.W. and Sullivan, K.M. A Strategy for Assessing the Requirements for Trapping Power Station Fly Ash. Proceedings of CSIRO Conference on Electrostatic Precipitation, Leura, N.S.W., Australia, August 1978.

8. Sullivan, K.M. Evaluation of Coal for Electrostatic Precipitator Design. Proceedings of Conference on Pulverised Coal Firing, Mineral Matter and its Effects, The University of Newcastle, Newcastle, N.S.W., Australia, August 1979.

COMPUTER SIMULATION OF THE WIDE PLATE SPACING EFFECT

By: Eric A. Samuel
Buell Emission Control Division
Envirotech Corporation
Lebanon, PA 17042

ABSTRACT

A numerical simulation code has been developed to analyze the coupled electro-aerodynamic phenomena within plate-wire precipitators. The electric field and space charge density are obtained by numerically solving Poisson's equation and the continuity equation simultaneously. The precipitator performance is evaluated by two methods: (i) the trajectory method, and (ii) the drift velocity method. The predictability of the wide plate spacing effect (WESP effect) for certain precipitator configurations is demonstrated using the simulation code. Evidence in favor of the equivalence between the trajectory method and drift velocity method of evaluating precipitator performance is presented in the Deutsch limit of infinitely rapid turbulent mixing.

INTRODUCTION

The emitting electrode diameter (2a), the spacing between successive emitting electrodes (2c), and the spacing between neighboring plates (2b) are three geometrical parameters which characterize a plate-wire electrostatic precipitator (Figure 1). The dependence of the precipitator collection efficiency on the above geometrical parameters has been subject to numerous experimental and theoretical studies (1-4). The effect of plate spacing on the collection efficiency has been one of the more far reaching discoveries of recent years (4). The collection efficiency has been found to be roughly independent of plate spacing in the range 0.2 to 0.6 m (8 to 24 in.). The independence of the collection efficiency on plate spacing is referred to in the literature as the wide plate spacing effect or the WESP effect. In terms of the classical Deutsch equation, one consequence of the WESP effect is the linear dependence of the drift velocity on plate spacing.

Masuda (4) has reviewed the various theories which have been proposed for explaining the WESP effect. Higher electric field at the plate, higher level of corona stability, lower level of rapping reentrainment and turbulent diffusion are among the advantageous effects thought to contribute to the wide plate phenomenon. The primary objective of the present paper is to demonstrate the predictability of the WESP effect for certain combinations of the precipitator geometrical and electrical parameters using two presently known numerical methods of evaluating precipitator performance. The results presented in this paper in support of the predictability of the WESP effect will also serve to compare the predictions of the two different numerical approaches for precipitator performance evaluation: (i) the particle trajectory method (3), and (ii) the drift velocity method (1,5). In an earlier investigation, the trajectory method yielded results which compared favorably with experimental efficiency results from model precipitators obtained using laser light scattering techniques. The trajectory method was also used previously to

predict an optimal wire spacing for a given plate spacing. The drift velocity method is used in the computer code developed by McDonald (5).

METHOD OF CALCULATION

Electric Field and Space Charge Density

In a previous numerical code (3), the electric field and space charge density were obtained by dynamically simulating the motion of electrons and ions within the precipitator until a steady state space charge distribution was reached. The above method, which avoided solving differential equations, was amenable to the inclusion of the effects of negative ion formation and fluid flow around the emitting wires. Since the objective of the present study is to obtain only trends in precipitator performance with respect to plate spacing, three simplifying assumptions are made: (i) the negative charge carriers have a single mobility which varies inversely with gas density, (ii) the effect of fluid flow on the corona characteristic is negligible, and (iii) the perturbation of the fluid flow field by the emitting wires is also negligible. With the above simplification, it is possible to obtain the electric field, $\underline{E}(x,y)$ and the space charge density, $\rho(x,y)$, by solving Poisson's equation and the continuity equation simultaneously:

$$\nabla^2 V(x,y) = -\rho(x,y)/\varepsilon_0 \quad ; \quad \underline{\nabla} V(x,y) \cdot \underline{\nabla}\rho(x,y) = \rho^2(x,y)/\varepsilon_0 \qquad (1)$$

subject to the boundary conditions: $V = 0$ on collecting plates and $V = V_w$ on emitting wires. In the above equations, ε_0 is the free space permittivity, $V(x,y)$ the potential and V_w the wire voltage. Cooperman (2) obtained an approximate solution to the above equations by assuming the space charge density to be constant everywhere within the precipitator. In the present study, the wire voltage, the potential, electric field and space charge distributions corresponding to a given average current density at the plate are obtained by following the numerical method proposed by Leutert and Böhlen (6) and by McDonald, Smith, Spencer and Sparks (7). The electrical characteristics obtained as described above are checked for consistency and accuracy by three methods which require: (i) agreement of the static potential distribution (space charge free) with the analytical results obtained from conformal mapping (3), (ii) agreement with Gauss' theorem for Gauss surfaces in Figure 1:

$$\oint \underline{E} \cdot d\underline{n} = \rho dv/\varepsilon_0 \quad ; \quad \underline{E} = -\underline{\nabla} V \qquad (2)$$

and (iii) agreement with the current continuity equation in the form:

$$k \int_{-c}^{c} \rho(x,y)\, E_x(x,y)\, dy = 2\, c\, j_p \qquad (3)$$

for arbitrary x, where k is the average negative ion mobility, E_x is the x-component of the electric field and j_p is the average current density at the collecting plate.

Methods of Evaluating Precipitator Performance

Three methods of evaluating precipitator performance are found in the literature: (i) trajectory method (3), (ii) drift velocity method (1,5), and (iii) particle transport equation method (8). All three methods can be traced to the continuity equation for mass flow. Leonard, Mitchner and Self (8) have

demonstrated that the particle transport equation method is equivalent to the drift velocity method in the Deutsch limit of infinitely rapid turbulent mixing (in the limit the eddy diffusion coefficient, $D \to \infty$). The trajectory method, in principle, should be valid for both laminar flow ($D = 0$) and for turbulent flow ($D \neq 0$) provided the time average of the fluctuating component of the velocity flow field is zero.

Trajectory Method

The trajectory method consists of following the path of a particle in the space between plate (gas passage) in small time steps, Δt. The position of a particle of radius r, at time $t = n\,\Delta t$, is given by the alogarithm:

$$x_n = x'_{n-2} + v_x(x_{n-1}, y_{n-1})\ (2\,\Delta t)$$

$$x'_{n-1} = x'_{n-2} + 0.5\ [\ v_x(x_{n-1}, y_{n-1}) + v_x(x'_{n-2}, y'_{n-2})\ ]\ \Delta t \qquad (4)$$

with similar equations for the y-coordinate. The particle velocity $\underline{v} = (v_x, v_y)$ is given in terms of the particle mobility, $k_p = q(t)/(6\pi\mu r)$, by:

$$v_x(x,y) = k_p\, E_x(x,y)\ ;\quad v_y(x,y) = k_p\, E_y(x,y) + v_o(x) \qquad (5)$$

where $q(t)$ is the charge on the particle at time t and μ is the gas viscosity. The velocity $\underline{v}_o$ represents the velocity profile of the gas flowing in a passage. Particles of a given radius, r, enter the precipitator at a chosen number of equally spaced inlet positions. The collection efficiency, by number density, is obtained by following the trajectories of the particles until they either reach the collecting plates or exit the precipitator comprising a chosen number of geometrically and electrically identical wires. The effect of the particle charge on the corona characteristic is ignored.

Drift Velocity Method

The drift velocity method of evaluating precipitator performance is applicable in the Deutsch limit in which rapid turbulent mixing causes the particle concentration to be a function only of the distance along the gas passage (y direction). In the above limit, the collection efficiency for particles of radius r is given by the Deutsch equation (1):

$$\eta(y) = 1 - \exp\ [\ -\omega\, y/(v_{av}\, b)\ ] \qquad (6)$$

where 2b is the plate spacing and v_{av} is the average velocity of flow in the y direction. The drift velocity, ω, is given in the Deutsch limit by:

$$\omega = [\ (2c)\ (6\pi\mu r)\ ]^{-1} \int_{-c}^{c} q_o(y)\, E_x(b,y)\, dy \qquad (7)$$

where q_o is the saturation charge corresponding to the average field within a gas passage at a distance y along the gas passage, given by:

$$q_o(y) = \frac{f}{b}\,\frac{3\kappa_p}{\kappa_p + 2}\, 4\pi\varepsilon_o r^2 \int_{o}^{b} [\ E_x^2(x,y) + E_y^2(x,y)\ ]^{\frac{1}{2}}\, dx \qquad (8)$$

In the integration given by equation (7), q_o is allowed to only increase or remain constant at its maximum value when moving in a low field region.

Particle Charging

Particles of diameter equal to or larger than 2 micron are assumed to be charged predominantly by the field charging mechanism. For the above mechanism, the charge on a particle of radius r at time t is given by (1):

$$q(t) = q_o t/(t + t_o) \; ; \quad q_o = f(4\pi\varepsilon_o)[3\kappa_p/(\kappa_p + 2)] \; |\underline{E}| \; r^2 \; ; \quad t_o = 4\varepsilon_o/(\rho k) \tag{9}$$

In the above equations, q_o is the saturation charge, $|\underline{E}|$ the magnitude of the total electric field, and κ_p the dielectric constant of the material comprising the particle. Because there is some doubt expressed in the literature regarding the accuracy of the saturation limit (3,9), an effectiveness factor, f, is introduced here. In the trajectory calculation, the increment in charge during a time step, Δt, is given by:

$$\Delta q = (q_o/t_o)\,(1 - q/q_o)\,[\,(1 - q/q_o)\,\Delta t - (q/q_o)\,\Delta t_o\,] + (q/q_o)\,\Delta q_o \tag{10}$$

The above equation takes into account the changes in particle charging rate due to changes in electric field and space charge density. During the flight of a particle within the precipitator, its charge is allowed to either increase or stay constant; no mechanism is considered for charge loss.

Velocity Flow Field

Two flow profiles are used in the present study: (i) the Poisuelle flow profile characteristic of laminar flow, and (ii) the uniform flow profile characteristic of fully developed turbulent flow. At typical operating gas velocities the Reynolds number for flow in the precipitator gas passages is higher than the critical value for the onset of turbulence. Despite the above fact, the intention in considering the Poisuelle flow field here is to compare differences in performance, as evaluated by the trajectory method, attributable to differences in the flow distribution. The intention in considering the uniform flow profile with the trajectory method is to compare the predictions of the trajectory and drift velocity methods for fully developed turbulent flow.

PRECIPITATOR CONFIGURATIONS

Four configurations are evaluated in this paper. These are illustrated in Figure 2. Seven plate spacings in the range 6 in. to 24 in. are considered within each scheme. The variations in the geometrical parameters within the schemes are as follows: Scheme 1 - b varied, keeping a and c fixed; Scheme 2 - b and a varied such that b/a = 85.7, keeping c fixed; Scheme 3 - b and c varied such that bc = 20.25, keeping a fixed (this scheme corresponds to maintaining the same density of wires per unit cross-sectional area perpendicular to the wires containing the direction of flow); Scheme 4 - a,b,c all varied such that b/a = 85.7 and bc = 20.25. In each of the above schemes, the precipitator with 2a = 0.105 in. and 2b = 9 in. is used as the reference for comparing the performance of the other precipitators. The average current density at the plate is maintained constant at 0.4 ma/m^2 (0.04 ma/ft^2). The following constants have been used in all of the calculations performed under the present study: gas temperature = 176°C (350°F); v_{av} = 1.2 m/s (3.93 ft/s); f = 0.5; κ_p = 2; μ = 2.31 X 10^{-5} kg/(m-s); k = 3.87 X 10^{-4} m^2/(V-s).

RESULTS AND DISCUSSIONS

Table 1 displays a summary of the main electrical characteristics of the plate-wire precipitators belonging to the four schemes described above (see Figure 2). The average field at the plate is in general higher than that in the air gap. The above fact is a peculiarity of plate-wire precipitators. Cylinder-wire precipitators display the opposite trend. Table 1 also shows the wire voltages calculated for the different precipitator configurations. While close agreement between the calculated wire voltages and those measured for field precipitators is not expected, the calculated voltages appear to display the correct trends with respect to precipitator geometry. The average fields at the plate as well as in the air gap appear to increase with increasing plate spacing, consistent with the explanation of the WESP effect proposed by Misaka, sugimoto and Yamada (see ref. (4)). The increase in the electric field with plate spacing is partly attributable to the increase in the total space charge enclosed by a gas passage of fixed length with increase in the plate spacing.

Figures 3(a) to 3(d) show the effective drift velocities obtained by the trajectory method for the four precipitator configurations described above. The drift velocities plotted in these figures are obtained by least-squares fitting the efficiency data to the Deutsch equation (equation (6)). For larger particles, which are captured in the first few wire sections, the analysis in terms of an exponential equation becomes an artifact; thus the lack of smooth trends in the drift velocities derived from the trajectory method for larger particles. Figures 4(a) to 4(d) display the drift velocities for the four precipitator configurations, evaluated on the basis of the drift velocity method. The trends in the drift velocity with respect to plate spacing are much smoother in this case, as would be expected from a method based on the Deutsch equation. For each precipitator scheme, the predictions of the trajectory method and the drift velocity method display closely similar trends, differing only in their absolute values. The above comparison provides some evidence that the trajectory method and the drift velocity are equivalent in the Deutsch limit. It appears that the trajectory method is a valid method of evaluating precipitator performance even in the presence of turbulent diffusion, provided the average velocity due to fluctuations is zero.

The dotted lines in Figures 3(a) to 3(d) and Figures 4(a) to 4(d) indicate the variations in the drift velocity expected on the basis of the WESP effect. The 9 in. plate spacing serves as the reference for the straight lines defining the WESP effect. It is evident from the figures that the WESP effect does not appear when only plate spacing is varied (scheme 1) for the entire range of plate spacings considered. A linear variation in the drift velocity does appear beyond a plate spacing of 12 in., but at a lower efficiency level. Scheme 2 and scheme 3 precipitators both appear to display the WESP effect. The increase in wire radius or the increase in the number of wires in conjunction with the increase in plate spacing appear to produce the same level of precipitator performance. Precipitators belonging to scheme 4 appear to display the best performance, far exceeding the expections based on the WESP effect.

Tables 2,3,4 and 5 display the numbers plotted in figures 3 and 4. In

addition, the above tables compare the drift velocities derived from the trajectory method corresponding to the Poisuelle flow field (method A) and the uniform flow field (method B). It appears, in general, that the trajectory method predicts a lower drift velocity for the Poisuelle flow distribution than for the uniform flow distribution. The above trend is not unreasonable since the particles near the middle of a gas passage, which in the laminar flow limit travel at velocities higher than the average velocity, require a greater length of travel along the gas passage to be collected.

REFERENCES

1. White, H. J. Industrial Electrostatic Precipitators. Addison Wesley, 1963.

2. Cooperman, p. A Theory for Space-Charge-Limited Currents with Application to Electrical Precipitation. Trans. Am. Inst. Electr. Eng. I 75(64): 47-50, March 1960.

3. Kim, Y. W. and E. A. Samuel. Electrostatic Precipitators II: The efficiency and Wire-to-Plate Scaling Ratio. Physics of Fluids Technical Report No. 27, Lehigh University, 1978.

4. Masuda, S. Present Status of Wide-Spacing Type Precipitators in Japan. In: Proceedings of the Second EPA Symposium on the Transfer and Utilization of Particulate Control Technology, Vol. II. Electrostatic Precipitators, EPA-600/9-80-039b, U. S. Environmental Protection Agency, Research Triangle Park, NC, Spetember 1980. p. 483-501.

5. McDonald, J. R. A Mathematical Model of Electrostatic Precipitation. Vol. I, Modeling and Programming, EPA-600/7-78-111a, U. S. Environmental Protection Agency, Research Triangle Park, NC, 1978.

6. Leutert, G. and B. Böhlen. The Spatial Trend of Electric Field Strength and Space Charge Density in Plate-Type Electrostatic Precipitators. Staub-Reinhalt. Luft. 32(7): 27-33, July 1972.

7. McDonald, J. R., W. B. Smith, H. W. Spencer and L. E. Sparks. A Mathematical Model for Calculating Electrical Conditions in Wire-Duct Electrostatic Precipitation Devices. J. Appld. Phys. 48(6): 2231-2243, June 1977.

8. Leonard, G., M. Mitchner and S. A. Self. Particle Transport in Electrostatic Precipitators. In: Proceedings of the Second EPA Symposium on the Transfer and Utilization of Particulate Control Technology, Vol. II. Electrostatic Precipitators, EPA-600/9-80-039b, U. S. Environmental Protection Agency, Research Triangle Park, NC, September 1980. p. 146-167.

9. Masuda, S. and M. Washizu. Ionic Charging of a Very High Resistivity Spherical Particle. J. Electrostatics. 6(1): 57-68, Feb. 1979.

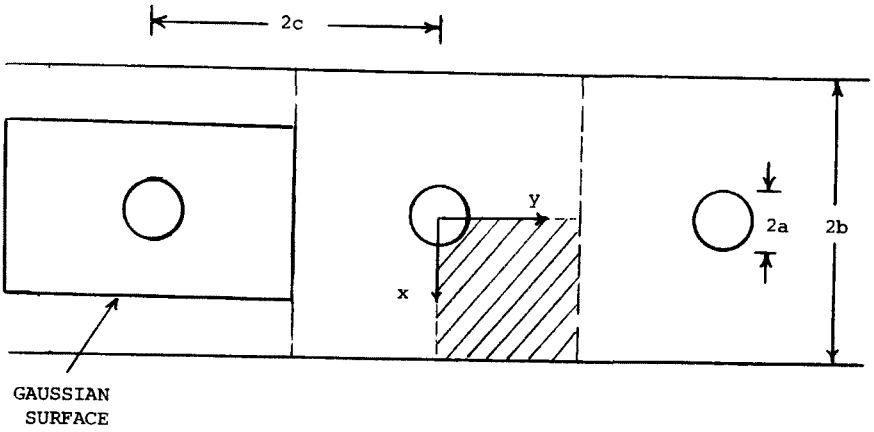

Figure 1 - Geometrical parameters which characterize a plate-wire electrostatic precipitator. The shaded area is the region within which the electric field and space charge density are solved. A Gaussian surface is also shown for use in verifying the numerical results for the electric field and space charge density.

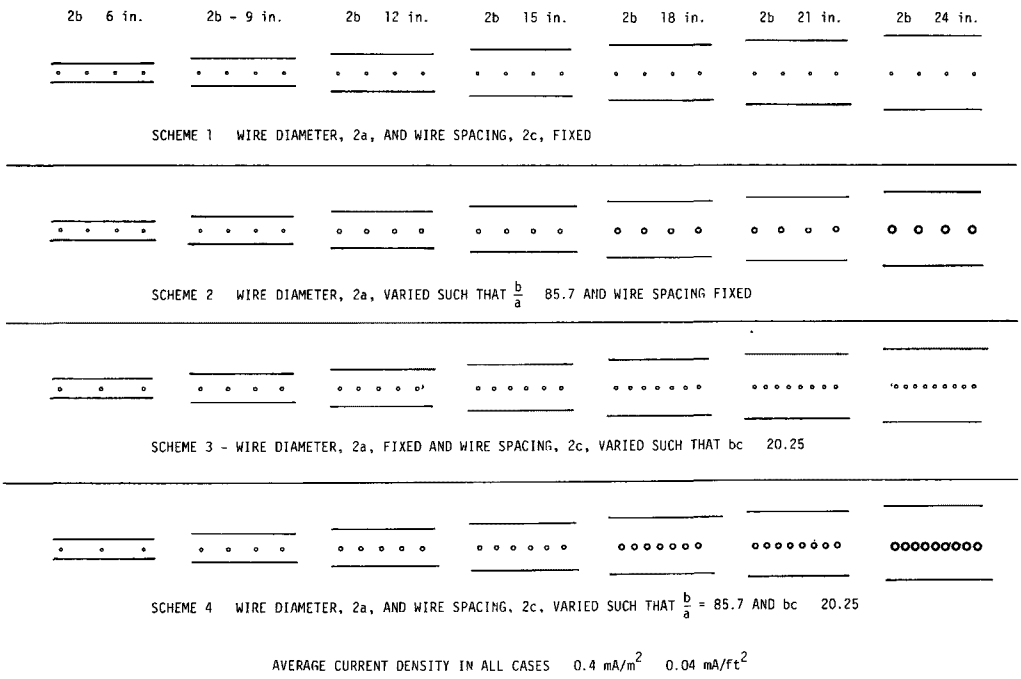

Figure 2 - Precipitator configurations evaluated for the WESP effect.

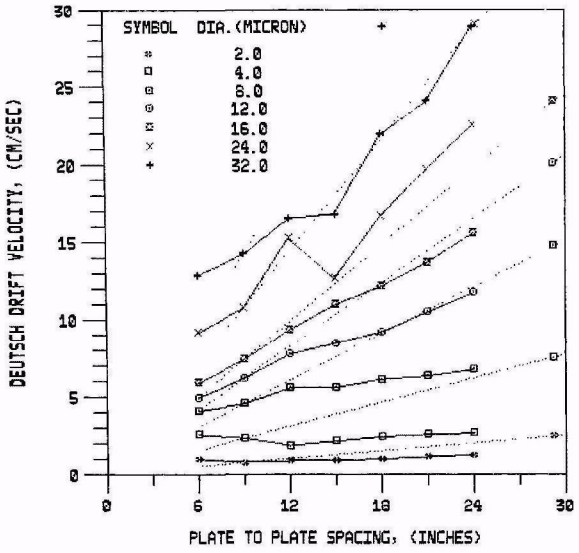

Figure 3(a) - Variation of the average drift velocity with plate spacing and particle size for scheme 1 precipitators in which the plate spacing, 2b, is varied with the wire diameter, 2a, and the wire spacing, 2c, held constant. The drift velocity is derived from the trajectory method with a uniform velocity flow profile.

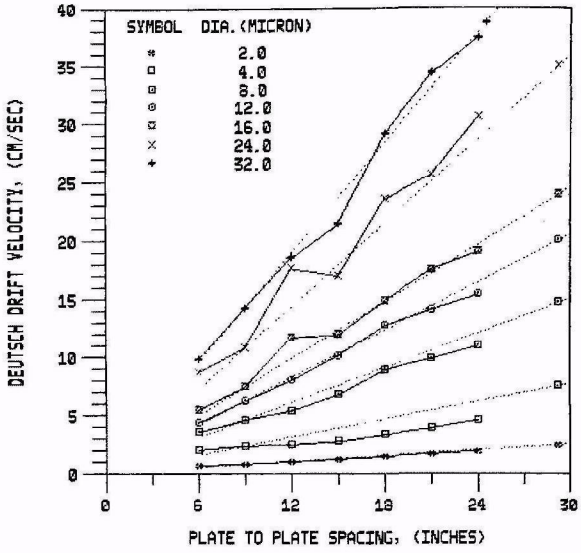

Figure 3(b) Variation of the average drift velocity with plate spacing for scheme 2 precipitators in which the plate spacing, 2b, and the wire diameter, 2a, are varied such that b/a = 85.7 with the wire spacing, 2c, held constant. The drift velocity is derived from the trajectory method with a uniform velocity flow profile.

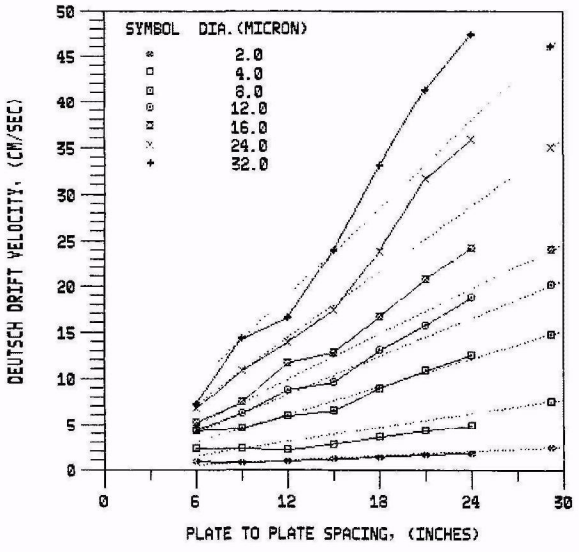

Figure 3(c) Variation of the average drift velocity with plate spacing for scheme 3 precipitators in which the plate spacing, 2b, and the wire spacing, 2c, are varied such that bc = 20.25 with the wire diameter, 2a, held constant. The drift velocity is derived from the trajectory method with a uniform velocity flow profile.

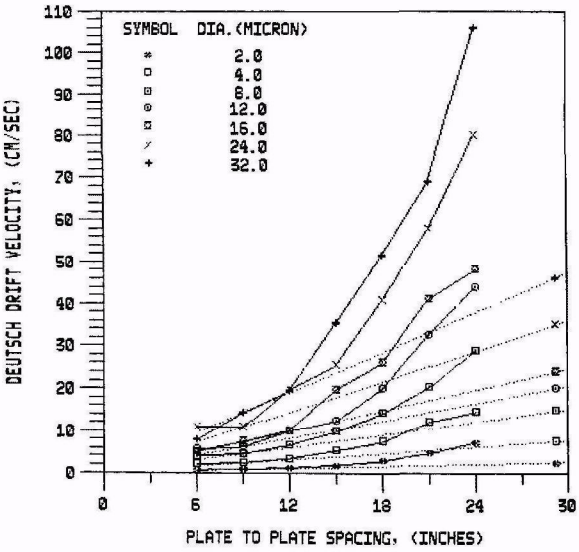

Figure 3(d) Variation of the average drift velocity with plate spacing for scheme 4 precipitators in which the plate spacing, 2b, the wire spacing, 2c, and the wire diameter, 2a, are all varied such that b/a = 85.7 and bc 20.25. The drift velocity is derived from the trajectory method with a uniform velocity flow profile.

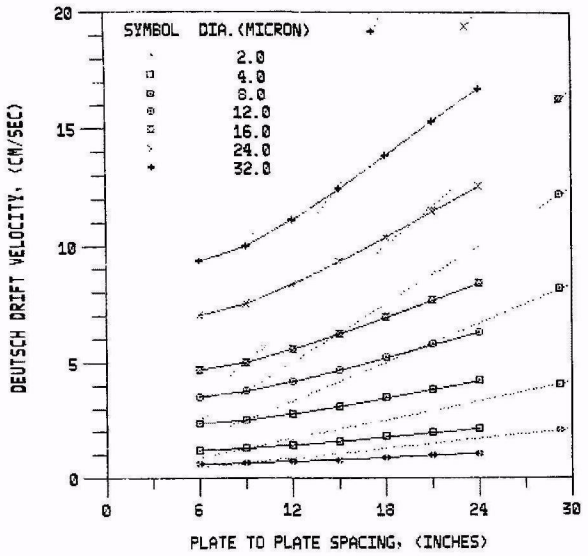

Figure 4(a) Variation of the average drift velocity with plate spacing for scheme 1 precipitators in which the plate spacing, 2b, is varied with the wire diameter, 2a, and the wire spacing, 2c, held constant. The drift velocity is derived from the drift velocity method with a uniform velocity flow profile.

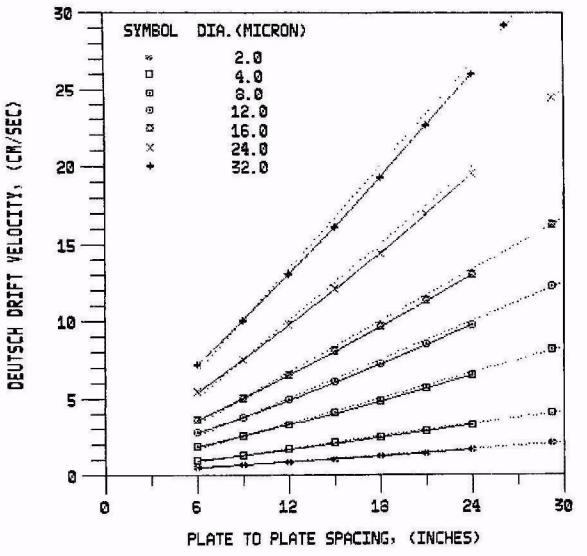

Figure 4(b) Variation of the average drift velocity with plate spacing for scheme 2 precipitators in which the plate spacing, 2b, and the wire diameter, 2a, are varied such that b/a 85.7 with the wire spacing, 2c, held constant. The drift velocity is derived from the drift velocity method with a uniform velocity flow profile.

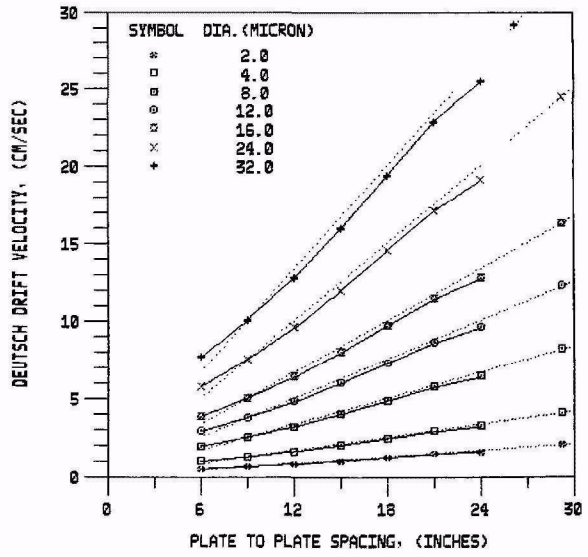

Figure 4(c) Variation of the average drift velocity with plate spacing for scheme 3 precipitators in which the plate spacing, 2b, and the wire spacing, 2c, are varied such that bc = 20.25 with the wire diameter, 2a, held constant. The drift velocity is derived from the drift velocity method with a uniform velocity flow profile.

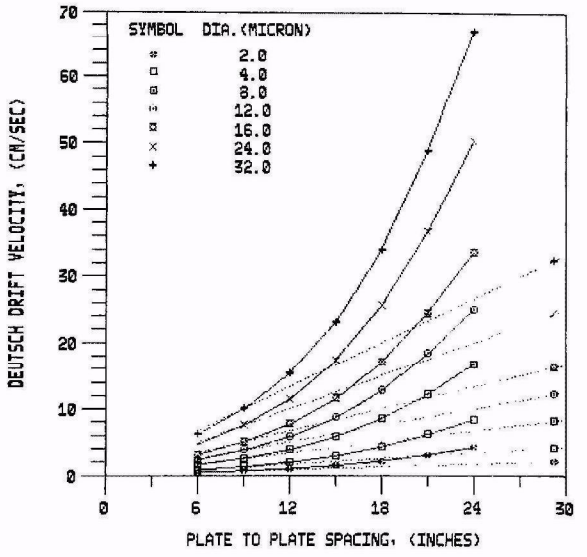

Figure 4(d) Variation of the average drift velocity with plate spacing for scheme 4 precipitators in which the plate spacing, 2b, the wire spacing, 2c, and the wire diameter, 2a, are all varied such that b/a = 85.7 and bc = 20.25. The drift velocity is derived from the drift velocity method with a uniform velocity flow profile.

TABLE 1. SOME CALCULATED ELECTRICAL CHARACTERISTICS OF WIRE-PLATE PRECIPITATORS AT A CONSTANT AVERAGE PLATE CURRENT DENSITY OF 0.4 mA/m^2 (0.04 mA/ft^2)

2a in.	2b in.	2c in.	Wire Voltage, kV	Electric Field Average, kV/m E_x *	E_y +	E_p #	Average Space Charge Density, 10^{-6} Coul./m^3	Total Space Charge Per Section, 10^{-7} Coul./m
0.105	6.0	9.0	24.6	111	50.1	141	8.1	2.8
0.105	9.0	9.0	30.1	128	40.5	169	7.6	4.0
0.105	12.0	9.0	36.4	142	33.3	193	7.1	4.9
0.105	15.0	9.0	43.5	155	27.9	213	6.7	5.8
0.105	18.0	9.0	51.5	167	24.3	232	6.3	6.6
0.105	21.0	9.0	60.2	179	21.3	249	6.0	7.3
0.105	24.0	9.0	69.6	189	19.2	265	5.8	8.0
0.070	6.0	9.0	19.7	98	40.8	131	9.2	3.2
0.105	9.0	9.0	30.1	128	40.5	169	7.6	4.0
0.140	12.0	9.0	41.4	154	38.4	201	6.5	4.6
0.175	15.0	9.0	53.8	178	36.3	229	5.8	5.0
0.210	18.0	9.0	67.4	200	34.5	255	5.2	5.4
0.245	21.0	9.0	82.0	221	33.0	280	4.7	5.7
0.280	24.0	9.0	97.8	241	31.8	303	4.3	6.0
0.105	6.0	13.50	24.0	90	44.4	121	8.6	4.5
0.105	9.0	9.00	30.1	128	40.5	169	7.6	4.0
0.105	12.0	6.75	37.6	160	30.6	206	6.4	3.4
0.105	15.0	5.40	47.2	189	24.0	238	5.5	2.9
0.105	18.0	4.50	60.0	217	19.5	267	4.8	2.5
0.105	21.0	3.86	72.7	242	16.8	290	4.3	2.3
0.105	24.0	3.38	88.2	266	15.3	300	3.9	2.1
0.070	6.0	13.50	19.7	81	38.1	116	9.4	4.9
0.105	9.0	9.00	30.1	128	40.5	169	7.6	4.0
0.140	12.0	6.75	43.2	176	36.6	218	5.8	3.0
0.175	15.0	5.40	60.6	233	33.6	273	4.4	2.3
0.210	18.0	4.50	83.9	298	31.8	336	3.5	1.8
0.245	21.0	3.86	114.5	372	31.2	399	2.8	1.5
0.280	24.0	3.38	153.8	456	31.5	459	2.3	1.2

* E_x is average field in gap between plates in a direction perpendicular to the plates.

+ E_y is average field in gap between plates in a direction parallel to the plates.

E_p is the average total field at the plate.

All calculations are performed for a gas temperature of 177°C (350°F) corresponding to an average mobility of 3.87x10^{-4} (m/s)/ (v/m) for negative charge carriers. The emitting electrode smoothness factor is unity.

TABLE 2. AVERAGE DRIFT VELOCITY AS A FUNCTION OF PARTICLE SIZE FOR VARIATION IN b, WITH FIXED a, c

2a in.	2b in.	2c in.	METHOD*	AVERAGE MIGRATION VELOCITY (cm/sec) AS A FUNCTION OF PARTICLE DIAMETER (micron) 2.0	4.0	8.0	12.0	16.0	24.0	32.0	MEAN
0.105	6.0	9.0	A	0.81	2.27	4.31	5.92	8.41	9.42	13.56	4.09
			B	0.94	2.52	4.02	4.88	5.84	9.11	12.82	4.81
			C	0.58	1.17	2.33	3.50	4.66	6.99	9.32	1.56
0.105	9.0	9.0	A	0.89	1.53	3.92	5.91	7.60	9.93	11.21	3.75
			B	0.75	2.31	4.52	6.16	7.37	10.74	14.19	4.61
			C	0.62	1.25	2.50	3.74	4.99	7.49	9.99	1.90
0.105	12.0	9.0	A	0.97	1.77	4.08	6.26	8.32	11.31	13.21	4.06
			B	0.84	1.83	5.50	7.70	9.28	15.24	16.47	4.87
			C	0.69	1.39	2.77	4.16	5.55	8.32	11.09	2.26
0.105	15.0	9.0	A	1.16	2.02	3.69	5.87	7.82	11.34	15.56	4.40
			B	0.86	2.11	5.56	8.41	10.95	12.63	16.75	5.52
			C	0.78	1.55	3.10	4.65	6.20	9.30	12.40	2.64
0.105	18.0	9.0	A	1.37	2.16	4.15	7.03	9.26	13.59	18.56	4.84
			B	0.95	2.38	6.07	9.15	12.11	16.59	21.87	6.00
			C	0.86	1.73	3.45	5.18	6.91	10.36	13.81	3.01
0.105	21.0	9.0	A	1.57	2.49	4.61	7.07	10.24	15.36	20.50	5.38
			B	1.09	2.52	6.28	10.43	13.66	19.64	23.94	6.58
			C	0.95	1.91	3.82	5.73	7.63	11.45	15.27	3.39
0.105	24.0	9.0	A	1.79	2.82	4.89	7.71	11.20	16.58	21.22	5.90
			B	1.23	2.61	6.70	11.67	15.51	22.45	28.83	7.13
			C	1.04	2.09	4.18	6.27	8.35	12.53	16.71	3.77

* A - trajectory method for Poisuelle flow field
B trajectory method for uniform flow field
C drift velocity method for uniform flow field
Mean value of drift velocity is evaluated on the basis of number density for a log normal size distribution with d_{50} - 5.0 micron and σ = 2.0.

Average velocity and average plate current density for all determinations are 1.2 m/s (3.94 ft/s) and 0.4 mA/m^2 (0.04 mA/ft^2) respectively.

TABLE 3. AVERAGE DRIFT VELOCITY AS A FUNCTION OF PARTICLE SIZE FOR VARIATION IN a AND b SUCH THAT b/a = 85.7, WITH FIXED c

2a in.	2b in.	2c in.	METHOD*	AVERAGE MIGRATION VELOCITY (cm/sec) AS A FUNCTION OF PARTICLE DIAMETER (micron) 2.0	4.0	8.0	12.0	16.0	24.0	32.0	MEAN
0.070	6.0	9.0	A	0.66	1.35	3.28	4.86	5.64	7.77	11.09	2.92
			B	0.61	1.96	3.46	4.27	5.39	8.63	9.68	3.95
			C	0.44	0.89	1.78	2.67	3.56	5.34	7.12	1.32
0.105	9.0	9.0	A	0.89	1.53	3.92	5.91	7.60	9.93	11.21	3.75
			B	0.75	2.31	4.52	6.16	7.37	10.74	14.19	4.61
			C	0.62	1.25	2.50	3.74	4.99	7.49	9.99	1.90
0.140	12.0	9.0	A	1.13	1.94	4.91	7.21	9.70	11.27	14.79	4.69
			B	0.95	2.40	5.31	7.93	11.62	17.57	18.48	5.57
			C	0.81	1.62	3.23	4.85	6.47	9.70	12.93	2.49
0.175	15.0	9.0	A	1.34	2.40	5.67	8.01	10.83	15.96	21.74	5.65
			B	1.18	2.68	6.71	10.11	11.90	16.93	21.35	6.63
			C	1.00	2.00	4.00	6.00	8.00	12.00	16.01	3.10
0.210	18.0	9.0	A	1.57	2.89	6.74	9.85	12.31	18.55	23.01	6.65
			B	1.40	3.24	8.86	12.70	14.85	23.47	29.02	7.95
			C	1.20	2.40	4.80	7.21	9.61	14.41	19.21	3.72
0.245	21.0	9.0	A	1.86	3.36	7.42	11.03	12.90	17.87	25.44	7.68
			B	1.63	3.84	9.85	14.08	17.56	25.66	34.26	9.24
			C	1.41	2.82	5.63	8.45	11.26	16.89	22.52	4.35
0.280	24.0	9.0	A	2.17	3.89	8.13	11.86	14.61	24.21	28.75	8.75
			B	1.87	4.53	10.92	15.37	19.03	30.53	37.33	10.67
			C	1.62	3.24	6.49	9.73	12.98	19.46	25.95	5.00

* A - trajectory method for Poisuelle flow field
B - trajectory method for uniform flow field
C - drift velocity method for uniform flow field
Mean value of drift velocity is evaluated on the basis of number density for a log normal size distribution with d_{50} = 5.0 micron and σ = 2.0.

Average velocity and average plate current density for all determinations are 1.2 m/s (3.94 ft/s) and 0.4 mA/m^2 (0.04 mA/ft^2) respectively.

TABLE 4. AVERAGE DRIFT VELOCITY AS A FUNCTION OF PARTICLE SIZE FOR VARIATION IN b AND c SUCH THAT bc = 20.25, WITH FIXED c

2a in.	2b in.	2c in.	METHOD*	AVERAGE MIGRATION VELOCITY (cm/sec) AS A FUNCTION OF PARTICLE DIAMETER (micron) 2.0	4.0	3.0	12.0	16.0	24.0	32.0	MEAN
0.105	6.0	13.50	A	0.76	2.29	3.84	5.35	7.47	7.21	14.38	3.95
			B	0.87	2.25	4.27	4.37	5.20	6.72	7.09	4.66
			C	0.48	0.95	1.91	2.86	3.82	5.73	7.64	1.37
0.105	9.0	9.0	A	0.89	1.53	3.92	5.91	7.60	9.93	11.21	3.75
			B	0.75	2.31	4.52	6.16	7.37	10.74	14.19	4.61
			C	0.62	1.25	2.50	3.74	4.99	7.49	9.99	1.90
0.105	12.0	6.75	A	1.05	1.92	4.61	6.74	8.57	11.92	15.79	4.47
			B	0.92	2.11	5.89	8.68	11.62	13.85	16.46	5.27
			C	0.79	1.58	3.17	4.75	6.34	9.50	12.67	2.47
0.105	15.0	5.40	A	1.34	2.38	5.26	7.77	9.99	14.49	17.62	5.33
			B	1.12	2.78	6.44	9.49	12.74	17.30	23.83	6.62
			C	0.99	1.98	3.97	5.95	7.93	11.90	15.87	3.08
0.105	18.0	4.50	A	1.67	2.93	6.56	9.97	12.66	17.79	25.31	6.49
			B	1.36	3.51	8.89	12.93	16.56	23.74	32.95	8.10
			C	1.21	2.41	4.83	7.24	9.65	14.48	19.31	3.74
0.105	21.0	3.86	A	1.99	3.32	7.98	11.69	15.65	23.13	30.81	7.60
			B	1.61	4.22	10.72	15.65	20.66	31.58	41.14	9.62
			C	1.42	2.84	5.68	8.51	11.35	17.03	22.70	4.39
0.105	24.0	3.38	A	2.18	3.71	9.41	13.91	18.50	26.63	33.92	8.67
			B	1.74	4.74	12.47	18.67	24.16	35.78	47.28	10.87
			C	1.58	3.17	6.34	9.51	12.68	19.01	25.35	4.91

* A - trajectory method for Poisuelle flow field
B - trajectory method for uniform flow field
C - drift velocity method for uniform flow field
Mean value of drift velocity is evaluated on the basis of number density for a log normal size distribution with d_{50} = 5.0 micron and σ 2.0.

Average velocity and average plate current density for all determinations are 1.2 m/s (3.94 ft/s) and 0.4 mA/m^2 (0.04 mA/ft^2) respectively.

TABLE 5. AVERAGE DRIFT VELOCITY AS A FUNCTION OF PARTICLE SIZE FOR VARIATION IN a, b AND c SUCH THAT b/a = 85.7 AND bc = 20.25

2a in.	2b in.	2c in.	METHOD*	AVERAGE MIGRATION VELOCITY (cm/sec) AS A FUNCTION OF PARTICLE DIAMETER (micron) 2.0	4.0	8.0	12.0	16.0	24.0	32.0	MEAN
0.070	6.0	13.50	A	0.63	1.33	3.33	4.26	4.74	7.30	7.48	2.87
			B	0.58	1.98	3.96	5.54	5.15	10.73	7.78	3.91
			C	0.38	0.77	1.54	2.30	3.07	4.61	6.14	1.20
0.105	9.0	9.00	A	0.89	1.53	3.92	5.91	7.60	9.93	11.21	3.75
			B	0.75	2.31	4.52	6.16	7.37	10.74	14.19	4.61
			C	0.62	1.25	2.50	3.74	4.99	7.49	9.99	1.90
0.140	12.0	6.75	A	1.23	2.19	5.58	8.42	9.66	15.04	19.39	5.18
			B	1.10	3.36	6.62	9.88	10.02	19.66	19.37	6.53
			C	0.96	1.91	3.82	5.73	7.64	11.47	15.29	2.77
0.175	15.0	5.40	A	1.71	3.29	7.60	11.78	14.50	19.70	27.79	7.18
			B	1.76	5.31	9.78	12.25	19.77	25.38	35.30	9.77
			C	1.44	2.88	5.76	8.63	11.51	17.27	23.03	3.87
0.210	18.0	4.50	A	2.59	5.46	11.70	16.35	22.47	32.25	37.74	9.97
			B	2.83	7.40	14.09	20.01	26.01	40.79	51.63	13.73
			C	2.13	4.25	8.50	12.75	17.00	25.51	34.01	5.29
0.245	21.0	3.86	A	3.66	9.14	16.23	22.18	31.35	45.38	56.38	14.27
			B	4.66	12.04	20.22	32.65	41.17	57.97	68.92	17.63
			C	3.05	6.10	12.20	18.31	24.41	36.61	48.82	7.04
0.280	24.0	3.38	A	5.12	12.20	22.56	30.41	40.35	62.95	75.84	18.82
			B	7.30	14.38	28.83	43.94	48.05	80.03	105.70	21.28
			C	4.18	8.36	16.72	25.09	33.45	50.17	66.89	9.01

* A - trajectory method for Poisuelle flow field
B - trajectory method for uniform flow field
C - drift velocity method for uniform flow field
Mean value of drift velocity is evaluated on the basis of number density for a log normal size distribution with d_{50} - 5.0 micron and σ = 2.0.

Average velocity and average plate current density for all determinations are 1.2 m/s (3.94 ft/s) and 0.4 mA/m^2 (0.04 mA/ft^2) respectively.

SIMULTANEOUS MEASUREMENTS OF AERODYNAMIC SIZE AND ELECTRIC CHARGE OF AEROSOL PARTICLES IN REAL TIME ON A SINGLE PARTICLE BASIS

By
M. K. Mazumder, R. G. Renninger, T. H. Chang
R. W. Raible, W. G. Hood, R. E. Ware, and R. A. Sims

Department of Electronics and Instrumentation
University of Arkansas Graduate Institute of Technology
P. O. Box 3017
Little Rock, Arkansas 72203

ABSTRACT

An instrument has been developed for measuring the aerodynamic relaxation time τ_p and electrical mobility Z of aerosol particles in real time and on an individual particle basis in the range from 0.3 to 10.0 μm in diameter. The instrument, an electrical single particle aerodynamic relaxation time (E-SPART) analyzer, employs a laser Doppler velocimeter (LDV) for measuring particle motion in an applied electric field. It operates by electrically charging the particles, subjecting them to an oscillatory electric field and then measuring the amplitude V_p and relative phase lag ϕ of the particles with respect to the electric field. The phase lag ϕ is given by $\tan^{-1}(\omega\tau_p)$ where ω is the frequency of electrical excitation and V_p is related to the particle charge q. A microcomputer-controlled signal processing and data storage system measures both ϕ and V_p, computes d_a and q for individual particles, and stores the data to generate the size and charge distributions of the aerosol particles. The application of this instrument in an electrostatic precipitator is briefly discussed.

INTRODUCTION

Measurement of the charge distribution acquired by the particles inside an electrostatic precipitator may give an insight into the effectiveness of charging as a function of the magnitude and polarity of the electric field, the geometry of the discharge electrode, and the resistivity of the flyash inside the precipitator. Such measurements can also be used as a diagnostic tool for determining the effect of back corona, particle sneakage, and reentrainment. Particle charge is usually measured using the Faraday cage method originally developed by Masters (1) and later modified by a number of researchers (2). Recently McDonald, Anderson, and Mosley (3) reported a method of measuring the charge on individual particles using a Millikan cell. They applied this technique to

measuring the charge on flyash particles in the range 0.3 to 1.5 μm at ambient temperatures ranging from 38°C to 343°C. While producing useful data, this method is inherently slow because it requires the visual observation of individual particles inside the Millikan cell. The method discussed here is capable of measuring a particle's charge and its aerodynamic diameter on a single particle basis and at a rate of 100 particles per second. Similar in principle to a Millikan cell, the method measures the electrical mobility of charged particles in an electric field at 40 kHz to determine the charge and also measures the phase lag to determine the aerodynamic diameter.

PRINCIPLES OF OPERATION

The basic principle for measuring the size as well as the charge on an individual particle basis is similar to that of the single particle aerodynamic relaxation time (SPART) analyzer (4). The SPART analyzer determines aerodynamic diameter by subjecting particles to an acoustic field of known frequency. The oscillatory motion induced on the particle is measured by using a frequency-biased differential laser Doppler velocimeter, LDV, (5). The particle motion lags behind the acoustic excitation because of its inertia, and, consequently, the phase lag ϕ between the particle motion and the acoustic excitation provides a measurement of the aerodynamic diameter of the particle. In the present technique, an electrical excitation replaces the acoustic excitation. Since it is possible to measure both the velocity amplitude and the phase lag of charged particles inside the analyzer, the electrical SPART analyzer (6) is capable of measuring both the electrical mobility Z and the aerodynamic relaxation time τ_p of individual charged particles in real time. From the measured value of τ_p and Z, the aerodynamic diameter d_a and the particle charge q are determined.

Measurement of Electrical Mobility

The equation of motion of an electrically charged particle suspended in air within a uniform AC electric field can be written as

$$\tau_p(dV_p/dt) + V_p = ZE_d \sin \omega t \qquad (1)$$

where τ_p is the aerodynamic relaxation time of the particle, given by

$$\tau_p = \rho_0 d_a^2 C_{ca}/18\eta \ , \qquad (2)$$

where d_a is the aerodynamic diameter, ρ_0 equals 1 gm/cc, C_{ca} represents the

Cunningham correction factor for molecular slip evaluated as a function of d_a, and η is the viscosity of air. In Equation 1, V_p is the particle velocity, E_d is the amplitude of the driving field and ω is the angular frequency of the electric field. The electrical mobility Z is a function of both the charge q and the particle size. For a particle of aerodynamic diameter d_a,

$$Z = qC_{ca}/3\pi\eta d_a \quad . \tag{3}$$

The steady-state solution of Equation 1 can be written as

$$V_p(t) = [ZE_d/(1 + \omega^2\tau_p^2)^{1/2}] \sin(\omega t - \phi) \quad , \tag{4}$$

where

$$\tan \phi = \omega\tau_p \quad .$$

The phase lag ϕ is therefore independent of both the driving field amplitude E_d and the particle charge q. From Equation 2, the amplitude of the particle velocity is given by

$$V_p = ZE_d/(1 + \omega^2\tau_p^2)^{1/2} \tag{5}$$

which depends upon q, E_d, and d_a. All other quantities are known. Since ϕ is measured independently from V_p, it is possible to measure the electrical mobility or the particle charge q by using Equation 5.

Since both the phase lag ϕ and the velocity amplitude V_p are available for each particle, the electrical SPART analyzer can measure the aerodynamic diameter and the electric charge of individual aerosol particles in real time.

EXPERIMENTAL SETUP

Figure 1 shows the relaxation chamber of the electrical SPART analyzer. An aerosol charging device, similar to that described by Langer et al. (5) is currently used for charging the particles so that the size and charge distribution measurements can be performed on particles that initially are electrically neutral. The charging section will be disconnected when the electrical SPART analyzer is used to measure the charge and size distribution of particles that are sampled from inside of

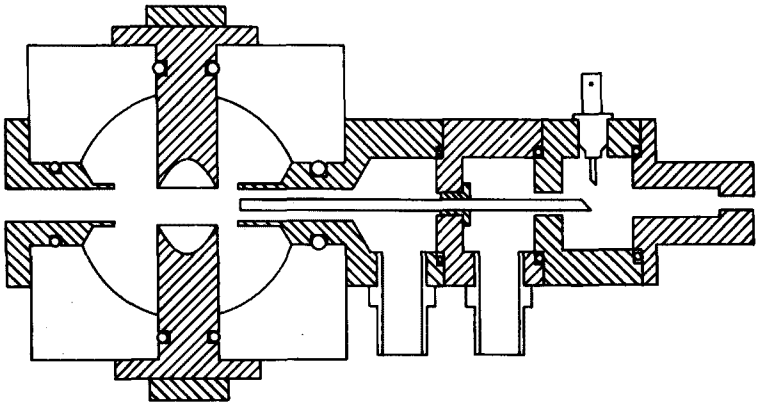

Figure 1. Schematic of the relaxation cell of the E-SPART analyzer for measuring charge and aerodynamic diameter simultaneously.

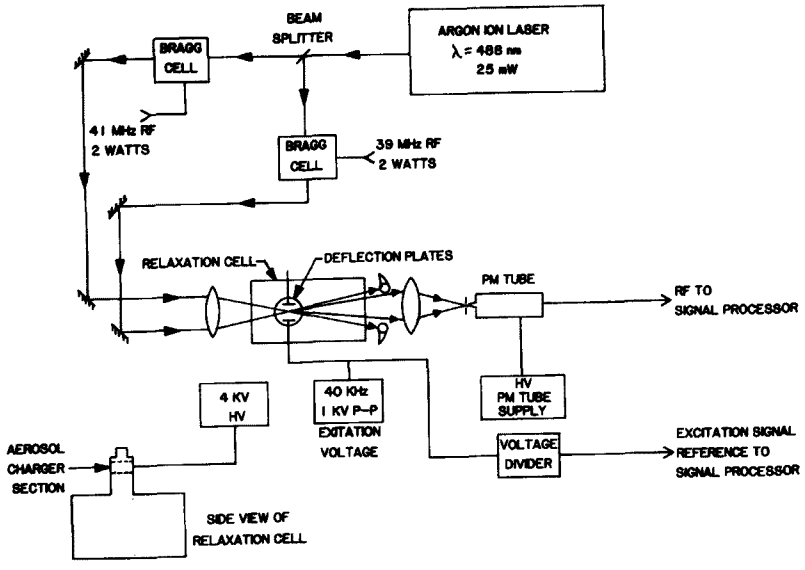

Figure 2. Schematic of the LDV optics and electrical high voltage drive circuits of E-SPART analyzer.

an electrostatic precipitator.

In the charging section, the aerosol is first exposed to a DC corona established at a pointed electrode as shown in Figure 1. The aerosol delivery tube to the relaxation cell is made of copper and serves as the ground electrode. The charger is mounted at the top of the relaxation chamber to minimize particle deposition inside the delivery tube between the charger and the sensing volume of the LDV. The sensing volume is positioned between electrodes across which a high voltage signal (6500 V_{p-p}) at 40 kHz is applied. The two electrodes are positioned symmetrically across the LDV sensing volume. Figure 2 shows a block diagram of the high voltage drive circuits, the laser Doppler velocimeter, and the associated electronics. Figure 3 shows the electronic data processing and the microprocessor based storage and display system.

A signal generator at 40 kHz, an RF power amplifier and a step up transformer provide the high voltage drive input to the electrodes. A voltage divider is used to monitor the applied voltage and to serve as the reference for measuring the relative phase difference between the particle motion and the electrical drive.

As the aerosol sample passes through the charger, the particles acquire an electric charge. The charged particles experience the oscillating electric field while passing through the LDV sensing volume. Light scattered by particles transiting the sensing volume is detected by a photomultiplier tube whose output is connected to the signal processing circuits. These circuits, shown schematically in Figures 2 and 3, recover the phase and amplitude of each particle's induced velocity.

The phase measuring circuit measures the relative phase difference between the particle motion and the electrical drive, and assigns a channel number based on particle size corresponding to one of 128 microcomputer memory locations. During the phase measurement, an analog-to-digital converter (ADC) is used to measure the velocity amplitude of the particle and its output is processed through the microcomputer, which determines the particle charge based on the measurement of V_p and the size information given by channel number.

RESULTS AND DISCUSSION

To determine the size resolution of the electrical SPART analyzer, monodisperse aerosols containing polystyrene latex spheres (PLS) were used as standards. Figure 4 shows the typical size resolution of the instrument, giving the distribution $dN/d(\log d_a)$ of PLS aerosols containing 0.82, 1.09, and 2.02 μm particles. The distributions show that the resolution obtained was similar to that obtained from the acoustic SPART analyzer (4). Figure 5 shows charge distributions measured on PLS particles of different sizes. The experimental results on charge indicate that particle charges were higher for larger particles, but because of the

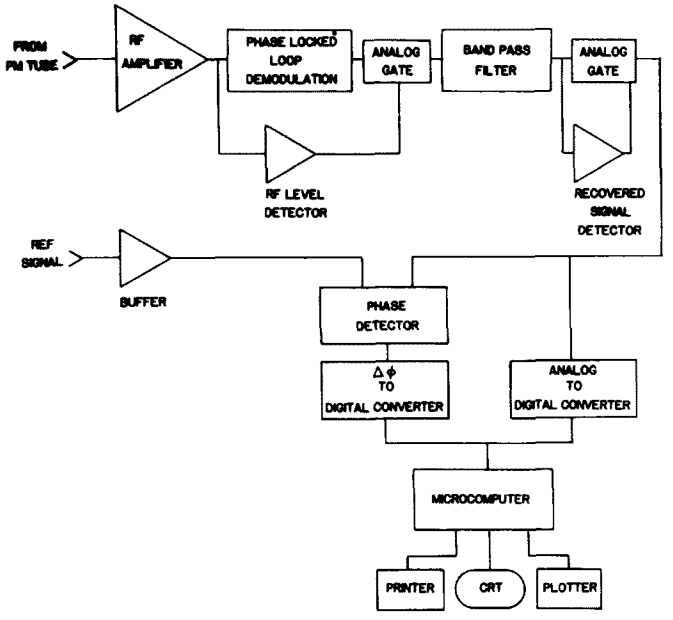

Figure 3. Signal and data processing circuits for E-SPART analyzer.

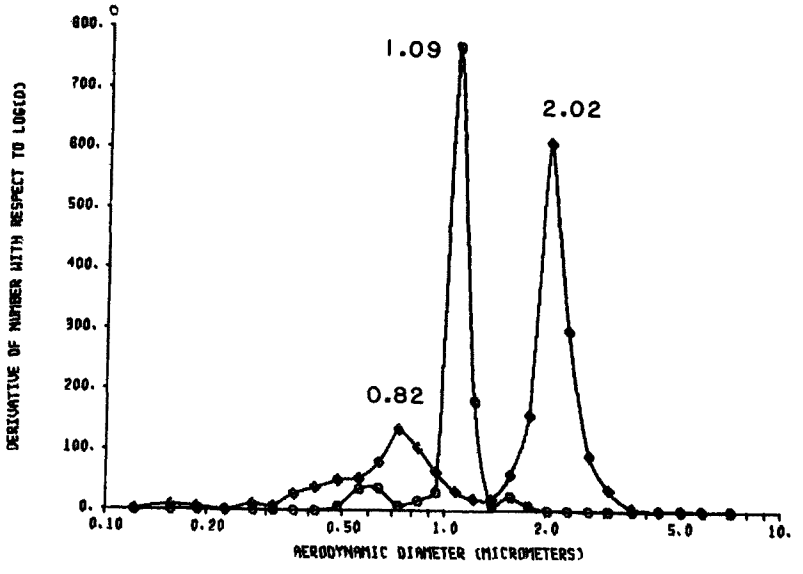

Figure 4. Size distributions of polystyrene latex sphere (PLS) aerosols as measured by the E-SPART analyzer.

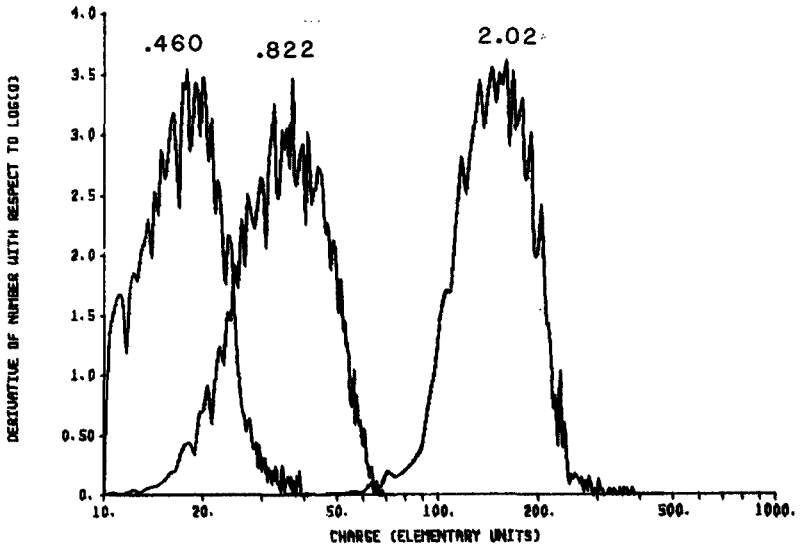

Figure 5. Charge distributions of polystyrene latex sphere (PLS) aerosols as measured by the E-SPART analyzer.

lack of any instrument which could be used to measure the particle charge independently, it was difficult to perform a comparative test. Experiments are now in progress to use a charge analyzer having a Millikan cell similar to the one developed by Gooch et al. for comparative studies.

CONCLUSION

Preliminary test results indicate that the electrical SPART analyzer can be conveniently used for measuring particle charge and size simultaneously in real time. It will also be possible to use the electrical SPART analyzer to determine the fraction of particles of a given size that acquire charge by noting the number of particles that pass through the sensing volume without any oscillatory motion.

ACKNOWLEDGEMENT

The authors thank J. D. Wilson, K. Kalb, and R. Chen for their technical assistance and constructive criticism, and P. Roberson, M. Elms, D. Watson, and P. T. Archer for their assistance in preparing the manuscript. This work has been supported by the U. S. Environmental Protection Agency under Grant No. R806192.

ENDNOTES

1. Masters, J. I. An Aerosol Analyzer. Rev. of Sci. Instrum. 24:586-588, 1953.

2. Langer, G., J. Pierrard, and G. Yamak. Further Development of An Electrostatic Classifier for Submicron Airborne Particles. Int. J. Air Wat. Poll. 8:167-176, 1964.

3. McDonald, J. R., M. H. Anderson, and R. B. Mosley. Charge Measurements of Particles Exiting Electrostatic Precipitators. EPA 600/7-80-077, 1980.

4. Mazumder, M. K., R. E. Ware, J. D. Wilson, R. G. Renninger, F. C. Hiller, P. C. McLeod, R. W. Raible, and M. K. Testerman. SPART Analyzer: Its Application to Aerodynamic Size Distribution Measurement. J. Aerosol Sci. 10:561-569, 1979.

5. Mazumder, M. K. Laser Doppler Velocity Measurement Without Directional Ambiguity by Using Frequency Shifted Incident Beams. Appl. Phys. Letts. 16:462, 1970.

6. Renninger, R. G., M. K. Mazumder, and M. K. Testerman. Particle Sizing by Electrical Single Particle Aerodynamic Relaxation Time Analyzer. Rev. Sci. Instrum. In press.

APPLICATION OF LASER DOPPLER INSTRUMENTATION TO PARTICLE TRANSPORT MEASUREMENTS IN AN ELECTROSTATIC PRECIPITATOR

By
M. K. Mazumder, W. T. Clark III, R. E. Ware
P. C. McLeod, W. G. Hood, J. E. Straub, and S. Wanchoo

Department of Electronics and Instrumentation
University of Arkansas Graduate Institute of Technology
P. O. Box 3017
Little Rock, Arkansas 72203

ABSTRACT

The two-color frequency biased laser Doppler velocimeter (LDV) and the single particle aerodynamic relaxation time (SPART) analyzer are two laser based instruments. Their development and application to electrostatic precipitators are briefly discussed. The LDV is designed to provide simultaneous measurements of two orthogonal velocity components: one along the flow direction and the other along the electric field direction. The instrument is mounted on a three-dimensional traversing stage which permits measurements of flyash trajectories at any desired point inside the precipitator. The SPART analyzer has been developed for measuring, in real time, the aerodynamic size distribution of aerosol particulates in the respirable range 0.3 to 10.0 μm in diameter. The instrument is capable of measuring and storing the size distributions of aerosols sampled from the two ends of the precipitator and computing the fractional efficiency as a function of particle size. Experiments are in progress on the measurements of particle trajectories and penetration inside a flow model precipitator. The preliminary experimental data are presented.

INTRODUCTION

Recently there has been considerable interest in understanding the particle transport properties, particularly the role of turbulence, that affect particle migration velocity inside an electrostatic precipitator (1,2). Both mathematical modeling and experimental observations are needed to understand the complex interaction of the Coulomb force on the particle, the turbulent diffusion, and the electric wind that govern the particle motion. Experimental studies on the particle transport and fluid flow properties are difficult to perform because ambient conditions inside the precipitator prohibit conventional instruments, such as the hot wire anemometer, to be placed inside the precipitator. The high voltage applied to the discharge electrodes, the high electrical field, and the high

particulate concentration inside the precipitator are not conducive to placing any physical probe in the precipitator for studying the flow properties. The laser Doppler velocimeter (LDV) overcomes most of the difficulties associated with making particle transport studies inside the precipitator. The LDV can measure the localized particle velocity at any given point inside the precipitator; however, such measurements may not yield the properties of fluid flow since the electrical field acting on the charged particle deviates the particle motion considerably from the flow of fluid. The objective of this project was to develop a two-dimensional LDV and particle seeding techniques for measuring: a) electrical migration velocity components, b) turbulence, and c) electrical wind inside a precipitator.

By sampling aerosol from both upstream and downstream of the precipitator, a single aerodynamic relaxation time (SPART) analyzer was used to measure in real time the fractional efficiency of an electrostatic precipitator. A brief discussion of the experimental design and preliminary data are presented.

EXPERIMENTAL SETUP

Experiments are being carried out using a flow model electrostatic precipitator designed and built in such a manner that the particle transport and turbulence properties can be studied along the entire length of the precipitator using a two-dimensional LDV. The experimental arrangement consists of the precipitator, the LDV mounted on a traversing stage, an aerosol generator for seeding the precipitator, and a SPART analyzer for measuring the fractional efficiency.

Flow Model Electrostatic Precipitator

A laboratory model electrostatic precipitator (Figure 1) made of Plexiglas was used with the following dimensions: 46 cm in height, 2.7 m in length with wire-to-distance variable from five to 13 cm and a wire-to-wire spacing of 15 m. The collection electrodes were made of six mm-thick plates of NESA glass which had a conductive coating for electrical connection but were transparent, thus permitting optical probing with an LDV. The mean velocity inside the precipitator was adjusted to approximately two m/sec with the free stream turbulence intensity approximately three percent. The high voltage applied to the discharge electrodes, with wire diameter of 0.25 cm, could be varied from zero to -50kV. The applied high voltage and the corona current collected by each plate were measured (Figure 2).

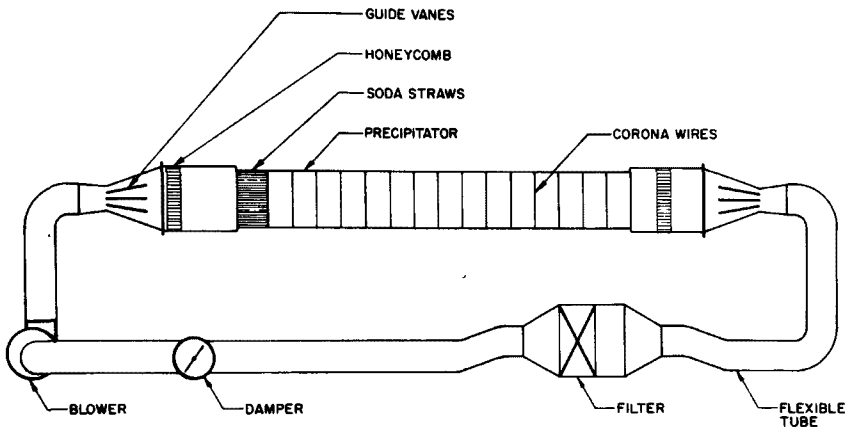

Figure 1. Schematic diagram of the laboratory model electrostatic precipitator.

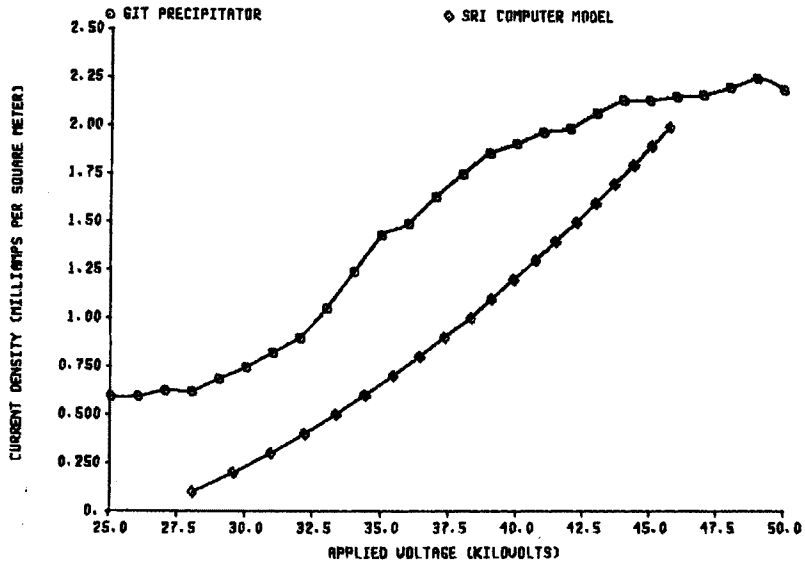

Figure 2. Experimentally determined V-I curve of the flow model precipitator compared with the computed results from SRI mathematical model.

Laser Doppler Velocimeter

An LDV (Figure 3) for measuring two-dimensional velocity components is used to measure the velocity distribution along the flow direction (x-axis) and the direction of electrical migration velocity (y-axis) of the particles. The transmission optics of the LDV contain two dual-beam, frequency-biased (3) LDV's with their optical axes at $\pm 45^0$ to the y-axis. The receiving optics consist of two light-collection and detection optical systems that are mounted on a platform opposite the transmission optics. This arrangement allows the forward scattered light to be collected by the receiving optics. A three-dimensional translational stage is used for mounting the LDV transmission and receiving optics; the stage also facilitates velocity mapping in the x-y-z-directions.

The optical system is designed for two-color, two-dimensional, simultaneous velocity measurement on a given particle. The system currently is used with only one color (514.5 nm) while velocity measurements are performed at $+45^0$ and then at -45^o sequentially. The experimental data are then processed to determine the x-y velocity components on a statistical basis (4). The measurement process requires the use of monodisperse aerosols with no alteration of process variables between two successive measurements.

Aerosol Generators

Currently two aerosol generators are used to seed the flow model precipitator. One, a Rapaport-Weinstock aerosol generator, produces bis (2-3,ethyl hexyl) sebacate (BES) aerosol in the size range 0.1 to 1.0 μm in aerodynamic diameter by a vaporization-condensation process. The second is a Wright Dust Feed mechanism which is used to generate flyash and talcum powder aerosol in the size range 0.5 to 5.0 μm in aerodynamic diameter.

SPART Analyzer

The SPART analyzer determines the aerodynamic diameter (d_a) by measuring the relaxation time (τ_p) of individual particles and droplets in real time. The aerodynamic diameter is defined as the diameter of a unit density sphere having the same aerodynamic properties as the particle in question. The aerodynamic diameter takes into account the size, shape, density, and surface properties that effect the behavior of a particle in air. The principle of operation and the description of the SPART analyzer (5) were previously discussed.

The performance of the SPART analyzer can be summarized as follows: The dynmamic size range of particles measured by the analyzer is currently

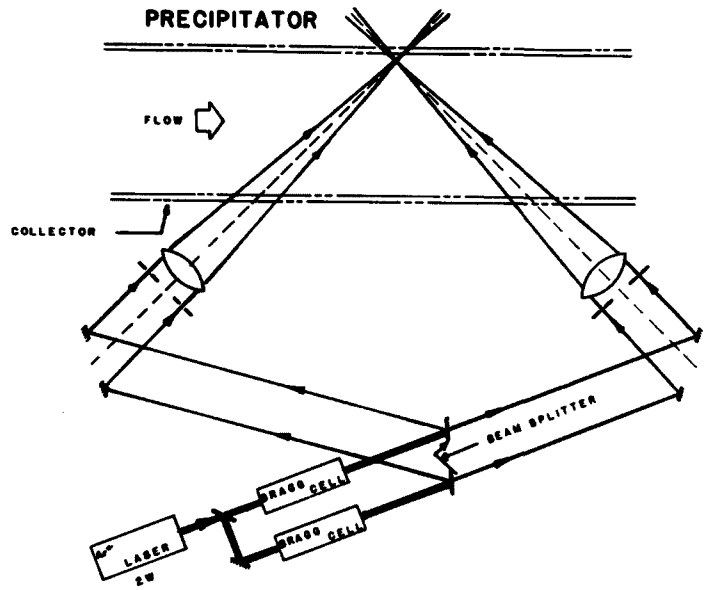

Figure 3. Schematic of the LDV transmission optics for measuring two-dimensional velocity components.

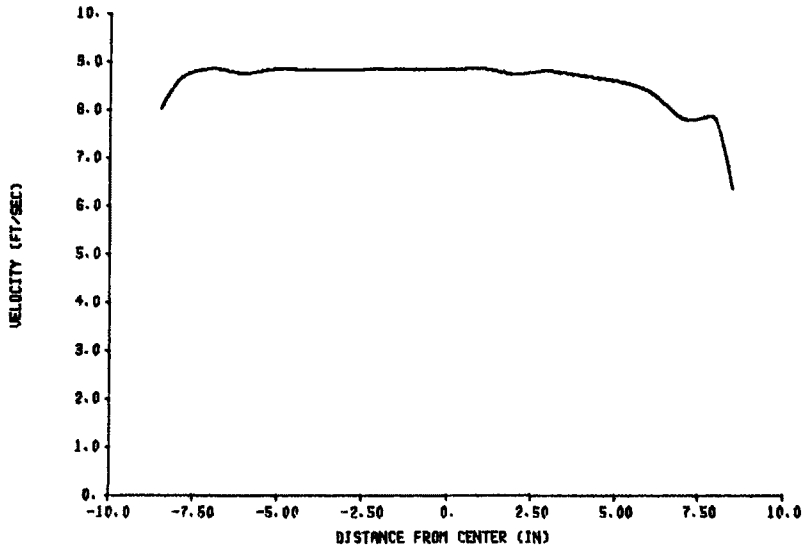

Figure 4. Velocity profile inside the flow model precipitator as measured by a hot wire anemometer.

0.3 to 5.0 μm in aerodynamic diameter measured in 119 channels or in 30 channels. The resolution of this instrument is dependent upon the frequency of acoustic excitation. The current instrument, operated at a frequency of 23 kH, has a maximum resolution in the range 0.5 to 2.0 μm. The sensing volume of the instrument is approximately 5×10^{-6} cc. The instrument samples at a rate of 200 cc per minute. The highest count rate is approximately 400 counts per second, although in actual measurements the count rate is never allowed to exceed 100 particles per cc in order to reduce the coincidence error below five percent. The maximum number of counts in any channel is approximately 1,000,000. The instrument can store two size distributions, such as one for aerosol at the upstream and the other for aerosol at the downstream of the precipitator. It can operate in automatic or in manual modes. Data from the SPART analyzer can be obtained on a line printer or on punched paper tape in the following format:

1) the total time in seconds during which the aerosol has been sampled,
2) the channel number,
3) the diameter in micrometers,
4) the total number of counts in that channel,
5) $dN/d(\log d_a)$, and
6) $dV/d(\log d_a)$.

Items 2 through 4 are repeated for all channels. The output of the analyzer is connected to a microcomputer which reads the data directly from the microprocessor memory and computes 1) the count median aerodynamic diameter (CMAD), 2) the mass median aerodynamic (MMAD), 3) the standard deviation (σ_g), and mass concentration in $\mu g/m^3$. The microcomputer is programmed to compute the fractional efficiency of the precipitator using the size distributions of the aerosol present at the upstream and the downstream of the precipitator.

RESULTS AND DISCUSSION

Velocity Profile

Only preliminary experimental data are presented here. Figure 4 shows a typical high velocity profile that was measured with a hot wire anemometer across the precipitator. No high voltage was applied and the precipitator was not seeded with aerosols. The velocity profile was mapped at different values of x from the inlet of the precipitator and it was found to be fairly uniform.

Migration Velocity

Measurement of migration velocity is currently performed on aerosol particles inside the precipitator while the mean velocity of air along the x-axis is maintained at or near zero. In this experiment, the precipitator

is seeded locally with a line source of aerosol placed at an upstream point with respect to the point of measurement and close to a discharge wire. The blower, used to maintain the air flow through the precipitator, is turned off during this experiment. The aerosol particles, after injection inside the precipitator, acquire charge in the electrical field and migrate immediately in the direction of the wall. Effective velocity is determined by the electrical migration velocity and by the electrical wind. The velocity components in the x and y directions are measured at several points. Figure 5 shows a map of velocity measurements at a given applied voltage. Figure 6 shows the change of velocity at four given points as a function of applied voltage. It is of interest to note that there is a velocity (w_y) reversal in Figures 6 and 7 which suggests a strong effect from the electric wind inside the precipitator.

Measurement of Aerodynamic Size Distribution and Fractional Efficiency

The aerodynamic size distribution measurements of the test aerosols used in the precipitator were performed with the SPART analyzer. For measuring the fractional efficiency of the precipitator, a polydisperse aerosol in the size range 0.5 to 5.0 μm was used and the size distributions at the upstream and downstream were measured. The calculated fractional efficiency is shown in Figure 8. Since the measurements are made in real time, it is possible to determine the fractional efficiency as functions of high voltages applied to the discharge electrodes and the physical characteristics of test aerosols.

CONCLUSION

Preliminary experimental data indicate the feasibility of applying the LDV based techniques to measuring particle transport inside the precipitator and to measuring the fractional efficiency of the precipitator in real time. It appears possible that such measurements could yield data which may augment the recently developed mathematical models incorporating turbulent diffusion.

ACKNOWLEDGEMENT

The authors wish to thank R. W. Raible, R. L. Bond and R. A. Sims for their technical contributions in the project; P. Roberson, M. Elms, P. T. Archer, and D. Watson for editorial assistance. The authors appreciate the valuable guidance and several comments received during the entire phase of this work from L. E. Sparks, Project Monitor. This work was supported by EPA Grant R806192.

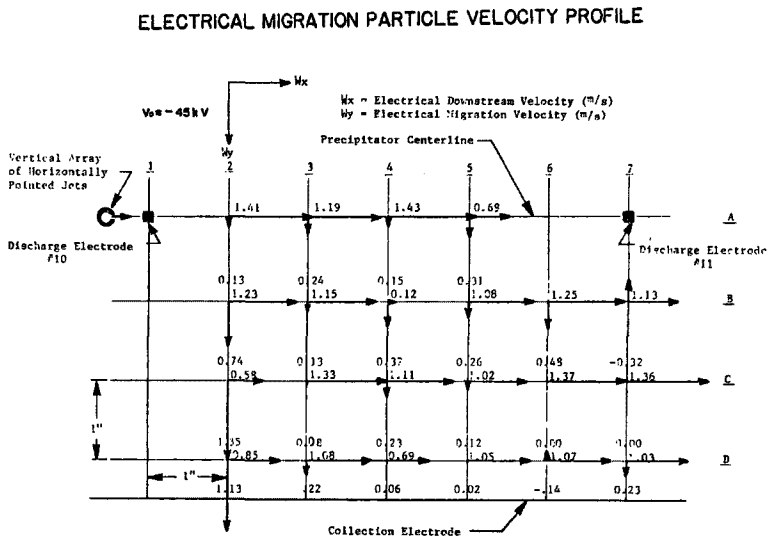

Figure 5. Two-dimensional migration velocity components (W_x and W_y) measured at 2.5cm x 2.5cm grids inside the precipitator.

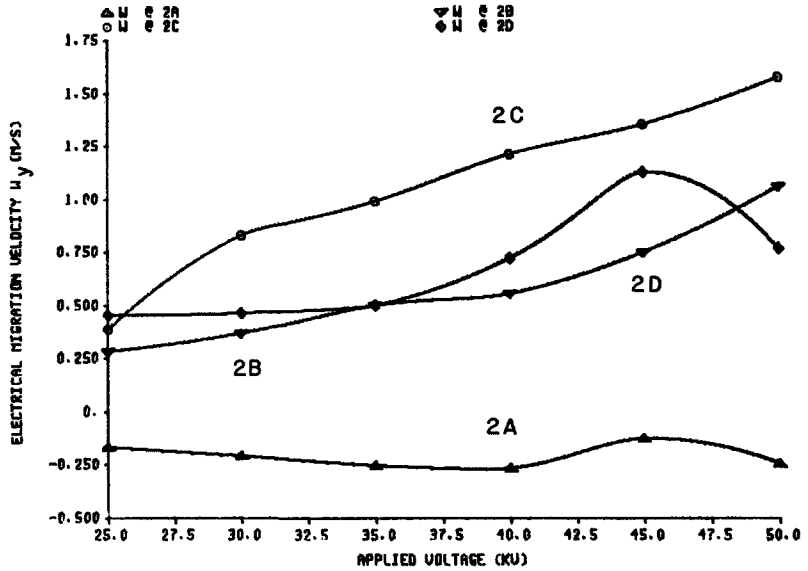

Figure 6. Variation of W_y with applied voltage measured at different points (see Figure 5) inside the precipitator.

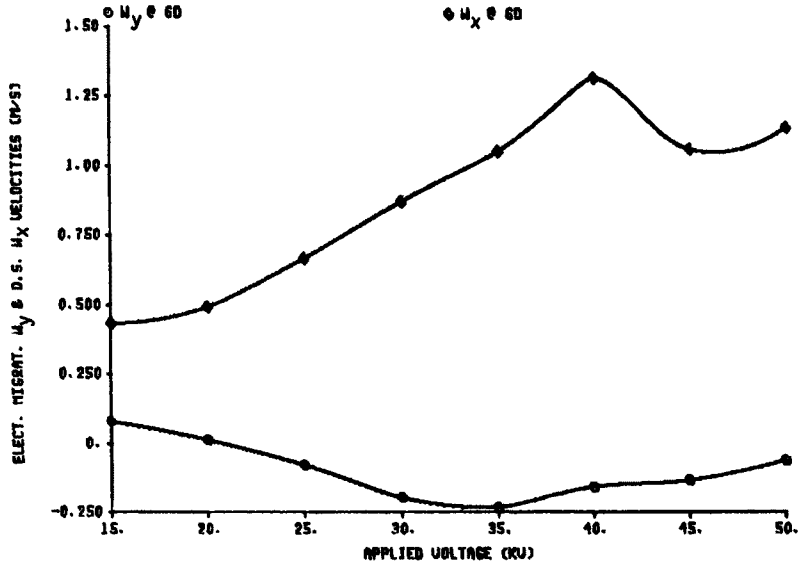

Figure 7. Variation of W_x and W_y with applied voltage. W_y was negative (particles moving away from the wall) at the point 6D (see Figure 5).

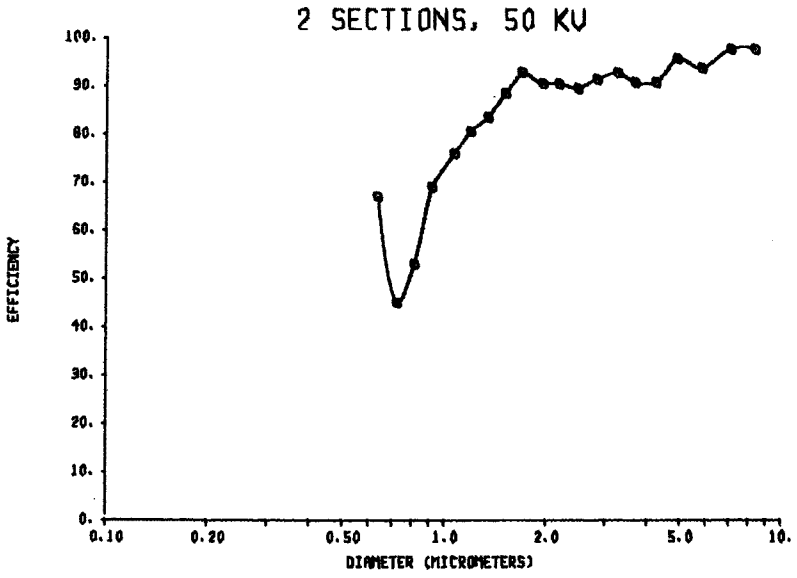

Figure 8. Fractional efficiency of the flow model precipitator as measured by the SPART analyzer.

ENDNOTES

1. Robinson, M. Turbulence in Electrostatic Precipitators. Minerals Processing. 9:13, 1968.

2. Leonard, G., M. Mitchner, and S. A. Self. Particle Transport in Electrostatic Precipitators. Atmospheric Environment. 14:1289, 1980.

3. Mazumder, M. K. Laser Doppler Velocity Measurement Without Directional Ambiguity by Using Frequency Shifted Incident Beams. Appl. Phys. Letts. 16:462, 1970.

4. Johnson, D. A. and W. C. Rose. Measurement of Turbulent Transport Properties in a Supersonic Boundary-Layer Flow Using Laser Velocimeter and Hot Wire Anemometer Techniques. AIAA Paper 73-1045, 1973.

5. Mazumder, M. K. and K. J. Kirsch. Single Particle Aerodynamic Relaxation Time Analyzer. Rev. Sci. Instrum. 48:622, 1977.

THE APPLICATION OF MEASUREMENTS OF AEROSOL CHARGE ACQUISITION BY BIPOLAR IONS TO THE PROBLEM OF BACK CORONA

By: R.A. Fjeld
Environmental Systems Engineering
Clemson University
Clemson, SC 29631

R.O. Gauntt, G.J. Laughlin, A.R. McFarland
Air Quality Laboratory
Texas A&M University
College Station, TX 77843

ABSTRACT

Measurements relevant to the impact of bipolar ions on particle charge acquisition are presented. Experiments were conducted to determine charge acquisition by aerosols exposed simultaneously to positive and negative ions of unequal current densities. Initially uncharged, highly monodisperse aerosols in the micrometer to submicrometer diameter size range were subjected to counter currents of positive and negative ions in the presence of an electric field. Measured charge is found to be significantly larger than that calculated by classical bipolar field charging theory. Substantial charge degradation can occur under bipolar conditions, but the extent of degradation exhibits a strong time dependence. The time behavior could be an important factor in assessments of the effect of back corona on charge levels in electrostatic precipitation.

INTRODUCTION

Back corona occurs in electrostatic precipitators when a large voltage drop develops across the dust layer on the collecting electrode. The voltage drop is due to highly resistive particles or high ionic current densities, and it causes dielectric breakdown in the dust. A counter current of ions of opposite polarity results, transforming the formerly unipolar charging region to a bipolar region. A reduced voltage drop across the inter-electrode region accompanies the change in charging currents. Lowered particle charge levels and depressed electric fields which result from these changes in electrical conditions cause precipitator collection efficiency to decrease (1).

A thorough understanding of back corona and its impact on precipitator performance thus requires knowledge of the electrical conditions (electric field strength, ionic current densities) which exist and the fundamental processes which occur. These processes include dielectric breakdown and ion generation, ion transport to the charging region, and particle charge acquisition in the presence of bipolar ions. Pioneering work was conducted in some of these areas by Pauthenier, Penney, Cooperman and White. Present day efforts, motivated in large part by the relatively recent trend toward low sulfur coal and the high resistivity ash accompanying its combustion, are building on the foundations provided by the early studies.

Bipolar charge acquisition and its role in precipitators experiencing back corona was first examined by Pauthenier in the 1950's. In this present paper the results of recent experimental measurements on charge acquisition by aerosols exposed to positive and negative ions of unequal current densities are presented and compared to calculations based on field charging theory. These charging data, in combination with recent measurements of ionic current densities in back corona, are then utilized to infer the potential impact of back corona on particle charge levels.

THEORY

The bipolar field charging theory of Pauthenier (2) is identical to classical unipolar field charging, with the exception that the transport of ions of opposite polarity to the back side of the particle is also considered. The mean charging rate is calculated as the difference between the rates at which ions of opposite polarity collide with the particle. When the two rates equalize, net charge acquisition ceases; and the particle maintains a steady state charge level given by

$$n_{ss}=n_{sat}[(\sqrt{\gamma}-1)/(\sqrt{\gamma}+1)], \quad (1)$$

where n_{ss} is the steady state charge level, γ is the ion current density ratio, and n_{sat} is the unipolar saturation charge. This latter quantity is given by

$$n_{sat}=(\pi\varepsilon_o D_p^2/q_e)[3K/(K+2)]E; \quad (2)$$

where D_p is the particle diameter (m), ε_o is the permittivity (8.85×10^{-12} coul^2/j.m), q_e is the elementary charge unit (1.6×10^{-19} coul), K is the particle dielectric constant, and E is the electric field strength (V/m). In field theory it is assumed that diffusional transport of ions is negligible and that the predominant mechanism for charge acquisition is ion drift along electric field lines.

The bipolar field charging equations have been used to predict charge levels under back corona conditions, but the theory has not been thoroughly tested experimentally. Measurements (3,4,5) on large particles (D_p>20μm) lend support for the calculations, but are limited in scope and do not provide unqualified experimental verification. Experimentally measured charge on submicrometer diameter particles in low fields is substantially higher than that predicted by the Pauthenier theory; the failure of the Pauthenier theory being attributed to its neglect of ionic diffusion (6). This observation is consistent with unipolar comparisons (7), where it is found that field theory yields charge levels significantly lower than experimental measurements. This is especially true for particles of micrometer size and smaller. Thus, there is some question as to the applicability of Pauthenier's theory to the prediction of charge acquisition during back corona.

EXPERIMENT

An experimental program has been established to provide a data base on

bipolar charge acquisition (8). Initially uncharged, monodisperse aerosols in the micrometer and submicrometer diameter size range are exposed to counter currents of positive and negative ions in the presence of an external electric field. Control variables are particle size (D_p), electric field strength (E), ion current density ratio (γ), and μNt product; where N is the ion density of the dominant ion species, μ is ionic mobility and t is charging time.

The experimental apparatus (Figure 1) includes an aerosol generator for polystyrene latex spheres, a bipolar charger, and a particle charge analyzer. The aerosol generator is comprised of an air blast atomizer and ^{85}Kr charge neutralizer. The charger consists of three regions (A,B, and C) bounded by parallel plate electrodes. The outer plates (1 and 4) contain radioactive sources (^{241}Am) which emit alpha particles into regions A and C. Ions generated in these regions by the radiation are driven by applied electric fields to electrodes 2 and 3, where a fraction penetrate wire screens and enter the charging region, B. For the electrode polarities indicated in Figure 1, positive ions enter the charging region through electrode 2 and negative ions enter through electrode 3. The potential to electrode 3 is applied in the form of a square wave. During the first half cycle particles are exposed to the ions and may experience lateral movement in the applied field. During the second half cycle the field in the charging region is reversed, preventing ions from entering the region and reversing the lateral direction of particle travel. This prevents particle migration to an electrode. Charging conditions, ie. ionic current densities and charging fields, are chosen such that space charge perturbations of the applied field and recombination are small.

Particles extracted from the charger are routed to an integral mobility analyzer. Those which pass through the analyzer are counted by an optical particle counter, and mean charge is determined by integral mobility analysis (9).

In the results presented below positive ions are dominant; that is, positive ionic current densities are greater than negative current densities. Tests were also conducted with the negative ions dominant and, within the limits of experimental error, the absolute value of charge was found to be independent of the dominant species. Thus, the results should apply equally well to either case.

RESULTS

Data presented in Figure 2 illustrate the effect of particle size and ion current density ratio on charge. In this case the electric field strength is 50KV/m and the μNt product is 1.9×10^9/Vm. A current density ratio of infinity corresponds to unipolar conditions. For particles of a given size, it is seen that charge levels are reduced as the current density ratio decreases. For a given current density ratio, charge increases with increasing particle size.

Comparisons of the data with classical field charging theory (Figure 3) show the measured charge to be significantly higher than that predicted by theory. These data are for 1.09μm diameter particles with $\mu Nt = 6.3 \times 10^8$/Vm,

γ=10 and electric fields ranging from 25 KV/m to 300 KV/m. An interesting aspect of this figure is that it reveals the experimental and theoretical slopes to compare favorably, yielding an approximately constant difference of 25 to 30 charges. If the charge level calculated from continuum diffusion theory (approximately 21 for this case) is added to the charge calculated from field charging theory, the result is only about 20 per cent less than the experimental measurement. For other ratios this calculation yields even better results, being well within experimental uncertainty for γ=3 and γ=100, and approximately ten per cent less than experiment for the unipolar case. This empirical practice of summing charge obtained from independent field theory and diffusion theory calculations has been found to compare reasonably well with unipolar measurements also (7), although in the above referenced comparison White's theory was utilized rather than the continuum model used in the present calculations.

In Figure 4 the ratio of bipolar charge to unipolar charge has been plotted as a function of μNt. This ratio is an indicator of the impact of bipolar ions on charge levels. The curve was obtained by plotting time dependent data for various bipolar ratios and for the unipolar case, graphically fitting a smooth curve to the data and computing ratios based on the curves. It is seen here that the fractional bipolar charge decreases with time. This decrease occurs because unipolar charge continues to increase in time while the bipolar charge reaches a constant steady state level. These curves illustrate that time dependent behavior is an important consideration in assessing the degradation of charge under bipolar conditions.

To determine the impact of back corona on charge levels it is necessary to know the initial charge state, the electrical conditions (ion current density ratio and electric field strength), and, as evident from Figure 4, the μNt product. Such data are not generally available, although a mathematical model of electrical conditions in wire-duct precipitators is being developed (10), and measurements of ion currents under simulated back corona have recently been reported (11, 12). The data of Masuda *et al* (12) may be utilized to make a preliminary assessment of charging in precipitators experiencing back corona. They report a current density ratio of approximately three for what is termed severe back corona. Using the data in Figure 4 it is seen that a neutral particle entering a uniform region of back corona with γ=3 would acquire about 60 per cent of the charge it would have acquired under unipolar conditions for μNt = 5 x 10^7/Vm and 15 per cent for μNt = 5 x 10^9/Vm. For γ=10, the corresponding percentages are approximately 95 per cent and 40 per cent, respectively. In these estimates of charge degradation the charging field is assumed to be the same for unipolar and bipolar conditions. If the field were depressed due to large voltage drop across the dust layer, the charge degradation would be substantially greater.

For the case of localized back corona, the above calculation would obviously not be appropriate. In such a situation a highly charged particle might move from a unipolar, high field region to one characterized by a reduced field and bipolar ions. Assessing charge degradation under these concitions is not possible with the data presented here.

SUMMARY

Measurements relevant to the impact of bipolar ions on particle charge acquisition have been presented. Measured charge levels are significantly larger than those predicted by classical bipolar field charging theory. However, the empirical practice of adding the charge obtained by field theory to that obtained by diffusion theory yields a good estimate of the measured charge, at least for 1.09 μm diameter polystyrene.

Substantial charge degradation can occur in bipolar regions, especially for ionic current density ratios less than ten; but the extent of degradation exhibits a strong time dependence. This time behavior could be significant in assessing the effect of back corona on unipolar charge levels.

ACKNOWLEDGEMENT

This material is based upon work supported by The National Science Foundation under Grant ENG-77-01130.

ENDNOTES

1. White, H.J. "Resistivity Problems in Electrostatic Precipitation." J. Air Pollut. Contr. Assoc. 24, 314 (1974).

2. Pauthenier, M., R. Cochet, and J. Dupuy, "Probléme Général de la Charge Acquise par une Particule Sphérique dans en Champ Electritrique Bi-ionisé," C.R. Acad. Sci. Paris 243, 1606 (1956).

3. Phillips, B.B. and R. Gunn, "Measurements of the Electrification of Spheres by Moving Ionized Air," J. Meteorol. 11, 348 (1954).

4. Gunn, R., "The Hyperelectrification of Raindrops by Atmospheric Electric Fields," J. Meteorol. 13, 283 (1956).

5. Fjeld, R.A., R.J. Heinsohn and S.H. Levine, "Nonequilibrium Bipolar Charging of Aerosol Particles: Theory and Experiment," J. Colloid Interface Sci. 62, 69 (1977).

6. Fjeld, R.A., R.O. Gauntt, G.J. Laughlin and A.R. McFarland, "Measurement of the Charge on Submicrometer Aerosol Exposed to Bipolar Ions," Conf. Rec. IEEE 1980 Annu. Meet. Ind. Appl. Soc., 1063 (1980).

7. Smith, W.B., L.G. Felix, D.H. Hussey, D.H. Pontius and L.E. Sparks, "Experimental Investigations of Fine Particle Charging By Unipolar Ions," J. Aerosol Sci. 9, 101 (1977).

8. Fjeld, R.A., R.O. Gauntt and A.R. McFarland, "Aerosol Charging By Bipolar Ions of Unequal Current Densities: Experiments in Low Electric Fields," accepted for publication by J. Colloid Interface Sci.

9. Gauntt, R.O., R.A. Fjeld and A.R. McFarland, "Characterization of Aerosol Mobility Distributions by Integral Mobility Analysis-The Method of Mobility Moments," J. Aerosol Sci. 12 (1981).

10. Lawless, P.A. and L.E. Sparks, "A Mathematical Model for Calculating Effects of Back Corona in Wire-duct Electrostatic Precipitators," J. Appl. Phys. 51, 242 (1979).

11. McKay, R.B. and I.I. Inculet, "Bi-ionized Space Charges Generated by Means of Corona," Conf. Rec. IEEE 1977 Annu. Meet. Ind. Appl. Soc., 717 (1977).

12. Masuda, S. and Y. Nonogaki, "Detection of Back Discharge in Electrostatic Precipitators," Conf. Rec. IEEE 1980 Annu. Meet. Ind. Appl. Soc., 912 (1980).

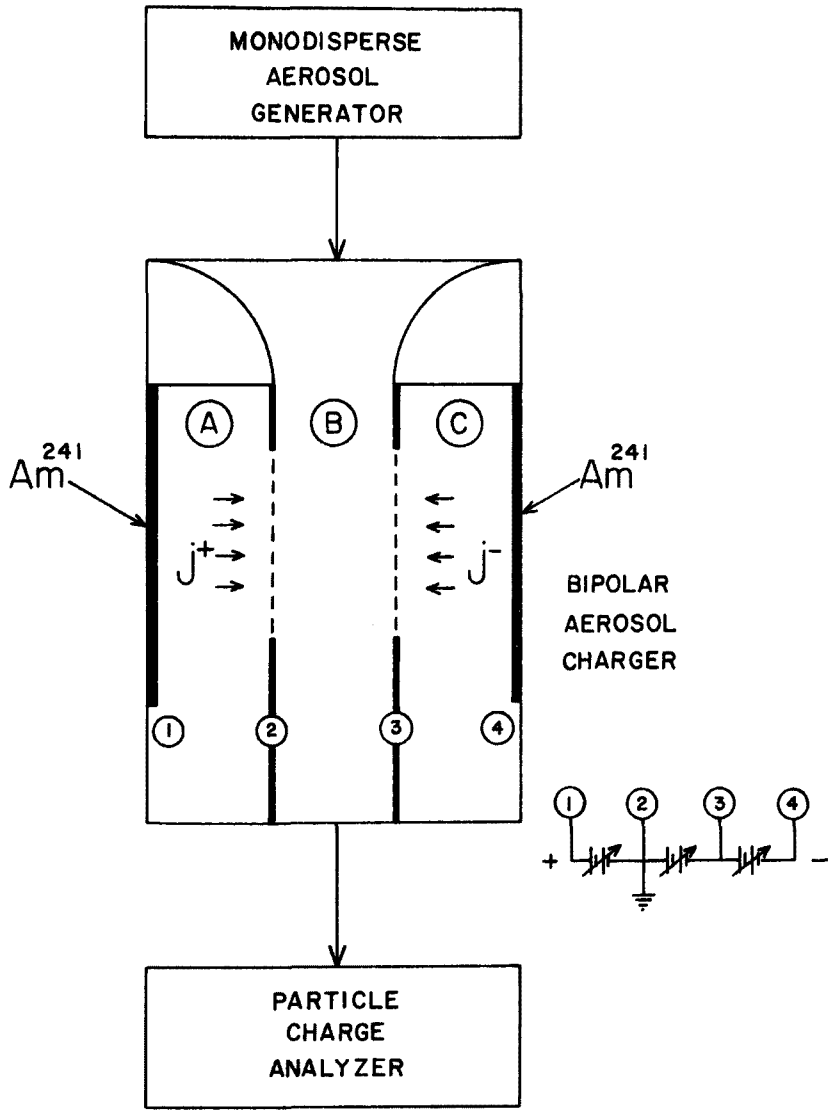

Figure 1: Schematic of the experimental apparatus (6).

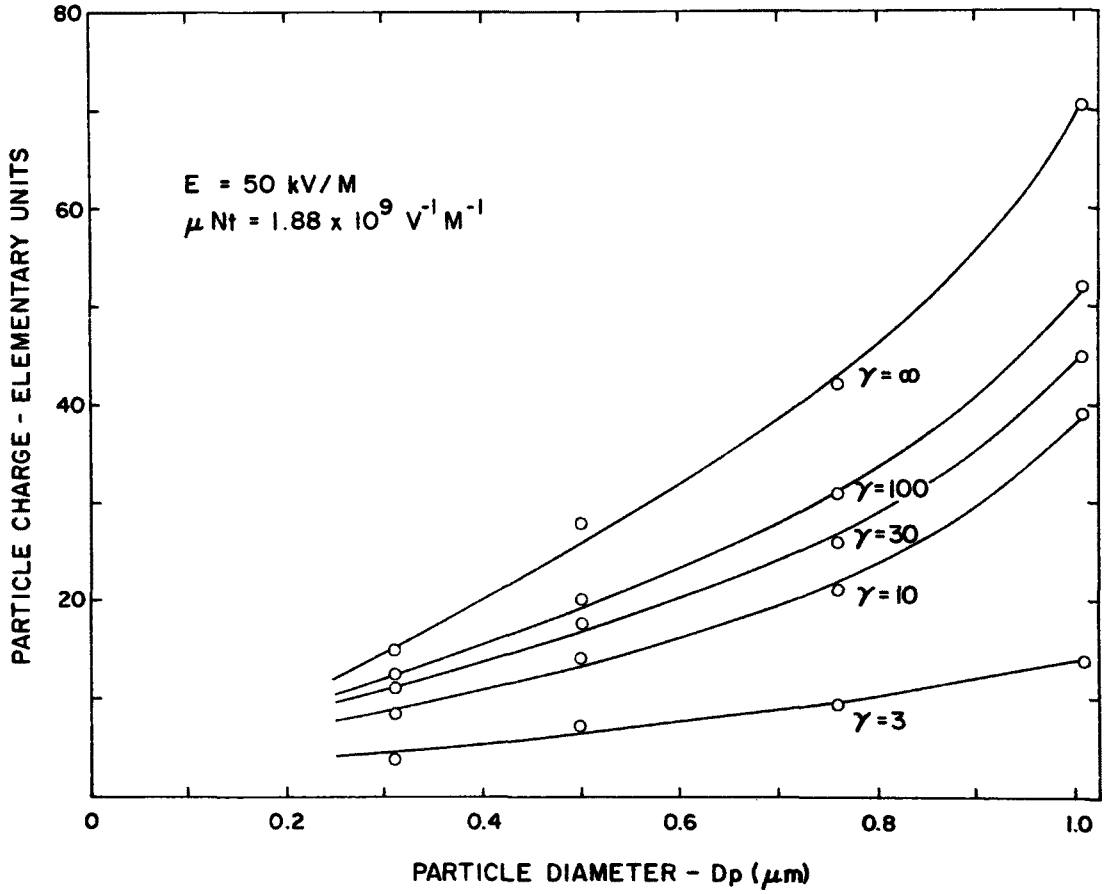

Figure 2: Measured charge as a function of particle diameter for various current density ratios. E = 50 KV/m and μNt = 1.9 x 10^9/Vm.

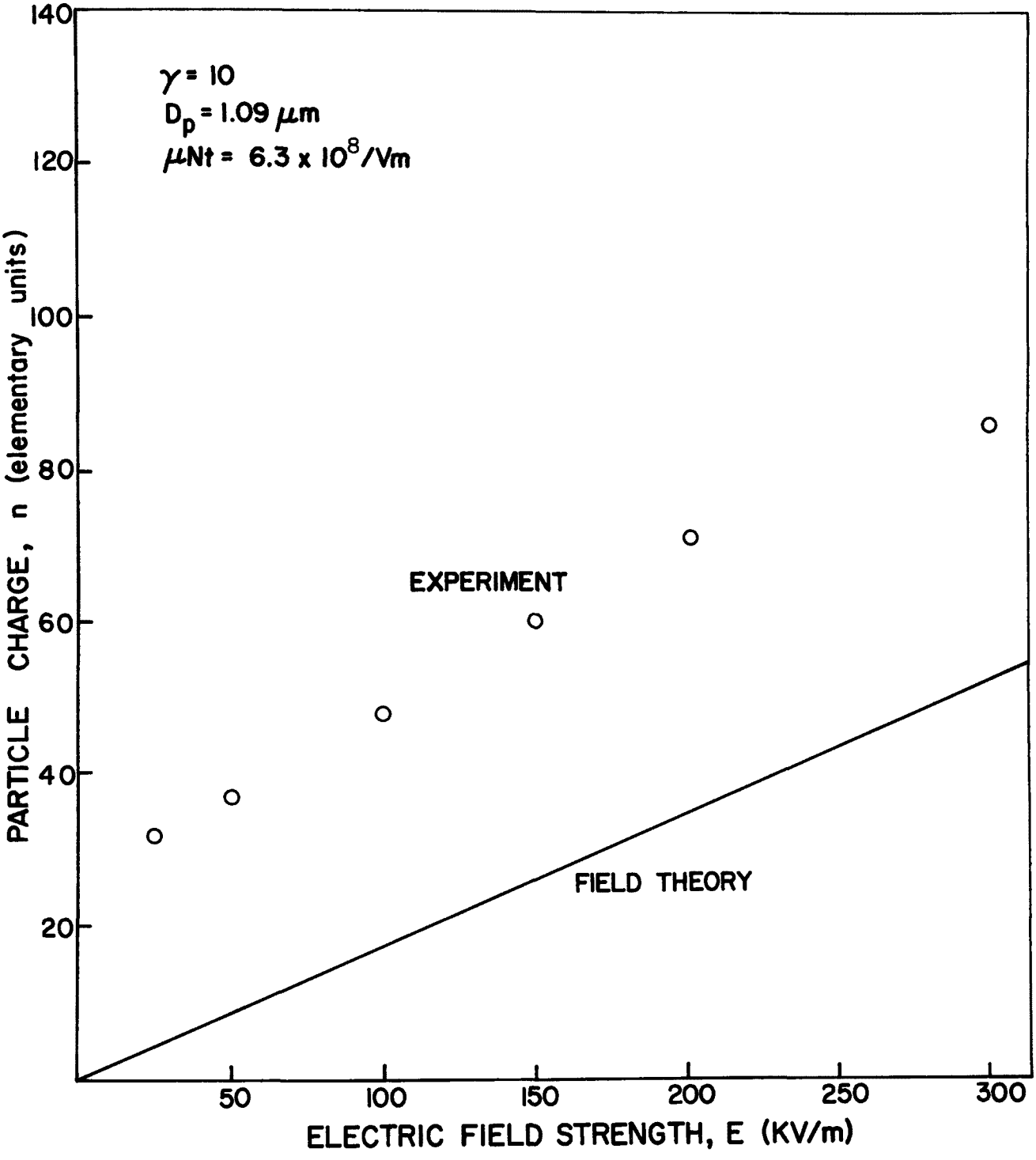

Figure 3: Comparison of experimental charge to field theory calculation. D_p = 1.09 μm, μNt = 6.3 x 10^8/Vm and γ = 10.

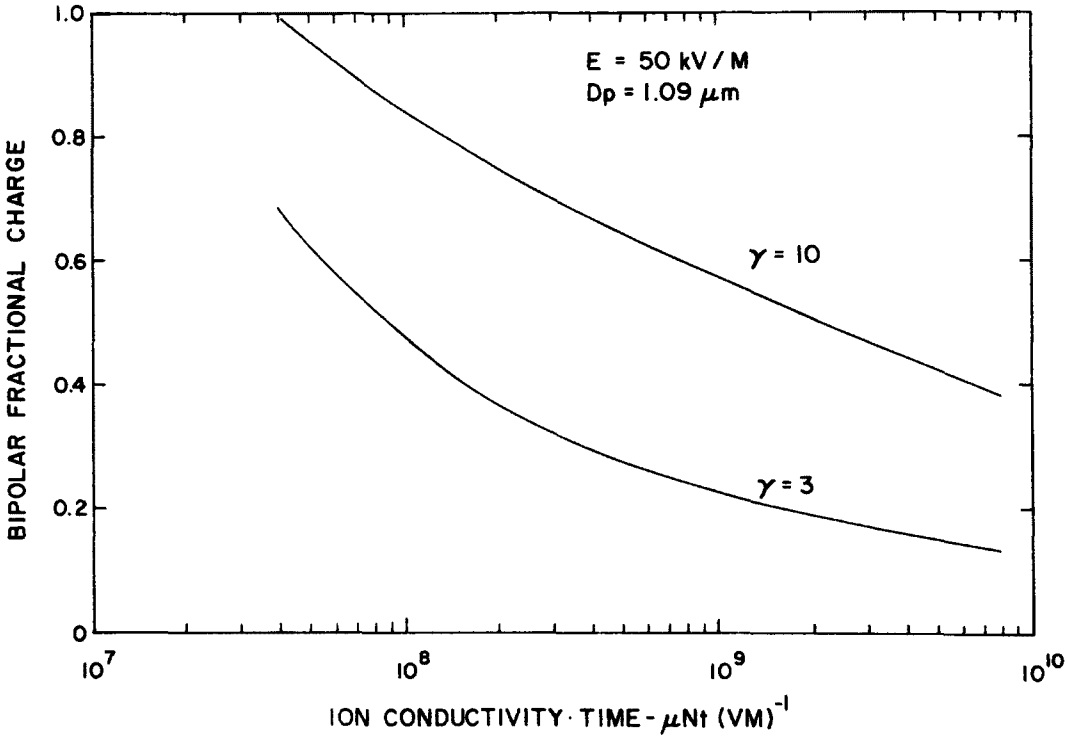

Figure 4: Ratio of bipolar charge to unipolar charge as a function of μNt for $\gamma = 3$ and $\gamma = 10$.

IDENTIFICATION OF BACK DISCHARGE SEVERITY

By: Senichi Masuda and Yutaka Nonogaki
Department of Electrical Engineering
University of Tokyo
7-3-1, Hongo, Bunkyo-ku, Tokyo 113
Japan

ABSTRACT

The effect of back discharge on collection performance of ESP's are examined, and a quantitative expression of its severity based on the measurable parameters is presented. A linear relationship is observed to exist between the measured charge-to-mass ratio and apparent migration velocity. In this case the charge-to-mass ratio measured at the outlet can be assumed to represent approximately its average value inside the collection field. It is evident that its outlet value should become greatly different from its in-field value with increasing length of collection field because the highly charged, larger particles are more rapidly collected whereas the smaller particles, difficult to collect, tends to raise the level of an overall charge-to-mass ratio at the outlet. In order to avoid this difficulty in the diagnosis of back discharge severity a bipolar current probe has been developed by the authors which enables a separate measurement of negative and positive ionic current density in a bipolar ionic atmosphere such as in the back-discharging field. These two quantities make possible a theoretical prediction of the charge-to-mass ratio in the back-discharging field, and thus the collection efficiency of an ESP, too.

INTRODUCTION

The effect of back discharge on the collection performance of an ESP is twofold. One is the reduction of field intensity, E, in charging and collecting fields owing to the lowering of sparking voltage itself (excessive sparking) or an abnormal increase in current at a lower voltage which cannot be raised because of a limited current capacity of a power supply. Another effect of back discharge is the production of false (positive) ions which reduce the particle charge, q. Since the apparent dust migration velocity, w, in Deutsch's equation is proportional to qE, the reduction in q and E impairs the performance through the lowering of w. As a result an impairment factor of migration velocity for identifying the overall back discharge severity may be estimated from two measurable parameters, the impairment factors of E and q.

In the ordinary collection field with a longer residence time the charge-to-mass ratio measured at the outlet mostly differs much from its value dominating in the collection process. Theory predicts, however, that the particle charge in the back-discharging field can be calculated, provided the quantities of negative and positive ionic current density can be measured. So, a particular probe (bipolar current probe) is developed to enable this measurement. This provides a possibility of identifying the back discharge severity through the current density of positive and negative ions, i_+ and i_-, and its

ratio, i_+/i_-. These quantities are the more meaningful parameters which precisely describe the bipolar ionic structure of the back-discharging field.

1. Theoretical Considerations

1.1 Expression of Back Discharge Severity

The electrical collection efficiency of an ESP after correction of mechanical contribution can be given, even under back discharge condition, by a well-known Deutsch's equation (1):

$$\eta = 1 - \exp(-wf) \tag{1}$$

where $$w = KqE = \text{apparent migration velocity of dust} \tag{2}$$

and f = specific collection area, q = average particle charge, and K = constant.

The quantities, q and E, are lowered by back discharge from their ideal values, q_o and E_o, under no back discharge conditions to become

$$q = \alpha q_o , \qquad E = \beta E_o \tag{3), (4}$$

and we get

$$w = \zeta w_o \tag{5}$$

where w_o = ideal value of w, and α, β, and $\zeta(= \alpha\beta)$ are constants. The magnitude of w_o is a function of all the variables in a ESP other than ρd, whereas the constants, α, β, and ζ, are specific to each back discharge condition which is determined by ρd, gas composition, gas temperature, particle size, dust composition etc. It is evident from equations (1) and (5) that overall effect of performance impairment by back discharge is represented by ζ, which can be numerically grasped from the measurable quantities, α and β. So, we name ζ the "impairment factor of apparent dust migration velocity" to specify the severity of respective back discharge condition.

Among the quantities, q and E, needed to estimate ζ the former is not only difficult to measure accurately, but also represents a secondary quantity determined by the more fundamental quantities to specify back discharge: the current density of negative and positive ions, its ratio, and field intensity, E. Based on these quantities it is possible to predict theoretically the magnitude of particle charge in the charging process in a bipolar ionic atmosphere, its saturation value, and its charging speed (charging time constant), not only in the case of a conventional ESP, but also in the case when a precharger is being used. This supports the use of these intrinsic quantities as the most essential parameters to identify the back discharge severity.

1.2 Particle Charge in Bipolar Ionic Atmosphere

The two different cases are considered separately: one being the case when the particles enter into the charging and collecting field of a conventional ESP without any initial charge (Case I), and another being the case when the particles are highly precharged (Case II). The field charging is assumed in both cases as the charging mechanism. The case of diffusional charging is considered in reference (2).

1.2.1. Case I (field charging without precharging)

The magnitude of charge of a single spherical particle in this case is given by Pauthenier (2) as

$$q_f = q_{f\infty} \frac{1 - \exp(-t/\tau)}{1 - \{(1-\gamma)/(1+\gamma)\}^2 \exp(-t/\tau)} \quad (C) \tag{6}$$

where

$$q_{f\infty} = q_{f\infty}^* \{(1-\gamma)/(1+\gamma)\} = \text{saturation charge under bipolar condition} \tag{7}$$

$$q_{f\infty}^* = 4\pi\varepsilon_o\{3\varepsilon_s/(\varepsilon_s+2)\}a^2E = \text{saturation charge under monopolar condition} \tag{8}$$

$$\gamma = \sqrt{\mu_+\rho_+/\mu_-\rho_-} = \sqrt{i_+/i_-} = \text{current parameter} \tag{9}$$

$$\tau = \varepsilon_o/\sqrt{\mu_+\rho_+\mu_-\rho_-} = \varepsilon_o E/\sqrt{i_+ i_-} = \sqrt{\tau_+\tau_-/4} \quad (s) \tag{10}$$

and

$$t = \text{time} \quad (s)$$

where ε_o = dielectric constant of vacuum = 8.842×10^{-12}(F/m), ε_s = specific dielectric constant of particle, a = particle radius (m), μ_+ and μ_- = mobilities of positive and negaive ions (m^2/Vs), ρ_+ and ρ_- = space charge density of positive and negative ions (C/m^3), i_+ and i- = current density of positive and negative ions (A/m^2) and

$$\tau_o = 4\varepsilon_o E/i = \text{charging time constant under monopolar condition at current density } i = i_+ + i_- \tag{11}$$

$$\tau_+ = 4\varepsilon_o E/i_+ = \text{" " at current density } i_+ \tag{12}$$

$$\tau_- = 4\varepsilon_o E/i_- = \text{" " at current density } i_- \tag{13}$$

It can be seen from equation (7) that the saturation charge in a bipolar ionic atmosphere lowers with increasing current density ratio, i_+/i_-. Figure 1 shows the particle charge normalized with its ideal value in a monopolar ionic atmosphere, $q_{f\infty}/q_{f\infty}^*$, as a function of the current density ratio, i_+/i_-. It should be noted that the particle charge is almost halved (52%) by a slight supply of positive ions at $i_+/i_- = 10\%$. Equation (7) also indicates that particles can be positively charged in the local area where i_+ exceeds i-. Figure 2 shows for different values of i+/i- the increase of particle charge, denoted by $q_f/q_{f\infty}^*$, as a function of charging time, t.

1.2.2 Case II (field charging with precharging)

The highly precharged particles lose their charge in a bipolar ionic atmosphere owing to charge elimination by positive ions, finally to obtain the saturation charge (7) specific to the back discharge condition. This process differs depending on a level of the initial charge, q_o, in relation to the value of ideal saturation charge, $q_{f\infty}^*$.

i) Range where $q_{f\infty} \geq q_{f\infty}^*$: The charge lowers to $q_{f\infty}^*$ according to the following relation derived by the authors (5):

$$q_f = q_o \exp(-4t/\tau_+) = q_{f\infty}^* \exp\{4(\Theta-t)/\tau_+\} \tag{14}$$

where

$$\Theta = (\tau_+/4)\ln(q_o/q_{f\infty}^*) = \text{time necessary for } q_o \to q_{f\infty}^* \qquad (15)$$

The charge elimination proceeds in this range without being affected by negative ions because the particle potential is excessively higher than the original local potential at the particle position.

ii) Range where $q_{f\infty}^* > q_f \geq q_{f\infty}$: In this range the particle potential is lower than in range i), so that negative ions interfere with the charge elimination process by positive ions, and the following relation holds for charge reduction (4):

$$q_f = q_{f\infty} \frac{1 + \{(1+\gamma)/(1-\gamma)\}\exp(-t/\tau)}{1 + \{(1-\gamma)/(1+\gamma)\}\exp(-t/\tau)} \qquad (16)$$

Figure 3 shows for different values of i_+/i_- the time decrease in particle charge from $q_{f\infty}^*$ to $q_{f\infty}$ according to equation (16).

Curves in figure 4 shows, for the cases of $i_+/i_- = 0.02$ (low severity of back discharge) and $i_+/i_- = 0.10$ (medium severity) respectively, the time decrease in particle charge from its initial value q_o ($>q_{f\infty}^*$) to $q_{f\infty}^*$ and further to the saturation value, $q_{f\infty}$, plotted in its actual value. A great difference can be seen in both the saturation value, $q_{f\infty}$, and the charge reduction speed , depending upon the difference in the magnitude of i_+/i_-. The lower curves in this figure represent the charging process starting from zero initial charge according to equation (6) depicted for the purpose of reference.

1.3 Relationthip between Charge Impairment Factor and Bipolar Current Density

It is evedent that the charge impairment factor, , defined by equation (3), can be easilly calculated using the time averages over the residence time of the values (q_f in equation (6)) and (q_f^* given by the following equation) for the case I:

$$q_f^* = q_{f\infty}^* \{(t/\tau_o)/(1+t/\tau_o)\} = \text{time increase of charge under no back discharge condition} \qquad (17)$$

In the case II where precharging is made for enhancing the collection performance, the charge enhancement factor, $\phi = q/q_o$ (>1), and the enhancement factor of apparent dust migration velocity, $\psi = w/w_o$, come into question. As the particle charge lowers in time in the succeeding collection field because of charge elimination, its time average must be taken in calculation of ϕ and ψ using equations (6), (14) and (16).

Since equations (6), (14) and (16) for the field charging are the functions of the residence time, t, field intensity, E, and the magnitudes of positive and negative ionic current density, i_+ and i_-, as in the forms of its ratio, i_+/i_-, and the square root, $\sqrt{i_+/i_-}$, it is theoretically possible to estimate the values of α, β, ζ, ϕ, and ψ from these quantities.

1.4 Theory of Bipolar Current Probe

Figure 5 shows the schematic of the bipolar current probes of both spherical and cylindrical types, each having three electrodes A, B. and C. The probes are inserted into a bipolar ionic atmosphere so that the central plane D becomes perpendicular to the local electric field, as illustrated in figure 6. The measuring electrodes A and B, and the detection electrode C are

connected through a current meter and wires to a variable dc high voltage source to be applied with the same voltage, V_o (figure 7). When the magnitude of V_o is adjusted to become equal to the original local potential of the probe center point, the electric lines of force in its surrounding takes a symmetric configuration respect to the central plane D (figure 6). Then, the measuring electrodes, A and B, accept respectively only the negative and positive ionic current, I_- and I_+, which can be easily calculated as (6):

(a) Spherical Probe: $I_- = -3\pi a^2 i_- \cos^2(d/2a)$, $I_+ = 3\pi a^2 i_+ \cos^2(d/2a)$ (18)

(b) Cylindrical Probe: $I_- = -4al\, i_- \cos(d/2a)$, $I_+ = 4al\, i_+ \cos(d/2a)$ (19)

where a = radius of probe, d = width of electrode C, and l = length of C in a cylindrical probe. Under this "balanced condition", the number of electric lines of force entering into the electrode C is equal to that leaving from it. But, a slight current is detected by C owing to the difference in the mobility and space concentration of positive and negative ions. It is evident that this probe can also be used in the usual monopolar ionic atmosphere. The values of I_- and I_+ at the balanced condition can be derived by the following methods:

i) Graphical Method: Figures 8 and 9 shows, for the monopolar and bipolar ionic atmosphere respectively, the values of I_+, I_- and I_c (= current flowing into electrode C) as the functions of probe potential, V_o. Theory predicts that each curves in both monopolar and bipolar cases consists of three parts, two straight lines with different gradients (L and N) and a curved line connecting them (M). In the monopolar case the second straight branches conincide with the horizontal axis. Theory further tells that the extrapolation of these two straight line branches provides a crossing point p on the horizontal axis, which corresponds to the balanced potential. This method requires a tedious procedure, and the ionic field may subject to disturbances in the mean time.

ii) Use of Correction Factors at "Quasi-Balanced Potential": It is much easier in the bipolar ionic atmosphere to determine the probe potential at $I_c = 0$. This potential, called "quasi-balanced potential", slightly differs from the true balanced potential owing to the difference in positive and negative ionic current density (point q in figures 8 and 9). But its deviation as well as deviations of I_+ and I_- can be calculated throretically . Thus, the values of I_+ and I_- at the true balanced potential to be used in equations (18) and (19) can be obtained by dividing their values at the quasi-balanced potential by the correction factors k_+ and k_- indicated in figure 10. These correction factors are calculated for different values of the probe parameters, d/2a, and depicted as the functions of I_+/I_- at $I_c = 0$.

In the monopolar case the method as described above fails because the exact determination of the quasi-balanced potential becomes extremely difficult (see point q in figure 8). However, theory indicates that, at the balanced potential in this case, the ratio of I_c/I_- takes a definite value depending upon the type and geometry of the probe:

(a) Spherical Probe: $I_c/I_- = \tan^2(d/2a)$ (20)

(b) Cylindrical Probe: $I_c/I_- = \sec(d/2a) - 1$ (21)

In the use of this probe in a back-discharging field the negative ionic current from the discharge electrode is partly obstructed by the probe to produce its shadow on the dust deposit on the collecting electrode. As a result no back discharge occurs (figures 11 and 12). Then, the positive ionic current detected by the lower electrode becomes extremely low or almost zero. This error can be avoided by providing a gas flow perpendicular to the field lines at a low velocity, the magnitude of which must be determined by the probe dimension and its distance from the collecting electrode.

2. Results of Experiments

2.1 Migration Velocity and Charge-to-Mass Ratio

The effect of charge-to-mass ratio of dust, q/m, on the apparent migration velocity of dust is investigated at a short collection field (two ducts in parallel, plate-to-plate spacing = 30 cm, height = 70 cm, length in gas flow direction = 50 cm) located in a laboratory race-track system, using fly-ash at gas temperature of 130°C. The dust resistivity, ρ_d, is 10^{11}- 10^{12} Ω·cm. When the collecting electrodes are cleaned by thorough rapping, back discharge dissappears at this resistivity level resulting in a normal current density and a high charge-to-mass ratio. Then, the current rises gradually with increasing dust deposit owing to the increase in back discharge severity to cause the drop in charge-to-mass ratio and collection performance. The charge-to-mass ratio is measured at the outlet of the collection field. The inlet and outlet mass-loading of dust are measured at the same time to evaluate the apparent migration velocity of dust. It is considered in this short field that the charge-to-mass ratio measured at the outlet is approximately representing its "in-field" value governing the collection performance. In the present system ca. 50 % of the inlet-dust in collected mechanically, and the apparent migration velocity is derived from the electrical collection efficiency, η_e, after subtracting the effect of mechanical collection. The magnitude of the apparent migration velocity, w, is considered to be propotional to $\ln(1 - \eta_e)$.

Figure 13 indicates the relationship between the measured values of charge-to-mass ratio and those of apparent migration velocity, both plotted in the normalized form, $\alpha = (q/m)/(q/m)_o$ and $\zeta = w/w_o$. The subscript o denotes the reference quantities under no back discharge condition just after the electrode cleaning. As a first approxomation a linear relationship can be seen to exist between α and ζ . However, a closer examination of the plots shows that the collection performance becomes superior to the linear line with the decrease in charge-to-mass ratio which is resulted by increasing the severity of back discharge.

2.2 Tests of Probe Diagnosis of Back Discharge Severity

Prior to the probe diagnosis of the collection field, the magnitudes of i_+ and i_- are measured under back discharge condition in a point-to-plane electrode system (figure 7) using different dust samples where the dust resistivity is altered in air by changing ambient temperature(5). Figure 14 shows the results obtaines for fly-ash with the spherical and cylindrical probes, both providing the same results in this particular case.

2.2.1 Charge-to Mass Ratio and Current Density Ratio

The bipolar current probe of cylindrical type (a = d = 1 mm, 1 = 10 mm) is inserted into the short collection field in the race-track system as previously descrived. The probe is located throughout the present experiments between the 6th wire and a plate. The probe can be moved vertically along the axis y parallel to the wire, with the distance from the plate kept constant at z = 10 cm. The charge-to-mass ratio of dust, i_+ and i_- are measured under different back discharge severity. Figure 15 indicates one of the probe diagnosis results under back discharge condition. It must be noted that the values of i_+ and i_-, as well as i_+/i_-, are extremely non-uniform in space. This fact strongly suggests that the multi-point measurement must be made in its application for predicting the collection performance.

Figure 16 indicates the normalized charge-to-mass ratio, $\alpha = (q/m)/q/m)_o$, plotted against the average current density ratio, $\bar{\xi} = \bar{i}_+/\bar{i}_-$, measured at the points along y-axis. The solid curve represents a theoretical curve according to equation (7). The agreement between the experimental and theoretical values is satisfactory.

2.2.2 Migration Velocity and Current Density Ratio

The inlet and outlet mass-loading of dust are measured at the same time when the probe diagnosis as in 2.2.1 is being made. The collection efficiency is calculated from the mass-loading , and $\zeta = w/w_o$ derived. The normalized charge-to-mass ratio is calculated from the measured value of $\bar{\xi} = \bar{i}_+/\bar{i}_-$ using equation (7). Figure 17 shows the relationship between the values of ζ and α thus obtained. A propotionality exists approximately between these quantities.

3. Conclusions

The following conclusions are derived from the present investigations;

1) Charge-to-mass ratio of dust provides an usable parameter to identify back discharge severity.
2) The magnitudes of positive and negative ionic current density, i_+ and i_-, and its ratio, i_+/i_-, can also be used as the most essential parameters for specifying back discharge severity, provided the distribution of back discharge be considered.
3) The bipolar current probes of three electrode type provides a usable means for diagnosing a bipolar ionic field.

References

(1) S.Masuda, A.Mizuno and H.Nakatani, Proc. US-Japan Seminar on Measurement and Control of Particulate Generated from Human Activities, Kyoto(1980), p.193.
(2) S.Masuda, Y.Nonogaki, H.Nakatani and T.Oda, ibid., p.66.
(3) M.Pauthenier, La Physique des Forces Electrostatiques et leurs Applications , Centre National de la Recherche Scientifique, Paris(1961), p.279.
(4) S.Masuda and Y.Nonogaki, Memorandum presented at Committee Electrical Engineering for Pollution Control, Inst. Elect. Engrs. Japan (July 1,1980).
(5) S.Masuda and Y.Nonogaki, Conf. Rec., IEEE/IAS 1980 Annual Meeting, p.912.
(6) S.Masuda and Y.Nonogaki, to be presented at the 4th International Congress on Electrostatics (1981, Hague).

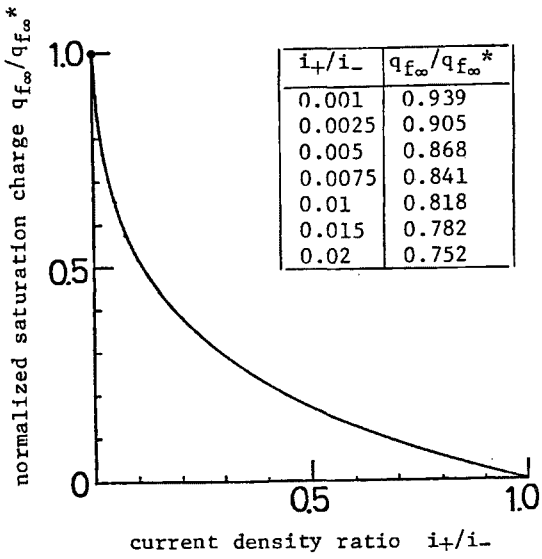

i_+/i_-	$q_{f\infty}/q_{f\infty}^*$
0.001	0.939
0.0025	0.905
0.005	0.868
0.0075	0.841
0.01	0.818
0.015	0.782
0.02	0.752

Fig. 1 Saturation Charge in Bipolar Ionic Atmosphere vs. i_+/i_-.

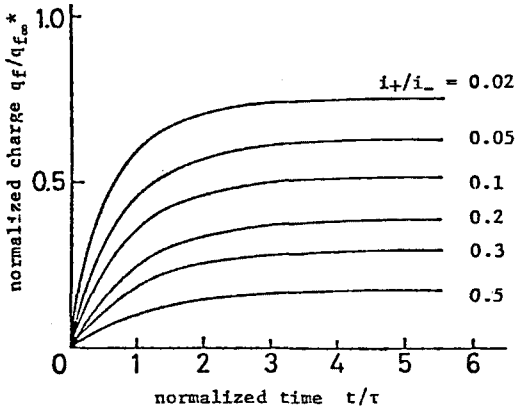

Fig. 2 Time Increase in Particle Charge in Bipolar Ionic Atmosphere

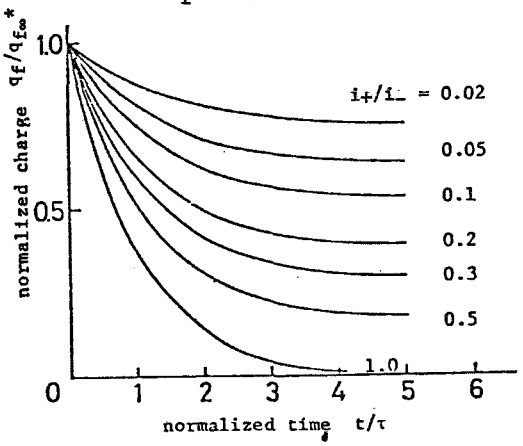

Fig. 3 Time Decrease in Particle Charge in Bipolar Ionic Atmosphere

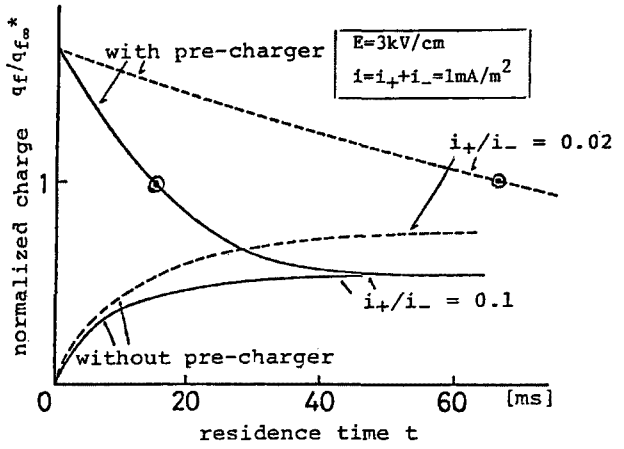

Fig. 4 Time Decrease in Particle Charge in Back Discharge Field of low and medium Severity Level

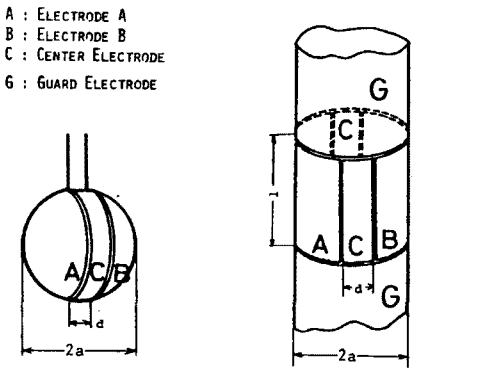

(a) Spherical Type
2a=4.6mm, d=1.2mm

(b) Cylindrical Type
2a=3.0mm, d=1.0mm
l=10.0mm

Fig. 5 Bipolar Ionic Current Probe

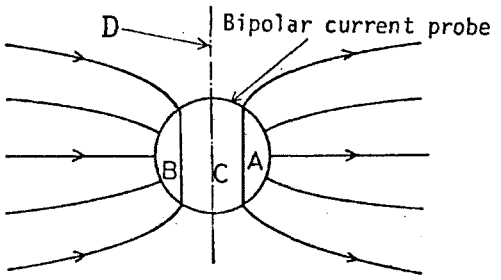

Fig. 6 Field Configuration around Probe at Balanced Potential

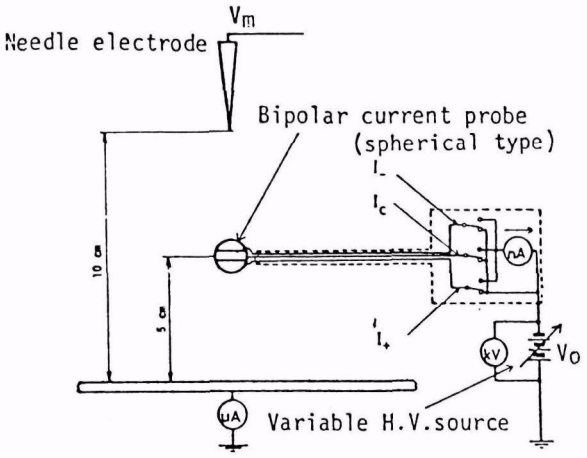

Fig. 7 Diagnosis of Needle-to-Plane Field by Bipolar Current Probe

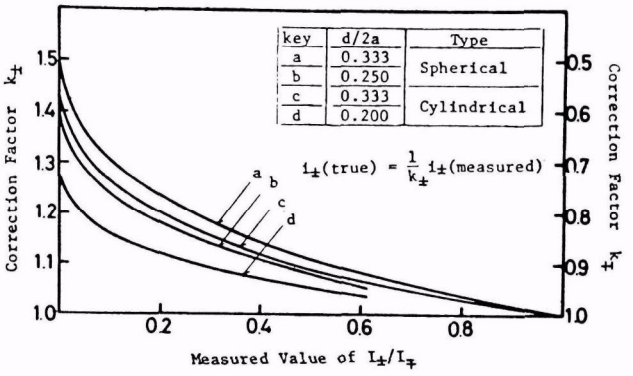

Fig. 10 Correction Factors K_+ and K_-

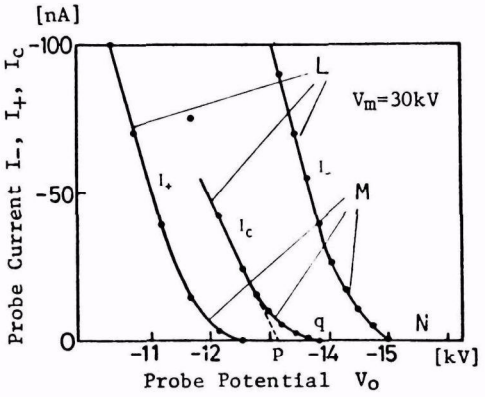

Fig. 8 Probe Currents vs. Probe Potential (monopolar ionic atmosphere; spherical probe)

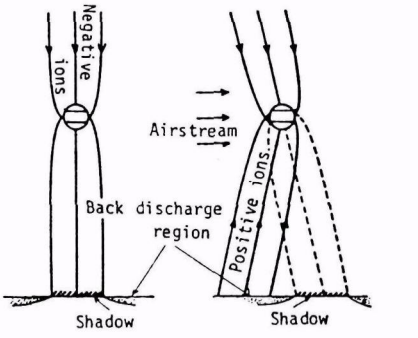

(a) without airstream (b) with airstream

Fig. 11 Formation of Negative Ion Shadow and Its Movement by Air Flow

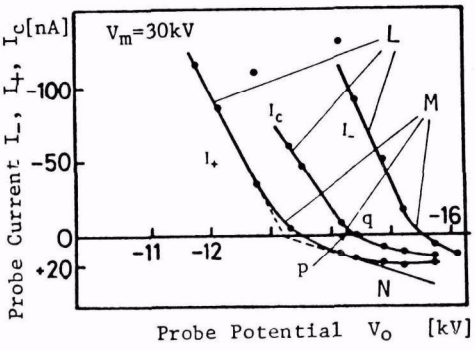

Fig. 9 Probe Currents and Probe Potential (bipolar ionic atmosphere; spherical probe)

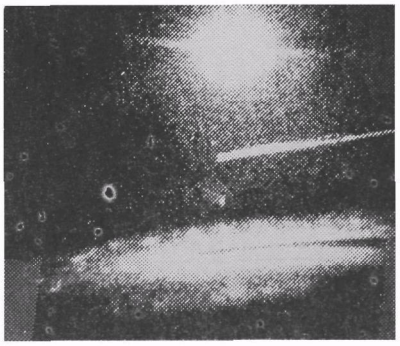

Fig. 12 Photograph of Probe Diagnosis and Negative Ion Shadow (cylindrical probe)

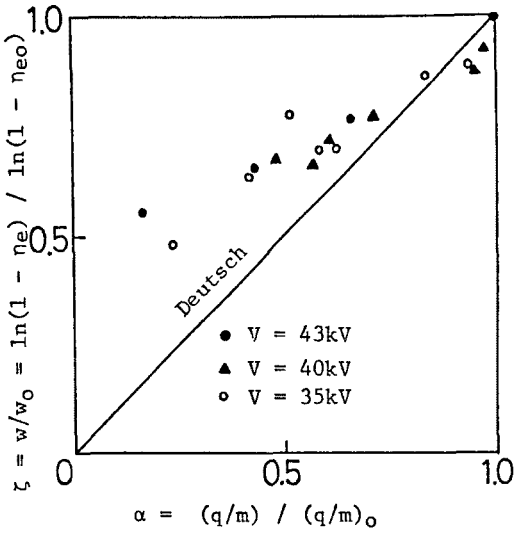

Fig. 13 Apparent Migration Verocity vs. Charge-to-Mass Ratio

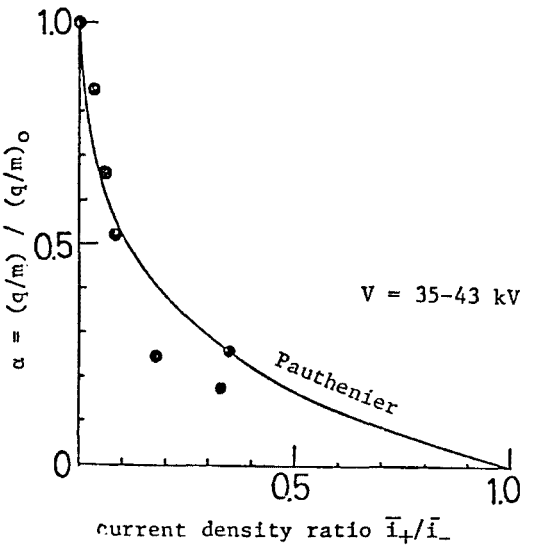

Fig. 16 Charge-to-Mass Ratio vs. Current Density Ratio

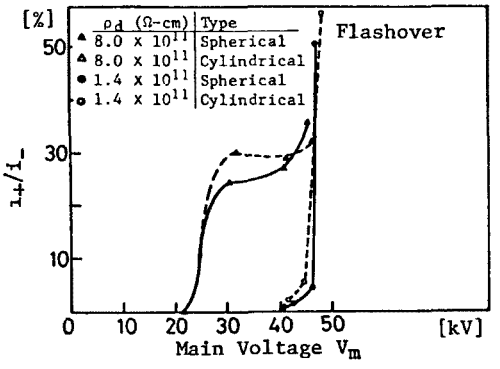

Fig. 14 Current Density Ratio vs. Applied Voltage (figure 7, fly-ash, 50-80°C)

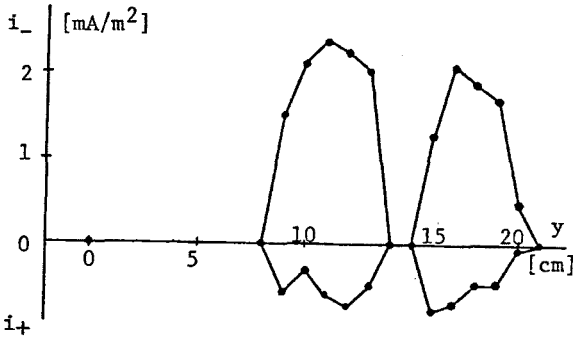

Fig. 15 Spacial Distribution of Ionic Current Density along y-axis ,V = 38kV

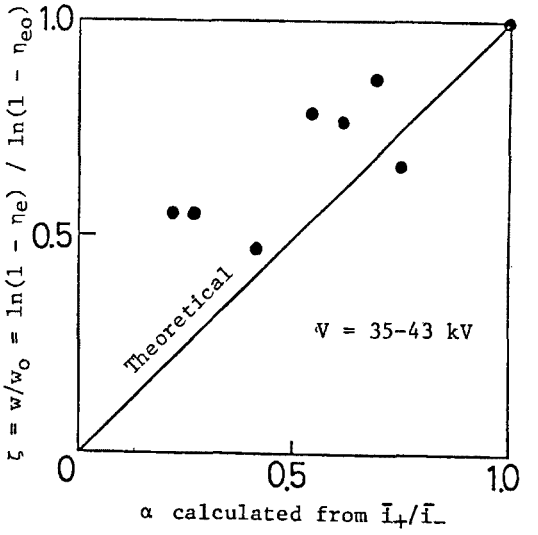

Fig. 17 Apparent Migration Velocity vs. Calculated Charge-to-Mass Ratio

MODELING OF ELECTROSTATIC PRECIPITATORS WITH RESPECT TO RAPPING REENTRAINMENT AND OUTLET OPACITY

By: M. Greg Faulkner, William E. Farthing, Jack R. McDonald
Southern Research Institute
2000 Ninth Avenue, South
Birmingham, Alabama 35255

Leslie E. Sparks
Industrial Environmental Research Laboratory
U.S. Environmental Protection Agency
Research Triangle Park, N.C. 27711

ABSTRACT

Revisions of the Environmental Protection Agency's mathematical model of electrostatic precipitation which allow a dynamic, time-dependent representation of rapping reentrainment and predictions of outlet opacity are discussed. The new rapping reentrainment scheme allows different rapping schedules for the various independent sections, reentrainment due to rapping of a specified percentage of the total mass collected in a given increment of length with a specified particle size distribution, recharging and recollection of reentrained particles, a representation of hopper boil-up, and a time history of dust layer thickness. The addition of opacity calculations based on Mie theory allows the prediction of total and fractional opacities based on predicted outlet mass loadings and particle size distributions, a specified complex index of refraction, particle density, and stack diameter. Simulations demonstrating the predicted effects on outlet particulate emissions and opacity are presented.

INTRODUCTION

The Environmental Protection Agency's mathematical model of electrostatic precipitation is undergoing revision and improvement at the Southern Research Institute. One recently completed modification alters the calculation procedure for rapping reentrainment and another provides the mechanism to calculate outlet opacity. In the present model, the outlet dust loading contributed by rapping reentrainment is determined by an empirical process which estimates the reentrained mass in the last section of the precipitator, fits that mass to a size distribution, and adds the result to the effluent size distribution of the precipitator. The revised version introduces the reentrained mass into the gas flow at the point where it was rapped loose and then follows the dust through the collection process to determine the outlet dust loading due to the rap. Opacity is not calculated in the present model. In the revised version, opacity calculations utilize Mie theory to predict total and fractional opacities based on the outlet mass loading and particle size distribution.

RAPPING REENTRAINMENT

In order to properly model the rapping reentrainment process it is necessary to understand what takes place when the rap occurs. When the

plates are rapped, the collected dust layer fractures and separates from the collection plates. Some of this dust is reentrained directly into the gas flow but most of it falls into a collection hopper where it is broken up by the impact. A large dust cloud then billows up out of the hopper and is reentrained into the gas flow. A study of a pilot precipitator demonstrated that this dust cloud contributes most of the reentrained particles.[1] The amount of particles carried aloft in this cloud will be a function of time as the cloud builds up and subsides or is carried away by the gas flow. The particle size distribution in the dust cloud is also expected to vary with time as large particles have a higher settling rate than smaller ones. Experiments have shown that the particle size distribution due to rapping found at the top of the precipitator is different from that near the bottom, where a higher concentration of large particles is found.

In the computer model, each electrical section of the precipitator is divided into several increments to allow a finer calculation of the efficiency in each section and of the dust layer growth rate. The rapping subroutine calculates the thickness of the dust layer in each increment at the time of each rap so that the amount of dust to be reentrained can be determined. Figure 1 shows a record of the dust layer thickness for a hypothetical three-section precipitator before and after two raps. The rapped sections are shaded for easy identification. When a rap occurs, a portion of the mass removed from each rapped increment is fitted to a size distribution and the resulting information is stored in the form of numbers of particles in each size band. The program is then returned to the beginning of the efficiency calculation procedure for the calculation of collection efficiency during the rapping puff. During this calculation, at the beginning of each increment, the computer checks the storage register to obtain the number of particles in each size band reentrained by the preceding increment. These numbers are added to the numbers of particles already present at that point in the precipitator and the calculation of particle collection in that increment proceeds in the usual manner. This mechanism implies instantaneous recharging of the reentrained dust particles to the value of charge that the same size particles in the regular flow have at that point. This is an approximation made to simplify the calculation. In the actual process, the charges on these particles, and therefore the rate at which they recharge, are unknown.

In order to more closely approximate the actual rapping puff, the reentrained dust is shaped according to a rapping profile. This is an array of numbers which describes the quantity and the size distribution of the reentrained dust as a function of time. This will allow the shaping of the reentrainment puff to closely approximate an experimentally observed puff. An example of this is shown in Figure 2, in which an actual rapping puff observed by Spencer[1] on a pilot precipitator has been duplicated.

This model has been used to examine the collection efficiency of a power plant precipitator.[2] The particular unit studied had three electrical sections, each having a collection area of 2500 m^2 (26,000 ft^2). This gives a specific collection area of 34.5 $m^2/(m^3/sec)$ or 175 $ft^2/1000$ acfm for the design volume flow of 214 m^3/sec (453,000 acfm). There are 42 lanes spaced 28 cm (11 in.) apart with 12 wires per lane per field. The first section is rapped 10 times/hour, the second field is rapped 6 times/hour, and the third field is rapped 1 time/hour. The plates are rapped two at a time.

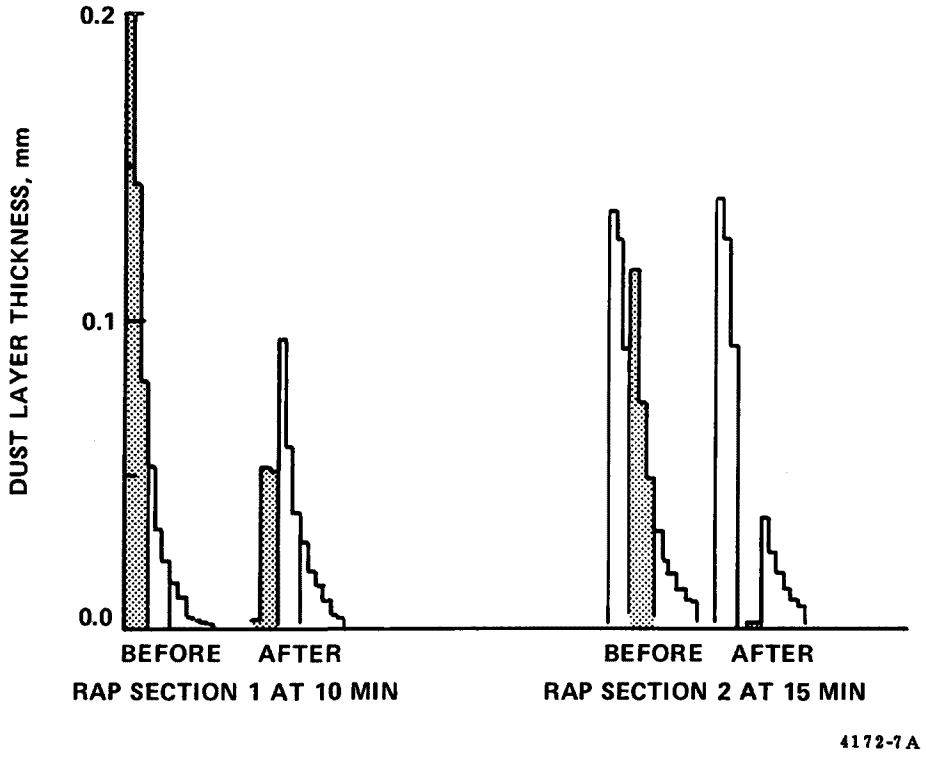

Figure 1. Thickness of dust layer before and after rap.

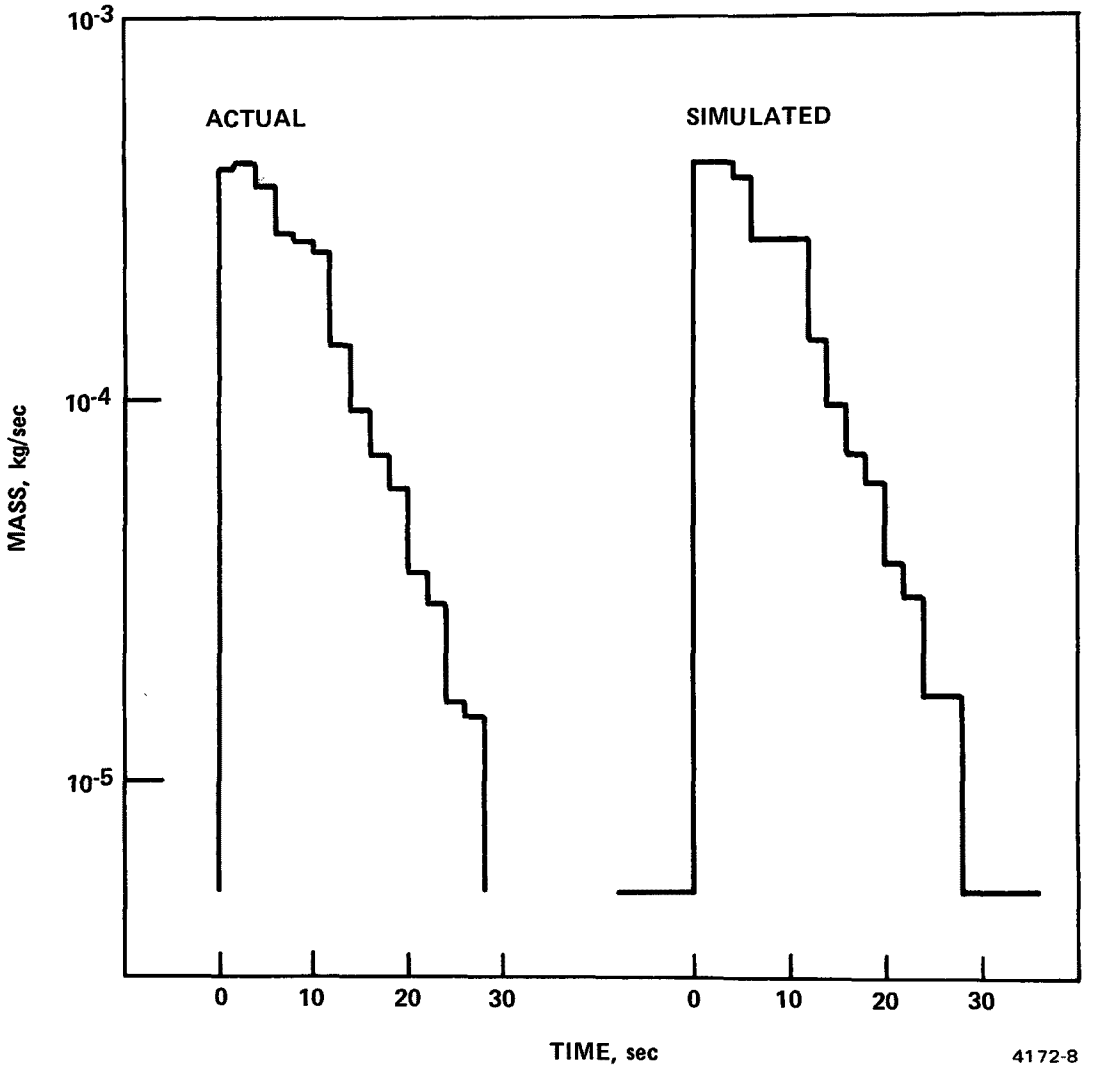

Figure 2. Simulation of rapping puff.

Figure 3 shows the experimental data for the plant and a comparison between the new rapping simulation and the old simulation: the new calculation more closely approximates the experimental curve. Overall collection efficiencies are 99.55% by actual measurement, 99.20% using the old rapping calculation, and 99.68% using the new procedure. The new procedure was run using an assumed 10 μm mass median diameter for the reentrained particles which were introduced into the gas stream in the form of a dust cloud which lasted 4 seconds. Each of the 42 lanes was considered to be independent from its neighbor during the rapping process. Seventeen separate rapping calculations were performed to simulate the complete rapping scheme, resulting in an increase in computer time from 4 minutes (no rap case) to 40 minutes. If only the rap of the final ESP section is simulated, similar results can be obtained with 7 minutes of computer time.

The flexibility of the new rapping procedure is much greater than that of the estimation procedure found in the present precipitator model. However, before the procedure can be widely used, a data base of size distributions and quantities of reentrained dust measured at the point of reentrainment must be obtained.

OPACITY

The reduction in the transmission of light passing through suspended particles occurs by scattering and absorption by these particles. The degree of reduction is a function of particle size, concentration, and composition, and the optical path through the aerosol. For particles with diameters greater than about 1 μm, the extinction of light is essentially determined by the total projected area of the aerosol particles. For smaller sizes, particle composition becomes important. Consequently, for general applications, the calculation of opacity must be performed using a mathematical solution to Maxwell's equations. The theory used in this development is that of Gustav Mie[3] which gives, among other parameters, the extinction efficiency, Q_{ext}, in terms of the particle refractive index, n, and size parameter $\pi D/\lambda$ for isotropic homogeneous spheres. D and λ are the particle diameter and the wavelength of the light beam, respectively. The extinction efficiency represents the effective projected area of a particle for removing light from a light beam compared to its geometrical projected area. This is related to opacity by

$$\text{Opacity} = 1-\exp(-EL) = 1-\exp(-NAQ_{ext}L),$$

where

E = Extinction coefficient (m^{-1}),
L = Pathlength of the light beam (m),
N = Particle concentration (number/m^3), and
A = Particle projected area (m^2).

Figure 4 shows the extinction efficiency as a function of the particle size parameter for four complex refractive indices. The actual computer code for Mie

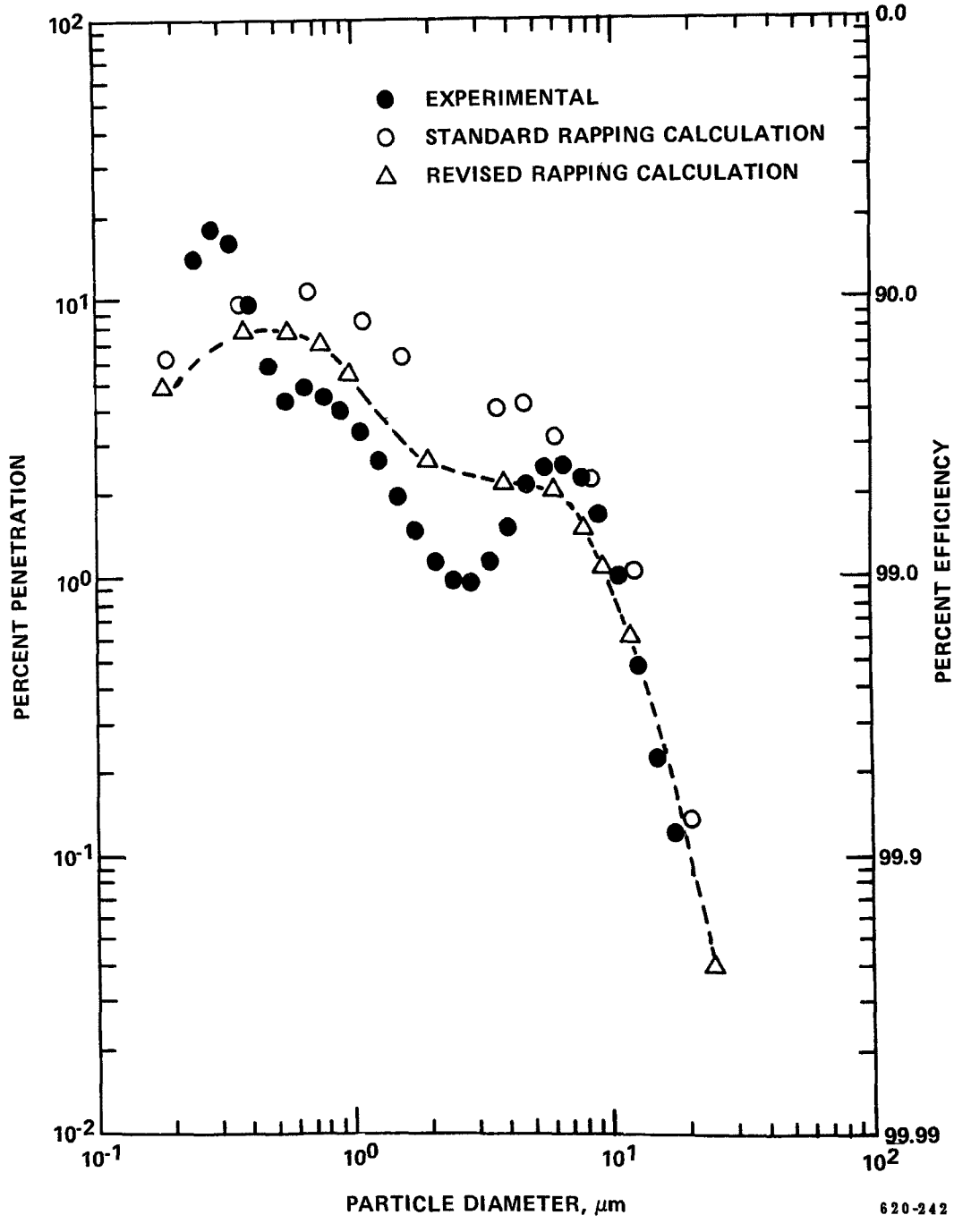

Figure 3. Comparison of standard and revised rapping reentrainment calculations.

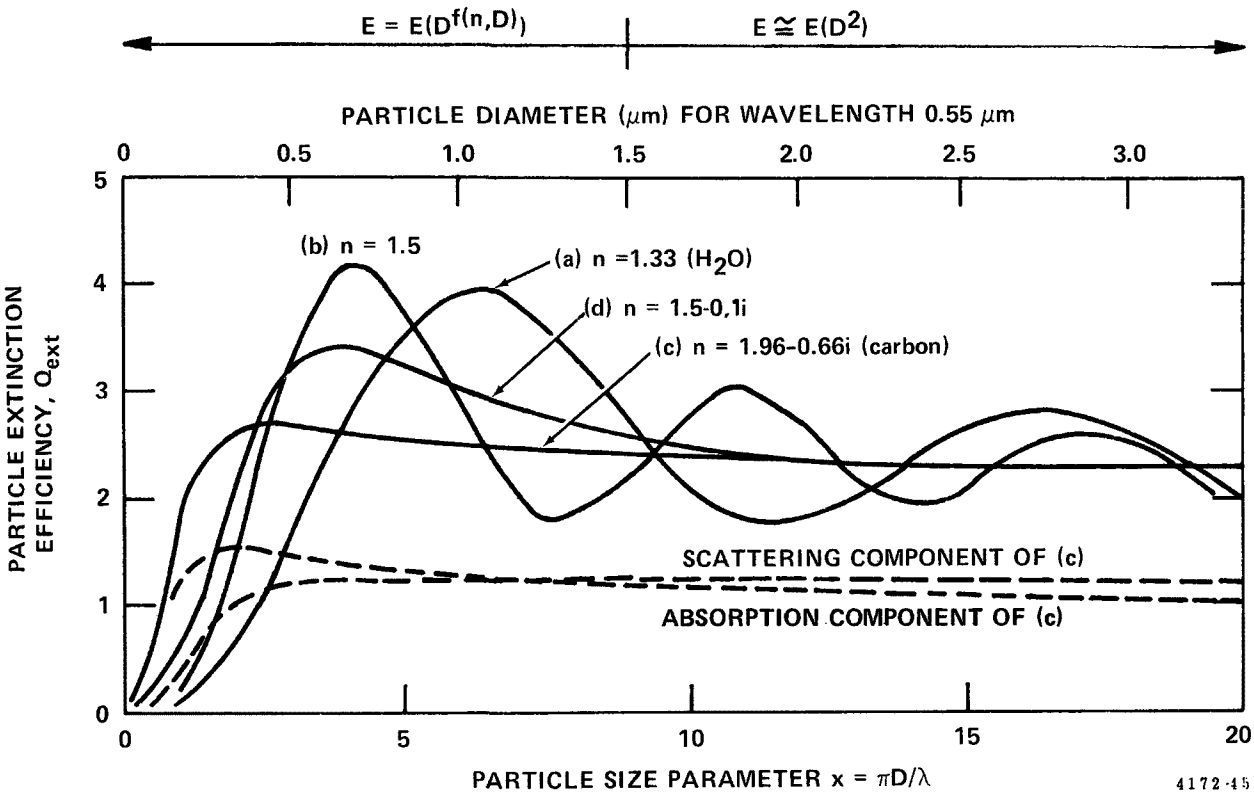

Figure 4. Particle extinction efficiency as a function of particle size parameter.

theory used in the ESP model is that of Moore[4] which employs the criteria of Deirmendjian[5] to determine a sufficient number of terms to achieve convergence of Mie's series solution.

The ESP model predicts the size distribution of the aerosol exiting the ESP for the no-rap case and for the rapping puff. The extinction coefficient for each size band of each case is calculated and printed along with the total extinction coefficients. The value of extinction efficiency, Q_{ext}, normally used for each size band is the average of Q_{ext} at 10 wavelengths weighted according the the photopic color response of the human eye. EPA approved opacity monitors must simulate this color response which is maximum at $\lambda = 0.55$ μm and has a width at half maximum of 0.1 μm. The option to perform the calculations at $\lambda = 0.55$ μm is available to reduce the required computer time. The resulting error depends upon the size distribution. Typical errors found thus far are about 5% in the total extinction coefficient. Computation time required for the calculations at all wavelengths is about 1 minute compared to about 45 seconds at one wavelength using the DEC 2020 computer. This is small relative to the hour typically required for the entire model.

The opacity calculations can be performed for several refractive indices for each run of the model if desired. The two default values of 1.5-0.0i and 1.5-0.1i will be used if the user does not supply this information. In addition, the variation of refractive index with wavelength can be taken into account by the program if these data are available.

The program output lists the contribution of each particle size band to the extinction coefficient, dE/dlogD, for the no-rap condition, the time-averaged rapping puff contribution, and the combined emissions. Following the fractional extinction coefficients, the total extinction coefficient, E, is given for the no-rap, rap, and combined cases. The extinction coefficient per unit mass loading, SPE, and the K parameter initiated by Pilat and Ensor[6] are also given. These quantities are related to opacity by

$$\text{Opacity} = 1-\exp(-(\text{SPE})\text{WL}) = 1-\exp(-\text{WL}/\text{PK}),$$

where

W = outlet particulate mass loading,
P = particle density,
and the other quantities are as previously defined.

The opacity calculation has been performed for the power plant described in the section on rapping reentrainment. Since no information on the refractive index was available for this plant, the default values were used. The opacities calculated for a refractive index of 1.5 were 13.5% for no-rapping, 2% for the rapping puff, and 15% for the combined case. For an index of 1.5-0.1i, the values were 12%, 2%, and 14%. The actual plant opacity at the time that these data were taken was estimated to be between 10 and 15%.

The opacity calculation developed for the ESP model is a highly flexible approach to the calculation of opacity. Based on the ESP emissions predicted

by this model, the new routine can calculate the opacity of the plume when only the pathlength of the light is available. However, for more exact calculations, more exact data may be supplied. In addition to the total opacity, this routine furnishes the contributions to the opacity from each particle size band.

ENDNOTES

1. Spencer, H. W., III. Rapping Reentrainment in a Nearly Full Scale Pilot Electrostatic Precipitator. EPA-600/2-76-140 (NTIS PB255 984), U.S. EPA, Industrial Environmental Research Laboratory, Research Triangle Park, NC, May 1976.

2. Gooch, J. P., and G. H. Marchant, Jr. Electrostatic Precipitator Rapping Reentrainment and Computer Model Studies. EPRI Contract RP413-1, The Electric Power Research Institute, Palo Alto, CA, June 1978.

3. Mie, G. Beitrage zur Optik truber Medien, Speziell Kolloidaler Metallosunge. Ann. Physik. 25:377-445, 1908.

4. Moore, J. D. M. 1968. Tests of Approximations to Electromagnetic Scattering by Spherical Particles. M.S. Thesis. Auburn University, Auburn, AL.

5. Deirmendjian, D., and R. J. Clason. 1962. Light Scattering on Partially Absorbing Homogeneous Spheres of Finite Size. Paper R393-PR, The RAND Corporation, Santa Monica, CA.

6. Pilat, M. J., and D. S. Ensor. Plume Opacity and Particulate Mass Concentration. Atmos. Environ. 4:163-167, 1970.

NEW PRECIPITATOR TECHNOLOGY FOR PARTICULATE CONTROL

By: J. R. Zarfoss
Environmental Elements Corporation
Subsidiary of Koppers Company, Inc.
Post Office Box 1318
Baltimore, Maryland 21203

ABSTRACT

All precipitator designs must accommodate the requirement of adequately cleaning the internal components. However, the collection of highly resistive particulate matter from boilers burning low sulphur coal is considered to be one of the more demanding applications. The fundamental capabilities needed to meet this challenge are the collecting surface response to rapping and the electrical characteristics of the discharge electrodes. This paper outlines a development program on this subject which spans six years, beginning with laboratory studies and concluding with the results from working installations. One of the basic studies quantifies and compares the rapping response, full size, of three popular collection surface designs. No evidence has been found to indicate that a comparison of this type has ever been attempted before. Levels of surface acceleration, frequency and uniformity are described. Techniques for altering the voltage and current characteristics of the discharge electrodes are also presented. This is not a theoretical study. All of the information relates to actual measurements and is useful in all precipitator designs.

INTRODUCTION

During the evolution of the electrostatic precipitator as a control device for particulate matter, each variable pertinent to collection efficiency has been reviewed many times. The objective each time has been to achieve higher efficiency and, in particular, accomplish this under the most difficult circumstances. Currently, manufacturers are faced with the problem of collecting high resistive particulate matter from boilers burning low sulphur coal. One of the variables of interest in this application is the proper dislodgement of the particulate matter from the collection surfaces and discharge electrodes. The basic motivation is to minimize the influence of the collection and removal of this ash on the voltage and current characteristics of these two fundamental precipitator components.

It is generally accepted that if the collected layer of high resistive material is thin, it will not unduly diminish the level of charging current. As a result, collection surface rapping response specifications often require 50 G's acceleration as a minimum acceptable level. When these requirements were first released, precipitator manufacturers responded with claims for their equipment that were disimilar. This apparent inconsistency, all based on credible records, gave rise to the question as to whether there was a single rapping technique more desirable than any other.

To resolve this question we initiated a multi-phase program to study the dynamics of rapping and develop appropriate hardware. The project was comprised of a literature search, a field pilot study, a comparison of rapping response on three different full size collection surfaces and the design and testing of new hardware.

This paper is a brief report on selected subjects from these studies.

Background

The published literature related to rapping was collected and reviewed. This information was compared to our knowledge of rapping, which had its beginning in 1962 with our first full size mechanical test facility. Following are some of the subjects on which there is general agreement.

Ninety percent of the authors agree with our experience that the most relevant directional component of acceleration for consistently predicting the removal of dust is the one perpendicular to the surface.

Measurements made during the subject project confirm published test results and therories that the sheet metal acutally buckles when struck in the plane of the metal. It physically moves in a serpentine manner.

The rapping shock and resulting wave transmission is similar to dropping a pebble into a pond of water surrounded by irregular boundaries in that the resulting ripples and their reflections add, subtract or cancel at different locations. It should also be understood that the shock waves on a collection surface are comprised of a spectrum of frequencies. The resulting sheet metal motion is therefore extremely complex. As a result, even under controlled conditions, repeatability of measurement is a problem. Add to this the fact that the impact energy diminishes as it moves away from the source and it is easily understood that the collection surface response to a rapper cannot be uniform.

As a rule of thumb, the acceleration of the metal controls the thickness of the collected layer and the rapping rate is related to the rate of deposit.

When a rapper strikes a collecting surface in an energized precipitator, only a small amount of material breaks free. The agglomerated dust breaks free only in those places where the shock wave can upset the balance between the mechanical forces within the layer, the electrostatic forces and gravity. Visual and photographic observations show that the removal of material looks like a miniature explosion in that the particulate matter is violently projected horizontally. The large agglomerates fall and the finely divided material moves downstream until it is recollected. If too much material is removed at one time, the resulting surge in dust concentration can influence the downstream voltage and current characteristics, and from an outlet field, the result will be a sudden increase in stack opacity.

Pilot Phase

In order to quantify the level of acceleration best suited to ash removal, a pliot precipitator was installed at a power station burning low sulphur coal and equipped with a hot side precipitator. The pilot was connected in a manner which permitted a portion of the flue gas to be taken from either before or after the large precipitator. In addition, a heat exchanger was installed ahead of the pilot unit to vary the temperature as desired. The collection surface response to rapping was measured before operation began making the unit a calibrated instrument. The results show that rapping requirements can vary with temperature. At both cold side and hot side temperatures the unit performing as an inlet field was best rapped at between 15 and 25 G's (average). When performing as an outlet field at the hot side condition, no change was required in rapper intensity, however, at cold side temperatures, a range of 65 to 85 G's (average) was required for best performance. Raising the rapping intensity above these levels always caused excessive reentrainment and created a significant increase in the scatter of efficiency data.

The conclusion is that 50 G minimum is acceptable as a design specification. That is, the equipment should be capable of achieving this level, but the actual operating values must be selected wisely because even high resistivity ash can be rapped excessively.

Full Size Test Tower Evaluation

In order to establish an understanding of accepted rapping practice in the air cleaning industry, three different types of collection surface configurations were selected for comparison. One configuration consisted of separated vertical panels joined only at the top and bottom by a common member and rapped at the bottom. The second was a structural frame with many sheet metal panels attached to it. The third was made of vertical panels interlocked along their adjacent edges and attached to a stiffener at the top and bottom. The latter two styles are top rapped. Each of the three designs has a long history of good performance and in combination they are believed to adequately establish a typical range of usable characteristics.

Test specimens of types one and two were direct copies of other manufacturers equipment and the third was our standard design. The corresponding suspension system was also duplicated for each system. All were installed in the largest and newest of our two test towers. All of the collection surfaces were the same size, 3.94 meters wide by 14.76 meters high.

The analytical experience used for this phase of the project was accumulated from the many tests conducted over the years in our mechanical test facilities. This background provided a complete awareness of the complexity of this kind of measurement and a concerted effort was made to control as many variables as practical. Instrumentation and techniques were selected with care, in fact, as many as fifty accelerometers were used in order to eliminate variations resulting from relocation and

attachment. In this way a variety of tests could be conducted without disturbing the instruments or the test specimen. The measurement system had a flat frequency response to 30 KHz. The accelerometers weighed 0.4 grams and were attached with a quick curing adhesive. The acceleration from each location was measured with a peak reading voltmeter (zero to peak). A frequency spectrum analyzer was among the instruments used.

Rapping for all tests was of the single impulse type; specifically, a mass falling by gravity. Each surface received an impulse of 13.56 joules (10 ft. lbs.). This value was selected arbitrarily and does not represent field practice. To be consistent, a 27 joule (20 ft. lbs.) impact was used for the two systems which rap two plates simultaneously.

The two top rapped systems typically use two rappers, one near the leading edge and one near the trailing edge. Previous testing experience demonstrated that the two rappers essentially act independently, therefore, the response to rapping was assumed to be symetrical about the vertical centerline. The bottom rapped plate was fully instrumented because only one rapper was used. This technique is consistent with the understanding of dust removal as described earlier. That is, the layer thickness is determined by the rapper closest to the location in question (maximum acceleration).

The patterns of acceleration are shown in Figures 1, 2, and 3. The differences are the result of the methods of construction and the influence this has on the characteristics of wave propagation and the frequency composition of the response. The frame or drum head construction produced the strongest low frequencies, the lowest acceleration levels and, therefore, the greatest displacement. The separated slender panels contained the highest frequencies, highest acceleration and, therefore, smaller metal displacement. The interconnected panels produced a response characteristic between and overlapping the other two responses. The three styles are similar in their lack of uniform distribution.

The significant frequencies ranged from 10's of Hz to 10,000 Hz. One frequency spectrum for each style is shown below. Actually, the frequency composition is not consistent over the surface of any of the test specimens. The cause of this is the complexity of the wave motion as mentioned in the background section of this paper. Therefore, these data samples serve only to graphically display our analysis and cannot indicate the variety of characteristics that can be found.

FREQUENCY SPECTRUM
0 TO 10KHz

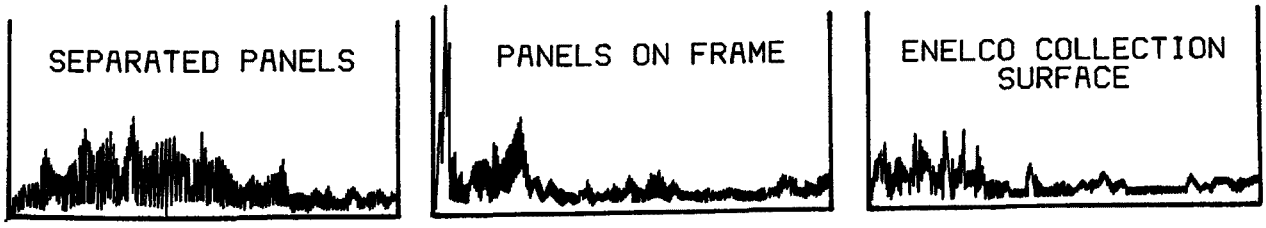

ENELCO COLLECTION SURFACE PANELS ATTACHED TO FRAME

RAPPING RESPONSE (G)
SIZE - 3.94m X 14.76m
FREQUENCY RANGE TO 30 KHz
RAPPING ENERGY-13.56 JOULES

RAPPER RAPPER

315	863	465	338	338	465	863	315
325	782	380	220	220	380	782	325
263	587	423	188	188	423	587	263
183	320	260	253	253	260	320	183
187	340	220	135	135	220	340	187
177	338	258	107	107	258	338	177
167	350	203	193	193	203	350	167
138	233	218	140	140	218	233	138
120	198	175	127	127	175	198	120
173	305	197	122	122	197	305	173

FIGURE 1

RAPPER RAPPER

195	193	193	195
133	132	132	133
107	78	78	107
83	65	65	83
70	75	75	70
100	68	68	100
88	90	90	88

FIGURE 2

SEPARATED PANELS
RAPPING RESPONSE (G)
RAPPING ENERGY-13.56 JOULES
FREQUENCY RANGE TO 30 KHz

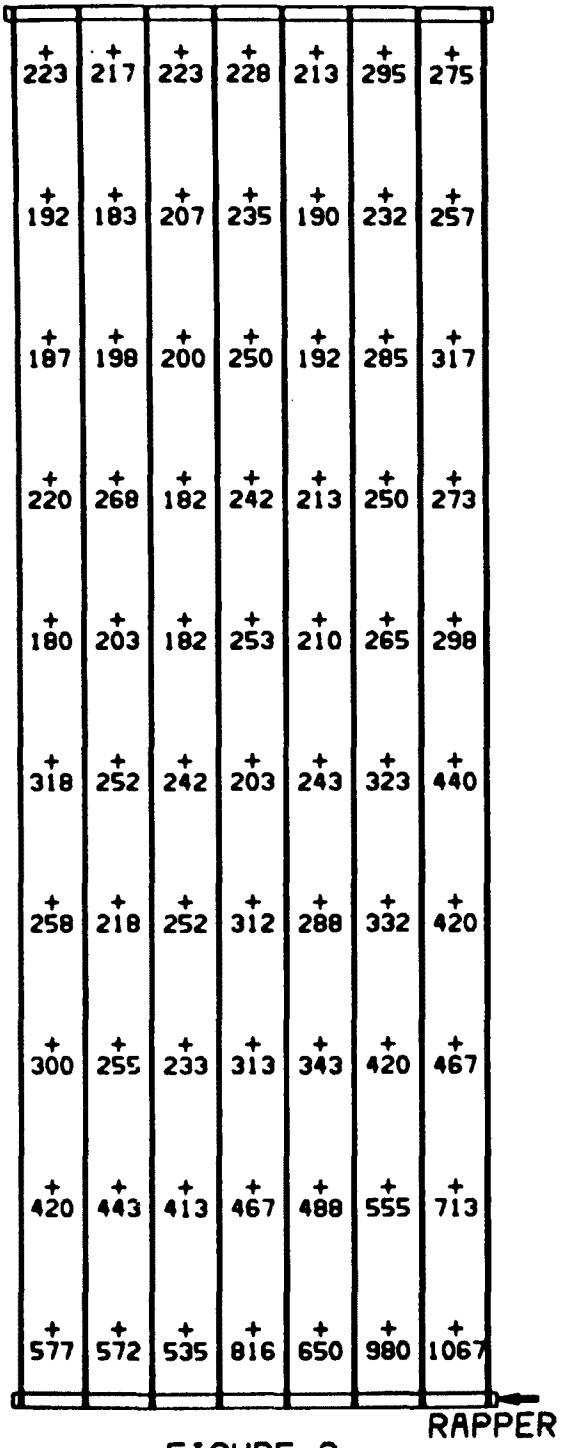

FIGURE 3

ENELCO COLLECTION SURFACE
RAPPING RESPONSE (G)
RAPPING ENERGY-6.8 JOULES
FREQUENCY RANGE TO 30 KHz

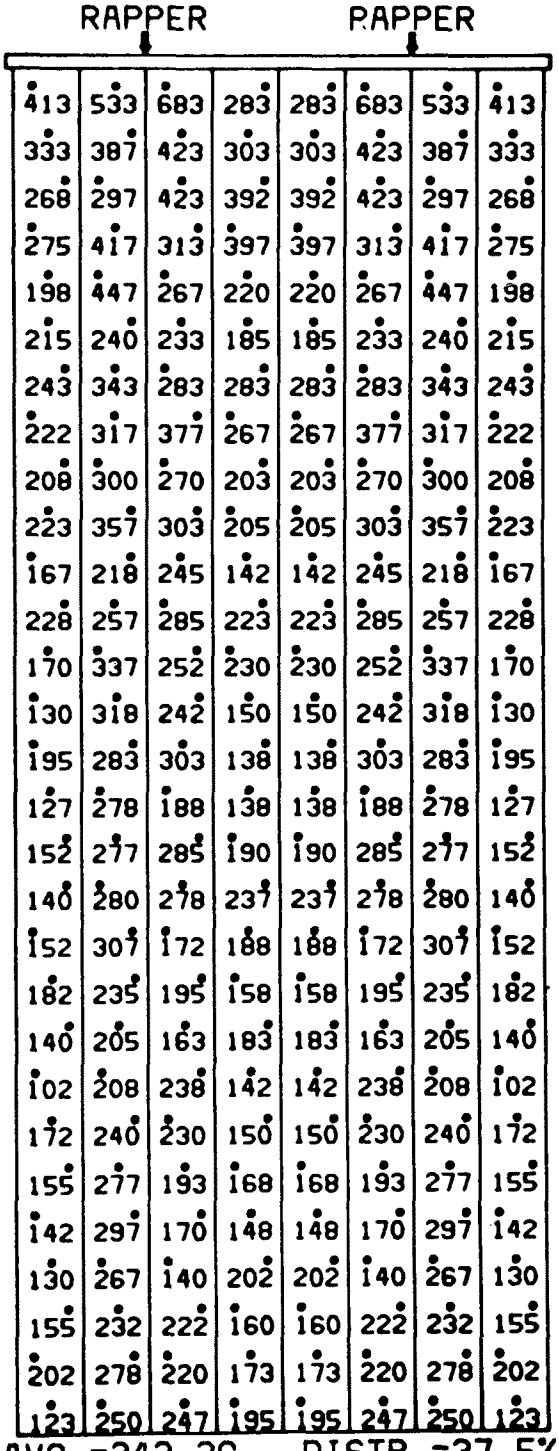

AVG.=243.3G DISTR.=37.5%

FIGURE 4

Realizing that all three styles of collecting surfaces are capable of providing good performance and discounting the influence of the mass of the dust on the frequency content, it could be conjectured from their wide range that frequency and displacement are variables of no practical value. However, if there are desirable frequencies they would most likely be found below 3,000 Hz which is the upper limit of the common frequencies on these three clean surfaces.

The analysis of the data below 3000 Hz does not permit a selection of one combination of acceleration and frequency as being typical and therefore the best. In fact, based on the variations found on an individual surface, it appears that a variety of combinations must be accepted. Even if a good combination exists it is probable that the practical limitations for design and fabrication leave acceleration as the only controllable variable; which is what the single specification of minimum acceleration implies. This is disappointing from a technical viewpoint but it does relieve the difficulty and added cost of precision engineering.

Additional testing of the interconnected panel design revealed that a stronger top stiffener would improve rapping transmission and durability. Test specimens using a new stiffener were installed for further testing.

The improved interconnected panel specimens were evaluated with a higher density of measurement locations. The locations were spaced uniformly vertically, but, one of three positions was randomly selected horizontally to lessen the influence of instrument location. Two sets of data were collected. The first contained all frequencies up to 30 KHz. The second contained only those frequencies below 3 KHz because of the observation described previously. See Figures 4 and 5. It is interesting to note that the level of indicated acceleration was changed by altering the frequency content but the distribution was not. (Distribution is defined as the standard deviation expressed as a percentage of the average.)

The 3 KHz test was continued in order to determine the energy required to meet two logical forms of a 50 G specification. One form is the minimum and the other is the average. Because of the transmission efficiency resulting from directly striking the new top stiffener, only 4.3 joules (3.2 ft. lbs.) were required to provide a 50 G minimum. The corresponding average value, however, is greater than the average value indicated in the pilot study inplying that this amount of energy is not always necessary. See Figure 6. An input of 1.15 joules (0.85 ft. lbs.) produced a response pattern with an average of 46 G and a minimum of 26 G. Which of these forms is the best is not clear but knowing the range of dynamic response is fundamental to selecting operating parameters and maintaining a history of performance.

Additional information, for use when designing rappers for the top rapped interconnected panel, was obtained by comparing the response from a magnetically, pneumatically and gravity driven cylinder of metal. There was no significant difference in response characteristics. Following this,

ENELCO COLLECTION SURFACE
RAPPING RESPONSE (G)
FREQUENCY RANGE TO 3 KHz

RAPPING ENERGY-6.8 JOULES

RAPPER RAPPER

187	270	293	222	222	293	270	187
243	240	208	233	233	208	240	243
118	185	170	220	220	170	185	118
120	217	213	185	185	213	217	120
100	200	130	143	143	130	200	100
108	120	147	115	115	147	120	108
117	207	153	130	130	153	207	117
92	122	120	160	160	120	122	92
110	138	160	120	120	160	138	110
112	140	137	102	102	137	140	112
72	145	128	92	92	128	145	72
88	158	175	107	107	175	158	88
97	150	130	115	115	130	150	97
92	125	140	97	97	140	125	92
98	123	117	83	83	117	123	98
60	105	87	100	100	87	105	60
82	108	105	98	98	105	108	82
75	147	100	90	90	100	147	75
70	92	102	80	80	102	92	70
88	145	105	87	87	105	145	88
77	145	98	90	90	98	145	77
70	138	115	78	78	115	138	70
75	85	85	83	83	85	85	75
83	118	90	77	77	90	118	83
80	147	97	80	80	97	147	80
80	105	63	98	98	63	105	80
83	98	108	88	88	108	98	83
82	110	98	77	77	98	110	82
90	137	102	75	75	102	137	90

AVG.=122G DISTR.=38.1%

FIGURE 5

RAPPING ENERGY-4.3 JOULES

RAPPER RAPPER

178	228	217	182	182	217	228	178
183	168	162	157	157	162	168	183
133	188	117	125	125	117	188	133
128	185	170	150	150	170	185	128
87	185	105	118	118	105	185	87
95	120	125	112	112	125	120	95
105	180	142	105	105	142	180	105
97	103	107	140	140	107	103	97
118	152	103	102	102	103	152	118
87	133	132	93	93	132	133	87
78	118	102	64	64	102	118	78
88	163	152	87	87	152	163	88
69	120	123	92	92	123	120	69
80	107	117	79	79	117	107	80
95	108	86	56	56	86	108	95
50	92	63	77	77	63	92	50
59	110	77	63	63	77	110	59
61	95	77	63	63	77	95	61
52	85	69	65	65	69	85	52
63	115	89	65	65	89	115	63
67	105	70	73	73	70	105	67
67	102	91	67	67	91	102	67
58	81	93	81	81	93	81	58
69	102	72	61	61	72	102	69
76	101	73	76	76	73	101	76
77	87	55	65	65	55	87	77
69	94	94	80	80	94	94	69
69	91	74	61	61	74	91	69
67	114	81	77	77	81	114	67

AVG.=102G DISTR.=37.1%

FIGURE 6

the gravity device was used to evaluate the influence of velocity at time of impact. Using a constant 27 joules (20 ft. lbs.), various weights were dropped from corresponding heights up to 3.28 meters (10 ft.). In general the response had the same frequency components under all conditions. However, the low velocity impact slightly raised the signal level of some of the low frequencies and the high velocity strengthened the upper end of the spectrum, but the difference is considered to be insignificant. It is therefore possible to conclude that the single impulse rapper mechanism for the interconnected panel style may be selected on the basis of economics and preference, assuming the energy output is acceptable. The required energy is of course a function of each system design.

Discharge Electrode Development

The challenge of collecting high resistivity dust with very high efficiency has also influenced the requirements for discharge electrodes. These now include the following.

1. Be suitable for tall systems, which are becoming more prevelant in this application.
2. Possess cleaning characteristics like those of the collection surfaces.
3. Enhance the collection efficiency as compared to wire electrodes.
4. Have high spark over voltage.
5. Have selectable voltage/current characteristics.
6. Be tolerant of in service abuse.

The electrode developed to meet these requirements is based on a tubular shape. This characteristic alone responds to many of these specifications. The tubes provide good vibration characteristics, significnt additional collecting surface, durability, a strong electrical field and high spark over voltage. Pointed corona emitters attached to the tube provide early corona onset and the number of emitters per length of tube determine the voltage/current characteristic.

The variability of the voltage/current relationship has a significantly wide range considering that the large diameter tube extends the voltage capability by raising the spark over limit. An example of this flexibility is shown in Figure 7. It is evident that the slope of the EI curve can be varied to achieve the two best characteristics, i.e., early corona onset combined with reasonable current usage at high voltage. These data were obtained in air in the laboratory but the relationship has been confirmed in actual operation.

It is typical of the breakdown voltage of air in the laboratory to vary with temperature and humidity. Figure 8 demonstrates the spark over advantage of the tubular shape during a time when the wire electrodes were limited by sparking. The full size installations containing this electrode exhibit little or no sparking after the inlet field, which, compared to past experience, confirms the lab prediction. From earlier field observations and this small amount of evidence, it is possible to conjecture that a significant amount of sparking in weighted wire systems

collecting high resitivity ash occurs in the vicinity of where the wires pass the top and bottom of the collection surface.

DISCHARGE ELECTRODE
VOLTAGE AND CURRENT RELATIONSHIP

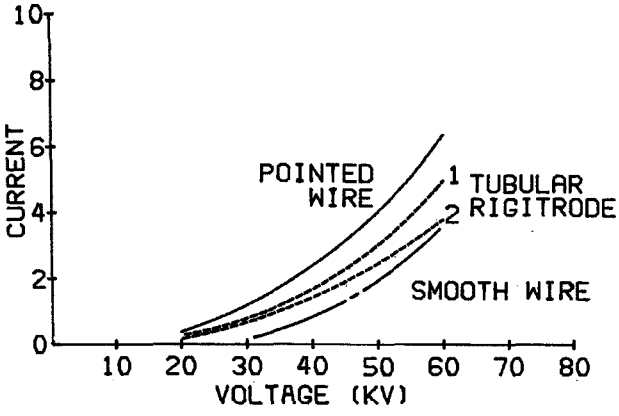

FIGURE 7

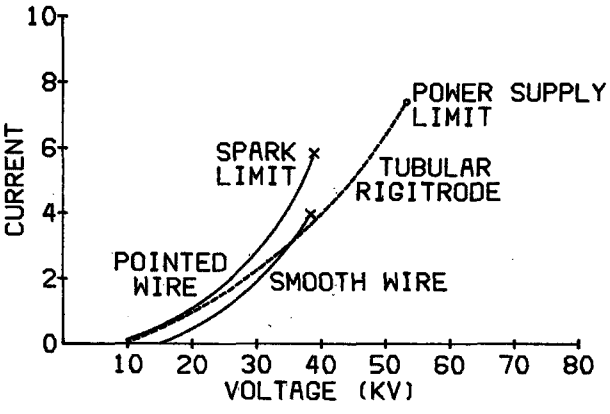

FIGURE 8

The cleaning characteristic of these electrodes is interesting. In addition to being capable of a 50 G minimum surface acceleration, the vibration is sustained. In a clean state, the motion is not totally damped for as long as 2 to 4 seconds. This action is similar to a musical chime. The pointed pins, being attached to the highly active surface, remain dependable corona emitters because they do not retain excessive dust coatings.

Total System Capability

Three precipitators containing this new technology are in service and three are under construction. The collection surface rapping is the same for all collection surfaces in the operating units. A midrange value of 3.05 joules (2.25 ft. lbs.) per collection surface was selected. It will be difficult at best, and certainly premature at this time, to quantify an enhancement factor over weighted wire for the new system. The only firm data in hand is a 25% improvement in drift velocity determined by pilot tests. Nevertheless, the test results from the first three installations support the expectation that an exciting improvement in precipitator technology has been achieved.

Acknowledgement

The test measurements and analysis were supervised by K. Teel, a member of the Technical Department at the time, and his fine work contributed to the success of the project.

AN APPLICATION SUMMARY OF HIGH ENERGY SONIC CLEANING APPLIED TO ELECTROSTATIC PRECIPITATORS

By:

Michael J. Berlant
KVB, INC.
18006 Skypark Blvd.
Irvine, CA 92714

ABSTRACT

Acousticlean sonic sootblowers, or "horns", are low frequency, high energy acoustic devices that have demonstrated an ability to solve many of the particulate buildup problems associated with the operation of electrostatic precipitators. Particles clinging to surfaces are dislodged by sound wave vibrational energy.

The paper describes four applications reducing particulate buildup in the precipitator. The areas cleaned are the inlet duct, turning vanes, distribution plates, and wires and collector plates. The result of using the sonic cleaner has been an extension of precipitator on-line times and an increase in efficiency.

INTRODUCTION

Low frequency, high energy sonic cleaning provides an operational and economic alternative to traditional methods of cleaning particulate buildup in electrostatic precipitators. Initially used by Inspiration Consolidated Copper (ICC) company to mitigate particulate buildup on a precipitator inlet distribution plate, the Acousticlean sonic sootblower is currently used to clean particulate buildup throughout the precipitator. The results of applications that followed ICC have been extended precipitator on-line times and increased precipitator efficiency. These results are due to continuous particulate removal provided by short, but frequent, blowing of the sonic cleaners.

Areas of Particulate Buildup in the Precipitators

A wide variety of industries use electrostatic precipitators to remove solid particles from their flue gas discharge. The particulate in the flue gas varies from pulp mill salt cake to copper smelter metallic oxides to utility coal ash. The particulate may build up in one or more of the following areas in the precipitator:

- inlet duct
- turning vanes
- distributor plates
- wire electrodes and collector plates
- ash hoppers
- outlet duct

Particulate buildup in these areas can require frequent shut-downs for cleaning and can reduce operating efficiencies. Strategically located sonic horns can mitigate or eliminate buildup in these areas.

Before discussing typical sonic horn applications in these problem areas, the next section describes the horn.

The KVB Acousticlean Sonic Sootblower (Horn)

Figure 1 is a picture of the KVB horn. Horns are low frequency, high energy acoustic devices--250 Hz and 145 dB. The bell is made of cast stainless steel and is good for temperatures of 1900°F (1040°C). There is only one moving part--a titanium diaphragm.

The horns operate on compressed air in the 60 to 80 psi range. Plant air is satisfactory and instrument air is not required. Air consumption during insonation is about 60 SCFM. They are turned on and off by actuating a 110 volt, normally closed, solenoid valve. In operation this valve is controlled by an automatic electric timer.

Each horn weighs 55 pounds and measures about two feet in length and one foot in diameter at the mouth of the bell. The bell is bolted to the housing to facilitate installation. Diaphragms--which should last six months to one year--are replaced by simply unbolting the back of the diaphragm housing. An oil mister in the air inlet line can be used to extend the life of the diaphragm. In operation the diaphragm is cooled by a continuous air flow of three to five SCFM.

Soot and other particles clinging to surfaces are dislodged by sound wave vibrational energy. The wave pressure fluidizes particles by breaking their bond with other particles and the surfaces to which they cling. Once "fluidized," particles will flow from surfaces by gravity or gas stream pressure.

Sound pressure level is a physical measure of the strength of a sound and is defined by the following equation:

$$L_p = 10 \log \left(\frac{p}{p_o}\right)^2 = 20 \log \frac{p}{p_o}$$

L_p = sound pressure level in dB
p = sound pressure in Pa
p_o = reference sound pressure, 2×10^{-5} Pa

Sounding two horns simultaneously will double the sound pressure or increase the energy level by 3 dB.

The "fluidizing" effect is compounded in an enclosed space where large, solid surfaces reflect sound waves, creating a homogeneous vibrational energy field.

PAPER AND PULP MILL RECOVERY BOILER EXIT DUCTS/ PRECIPITATOR INLET DUCTS

Weyerhaeuser Company in Longview, Washington, is using ten horns in its recovery boiler economizer hoppers and exit ducts/precipitator inlet ducts. Saltcake buildup in the ducts gradually restricted load on the boiler and channeled inlet air adversly to the precipitator.

This recovery boiler is a 1,090,000 Kilograms per day (1200 TPD) low-odor design in which the flue gas flows directly from the economizer outlet to an electrostatic precipitator. The exit ducts to the precipitator are inclined upward at a 45° angle, as shown in Figure 2. Saltcake build-ups tend to occur in the rear sections of the economizer hoppers and in the inclined exit ducts. The problem is believed to stem partly from high-sulfidity pulping, which appears to produce unusually sticky ash, as well as from the sharp turn the flue gas must negotiate as it exits the boiler. The problem was sufficiently severe that it gradually reduced maximum load on the unit as each scheduled maintenance and cleaning period approached.

The mill rejected the addition of more steam lances to solve this problem because of their relatively high initial cost and the continuing steam penalty required to operate them. Vibrators were also rejected because they would apply unwanted stress to the ductwork and also because they are intended to flow the solids downhill, which in this case is against the gas flow. Horns were selected primarily because they would fluidize the solids so that they would be carried with the flue gas into the precipitator.

During the Christmas outage of 1978, four horns were installed in the economizer hoppers and exit ducts as shown in Figure 2. Due to the rapid rate of saltcake buildup and the sticky nature of the saltcake, it was found best to sound the horns rather frequently. They each operate for 10 seconds at three minute intervals. The horns have proven successful in reducing the buildup problem to the extent that it no longer restricts load on the unit.

Due to the shallowness of the exit ducts, which are only 1.22m (four feet) deep, the sound energy from the horns does not have an opportunity to spread very much before reaching the bottom of the ducts. Therefore, each horn cleans only a fraction of the duct in which it is located. Each horn appears to clean an area approximately 1.53m (five feet) in diameter. In order to keep larger fractions of the ducts open, and thus provide a more comfortable margin of pluggage protection, Weyerhaeuser installed four horns in these ducts.

PAPER AND PULP MILL PRECIPITATOR TURNING VANES

Horns have been used by ITT-Rayonier at Jesup, Georgia, to reduce saltcake buildup at the inlets of two recovery boiler precipitators.

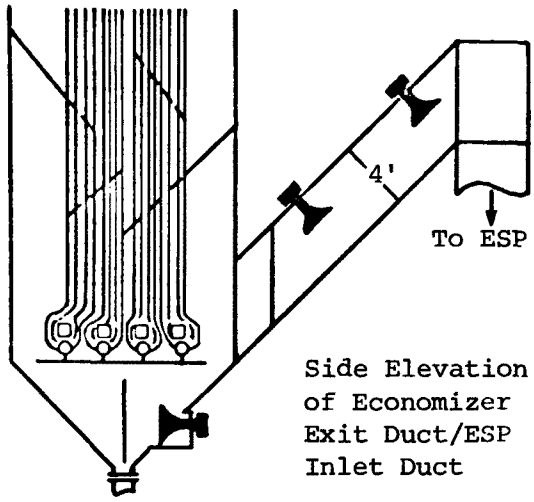

Side Elevation
of Economizer
Exit Duct/ESP
Inlet Duct

Not to Scale
One Foot = 0.305m

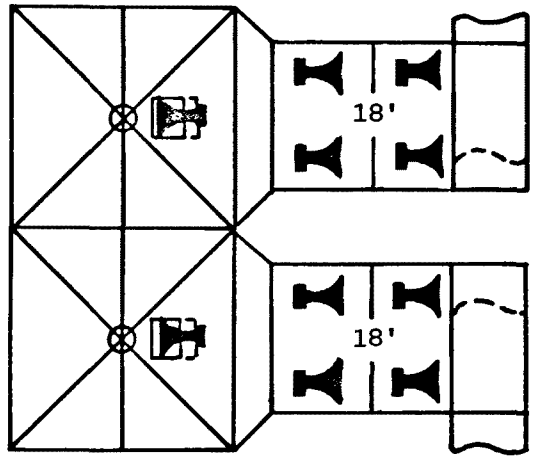

PLAN VIEW OF ECONOMIZER EXIT DUCTS/ESP INLET DUCTS

FIGURE 2. Application of Horns to Recovery Boiler Economizer Exit Ducts/ Precipitator Inlet Duct.

A secondary precipitator at the mill treats half the flue gas from three recovery boilers having a combined rating of 682,000 kilograms per day (750 TPD) of pulp. The precipitator has a history of saltcake buildup between turning vanes located in the inlet plenum. These deposits were observed at all scheduled maintenance outages and were normally removed by washing. During the Labor Day outage in 1979, two horns were installed on the top of the precipitator inlet plenum as shown in Figure 3.

The horns were set to operate simultaneously for 30 seconds at ten minute intervals.

At the Christmas outage in 1979, after nearly four months of horn operation, the turning vanes were observed to be free from saltcake build-ups with the exception of those parts of the top vanes lying outside of the conical sound patterns produced by the horns. The mill concluded that the horns were effective in controlling saltcake buildups.

COPPER SMELTER PRECIPITATOR INLET DISTRIBUTION PLATES

Two horns have been operating in an electrostatic precipitator that serves the flue gas from a copper smelter reverbatory furnace since July 1979. Prior to installation of the horns ash buildup in the inlet nozzle would bridge the gap between the inlet distribution plates. The ash would build upon itself until the flue gas was effectively channeled, resulting in the nozzle being blanked off by plant personnel for cleaning every two to three months. In January of this year the plant reported that after eighteen months of operation with the horns that the distributor plates have been clean and that the inlet nozzle has not been blanked off.

The copper smelter's reverbatory furnace is coal fired. The flue gas from the furnace contains coal ash and smelter dust (metallic oxides). The flue gas from the furnace enters the precipitator at 330°C (625°F) at a gas flow rate of about 5700 m^3/minute (200,000 ACFM). The flue gas is divided into three inlet nozzles one of which is currently blanked off. Each nozzle has distribution grids of 7.3m x 7.3m (24 feet x 24 feet) and 9.2m x 9.2m (30 feet x 30 feet), 76.2 centimeters (30 inches) apart.

The horns are installed forward of the first plate about mid-way in elevation as shown in Figure 4. The horns are operated simultaneously for 30 seconds every 20 minutes. The plant has not replaced the original diaphragms during the eighteen months of continuous operation.

The overall results of utilizing the KVB low frequency acoustic horns have produced several significant benefits. Use of the horns has increased total precipitator running time by eliminating the periodic shut downs to clean the inlet nozzles. The efficiency of the precipitator has increased from the even distribution of flue gas. The plant has saved the labor cost of cleaning the plates and the inlet nozzle.

COAL FIRED UTILITY PRECIPITATOR

A coal-fired utility in Spain began using horns in their electrostatic precipitator as a supplement to their rappers and vibrators about eighteen

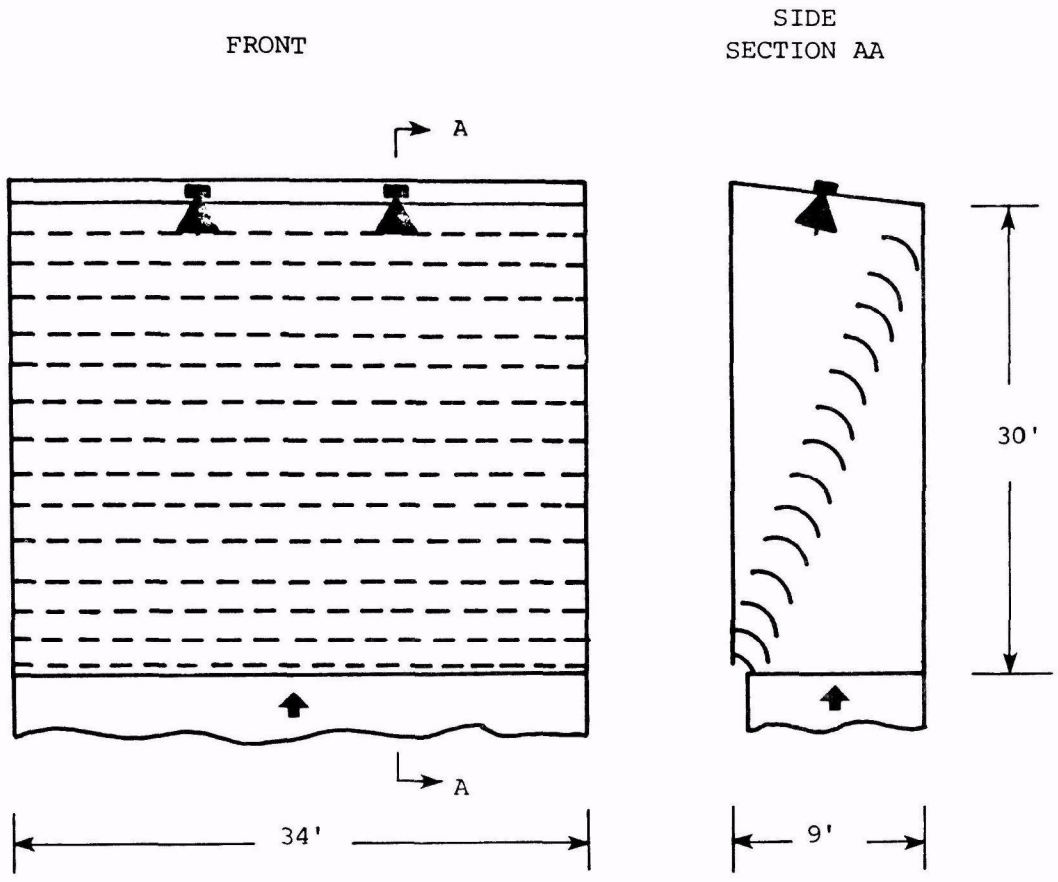

FIGURE 3. Application of Horns to clean turning vanes in Recovery Boiler Precipitator Inlet Plenum.

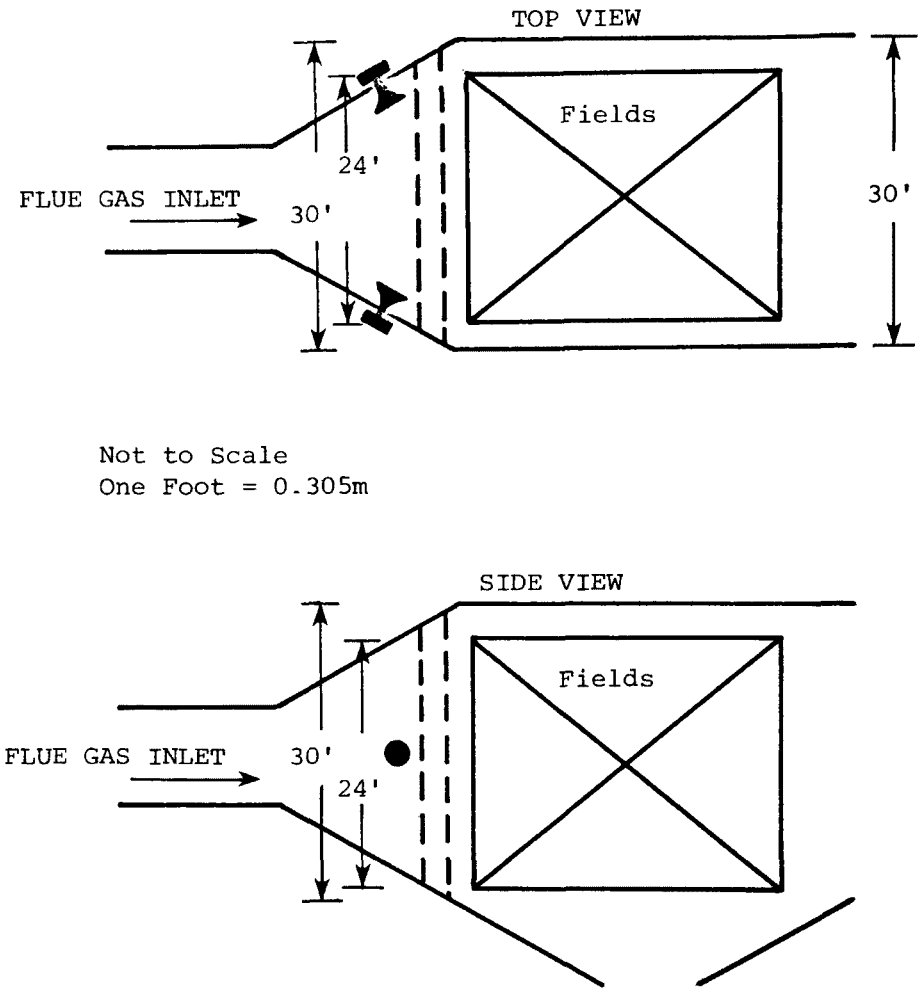

FIGURE 4. Application of Horns to clean Inlet Distributor Plates on Copper Smelter Precipitator.

months ago. The utility's Puertollano Station installed the horn in the roof of one precipitator chamber as shown in Figure 5.

The horns were installed after the plant had experienced problems that were related to the firing of low-sulfur coal (high resistivity/low conductivity ash). Heavy buildups of ash would occur rapidly on the plates causing sparking with the precipitator. The sparking would continue until an electrode would break. Electrode breakage was on the order of one per week. Operation would continue with one field grounded but the loss of a second field required shut down. Shut downs would occur every two weeks.

The horns are installed in a French design precipitator that serves a 220 megawatt, oil-or coal-fired boiler. Typically, the unit fires a low-sulfur Bituminous coal with an approximate ash content of 37%.

The precipitator at the Puertollano Station is a two-chamber unit with three fields per chamber as shown in Figure 6. The flue gas velocity through the precipitator chambers is about 2 meters per second (6-7 feet per second) at 100°C (212°F).

Because of the frequent precipitator shut downs, the plant initially tried steam injection to alleviate the ash buildups. The steam lowered the resistivity and increased the conductivity of the ash eliminating the heavy buildup on the wires but at a daily cost of $3,000. Due to the high operating costs with steam, the plant installed the horns.

Since initial horn operation began one and one half years ago, the precipitator has not had to come down because of an electrode failure. In addition to the elimination of steam injection, plant personnel have noted that the precipitator chamber with the horns removes higher levels of fly ash. This is evident when they compare the ash handling between the chambers.

The horns operate in series, with five seconds of operation and a two second delay between each horn on a continuous basis. The wire rapper cycle is one minute and fifty five seconds every ten minutes. There are fourteen collecting plate rappers that rap eight seconds each in a ten minute cycle.

The horn diaphragms are replaced every four to five months. The plant is not using an oil mister that could extend diaphragm life. Plant personnel are very impressed with the effectiveness of the horns and they intend to install nine additional horns in the second chamber of the precipitator.

CONCLUSIONS

The use of low frequency, high-energy acoustic horns significantly reduced particulate collection problems in electrostatic precipitators. The horns are effective on a variety of particulate types in a variety of industrial categories.

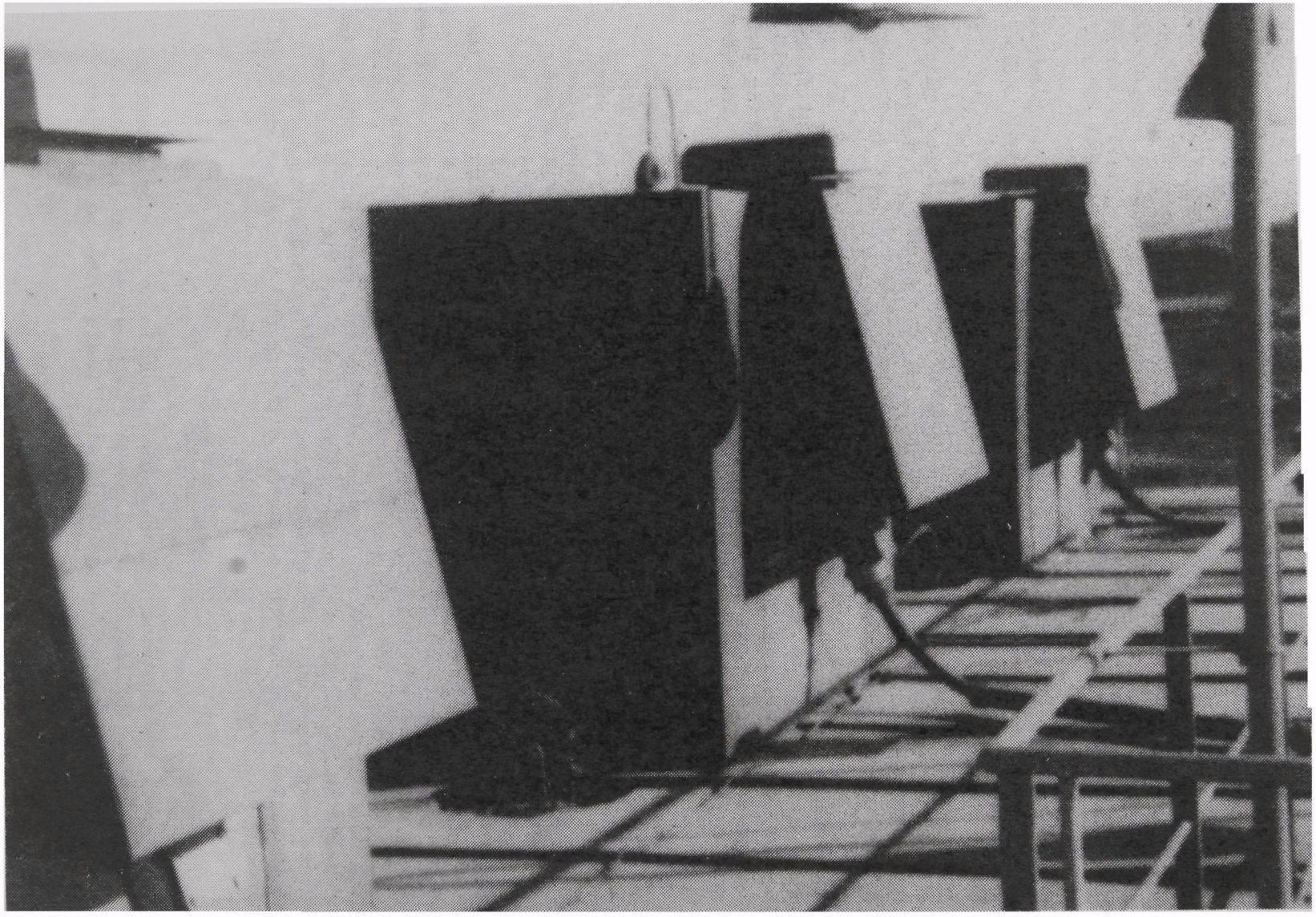

FIGURE 5. Horn Installation in Roof of Utility Precipitator.

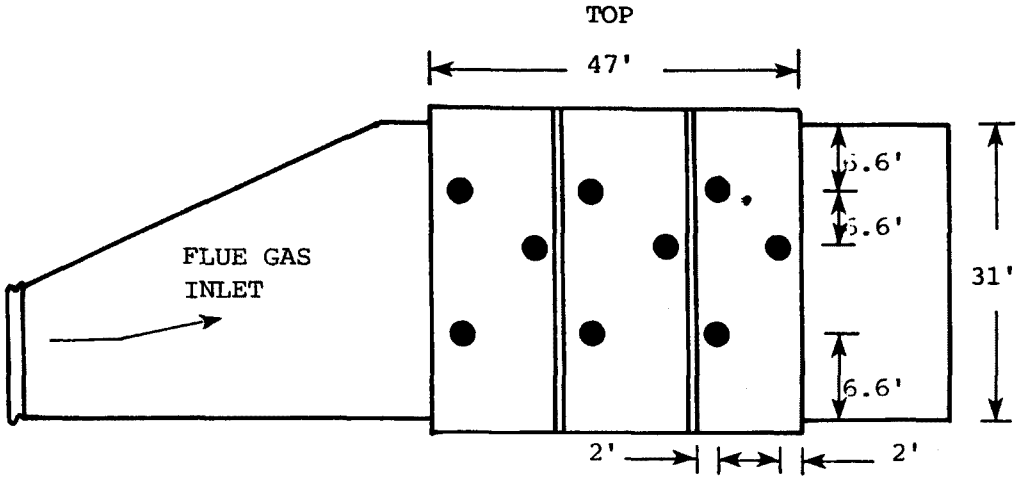

Not to Scale
One Foot = 0.305m

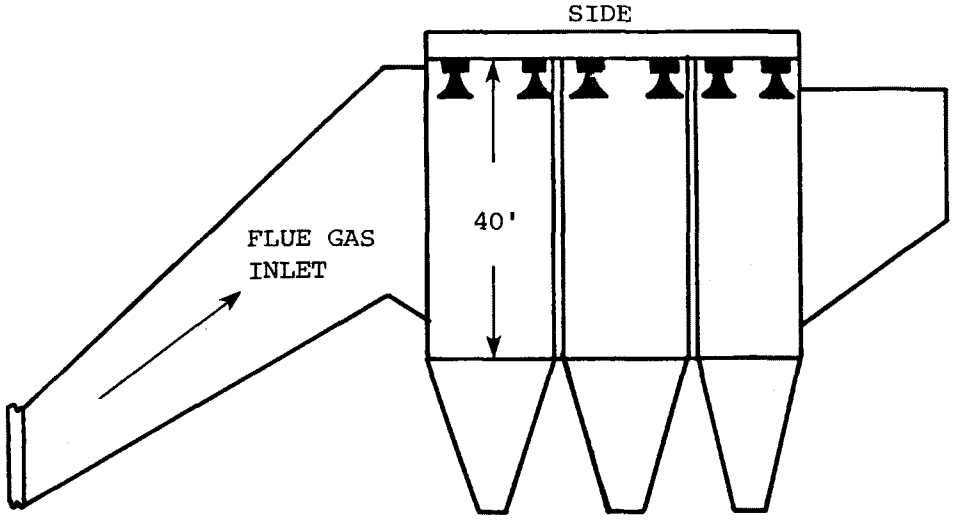

FIGURE 6. Application of Horns to Plates and Wires in Coal-Fired Utility Precipitator.

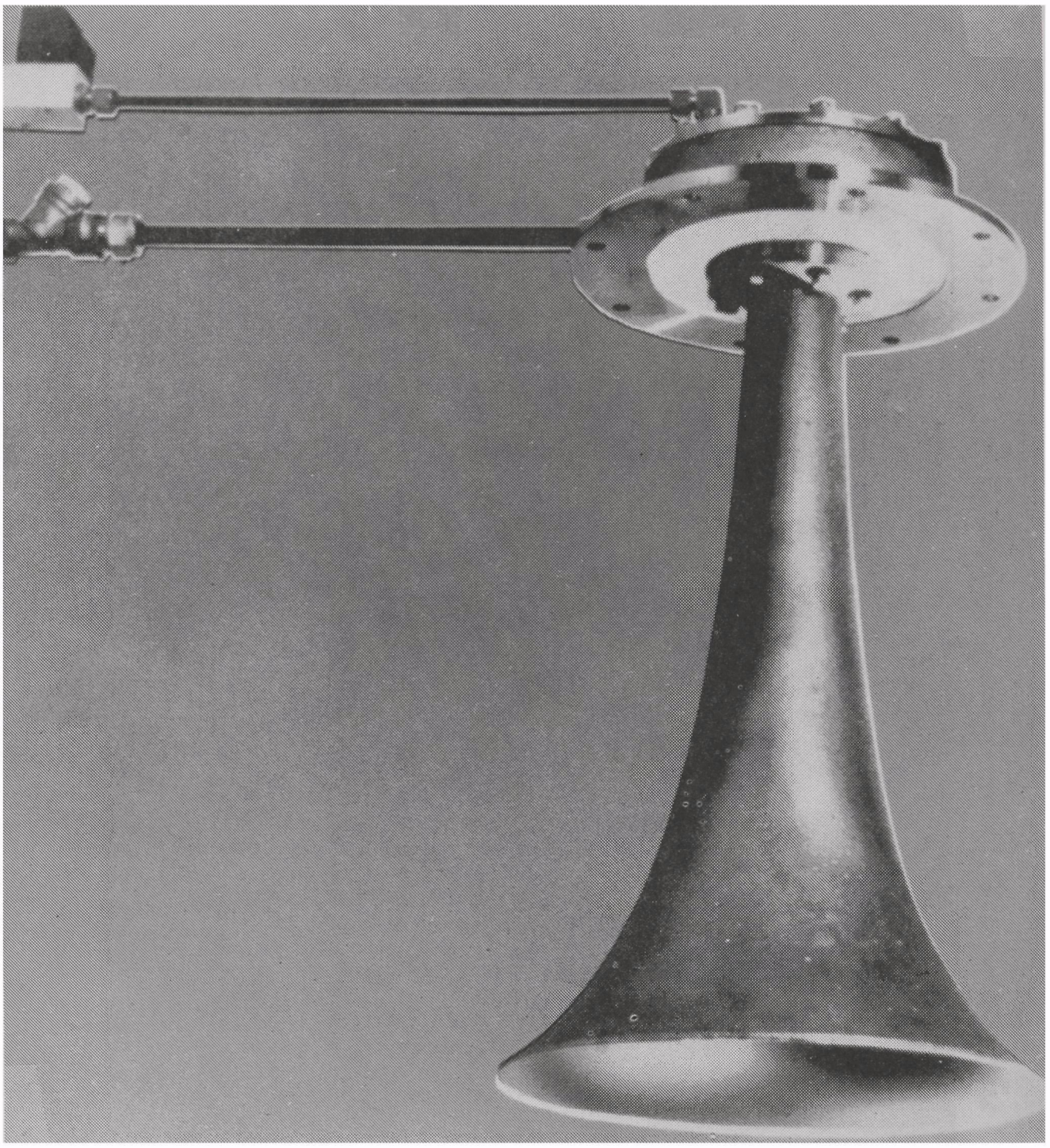

FIGURE 1. Acousticlean Sonic Sootblower.

The horns effectively reduced particulate buildup around the precipitator inlet ducts, turning vanes, distribution plates, and wire electrodes and collection plates. Plants using the horns have saved labor costs, reduced more costly alternative cleaning methods, extended the on-line time for the precipitator and, in some cases, observed an increase in precipitator efficiency.

THE IMPACT OF INTELLIGENT PRECIPITATOR CONTROLS

By: Dr. Norman Z. Shilling

Robert O. Reese

Jeff A. Fackler

Buell Emission Control Division
Envirotech Corporation
Lebanon, Pennsylvania 17042

ABSTRACT

This paper describes both operational hardware and supporting software which have been developed for microcomputer control of an electrostatic precipitator. Particular emphasis is placed upon operator-computer interaction and the need to ensure acceptance of the control concept at the plant level.

Specific examples of normal operator/control system interactions are drawn from an actual microcomputer-controlled precipitator which is serving a utility boiler. The microcomputer provides a significant scope of flexibility to obtain maximum precipitator performance consistent with low power consumption. Transformer-rectifier power disposition and rapping parameters are controlled by opacity feedback and other key precipitator operating parameters. The logical structure of the adaptive/recursive software which provides this control is described. Features of microcomputer control are outlined which will provide increased reliability and nearly failsafe operation.

INTRODUCTION

Intelligence is defined as the capacity for reasoning and understanding. With regard to a microprocessor/microcomputer-controlled (i.e., intelligent) precipitator, we would modify this definition to "the ability to provide a logical sequence of responses based upon a perception of operating conditions". The endowment of mental faculties to equipment that sometimes is viewed as the manifestation of black magic may bring shivers to some. Hopefully, this paper will put such fears to rest by rigorous definition of the benefits attainable with microprocessor control. The questions which are addressed here are, in turn, (1) how is it implemented in terms of both hardware and software, (2) how is it structured to ensure acceptance and proper utilization by plant personnel, and at the bottom line, (3) how is it expected to impact plant operation?

In answer to the last question, and as a capsule summary of this presentation, the Intelligent Precipitator will impact immediately on two fronts -- specifically, improved maintainability (and ultimately availability) and reduced operating power consumption. In plant operation, previously the sole edict which came from "on high" was to keep the plant operating. Now the directive is to keep the plant running and do it efficiently.

The hardware and interactive software described here are presently in

service at an operating power plant. The high level software which provides performance optimization is now being qualified. There are no technology barriers standing between this point in time and universal adoption of this concept. However, achievement of the full potential of computer control in the plant will, in large part, depend upon acceptance in the "trenches" through day-to-day operation, how it treats, and how it is treated by operating plant personnel. This aspect of operation constitutes a very important aspect. Appropriately, it is discussed first.

OPERATOR/INTELLIGENT PRECIPITATOR COMMUNICATION

In the Buell Intelligent Precipitator, operational control proceeds on two levels. Monitoring, logging and direct operator control constitute the primary level. Here, detailed error and failure conditions are provided to the operator, as well as key precipitator operational parameters via CRT, typewriter, and control panel annunciation. At the operator's discretion, and similar to present standard precipitator control systems, he can choose normal threshold of sparking control in which the microcomputer defers TR control to the stand-alone microprocessors (AVCON 2000 Boards). These would normally have full responsibility for control in a standard system. The operator also has the choice of using default rapping parameters or entering his own. But this is where the functional similarity ends between standard and Intelligent Precipitator controls.

With Intelligent Precipitator controls, the operator has the option to make the control of rapper parameters and TR set operation the responsibility of the microcomputer. Adaptive control decisions can be made by the Intelligent Precipitator on the combined basis of opacity and long-term electrical performance trends which are normally transparent to an operator during a single shift, or even a 24-hour period.

First, however, we illustrate interactions at the primary level.

THE CRT

The first and most striking physical difference between standard and computer controls begins at the CRT and chassis for the Intelligent Precipitator (Figure 1). These controls will be located in the plant Control Room, rather than at an area remote from other data. This simple physical change in location will likely impact the operator's fundamental attitude towards the precipitator, helping him to recognize it as an integral part of the plant.

To give an idea of the control flexibility, available commands include the following:

Rapper System

1. Change of a rapper row round trip time
2. Change of a specific rapper frequency
3. Change of a rapper row lift (ft/lbs)
4. Change of a specific rapper lift (ft/lbs)
5. Obtain a graphic illustration of rapper configuration by number and location
6. Display round trip summary

7. Choose a high level rapper system control

TR System

8. Change TR control set point as a % of full KVA
9. Display TR control operating point summary
10. Display electrical condition operating summary
11. Choose high level control of TR voltages (power consumption minimization)

General System

12. Display time
13. Set real time clock
14. Program tape copy
15. Copy from CRT or tape to keyboard

Actual CRT displays which, for example, are obtained for Commands #5, #6 and #10 are shown in Figures 2, 3 and 4, respectively. With these controls and commands in closer proximity to both operation and plant data, it is likely that anticipatory changes in control corresponding to operating plant conditions will be made. Also, precipitator operating trends leading to possible fault conditions will be more easily perceived due to detailed graphic display and 24-hour data summary which can be called on the CRT.

FAULT DETECTION

The primary control level detects and announces various faults on the terminal screen, performs automatic initial action, and logs the type and time of failure in hardcopy on the typewriter and system tape. For a specific example of how major fault conditions are handled, consider the response to a rapper short circuit: This fault will cause the computer to interrupt any present tasks and handle the shorted rapper in the following manner:

1. Power is removed from the rapper upon completion of the present half cycle.
2. A special program determines the rapper number and saves it.
3. An alarm sounds, alerting the operator.
4. The TIME, DATE and RAPPER NUMBER are displayed on the Terminal screen.
5. The above sequence will be repeated until the rapper is taken out of service for repairs.

Some other faults that are addressed by the system are:

Rapper Open Circuit

Rapper High Current

Rapper Low Lift

Field Box -- cable open condition

Field Box -- power loss

TR Short

TR Open Circuit

TR Over Temperature

Precipitator Below Energization Temperature

Precipitator High Temperature

Purge System Failure -- fan or heaters

And, of course, any other additional precipitator or plant paramaters as necessity or whim requires. The specific hardware configuration which accomplishes this is described in the next section.

INTELLIGENT PRECIPITATOR CONTROL ARRANGEMENT

The Intelligent Precipitator operates in a real time mode and implements distributed rapper control, TR control, and analog/digital I/O control, all connected to a central microcomputer via several data bus pathways. Figure 5 shows the Intelligent Precipitator layout. This arrangement reduces wiring and installation cost while increasing precipitator control reliability.

The control system for the rapper matrix are microprocessor-based and function independently of the host computer. They can be downloaded from the host computer or connected to a local terminal via a serial data bus. The TR controllers can be programmed to send and write data to the host computer via a serial data bus. As previously mentioned, the T/R controllers can also function independently of the host computer.

The various subsystems that comprise the control system are: (Figure 5)

I. AVC Control Center

The AVC Control Center is comprised of T/R automatic voltage control cabinets, each having a full complement of analog meters, start-stop switches, low voltage contactors, and power silicon control rectifiers (SCR's). In addition, each T/R Automatic Voltage Control (AVC) cabinet contains two companion boards:

a. The AVCON 2000 Automatic Voltage Controller Board monitors T/R secondary current changes and closes the loop by phase-controlling the power SCR's in the T/R primary circuit.

b. The Communications Board provides a serial interface between the Host Computer and its associated AVCON 2000 board. T/R primary and secondary currents and voltages along with spark rate date are multiplexed, digitized and transmitted on the bus to the Host Computer. The Host sends formatted control data to each T/R AVC board through the Communication Board interface.

The present configuration is comprised of a three-wire serial bus. AVCON 2000 boards are daisy-chained on the serial bus up to a distance of 500 feet from the Host Computer. In the event the Host Computer is out of service, the AVCON 2000's revert to automatic mode.

II. Rapper Controller

Each Rapper Controller is microprocessor-based and functions independently of the Host Computer. A precision zero crossing detector serves as the master clock signal to time the operations. In addition, a hand-held portable terminal can be used in place of the Host Computer interface port to enter lift and timing data as well as display rapper status.

Round trip times and lift values in foot-pounds can be downloaded to each Rapper Controller via the serial interface bus at initialization time. In the event of a power failure, the battery back-up mode of operation is invoked and the Rapper Control continues to function.

In the event of a rapper failure, the RAPPER NUMBER, FAULT, TIME AND DATE are locally displayed on the local rapper status display and the same data is transmitted to the Host Computer via the serial interface bus.

The present configuration is comprised of a three-wire serial bus. Rapper controllers can also be daisy-chained on the serial bus to a distance of 500 feet from the Host Computer.

III. Analog and Digital Input/Output Controller

The Analog and Digital I/O Controller is microprocessor-based and functions independently of the Host Computer. Under this control, analog signals such as temperature, pressure and opacity are multiplexed into local memory buffers to be accessed subsequently by the Host Computer via the serial interface bus. Contact closures are monitored and controlled by the microprocessor controller, and status information is formatted to be evaluated as required by the Host Computer. In the event of a power failure, the battery back-up mode of operation is invoked and the I/O Controller will continue to function.

IV. Fault Detection and Annunciation

In the event of a contact closure or loss of signal, the fault is displayed on the local status panel of the I/O Controller. Additionally, an error message is formatted and sent to the Host Computer for further action. The present configuration is comprised of a three-wire serial bus. Four I/O Controllers can be daisy-chained on the bus (700 I/O lines).

V. Host Computer

The Host Computer functions as the master control center, sending and gathering information to and from the various remote control units distributed over the several serial bus pathways. The Host Computer operates as a single job monitor in a real time operating environment. Tied to the Host Computer is a special peripheral serial bus containing the CRT display, input keyboard, data logging typewriter, and a dual cartridge

tape storage unit. Specific equipment provided at the plant central room is:

a. Standard ASCII Keyboard used as the medium for operational interface with the control system. At this keyboard, the operator can initiate start-up or shutdown operations for all the T/Rs and rapper controllers as well as the I/O Controller. In addition, the operator can request printouts or invoke high level system algorithms for power consumption minimization or rapping control.

b. A CRT for the display of all T/R and rapper status information. Also, alarm messages relative to the various precipitator controls are displayed.

c. A data-logging typewriter providing an hourly hard copy summary of T/R primary and secondary currents and voltages. In addition, all alarms displayed on the CRT are printed out.

d. Cartridge Tape Storage

   A dual Cartridge Tape unit provides the following:

   1. Unit #Ø contains the Master Precipitator Control Program.

   2. Unit #1 contains a Scratch Tape to be used as the medium to collect system status and faults on an hourly basis.

Upon initial system start-up or in the event of a power failure, an automatic bootstrap loader program begins to read the program contained on the Master Tape Cartridge into the Host Computer Memory. The Master Program has a self-start feature and, through prompting, the operator can enter, via the keyboard, precipitator parameters.

ADAPTIVE CONTROL SOFTWARE

As stated previously, the operator can defer rapping and TR control to the Intelligent Precipitator. The Intelligent Precipitator has two adaptive feedback control loops which control overall TR power levels and system rapping parameters. This level of control adds another dimension to the capabilities and benefits of Intelligent Precipitator control.

I. Power Consumption Minimization

ESPs, although relatively efficient in terms of power consumption when compared to scrubbers, fabric filters or mechanical collectors, do expend power in excess of that minimally required to solely charge and collect particles. These losses are primarily due to electrical currents between collector and emitter which are not directly involved in the precipitation process. Such losses are sensitive to precipitator mechanical design (i.e., electrode design, plate spacing, etc.) and powering strategy (i.e., high electrical sectionalization). For ESPs which are serving a base loaded process, the possible reduction in TR power will

generally be small and proportional to precipitator design margin for statistical variability in coal and ash composition, uneven particle size distribution, grinding mill variability, and temperature variations which occur between regenerator cleanings. In this case, infrequent manual adjustment of the TR controls will probably be satisfactory to obtain the major portion of potential power savings. Power is reduced so as to maintain the opacity within either regulatory opacity limits, or to limits correlated with specific mass loadings.

For cyclic operation, the increase in specific collection area (SCA) corresponding to load reduction provides the greatest potential for power savings with microprocessor control. Generally, uncontrolled power increases during boiler load reductions due to lowered flue gas temperature and corresponding flyash resistivity reduction.

The magnitude of power savings possible is extremely site specific so that it is misleading to quote general numbers. However, power distribution within a precipitator can have a significant effect upon the efficiency obtainable for a given power consumption, or the converse problem - power consumption required to obtain a given efficiency.

This effect is demonstrated by test data shown in Table 1 obtained on a Buell rigid frame precipitator. Even with only four fields in depth, it was possible to obtain performance improvement by modifying the distribution of power to the fields. For example, in Test A, the power was controlled at threshold of sparking by automatic voltage control. An efficiency of 99.73% was obtained with 34.9 KW corona power. When the power distribution from front to back was changed in Test B, the efficiency increased to 99.85% at an overall power consumption of 29.56 KW--a net increase in performance with a decrease in overall power consumption. This type of power distribution is consistently and automatically sought by the Intelligent Precipitator controls.

Table 1 - Effect of Improved Power Distribution

Test A	Volume (ACFM)	Cabinet Power (KW) A	B	C	D	Precipitator Efficiency %
1A	138,278	2.12	8.84	9.35	12.42	99.76
2A	143,507	2.55	9.00	7.70	13.75	99.78
3A	144,968	2.34	13.20	12.00	11.44	99.72
		Mean Total KW = 34.9 KW				Mean 99.73
Test B						
1B	137,741	5.60	9.72	6.24	8.48	99.88
2B	140,627	5.00	10.08	6.24	8.48	99.84
3B	144,279	3.91	10.26	6.36	8.32	99.84
		Mean Total KW = 29.56				Mean 99.85

In this particular case, power was reduced to electrical fields which were operating in current limited mode, so that excessive current could be trimmed without a significant reduction in collection field strength.

In some instances, it will be possible to achieve relative decreases in power consumption which exceed the relative load reduction. The control loop capable of performing this function is shown in Figure 6b. Operationally, there are various levels of complexity that could be chosen at the customer's preference. Although the control loop in Figure 6 b is relatively complex, this configuration offers maximum flexibility and potential for power savings. The key control parameters are suitable integrated opacity level and individual TR secondary voltages V and currents I. Additionally, the Intelligent control periodically perturbs the TR currents to determine the local slopes of each of the V-I curves. This latter feature of adaptive control--to specifically and continually test to determine where operation is and where it should be to maximize collection efficiency for a given power consumption--is where the Intelligent Precipitator earns its name.

Changes in overall power level are made so as to maintain the outlet opacity within the limits of $\emptyset_{LL}$ and $\emptyset_{LU}$ (Figure 6a). The band upper opacity limit $\emptyset_{LU}$ is chosen to fall below the regulated opacity limit $\emptyset_R$ by a margin ε_L. This provides suitable reaction time when opacity exceeds $\emptyset_{LU}$. Total TR power is changed in discrete increments--positive when the opacity signal exceeds the upper limit and negative when the opacity falls below the lower limit. The control then applies this power alteration to the TR which will yield the largest gain in overall efficiency for a power increase, and the smallest decrease in overall efficiency if a power reduction is called for.

Following the change in operating voltage, a pause period τ_1 is required prior to acquisition of the next opacity level. This allows the effects of any prior changes made by the control system to take hold. The integration period is τ_2 and should either τ_1 or τ_2 be too short, unstable operation will result. If too long, significant drift of the signal may occur between corrections.

Major activity in power disposition is likely to be concentrated in the outlet fields of the precipitator; of course, a major power reduction, if optimally performed, will generally involve simultaneous power reduction over several fields.

Finally, the Intelligent Precipitator is capable of discerning back corona and will automatically adjust powering to TRs in this condition so as to be operating at the maximum secondary voltage achievable.

II. Rapper Control

Rapping parameters are adjusted based on secondary voltage characteristics. Rapper adjustment routines are invoked by the operator (after a change in coal, for example) or by the main routine periodically, or in response to a detected condition (such as excessive spark rate, back corona, or low corona current).

The rapping adjustment routines measure and log corona onset voltage

and voltage corresponding to a given spark rate. Corona onset voltage is functionally defined as that point where secondary TR current exceeds a specified threshold value.

Measured corona onset voltage is compared to a normal operating range. If the measured value falls outside this range, emitter rapping is increased. Similarly, measured sparking voltages are compared to the normal ranges. If the measured value falls outside this range, rapping to the associated plates is increased or decreased, depending on whether the voltage is below or above this range.

If any rapping change is made, the parameter in question (corona onset or sparking voltage) is measured again after a specific number of rapping cycles to monitor response. This cycle may repeat several times until either deterioration ceases, or rapping frequency or intensity reach maximum allowable values. At this point, the operator is notified. This situation could arise from a change in ash or flue gas characteristics, invalidating the "normal" values of sparking and corona onset voltages. These values should, in this case, be updated by the operator.

Another routine is available to automatically control the precipitator during boiler startup. This routine energizes only portions of the precipitator as needed, starting from the precipitator back end, based upon opacity feedback. Rapping intensity and frequency are held at their maximum allowable value throughout startup while operating temperatures are low. This routine reverts to normal operating mode when the flue gas is above the dewpoint range.

Optionally, the Intelligent Precipitator can be configured to respond to unusual or dangerous operating conditions. For example, boiler flame and combustible detectors can be monitored and used as inputs to initiate rapid precipitator shut-down. Parameters, such as coal feed rate and boiler load can be input to the Intelligent Precipitator to take advantage of its data logging capability or can also be used as feed-forward signals to the power control algorithms.

SUMMARY AND CONCLUSIONS

It has been seen that precipitators constitute a very fertile ground for minicomputer control. The advantages which will accrue from the adoption of such control include simplified high voltage and rapper control wiring, more convenient operator control, improved and more complete operator awareness of precipitator operating trends and higher control system and precipitator reliability. Adaptive feedback control will reduce precipitator corona power close to the minimum required for given operating conditions, and will control rapping to optimum values consistent with low emissions and maximum component mechanical life. Intelligent Precipitator control will result in reduced operating costs and higher reliability.

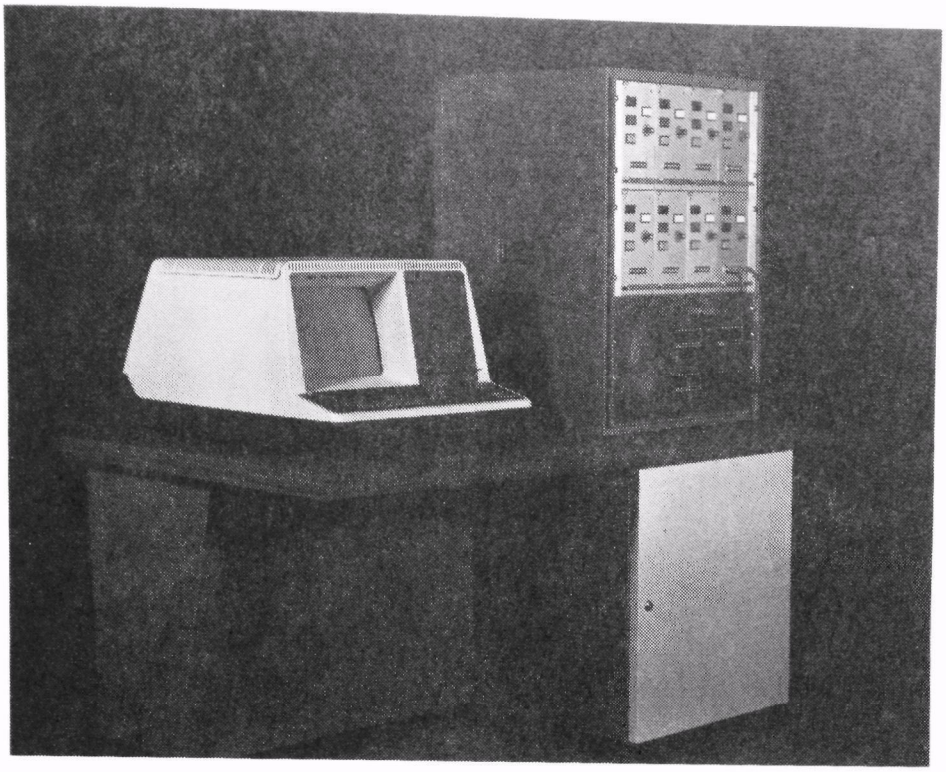

Figure 1. Intelligent Precipitator CRT and Chassis

PRECIPITATOR COLLECTING AND EMITTING
RAPPER MATRIX CONFIGURATION

R9	144	(145)	146	147	(148)	149
R8	128	(129)	130	131	(132)	133
R7	112	(113)	114	115	(116)	117
R6	96	(97)	98	99	(100)	101
R5	80	(81)	82	83	(84)	85
R4	64	(65)	66	67	(68)	69
R3	48	(49)	50	51	(52)	53
R2	32	(33)	34	35	(36)	37
R1	16	(17)	18	19	(20)	21
R0	0	(1)	2	3	(4)	5
	C0	C1	C2	C3	C4	C5

NOTE: 1) THE BRACKETED RAPPERS ARE THE EMITTING TYPE. INTENSITIES CAN NEVER EXCEED 5 FOOT-POUNDS.

Figure 2. CRT Rapper Configuration Display

RAPPER PARAMETER SUMMARY LISTING

ROW NO.	RAPPER NO.	OPERATING EVERY	LIFT FT-LBS	RAPS
Ø	ØØØ	1Ø MIN.	5	1
	(ØØ1)	1Ø MIN.	2Ø	1
	ØØ2	1Ø MIN.	2Ø	1
	ØØ3	1Ø MIN.	15	1
	(ØØ4)	1Ø MIN.	15	1
	ØØ5	5M MIN.	2Ø	1

NOTE: THE ( ) ABOVE DENOTES THE EMITTING RAPPERS. ANY "LIFT" VALUE GREATER THAN 5 FT-LBS WILL BE SET TO 5 FT-LBS AT OUTPUT TIME.

Figure 3. CRT Display Following Change of an Individual Rapper Time

PRECIPITATOR SUMMARY DATA

WED 02-18-81 TIME 10:49:00

UNIT NO. 1

	PRIMARY CURRENT	PRIMARY VOLTAGE	SECONDARY CURRENT	SECONDARY VOLTAGE	SPARK RATE	OPERATING STATUS
TR #1A	056 AMPS	270 VAC	213 MA	054 KV	16' MIN	
TR #1B	090 AMPS	244 VAC	313 MA	050 KV	14' MIN	
TR #1C	076 AMPS	280 VAC	212 MA	043 KV	3' MIN	
TR #1D	081 AMPS	285 VAC	640 MA	047 KV	10' MIN	

UNIT NO. 2

TR #2A	048 AMPS	327 VAC	306 MA	050 KV	6' MIN	
TR #2B	070 AMPS	228 VAC	306 MA	050 KV	7' MIN	
TR #2C	071 AMPS	232 VAC	540 MA	049 KV	10' MIN	
TR #2D	090 AMPS	243 VAC	600 MA	046 KV	7' MIN	

Figure 4. CRT Display - Electrical Operating Condition Summary

Figure 5. Real-Time Intelligent Precipitator Control Arrangement

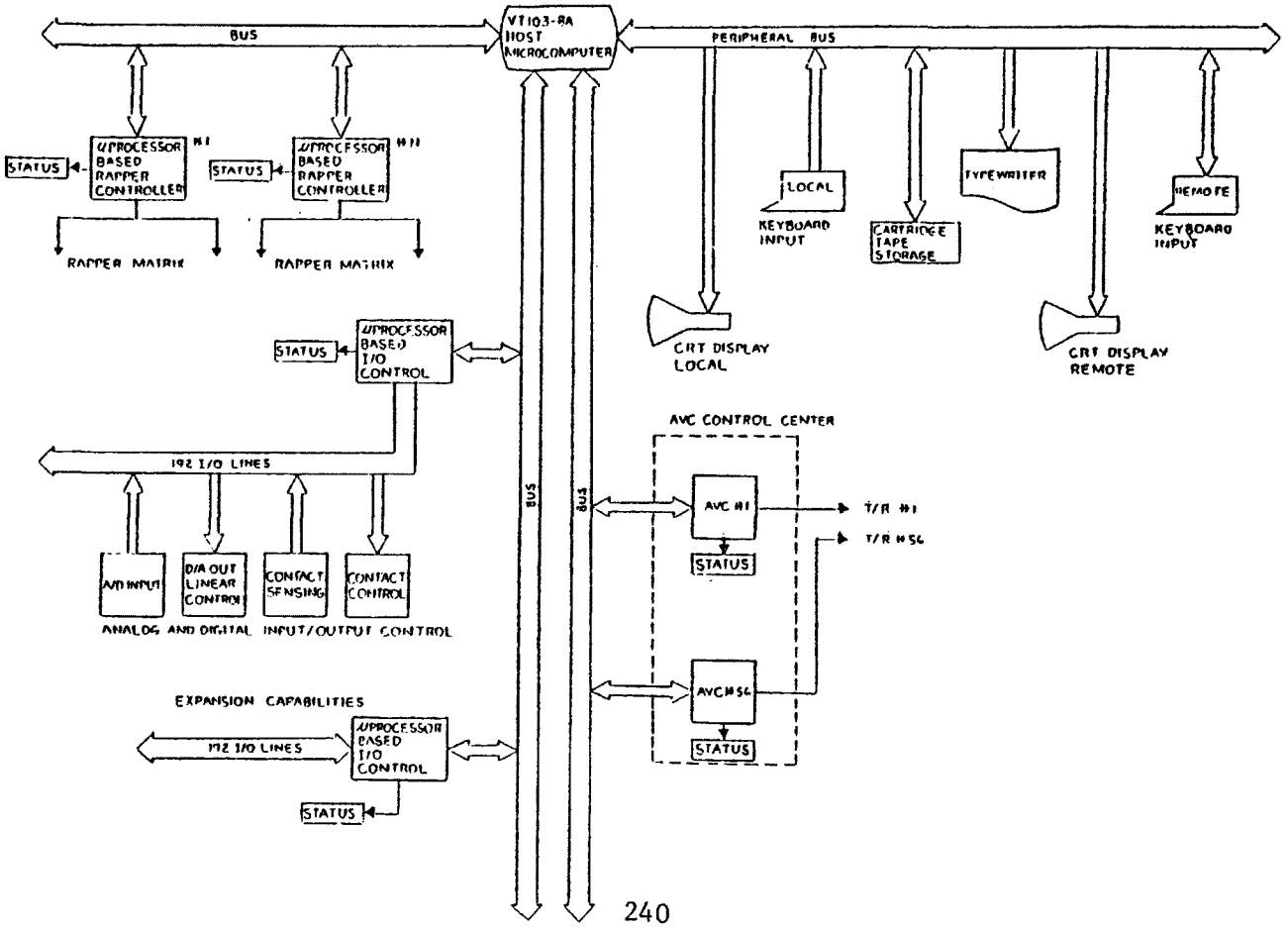

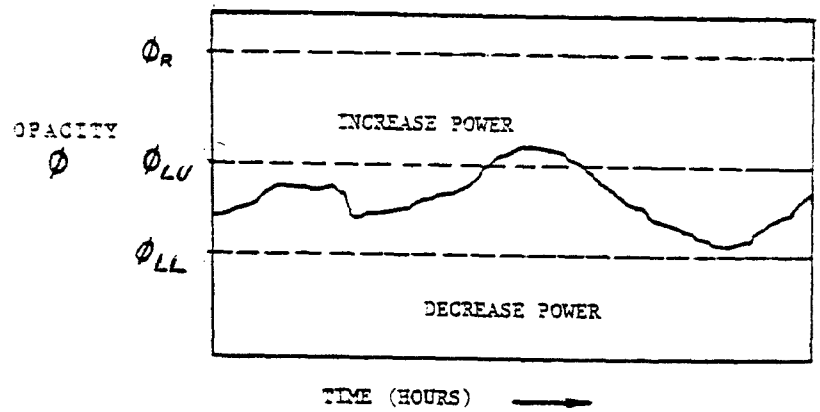

6a. Definition of Opacity Deadband Limits

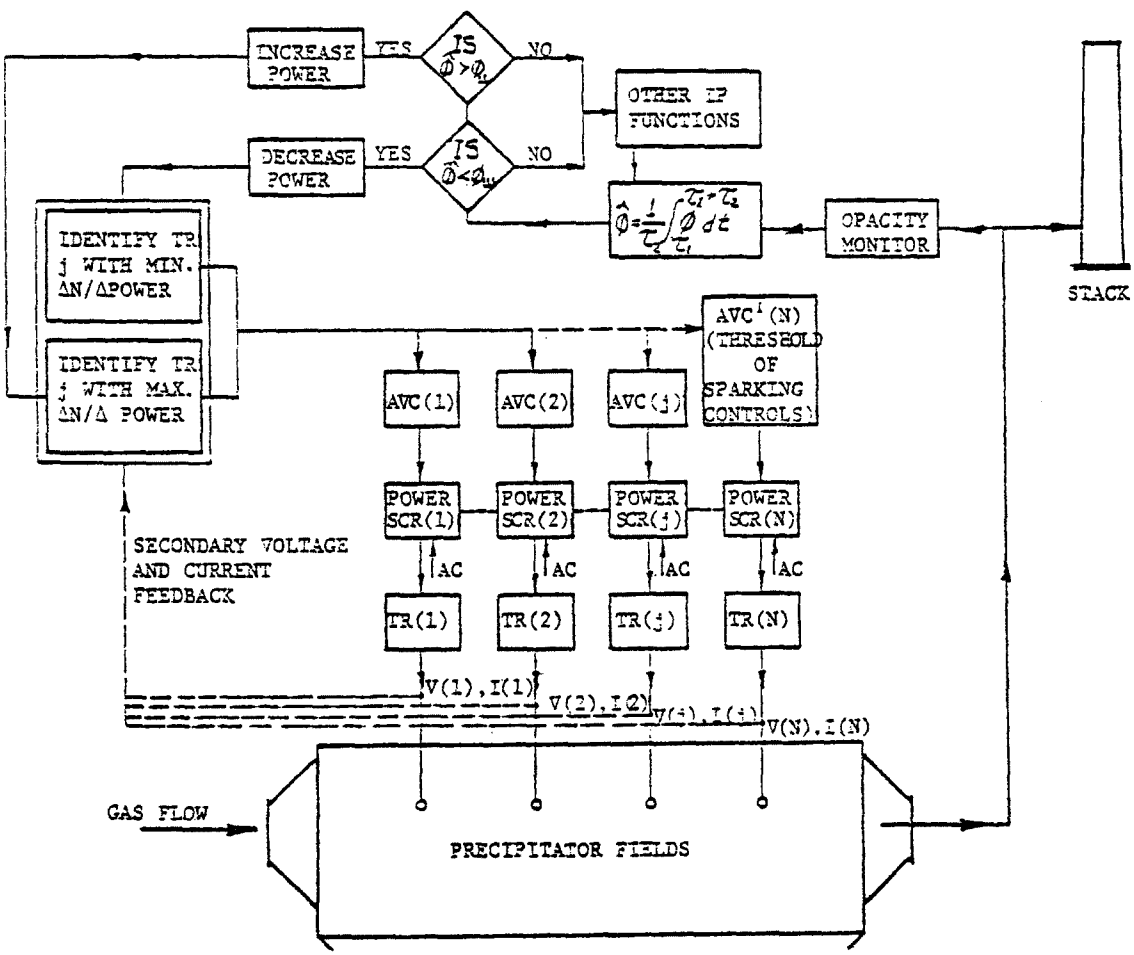

6b. Feedback Control Loop

Figure 6. Power Consumption Control Loop

AN ENERGY MANAGEMENT SYSTEM FOR ELECTROSTATIC PRECIPITATORS

By: Robert R. Crynack and Martin P. Downey
Wheelabrator-Frye Inc.
Air Pollution Control Division
600 Grant Street
Pittsburgh, PA 15219

ABSTRACT

As the emphasis of air pollution control regulation shifts toward maintaining daily compliance with stringent standards, the user must direct more attention to maintaining optimum performance from his control equipment. Modern electrostatic preicipitators have become increasingly larger with more power supplies and electrical auxiliaries which demand monitoring by operating personnel to ensure code compliance. An Energy Management System is proposed which can monitor precipitator electrical equipment and optimize energy consumption while maintaining continuous compliance. The Energy Management System is a microprocessor-based device which is connected to the power supply controls and auxiliaries and regulates electrical power in response to actual on-line precipitator operational needs. A prototype Energy Management System, which controls the corona power, has been operating for over one year with a high degree of success on a precipitator serving a utility boiler.

INTRODUCTION

In recent years industry has been forced to purchase more conservatively designed air pollution control equipment to assure daily compliance with stringent standards. In the area of electrostatic precipitators on large scale industrial processes, users have found it necessary to specify and purchase larger units, often with redundant collecting area and a high degree of electrical sectionalization. This has resulted in higher maintenance and operating costs of the equipment.

Good engineering design practice demands a reasonable amount of conservativism for any equipment that must withstand the rigors of a heavy industrial environment. This can be illustrated in the case of an electrostatic precipitator serving a utility coal-fired boiler. Modern power plants are generally designed for a 20 to 30 year life, during which time the coal supply may come from a variety of sources that demand a range of design tolerances. When dealing with a range of coal characteristics, a boiler designer must size his furnace for the lowest heating value, highest moisture and highest ash content. This in turn presents the worst case sizing parameter for the precipitator because of the resulting largest flue gas volume and highest dust loading. The precipitator and the boiler must be sized to handle the worst conditions that can be anticipated over their projected design life. Yet during actual operation more favorable conditions may be encountered. For instance,

fuels may be used that produce a more collectable ash or the boiler may not operate at its maximum continuous rating (MCR).

ENERGY MANAGEMENT CONCEPT

The concept of the Energy Management System (EMS) is to provide a means of monitoring and controlling all sub-systems of the electrostatic precipitator. The EMS will ultimately provide the user with operational and equipment status information to allow him to operate and maintain good efficiency of the precipitator. The EMS provides a single source of precipitator control rather than individual controls operating independently. More effective utilization of corona power is possible. At the same time, power consumption can be reduced while maintaining emissions below compliance levels. The EMS can automatically respond to changes in process conditions and increase precipitator power when operating conditions demand it.

The transformer/rectifier (T/R) sets and controls which supply corona power to the precipitator, consume the most significant portion of power. The primary function of the EMS will be to monitor and control corona power and still meet mass emission requirements. The EMS obtains an input signal from a tranmissometer (opacity meter) and adjusts the precipitator power to maintain a preset opacity level. The opacity, used as a measure of the mass emission rate, can be maintained at a specified level through a variety of operating conditions.

CORONA POWER

As defined by the Deutsch-Anderson equation, for a given migration velocity the size of the precipitator increases with increasing efficiencies and gas volumes. The relationship between corona power and collection has been explored in theory and supported with field data by White (1). The corona power density, expressed in watts per square foot of collecting area, has good correlation with efficiency up to 98 percent. For higher efficiencies, White's data has shown that a higher rate of corona power is required for increasing efficiency. For these efficiencies corona power was examined in watts per thousand ACFM, referred to as specific corona power. Figure 1 shows the relationship of efficiency versus specific corona power, where both White's curve and WFI data for one specific installation are plotted. The significance of this data is that the rate of increase in efficiency diminishes with increasing specific corona power. A similar trend can be seen in the relationship between outlet residual and specific corona power for the same installation as shown in Figure 2.

Correlation between corona power and collecting area can be derived mathematically by examining the relationships among corona power density, specific corona power, and specific collection area (SCA). In high resistivity applications where corona power density is low, a large SCA is required to obtain the specific corona power necessary to obtain a given efficiency. For low resistivity applications where corona power densities are relatively high, a small SCA is required to obtain the

same specific corona power and efficiency.

For a given application, a specific corona power can be selected to achieve a specified efficiency. However, good practice demands providing power supplies that are capable of delivering higher power densities than are required. When sizing a T/R, consideration must be given to variations in operating conditions and ash resistivity. At the same time, present precipitator control logic centers around the concept of seeking the highest level of corona power regardless of dust concentration or gas volume. Standard precipitator controls automatically seek the highest spark level or maximum rated current of the T/R.

When all of these worst case conditions are present, all of these sizing precautions are necessary. However, if process conditions change and operation becomes more favorable for precipitation, power in a precipitator will tend to increase. Process conditions such as a reduction in boiler load and favorable particulate chemistry will create this situation. This increased corona power comes at a time when less corona power is required to maintain emission levels.

PRECIPITATOR POWER REQUIREMENTS

The design and electrical load requirements for a precipitator on a coal-fired boiler unit will be examined. Table I shows a summary of typical design parameters for a cold side ESP to serve a large size utility boiler. Present code requirements for particulate mandate a maximum outlet of 0.03 lbs/MBTU, which typically corresponds to an outlet residual of 0.008 gr/ACF and an efficiency of 99.8% for a Western sub-bituminous coal. Redundancy in the collecting area is often specified to allow for the loss of electrical bus sections due to potential failure of the material handling equipment, high voltage electrodes and electrical energization equipment.

Table II shows an electrical load summary for a precipitator system. No consideration has been given to power consumption of the I.D. fans or of the ash removal equipment. A significant point from the summary is that there is a large number of subsystems which will require service and maintenance. In addition, with larger precipitators having a large number of T/R units, it becomes very difficult to understand the operational status of the unit at any one time. For instance, a plant operator taking T/R control cabinet readings has a difficult time interpreting any more than if the power is up or down in the precipitator and has no concept of whether this indicates higher or lower particulate emissions. In the current state of the art design, all of these subsystems operate in a open loop mode, operating independently with no central monitor or control.

Regarding the electrical load summary in Table II, the connected load tabulates power required at the distribution transformer, while the expected power summarizes the operating power consumption that could be anticipated at MCR. Note that the T/R's and controls consume approximately 79% of the total normal operating load. A value of 500 watts/1000

ACFM was selected as a reasonable specific corona power required to meet the outlet emissions. This calculates to a corona power of 1500 KW for the volume given in this example. Then the corona power was converted to line power using a factor of 1.25, which approximates the power losses in the T/R unit, linear reactor and the thyristor package. This yields the final value of 1875 KW, which represents the line power required from the plant distribution transformers.

OPACITY AND PARTICLE CONCENTRATION RELATIONSHIP

The opacity signal from a transmissometer is the key input to the EMS. According to Bouguer's Law, the optical density is proportional to the particle concentration in the gas. The constant of proportionality differs with density, size and optical properties of the particulate. The constants of proportionality can be calculated if all parameters are known, but these parameters are difficult to establish. It is more practical to determine the proportionality constants experimentally. Through a series of tests, the relationship between optical density and particulate concentration can be established along with its confidence limits.

A transmissometer measures the ratio of the amount of light transmitted through the gas stream (I) to the initial amount of light (I_o). The transmittance (T) is defined as the ratio of I/I_o. Opacity is then defined as:

$$\text{Opacity} = 1 - T = 1 - (I/I_o)$$

The relationship between optical density and opacity is given as:

$$\text{Optical Density (OD)} = \log_{10}\left(\frac{1}{1-\text{Opacity}}\right) = \log_{10}(1/T).$$

Although a transmissometer measures transmittance and thus opacity, the relationship between opacity and optical density is defined. Many transmissometers will provide a readout of both opacity and optical density. Thus, particle concentration can be correlated with either optical density or opacity. This relationship has been experimentally shown in a variety of applications (2,3).

THE EQUIPMENT

The EMS hardware can take on any level of sophistication, depending on the number of inputs, complexity of operation, and number of outputs. The equipment described here is a developmental prototype system used to test the applicability and capability of such a system under actual operating field conditions. This system monitors and controls the corona power which is the most significant portion of the precipitator electrical load.

The EMS is structured around a programmable controller and an interface panel. The function of the programmable controller is to continuously monitor all incoming signals (inputs), perform basic operations based on these inputs, and provide outgoing signals (outputs) on the basis of the programmed logic. Using relay format (ladder diagram) programming, this microprocessor based device performs the

logic, timing, counting, and simple arithmetic functions needed to perform the desired control algorithm. The interface panel contains hardware to (a) monitor and display opacity, (b) provide system inputs to modify EMS operation, (c) indicate power reduction levels and (d) digital to analog (D/A) converters to provide signals to regulate the power in individual analog T/R controls.

Although the EMS program can be modified using a programming panel, the interface panel provides for changing three inputs to the EMS. In this prototype thumbwheel switches are used for this purpose. These three control inputs are (a) opacity setpoint, (b) response period and (c) priority level. The opacity setpoint can be adjusted to the desired value using a two-digit, 10 segment thumbwheel switch. The opacity feedback signal from the transmissometer is compared to the setpoint and power is adjusted so as to force the two values to be equal. The response period is the parameter that controls the rate at which the EMS will react to an opacity error. The rate at which power is changed depends upon the opacity error as well as the setting of the response period. Each controllable precipitator section is assigned a priority level from 0 to 9, selectable using a single-digit thumbwheel switch. This level assignment determines the order in which power is increased or decreased in the various precipitator sections.

The EMS interface panel has a series of seven segment readouts to indicate the corona current level of the individual precipitator sections. A "9" indicates a 90% reduction while a zero indicates no reduction (full power).

THE OPERATION

The EMS samples the opacity signal and updates the stored opacity value using a digital filter. The opacity value is compared to the preset opacity setpoint input from the interface panel. The EMS then adjusts the precipitator power upward or downward to maintain the opacity at the setpoint. The EMS responds differently depending on whether the opacity exceeds the setpoint or is less than the setpoint. The speed of response is determined by the response period input from the interface panel and the magnitude of the opacity error (difference between actual opacity and setpoint opacity).

Upon initialization of the system, if the opacity is below the set point opacity, the power is first reduced in 10% (corona current) steps with "0" priority controls until the minimum power level is reached. The EMS will then begin to reduce the power on priority level "1" controls. This will continue until all priority levels are completed or until the opacity equals the set point. If actual opacity is above the set point, the EMS will increase precipitator power in 10% increments. The power will be increased in successively lower priority controls until maximum power is reached or until the opacity setpoint is reached. The rate at which power is adjusted is a function of (1) selected response time, (2) opacity error and (3) opacity being above or below the set point. The level of power reduction is displayed on the single

digit readout for each precipitator control panel.

THE TEST SITE

A prototype Energy Management System for corona power was installed on a 156 MW coal-fired boiler in November 1979. The rated gas volume is 751,000 ACFM at a temperature of 300°F at the precipitator inlet. The design SCA is 716 and plate spacing is 10 inches. This is a two chamber, six field precipitator. Each field of each chamber is powered by one T/R set rated at 45 kv and 2500 ma.

The coal burned at this station is referred to as Decker Coal, mined in southern Montana. The sulfur content of the coal is approximately 0.6%. When these units were sized in 1974, it was thought that this would be a very difficult ash to collect because of the low sulfur content of the coal. At that time, the effect of sodium in the coal was not known. The sodium in the ash (reported as sodium oxide) is about 8.7%. It has been established that ash from low-sulfur coal is not difficult to collect if the sodium content is relatively high. The performance of these precipitators substantiates this fact.

In May 1978, a series of reduced power tests were conducted on these precipitators. Under normal operating conditions, all fields except the first field operate at full rated (2500 ma) corona current. The inlet field generally operates in a sparking mode at less than 1000 ma. Although precipitator voltage (KV) meters were not supplied with these units, measurements showed that the precipitator voltage is about 40-47 kv at full-rated corona current. It was determined that precipitator performance remained approximately the same whether 6, 5 or 4 fields were in operation at full corona power. The outlet emission level was less than 2.3 mg/cu.m. (0.001 gr./cu.ft.). Reducing the corona power to 75% and then to 50% of full-rated corona current with four field operation showed almost no change in outlet particulate concentration or in the opacity level of 0 to 1%. It was when only two fields were energized at a corona power of 25% of rated current value that the mass emission level increased by a factor of 10 and the opacity jumped above 10%. This is the data plotted in Figures 1 and 2. These results indicate that an EMS would provide a substantial savings in energy with no significant impact on emissions.

OPERATING EXPERIENCE

The prototype EMS was installed and commissioned during the week of November 5, 1979. The EMS has worked effectively in over sixteen months of operation. The EMS automatically increases and decreases corona power in response to changes in opacity, and thus mass emission. The EMS has automatically responded to boiler upsets, boiler load changes, and electrical failure of the enegization equipment. Little maintenance has been required for the EMS, but periodic cleaning of the optics of the transmissometer is required to provide an accurate opacity measurement.

Before installation of the EMS, plant personnel manually reduced

corona current to about 50% of rated values in order to conserve on power. The installation of the EMS resulted in significantly more power savings. Furthermore, the automatic response of the EMS eliminated the need for operating personnel to monitor and adjust the power when opacity levels began to increase. The EMS is able to reduce the corona current in the entire precipitator to 10% of the full rated value and maintain that level of power with opacity increasing to only 5%. There is a substantial energy savings at this installation. One must bear in mind that this Decker coal, together with the large SCA precipitator, provide an extreme case but an excellent test facility.

COST ANALYSIS

Based on statistical information published by the Edison Electric Institute (4), the energy consumption costs of a precipitator can be calculated. In 1979, the average cost of fuel for a coal-fired boiler was approximately 1.33 cents per net kilowatt-hour (KWH). Based on average operating expenses for investor-owned electric utilities, the cost of generation (including fuel), was about three cents per KWH. Bear in mind these numbers are for 1979 and the 1981 figures would be higher.

The amount of power consumption savings and cost per KWH are site specific. Using the above costs of energy, a 10% reduction in the corona power for one year would result in a savings of over $21,000 per year in fuel costs alone and a savings of over $49,000 in production costs. Based on an installed cost of approximately $100,000 for this EMS equipment on a typical 750 MW boiler, the payback period would be about five years if fuel costs are considered and only 2 years if production costs are considered. These figures are based on the average expected power consumption of 1875 KW given in the example in Table II. These figures do not consider the advantages of central monitoring and control of the corona power that result in simplified operation and maintenance of the electrostatic precipitator.

SUMMARY

Conservatively designed precipitators are necessary to maintain daily compliance with stringent air pollution control codes. An Energy Management System (EMS) is proposed to effectively monitor and control corona power. Over sixteen months of field operation of a prototype EMS has verified its capability and reliability. This microprocessor-based device monitors opacity and automatically regulates corona power to maintain a maximum opacity level, and thus, a maximum emission level. The relationship between power consumption and precipitator performance and between opacity and particulate emissions are discussed. Reduced power tests were performed on a 156 MW coal-fired boiler which demonstrated the need for a central management and power reduction controller.

While the EMS is monitoring and automatically responding to variations in operating conditions, power consumption savings can be

significant on installations where worst case design limits are not reached. Although the amount of power savings depends on many factors, a ten percent reduction in power consumption would offset the cost of the EMS in a few years. Although this paper is directed toward utility applications where precipitators are larger and more conservatively sized, the EMS is applicable to industrial applications as well. In the future the EMS will be expanded to monitor and control most of the subsystems and auxiliaries of an electrostatic precipitator.

REFERENCES

1. White, Harry J. Electrostatic Precipitation of Fly Ash. Pittsburgh, Air Pollution Control Association Reprint Series, 1977. p. 22-23.

2. Beutner, Heinz P. Smoke Density Measurement With an On-Stack Transmissometer. APCA Journal. 24:865-871, September, 1974.

3. Brennan, R. J., et al., Review of Concurrent Mass Emission and Opacity Measurements for Coal-burning Utility and Industrial Boilers. EPA Report No. 600/7-80-062. March, 1980.

4. Statistical Year Book of the Electric Utility Industry - 1979. Washington, D.C. Edison Electric Institute. November, 1980.

FIGURE: 1 RELATIONSHIP OF SPECIFIC CORONA POWER AND EFFICIENCY

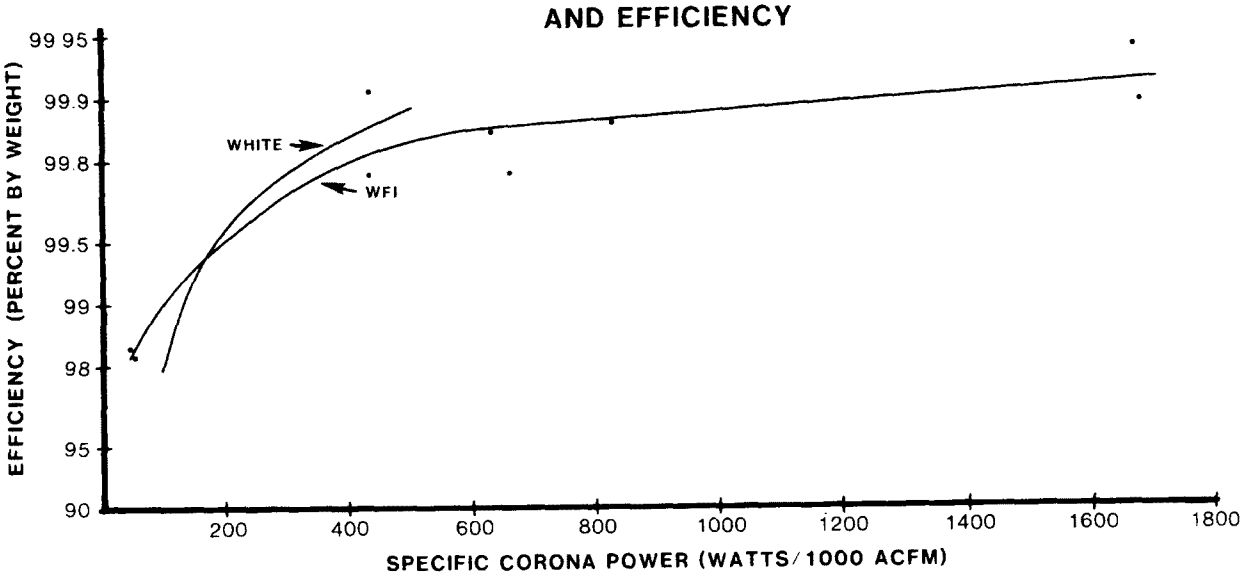

FIGURE: 2 RELATIONSHIP OF SPECIFIC CORONA POWER AND OUTLET RESIDUAL

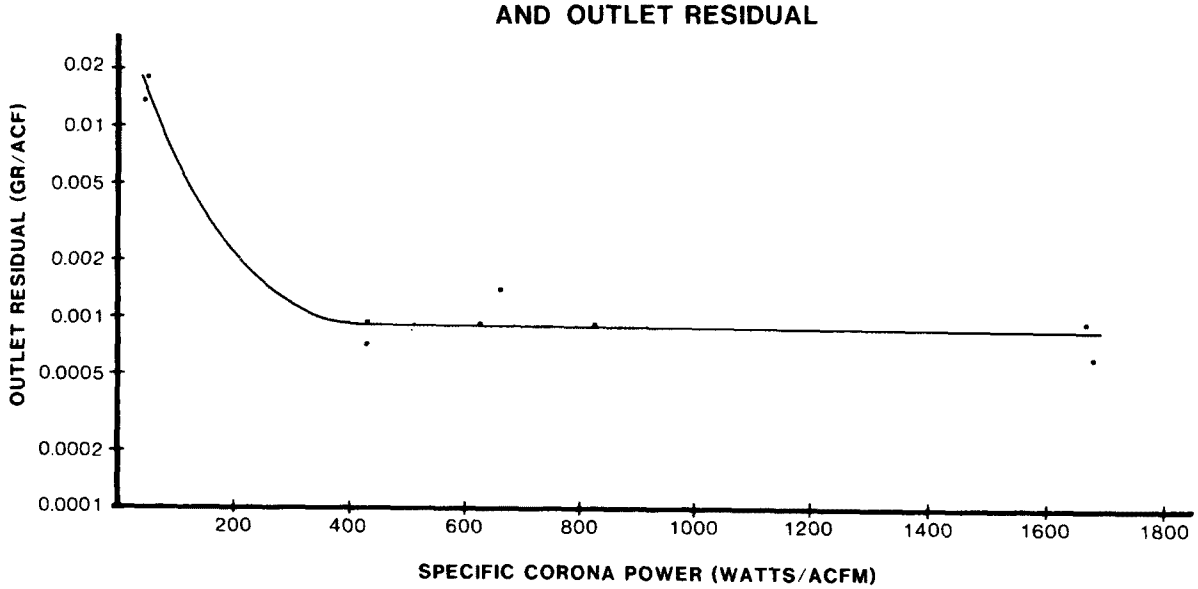

TABLE I - SPECIFIED DESIGN PARAMETER SUMMARY

Station Nominal Generating Capacity -	750 MW
Type of Fuel -	Western Sub-bituminous Coal (Low Sulfur - Low Sodium)
Air Pollution Code Requirements for Particulate -	
Maximum Allowable Particulate Emission	0.03 lbs./MBTU
Maximum Allowable Opacity	20%
Maximum Flue Gas Volume at Air Heater Outlet	3,000,000 ACFM
Precipitator Inlet Grain Loading	4.0 gr/ACF
Outlet Residual (Equiv. to 0.03 lbs/MBTU)	0.008 gr/ACF
Design Efficiency	99.8%
Design Specific Collection Area (SCA)	650 $ft.^2$/1000 ACFM
Collecting Area Redundancy	10%
Total Installed SCA Required	715 $ft.^2$/1000 ACFM

TABLE II - ELECTROSTATIC PRECIPITATOR LOAD SUMMARY

Subsystem	No. of Units	Connected Power (KW)	Expected Power At MCR (KW)
1) T/R's and Controls	96	4750	1875
2) Hopper Heating Units	112	730	365
3) Rapper Motors	114	65	54
4) Insulator Heaters	448	358	0
5) Insulator Purge Sys.	8	484	0
6) Insolation & Louvered Dampers	12	149	0
7) Hopper Vibrators	112	19	3
8) Hopper Level Indicators	112	5	5
9) Control Room - HVAC	2	48	48
10) Roof Weather Enclosure Ventilating Equip.	8	16	16
11) Area Lighting		30	15
	TOTAL	6654	2381

RELATIONSHIP BETWEEN ELECTROSTATIC PRECIPITATOR PERFORMANCE AND RECORDKEEPING PRACTICES

By: S. P. Schliesser
PEDCo Environmental, Inc.
505 S. Duke St., Suite 503
Durham, N.C. 27701

ABSTRACT

This paper discusses the sensitive relationship between the performance of electrostatic precipitators (ESPs) to the quality of recordkeeping, specific to the analysis of voltage current (V-I) curves and corona power-mass emission correlations. The author contends that improved recordkeeping practices will mutually benefit both the operator and regulatory agency. Strategic recordkeeping will permit the operator to effectively diagnose restrictive performance problems, enabling corrective changes to be made on a more timely and regular basis. For regulatory agencies, these records provide a means other than opacity to evaluate the compliance status of the unit. V-I curves and corona power levels constitute the basis for evaluating ESP operation and maintenance (O&M) levels, along with continuous particulate emission levels. A fundamental characterization of ESPs is presented, limited to using organized electrical data as the guideline for behavior and performance.

INTRODUCTION

Qualitative evidence recently acquired demonstrates a strong relationship between ESP performance and recordkeeping practices.(1) The investigation evaluated several ESPs by classifying performance and recordkeeping levels into five designated categories. A detailed inspection and file review determined the performance and recordkeeping level assigned to each source. Table 1 identifies the criteria used in this study to classify the performance and recordkeeping levels. Figure 1 illustrates the results of the classification and shows the strong relationship between performance and recordkeeping levels. Note that the correlation applies across the range of recordkeeping/performance levels and industrial source categories studied (i.e., utilities, portland cement, and kraft pulp industries). The conclusions drawn by the author are that a relationship exists between performance and recordkeeping at most sources and that this relationship becomes causal when records are used for diagnostic purposes. These conclusions are supported by the author's experience with EPA's mobile ESP.

STRATEGIC RECORDKEEPING

Strategic ESP recordkeeping practices consist of obtaining, organizing, and comparing transformer-rectifier (T-R) set voltage and current levels. The initial collection of this electrical data begins with the design specifications and the set of air load V-I curves conducted during equipment check out. The V-I curves and corona power levels experienced and collected during the initial performance test will constitute the technical base for initial

and continuous compliance determinations. Continued collection of this voltage-current data during air load tests and regular operation will continue to serve as the measure of equipment readiness and performance. Thus, a complete ESP recordkeeping package consists of electrical data collected from all phases of equipment design, initial check-out and performance testing, and continued operation and maintenance periods. Both V-I curves and corona power levels are the supplemental means of an ESP evaluation, available for common use by operators, regulators, manufacturers, and consultants.

INSTRUMENTATION AND KEY PARAMETER RECORDKEEPING

The most important ESP parameters for regular recording are the secondary electrical levels. The secondary voltage and current readings for each transformer-rectifier (T-R) set should be logged at least once per shift, and spark rate meter levels should also be recorded. Even though primary electrical meters are more commonly used, secondary meters are now being recommended by vendors,(2) enlightened users,(3) and consultants.(4) Secondary metering is preferred since it directly measures the electrical levels to the discharge wires; primary meters monitor the electrical levels fed to the T-R sets, and obscure the diagnosis of common problems within the unit. Other essential data sets to be regularly logged are provided in reference 2, and include source operating data, fuel analysis, ash analysis, electrode cleaning equipment data, ash removal system data, internal component inspection data, and replacement parts log.

RECORDKEEPING - A MEANS OF MINIMIZING MAINTENANCE

Two key engineering tools can be incorporated into a maintenance and recordkeeping program to improve ESP performance with minimum manpower requirements. These two tools are 1) the voltage-current curves and 2) the corona power-emissions correlation.

The key maintenance tool is the V-I curve. The characteristic profile of the V-I relationship can be used during off-line (air load) and on-line (gas load) conditions to understand the behavior of an ESP. It will serve as an "eyeball" to ESP operators by graphically illustrating the conditions of the internal wires and plates. Interpretation of V-I curves does not require extensive training, and it will accomplish the following: 1) assure proper operating status, 2) define high-voltage power loss from the T-R set to the internal bus bars, 3) indicate short or open circuiting in bus sections, 4) indicate effective changes in discharge wire size, either wire shrinkage or ash buildup, 5) indicate alignment problems between wires and plates, 6) indicate excessive deposits on collection plates, 7) indicate sharp edges on plates, baffles, 8) indicate air inleakage, 9) indicate ash buildup into the energized region, and 10) indicate changes in gas composition, temperature, resistivity, conditioning agents, space charge effects and gas throughput.(4,5)

A V-I curve can be obtained in less than 5 minutes, since a minimum of 4 voltage-current data sets is sufficient to map a curve. The corona initiation point and the critical operating limit need to be determined, along with at least two intermediate points. The controller needs to be put in the

manual, and not the automatic, mode. The corona initiation point is determined by gradually energizing the T-R set until a detectable secondary current level is achieved. Generally, corona is initiated in the range of 16 to 22 kV. Record the secondary voltage and corresponding secondary current level. Continue to incrementally energize the field in increasing power levels and record the respective voltage and current levels at a minimum of 3 more points. As each energization level becomes stable, the electrical readings are recorded. Any of three critical limits will determine the maximum corona point achievable for the prevailing conditions: 1) T-R set current limit, 2) T-R set voltage limit, and 3) spark limit. Note and record the limiting case. A standardized form with electrical data formating and a grid with voltage and current graduations should be used to expedite this exercise (see reference 2).

Because of the complexity of ESP units, a staged troubleshooting approach is necessary to isolate conditions and to assure that each element is operational. Air load V-I curves provide the first set of data necessary for troubleshooting an ESP before it goes on line. A comparison of air load V-I curves taken after an outage with those taken during a time of suitable credibility (i.e., initial installation), one can assess the operational status of an ESP. Reasonable agreement between the reference and outage air load V-I curve is evidence that the particular field is fully operational. Lack of reasonable agreement between the curves is evidence that a problem exists. The compilation and comparison of air load V-I curves for each T-R set in the ESP system provide evidence as to which fields are ready and which need attention. Figure 2 presents a series of air load V-I curves. Each shows reasonable agreement with the other with the exception of field 3, which shows a secondary power leakage problem. With reasonable experience or training one can determine the nature of the problem by interpreting the deviant character of the V-I curve.

The air-load procedure includes: 1) preparing the ESP system for regular operation, 2) providing a nominal level of ambient airflow through the ESP, 3) placing the controller in the manual mode, 4) energizing each T-R set and recording voltage and corresponding current levels over the achievable range of electrical operating conditions, 5) graphing the tabulated secondary voltage-current data sets, and 6) comparing the graphed secondary V-I results for each field (or T-R set) with a) the other fields (under the same environmental conditions) and b) the V-I curves taken in the past (under similar environmental conditions). Elaboration of this sequence of activities and their significance is contained in reference 1. It is strongly recommended that operators follow the manufacturer's procedures during this exercise. Substantial levels of ozone will be generated from corona formation during air-load measurements, and the ozone needs to be safely vented before reentering the unit.

Figure 3 depicts the theoretical relationship between air load and gas load V-I curves. The uppermost curve, labelled "no mass loading," represents an air load V-I curve in that it describes the V-I relationship without the presence and effect of particulate. The middle V-I curve represents an outlet field voltage-current relationship. The bottom curve represents an inlet field V-I profile. Note the progressive shift in the V-I curves

resulting from the relative amount of particulate flux experienced for these three conditions. Particulate flux is equivalent to the surface areal rate of particulate and is dependent on particle size distribution and gas throughput levels. Generally speaking, then, the air load V-I curves will resemble gas load curves, but typically will be shifted to the left because of the absence of particulate flux.

One method of checking gas load V-I curves is the same as that used for air load curves (i.e., compare the reference V-I curve with the one in question). Another method consists of common graphing of the V-I curves for each ESP field, as shown in Figure 4. This figure shows a series of V-I curves taken during normal operation of a cold-side ESP treating high sulfur fly ash. Note the progressive shift in the V-I curves resulting from the relative amount of particulate flux experienced for the three fields. Also note the gradual decrease in the operating voltage and the gradual increase in the current density from inlet to outlet. The slopes and sequences of these V-I curves provide evidence that this ESP is operating and performing properly. Deviations from these slopes and sequencing are evidence that the respective field is experiencing some kind of trouble. Again, one can interpret the problem from the nature of the deviant V-I curve.

This organized approach to the use of air load and gas load V-I curves can serve as an important part of an O&M plan for any ESP and will apply to all manufacturer types and vintages. Note, however, that the V-I curves in this report demonstrate the general use of this approach. The practical use of this approach requires obtaining site-specific and manufacturer-specific V-I curves. Once this V-I approach is integrated into regular O&M plans, it can be used to prioritize the fields warranting attention before an outage. It will provide evidence as to which fields need repair and which fields are operationally sound.

CORONA POWER - EMISSIONS CORRELATION

Now that voltage and current levels are realized to provide evidence of performance for each field, a second engineering tool, corona power, can be used to indicate the particulate removal performance level of the total ESP system. Corona power is a measure of the presence and intensity of the electrical energy effectively used in the precipitation process. Effective use of corona power excludes secondary power leakage levels and reverse corona conditions, both definable from V-I curves. Corona power is the product of the average voltage and average current from all T-R sets. Corona power density is related to collection efficiency through the equation:(6)

$$n = 1-e^{-0.06k_1(P_c/V)} \qquad \text{(Eq. 1)}$$

where

n = collection efficiency

k_1 = empirical parameter; for fly ash, typically 0.5 to 0.7

V_{avg} = corona voltage, volts (secondary voltage)

I_{avg} = corona current, amps (secondary current)

$P_c = (V_{avg})(I_{avg})$

P_c/V = corona power density, watts/1000 acfm

For a multifield precipitator, P_c is the sum of the individual corona power levels for each T-R set. Figure 5 shows actual performance results on ESP efficiency through the use of corona power density levels from many fly ash studies. Emission levels have been correlated with ESP collection efficiency to illustrate that corona power density levels are directly indicative of emission levels. Note, however, that the numbers in Figure 5 are purely illustrative and do not represent all fly ash cases. Again, site-specific and manufacturer-specific data would have to be collected to correlate corona power density levels with specific levels of ESP fly ash emissions. The corona power density relationship with removal efficiency is not limited to only fly ash collection, as characteristic relationships have been found for other industrial applications.(7) These industries include pulp and paper, cement, municipal incinerators, and steel source categories. As continuous compliance and recordkeeping practices are implemented, a corona power-emission level relationship could become a viable method of accounting for continuous ESP performance levels in most industrial source categories.

CONCLUSION

Strategic recordkeeping of voltage and current data has been demonstrated to be an effective method to characterize and diagnose ESP behavior. Voltage-current data collected and organized into V-I curves and corona power density units are the supplemental tools to characterize ESP O&M and performance. Benefits to the operator and regulatory agency can be realized as this methodology is practiced and understood.

ACKNOWLEDGEMENTS

The author needs to acknowledge that the entirety of this report is referenced literature, merely compiled and limited to 10 pages. The principal investigators behind this material are present or previous members of Southern Research Institute and Research-Cottrell, Inc., partially represented by the authors listed in the endnotes.

ENDNOTES

1. Schliesser, S. P., and J. R. Richards. Development of Guideline Document for State Operating and Maintenance Recordkeeping Programs (draft), December 1980.

2. Bibbo, P. P., and P. Aa. Increasing Precipitator Reliability by Proper Logging and Interpretation of Operational Parameters - An Operator's Guide. In: Second Symposium on the Transfer and Utilization of Particulate Control Technology, Vol. II, Electrostatic Precipitators. EPA-600-/9-80-039b, September 1980. pp. 219-241.

3. Raymond, R. K. Electrostatic Precipitators - Electrical Problems and Solutions. In: Second Symposium on the Transfer and Utilization of Particulate Control Technology, Vol. II, Electrostatic Precipitators. EPA-600/9-80-039b, September 1980. pp. 173-188.

4. McDonald, J. P., and A. H. Dean. A Manual for the Use of Electrostatic Precipitation to Collect Flyash Particles. EPA-600/8-80-025, May 1980.

5. Banks, S. M., J. R. McDonald, and L. E. Sparks. Voltage-Current Data from Electrostatic Precipitators Under Normal and Abnormal Conditions. In: Proceedings: Particulate Collection Problems Using ESP's in the Metallurgical Industry. EPA-600/2-77-208, October 1977.

6. White, H. J. Electrostatic Precipitation of Flyash. APCA Reprint Series, July 1977. pp. 22, 23.

7. Oglesby, S., and G. B. Nichols. A Manual of Electrostatic Precipitator Technology, Parts I and II, PB 196 380 and PB 196 381. August 1970.

TABLE 1. CRITERIA FOR RECORDKEEPING AND PERFORMANCE LEVELS

Level of Recordkeeping	Level of Performance
1. The air pollution control equipment and fan systems are devoid of monitoring instruments. No operating records can be taken.	1. The air pollution control device is in an advanced state of deterioration. Excursions above mass and visible emission levels are probably frequent and substantial.
2. Air pollution control systems have some of the necessary instruments, however, it is difficult to ensure compliance. These instruments are not always properly maintained and some will be inoperative a large fraction of the operating hours. Operating records are not taken.	2. There are frequent excess emission incidents which are largely preventable. Problems are not corrected in a timely manner. Nevertheless, the units are kept in compliance or near design limitations a majority (>50%) of the time by corrective maintenance.
3. All the instruments considered necessary to evaluate compliance are available. Because these instruments are checked regularly, most are operational at any given time. Although operating records are maintained routinely, they are often incomplete.	3. Excess emission incidents are relatively infrequent and at least ½ are due to "nonpreventable" factors. Units remain in compliance or near design limitations at least 90% of the operating hours and malfunctions are quickly identified.
4. All the instruments considered necessary to evaluate compliance are available. These instruments are checked and calibrated on a regular schedule, therefore, most are operational and indicates correct data at any given time. Operating records are complete and these are reviewed routinely to identify possible compliance problems.	4. Air pollution control devices remain in compliance or near design limitations a high percentage (>98%) of the time. Malfunctions and/or upsets are generally of the "nonpreventable" type only.
5. Sophisticated instrument systems useful for evaluating compliance and optimizing performance are available. These instruments are checked and calibrated regularly to ensure quality data. Operating records are reviewed regularly to ensure compliance and to optimize performance. A diagnostic repair log is maintained for each control device.	5. Operation of control devices is optimized to levels well below applicable mass and visisble emissions requirements. Malfunctions or upsets are very infrefrequent and only due to unpredictable, "nonpreventable" incidents.

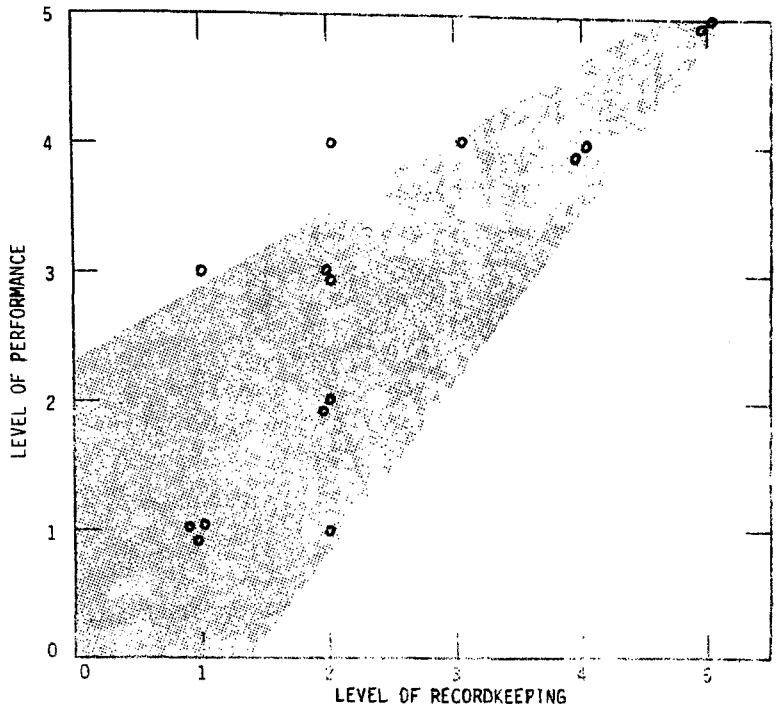

Figure 1. Relationship between performance and recordkeeping for several ESP cases.(1)

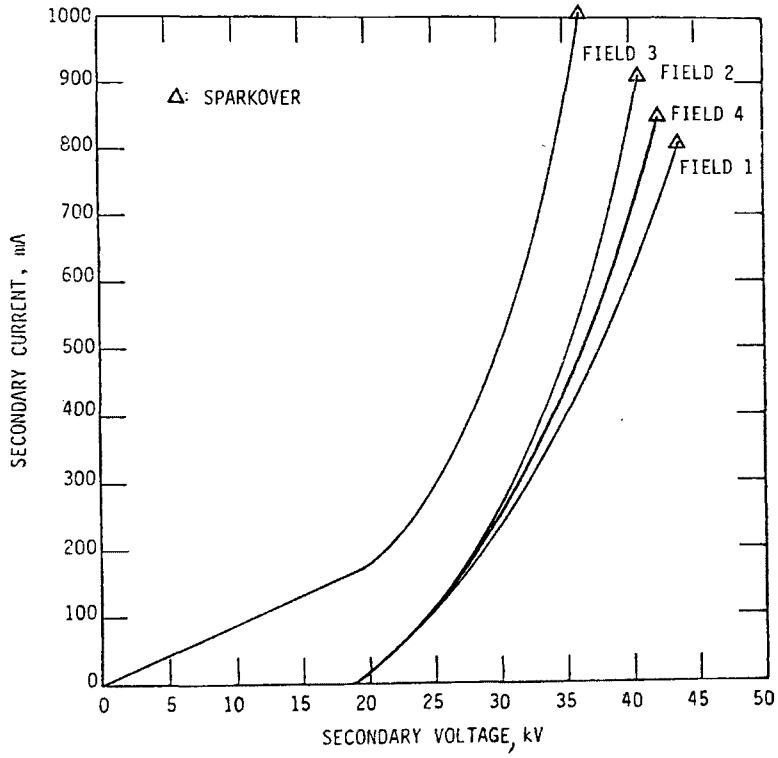

Figure 2. Examples of air load voltage-current curves for an ESP off-line.(1)

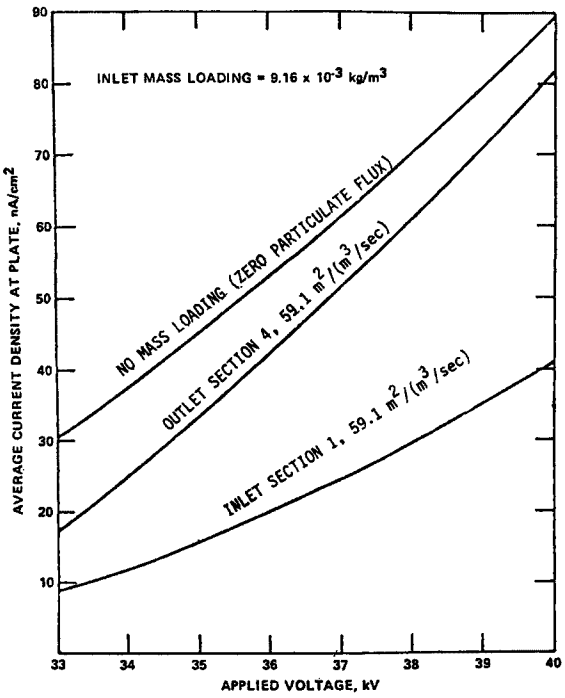

Figure 3. Comparison of theoretical voltage-current curves for different particulate flue conditions.(4)

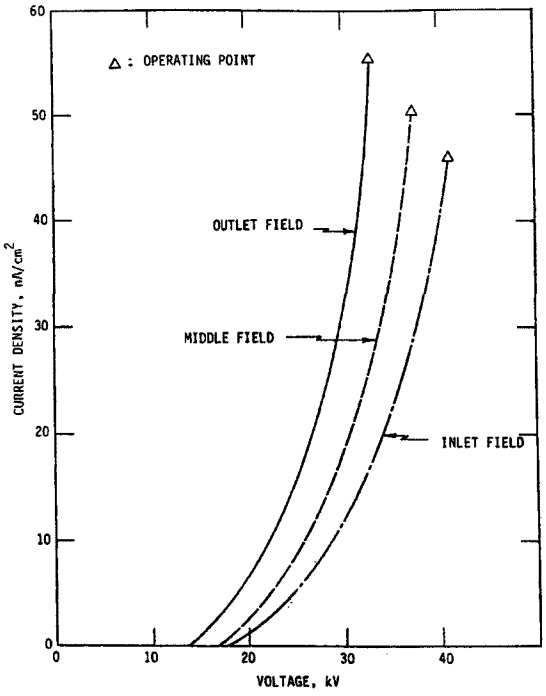

Figure 4. Secondary voltage-current curves demonstrating good operating conditions for a cold-side ESP.(4)

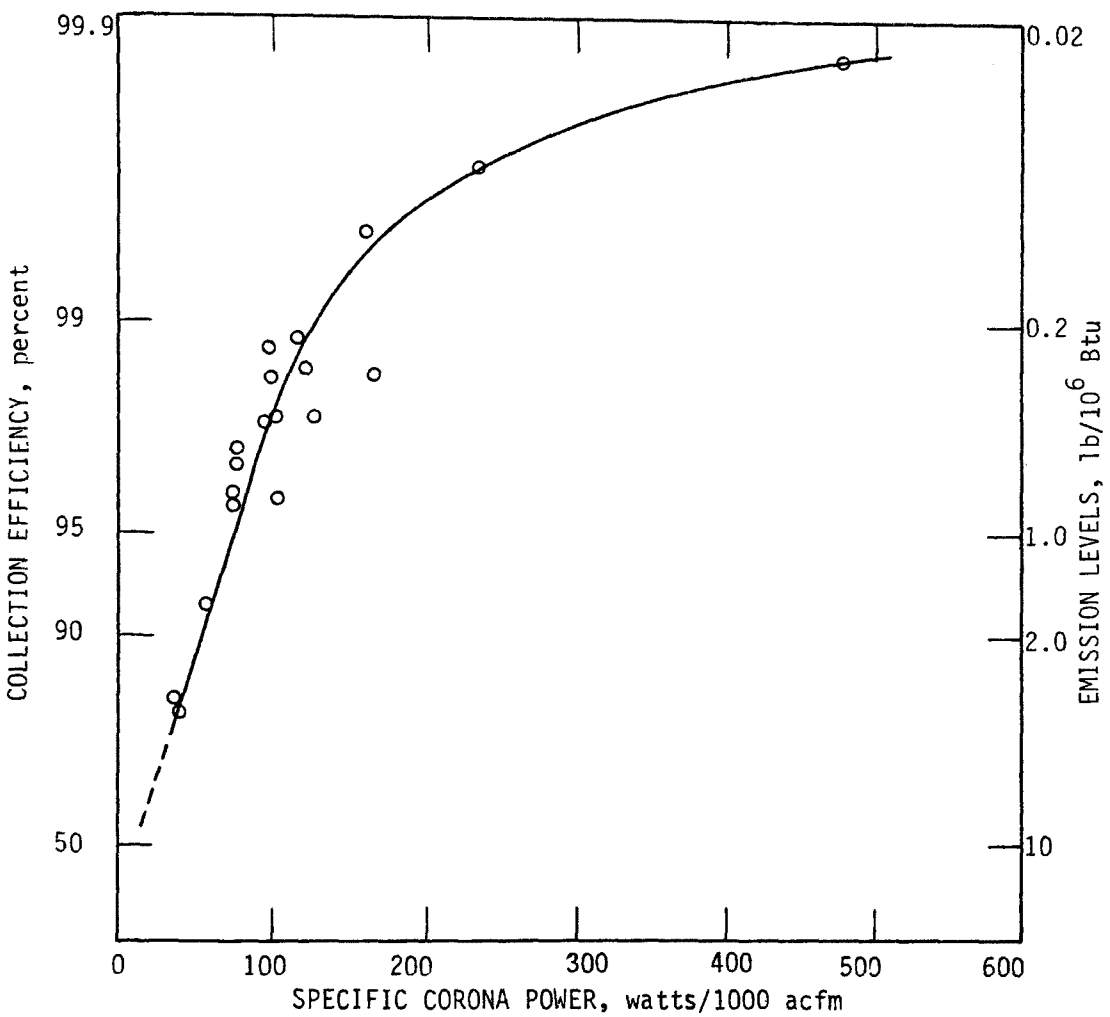

Figure 5. Efficiency versus specific corona power density extended to high collection efficiencies, based on field test data.(6)

AN OPERATION AND MAINTENANCE PROGRAM FOR A PHOSPHATE ROCK ELECTROSTATIC PRECIPITATOR

By: D. B. Rimberg, Ph.D.
North American PEMCO Inc.
P.O. Box 655
Bardonia, N.Y. 10954

ABSTRACT

An extensive investigation was performed on a weighted wire electrostatic precipitator to improve its performance on opacity. The application was on a phosphate rock fertilizer calciner. The program was designed to upgrade precipitator performance without major investment in new pollution control equipment. An extensive inspection, repair and replacement program was commenced to identify and rectify electro/mechanical problems. Through a sampling and testing program, it was determined that resistivity conditioning by moisture control was required. The program resulted in achieving compliance with no capital equipment investment. Sampled grain loading were reduced by a factor of ten. A regulated preventive maintenance program was instituted, thereby maintaining continuous mass and more importantly, opacity compliance status.

INTRODUCTION

The principle purpose of the phosphate fertilizer industry is to convert insoluble phosphate rock into water soluble phosphorus fertilizers for plant uptake. Florida possesses major phosphate rock deposits and accounts for approximately 78% of the nation's rock fertilizer production, the western states about 14%, the remaining from Tennessee and North Carolina.

Typically, phosphate fertilizer production initiates with crushing the phosphate rock and mixing it with aqueous sulfuric acid to produce phosphoric acid, insoluble calcium sulfate dihydrate (gypsum) and fluorine compounds. This reaction is approximated by the equation:

$$2H_2O + Ca_3(PO_4) + 3H_2SO_4 \rightarrow 2H_3PO_4 + 3CaSO_4 + 2H_2O$$

Water+Phosphate Ore+Sulfuric Acid→Phosphoric Acid +Gypsum

The phosphoric acid produced is 30-32% P_2O_5. This acid is then used to make various grades of fertilizers.

The precipitated gypsum is filtered from the acid, sluiced with recycled pond water and pumped to a gypsum pond. Fumes from the attact vessel are usually vented to scrubbers for fluoride removal before being passed to the atmosphere.

When utilizing western rock, a preliminary processing step is required before rock grinding, namely roasting (calcining). This process is necessary to handle undesirable organic matter (2%-8% by weight). This organic matter if not removed tends to stabilize a foam layer on the surface of the acid reactors. The presence of the organic material also produces a slimy gypsum

filter cake which is slow filtering and difficult to wash.

Calcining also supports the decomposition of carbonates which are present in the rock. Reduction in carbonate concentration reduces the release of carbon dioxide gas which would otherwise add to the foam problem.

Current practices in calcining allow for the roasting to occur at 1200°F to 1600°F in a multi-stage fluid roaster. The fluid bed roasters are normally equipped with cyclone collectors to capture particles which are liberated from the fluidized bed and returned to the process (Figure 1). However, extremely small particles pass through the cyclone and require additional collection equipment such as scrubbers or electrostatic precipitators. In the present application, an electrostatic precipitator was employed to collect cyclone throughput.

Problem Background and Troubleshooting Program

The subject electrostatic precipitator, although in compliance for mass emissions, could not constantly comply with opacity regulations. (Intermittent puffing from the stack was prevelant). Also, the precipitator often exhibited excessive sparking and reduced operating voltage. An expensive automatic voltage control system was installed and still the problem persisted. A replacement electrostatic precipitator system was being considered as a solution for an installed cost of $500,000 (1978 dollars).

Analysis of the problem was subsequently categorized into two areas: (1) characterization of the contaminants outlet of the calciner, aftercooler and electrostatic precipitator inlet and outlet: (2) electrostatic precipitator equipment mechanical/electrical malfunction.

A multiphase program was implemented to diagnose the various problems. The phases were divided in the following manner:

Phase I: Problem Identification
Phase II: Implementation
Phase III: Sampling & Testing
Phase IV: Preventive Maintenance

Equipment Description

The design specifications for the electrostatic precipitator employed to control the calciner emissions are provided in Table I.

The precipitator was installed in 1966/1967 and subsequently became subject to State emission regulations rate and an opacity of 40% for existing sources. (Needless to say, 1980 regulations are much more stringent).

Phase I: Problem Identification

General Observations/Interpretation-

The pretreatment simple cyclones and aftercooler cyclone were not signi-

ficantly reducing particulate loading to the precipitator. This was apparent from previously obtained particle size sampling data, (Table Test G) which revealed particles approximately 50 percent by weight larger than 10 microns downstream of the cyclones. Accordingly, this size particle should be easily removed by the existing cyclones.

Inspection of interconnecting material's handling system revealed that the product elevator duct allowed ambient air into the system. Aside from the duct handling particulate emissions from the conveyor system, the ambient air with entrained moisture was suspected to promote sporadic condensation with subsequent contaminant buildup in the fan and precipitator.

Previous information and onsite observations indicated correlation of stream moisture and opacity. A major portion of the moisture entered the stream through cooling water injection nozzles in the aftercooler (Figure 1). The moisture was believed to affect particle resistivity.

Frequent temperature changes in process were thought to be reaching dew point in the precipitator.

Rappers-Nine of the 17 rappers (vibrators) were inoperative, malfunctioning, or missing. The complete rapper system contained many inoperable components.

Timer-Rappers were not sequenced or timed properly.

Insulators-One high voltage insulator was cracked.

Wire Frame Stabilizer-Loose insulation.

High Voltage Bus Ducts-Gasketing and several bolts on three bus duct hatches missing.

Insulator Compartment Ventilation System-Contained air leaks and dirty filters; blower was incapable of overcoming positive pressure in the precipitator housing.

Additional Equipment Required-No temperature monitor was present at the inlet of the precipitator.

Recommendations-

Observe stack opacity while manually controlling water injection.

Renovate, repair and replace old rappers.

Replace broken insulator.

Secure stabilizer insulators.

Install new gaskets and insulator compartment blower and filter.

Install thermocouple probe upstream of precipitator to determine if dew point is reached.

Inspect and clean cyclones.

A sampling and testing program was devised to characterize the cyclones and precipitator inlet and outlet streams. Parameters measured included grain loading (ASME-WP50), particle size (impactor and electron microscope), moisture grainmetric), temperature, opacity, and pertinent process variables. A prerequisite in acquiring the data was to minimize sampling duration (five minutes or less) to permit observations of peak concentrations.

Phase II: Implementation

Rapper Units-Nine new rapper units were installed and adjusted. The remaining seven units were rebuilt and adjusted. One of the two gas inlet distribution plate rappers (which had been missing since the precipitator was originally installed) was not replaced since previous operating experience revealed no contaminant buildup and therefore the single existing rapper was considered sufficient.

Rapper Mounts-All twelve of the plate rapper mounts were disassembled, and reinstalled. Three worn anvils and pins were replaced.

The four wire frame rapper mounts were disassembled and cleaned. Four new shaft insulators were installed. (It was suspected that these insulators had probably never been inspected, cleaned or replaced since the precipitator was installed). A new cap for one of the insulators was machined and installed.

Rapper Timers-New contacts and cam followers were installed in the timers. Cam timing and contact clearances were adjusted.

A new starting capacitor was installed in the motor drive circuit.

Insulators-All insulators were inspected, cleaned and coated with silicone. Two insulators which could not be cleaned properly were replaced.

All insulator bushing gaskets were replaced.

Wire Frame Stabilizers-All four stabilizers at the bottom of the wire frames were cleaned and securely fastened to the wire frames. New asbestos pads were also installed.

Bus Ducts Insulator Housings, Hatches-The bus ducts and insulator housings were cleaned. New gasketing was installed on all hatches and all missing bolts were replaced; new studs were installed where required.

Insulator Compartment and Ventilating System-New air filters were installed. Heater and fan operation were checked.

Duct air leaks around the heater was repaired.

Air distribution ducting was unplugged and cleaned. Baffling at the entrance to the insulator housings was modified to provide less restrictions to airflow.

Internal Inspection-An internal inspection of wires, frames and housing, was performed. All wires and other components were found to be intact.

The internal components of the precipitator were cleaned as required.

Temperature Sensors-Thermocouple probes monitoring precipitator inlet and outlet temperatures were installed. A chart recorder and digital readout were provided in the control room to continuously monitor the respective temperatures.

Phase III: Sampling & Testing

To ascertain the effectiveness of the aforementioned mechanical service, repair and replacement phase, a sampling and testing program was commenced. At the outset, an airload test was performed to establish the baseline pre-

cipitator operating conditions. Following this, the sampling and testing program was initiated. These tests were designed to acquire inlet and outlet particle size distribution by both inertial impaction and electron microscopy methods. Also, sampling for grainloading, along the opacity observations, were continuously performed during the entire sampling period.

The test program was initiated and evaluated for a given production rate (Test A) and then at a higher rate (Test B). Opacity observations of the frequency and duration of "puffs" were simultaneously recorded. To examine the effect of aftercooler water injection, Test C was performed at Test A production rate. The water injection rate during Test C was manually controlled and maintained above 10gpm minimum while quantitative sampling was performed. The results of these tests are shown in Table II. For comparison purposes, previous sampling tests are also given in Table II.

To expedite particulate sampling, single point isokinetic samples were extracted after the average flow rate was determined. Inlet and outlet sampling was performed for five and twenty minutes respectively.

Sampling for scanning electron microscopy (SEM) particle size distribution was performed by "in stack" membrane (0.30 micron) filters. Sampling duration at the inlet was one second, and outlet twenty seconds.

Sampling and Testing Results-

Grainloading, Particle Size (Impactor)-Quantitative and qualitative results from Table II for Test C indicate an outlet concentration of 0.014 GR/AFC and opacity less than 5% with an efficiency of 99.7%. These results compared with previous outlet data (>.109) GR/AFC) were the most gratifying to date. The reason for this was primarily due to the manual control of the aftercooler water rate and the recently completed electrostatic precipitator service and maintenance program.

The apparent decrease in precipitator inlet particle size from 10.7 microns in Test G to less than four microns during Test A and C, reflected the maintenance work performed on the cyclones. However, the corresponding inlet dust load still was less than anticipated.

Since the variation of the production rates for Tests A and B were significant, it was concluded that emissions reduction was strictly related to improved precipitator performance. Generally speaking, Tests A and B showed substantial improvement in precipitator performance compared with the previous Tests D-H given in Table III.

Particle Size (Scanning Electron Microscopy)-Since visibility or light scattering from a plume is largely determined by geometric particle size (and refractive index) it was deemed necessary to characterize submicron size distribution by SEM in the range from 0.2-1.0 micron (in intervals of 0.2 microns; Table III). The cumulative frequency size distribution by number and weight with their corresponding number (NMD) and mass median diameters (MMD) and geometric standard deviation are given in Table III. Larger parti-

cles (>1.0 micron) were not counted since they do not produce significant light scattering and would also require numerous SEM's to be produced and evaluated at low magnification.

The size distribution obtained from the SEM's regardless of their inlet and outlet conditions, reveal a number medium diameter (NMD) range from 0.19-.32 microns the data of which is given in Table III. These results are expected since electrostatic precipitators are relatively inefficient for collection of particles of less than one micron. Since number concentration measurements (particles per unit volume) could not be obtained because of the difficulty in controlling inlet sampling time (approximately one second) a valid comparison between submicron inlet and outlet number concentrations could not be made.

The major value in acquiring the SEM's was to verify that the plume opacity was produced by high numbers of submicron particles. One could easily be mislead if the impactor data only was considered since size distribution obtained in this manner give an outlet MMD of 1.2. microns and greater.

Critical Service Items-

The following items were critical to proper precipitator operation and it was recommended that plant personnel check them regularly:

Rapper System (Weekly)-Check and adjust rappers in place at thirty percent power (30%).
Check rapper shafts for freedom of movement where it passes through the housing.
Check timer for burned contacts.
Insulators (when excessive arcing occurs)-Check all insulators for cracks, excessive dust buildup (more than 1/8" thick), and arcing tracks. (Be sure to check rapper rod insulators in insulator housings).
Check lower stabilizers.
Recoat insulators with silicone after cleaning.
Vent and Heater System (Monthly)-Check heater for proper temperature.
Check air filters.
Check system for adequate airflow at insulator housings.
Bus Ducts (when open)-Be sure gasketing and bolts on all hatches are intact.

CONCLUSIONS

Precipitator Capability

When properly serviced and maintained, the existing equipment was capable of adequately controlling the calciner emissions within the environmental requirements.

Calciner Liquid Flow Rates

To minimize the periodic "puffing" of the exhaust plume an automatic

water control system on the aftercooler was installed. The controlled moisture content of the airstream will increase the overall precipitator collection efficiency.

Temperature Monitors

The temperature monitors on the precipitator inlet and outlet aided the operators in maintaining the optimum temperature in the precipitator required for efficient collection. This also prevented moisture from condensing in the precipitator.

Opacity

Plume opacity occurred when the airstream contained high concentrations of submicron particles less than 0.32 microns.

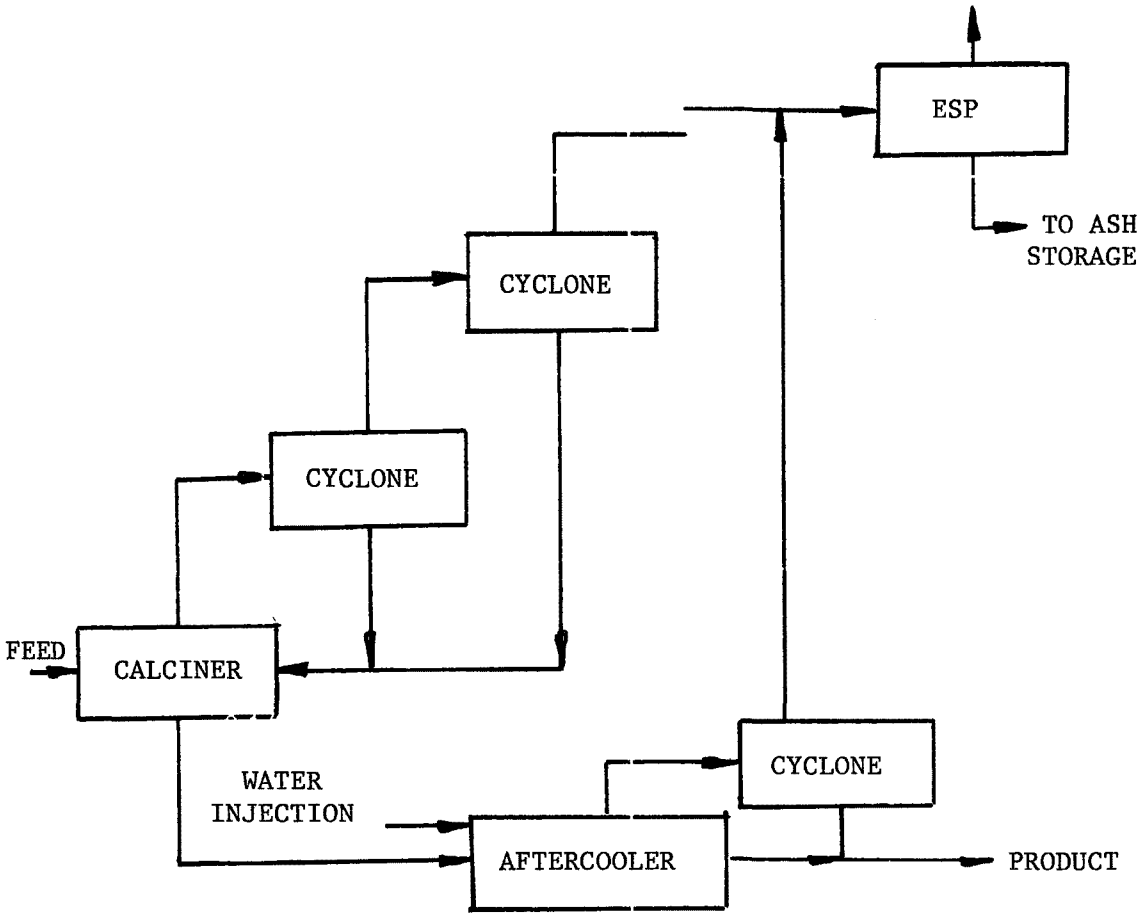

Figure 1. SCHEMATIC DIAGRAM OF CALCINER SYSTEM

TABLE I. ELECTROSTATIC PRECIPITATOR - DESIGN SPECIFICATIONS

Normal Operating Conditions

Flowrate:	70,000 CFM (nominal)
Temperature:	234 - 285 ^{o}F
Pressure:	Positive
Inlet loading, approximate:	6 - 7.5 gr/acf
Gas velocity thru collector:	3.26 fps
Retention time:	5.51 sec
Type of suspended matter:	phosphate dust

Estimated Operating Requirements

Draft loss (pressure drop from the inlet to the outlet of the collection equipment, not including nozzles):	0.5" VWC
Total connected load, base offering:	81 KW
Electrical characteristics:	440 v, 60 cy, 3 ph

Collection Equipment

Number of electrostatic precipitators:	1
Number of cells per precipitator width:	1
Number of fields per precipitator length:	2
Design pressure, positive:	15" VWC
Casing thickness:	3/16"
Collecting surfaces -	
Gas passages per cell-field:	24
Spacing of gas passages:	9"
Surface size:	9' x 20'
High voltage electrode diameter:	.1055"
Collecting surface rappers per cell-field:	5
High voltage system rappers per cell-field:	2
Destribution device rappers, total:	2

Electrical Energizer and Control Equipment

Energizer sets:	1
Transformer ratings:	50 KV 1200 MA
Rectifier circuit:	full wave
Rapper control panel:	1

TABLE II. RESULTS OF SAMPLING

	LOCATION	TEMP °F	FLOWRATE ACFM	MOISTURE % VOLUME	CONC. GR/ACF	DUST LOAD LB/HR.	MASS MED. DIA. (MICRON)*	NO. MED. DIA. (MICRON)*	PRODUCTION RATE (TPH)	EFFICIENCY %	OPACITY %	NO. PUFFS HR.	DURATION SEC.
C	INLET	265±3	-	17	4.1	2199	4.0 (0.74)	0.32	C	99.7	-	-	-
	OUTLET	265±3	61940	28	0.014	7.56	1.2 (0.80)	0.19			<5	~ 10	10 SEC.
B	INLET	265±3	-	18.3	3.8	2160	2.7 (0.68)	0.22	B	99.3	-	-	-
	OUTLET	265±3	65755	22.5	0.027	15.2	1.8 (0.80)	0.29			<10	~ 30	10-30 SEC.
A	INLET	265±3	-	22.6	5.3	3190	4.0 (0.68)	0.19	A	99.6	-	-	-
	OUTLET	265±3	70120	24.4	0.022	13.2	1.2 (0.69)	0.24			<10	~ 30	10-30 SEC.
D	INLET	325	-	17.6	6.2	3454	NA	NA	D	99.2	-	-	-
	OUTLET	313	65000	22.1	0.5	278	NA	NA					
E	INLET	330	-	14.3	8.01	4874	NA	NA	E	98.6	-	-	-
	OUTLET	312	71000	27.7	0.109	66.3	NA	NA					
F	INLET	335	-	14.1	NA	NA	NA	NA	F	-	-	-	-
	OUTLET	320	63100	17.7	0.192	103.8	NA	NA					
G	INLET	331	-	14.3	6.430	3505	10.7	NA	G	98.3	-	-	-
	OUTLET	310	63600	16.7	0.107	58.3	NA	NA					
H	INLET	335	-	11.3	4.590	2227	NA	NA	H	97.4	-	-	-
	OUTLET	313	56600	28.5	0.121	58.7	NA	NA					

* MMD AND NMB OBTAINED BY SEM BELOW ONE MICRON ONLY
\+ BY IMPACTOR

TABLE III. PARTICLE SIZE DISTRIBUTION
SCANNING ELECTRON MICROSCOPY

TEST			0.2	0.2 - 0.4	0.4 - 0.6	0.6 - 0.8	0.8 - 0.10	NMF MMD σ_g
	- INLET	NO %	26.44	26.44	28.81	10.85	7.46	0.32
		CUM %	26.44	52.88	81.69	92.54	100.00	2.0
A		WT %	0.20	5.29	26.68	27.56	40.27	0.74
		CUM %	0.20	5.49	32.17	59.75	100.00	1.54
	- OUTLET	NO %	54.06	22.10	11.72	6.89	5.24	0.19
		CUM %	54.06	76.16	87.88	94.77	100.00	2.58
		WT %	0.65	7.19	17.65	28.46	46.06	0.80
		CUM %	0.65	7.84	25.49	53.95	100.00	1.66
	- INLET	NO %	48.08	28.02	15.93	4.87	3.10	0.22
		CUM %	48.08	76.10	92.03	96.90	100.00	2.0
B		WT %	0.72	11.25	29.62	24.83	33.58	0.68
		CUM %	0.72	11.97	41.59	66.42	100.00	1.6
	- OUTLET	NO %	31.88	33.15	19.49	8.20	7.29	0.29
		CUM %	31.88	65.03	84.52	92.72	100.00	2.1
		WT %	0.28	7.79	21.21	24.48	46.24	0.8
		CUM %	0.28	8.07	29.28	53.76	100.00	1.7
	- INLET	NO %	53.44	28.07	10.80	5.13	2.56	0.19
		CUM %	53.44	81.51	92.31	97.44	100.00	2.1
C		WT %	0.92	13.09	23.31	30.38	32.29	0.68
		CUM %	0.92	14.01	37.32	67.70	100.00	1.7
	- OUTLET	NO %	43.63	32.67	17.29	3.68	2.74	0.24
		CUM %	43.63	76.30	93.59	97.27	100.00	1.9
		WT %	0.69	13.90	34.04	19.91	31.46	0.69
		CUM %	0.69	14.59	48.63	68.54	100.00	1.7

ELECTROSTATIC PRECIPITATOR PERFORMANCE WITH PULSE EXCITATION

by

Donald Rugg
Michael Durham
George Rinard

Denver Research Institute, Denver, Colorado

and

Leslie Sparks

Industrial Environmental Research Laboratory
Environmental Protection Agency
Research Triangle Park, North Carolina

ABSTRACT

A laboratory electrostatic precipitator was energized by pulse power supplies. The voltage-current characteristics were measured under clean and high-resistivity dust conditions. The results, which illustrate the relationships between corona current and the peak and average voltages, are shown. Charge-to-mass ratios, particle-size distributions, and mass efficiencies were measured. The data were analyzed to determine the major factors which account for the increase in mass efficiency for pulse excitation compared to efficiencies obtained with dc excitation. The data and the results of the analysis are presented.

INTRODUCTION

Pulse excitation, consisting of an average voltage with a pulse voltage superimposed upon it, was applied to a laboratory electrostatic precipitator (ESP). Measurements were made to obtain experimental data which would assist in understanding and evaluating the basic concepts of pulse excitation.

The electrical characteristics of interest were the peak voltage, average voltage, average current, and current distribution over the collector plates. These characteristics were measured at 150°C (300°F) under both clean and high-resistivity dust (6×10^{12} ohm-cm) conditions. The results show the changes in the voltage-current relationship due to high-resistivity dusts and also provide a basis for selecting the operating levels of peak voltage, average voltage, and average current for optimum ESP performance.

Charge-to-mass ratios and mass penetration measurements were made to determine the charging and collecting characteristics of the ESP with pulse excitation. Also, a Meteorology Research Incorporated (MRI) Plant Process Visiometer (PPV) was used to monitor the relative outlet opacity. These

results were compared to measurements made using dc excitation in an attempt to determine if improvement in efficiency was due to higher charge on the particles or to higher field strength for particle collection.

DESCRIPTION OF PULSE POWER SUPPLY

A sketch of the pulse power supply is shown in Figure 1. The circuit is similar to the ones described by Lausen [1] and Masuda [2].

The controls consist of a variable pulse repetition rate (PRR) of 0 to 110 pulses per second (pps) and a variable pulse amplitude of 0 to 55 kV. A capacitor in the primary of the 1:50 step-up transformer is charged to a voltage v_c which determines the pulse amplitude. The SCR switch is triggered by a timing circuit which determines the PRR, and the capacitor is connected to the pulse transformer for one cycle of primary current. Figure 2 (a) shows that the primary capacitor discharges during the first half-cycle of primary current and recharges during the second half-cycle. The output pulse v_o is shown in Figure 2 (b). The output voltage increases during the first half-cycle and decreases during the next half-cycle. This duration, which is considered to be the pulse width, is about 220 μs for one power supply and about 180 μs for the other.

The output pulse was capacitor-coupled to the corona discharge electrode. A dc bias voltage, variable from 0 to 60 kV, was added to the pulse voltage through a blocking diode. Therefore, the pulse power supply permitted independent control over peak and average voltages and PRR.

ESP VOLTAGE-CURRENT CHARACTERISTICS

Pulse excitation consists of an average voltage with a pulse voltage superimposed upon it. Measurements were made to determine the extent to which the corona current can be regarded as consisting of two independent components, one due to the pulse voltage, and the other due to the average voltage.

Wire electrodes 3.18 mm (1/8-in.) in diameter were placed in the ESP at a spacing of 22.9 cm (9 in.). Measurements were made at 150°C (300°F) for both clean and dirty conditions. The average current vs. average voltage (V_A/I_A) curves were measured using dc excitation and pulse excitation. For pulse excitation, the peak voltage, which is the sum of the pulse voltage and the average voltage, was maintained at 60 kV and the PRR was set at 110 pps.

The results of these measurements are shown in Figure 3. For clean conditions and dc excitation, the corona onset voltage was 26 kV. For clean conditions and pulse excitation, there was corona current due to the pulse voltage when the average voltage was only 5 kV. As the average voltage was increased and the peak voltage was held constant at 60 kV, the current increased until the average voltage was about 15 kV. This current increase was probably due to the increase in time that the pulse voltage was above corona onset. The current density remained constant at 12 nA/cm^2 as the average voltage was increased from 15 kV to 25 kV. This indicates that the current was due to the pulse voltage and was independent of the average

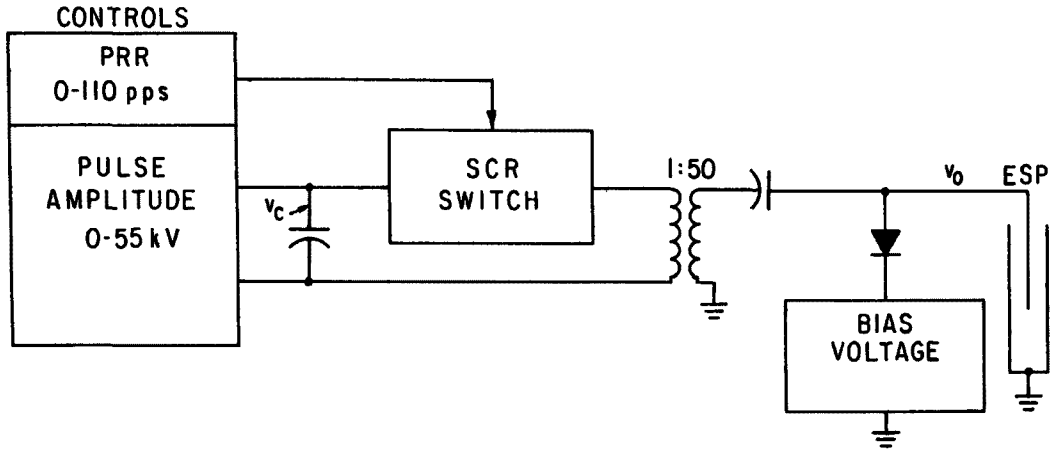

FIGURE 1. PULSE POWER SUPPLY

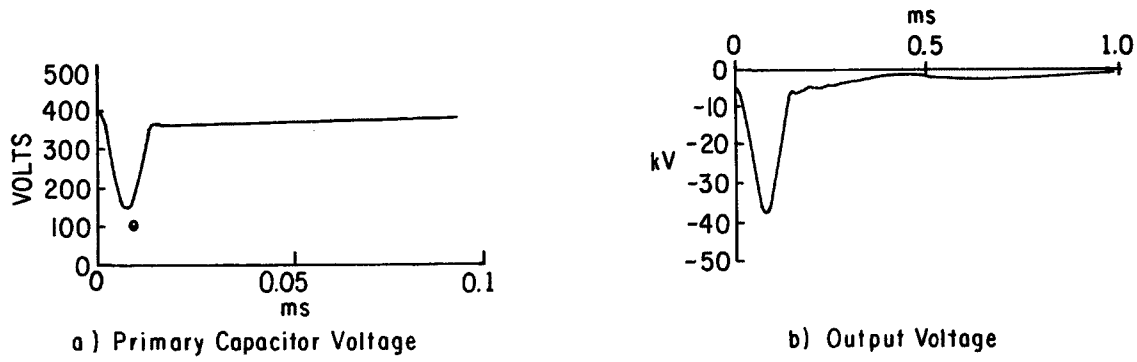

FIGURE 2. PULSE POWER SUPPLY WAVEFORMS

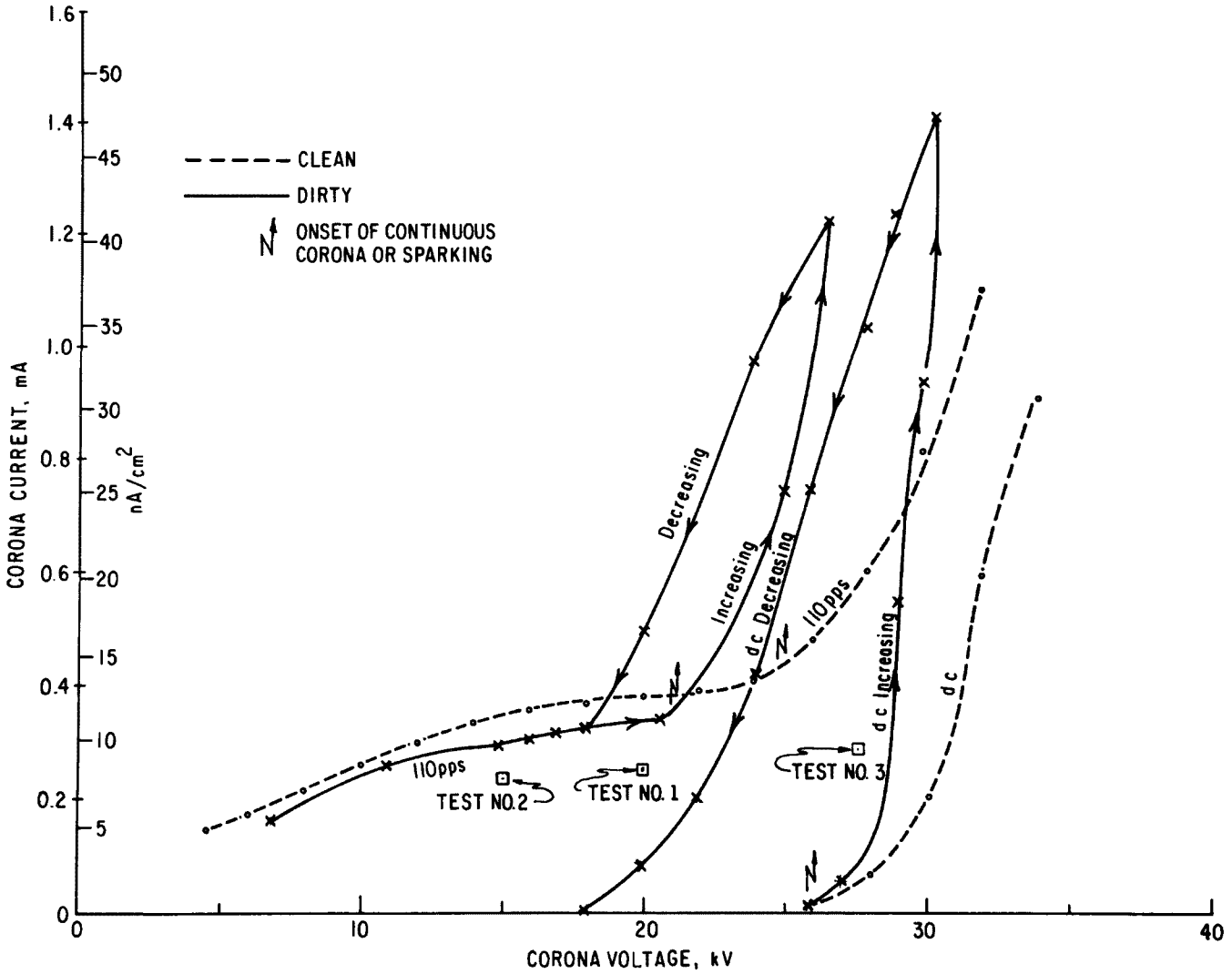

FIGURE 3. AVERAGE CURRENT vs AVERAGE VOLTAGE FOR 3.18 mm (1/8-in.) WIRE WITH/WITHOUT 60 kV PEAK PULSE.

voltage, which was below dc corona onset. For average voltages above 25 kV, the corona current increased rapidly as shown by the curve for clean conditions. This indicates that the corona current was being sustained between pulses by the average voltage. Occasionally, sparking rather than continuous corona would occur when the average voltage reached 25 kV.

For dirty conditions and dc excitation, the corona onset voltage was 26 kV (the same as for clean conditions). However, as the dc voltage was increased, the current increased abruptly, as shown in Figure 3. As the voltage was reduced, the corona current did not cease until the voltage was 18 kV. This hysteresis in the V_A/I_A curve indicated the presence of back corona.

For dirty conditions and pulse excitation, the V_A/I_A curve was similar to the clean-condition curve when the average voltage was below 21 kV. It appears that the current was due to the pulse voltage and not to the average voltage. As Figure 3 shows, when average voltage was increased above 21 kV and sparking did not occur, the current increased abruptly, indicating that the average voltage was sustaining corona current between pulses. Also, the hysteresis in the V_A/I_A curve for dirty conditions and pulse excitation indicates that back corona was produced and did not cease until the average voltage was reduced below 18 kV. This was the same voltage at which corona ceased with dc excitation.

The effects of reducing the PRR were observed. For average voltages below the onset of continuous corona, the corona current decreased as the PRR was decreased. However, corona current could be controlled by the PRR only if the average voltage was maintained below the onset of continuous corona.

Current distributions on the collector plate were measured under dirty high-resistivity conditions for dc and pulse excitation. A 0.279 m^2 (3 ft^2) area on one collector plate was divided into 96 isolated cells 29 cm^2 in area and the current to each cell was measured. For dc excitation and an average current density of 5 nA/cm^2, there was no current on 90% of the collector plate area and high current densities on a few cells. This indicates that back corona was established on these localized areas. For pulse excitation without continuous corona and at about the same average current density, the current was uniform over the collector plate. When the average voltage was high enough to produce continuous corona current, the additional current was not uniformly distributed over the collector plate. This again indicates that under pulse excitation, back corona was established when continuous corona current was present.

The curves in Figure 3 show that the corona current can be regarded as consisting of a component due to the pulse voltage and a component due to the average voltage. When corona current was due to only the pulse voltage, the current distribution was uniform and back corona did not exist for the high-resistivity dirty conditions. However, if the average voltage was high enough to sustain corona current between pulses, then it appeared that back corona existed. With dust, the onset of continuous corona occurred at average voltages of 18 kV to 26 kV, depending upon the amount of pulse corona current.

ESP CHARGING AND COLLECTING CHARACTERISTICS

Charge-to-mass ratio, particle size distribution, and mass penetration measurements were made to determine ESP charging and collecting characteristics of high-resistivity fly ash with pulse excitation. Since charging and collection of particles may be a function of both peak and average voltages [3], tests were run at two different average voltage levels to determine their effect upon charging and collecting. The test was repeated using dc voltage in order to make direct comparisons between the two types of excitation.

The laboratory ESP consisted of one 22.9 cm (9 in.) wide channel, which was 1.22 m (4 ft) high and 4.88 m (16 ft) long. The corona electrodes were 3.18 mm (1/8-in.) wires, spaced 22.9 cm (9 in.) apart, and the total collector plate area was 11.9 m^2 (128 ft^2). The gas velocity was 2 m/sec (6.65 ft/sec), which resulted in an SCA of 21 sec/m (107 ft^2/1000 acfm). Mass loading and impactor measurements were made across the inlet and outlet of the ESP. These measurements were made at three sampling ports (top, center, and bottom) at each location. Also, the charge and mass were measured at a center port located 1.22 m (4 ft) upstream from the outlet sampling ports. Mass penetration, inlet and outlet particle size distribution, and Q/M ratio were determined from these measurements.

The experimental results of the three tests are listed in Table I. In all three tests, the dust at the inlet had a mass median diameter of 4.9 μm and a geometric standard deviation of 3. In Test No. 1, the peak voltage was set at 60 kV, which was slightly below the sparking voltage; the average voltage was set at 20 kV, which was below the onset of continuous corona or back corona; and the current density was adjusted to 8.4 nA/cm^2 by the PRR. The measured Q/M was 19.6 μC/g and the mass penetration was 0.118. The modified migration velocity, ω_k, was 0.22 m/sec. Several investigators [4, 5] consider the empirically derived ω_k to be a measure of ESP performance, and ratios of ω_k are referred to as improvement factors.

Test No. 2 was the same as Test No. 1, except the average voltage was reduced from 20 kV to 15 kV. The Q/M ratio was 17.6 μC/g, which was 10% less than in the first test. The mass penetration of 0.115 and modified migration velocity of 0.22 m/sec were essentially unchanged. The mass median diameter of the particles at the outlet was 2.5 μm compared to 1.75 μm in Test No, 1. In part, this difference was probably a result of making only one impactor measurement at each of the three outlet sampling ports during a test. The effects of lowering the average voltage were not large enough to be determined from the results of Test No. 1 and Test No. 2.

In Test No. 3, dc excitation was used. The average voltage was 27.6 kV and the current density was about 9 nA/cm^2. This operating point, and the average voltage and current operating points for the first two tests, are shown in Figure 3. The dc operating point was kept near the increasing voltage V_A/I_A curve by manually decreasing and then increasing the voltage whenever the current rose above 12 to 14 nA/cm^2. This procedure kept the outlet opacity at a minimum level. Although the average voltage was higher

TABLE I: EXPERIMENTAL RESULTS

	Test No. 1	Test No. 2	Test No. 3
d_{in}, μm	4.9	4.9	4.9
σ_{in}	3.0	3.0	3.0
V_p, kV	60	60	--
V_A, kV	20	15	27.6
j_A, nA/cm^2	8.4	7.6	8.9
SCA, sec/m	21	21	21
Q/M, μC/g	19.6	17.6	6.0
M_{out}/M_{in}	0.118	0.115	0.248
ω_k*, m/sec	0.22	0.22	0.093
d_{out}, μm	1.75	2.5	3.0
σ_{out}	2.0	2.4	2.7

Resistivity = 6 x 10^{12} ohm-cm

*$\omega_k = [\ln (M_{out}M_{in})]^2/SCA$

than during the two pulse excitation tests, Q/M was only 6.0 μC/g, the mass penetration was 0.248, and ω_k was 0.093 m/sec. The outlet particles had a mass median diameter of 3 μm, which was larger than in the first two tests. The larger size particles were expected since the mass penetration was larger. In comparison to dc excitation, the improvement factor for pulse excitation was 2.36.

The effect of operating with the average voltage above the onset of continuous corona was determined by observing the PPV output which is a relative measure of the outlet opacity. Initially, the average voltage was set at 27 kV and the pulse source was off. Then a 25 kV pulse was added to the average voltage to produce a peak voltage of 52 kV and the outlet opacity decreased. The peak was kept at 52 kV and the average voltage decreased to 10 kV. Again, the outlet opacity decreased. These observations indicate that the best performance was achieved with pulse excitation when the average voltage was below the onset of continuous corona.

The Q/M ratio depends upon the particle size distribution, ion density, treatment time, and field strength. To assist in understanding this relationship, Q/M ratios were calculated as a function of applied dc voltage on the ESP for three different particle-size distributions, assuming constant

current density and constant treatment time. The results are shown in Figure 4. It appears that a dc charging voltage of 50 kV to 60 kV would produce the same Q/M ratios that were measured in the pulse excitation tests. This equivalent dc-charging voltage was considerably higher than the average voltage. The dc-charging voltage of 27.6 kV in Test No. 3 should have produced a Q/M ratio of 10 μC/g. Since the measured Q/M ratio was only 6 μC/g, it appears that many particles were never charged or that particles lost their charge through collection and reentrainment.

The ESP performance for various dc-charging and collecting voltages was calculated. The charge and penetration, as a function of particle size, were determined using field and diffusion charging theory and the classical Deutsch equation for collecting. The results were integrated to calculate the theoretical Q/M ratio and penetration. The modified migration velocity, ω_k, was calculated from the theoretical penetration. The inlet size distribution, current densities, and SCA were assumed to be the same as in the experimental tests.

Column A in Table II shows theoretical results for charging and collecting voltages of 20 kV. The calculated Q/M ratio was low and the penetration was high in comparison to Test No. 1. This indicated that both charging and collecting were better than for an ESP operating at 20 kV dc without high-resistivity dust problems. The theoretical results for 60 kV charging voltage and 20 kV collecting voltage are listed in Column B. In comparison to Test No. 1, the calculated Q/M was high, indicating that the effective charging voltage was less than the 60 kV peak voltage. The calculated penetration was high, indicating that the effective collecting voltage was higher than the 20 kV average. The dc conditions of Test No. 3 were used to calculate the values in Column C. The theoretical penetration was lower than measured values. This indicates that the ESP performance was low with dc excitation because of the high-resistivity dust.

TABLE II: CALCULATED ESP PERFORMANCE FOR VARIOUS CHARGING AND COLLECTING VOLTAGES

	A	B	C
d_{in}, μm	4.9	4.9	4.9
σ_{in}	3.0	3.0	3.0
Charging voltage, kV	20	60	27.6
Collecting voltage, kV	20	60	27.6
j_A, nA/cm^2	8.4	8.4	8.9
SCA, sec/m	21	21	21
Q/M, μC/g	9.3	25.9	13.4
M_{out}/M_{in}	0.348	0.145	0.206
ω_k*, m/sec	0.053	0.178	0.119

*$\omega_k = [\ln (M_{out}M_{in})]^2/SCA$

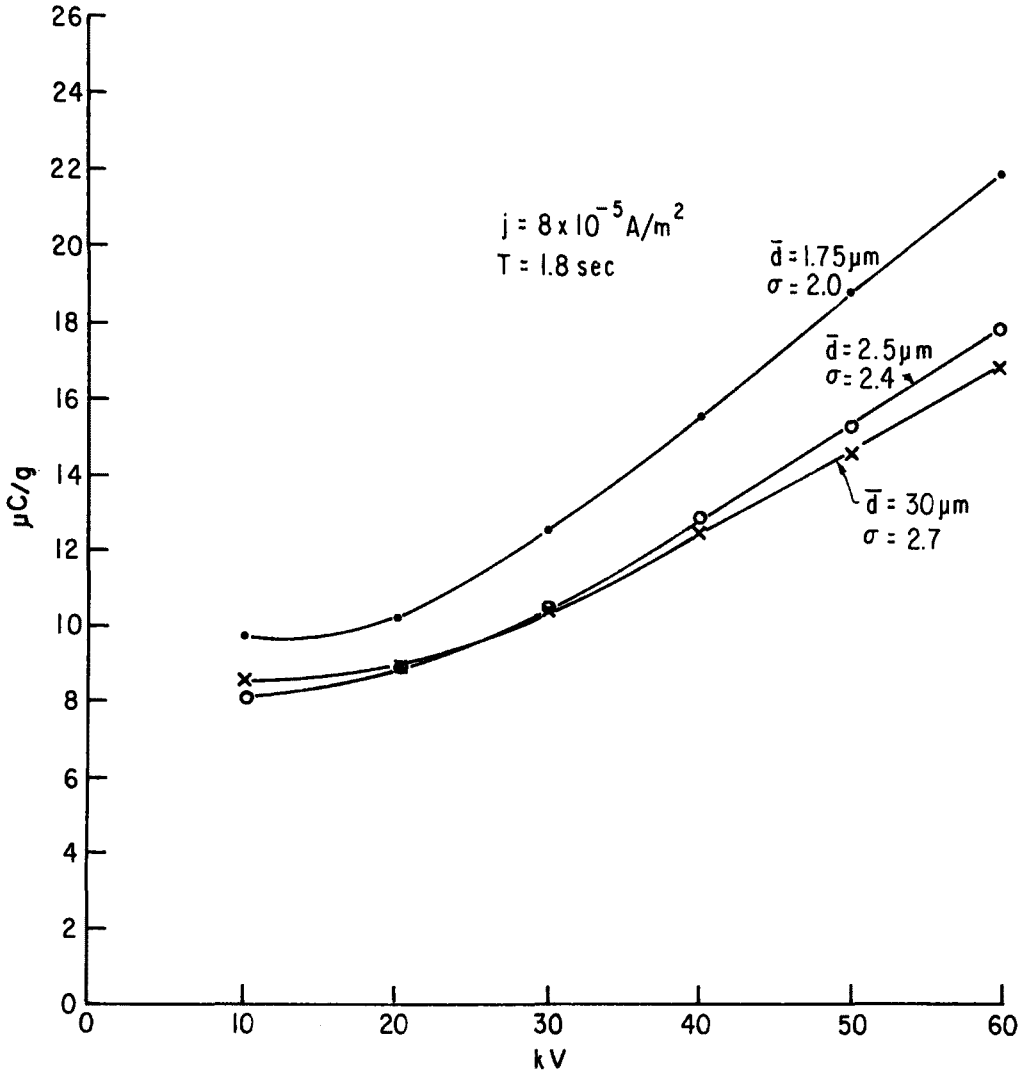

FIGURE 4. CALCULATED Q/M RATIOS FOR VARIOUS CHARGING VOLTAGES

CONCLUDING REMARKS

Maximum ESP efficiency was achieved by operating with the peak voltage slightly below sparking, the average voltage below the onset of continuous corona, and the PRR at its maximum rate. Under these conditions, the corona current was uniformly distributed over the collector plate and there was no indication of back corona. However, when the average voltage was high enough to sustain corona current, there were indications of back corona and the ESP outlet opacity increased. Therefore, in evaluating pulse excitation, it is important to know under which of the two average voltage conditions the ESP was operating.

The improvement in efficiency with pulse excitation in comparison to dc excitation appears to be due to a higher charge on the particles and a higher field strength for particle collection.

REFERENCES

[1] Lausen, P.; Henrikson, H.; and Petersen, H.; "Energy Conserving Pulse Energization of Precipitators;: IEEE-IAS Conference, Cleveland, Ohio; October, 1979.

[2] Masuda, S.; Obata, G.; and Hirai, J.; "A Pulse Voltage Source for Electrostatic Precipitators;" Proc. IEEE-IAS Conference, Toronto, Canada; October, 1978.

[3] Masuda, S.; and Mizuno, A.; "Maximum Charge of a Spherical Particle Imparted by Pulse Charging;" Proc. 1978 International Workshop on Electric Charges in Dielectrics, Kyoto, Japan; October, 1978.

[4] Petersen, H.; "New Trends in Electrostatic Precipitation - Wide Duct Spacing, Precharging, Pulse Energization;" IEEE Cement Industry Technical Conference, Toronto, Canada; May, 1980.

[5] Feldman, P.; and Milde, H.; "Pulse Energization for Enhanced Electrostatic Precipitation in High Resistivity Applications;" Symposium on Transfer and Utilization of Particulate Control Technology, Vol. 1, (Denver, CO; July, 1978); EPA-600/7-79-044a (NTIS No. PB 295226); February, 1979.

DEVELOPMENT OF A CHARGING DEVICE FOR HIGH-RESISTIVITY DUST USING HEATED AND COOLED ELECTRODES

By: G. Rinard, M. Durham, D. Rugg, Denver Research Institute, Denver, CO
L. Sparks, U.S. EPA, Industrial Environmental Research Laboratory, Research Triangle Park, NC

ABSTRACT

An efficient cooled-pipe charger/collector which is capable of controlling back ionization and allowing efficient charging of particles has been developed. It has also been shown to be an excellent collector. Feasibility tests were conducted, utilizing parallel heated-pipes and corona-discharge wires placed in a plane normal to gas flow, to determine if the dust resistivity, and thus back ionization, could be controlled by heating a small collector surface area. The success of these tests led to the development of a more practical design utilizing cooling on the collector pipes. Cooled pipes are more practical for many applications since they do not require the input of high quality heat. The results of the testing of the heated and cooled electrodes that led to the present design are given.

INTRODUCTION

The electrostatic precipitator offers advantages in controlling particulate emission for many industries. However, the operation of electrostatic precipitators in collecting fine, high-resistivity dust is a problem. The size of a standard Cottrell-type precipitator necessary for controlling these problem sources of dust is often not cost effective. The most important factor in the operation of a standard Cottrell-type precipitator is the electrical resistivity of the dust collected. The most common problem encountered in the use of Cottrell precipitators in industrial application occurs when the electrical resistivity of the dust is too high (greater than 10^{11} Ω-cm). In the presence of high-resistivity dust, the negative ions produced by corona generation produce an excessive field in the dust layer resulting in back ionization. Although the exact nature of back ionization is not completely understood, the electrical characteristics produced and the deleterious effect on particle collection are well known. Back ionization is characterized by an operating voltage considerably lower and operating current considerably higher than those obtainable under clean plate operating conditions. Since back ionization is produced stably at a voltage lower than that required for normal operation, effective uni-polar ionization is greatly reduced. This, in conjunction with the presence of positive ions produced at the plate, has an overall effect of greatly reducing the efficiency of charging and collecting the dust particles. Back-ionization effects can so overwhelm the operation of an electrostatic precipitator as to make it effectively useless as a dust collector.

The electrostatic precipitator would become more practical for collection of high-resistivity dust if it could be designed to eliminate the possibility of back corona being produced. A survey of the technology shows

that this is the goal of most novel precipitator concepts (Bush, et al., 1980; Gelfand, et al., 1980; Masuda, et al., 1978a; Pontius, et al., 1979). These concepts rely on means that attempt to separate the charging and collecting processes. The two processes may be separated and performed in different parts of the precipitator, in which case the unit is usually referred to as a two-stage electrostatic precipitator. The purpose of the first stage is to charge, without collecting, the particles, thus avoiding production of back ionization. The purpose of the second stage is to collect the particles under conditions of high electric field and low current, again avoiding production of back ionization. These two processes may also be separated in time by means of varying the precipitator corona voltage waveform. The high-voltage waveform used for this purpose is a DC voltage with an impressed pulse of long or short duration (Feldman and Milde, 1979; Lausen, et al., 1979; Masuda, et al., 1978b; White, 1952). This type of waveform is applied to two or three electrode designs.

In order to study a concept originally investigated by Penny (1950, 1962) and White (1956-59 as reported by White, 1974), a precharger was tested which consisted of parallel heated-pipes and corona discharge wires. These initial tests were conducted to determine if the dust resistivity, and thus back ionization, could be controlled by heating only a small (pipe) collector surface area. The primary objective was to determine the characteristics of a precharger when operating with high-resistivity dust but not in back corona. The results were very encouraging in that not only were the particles charged to a high level, but a considerable quantity of the dust was collected by this configuration. Further tests were conducted to optimize the heated-pipe charger/collector and determine its practicality. These tests, while encouraging, indicated that a considerable quantity of high-quality heat was required for heated-pipe operation. Therefore, tests were conducted with the same wire/pipe configuration except that the pipes were cooled to control resistivity. For these tests the moisture content of the test-gas stream was raised to levels normally encountered in flue-gas streams. The results of the tests on both the heated- and cooled-pipe charger/collector are given below. This work has led to an important concept in prechargers. The parameters necessary for good particle charging are the same as those necessary for good particle collection. Therefore, if the precharger can be designed to control back ionization due to collected high-resistivity dust, the overall collecting efficiency of the two stage-ESP can be greatly enhanced.

HEATED-PIPE TESTING

Initial testing of the heated-pipe system occurred in the 0.472 m^3/sec (1000 acfm) EPA pilot precipitator in Room H-300 of EPA's Environmental Research Center in Research Triangle Park, North Carolina. Two heated-pipe systems were set up with one in the first section and the other in the third section of the pilot-scale ESP. Each heated-pipe system consisted of two 6 cm (2-3/8 in.) pipes each containing two 1500 W electric heaters. The two pipes were mounted onto the collector plates directly across from each other in the front third of the section. The corona electrode consisted of a single 0.32 cm (1/8-in.) or 0.16 cm (1/16-in.) wire aligned with the center of the pipes. Two focusing electrodes consisting of 1.27 cm (1/2-in.) rods

were placed 7.62 cm (3 in.) upstream and downstream of the wire. The purpose of these electrodes was to focus the electric field in such a manner that all of the current would go to the heated pipes and not to the unheated collector plate.

The heaters were connected to a timer/control unit so that the duty cycle of the heater could be varied. No thermocouple was mounted on the outside of the pipe because it would interfere with the electrical conditions of the system, and because it would not measure the temperature of the outside surface of the dust layer that was of interest.

The laboratory-measured electrical resistivity for the dust used was 2×10^{12} Ω-cm for the experimental condition. Figure 1 is a plot of clean and dirty voltage current characteristics as a function of the internal temperature of the pipes. These tests are for 0.16 cm (1/16-in.) corona wire. Initially 0.32 cm (1/8-in.) wire was used but this produced only a small operating range between the corona onset and the sparking voltages. As can be seen from Figure 1, the clean curves all have about the same shape except that as the temperature of the pipe is increased, the current increases for a given voltage and the sparking voltage decreases. This can be expected from the change in the air density in the vicinity of the pipes. The unheated pipe, T = 165°C (330°F), displays the sharply rising characteristics of back ionization.

Mass-concentration tests were run on the inlet and outlet of the precipitator to determine the effect of these improvements in electrical conditions on collection efficiency. The precipitator was set up with the heated pipes in sections 1 and 3 and parallel-plate electrodes operating at 40 kV in sections 2 and 4. Three simultaneous inlet and outlet tests were run with the pipes unheated and the average penetration was 31.2 percent. The pipes were then heated to 595°C (1100°F) and seven tests were run, and the penetration was reduced to 7 percent. The field strength for the pipe section was 3.7 kV/cm.

Further testing was done with the pipe spacing increased to 27.9 cm (11 in.) which is more representative of a multichannel unit with 6 cm (2-3/8 in.) pipes on 22.9 cm (9 in.) centers. For this spacing the field strength could be increased to 4.5 kV/cm. For these tests the overall penetration was reduced to 3.8 percent. Charge-to-mass measurements were made following the pipe section. The average of five tests was 7.22 μC/g. These measurements also indicated that each pipe section had a collection efficiency of more than 50 percent.

After repeating the tests at Denver Research Institute's Cherry Creek Field Site on a multichannel unit, attempts were made to reduce the input power necessary to keep the pipes hot. Smaller pipes and various methods to reduce heat loss were tried. None proved sufficiently successful to make the heated-pipe concept practical. Another problem anticipated with heated pipes is that they could exhibit the same deteriorating performance over a period of time that is experienced in some hot-side precipitators.

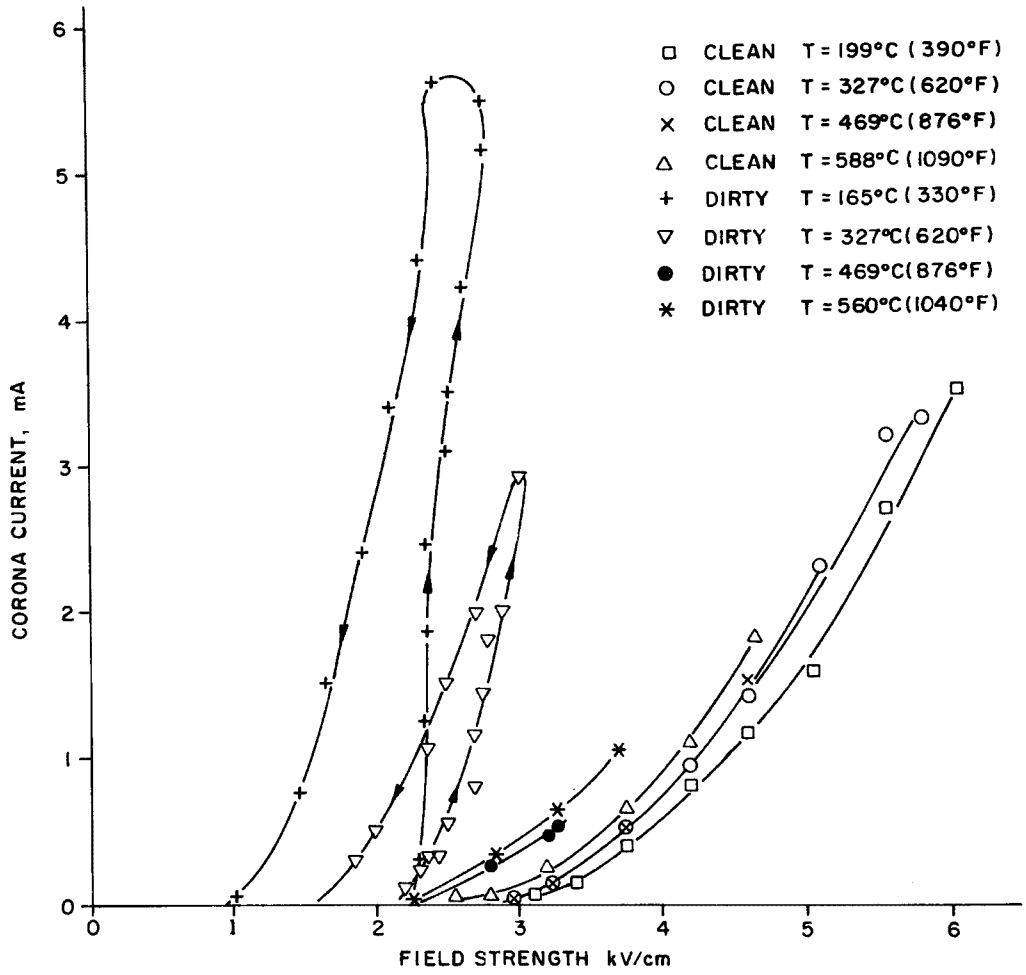

Figure 1. Voltage-Current Characteristics of Heated Electrodes as a Function of Internal Temperature.

COOLED-PIPE TESTING

Because of the practical problems with heated pipes it was decided to try to take advantage of the decreased resistivity on the cold side of the resistivity curve. Super cold-side precipitators have been demonstrated successfully in Japan (Drehmel, et al., 1979). In this case, the collecting plates of the entire ESP are cooled by means of water-filled compartments. The collected dust is removed from the collection surfaces by means of mechanical scrapers since the water-filled plates cannot be rapped by conventional means. This problem could be overcome using the wire/pipe design, since the area of the cooled surface would be greatly reduced. The cooled-pipe concept would have several advantages over the heated pipes if both work equally well. The cooled pipes would be removing a low-quality waste heat from the gas stream rather than adding high-quality heat to the gas. The cooled pipes would also be operating in the region of surface-controlled resistivity rather than bulk resistivity and would therefore be more a function of the components of the gas stream than the bulk material of the fly ash.

A water-pipe manifold and a cooling system were designed to test the cold-pipe concept. The manifold consists of seven pipes spaced 22.9 cm (9 in.) center to center welded to an upper and a lower header. Water enters the bottom header, rises through the cooled pipes, and exits on the opposite side of the upper header. Water temperature is measured at the inlet and the outlet of the system in order to monitor the temperature drop through the system and calculate the heat removed from the gas stream. Two separate systems were built using 6 cm (2-3/8 in.) and 3.81 cm (1-1/2 in.) outside diameter pipes.

The dust resistivity for these tests was the same as that used in the experiments at EPA's Environmental Research Center. The dust resistivity at cold-side temperatures is dependent on moisture content of the flue gas. Water was sprayed into the system at a constant rate and wet-bulb/dry-bulb measurements were made to determine the volumetric moisture content of the gas stream entering the precipitator. This can be controlled in the test unit from 0 to 14 percent. Most data were taken at 10-percent moisture, which is typical of power plant flue gas.

A series of tests were run which included voltage-current characteristics and charge/mass data for both sets of cooled pipes. The data for the 3.81 cm (1-1/2 in.) pipes are presented in Table 1, and the curves are plotted in Figure 2 for three different inlet-water temperatures. With no water in the pipes the VI curve is nearly vertical at about 20 kV. When the water was added to the pipes and the inlet temperature was adjusted to 29°C (85°F), 38°C (101°F), and 47°C (117°F), the electrical conditions improved and data all fell on the same curve. No clean-pipe data was taken at this time but later measurements indicate that the cooled-pipe data lie along the clean-pipe curve. The highest operating voltage, 49 kV, was obtained for the intermediate temperature of 38°C (101°F). At 8.3°C (15°F) below and above this temperature, sparking occurred at a lower voltage. When operating with an inlet temperature of 29°C (85°F), the lower header and

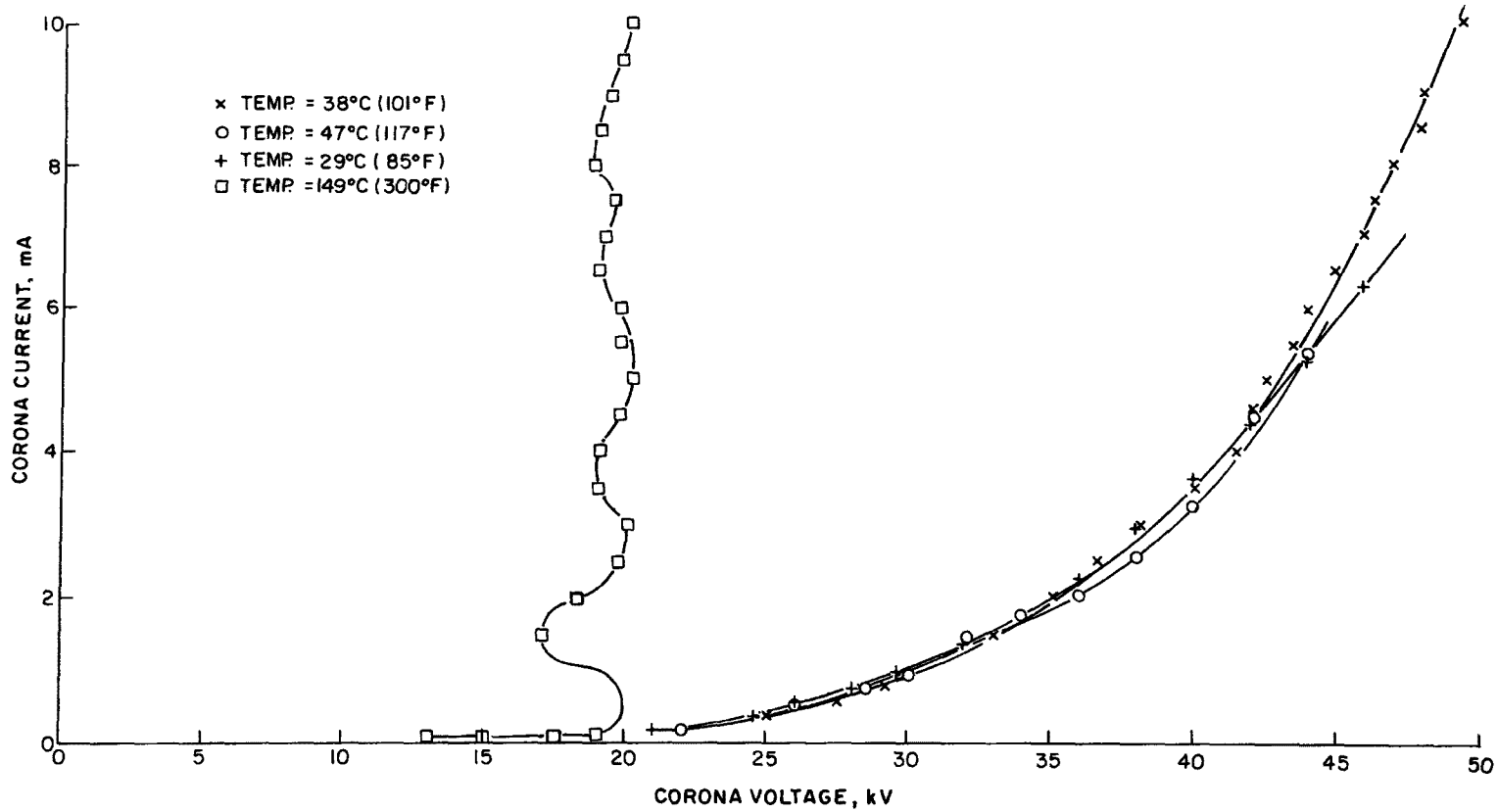

Figure 2. Voltage-Current Characteristics of the 3.8 cm (1.5 in.) Cooled-Pipe Electrodes

vertical pipes were dry but condensation was occurring on the upper header. This was probably due to the fact that the upper pipe is in an area of stagnant air flow. The condensate dripping from the upper pipe led to the lower operating voltage at this temperature, and a spark was initiated each time a drop of water fell from the manifold toward the high-voltage electrode. At both of the other temperatures the collected dust on all pipe surfaces was completely dry. It appears, therefore, that the cooled pipes operate best at a temperature above the water dew point of the gas stream.

TABLE 1. OPERATING CHARACTERISTICS OF THE 3.8 cm (1.5 in.) COOLED PIPES WITH 0.16 cm (1/16-in.) WIRES

Tin °C (°F)	V kV	I mA	Q/M μC/g	m/v g/m³/min	Heat Out W/m³/min
29 (85)	42	4.3	3.7	1.00	15.5
39 (102)	46	3.9	4.3	0.91	15.5
47 (117)	42	6.5	3.6	1.12	17.0

The data for the 6.0 cm (2.375 in.) cooled pipes, given in Table 2, is similar to that for the smaller ones. The VI curves are given in Figure 3. Without cooling, severe back ionization, resulting in very high current, occurs with operating voltages between 15 and 20 kV. Although no data were taken at 29°C (85°F), the data at 41.6°C (107°F) and 45.5°C (114°F) both fall close to the curve for clean conditions, with the higher operating voltages being obtained at 41.6°C (107°F). For both sets of pipes the temperature drop from the inlet to the outlet was maintained between 2.8 and 5.5°C (5 and 10°F). Comparing the data between the two sets of cooled pipes it can be seen that (as with the heated pipes), although higher voltages can be obtained with the smaller pipes, taking into account the increased gap between the corona wire and the pipes, the larger pipes had the higher field strengths.

TABLE 2. OPERATING CHARACTERISTICS OF THE 6.0 cm (2.375 in.) COOLED PIPES WITH 0.16 cm (1/16-in.) WIRES

Tin °C (°F)	V kV	I mA	Q/M μC/g	m/v g/m³/min	Heat Out W/m³/min
27 (80)	40	6.6	3.9	0.66	24.7
41.7 (107)	42	6.8	4.6	0.75	21.2
42 (108)	32	2.85	3.7	1.00	21.2

With the cooled pipes it was possible to operate at a voltage approximately 30 to 40 percent higher than with the heated pipes. However, the

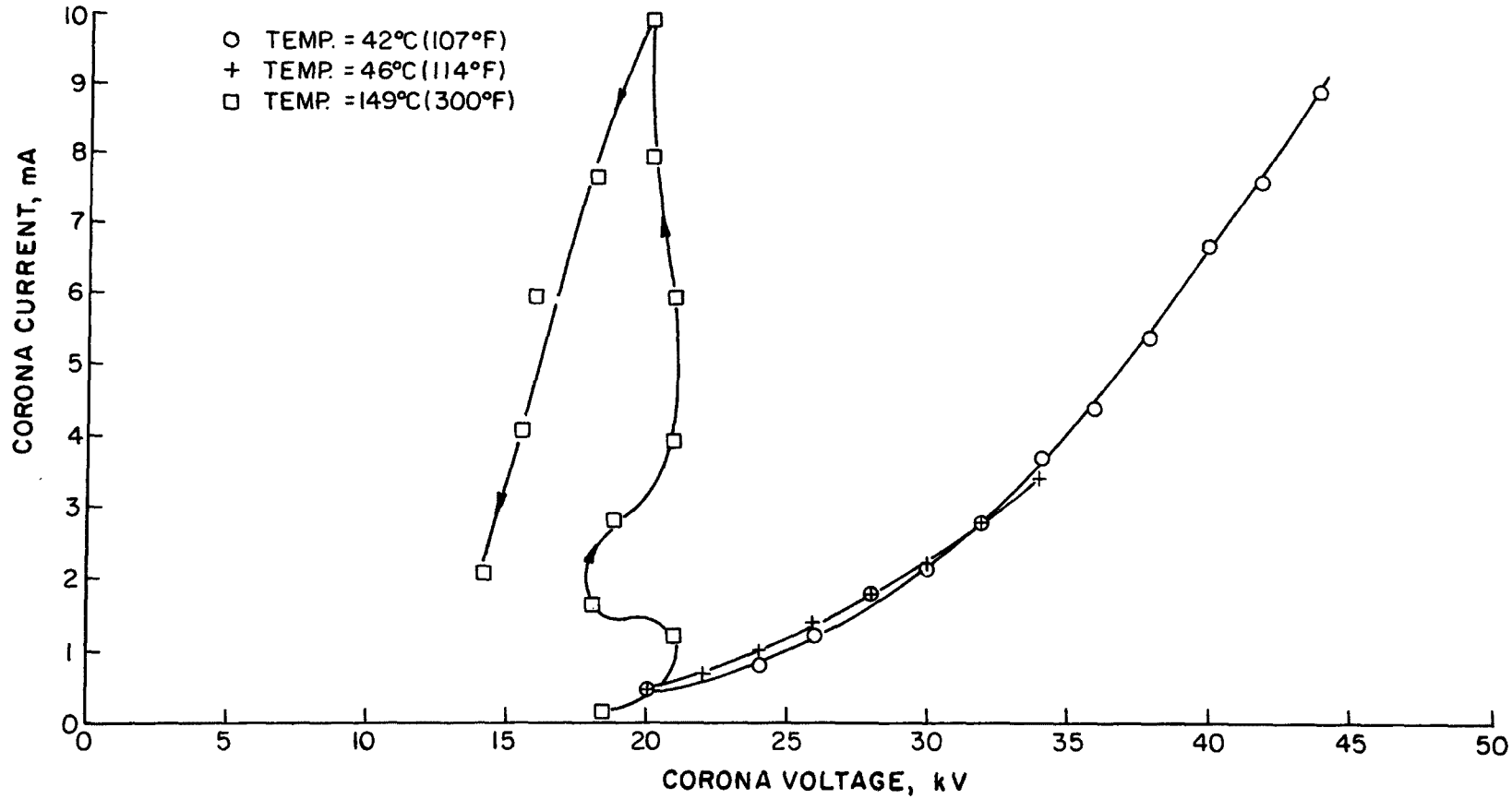

Figure 3. Voltage-Current Characteristics of the 6.0 cm (2.375 in.) Cooled-Pipe Electrodes

charge/mass values were not as high as those obtained at lower voltages with the heated pipes. This cannot be explained at this time. The mass loading following the cooled pipes was slightly higher, but the feed rate of dust was much higher for these tests than for the hot-pipe tests. It should be noted that the opacity monitors were much lower for the cooled pipes when the dust feed rate was the same as for the heated pipes. This indicates that the cooled pipes were better collectors than the heated pipes.

Besides the better operating conditions of the cooled pipes, the low-quality heat removed from the gas stream was less than half the quantity of the high-quality heat needed to be added to the heated pipes. The cooled pipes take less than 1 W of thermal energy from each ft^3 of air which has an effect of lowering the flue gas temperature 1.0°C (2°F) per section of cooled pipes.

EFFICIENCY TESTS WITH A SINGLE SECTION OF COOLED PIPES AND HIGH-VOLTAGE PLATES

The purpose of this series of mass-efficiency tests was to determine the collection efficiency of a single section of a precipitator with cooled pipes as a charger/collector and high-voltage plates as a collector. The charging section consisted of a set of seven 6 cm (2-3/8 in.) diameter pipes spaced 22.9 cm (9 in.) center to center with 3.18 mm (1/8 in.) corona wire electrodes. The collector section consisted of seven collecting plates spaced 22.9 cm (9 in.) alternating with six high-voltage plates. The nominal plate size was 1.1 × 1.6 m (3.6 × 5.2 ft) for a total collection area (excluding high-voltage plates) of 21 m^2 (225 ft^2). Dust resistivity at the operating gas temperature was 10^{12} Ω-cm.

The pipe voltage was set at 42-43 kV. The plates were operated at approximately 2 to 4 kV lower than the point where back corona started. This was approximately 48 kV. The results obtained were quite impressive. With a specific collection area of less than 11 sec/m (55 ft^2/1000 acfm), the collection efficiency was 84.4 percent. This is especially good on a test machine designed for testing mechanical characteristics and therefore didn't have any baffles to prevent sneakage.

TESTING OF COOLED-PIPE CONCEPT ON ACTUAL FLUE GAS

After successful tests of the cooled-pipe charger/collector in the laboratory, a small test unit was constructed for testing under actual flue-gas conditions. The purpose of the unit was to determine if there was any component in the actual flue gas which would prevent the cooled-pipe concept from working as it did in the laboratory. Tests were made with this "Tiny TEP" at the Coors Power Plant in Golden, Colorado, and at the Valmont Station near Boulder, Colorado.

The chamber in the Tiny TEP is a 0.31 m (1 ft) cube. The corona wire is 3.18 mm (1/8-in.) in diameter and uses four cooled pipes 3.1 cm (1.5 in.) in diameter with centers 11.43 cm (4.5 in.) from the corona wire. The corona wire is connected to a negative high-voltage power supply with meters which measure voltage and current.

The results of tests under actual flue-gas conditions at the Coors Power Plant are shown in Figure 4. The clean VI curve and the dirty VI curve with the internal cooled-pipe temperature at 118°C (244°F) are shown. The difference between the two curves shows that back corona occurs when the pipes are not cooled. Sparkover voltages and current were measured as the internal pipe temperature was varied. When the internal temperature of the cooled pipe was 31°C (88°F), the VI characteristics were essentially the same as if the pipes were clean, except sparkover occurred at about 49 kV as shown in Figure 4. As the temperature was increased to 36°C (96°F), the current and voltage at sparkover decreased. However, the sparkover point lies on the clean VI curve which indicates that when the dust layer breaks down, a spark (rather than stable back corona) results. At about 43°C (109°F) the current at sparkover started to increase indicating that positive ions from back corona were present. As the temperature was increased to 53°C (127°F) or above, the sparkover point lies near the 118°C (244°F) dirty VI curve showing that stable back corona was established on the collector electrodes. The dust layer thickness on the cooled pipes affected the temperature of the cooling water which was needed to operate the Tiny TEP at high sparkover voltages and currents.

The test results at the Valmont Station were similar to those obtained in the laboratory and at the Coors Power Plant. The Tiny TEP tests showed that the cooled pipes produced the desired electrical characteristics under actual flue-gas conditions. They also showed that the laboratory conditions, with reentrained Coors dust, accurately simulate actual power-plant stack conditions.

CONCLUDING REMARKS

The results of the above test program indicate that back corona can be effectively eliminated in the pipe-type precharger by either heating or cooling the pipes, the more practical device being when the pipes are cooled. When back corona is eliminated, the pipes can be operated at field intensities and current densities considerably higher than typical wire plate ESP's. The charger also exhibits appreciable collection efficiency in excess of 50 percent per pipe section.

REFERENCES

Bush, P.V., D.H. Pontius, W.B. Smith, and L.E. Sparks (1980), "Field Evaluation of the SoRI-EPA Precharger-Collector System," presented at the 73rd Annual Meeting of the Air Pollution Control Association, Montreal, Quebec, June 22-27.

Drehmel, D.C., C.H. Gooding, and G.B. Nichols (1979), "Particulate Control Highlights: Recent Developments in Japan," EPA-600/8-79-031a (NTIS PB 80-148802), November.

Feldman, P.L., and H.I. Milde (1979), "Pulsed Energization for Enhanced Electrostatic Precipitation in High Resistivity Applications," Symposium on the Transfer and Utilization of Particulate Control Technology: Volume 1. EPA-600/7-79-044a (NTIS PB 295226), February, pp. 253-274.

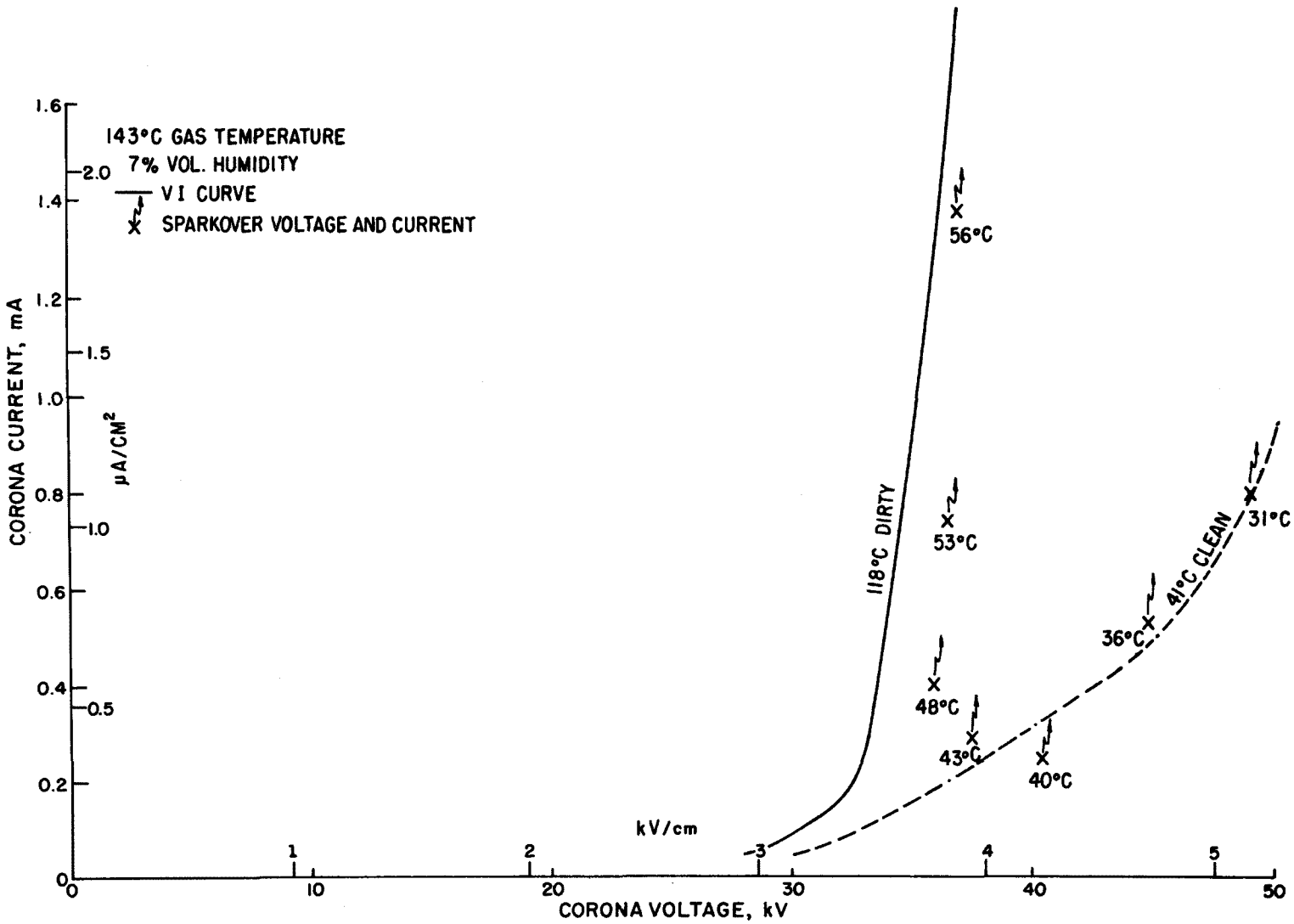

Figure 4. Effect of Water Temperature on the Sparkover Voltage of the Cooled-Pipe Electrodes Operating on an Actual Flue Gas Stream.

Gelfand, P.C., D. Norman, W.V. Piulle, H.W. Spenser, and O.J. Tassicker (1980), "Results of High Intensity Ionizer/Precipitator Evaluation at the EPRI Test Facility," presented at the 73rd Annual Meeting of the Air Pollution Control Association, Montreal, Quebec, June 22-27.

Lausen, P., H. Henriksen, and H. Petersen (1979), "Energy Conserving Pulse Energization of Precipitators," IEEE-IAS Conference, Cleveland, Ohio, October.

Masuda, S., M. Washizu, A. Mizuno, and K. Akutsu (1978a), "Boxer Charger - A Novel Charging Device for High Resistivity Powders," Proc. IEEE-IAS Annual Meeting, Toronto, Ontario, October.

Masuda, S., G. Obata, and J. Harai (1978b), "A Pulse Voltage Source for Electrostatic Precipitators," Proc. IEEE-IAS Conference, Toronto, Ontario, October.

Penny, G.W. (1950), British Patent 643,363, September 20.

Penny, G.W. (1962), Industrial Precipitator with Temperature Controlled Electrodes. U.S. Patent 3,026,964, March 27.

Pontius, D.H., P.V. Bush, and L.E. Sparks (1979), "A New Precharger for Two-Stage Electrostatic Precipitation of High Resistivity Dust," Proceedings: Symposium on the Transfer and Utilization of Particulate Control Technology: Volume 1. EPA-600/7-79-044a (NTIS PB 295227), February, pp. 275-285.

White, H.J. (1952), "A Pulse Method for Supplying High-Voltage Power for Electrostatic Precipitation," Trans. AIEE, November, pp. 326-329.

White, H.J. (1974), "Resistivity Problems in Electrostatic Precipitation," J. Air Poll. Control Assoc. 24 4, p. 313, April.

THE EVALUATION OF NOVEL ELECTROSTATIC PRECIPITATOR SYSTEMS USING A TRANSPORTABLE PROTOTYPE

By: G. Rinard, M. Durham, D. Rugg, J. Armstrong
Denver Research Institute, Denver, CO
L. Sparks, J. Abbott
U.S. EPA, Industrial Environmental Research Laboratory
Research Triangle Park, NC

ABSTRACT

A program is presently being conducted to advance the development of economically feasible, two-stage electrostatic precipitators for collection of high-resistivity dust. The objectives of this program are to: 1) evaluate alternative precipitator designs, 2) optimize the downstream collector for use with a precharger, and 3) evaluate the SoRI precharger on various sources of high-resistivity dust. These goals will be achieved through the design, fabrication, and testing of a transportable electrostatic precipitator (TEP) on problem sources of high-resistivity dust. In order to determine alternative precipitator designs for testing in the TEP, a program was undertaken to investigate novel precharger and collector technology. The design specifications for the TEP and configuration for the first series of testing are presented.

INTRODUCTION

Electrostatic precipitators have historically been the primary air pollution control device for controlling particulate matter from coal-fired boilers. Precipitators are used because they perform reliably and require minimum operating and maintenance costs. However, as more industrial and utility boilers were switched to coal and the burning of low sulfur coals increased, problems arose in the operation of precipitators. The burning of low-sulfur coals produces a high-resistivity fly ash (greater that 10^{11} ohm-cm). High-resistivity ash leads to back ionization which greatly reduces the operating performance of precipitators. To compensate for this, it was necessary to build precipitators many times larger than was previously required, and the use of precipitators became less attractive.

The Particulate Technology Branch of EPA's Industrial Environmental Research Laboratory at Research Triangle Park, NC, began performing in-house research and began funding contracted research to develop an economically feasible electrostatic device to collect high-resistivity dusts. From the early stages of this research, it was apparent that the effort should be directed toward developing a two-stage system in which the main functions of charging and collecting were separated. The first phase of research was directed toward developing a device to charge high-resistivity dusts. As part of this program, EPA and the Southern Research Institute (SoRI) developed a novel tri-electrode system to precharge particles before they entered a collecting device. This precharger was tested by SoRI in the laboratory on reentrained fly ash and in a pilot precipitator on a slipstream of a utility boiler.

To advance the research on two-stage precipitation, EPA awarded a grant to the Denver Research Institute. The main objectives of the grant were to:

- Evaluate alternative precipitator designs.
- Optimize the downstream collector for use with a precharger.
- Evaluate the SoRI precharger on other sources of high-resistivity dusts.

To attain these objectives DRI first undertook a program to investigate novel precipitator technology. This involved searching the literature, personal contacts with scientists and engineers working in this field, and continuously reviewing other related EPA funded projects. Concepts that were decided to be promising were then tested in the laboratory and in some cases in the field. In order to thoroughly evaluate these alternative precipitator designs, a testing program will be conducted. This program consists of:

- Design and fabrication of a transportable electrostatic precipitator (TEP).
- Testing of the TEP on problem sources of high-resistivity dust.

The design philosophy of the TEP was to develop a system which allowed for maximum flexibility, accuracy, and utility in the investigation of advanced two-stage electrostatic precipitator concepts. The mobility of the precipitator is important in order to be able to try these concepts directly on various problem sources at widely spaced geographical locations. In addition, the precipitator had to be large enough to provide meaningful engineering data for scale-up to full-sized precipitators. To fairly evaluate the novel precipitator design, its characteristics had to be compared with those of a standard Cottrell design. The electrical parameters of the collector segment of a two-stage unit may be considerably different than those of the standard single-stage design. In particular the electric field intensity should be higher, and the corona current lower than in the standard single-stage design. The TEP was so designed that it could be reconfigured from single-stage to two-stage operation.

DESIGN SPECIFICATIONS

A set of design specifications to define the parameter limits and operational characteristics of the TEP were first established. These specifications were then used as guidelines in the precipitator design. Consideration was given to the type of industry at which the TEP would be tested; the type of precipitator technology to be tested; the physical size necessary for producing data suitable for full scale-up; requirements for flexibility in reconfiguring the TEP to different precipitator technologies; practical operating pressures and temperatures; durability; safety; and ease of operation. The specifications established are:

- The TEP precharger (PC) and collector sections are of modular construction for ease of shipping and for flexibility in section configuration at various test sites. All disassembled components of the TEP are of a size suitable for transporting on standard flat-bed trailers.

- The high voltage electrode and collector plate assemblies of the PC and collector sections are designed for easy installation, reconfiguration, and removal from the TEP.

- The collector sections will accommodate collector plates 1.5 m (5 ft) long and 3.66 m (12 ft) high. The high-voltage supports are designed to accommodate various corona-generating structures as well as flat plates. The channel spacing of a collector section is variable and consists of six channels at a typical 22.9 cm (9 in.) plate-to-plate spacing.

- The precharger sections are sufficiently long to accommodate different precharger technologies. The tops of the precharger sections are independent and easily modified to accommodate the various precharger technologies.

- Each collecting and PC section is a separate electrical section. Power supplies and controls suitable for operation with all the various technologies are: 1) for the collector section operating with wire electrodes, a minimum of 50 kV and 100 mA; 2) in the collector section with plates, a minimum of 100 kV and 10 mA; 3) for the precharger section with pipe electrodes, a minimum of 50 kV and 50 mA; 4) for the SoRI precharger grid, a minimum of 15 kV and 200 mA; and 5) specially constructed pulsing supplies for operating collector sections with pulse excitation.

- The maximum TEP operating temperature is 427°C (800°F).

- The TEP operating gas flow range is 4.72-7.08 m^3/sec (10,000-15,000 acfm) with average gas velocities of 0.91-1.5 m/sec (3-5 ft/sec).

- At a 22.9 cm (9 in.) plate-to-plate spacing, the SCA per collector section is 14.2 sec/m (72 ft^2/1000 acfm) and 9.5 sec/m (48 ft^2/1000 acfm) for flow rates of 4.72 m^3/sec (10,000 acfm) and 7.08 m^3/sec (15,000 acfm), respectively.

- All TEP components are so constructed to be able to withstand a minimum negative pressure of 6.2 kPa (25 in. H_2O). A centrifugal blower is utilized to overcome all pressure drops in the gas flow system.

- Supplemental electrical heating is provided to maintain ducting and precipitator temperatures during operation and to preheat the TEP system upon start-up.

- Three 10.2 cm (4 in.) sampling ports are located on the downstream side of each precharger section: one near the top, one in the middle, and one near the bottom. Other ports for temperature measurement and gas sampling will be provided as required.

- A portable sampling trailer is provided for the purposes of gas sampling, particulate sampling, data acquisition, and data reduction.

- o A portable instrumentation trailer is provided for controlling the TEP, automatically recording TEP operating characteristics, and reduction of all TEP data.

- o Since the TEP utilizes hazardously high voltages, safety interlock systems and procedures have been established to eliminate any electrical hazards to the operating crew or any other personnel.

TEP DESIGN

A formal Preliminary Design Review was held between the project officers of EPA and appropriate DRI personnel. A comprehensive presentation of the conceptual design alternatives was conducted and design recommendations presented. Joint decisions were made concerning design philosophy, major operational objectives, and data acquisition and processing. Work on the final design was then started. The final design configuration is the result of the evaluation of the new technology, site surveys, provisions for data acquisition and processing requirements, operator safety and convenience, and the specifications of operating parameters with the established design goals.

The main TEP assembly is presented in Figure 1 which shows the elevation of the TEP unit including the inlet and outlet duct components. In this drawing the TEP has four collector sections each preceded by a PC section. Each collector section includes dust hoppers and an overhead compartment which houses the high-voltage feed-throughs and hanger supports for plate and corona frame assemblies. As stated above, the collector plates will be 1.5 m (5 ft) long and 3.66 m (12 ft) high. Each collector section is 2.1 m (7 ft) long. The final section will house a device to control rapping reentrainment.

Each PC section is designed so that it can be attached to either end of a collector section or another precharger section. The precharger sections are capable of accommodating various precharging concepts. These sections also include hoppers and overhead compartments for rappers, hanger supports for plate and/or grid assemblies, and HV feed-throughs. The precharger segments are 0.91 m (3 ft) long.

The direction of gas flow in this drawing is from the left to the right. Gas is slipstreamed from the source being sampled and is conveyed to the TEP through a thermally insulated circular duct having an inside diameter of 0.61 m (2 ft). This duct is attached to the first TEP inlet cone segment where the dust-laden flue gas begins to decelerate in a controlled manner. The TEP entrance cone design has been established through air flow modeling. The results of the modeling effort show that good quality gas flow which meets the IGCI standards can be maintained within the full-size TEP using a combination of inlet diverging cones having half angles of 15° and 20° and two 40 percent open diffuser plates. Once the gas passes through the TEP, it enters two 45° half angle converging cones which in turn are connected to a 0.61 m (2 ft) ID duct which returns the gas to the source being sampled. The exterior surfaces of the inlet and outlet cones are thermally insulated. A centrifugal blower is located in the return duct to overcome pressure drops through the TEP and the delivery and return ducting. A bypass branch connecting the inlet and outlet ducting is located at the blower position. An electric heater in the bypass branch is used to preheat the TEP during

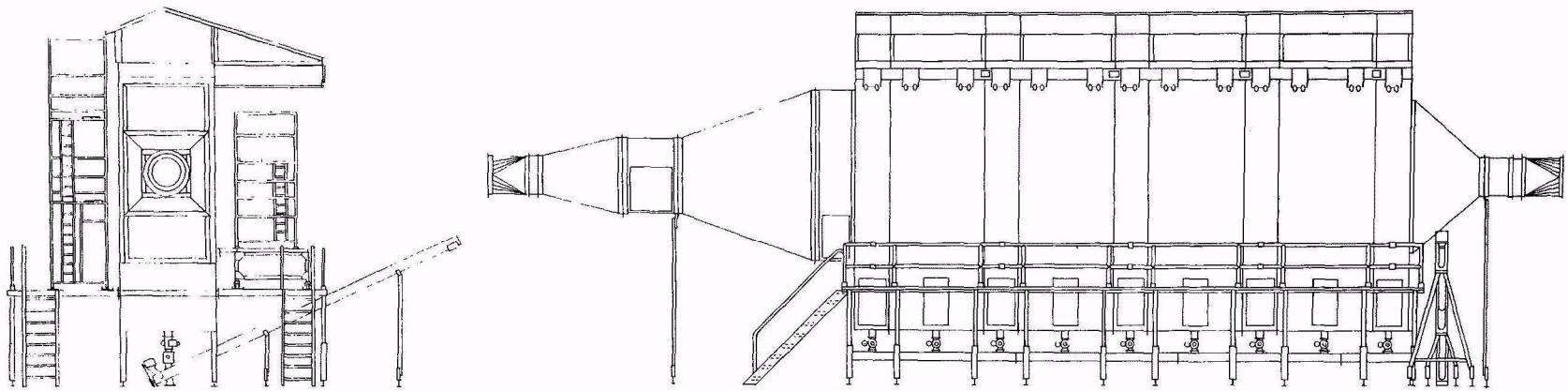

Figure 1. Elevation Views of the Transportable Electrostatic Precipitator.

start-up to prevent condensation in the TEP. Valves are used to control the gas flow through the TEP and to direct the gas through either the bypass branch in a closed loop mode or to sample gas from the source and to return it. Atmospheric air ports with control dampers in the closed-loop system allow for rapid cooling of the system during shutdown.

A scaffolding support structure extends outward toward the front and back of the main unit and is accessible by means of stairways. This structure is more clearly shown by the end elevation (lower left). On the back of the precipitator, commercial rolling scaffolding is erected for purposes of sampling and access to the upper portions of the precipitator. The front section of each collector section is accessible by means of doors as shown in Figure 2. A specially designed dolly rides along guide rails on the scaffolding support at the front of the precipitator. This dolly may be positioned in front of each collector section with collector doors open. Fold-down rails from the dolly are then placed in position to allow scaffolding riding on the dolly to be moved into the collector section. This allows access into the collector section for the purposes of installing and modifying collector plate and corona electrode components. A cantilevered outboard support is used for installing and removing the internal components of the precipitator. All internal components are mounted on slotted track. With the doors open, extensions of the slotted track may be installed and supported by the outboard support. When installing the internal components of the precipitator, each component is brought into position beneath the outdoor support by means of a fork lift. The component is then attached to the support and moved into the precipitator. The process is reversed when removing internal components.

Each PC and collector section has a separate hopper to minimize sneakage. Further reduction in sneakage is provided by simple baffles. Rotary air lock valves are used at the outlets of the hoppers so that collected dust can be removed independently from each hopper while the TEP is operating. The hoppers, which are thermally insulated, are equipped with dust level indicating devices and vibrators. The hoppers are emptied by means of two screw conveyors.

Figure 2 shows the collector section assembly. The overall outside dimensions of the collector assembly are 2.1 m by 2.1 m by 8.2 m (7 ft by 7 ft by 27 ft) tall. The unit is constructed of standard structural steel components. Each outside wall of the collector assembly contains 4 in. of internal fiberglass insulation. The primary feature of the collector section shown in Figure 2 is the access doors. These doors are suspended by specially designed hinges allowing the doors to close parallel to the sides of the precipitator in port-hole fashion. This simplifies gasketing and sealing of the doors. These hinges also allow the doors to open completely and lie flat along the side of the precipitator in the open position. The doors are secured when closed by means of quick release clamps along all sealing surfaces of each door. Since the precipitator is designed for operation under negative pressure, these simple door closures are sufficient. Sealing is accomplished on all sealing surfaces of the doors by means of a heat resistant, covered, Inconel mesh (tadpole) gasket. In addition the doors are restrained by means of a rigid plate to prevent complete collapse of the gaskets. These types of gaskets were chosen to provide the sealing necessary and yet allow for some

misalignment due to fabrication of the mechanical components. All panels of the collector section, as well as the rest of the TEP unit, are reinforced to withstand a total negative pressure of 6.2 kPa (25 in. H_2O) and 44.7 m/sec (100 mph) wind loading. Stress analyses have been conducted on all exterior components to ensure that the TEP is structurally sound.

Figure 2 also shows the support mechanism for the high-voltage electrodes and the collector plate. The voltage insulators are especially designed and fabricated by Coors Porcelain of Golden, Colorado. High voltage is conducted to the high-voltage carrier channel by means of the metal insulator rod. Support for the collector plates is very similar to that for the high-voltage electrode except that no high-voltage insulation is required. The collector plate suspension is extended through the top of the precipitator in such a manner that load cells may be used to measure the weight of each collector plate and thus determine the total accumulated dust loading. The high-voltage electrode and collector-plate carrier channels are so designed as to allow completely variable spacing of the high voltage and collector electrodes.

The construction of the precharger section is very similar to that of a collector section. The various components of the precharger section are assembled by bolting them to the ends of the collector section or flow straightening units. Access to the precharger sections is by means of the doors on the collection sections and removable panels on the precharger sections. This is necessary due to the geometric shape of the precharger section. With all high-voltage electrode and collector plates removed from, and the scaffolding inserted into, the collector section, the precharger section on either side of this collector section is completely accessible. The precharger assembly is designed to allow complete flexibility for the use of various precharger concepts. The only component of the precharger assembly requiring redesign for a new type precharger is the top section. This section is easily removable from the rest of the precharger section. Except for the shape, the hopper of the precharger assembly is identical for the collector section.

As stated above, the TEP is designed to operate to temperatures of 427°C (800°F). This will allow the system to be operated in either a cold-side, 149 to 204°C (300 to 400°F), or a hot-side, 371 to 427°C (700 to 800°F), mode. In addition, the system is capable of operating at sites located at sea level to altitudes of 1980 m (6,500 ft).

The rapping system which will be employed in the collector sections for the collector plates and the high-voltage wire frames or high-voltage plates will be series of hammers which strike the individual plates or wire frames. The selection of the hammer system is based on the results of laboratory tests which evaluated the effectiveness of using pneumatic impactors to rap complete fields of dust laden plates versus the individual hammer rapping of each plate.

The collection of reentrained dust is the reason for the provision of having PC sections preceding each collector section. Dust from upstream collector and PC that is returned to the gas stream due to rapping must be recharged by downstream PC sections so that it can be effectively recaptured. The TEP can be operated, however, with selected PC sections either de-energized or empty.

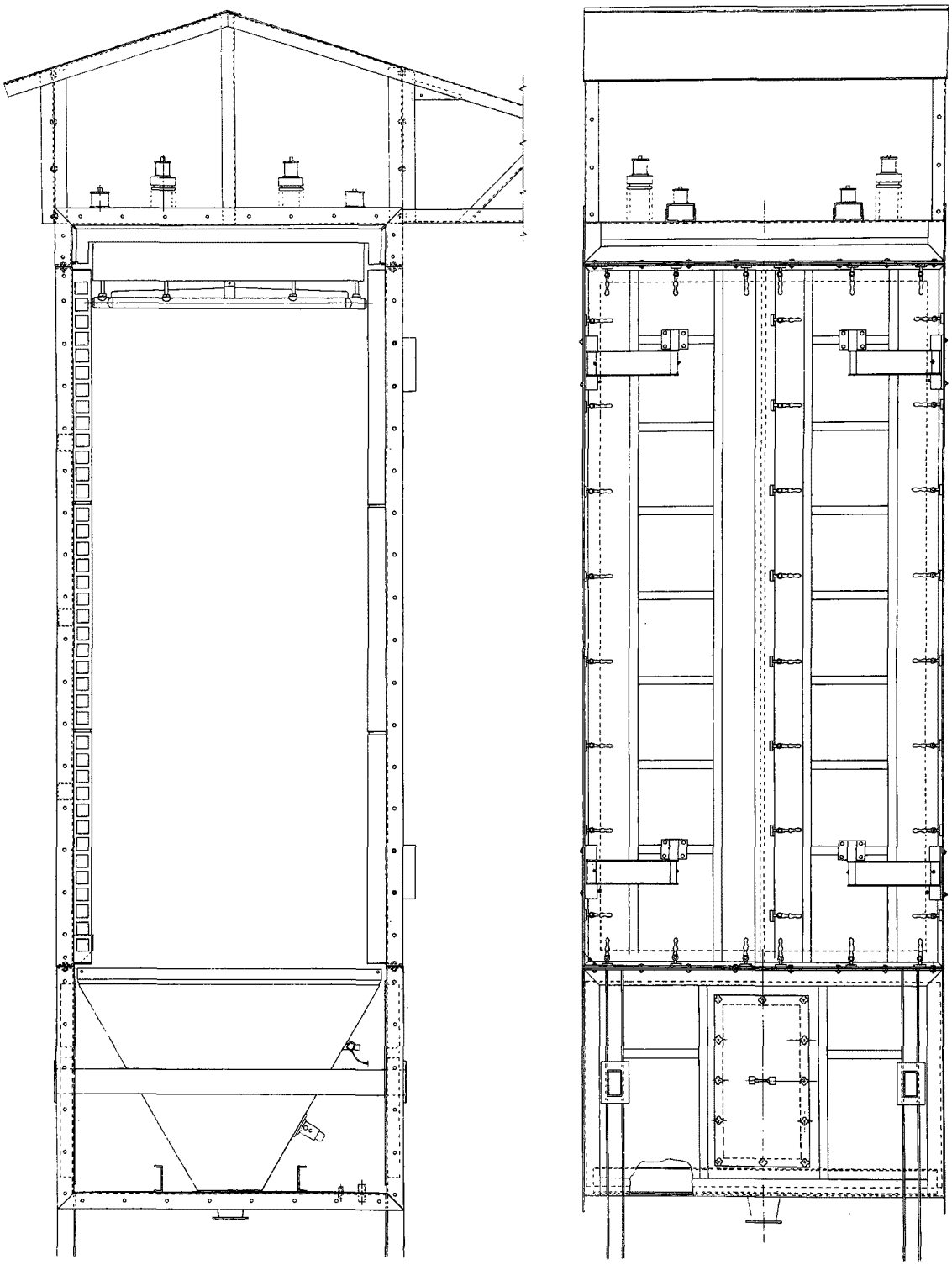

Figure 2. Side and Front Views of a Typical Collector Section.

TESTING AT THE VALMONT POWER PLANT

Work on the task of selecting appropriate test sites commenced early in the project. A survey of selected industries was made for determination of design parameters for the TEP. Design parameters were selected which would allow the operation of the TEP in virtually all industries except the cement industry. The excessively high negative pressures encountered in this industry imposed an unreasonable constraint on the design of the TEP.

Contact was made with officials of the Public Service Company of Colorado (PSCo) concerning the possibility of the utilization of one of PSCo's power generating stations for the first TEP test site. All of PSCo's plants were considered and the 180 MW Unit 5 at the Valmont Station in Boulder, Colorado, was selected. This is a base-loaded unit. Both in-situ and laboratory tests have been made on unconditioned fly ash at Valmont. The ash resistivity at cold-side temperatures is approximately $10^{13}\Omega$ cm.

Site preparation at Valmont is nearly complete. The major portion of the TEP has been constructed. Final assembly of the TEP at Valmont is scheduled for July 1981. The slipstream at Valmont will be taken before the preheater and cooled to cold-side temperatures by means of a heat exchanger. This will allow very flexible control of the operating temperature of the TEP.

The plan is to remain at Valmont for a series of evaluation and optimization testing. The first series of tests will consist of a SoRI precharger followed by two collector sections with parallel plate electrodes, a second SoRI precharger, again followed by two collector sections with parallel plate electrodes, and finally a third SoRI precharger as the last TEP section. The TEP configuration for the second series of tests will consist of replacing the first and second SoRI prechargers with cold pipe charger-collectors. In this manner a direct comparison will be made between the effectiveness of the SoRI and cold pipe concepts. It is envisioned that two additional units of whichever charger concept proves to be the better will be built in the future for inclusion in the initially empty charger sections of the TEP located between the first and second and the third and fourth TEP collector sections. The final series of tests at Valmont will be conducted to optimize the precipitator parameters.

FUTURE TESTING

The configuration of the TEP as established during the Valmont program will be tested at various sources of high-resistivity dust. Present plans are that the next two sites will be one more power plant and a steel mill. Testing at each site will be long enough to collect data and optimize precipitator performance characteristics for each source.

Further operation at these sources will be conducted to demonstrate the technology for each application. During this phase of the program, transfer of this technology to potential manufacturers and users will be pursued.

ANALYSIS OF THE ELECTRICAL AND CHARGING CHARACTERISTICS OF A THREE ELECTRODE PRECHARGER

By: K.J. McLean
University of Wollongong,
Wollongong. N.S.W. 2500, Australia.

ABSTRACT

The operation of the three electrode precharger is analysed using a comprehensive set of electrical and charge/mass measurements. The electrical measurements are made with clean and contaminated electrodes, smooth and perforated grids, and for a wide range of grid and corona voltages. Particular consideration is given to the magnitude and direction of the grid current flow. It is concluded that biasing the grid reduces the back corona component of the total current in the main gas stream for a restricted range of voltages and that the main action of the biased grid is to suppress or reduce the formation of back corona rather than to act as a collector of the positive ions.

INTRODUCTION

One of the most serious limitations of electrostatic precipitators is that their performance deteriorates when the particulate being collected has a high resistivity. A phenomenon, commonly called 'back corona', is formed on the deposited dust layer which degrades the precipitator's performance by reducing the sparkover voltage, producing reverse charging positive ions, distorting the electric field pattern and probably increasing particle re-entrainment.

A wide range of techniques have been investigated to overcome this high resistivity prolem of which one important group is the precharger (1,2,3,6). In the precharger, the effect of back corona is minimised by either reversing the field direction (1), introducing a biased third electrode to suppress back corona (2), using high gas velocities to prevent particle deposition (3) and reducing the resistivity of the ash on the collecting electrode by changing its temperature (6).

One of these units is a pilot scale precharger, designed by Southern Research Institute and installed at the U.S. Environmental Protection Agency's Industrial Environmental Research Laboratory, Research Triangle Park, N.C. The unit is described elsewhere (2) and some of its overall performance characteristics have been published (4).

The purpose of this paper is to establish a technique by which the operation of this type of precharger may be analysed from measurements of the

electrical parameters.

The specific results recorded in this paper are applicable only to this precharger, to the particular high resistivity fly ash tested and other operating conditions stated in this paper. However, the technique of analysis described should be universally applicable and the basic mode of operation for other units collecting different ashes can be expected to follow a similar pattern.

CURRENT FLOW PATTERN

The main currents that can be expected to flow in the precharger are shown in Figure 1.

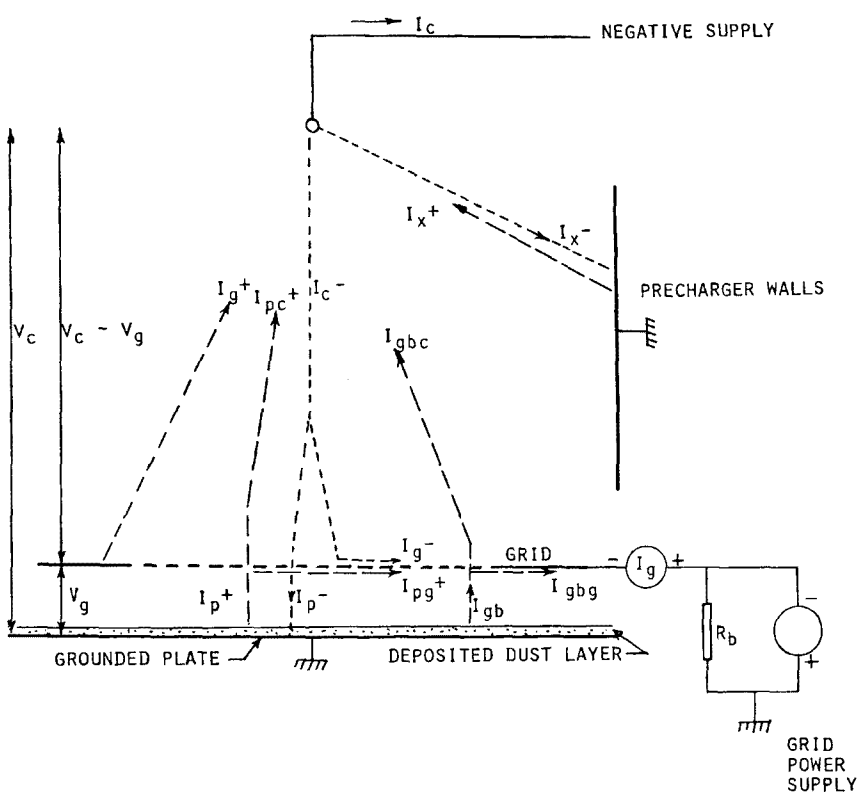

Figure 1: Diagrammatic Representation of Currents Flowing in Precharger.

Where:

I_c	Total corona current measured by an external meter
I_g	Total grid current measured by an external meter
I_{c^-}	Total negative ion corona current to the grid
I_{x^-}	Stray negative ion current
I_{g^-}	Corona negative ion current terminating on the grid
I_{p^-}	Corona negative ion current passing through the grid to the plate
I_{x^+}	Back corona positive ion current due to stray current
I_{g^+}	Back corona positive ion current from grid
I_{p^+}	Back corona positive ion current from the particle layer on the plate
I_{pg^+}	Part of I_{p^+} collected by the grid
I_{pc^+}	Part of I_{p^+} which passes through the grid openings into the gas space
I_{gb}	Grid to plate breakdown current
I_{gbc}	Proportion of I_{gb} injected into gas space
I_{gbg}	Proportion of I_{gb} collected by the grid

The resistance R_b is necessary to provide an impedance path for grid current when it flows from the supply to the grid. If this is not present, the grid power supply loses control of the grid voltage level.

The voltages present are:

V_c	Voltage of corona wire to ground
V_g	Voltage of grid to ground
(V_c-V_g)	Gas gap voltage

Some important current relationships are:

$$I_g = I_{g^-} + I_{g^+} - (I_{pg^+} + I_{gbg}) \quad (1)$$

$$I_c = I_{x^-} + I_{c^-} + I_{pc^+} + I_{g^+} + I_{gbc} + I_{x^+} \quad (2)$$

It is of particular importance to note the direction of the current flow in the grid circuit. If there is only corona negative ion current I_{g^-} and back corona off the grid I_{g^+}, an ammeter connected in the circuit as shown will give a positive reading. The presence of I_{pg^+} or I_{gbg} will at first reduce this value and then reverse the direction of the meter reading. Hence, the sign and the direction of variation in magnitude of this grid current can be used to determine which back corona currents are present.

The relative magnitudes of these currents will vary over a wide range of values and in some instances, certain currents will be insignificant and may be neglected.

EXPERIMENTAL RESULTS

Electrical Transparency

This is one of the most important parameters that affects the operation of the precharger. It is defined as the ratio of the current passing through

the grid to the plate, divided by the total current approaching the grid. Since it is not possible to measure the plate current directly, the electrical transparency is given by:

$$T_e = \frac{I_c - I_g}{I_c - I_e} \tag{3}$$

where I_e is an estimate of the current flowing to the smooth edges of the grid. Measurements were made with clean electrodes at 300°F and the results are shown in Figure 2. The characteristics show a dependence on current density.

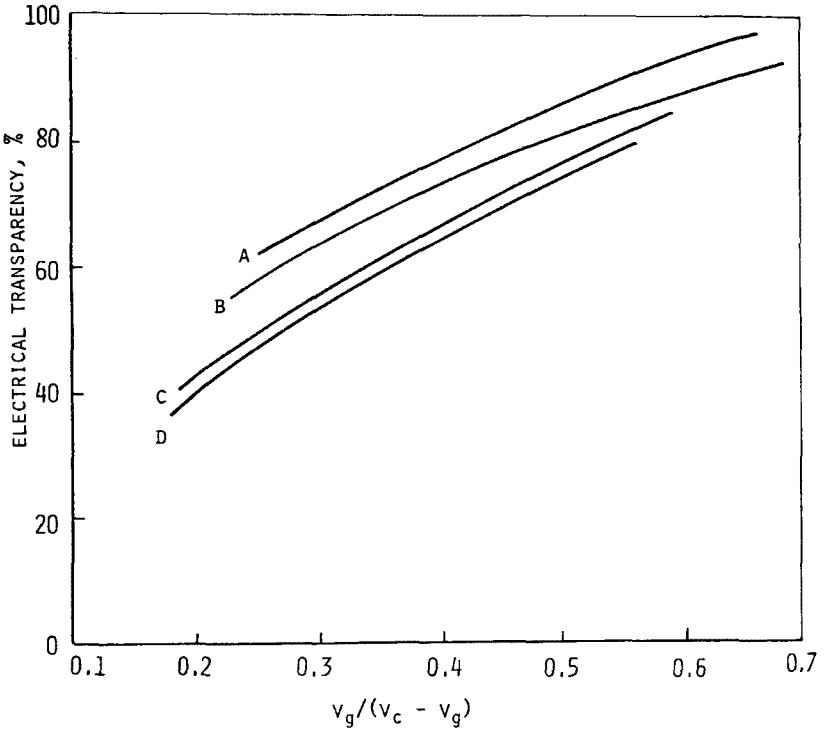

Figure 2: Electrical Transparency.

A. V_c-V_g = 11 kV I_c = 130 μA B. V_c-V_g = 13 kV I_c = 370 μA
C. = 15 kV 650 μA = 17 kV = 1000 μA

A careful set of laboratory scale measurements and a theoretical analysis (5) shows that the electrical transparency for a grid of constant optical transparency is a function of E_g/E_o and is given by:

$$T_e = \frac{2}{\pi} \tan^{-1}\left[\sqrt{\frac{1-K}{1+K}} \tan\ (\theta_o/2)\right] + \frac{2}{\pi}\frac{E_g}{E_o} \tan^{-1}\left[\sqrt{\frac{1-K}{1+K}} \cot\ (\theta_o/2)\right] \tag{4}$$

where: E_o the electric field just above the grid
E_g the electric field between the grid and plate
K constant
θ_o angle at which the field direction changes

In an ideal case, all the results plotted with E_g/E_o as an abcessor should fall on a single curve.

The reason for the electrical transparency curves of the precharger not coinciding for all current densities is probably due to variations in the values of E_o and E_g caused by the changes in space charge with current density.

Smooth Grid Electrical Characteristics

The perforated screens of the precharger grids were replaced with solid smooth aluminium sheets and the corona characteristics measured for both clean and contaminated grids. One set of results are plotted in Figure 3, for V_g = 5 KV.

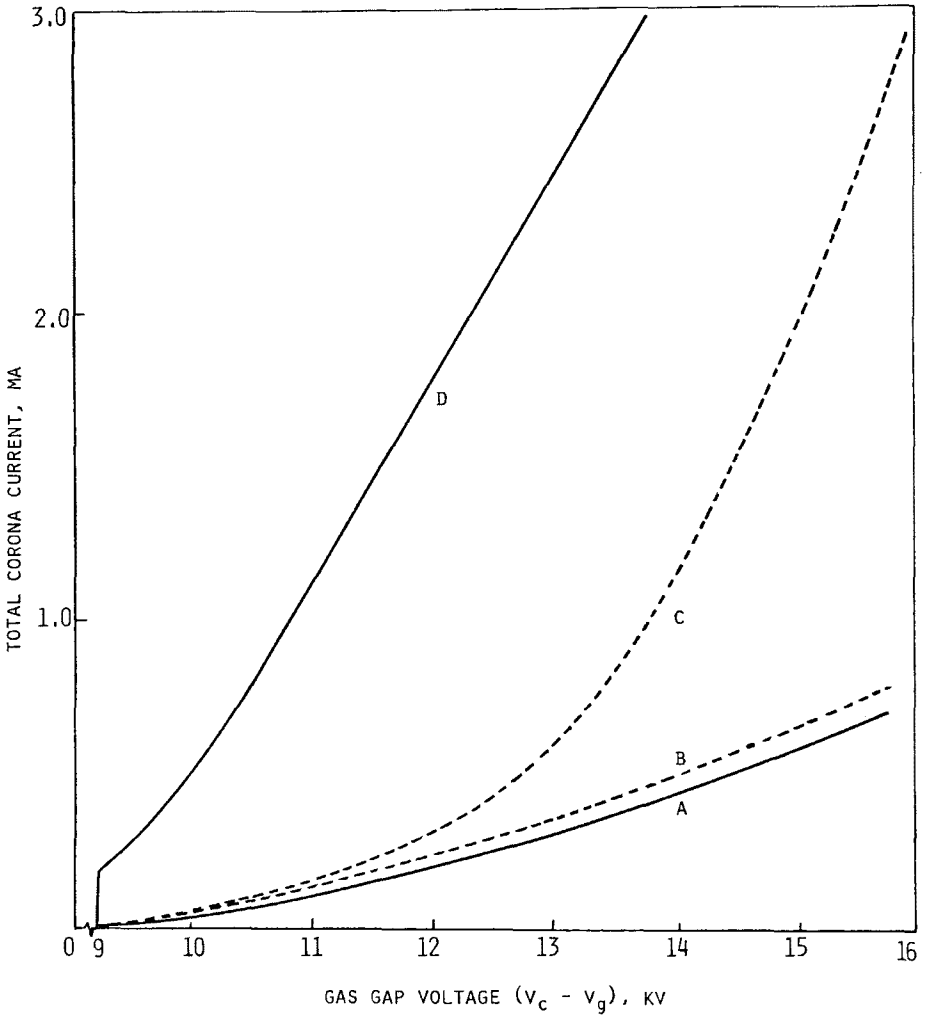

Figure 3: Total Corona Characteristics - V_g = 5 kV.
A. Clean smooth grid. B. Clean perforated grid.
C. Contaminated perforated grid. D. Contaminated smooth grid.

Perforated Grid Electrical Characteristics

The perforated screens were refitted to the grid and the clean electrical characteristics measured. Dust was injected with the grid biased as strongly as possible so as to reduce the amount of dust deposited on the grid itself. Conditions were allowed to stabilise and a range of electrical measurements made. One set of typical results are plotted in Figures 3 and 4.

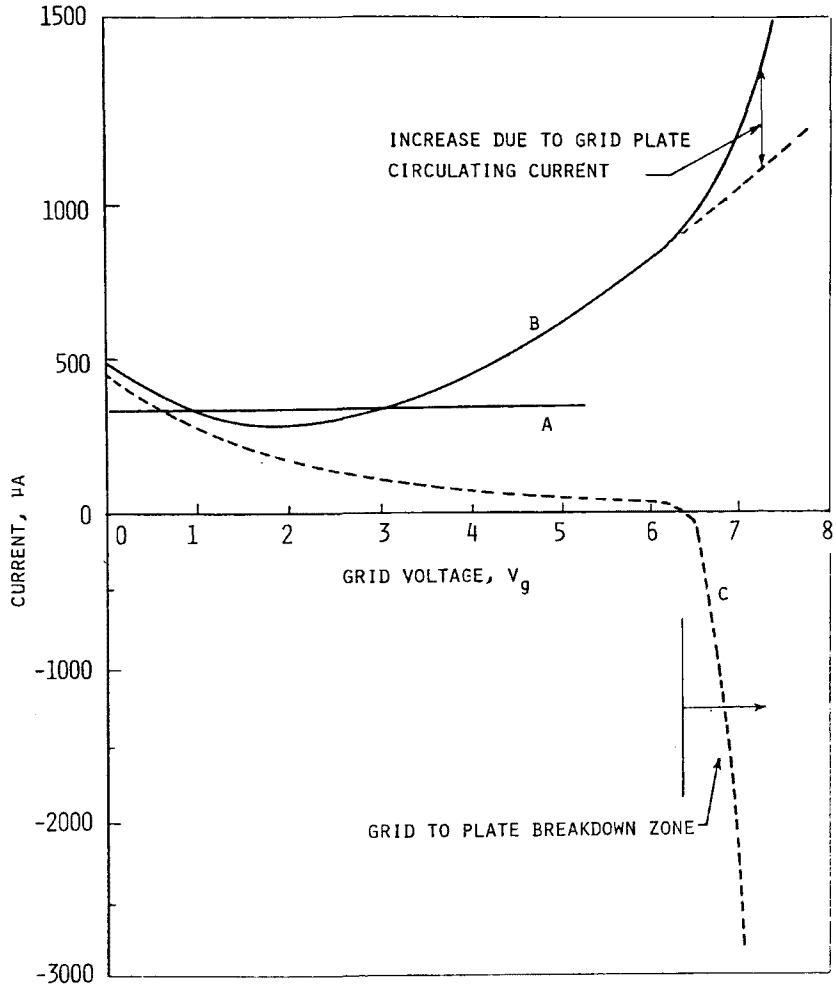

Figure 4: Typical Total Corona and Grid Current - V_C-V_g = 13 kV.
A. Total corona current with clean electrodes.
B. Total corona current with contaminated electrodes.
C. Grid current with contaminated electrodes.

The characteristics for other (V_c-V_g) values had this same general shape. Once the grid-to-plate breakdown occurred, the circulating current could be easily increased to about 10 mA and was independent of (V_c-V_g). This voltage could even be reduced to zero and the breakdown current would still flow if V_g is maintained. In all cases, the total corona current increased with the magnitude of the circulating current. The total back corona current appears to be controlled by grid biasing for (V_c-V_g) up to a maximum value which is approximately 14 kV for the conditions of the test. At higher values (i.e., 16 kV) the back corona current is substantially higher than the negative ion current.

Conditions were then established at ambient temperature to allow the grid to become very dirty. The electrical characteristics were then measued for various conditions at 300°F. A typical set of results are plotted on Figure 5.

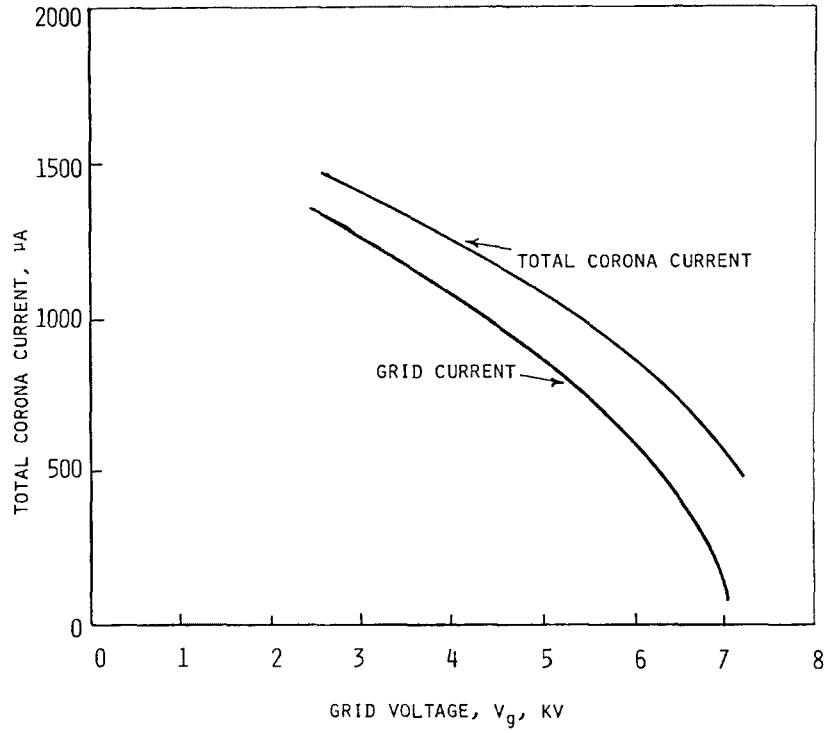

Figure 5: Typical Corona and Grid Currents for Very Dirty Electrodes - V_c-V_g = 13 kV.

Charge/Mass Measurements

The Southern Research Institute probe was used to make these charge/mass measurements. The input to the probe was located 50 mm off the centre line of the middle electrode, halfway up the duct immediately following the precharger. The total charge was measured by a 610 C, Keithley Electrometer and samples were taken over a three minute period.

In order to measure the effect of (V_c-Vg) and hence the relative magnitude of the back corona current, the grid voltage was fixed at 5 kV and Q/M measured for increasing values of (V_c-V_g). The results are shown plotted in Figure 6.

Similar measurements were also made with the grids in a very dirty condition corresponding to the electrical conditions which are also shown plotted in Figure 6.

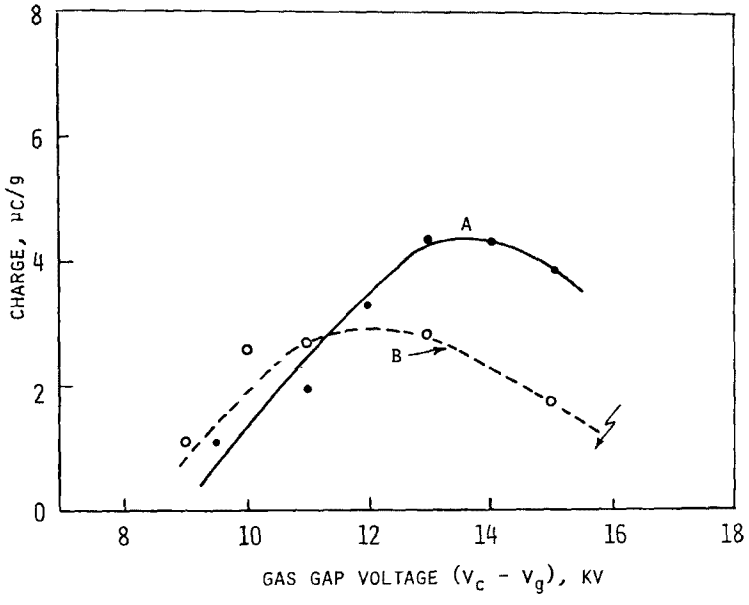

Figure 6: Variation of Q/M with Gas Gap Voltage - V_g = 5 kV.
A. Moderately dirty grid.
B. Very dirty grid.

DISCUSSION

From these tests, it may be concluded that the biased third electrode placed close to the collecting plate reduces the magnitude of the back corona compared with that in a conventional two electrode precipitator. This conclusion is supported by the following:

(1) Comparison of the total corona currents of the contaminated smooth and perforated grids as shown in Figure 3. For all values of (V_c-V_g) the total current is less with the perforated biased grid.

(2) Variation of the total corona current with different grid biases as shown in Figure 4. For a limited range of (V_c-V_g) and to a maximum grid voltage V_g, the total corona current is not much

greater than the clean electrode negative ion current, indicating a significant reduction in the generation of back corona current.

(3) Variation of total corona current with grid bias for very dirty grids, as shown in Figure 5.

(4) The Q/M measurements show that this ratio increases with increasing magnitudes of (V_c-V_g) to a maximum at about 14 kV and then begins to reduce. The turnover corresponds exactly with the value at which the back corona current begins to be a significant proportion of the electron current as shown in Figure 3. Charging is significantly lower when the grids are contaminated.

Although the formation of back corona can potentially take place from the grid surface and the plate, a careful examination of the magnitude and direction of the grid current, for a relatively clean grid, indicates that the grid is not emitting a significant proportion of positive ion current nor is it receiving a significant positive ion current from the plate. Hence, what positive ion current is being measured by I_c, must be coming direct from the plate and passing through the grid aperature to the discharge electrode; following the same flux lines that bring in the negative ions.

When breakdown occurs between the grid and the plate, a substantial current circulates in the grid loop. It is suggested that this breakdown is initiated when the electrical transparency is high, about 80%, and some of the positive ion back corona current is sufficiently close to the grid to be captured by it. Once this occurs a low impedance path is generated and a large current is circulated by the grid power supply.

No significant part of this current is generated by the incoming corona negative ions. The measurements however do indicate that some proportion of this current escapes into the gas space and flows to the discharge electrode. This breakdown occurs just on one grid and it is not unreasonable to speculate that it is very localised.

CONCLUSIONS AND COMMENTS

For the successful operation of the three electrode precipitator as a precharger it is necessary to carefully adjust the gas gap and grid voltages. The tests show that there is a mode of operation in which the back corona is suppressed and good charging of the inlet particles is possible.

An alternative application of the triode precipitator is to use it in a hybrid system as the final collecting stage. Its main function would be to provide a high collection efficiency zone which can charge and collect the reentrained fly ash. The aerodynamic shielding and electric field pattern produced by the grid should reduce any reentrainment when this last zone is rapped.

ACKNOWLEDGEMENT

This project was funded by the U.S. Environmental Protection Agency, Contract No.68-02-3143. The authors are grateful for the assistance given by G.H. Ramsey, B.E. Daniel and R.E. Valentine in carrying out the tests.

ENDNOTES

1. Masuda, S., Nakatani, H., and Mizuno, A. Boxer-charger, A Novel Charging Device. (Presented at the EPA-Symposium on Transfer and Utilisation of Particulate Control Technology, Denver, Colorado, 1979).

2. Pontius, D.H., Bush, P.V. and Smith, W.B. Electrostatic Precipitators for Collection of High Intensity Ash. Environmental Protection Agency Report No. EPA-600/7-79-189, August, 1979.

3. Air Pollution Systems, Inc. Development Program for an Ionizer-Precipitator Fine Particle Dust Collection System as Applied to Coal Fired Utility Steam Generators: Final Report, Vol.1: Technical and Economy Summary. EPRI FP-291. Palo Alto, C.A. 1976.

4. Sparks, L.E., Ramsey, G.H. and Daniel, B.E. Collection of Fly Ash with High REsistivity in a Pilot Plant Electrostatic Precipitator Preceded by the EPA/SORI Precharger. Air Poll. Cont. Ass., 29: 745-7, 1979.

5. McLean, K.J., Herceg, Z. and Boccola, R.I. Electrical Transparency of a Corona Triode. Jn. Electrostatics, 9: 211-222, January, 1981.

6. Rinard, G., Durham, M., Rugg, D. Development of a Charging Device for High Resistivity Dust using Heated and Cooling Electrodes. (Presented at the 3rd EPA-Symposium on Transfer and Utilisation of Particulate Control Technology, Orlando, Florida, 1981).

PARTICLE CHARGING IN AN ELECTROSTATIC PRECIPITATOR BY PULSE AND DC VOLTAGES

By: L. E. Sparks, G. H. Ramsey, R. E. Valentine, and J. H. Abbott
Industrial Environmental Research Laboratory
U. S. Environmental Protection Agency
Research Triangle Park, N. C. 27711

ABSTRACT

Measurements of particle charge as a function of particle radius for dc and pulse energization were made at the exit of a pilot plant electrostatic precipitator. A Milliken cell was used to make the measurements. Measurements were made at three values of dust electrical resistivity--low (2×10^{10} ohm-cm), moderate (2×10^{11} ohm-cm), and high (2×10^{12} ohm-cm). All experiments were conducted using a resuspended flyash. In order to compare the charging characteristics of dc and pulse supplies, the average current densities for both cases were kept identical. The results are compared with theory and previous experimental data. The data show that there is no difference in particle charge for pulse and dc when the dc is operated without back corona.

INTRODUCTION

Pulse power for electrostatic precipitators has been offered as a possible solution to the problems associated with collecting dust with high electrical resistivity in electrostatic precipitators. Petersen and Lausen,[1] Feldman and Milde,[2] and others have presented data to show a significant improvement in electrostatic precipitator performance for pulse versus dc power supply.

Because pulse power appeared to have significant performance advantages over dc, an experimental program was developed to investigate pulse power in cooperation with Denver Research Institute. Denver Research designed and built the pulse power supplies and then delivered them to the Particulate Technology Branch of EPA's Industrial Environmental Research Laboratory at Research Triangle Park, North Carolina (IERL-RTP). All of the experiments were conducted in the IERL-RTP in-house electrostatic precipitator.

The experiments discussed in this paper were designed to compare the particle charging characteristics of pulse and dc when the electrostatic precipitator was collecting dust with high, moderate, and low electrical resistivity. The results of these experiments are presented in this paper.

EXPERIMENTAL EQUIPMENT

The experiments were conducted in a single-lane pilot-plant electrostatic precipitator located at IERL-RTP. The electrostatic precipitator has been completely described by Lawless et al.[3] so only a brief description will be given here.

The electrostatic precipitator is shown in Figure 1. The electrostatic precipitator is a single-lane, four-electrical-section electrostatic precipitator. For these experiments Sections 1 and 2, and Sections 3 and 4 were electrically connected so that only two power supplies were needed to energize the electrostatic precipitator.

The pulse power supply was designed and constructed by Denver Research Institute. The pulse height and pulse rate were adjustable from 0 kV to about 50 kV and from 0 to about 110 pulses per second. The pulse width was about 100 μsec. A plot showing the pulse shape and width is shown in Figure 2.

A of the pulse power supply is shown in Figure 3. A capacitor in the primary of the 50:1 step-up transformer is charged to a voltage V_c which determines the pulse amplitude. The SCR switch is triggered by a timing circuit which determines the pulse repetition rate and the capacitor is connected to the pulse transformer for one cycle of primary current. The primary capacitor discharges during the first half cycle of the primary current and recharges during the second half cycle.

The output pulse was capacitor coupled to the corona discharge electrode system. A dc bias voltage, which was variable from 0 to 60 kV, was added to the pulse voltage through a blocking diode. Therefore, the pulse power supply permitted independent control over peak and average voltages.

For these experiments the pulse height and pulse rate were adjusted to give the highest allowable current density at the plate that did not give rise to sparking or back corona. The dc bias voltage was set below the corona onset voltage. The exact conditions depended on the dust resistivity and are given later.

The aerosol used for the experiments was flyash which was redispersed using sandblast guns fed with a vibrating screw feeder. Previous experience has shown that this is an excellent method of producing an aerosol.

MEASUREMENT APPARATUS

The charge and diameter of individual particles were determined using a technique and apparatus developed and described by McDonald et al.[4] The technique consists of extracting a sample gas volume from the ESP and directing part of the gas flow into a modified Milliken measurement cell. A single particle is then isolated and its upward and downward motion under the influence of a uniform electric field can be measured. The particle charge and diameter can be determined by knowing the time required to move up and down a given distance in the electric field.

Figure 4 shows a drawing of the apparatus inserted into an ESP. The gas sample is extracted through 5 cm diameter tubing. Because the technique is limited to particles with diameters less than 4 μm, isokinetic sampling is not required. The tubing leading to the test chamber contains a butterfly valve which controls the flow of aerosol into the test

chamber. The valve is opened when a sample is acquired and then closed while the measurements are being made. When the valve is open, the pump is turned on, and an aerosol sample is obtained. When a sufficient number of particles are in the measurement cell, the pump is turned off and the valve is turned off. A very short time after the valve is closed, particle motion due to the gas flow ceases and the motion of the particles is controlled solely by the gravitational field, viscous drag, and the electric field in the measurement cell.

Measurements are made only after all motion due to the gas flow has ceased.

After the particle motion due to gas flow has ceased, the time required for an individual particle to travel a known distance up and down in the electic field is measured. Typically the up and down time for a single particle is determined 3 to 4 times. A new particle is then selected and the process is repeated. Eventually, the particle concentration in the cell becomes very small, and a new sample is obtained.

Data from the Milliken experiment are reduced on a TRS-80 microcomputer. The computer calculates the particle charge and diameter for each measurement.

TEST PLAN

The experiments were designed to provide data on particle charge as a function of particle diameter for dc and pulse under three conditions of electrical resistivity of the dust--low resistivity (2×10^{10} ohm-cm), moderate resistivity (2×10^{11} ohm-cm), and high resistivity (2×10^{12} ohm-cm). The electrical resistivity was varied by changing the operating temperature of the electrostatic precipitator. The low resistivity runs were made at ambient temperature (23°C), the moderate resistivity runs at 218°C, and the high resistivity runs at 150°C.

The high resistivity runs were made with matched current densities at the plate. The current density was about 5 na/cm^2. Operation above this current density resulted in back corona and poor performance for both the pulse and dc cases. It was found that stable operation at this current density allowed both the pulse and dc to operate in optimum fashion.

The moderate resistivity runs were made again at matched current densities at the plate. The exact current density to use was determined by adjusting the pulse height and pulse rate to give the lowest reading on the opacity monitor. The current density at the plate for this case was 12 na/cm^2 which was found to be the best operating point for the dc also. The low resistivity experiments were conducted to determine if pulsing significantly affected the charge on the particles either due to the high pulse voltage or due to the pulse of ions produced by the pulse. Consequently, the experiments were conducted at low current densities similar to those used in the high resistivity experiments. By conducting the experiments with low resistivity dust, we were able

to compare the effects of pulsing without the confusing factors of back corona that existed when high resistivity dust was used.

It was quite easy to operate the pulser at the desired current densities for all cases. The dc was extremely difficult to operate at the desired current density for the high resistivity case. Even with extreme care, the dc tended to go into back corona at unpredictable times. Whenever the dc went into back corona, particle collection was reduced. The effects on particle charge are discussed later.

RESULTS

High Resistivity Dusts

The results for the high resistivity runs are shown in Figure 5. The most striking feature for the data is that there is no difference between the charge on the particles under conditions of pulse and dc energization of the electrostatic precipitator. The charge on the particles is in very good agreement with the charge predicted by a model based on the sum of the charging rates due to diffusion and field charging.

It is important to note that the results shown in Figure 5 are the charge on those particles that have charge. Whenever the dc went into back corona, significant numbers of uncharged particles were observed. But even under these conditions of back corona, those particles that had charge were charged to the expected values of charge. This behavior is consistent with the idea that the dc current density under conditions of back corona is very nonuniform. Consequently, particles are randomly exposed to areas of current or no current. Those particles that are exposed to current are charged as expected, while those particles that are not exposed to current are not charged.

All of the particles for the pulse charging experiments were charged all of the time. This is consistent with the data that showed that the current distribution at the plate was very uniform under pulsing conditions. Thus all of the particles are exposed to charging current.

The particle charge data that show that the particle charge is the same for both dc and pulse are consistent with particle collection data.

The main value of the pulse power supply appeared to be that it allowed stable operation for long periods of time with the high resistivity dust. Such operation was not possible with the dc. It should be emphasized that as soon as the dc was allowed to operate in back corona, the particle collection efficiency of the electrostatic precipitator dropped and significant numbers of uncharged particles were observed.

Moderate Resistivity

The results of the moderate resistivity experiments are shown in Figure 6. Again note that there is no significant difference between the dc and pulse data. The standard deviation for the particle charge

at a given particle diameter is about 25 percent as was the case for the high resistivity data.

These particle charge results are consistent with the measured collection efficiency of the electrostatic precipitator as shown by Figure 7 which is a plot of penetration (1-efficiency) versus particle diameter. There is no significant difference between the data for dc and pulse.

In this case there was no benefit to pulse power even as a control system. Stable operation was possible for both the dc and pulse under these conditions.

Low Resistivity Runs

As mentioned earlier, the low resistivity runs were conducted to see if there was any effect of the pulse on particle charge. The experiments were conducted at the low current densities used in the high resistivity experiments. The results are shown in Figure 8. Again note that there is no difference between the dc and pulse data.

DISCUSSION

The main conclusion we draw from these data is that there is no difference between the performance of an electrostatic precipitator using either dc or pulse power provided that the electrostatic precipitator is not allowed to go into back corona. As soon as the electrostatic precipitator is allowed to operate in back corona (most likely with dc), the particle collection efficiency decreases and significant numbers of uncharged particles are found.

The main advantage of using pulse power supplies is that good control of the electrical operating conditions of the electrostatic precipitator is possible, even when dusts with high electrical resistivity are being collected. Such good control is often not possible with dc. The value of good control should not be neglected and the fact that pulsing allows one to control the operation of an electrostatic precipitator is significant.

There is still the problem of reconciling these results with the data reported in the literature which show a major improvement with pulsing. It seems likely that much of the data comparing particle collection with pulse and dc were generated under conditions where the dc was operated under conditions of back corona. We observed similar results when pulse power was compared with dc in back corona. However, significant improvements in particle collection were obtained when the electrostatic precipitator was operated with dc out of back corona. For this reason we took extreme care to operate the dc so that back corona was avoided. The fact that the dc could not be operated for long times without going into back corona shows that pulsing for control of the electrical conditions is a significant advantage.

ENDNOTES

1. Petersen, H. H. and P. Lausen, "Precipitator Energization Utilizing an Energy Conserving Pulse Generator," in Second Symposium on the Transfer and Utilization of Particulate Control Technology: Volume II, EPA 600/9-80-39b. (NTIS PB81-122210), September 1980.

2. Feldman, P. L. and H. I. Milde, "Pulsed Energization for Enhanced Electrostatic Precipitation in High Resistivity Applications," in Symposium on the Transfer and Utilization of Particulate Control Technology, Volume I, EPA-600/7-79-044a (NTIS PB 295 226), February 1979.

3. Lawless, P., G. Ramsey, and B. Daniel, "Characterization of the EPA/IERL-RTP Pilot-Scale Precipitator," EPA-600/7-79-052 (NTIS PB 292-820), February 1979.

4. McDonald, J. R., M. H. Anderson, R. B. Mosely, and L. E. Sparks, "Charge Measurements on Individual Particles Exiting Laboratory Precipitators with Positive and Negative Corona at Various Temperatures." J. Appl. Phys. 51,3632 (1980).

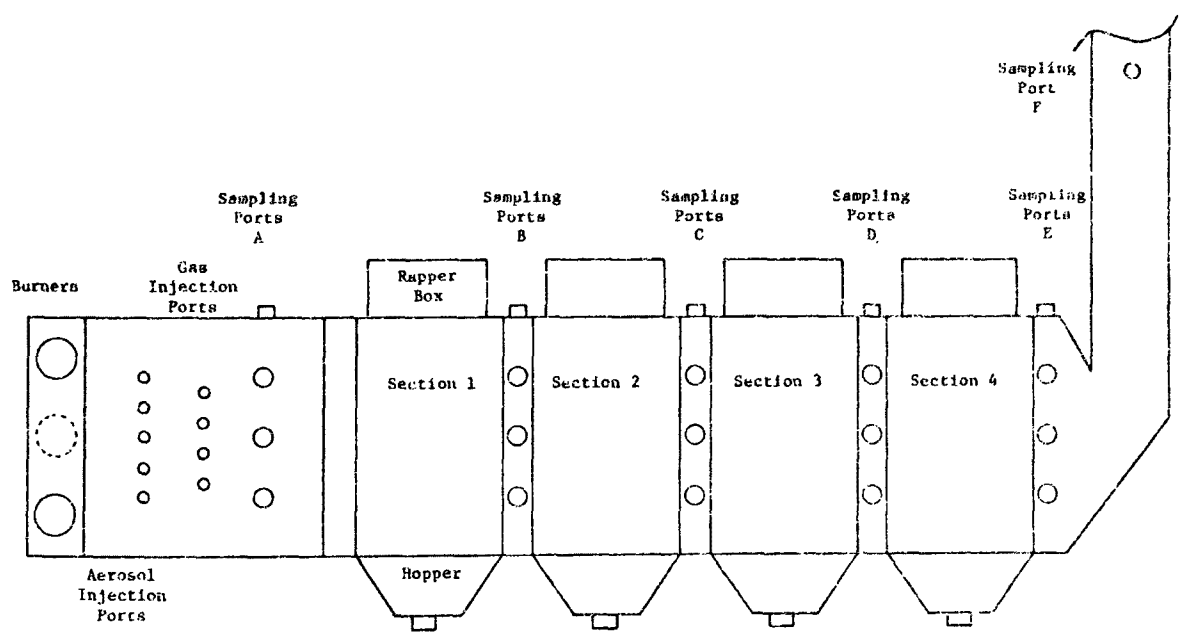

Figure 1. Diagram of pilot-scale ESP.

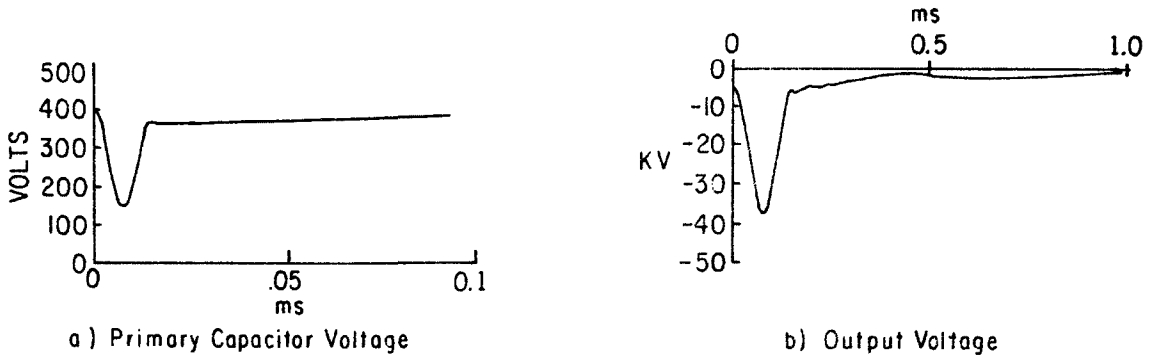

FIGURE 2. PULSE POWER SUPPLY WAVEFORMS

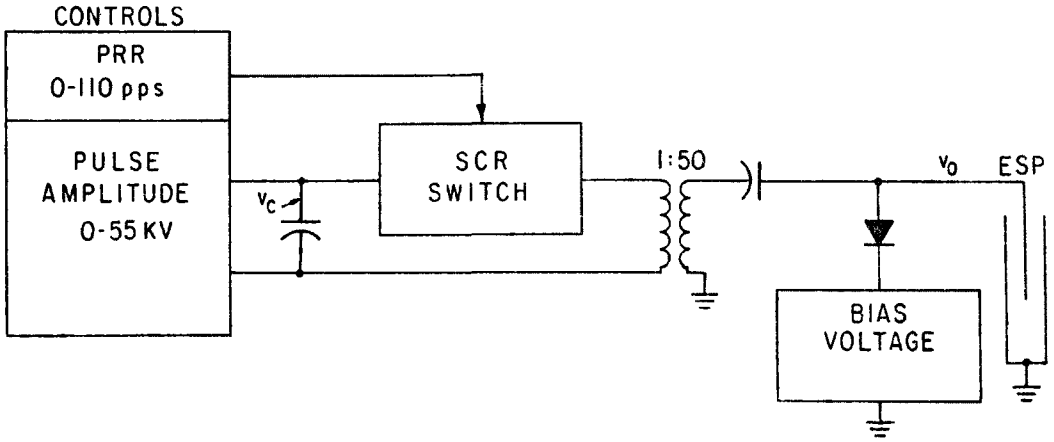

Figure 3. Pulse power supply circuit.

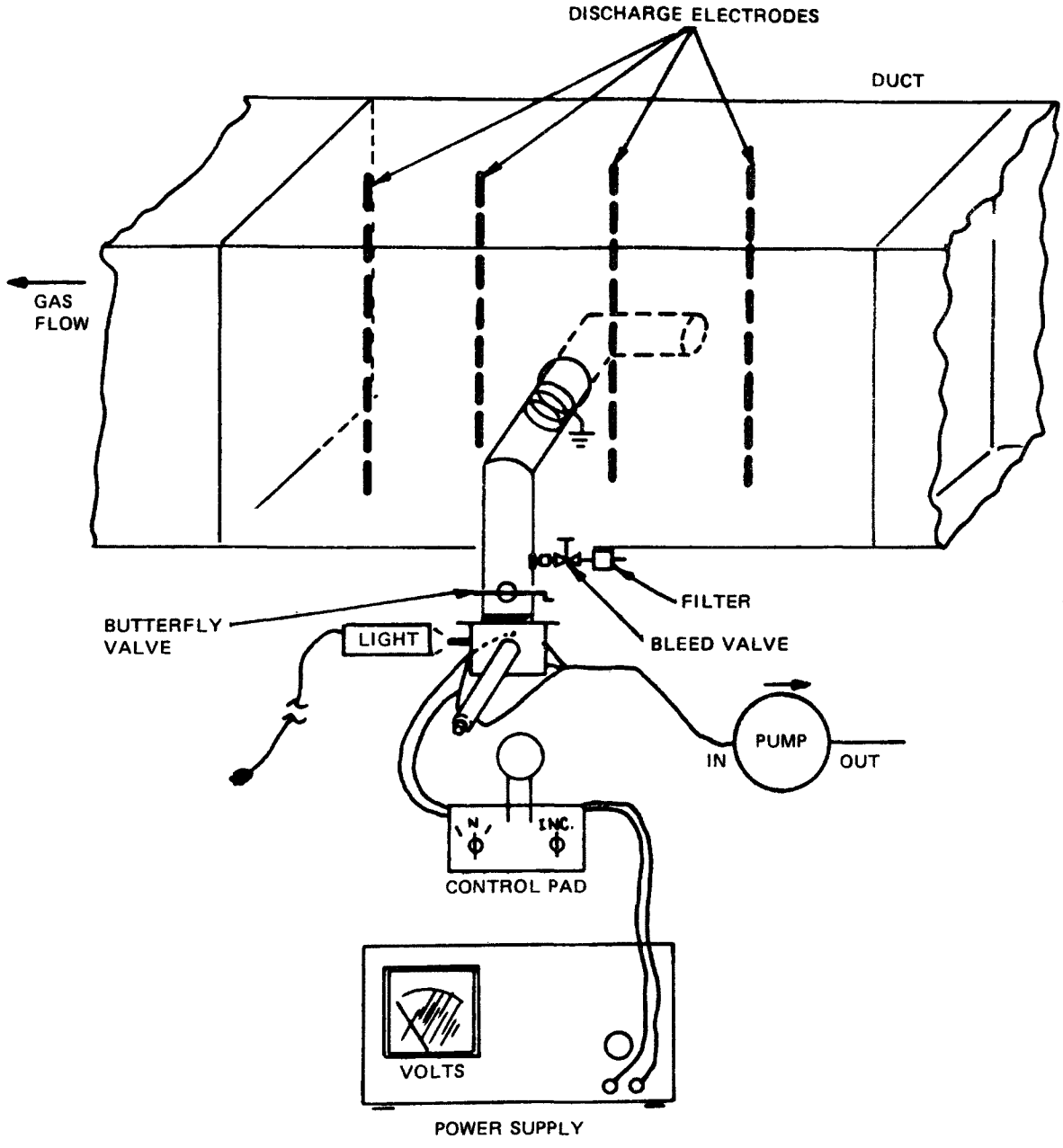

Figure 4. Experimental apparatus for measuring the diameter and charge of particles.

FIGURE 5. CHARGE VS RADIUS FOR HIGH RESISTIVITY
TEMPERATURE = 150 C

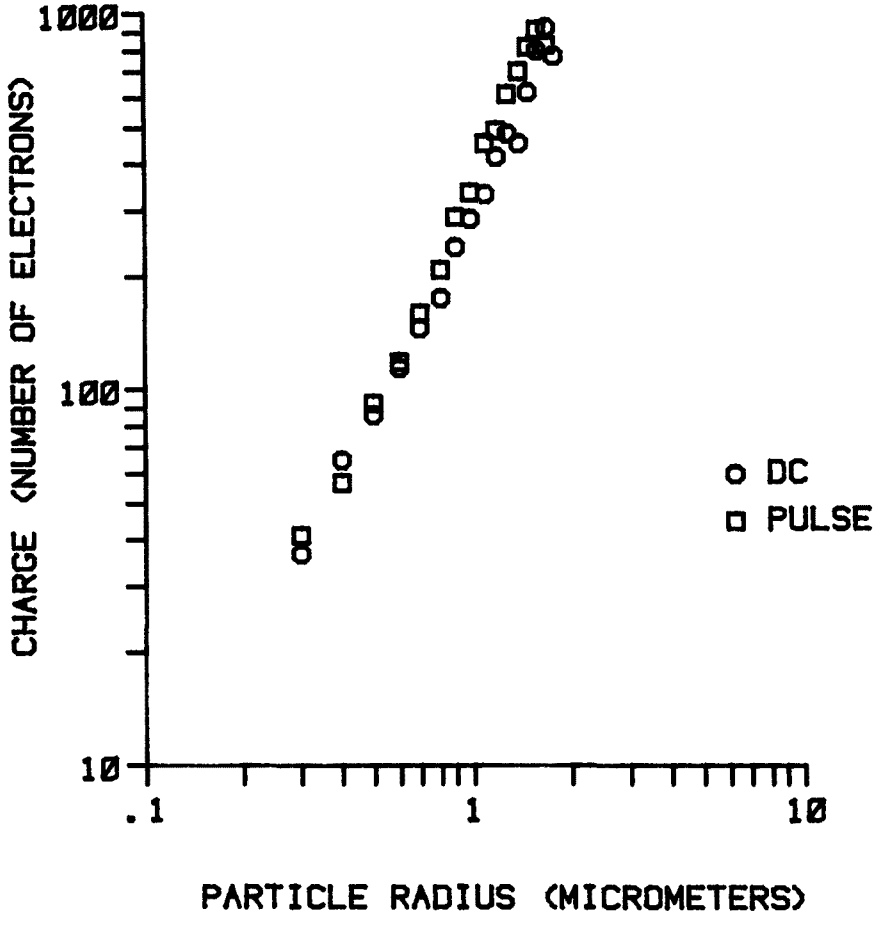

FIGURE 6. CHARGE VS. RADIUS FOR MODERATE RESISTIVITY
TEMPERATURE = 218 C

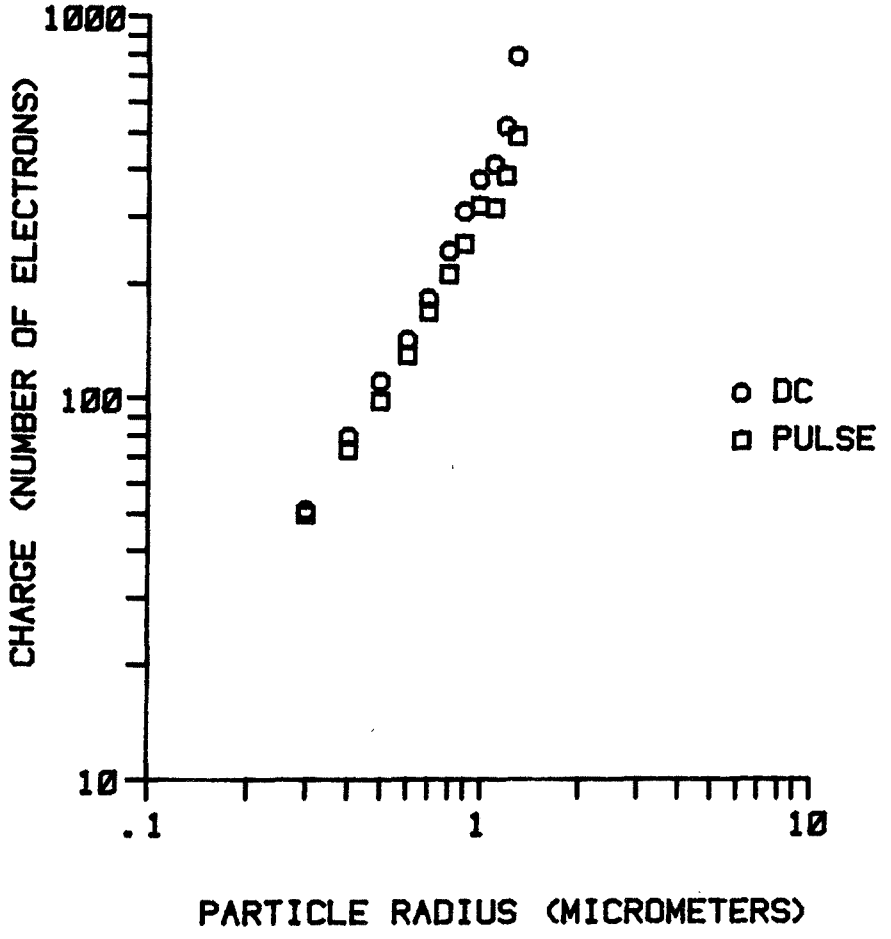

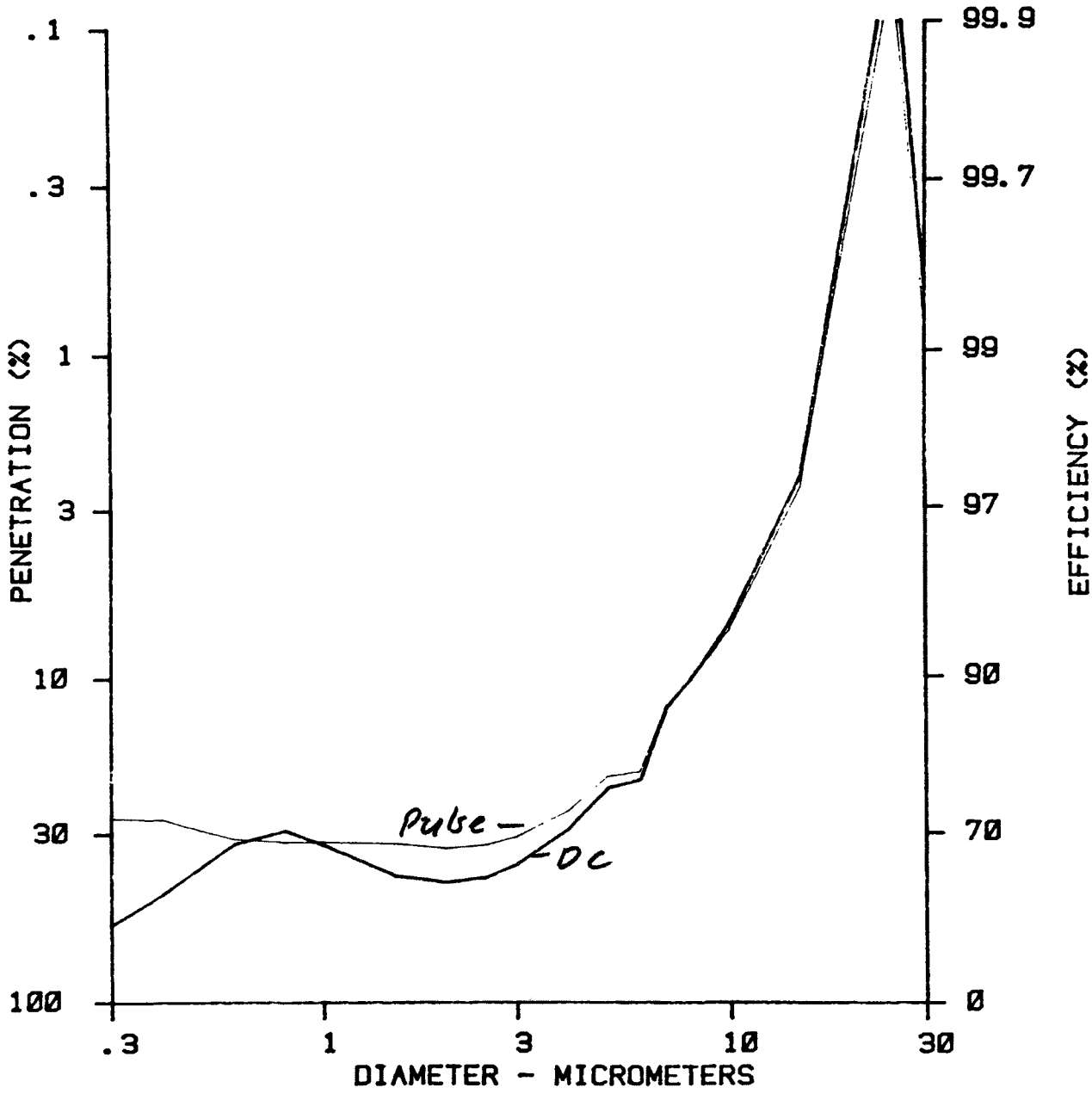

Figure 7. Penetration versus particle diameter for moderate resistivity.

FIGURE 8. CHARGE VS RADIUS FOR LOW RESISTIVITY EXPERIMENTS
TEMPERATURE = 24 C

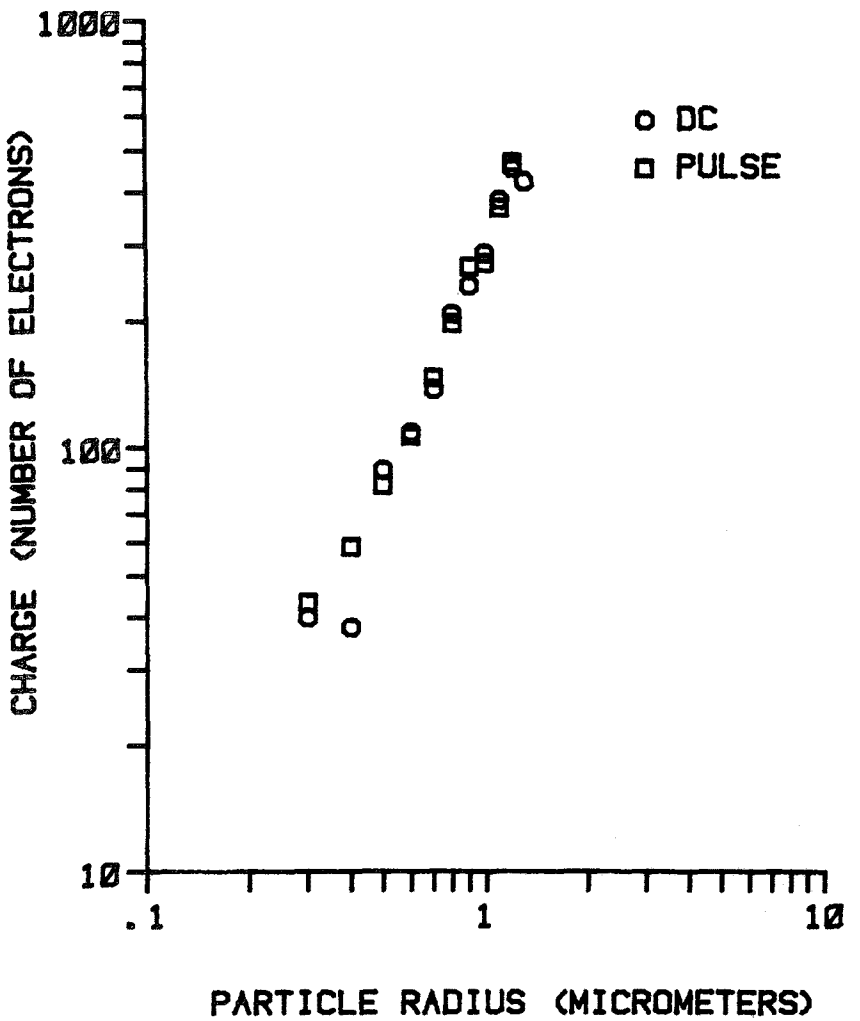

Particle Collection in a Two-Stage Electrostatic Precipitator with Various Collector Stages

by
L.E. Sparks, G.H. Ramsey, R.E. Valentine, and J.H. Abbott

Introduction

One of the major goals of the Environmental Protection Agency's electrostatic precipitator research and development program is the development of improved electrostatic precipitators for collecting dusts with high electrical resistivity. Fairly early in the program it became apparent that some two-stage electrostatic precipitator design was most likely to give the desired improvement. Consequently a major program was funded to develop and demonstrate a new two-stage electrostatic precipitator for collecting dusts with high electrical resistivity.

Early work concentrated on the development of a suitable precharger for the system. The precharger that came out of this work is a three-electrode precharger, shown in Figure 1, developed by Southern Research Institute under EPA's sponsorship. The three-electrode precharger is described by Pontius and Sparks[1].

The three-electrode precharger has been tested as part of a two-stage electrostatic precipitator system and the results reported by Sparks et al.[2] and Pontius et al[3]. The collector stage used in the previous work was a first generation collector and was essentially a conventional electrostatic precipitator with discharge electrodes consisting of either wire mesh or closely spaced wires.

The experimental results in References 2 and 3 showed that the first generation system was a significant improvement in electrostatic precipitator technology. However, the collector stage was not the optimum. Theoretical analysis and limited experimental data showed that additional improvements in electrostatic precipitator technology were possible if the collector stage could be improved.

Work to develop an improved collector stage, begun by EPA/IERL-RTP's Particulate Technology Branch using inhouse capabilities, is discussed in this paper.

Characteristic of Optimum Collector Stage

Because the collector stage is designed to collect previously charged particles, the highest possible electrical field should be maintained in the collector. If there were no reentrainment, the collector stage would not require any current. Unfortunately, reentrainment is present in any dry system. Thus, some current is necessary in the collector stage to minimize the reentrainment problem.

The major functions of the collector stage are to collect the charged particles from the precharger and to charge and recollect particles that

are reentrained. Because the size of reentrained material is large, the particle charging requirements of the collector stage are much less severe than the particle charging requirements of the precharger. This means that low current densities are acceptable in the collector stage.

The mesh and close-spaced wire discharge electrodes used in the first generation collector stage were selected to provide fairly high electric fields and low current densities. Pilot plant experiments with the mesh and wire discharge electrodes showed that, when the discharge and collection electrodes were clean or covered with low resistivity dust, the applied voltage (and thus the achievable electric field) was much higher than that obtained with conventional discharge electrodes. However, when the discharge and collection elecrodes were covered with high resistivity dust, there was no significant difference between the applied voltage obtained with the mesh or close-spaced wire discharge electrodes and the applied voltage obtained with conventional discharge electrodes. The stable electric operating points for all discharge electrode configurations were essentially the same[2]. The only exception was that flat plate discharge electrodes could be operated at high applied voltage and no current.

A downstream collector with flat plate discharge electrodes would be the ideal collector stage except for the problem of reentrainment. A system could be designed with precharger collector, precharger collector, etc. But reentrainment from the last collector stage would still be a problem. Also the use of the precharger to charge the large particles from reentrainment appears to be a non-optimum economic solution to the problem.

Analysis along the lines outlined above led to the idea that the optimum downstream collector would consist of sections with flat plate discharge electrodes in combination with something to handle the reentrainment. A pilot plant experimental study was begun to study various combinations of collector stage configurations. The configurations which were studied are shown in Table I.

Table I. Collector Stage Configurations.

1. Flat Plate, Wire, Flat Plate, Wire
2. Flat Plate, Flat Plate, Wire, Wire, dc power.
3. Flat Plate, Flat Plate, Wire, Wire, pulse power.

Experimental Electrostatic Precipitator

The experiments were conducted in a one-lane pilot plant electrostatic precipitator located in EPA's Industrial Environmental Research Laboratory, Research Triangle Park, NC. The electrostatic precipitator was operated with plate-to-plate spacing of 22.9 cm. The discharge electrodes were 0.318 cm diameter rods spaced 22.9 cm apart.

The aerosol used for this study was fly ash which was injected into the electrostatic precipitator through two sand blast guns fed by a vibrating screw feeder. The electrical resistivity of the fly ash was about $2x10^{12}$ ohm-cm for the experiments discussed in this paper. This corresponds to an electrostatic precipitator operating temperature of 150°C.

Additional information on the pilot plant electrostatic precipitator and the aerosol injection system is given by Lawless et al[4].

The overall mass particle collection efficiency of the system was determined using mass filters. The collection as a function of particle diameter was determined using Meteorology Research, Incorporated (MRI) cascade impactors calibrated by personnel of EPA/IERL-RTP's Particulate Technology Branch. Data reduction was done on a TRS-80 microcomputer using software developed by Denver Research Institute.

Results

The penetration as a function of particle diameter for the various configurations studied is shown in Figures 2-4. The results of the previous experiments with the mesh discharge electrode are shown in Figure 5. The performance of the pilot electrostatic precipitator as a conventional electrostatic precipitator is shown in Figure 6.

The results shown in the various figures show that the initial or first generation collector stage was not the optimum. The various flat plate configurations offer improved particulate collection when compared to the first generation collector. The results also show that changing the rapping cycle in the precharger had a major impact on the particle collection efficiency of the system.

Discussion and Conclusions

The results of the pilot plant experiments demonstrate that improved electrostatic precipitator technology requires both a good precharger and a good collector stage. The difference in particle collection between the best of the collector stages studied and the first generation system is almost as much as the difference in particle collection between the first generation system and the conventional electrostatic precipitator.

The experimental data were used to estimate the penetration versus specific collector area curve for a typical fly ash with a log-normal particle size distribution (mass mean diameter = 20 μm and geometric standard deviation = 5.0). The penetration for a given specific collector area was estimated by using the experimental particle diameter specific migration velocities and the specific collector area to calculate the penetration for each particle diameter from:

$$Pt(d)=\exp[-w(d)SCA] \qquad (1)$$

where Pt(d) is the penetration of particles of diameter d, w(d) is the migration velocity of particles with diameter d, and SCA is the specific collector area. The overall penetration was calculated from:

$$Pt_o = \Sigma_i \quad Pt(d_i)f(d_i) \qquad (2)$$

where $f(d_i)$ is the fraction of the particles with diameters between d_i and $d_i + dd$.

The migration velocity versus particle diameter for the conventional electrostatic precipitator, the first generation system, and the second generation system is shown in Figure 7.

The results of the calculation are shown in Figure 8. Note that because of particle size distribution effects, the performance gain of the two-stage system increases as the overall penetration decreases (as the overall efficiency increases).

The major unknown about the improved collector stage is its cost. Work is now underway to determine the costs of using all plate collector stages. Preliminary results are promising and show that the added cost of all plate stages is more than compensated by the improved performance. Additional work is necessary to improve the cost estimates before any quantitative information is released.

Also additional experimental work is planned to improve the performance of the system as a whole. This means that optimization of both the precharger and the collector stages is necessary.

References

1. Pontius, D.H. and L.E. Sparks. "A Novel Device for Charging High Resistivity Dust." J. Air Pollution Control Association, 28, 698 (1978).

2. Sparks, L.E., Ramsey, G.H., and B.E. Daniel. "Collection of Fly Ash with High Electrical Resistivity in a Pilot Plant Electrostatic Precipitator preceded by the EPA/SoRI Precharger." J. Air Pollution Control Association, 29, 745 (1979).

3. Pontius, D.H., P.V. Bush, and L.E. Sparks. "Field Evaluation of a Two Stage ESP for High Resistivity Dusts." Staub. (in press) (1980).

4. Lawless, P., G.H. Ramsey, and B.E. Daniel. "Characterization of the EPA/IERL-RTP Pilot-Scale Precipitator." EPA-600/7-79-052 (NTIS PB 292-820) (1979).

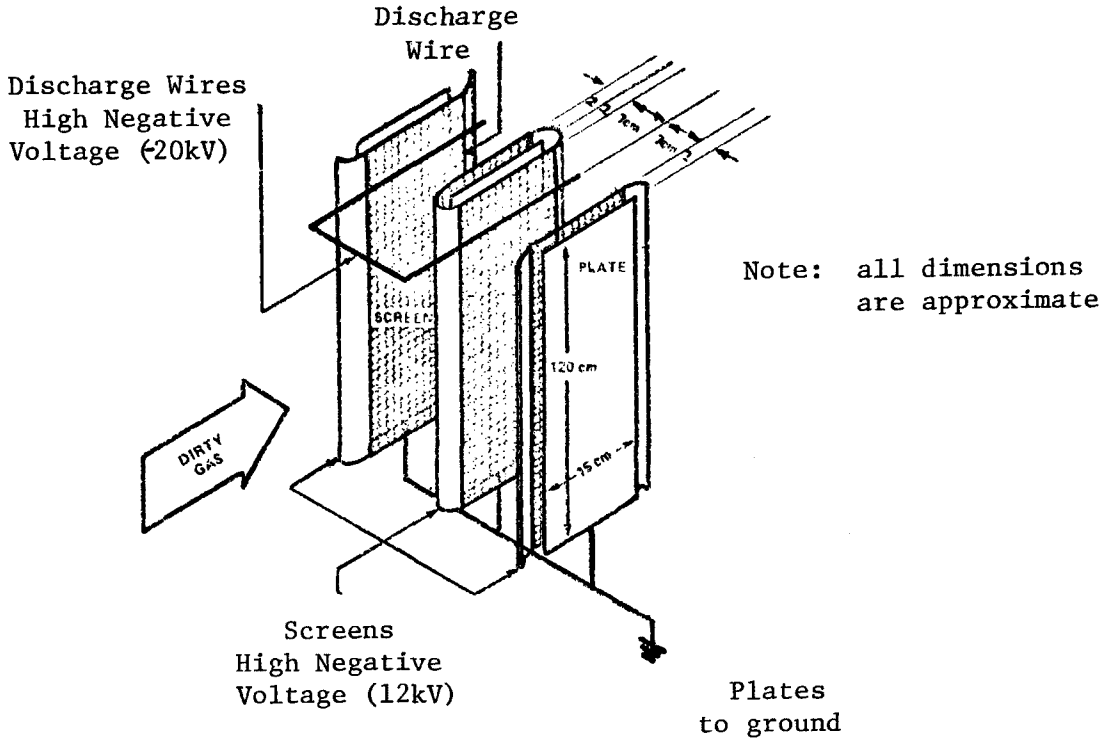

Figure 1. Schematic drawing of EPA/SoRI precharger.

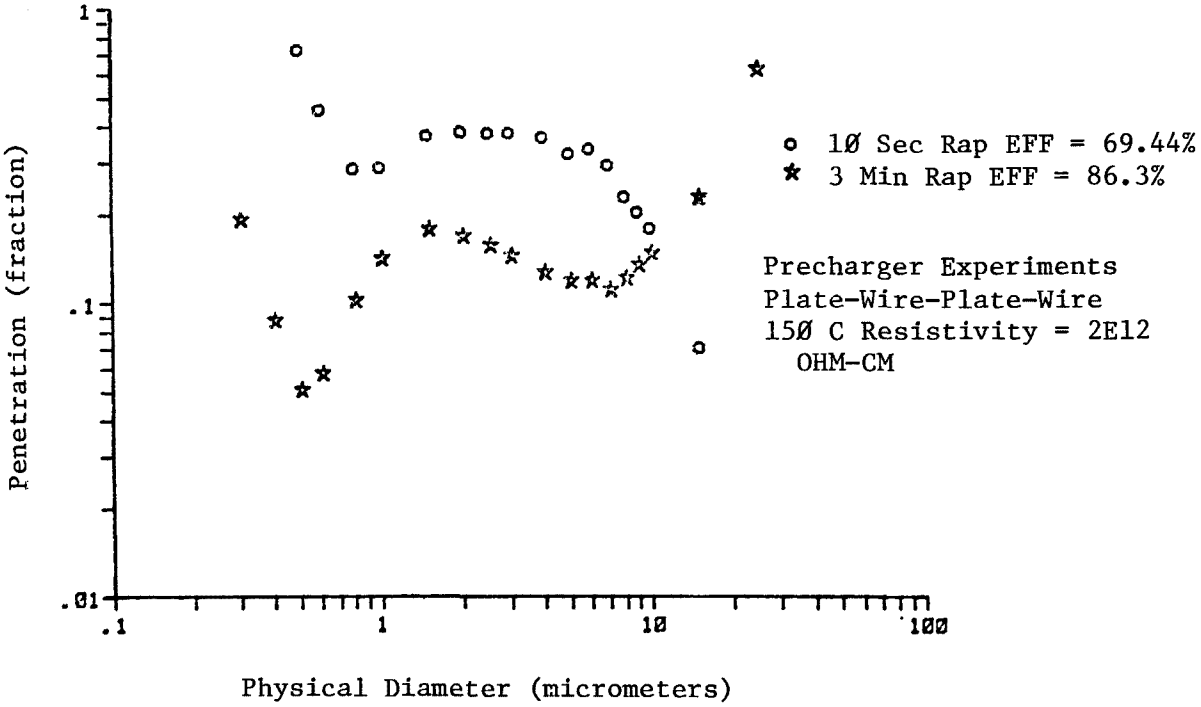

Figure 2. Penetration versus particle diameter for precharger followed by plate-wire-plate-wire collector.

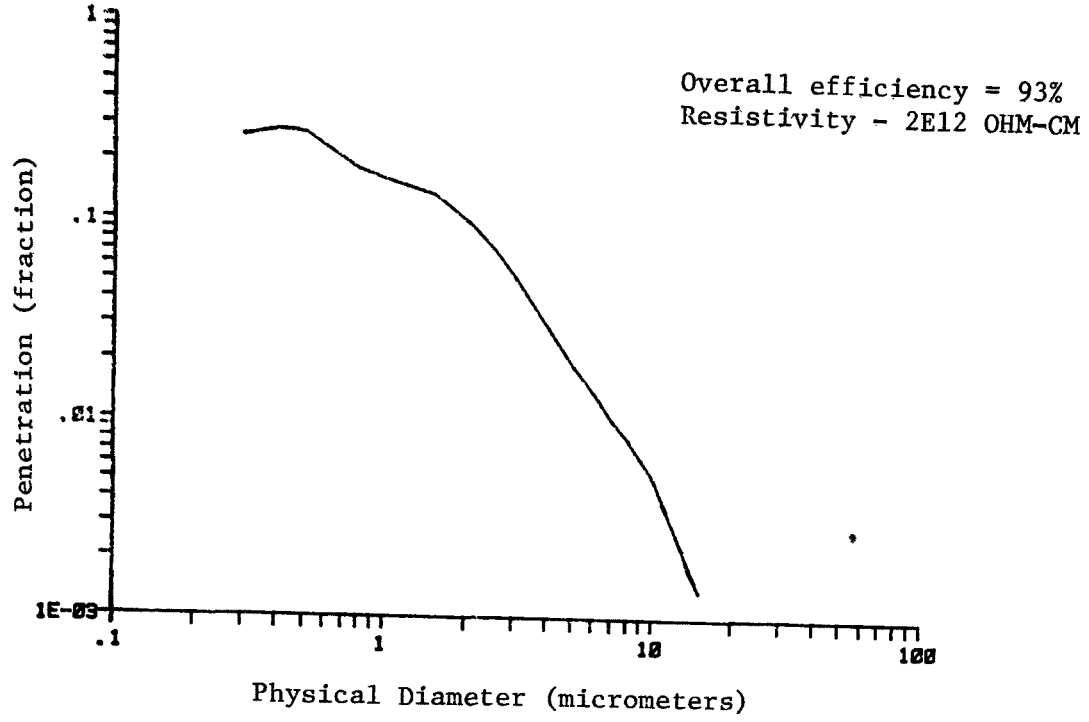

Figure 3. Penetration vs particle diameter for precharger plate-plate-wire-wire DC power.

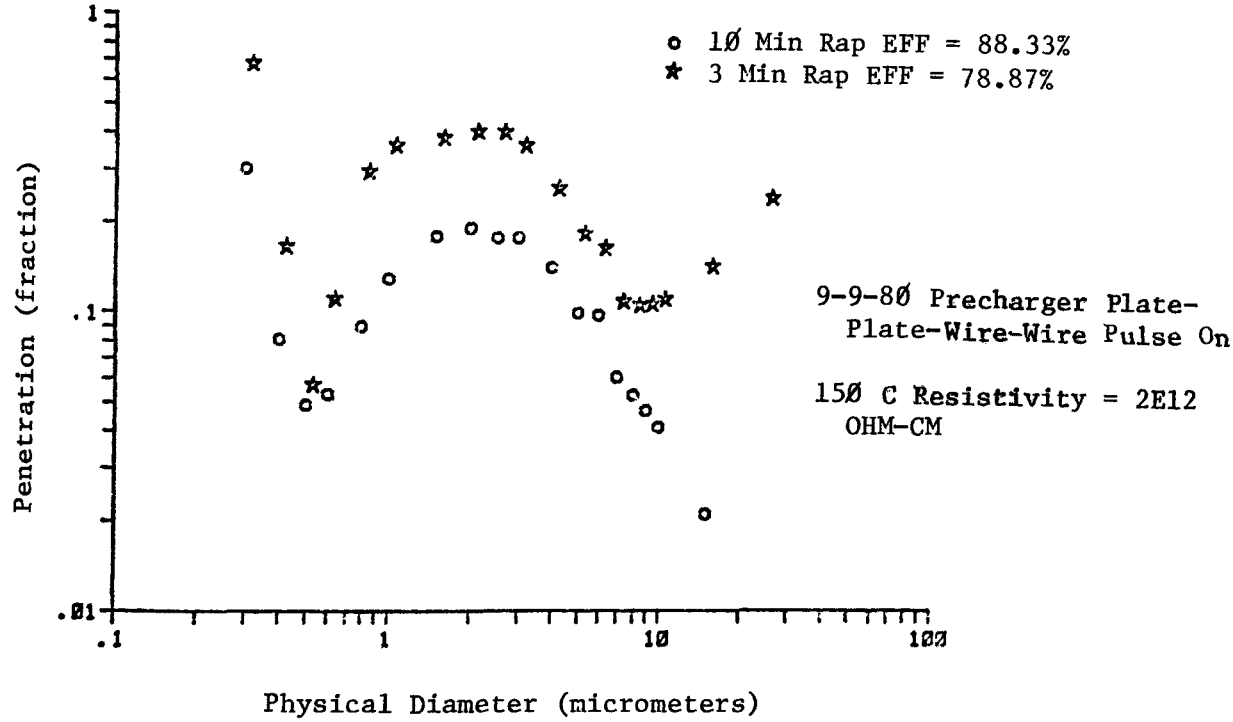

Figure 4. Penetration versus particle diameter for precharger followed by plate-plate-wire-wire collector with pulse power.

FIG. 5 1ST GENERATION PRECHARGER SYSTEM

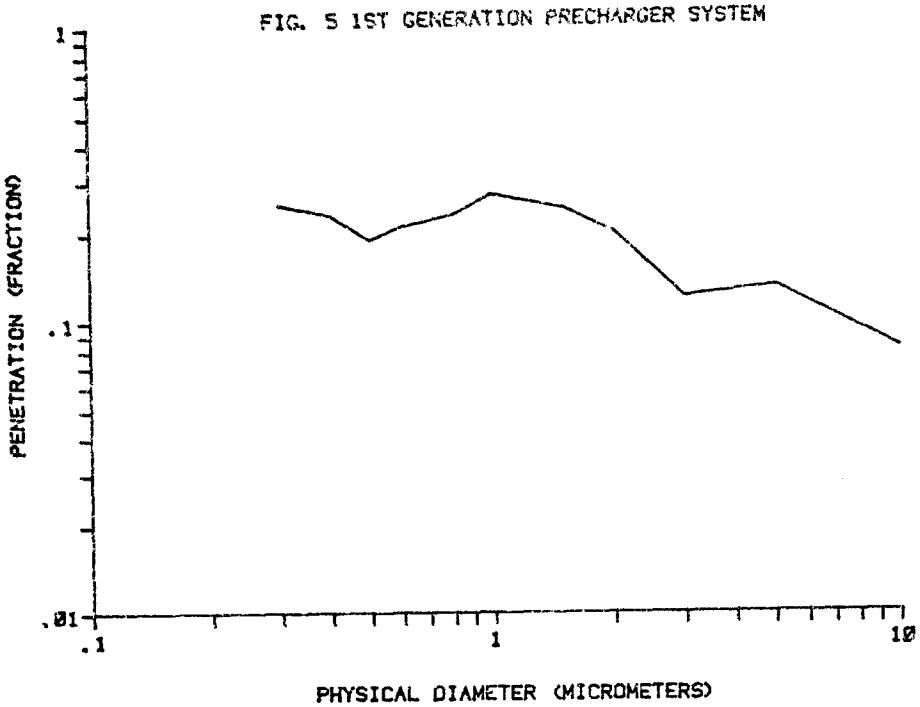

FIGURE 6. PENETRATION FOR PILOT ESP

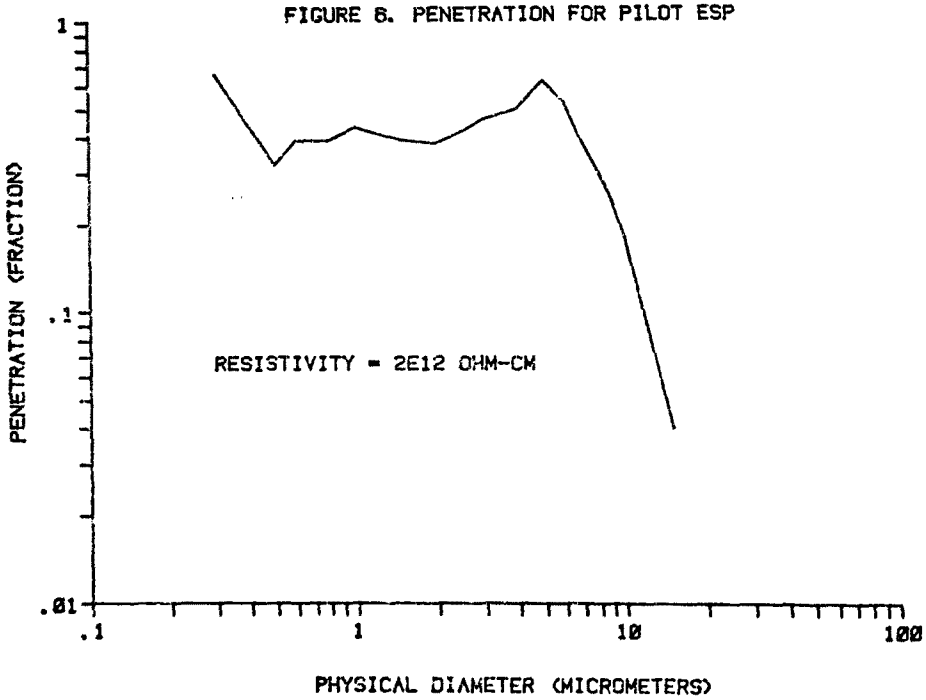

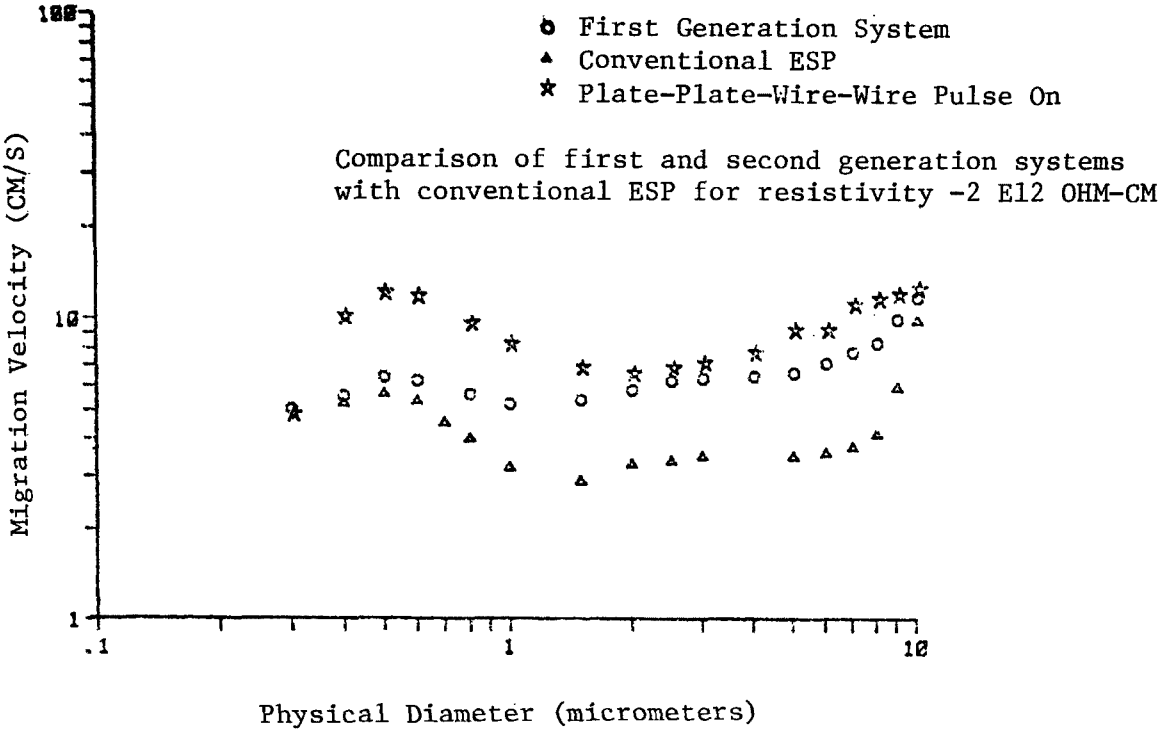

Figure 7. Effective migration velocity as a function of particle diameter for precharger followed by first and second generation collectors.

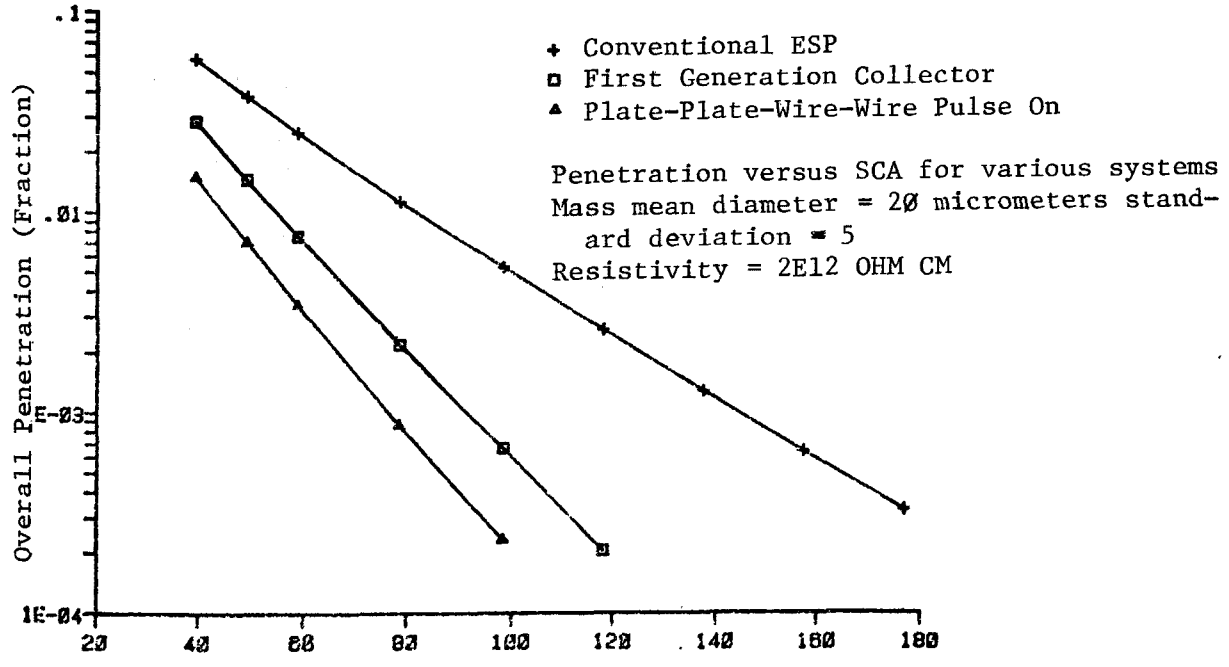

Figure 8. Overall penetration as a function of specific collector area for precharger followed by first and second generation collectors .

HIGH INTENSITY IONIZER DEVELOPMENT

By M. H. Anderson
J. R. McDonald
J. P. Gooch

Southern Research Institute
2000 Ninth Avenue South
Birmingham, Alabama 35255

and

D. V. Giovanni
Electric Power Research Institute
3412 Hillview Avenue
Palo Alto, California 94303

ABSTRACT

Results from parallel laboratory and field studies designed to characterize effects associated with a double-bellmouth, high intensity ionizer (HII) are presented. These studies include measurements after the HII of particle charge as a function of particle diameter in the fine particle size range for various voltage levels, particulate mass loadings, fly ash compositions, charge to mass ratio measurements after the HII for various HII and gas conditions, measurements of the gas velocity distribution after the HII for various main gas flows, temperatures, and anode purge air pressure drops in the HII, observations of effects in transition cavities containing highly charged particles, and observations of effects in small-scale HII/ESP combinations. The results of the studies show that the HII charges fine particles in accordance with field charging theory, the gas velocity distribution after the HII can be adjusted by varying the anode purge air conditions, space charge precipitation effects can be significant in transition cavities following the HII, and the HII provides improved performance of an ESP for small-scale HII/ESP combinations with the degree of improvement depending on ESP operating conditions.

INTRODUCTION

The electric utility industry is faced with the problem of finding cost effective procedures for upgrading the performance of electrostatic precipitators which are not in compliance with particulate matter emission regulations. One approach for accomplishing this objective is to provide a precharging device at the inlet of a conventional precipitator for the purpose of imparting a higher than normal value of charge to fly ash particles entering

the precipitator. Theoretical calculations have indicated that the precharging approach can provide significant improvements in the collection efficiency of a downstream precipitator.

Promising laboratory results and pilot plant trials with a precharging device known as the high-intensity ionizer prompted EPRI to initiate a research program in 1975 to respond to the need for finding practical methods to upgrade precipitator performance. As shown in Figure 1, the basic design of the ionizer consists of a disc electrode centered in a venturi shaped anode assembly equipped with a purge system. An array of ionizer assemblies is placed at the entrance to an ESP. For the combined HII-ESP system to be successful, three technical goals must be achieved:

1. The HII must impart an enhanced charge to the fly ash particles.

2. The particles must retain this high charge as they pass through the HII assembly and transition cavity into the ESP.

3. The ESP must respond by efficiently collecting these highly charged particles without deterioration of performance over time.

The initial research approach consisted of evaluation of the charging capabilities of a prototype HII system under controlled operating conditions at a scale representative of utility ESP installations. The evaluation was performed in 1978 on a 10 MW prototype ESP at EPRI's Advanced Emissions Control and Test Facility, at the Arapahoe Station of Public Service Company of Colorado. A schematic diagram of the prototype system is given in Figure 1. The HII system tested at Arapahoe in 1978 did not achieve the goals listed above. The collection efficiency of the 10 MW ESP prototype at Arapahoe did not improve sufficiently to warrant further scale up. As a result of these findings, the research effort was redirected towards identifying HII performance limitations and developing hardware and process improvements to overcome these limitations. The redirected research effort involved experiments on laboratory test stands in the APS laboratories and diagnostic tests and analyses on the 10 MW prototype system and a smaller ($\sim$5000 acfm) pilot unit at the Arapahoe Test Facility.

Diagnostic testing on the 10 MW prototype indicated that ionizer performance was limited by electrical breakdown associated with build-up of high resistivity ash on the anode vanes. Ionizer voltage vs. current measurements were performed, using ambient air, and using simulated flue gas corresponding to both natural gas and coal-fired boiler conditions.[1] Operating conditions were established at ambient and at elevated temperatures. It was found that the initial sparking point dropped from about 11 kV/cm to about 6 kV/cm after eight hours of operation (See Figure 2), unless the moisture content of the anode purge gas was increased to about 5 to 12% by volume. Typical required operating conditions for the anode purge gas were established at 6% by volume moisture, at a temperature of approximately 43°C (110°F), and purge air gas flows equal to about 8% of the main gas flow.

The necessity for conditioning the thin layers of ash deposited on the anode vanes can be explained by considering the electric field intensity in the ash layer that results from the high current fluxes at the anode surface, which are typically ~2500 nA/cm^2. Although the electric field intensity (breakdown strength) required to produce electrical breakdown in the ash layer can vary widely, values in the range of 10 to 20 kV/cm are considered typical. Since the maximum value of resistivity which can be tolerated without breakdown is equal to the breakdown strength divided by the operating current density, it can be shown that, if breakdown strength is in the 10 to 20 kV/cm range, the resistivity of ash on the anode must not exceed 4-8x10^9 ohm•cm. If the resistivity does exceed 4-8x10^9 ohm•cm, some means of reducing the resistivity will be required. It is therefore apparent that the effectiveness of the anode purge/conditioning system will depend upon the response of fly ash resistivity to the moisture content and reduced temperatures of the anode purge gas.

Although the addition of water vapor to the anode purge gas alleviated the degradation of ionizer electrical operating characteristics at Arapahoe, this remedial approach did not result in improved system performance for ionizer field strengths above 7 kV/cm. It was determined that 7 kV/cm was not an electric field value of sufficient intensity to accomplish the desired level of particle charge and that additional diagnostic testing and development efforts were required.

Further diagnostic testing provided the following conclusions:

- Charge loss within the ionizer assembly was occurring downstream of the discharge electrode, and the performance of the ionizer-precipitator system was limited by the charge loss.

- The charge loss was induced by the high space charge of the particles and was severe at higher mass loadings.

- The fiberglass exit cone enhanced the electric field at the fiberglass-metal interface where most of the discharge occurred.

As has been previously reported,[1] the original design of the HII evolved following a series of optimization tests to obtain both a high intensity electric field in the ionizer throat and a low gas pressure drop through the ionizer system. The inlet cone section was designed with a bellmouth configuration, but the outlet cone section was designed to recover kinetic energy from the main gas stream. Since charge loss in the ionizer assembly was found to be a major limiting factor in system performance, an experimental effort was initiated in the laboratory to minimize the charge loss. It was found that simply replacing the fiberglass cones with metal cones would not significantly improve particle charging performance because of resulting high space charge effects within the cone.

Promising results were obtained, however, by eliminating the fiberglass exit cone and metal diffuser and by using a double bellmouth design which has symmetric inlet and outlet geometries. A schematic drawing of this design is

given in Figure 3. With this new geometry, ionizer field strengths of 10 kV/cm and current densities on the order of 3000 nA/cm^2 have been obtained.

This paper will summarize results obtained with this ionizer geometry in a parallel effort, which is still in progress, conducted at the APS laboratories and at the Arapahoe Test Facility. The objectives of the research efforts are:

1. To quantify the particle charge values produced by the ionizer on fly ash particles under various conditions.

2. To determine the degree to which the fly ash particles retain charge imparted by the ionizer.

3. To quantify the increase in collection efficiency obtainable by precharging under various conditions.

Initially, Air Pollution Systems was primarily responsible for the development of the HII, and Western Precipitation was responsible for its field evaluation. When it was decided in the spring of 1979 that a return to smaller test units and the initiation of a diagnostic program were required, a Task Force composed of members from EPRI, APS, Western Precipitation, KVB and Kaiser Engineers was formed to direct the program. In November of 1979, Western asked to be relieved of their evaluation responsibilities, and Southern Research Institute (SoRI) was placed under contract to EPRI. The responsibilities of SoRI included the performance and analysis of the testing at Arapahoe and providing assistance in data acquisition and interpretation for the work underway at the APS laboratories.

Experimental Technique and Procedures

APS Laboratory

As was indicated earlier, the outlet geometry of the ionizer was changed by replacing the metal diffuser and fiberglass cone by a diffuser bellmouth in an attempt to alleviate the discharge activity associated with the diffuser/cone assembly. In order to evaluate the charging characteristics of both outlet geometries under similar test conditions, two test stands were set up in the APS lab. One of the test stands was equipped with a diffuser/cone outlet, and the other had a bellmouth outlet. The main gas flow for each test stand consisted of hot air from a natural gas fired combustor combined with ambient air. The inlet gas temperature was controlled by varying the ratio of combustor air to ambient air. A vibrating screw feeder was used to add the desired amount of fly ash to the gas stream. Each ionizer assembly consisted of a 25.4 cm (10 inch) vaned anode and a 11.43 cm (4.5 inch) discharge electrode. Also, a wire-pipe ESP was installed downstream of the double bellmouth ionizer to investigate HII/ESP interactions. The ESP could be operated either wet (to eliminate high resistivity problems) or dry at simulated flue gas conditions.

Arapahoe Test Facility

At the Arapahoe Facility, two nominally 5000 acfm mobile support units (MSUs) were used to obtain the data presented here. The first, (designated MSU-I) which was used to study the charging characteristics of the ionizer, consisted of a multiclone, a two field electrostatic precipitator, a two ionizer array, and a single-field precipitator. The ionizers had the double bellmouth geometry with 25 cm anodes, with the anodes and bellmouths isolated from ground, so that current flow from these components could be monitored. The precipitator fields were of the Western Precipitation design and each had 40.1 m^2 (432 ft^2) of plate area. Several isolated metal strips were placed near the wall of the cavity between the ionizers and the last field of precipitation. These "current strips" were used to get a qualitative feel for the manner in which charge migrated in the cavity and, also, to determine if particulate charge was being lost in the cavity.

MSU-I was adequate for the ionizer charging study, but it was not well suited for the evaluation of an HII-ESP combination. It was limited by low temperature (200-220°F) at the ionizer outlet and low SCA (80-90 ft^2/1000 acfm) in the downstream collector when operating at design flow. Therefore, it was replaced by a mobile unit (designated MSU-II) shown in Figure 4, which consisted of a two ionizer array followed by a three-field electrostatic precipitator. Each ionizer was of the double bellmouth design and had a 30.5 cm (12 inch) vaned anode with a 13.7 cm (5.4 inch) discharge electrode. Again the anodes and bellmouths were isolated from ground. The precipitator fields were of the Western design with 43.2 m^2 (465 ft^2) of plate area per field.

The charging capability of the ionizer was studied as a function of: inlet mass loading, main gas flow rate, ash resistivity, ionizer field strength and particle size. The charge as a function of particle size was determined using a modification of the Millikan Technique developed by Southern Research Institute.[2] The ratios of charge to mass and charge to volume were determined by measuring the charge which accumulated on a filter substrate while isokinetically sampling the mass concentration of the flue gas stream. Mass loadings, particle size distribution and velocity profiles were determined using standard techniques.

Experimental Results - APS Laboratory[3]

Charging Effectiveness

The work done to compare the charging capabilities of different ionizer geometries will be summarized briefly. For both geometries charge/mass (Q/M) was measured as a function of ionizer field strength for 0.5, 2, and 4 gr/acf. For the diffuser/cone geometry the values of Q/M were in fair agreement with predicted values for the low grain loading case but fell below predicted values for the higher grain loadings. The degradation in Q/M could be correlated with an increase in the current to a ring at the exit of the cone. The values of Q/M measured at the exit of the bellmouth for the same conditions displayed little or no dependence on grain loading and agreed with values predicted for the particle size distribution and ionizer setting. All subsequent work was performed using the double bellmouth geometry.

Since Q/M results can be seriously misleading because of their sensitivity to particle size distribution changes, considerable effort was directed toward quantifying the charging characteristics of the HII as a function of particle size. The charge given to individual particles was measured as a function of particle size at several different HII current-voltage settings for three different mass loadings; .5, 2.0, and 4.0 gr/acf. The results obtained for 2.0 gr/acf at the ionizer voltage setting of 71.5 kV are shown in Figure 5. Also shown in Figure 5 is a theoretical prediction of the charge as a function of particle size for particles exiting a highly efficient cold-side ESP and a theoretical prediction of charge for particles exiting the ionizer. It can be seen by comparison that, for the 71.5 kV case, particles exiting the HII obtain significantly more charge than would be obtained by traversing the ESP. These data also give direct proof that the ionizer is effective in charging submicron size particles. Also, the agreement shown between measured values of charges and those predicted by theory from conditions in the ionizer is considered to be acceptable.

In summary, the ionizer was found to charge particles to levels predicted by theory if the anode purge system was operating properly. If the moisture content of the purge air dropped below 5% by volume, sparking occurred in the ionizer and the charge levels measured were reduced. Also, when the moisture level rises above the saturation point, plugging of the anode vanes occurs. This eventually leads to back corona in these plugged regions with a decrease in the effectiveness of the ionizer.

Effect of Back Corona

In addition to the particle charge measurements and comparison with theory, it was of interest to determine in the laboratory the effect on outlet emissions of back corona in an ESP following an HII. Therefore, experiments were performed using the double bellmouth - HII and wire-pipe ESP laboratory test apparatus. Tests were conducted using fly ash from the D field of the pilot unit at Arapahoe. It was found that with this fly ash, the ESP went into back corona even at fairly low current levels. The presence of back corona was determined by evaluation of the current-voltage curves, by changes in electrical conditions with increasing ash thickness, and by ESP current-outlet optical density measurements. It should be noted, that in this work, optical density is used only as a qualitative indication of system performance and is not related to mass emissions or mass efficiency.

As mentioned previously, the ESP could be operated either wet or dry. The wet operation insured the absence of back corona. The test results for both wet and dry operation show a decrease in the outlet optical density as the HII current was increased. For the wet ESP, the effect of the HII on the outlet optical density appeared to decrease as the current level in the ESP was increased, which is consistent with theory. For the dry ESP case, the baseline optical density increased with time, and as the ESP deteriorated, the reduction in optical density produced by the ionizer decreased.

The results from these experiments with Arapahoe fly ash (dry ESP case) are shown in Figure 6. To determine if reentrainment emissions were influencing the results shown in Figure 6, the ash feeder was turned off after 3

hours of operation, and the optical density was monitored. It was found that the optical density dropped to zero even though the gas flow was maintained, indicating no significant reentrainment problems in the ESP under the conditions of the experiment. Although the ESP was in back corona at all current levels tested, the electrical characteristics of the ESP deteriorated as a function of time during the experiment. This indicates that the extent of the back-discharge was increasing as the dust layer thickness increased.

These results are significant because they illustrate that the HII will not restore an ESP in back corona to the performance levels which could be achieved in the absence of back corona. This observation is also consistent with results reported by Masuda,[4] where positive ions produced by back corona reduce the limiting negative charge which can be obtained.

Flow Distribution

Since the gas flow uniformity across the inlet of an ESP has a significant impact on performance, an experimental program was performed to study the interaction between the purge gas and main gas flow rates. The first series of tests were performed with no purge air flow. The main gas temperature was maintained at 300°F and four different flow rates from 1600 to 3200 acfm were used. The test results show the gas velocity profile to be in the jetting pattern for all flow rates with the degree of jetting decreasing as the main gas flow rate was decreased. Here "jetting" refers to a plume shaped velocity profile at the exit of the ionizer, and "non-jetting" is defined as a velocity profile in which the flow separates and follows the curvature of the bellmouth.

Next, the effect of purge air ΔP (which is related to purge gas flow rate) on the gas velocity profile downstream of the double bellmouth HII was studied for main gas flow rates of 1600, 2000, 2800, and 3200 acfm. Again the main gas temperature was maintained at 300°F, while the purge air temperature was maintained at 110°F. For the 1600 acfm flow rate the gas velocity profile was fairly uniform at the ΔP of 1.0" H_2O and switched to a non-jetting profile when the purge air ΔP was increased to 1.5" H_2O. For the 2400 acfm main gas flow rate, the gas velocity profile switched from jetting to a uniform profile when the purge air ΔP was increased from 1.5" to 2.0" H_2O, and to non-jetting between 2.0 and 2.5" H_2O ΔP.

In general, it was found that for all the main gas flow rates tested, the gas velocity jet downstream of the HII steadily broadened as the purge air ΔP was increased until it switched to the non-jetting profile. Also, it was observed that the purge air ΔP at which the gas velocity profile switched from a jetting to a non-jetting condition increased as the main gas flow was increased.

Figure 7 illustrates the interrelationship between main gas flow rate, purge air ΔP, and outlet velocity profile in the double bellmouth HII. The solid curve and the area above it is the jetting profile regime. The dotted curve and the area below are in the non-jetting profile regime. The gas velocity profile downstream of the double bellmouth HII switches from jetting to non-jetting or vice-versa in the area between the two curves. The practical

significance of these results is that the gas flow profile downstream of the double bellmouth ionizer design is reasonably uniform when the purge gas flow rate is about 16% of the main gas flow rate.

Experimental Results - Arapahoe Test Facility

Results from MSU-I

After the size-dependent charge measurement efforts in the laboratory produced encouraging results, it was decided to obtain similar data in the field at a point directly behind the ionizer for the three possible MSU configurations:

1. Multiclone - AB field - HII - C field (MABIC),
2. Multiclone - HII - C field (MIC), and,
3. HII - C field (IC).

For the IC configuration the ionizer inlet grain loading was on the order of 1.5 gr/acf, for the MIC case it was on the order of 0.4 gr/acf and for the MABIC case less than .1 gr/acf. In Figure 8, data obtained for the MIC configuration are compared to the charge as a function of particle size predicted by field charging theory for the three voltages at which data were obtained. This figure shows that reasonable agreement was obtained between the measurements and theory.

Figure 9 is a plot of charge as a function of ionizer electric field for several particle sizes for the $\sim$.4 gr/acf data. Due to the statistical nature of the data, there is some scatter present; but, in general, the charge increases with increasing electric field over the range of particle sizes.

These data confirm the results obtained with the laboratory test stands, and show that the double bellmouth ionizer design is capable of producing charge levels in approximate agreement with theoretical predictions. Agreement with theory was also obtained for the higher grain loading case (IC configuration), but it was found that the distribution of charged particles in the cavity was more highly dependent upon position. This is thought to result from higher space charge fields existing in the downstream cavity which accompany the higher mass loadings. The space charge field tends to force the charged particulate matter to the wall region of the cavity.

For all cases, the ability of the ionizer to achieve theoretical levels of charge was contingent upon sufficient conditioning of anode ash deposits by the steam-air mixture comprising the anode purge gas. Malfunctions in the steam generator system which produced either low water vapor concentrations, (below 6% by volume) or plugged anode vanes due to moisture carry-over, were accompanied by reduced charge levels on particles passing through the ionizer under these conditions.

As previously indicated, size distribution has a major effect on Q/M values measured downstream from an HII. This observation is illustrated by

the data and calculated charge values shown in Table 1. The size distribution data were obtained in the cavity region downstream from the HII in the MIC configuration, and the particle charge values were calculated from field charging theory using the HII applied voltage of 75 kV. The calculated sum of 35.7 μC/gm is in fair agreement with a measured value of 45 μC/gm obtained under similar conditions. Note that over 60% of the calculated charge is contained in the sub-micron diameter particles.

Test Plan and Results for MSU-II

Since the charge vs. size measurements at both Arapahoe and at the APS laboratory indicated that the double bellmouth ionizer design produced levels of charge in approximate agreement with theory, EPRI initiated a paper study designed to evaluate the market potential for HII technology. This study is described in another paper,[5] but some of the methods will be discussed briefly in this paper to illustrate the logic used in formulating a test plan for the Arapahoe MSU unit.

The evaluation of the market potential for HII-ESP systems is based in part on simulations performed with a modified version of the EPA/SoRI computer model. Typical results from simulations of a precipitator system with and without the ionizer are shown in Figure 10 for high (5 nA/cm^2) and low (40 nA/cm^2) resistivity conditions. The "with ionizer" curves do not consider the effect of purge gas, and therefore the indicated SCA for a given efficiency must be increased by approximately 16% for the with ionizer cases if purge gas is used to obtain uniform flow. The projected plate area gain as a result of ionizer energization for these hypothetical cases is approximately 17% at the 99% efficiency level for the low resistivity case, and 50% for the high resistivity case at the 95% efficiency level with the effects of purge air considered. These percentages are obtained by dividing the equivalent SCA decrease by the required SCA for the "without ionizer" cases. These examples are cited to illustrate the following point: The ionizer provided greater theoretical equivalent plate area gains for high resistivity cases than for low resistivity cases, if no charge loss is assumed to occur.

Since models for predicting the extent of back discharge and the resulting charge loss are not available, it is essential to determine whether the enhancements indicated by the computer simulation can, in fact, be obtained under realistic conditions. Therefore, the MSU-II system was installed at Arapahoe, and a test plan was designed to evaluate the effect of the HII on precipitator performance for both high and low resistivity conditions. Preliminary results from this effort are discussed in the following paragraphs.

During the time period that the MSU-II system has been available for testing, (approximately 2 months), brief experimental programs have been conducted with a moderate resistivity ash (Amax Coal) and with a high resistivity ash (Energy Coal). Resistivity vs. temperature predictions obtained from Bickelhaupt's[6] correlation, along with in situ data from the HII inlet area, are shown in Figure 11. At the operating temperature of 300°F, the resistivity of the Amax fly ash was $1\text{-}2 \times 10^{11}$ ohm•cm. As was discussed earlier, resistivities of $4\text{-}8 \times 10^{9}$ ohm•cm can lead to breakdown of the ash layer on the anode vanes. The estimated temperature of the anode is ∿200°F.

From Figure 11, it can be seen that the predicted resistivity would be ∿1 to $2x10^{10}$ ohm•cm with Amax ash, and 1 to $2x10^{11}$ with Energy ash. We conclude from these observations that some degree of back discharge is inevitable with the Energy coal at these conditions and is possible with the Amax coal.

The anode and bellmouth currents with Energy coal show evidence of some discharge occurring at higher ionizer current densities (2000 nA/cm^2). This discharge activity was not observed for the Amax Coal until a current density of 3000 nA/cm^2 was reached. It is important to note that the earlier charging data obtained with MSU-I were taken with anode temperatures estimated to be ∿170°F. Therefore, the more realistic temperatures achieved in the MSU-II unit require more resistivity reduction to be accomplished by the anode conditioning system.

With the Amax Coal, preliminary results from testing of the MSU-II system at Arapahoe indicate that the overall collection efficiency of the system was increased from 99.11 to 99.53 as a result of energization of the ionizer. These data were obtained for a specific collecting area of 300 ft^2/1000 acfm and include both mass train and impactor results. Fractional efficiency data obtained with impactors for this test series are given in Figure 12, along with calculated efficiencies using the test conditions as input data to SoRI's computer model. These data are encouraging in that the theoretical predictions of collection efficiency enhancement in the fine particle range were approximately obtained for particle sizes smaller than 0.6 μm diameter. For particle diameters larger than 1.5 μm, size resolution was not obtained with the impactors because of nozzle collection interference with upper stage cut points. This problem has now been corrected by using an in-line nozzle geometry.

With the Energy coal, (high resistivity ∿10^{12} ohm•cm) the following preliminary results have been obtained for overall efficiency:

300 ft^2/1000 acfm,	with ionizer:	99.3
	without ionizer:	98.8
200 ft^2/1000 acfm,	with ionizer:	92.9
	without ionizer:	92.8

The results for the higher flow rate (200 ft^2/1000 acfm) show that only small or insignificant enhancements were achieved, which are well below predicted values of enhancement in the absence of back discharge and charge loss. At the higher flow rate significant discharge activity was observed from the current strips in the cavity behind the ionizer. The particulate charge loss associated with this discharge phenomena is thought to be responsible for the lack of enhancement.

Figure 13 presents the mass efficiency data discussed above, along with projections of collection efficiency using the computer model with the conditions of the experiment as input data. This graph illustrates, that for all cases, the enhancement achieved in overall collection efficiency by energizing the ionizer was significantly below the values predicted by the computer model. The figure also indicates that the model was reasonably successful in

predicting the baseline collection efficiency of the MSU without the ionizer energized. This indicates that some charge loss still occurs in either the ionizer assembly, the cavity, or the ESP for resistivities on the order of 10^{11} ohm•cm.

Summary

The following conclusions have been derived from the laboratory and field studies with the double bellmouth ionizer geometry used in pilot-scale HII-ESP system.

- For high resistivity dusts, ($>10^{11}$ ohm•cm), an anode conditioning system is required to reduce ash resistivity on the anode vanes to 10^{9} to 10^{10} ohm•cm. Water vapor additions to the anode purge air have been shown to be a marginally effective means of reducing anode ash resistivity when high resistivity dusts (up to 10^{11}) are being treated. It is the opinion of the authors that steam purge air systems may not be practical in a power plant environment, and therefore another conditioning method should be developed if HII technology is to be successful for high resistivity dusts.

- The HII achieves levels of particle charge, within $\pm$ 10 to 20% of those predicted by field charging theory, when the anode conditioning system is conditioning the ash to the 10^{9} ohm•cm range, and this charge is retained as the particles pass through the ionizer assembly.

- Results obtained with moderate resistivity dust ($\sim 10^{11}$ ohm•cm) indicate that model projections have the potential for predicting HII-ESP performance under conditions where detrimental effects due to high resistivity ash in the cavity and in the ESP are eliminated.

Certain unresolved technical issues must be addressed if the ionizer is to become an effective means of upgrading precipitators. These issues are:

- To what extent does particle charge loss due to back discharge in the ESP or in the transition cavity negate the beneficial effects of charge imparted by the HII? The results obtained to date suggest that if an ESP is operating in back corona without the ionizer, then the beneficial effects of energizing the ionizer may be substantially neutralized.

- By what means does one obtain a good velocity profile downstream of the ionizer while minimizing the purge air requirements? With the double bellmouth design, the uniformity of gas flow downstream depends on the ratio of the purge gas and flue gas and flue gas flow rates. Preliminary results indicate that the gas flow profile is reasonably uniform (standard deviation of 25% in MSU-I) when the purge gas flow rate is about 16% of the

flue gas flow rate. This has the effect of offsetting the plate area gain by an amount approximately equal to 16% of the plate area requirement for an HII-ESP system. An alternative means of producing uniform flow profiles will probably be needed for an economically attractive system.

Continuing Work

Additional overall mass and size dependent efficiency data will be obtained at high resistivity conditions with the two selected values of specific collection area (200 and 300 $ft^2/1000$ acfm). Also, SO_3 conditioning will be used to obtain resistivity values of the order of 10^9 to 10^{10} ohm•cm. An experimental program will be conducted with these lowered resistivities to determine the enhancement which would be produced by the ionizer for a high resistivity ash if back discharge problems in the ionizer, cavity and precipitator were not present. Results from these measurements are expected to determine the potential for commercial development of HII-ESP systems.

ENDNOTES

1. Spencer, Herbert W., III, et. al. "Results of High Intensity Ionizer/ Precipitator Evaluation Tests at the EPRI Test Facility", paper 80-23.3, 73rd Annual Meeting, Air Pollution Control Association, Toronto, June, 1980.

2. McDonald, J. R., et. al. "Charge Measurements on Individual Particles Exiting Laboratory Precipitators with Positive and Negative Corona at Various Temperatures". J. Appl. Physics, 51(7):3632-3643 (July, 1980).

3. Unpublished reports by APS, Inc. to EPRI.

4. Masuda, S., and Y. Nonoyaki. "Detection of Back Discharge in Electrostatic Precipitators". IAS Annual Meeting, Cincinnati, Ohio, September 28 - October 3, 1980.

5. Lagarias, John S., and Jack R. McDonald. "Application of the High Intensity Ionizer to the Electric Utility Industry". Presented at the Third Symposium on the Transfer and Utilization of Particulate Control Technology.

6. Bickelhaupt, Roy E. "A Technique for Predicting Fly Ash Resistivity", EPA-600/7-79/204, Environmental Protection Agency, Research Triangle Park, NC, August, 1979.

Table 1

CALCULATION OF Q_s/M FROM MIC IMPACTOR AND CURRENT-VS.-VOLTAGE DATA

Dia. (μm)	Radius (μm)	Cum. % of Mass	Mass (gm)	Mass/Part. (gm)	No. of Particles	Charge/Part. (Cont)	Total Charge (μC)
.2	0.10	2	.02	9.802×10^{-15}	2.040×10^{12}	3.718×10^{-18}	7.585
.3	0.15	3.5	.015	3.308×10^{-14}	4.534×10^{11}	8.365×10^{-18}	3.793
.4	0.20	5.0	.015	7.841×10^{-14}	1.913×10^{11}	1.487×10^{-17}	2.845
.5	0.25	6.7	.017	1.532×10^{-13}	1.110×10^{11}	2.324×10^{-17}	2.580
.6	0.30	8.1	.014	2.646×10^{-13}	5.291×10^{10}	3.346×10^{-17}	1.770
.7	0.35	9.8	.017	4.203×10^{-13}	4.045×10^{10}	4.554×10^{-17}	1.842
.8	0.40	11.2	.014	6.273×10^{-13}	2.232×10^{10}	5.948×10^{-17}	1.328
.9	0.45	12.7	.015	8.932×10^{-13}	1.679×10^{10}	7.528×10^{-17}	1.278
1.0	0.5	14.2	.015	1.225×10^{-12}	1.225×10^{10}	9.294×10^{-17}	1.139
2.0	1.0	26.0	.118	9.802×10^{-12}	1.204×10^{10}	3.718×10^{-16}	4.552
3.0	1.5	34.5	.085	3.308×10^{-11}	2.570×10^{9}	8.360×10^{-16}	2.149
4.0	2.0	40.8	.063	7.841×10^{-11}	8.035×10^{8}	1.487×10^{-15}	1.195
5.0	2.5	46.8	.060	1.532×10^{-10}	3.916×10^{8}	2.324×10^{-15}	0.910
6.0	3.0	51.0	.042	2.646×10^{-10}	1.587×10^{8}	3.346×10^{-15}	0.531
7.0	3.5	54.6	.036	4.203×10^{-10}	8.565×10^{7}	4.554×10^{-15}	0.390
8.0	4.0	58.0	.034	6.273×10^{-10}	5.420×10^{7}	5.948×10^{-15}	0.322
9.0	4.5	60.8	.028	8.932×10^{-10}	3.135×10^{7}	7.528×10^{-15}	0.236
10.0	5.0	63.0	.022	1.225×10^{-9}	1.796×10^{7}	9.294×10^{-15}	0.167
14.0	7.0	70.5	.075	3.362×10^{-9}	2.251×10^{7}	1.822×10^{-14}	0.406
18.0	9.0	76.0	.055	7.145×10^{-9}	7.698×10^{6}	3.011×10^{-14}	0.232
22.0	11.0	78.5	.025	1.305×10^{-8}	1.916×10^{6}	4.498×10^{-14}	0.086
30.0	15.0	84.5	.060	3.308×10^{-8}	1.814×10^{6}	8.365×10^{-14}	0.152
60.0	30.0	100	.155	2.646×10^{-7}	5.858×10^{5}	3.346×10^{-13}	0.196

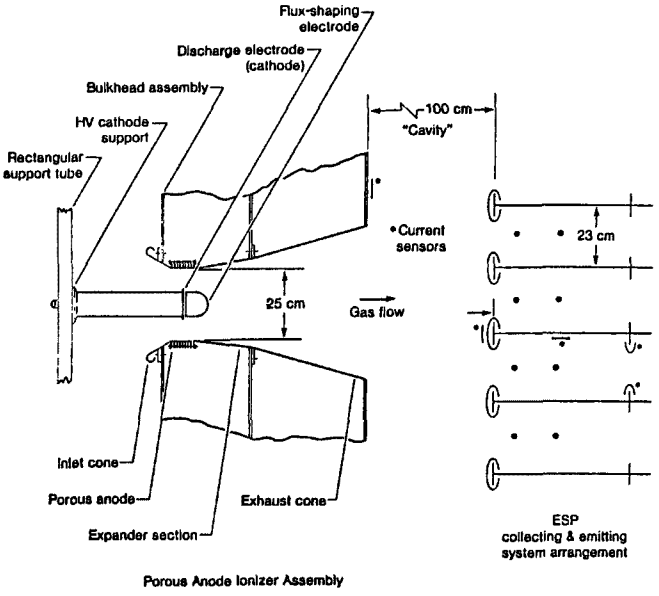

Figure 1. Initial Ionizer and Collector Field Arrangement, Unit 2

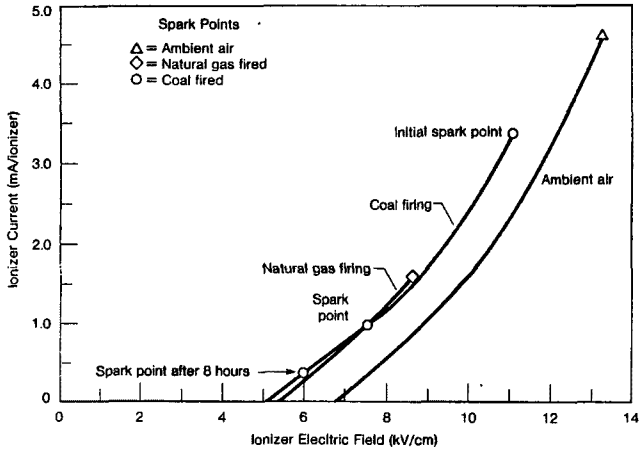

Figure 2. Ionizer current versus ionizer electrical field (33,000 ACFM) MICD configuration.

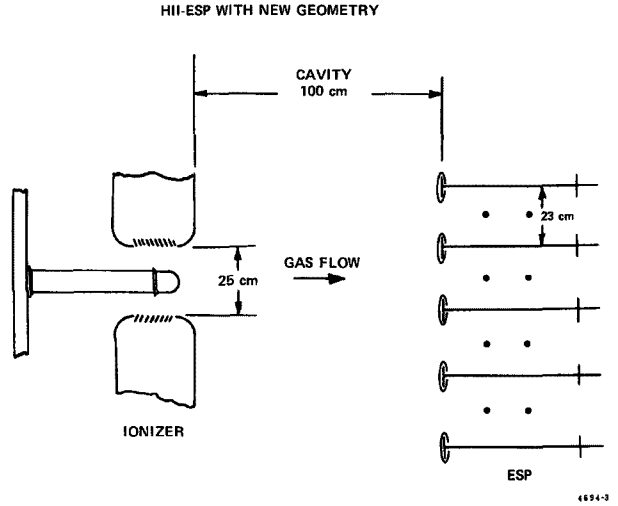

Figure 3. Double bellmouth high intensity ionizer followed by an electrostatic precipitator.

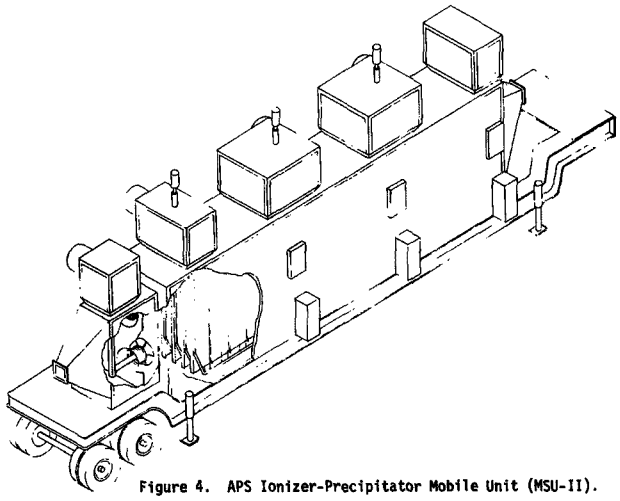

Figure 4. APS Ionizer-Precipitator Mobile Unit (MSU-II).

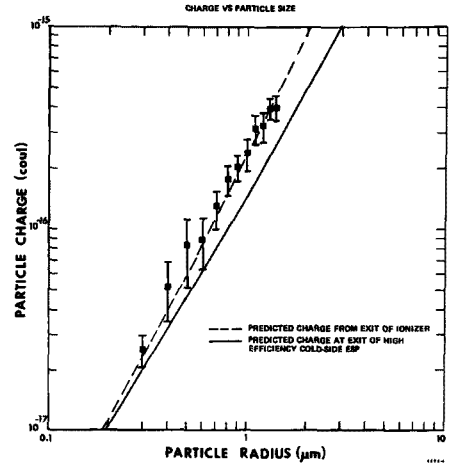

Figure 5. Laboratory measurements and predictions of particle charge at the outlet of the double bellmouth high intensity ionizer.

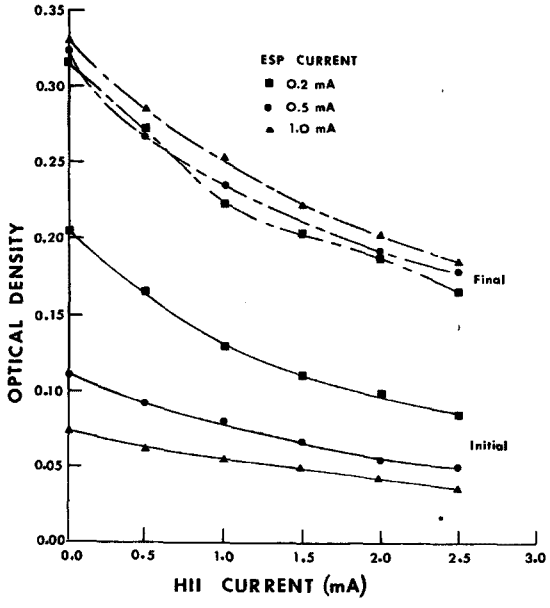

Figure 6. Outlet optical density versus Ionizer current for dry ESP operation.

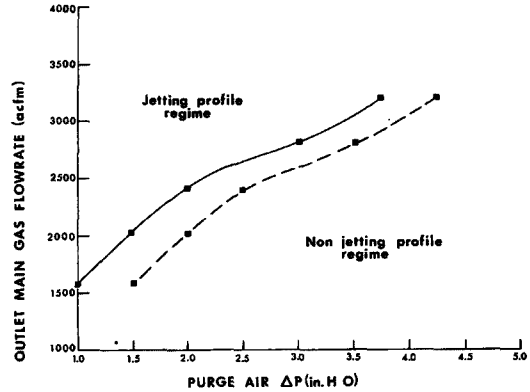

Figure 7. Plot of relationship between main gas flowrate and purge air flowrate for double bellmouth geometry.

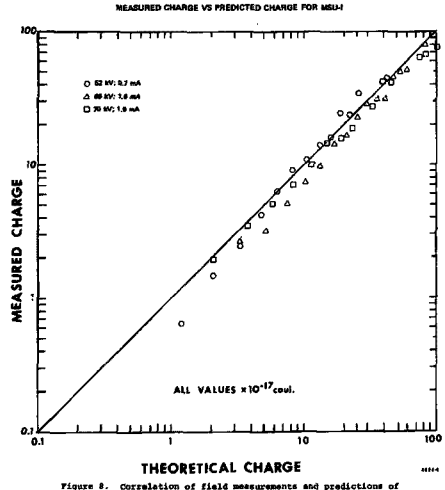

Figure 8. Correlation of field measurements and predictions of particle charge at the outlet of the double bellmouth high intensity ionizer.

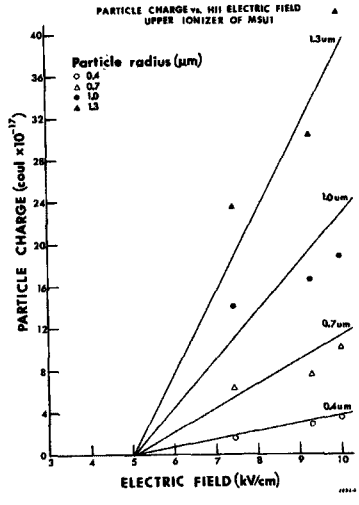

Figure 9. Particle charge at the outlet of the HII as a function of particle size and electric field.

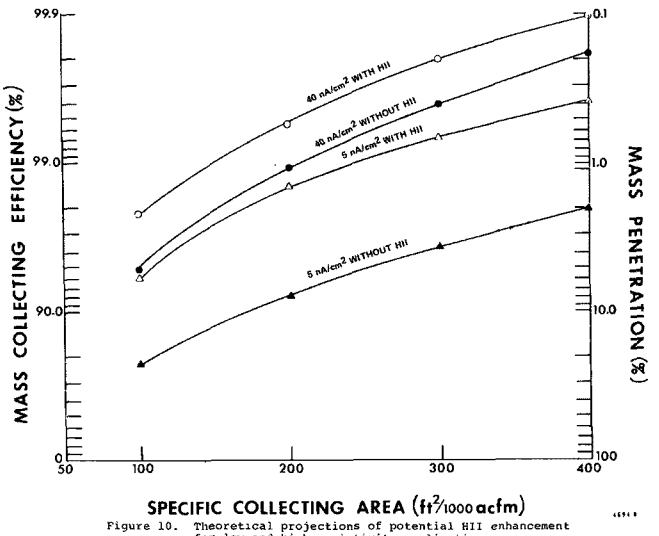

Figure 10. Theoretical projections of potential HII enhancement for low and high resistivity applications.

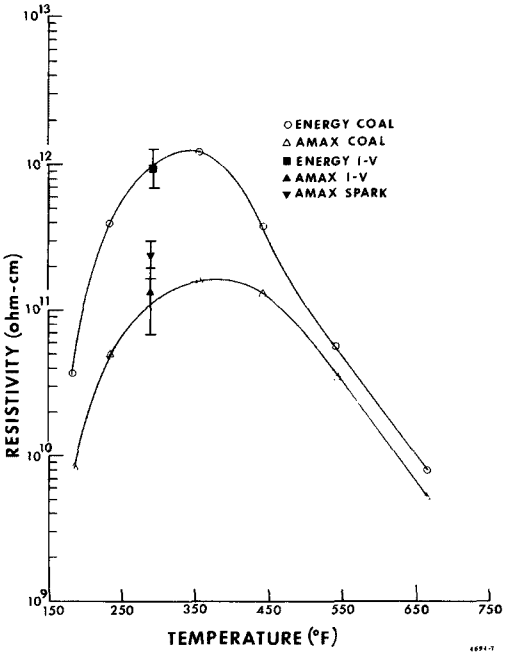

Figure 11. Predicted and measured ash resistivities for the coals burned at the Arapahoe Facility.

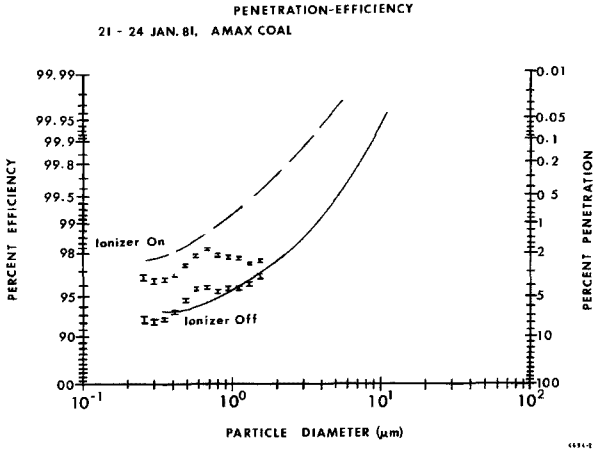

Figure 12. Measured and predicted fractional collection efficiencies without and with the high intensity ionizer and a moderate resistivity ash.

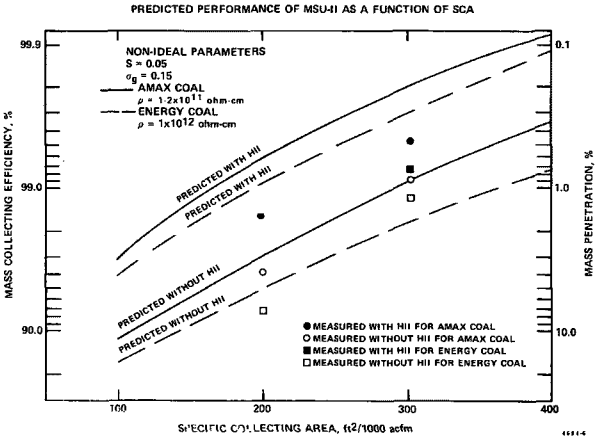

Figure 13. Measured and predicted overall mass collection efficiencies without and with the HII for two different coals.

DEMONSTRATION OF AIR POLLUTION SYSTEMS HIGH INTENSITY IONIZER/ELECTROSTATIC PRECIPITATOR ON AN OIL-FIRED BOILER

By: Gary A. Raemhild, Anil Prem
Air Pollution Systems, Inc.
18642 - 68th Avenue South
Kent, Washington 98031

Fred Weisz
Long Island Lighting Company
Northport Power Station
Eaton's Neck Road
Northport, New York 11768

ABSTRACT

A study was performed to evaluate the applicability of Air Pollution Systems High Intensity Ionizer (HII) to the electrostatic precipitation of particulate emissions from a high sulfur oil-fired boiler. The study was conducted on a 380 MW boiler at Long Island Lighting Company's Northport Station, Unit 1. The APS High Intensity Ionizer/Electrostatic Precipitator (HII/ESP) mobile pilot plant was utilized for this study. Simultaneous particulate measurements were initially performed at the inlet and outlet of the south side precipitator on Unit 1 to characterize the performance of the existing precipitator. Testing was done at 360 MW and 125 MW and included total mass samples, cascade impactor tests and ultra-fine particle analysis. The electrical and physical parameters for the three field precipitator in the mobile HII/ESP pilot plant were adjusted to simulate the south side precipitator on Unit 1 as closely as possible. Simultaneous inlet/outlet particulate sampling for the pilot unit was performed using the same methods as on the main precipitator. Performance tests were conducted with the HII both energized and de-energized at 14,273 M^3/hr.(8400 ACFM), 11,894 M^3/hr. (7000 ACFM), and 5947 M^3/hr. (3500 ACFM). All tests were performed with the boiler at a baseline load condition between 340 and 360 MW. The results show a significant decrease in particle penetration when the HII was energized. Due to certain delays in data reduction and analysis, the results have not yet been released. Upon release, the data shall be available to the public from ESEERCO, or Air Pollution Systems.

INTRODUCTION

The Empire State Electric Energy Research Corporation (ESSERCO) awarded a contract to Air Pollution Systems, Inc. to conduct a turnkey pilot plant program that would demonstrate the applicability of Air Pollution Systems' High Intensity Ionizer (HII) technology on oil-fired boiler emissions.

This program was carried out at Long Island Lighting's Northport Power Station. The first stage of the program was the characterization of the existing Unit #1 main precipitator by simultaneous inlet/outlet testing. The HII/ESP pilot plant was then evaluated with identical testing techniques using a slip stream off the same exhaust emissions. Comparative simultaneous tests were performed with the HII energized and de-energized. This provided the data necessary to define the reduction in particle penetration with the utilization of an HII for particle pre-charging upstream of an existing conventional precipitator.

TEST OBJECTIVES

The objectives of the test program are listed below:

1. Characterize the operating parameters and performance of the south side main electrostatic precipitator on Unit #1 at LILCO's Northport Power Station.

2. Using the APS HII/ESP pilot plant, determine quantitatively the improvement in performance of the ESP when an HII is used to precharge the particulate. This involves studying the effect of gas flow rate and specific collecting area (SCA).

3. Utilizing the pilot plant and main ESP data, predict the level of reduction in particulate emissions from the main (Unit #1) ESP with the addition of an HII array.

HIGH INTENSITY IONIZER TECHNOLOGY

The APS High Intensity Ionizer, due to its unique electrode geometry, is successful in maintaining a highly stable intense corona discharge. The cathode is a solid metal disc supported by a structurally reliable tube section centered in a cylindrical anode arrangement. An HII assembly is illustrated in Figure 1. The electrode configuration produces a substantially uniform three dimensional field which is a principle factor in the greater electrical stability. Typical operating field strengths of 10-13 kV/cm have been obtained compared to 3.5 kV/cm for wire electrode geometry in an industrial flue gas.

In addition to the very high electric fields, the HII electrode geometry produces a concentrated field with ion densities of 10^9 - 10^{10} ions/cc, many times that obtained in the wire electrade geometry. As a result of higher fields and ion densities, both the level of charge acquired by the particles and the rate of charging is significantly higher. For example, even with the significantly lower residence time in an HII compared to an electrostatic precipitator, the level of charge obtained by the particles exiting an HII are two to three times higher compared to the particles exiting an ESP.

The HII effectively charges particulate at velocities 7 to

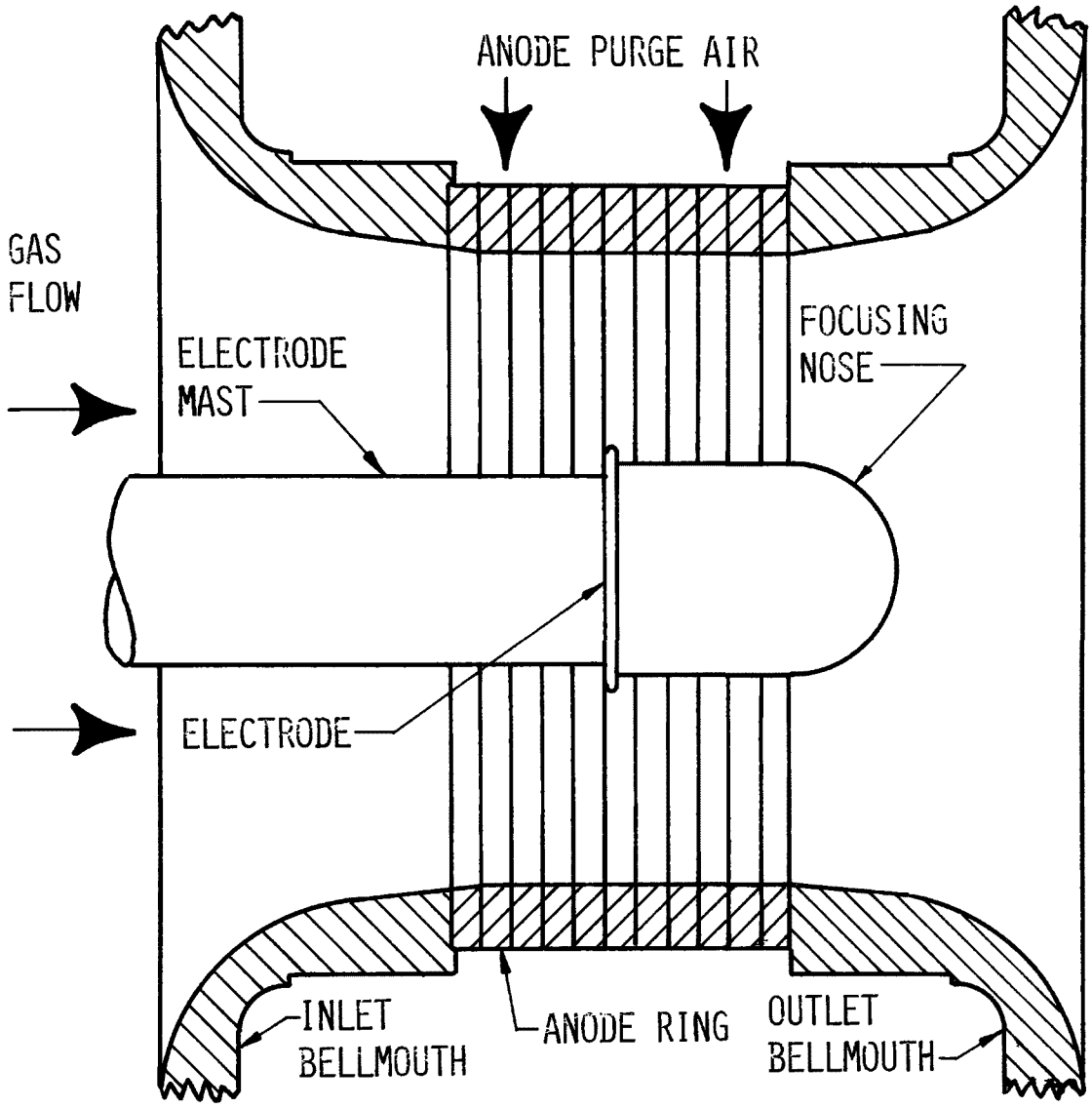

FIGURE 1 - HIGH INTENSITY IONIZER ASSEMBLY

10 times higher compared to the more conventional electrostatic geometries. Gas velocities in excess of 100 fps can be maintained through the HII with the charging time of a few milliseconds. This means particles can be charged to a high level in a very small volume resulting in a very compact system that can be retrofitted to the existing control devices.

A more detailed description of the HII technology can be found in the EPRI Report FP-291 (1).

HII/ESP MOBILE PILOT PLANT

The HII/ESP Mobile Pilot Plant combines an HII module with a conventional ESP for field demonstration work. The designed nominal flow rate for the pilot unit is 11,894 M^3/hr.(7000 ACFM). At the nominal flow condition the specific collection area (SCA) is 37.23 $M^2/(M^3/sec)$ (189 ft^2/1000 ACFM). Flow conditions for determining flow rates and SCA are measured at the pilot plant outlet. This is due to the HII anode purge air which is injected upstream of the first field in the ESP. A schematic diagram of the pilot unit is shown in Figure 2.

The pilot plant is a trailer mounted unit. It contains a conventional wire and plate precipitator with three electrically separate fields of equal size. The ESP is a solid harp frame design with flail hammer rappers for the collection plates and electrical vibrating rappers for the H.V. harp frame and wires. Heated purge air is injected into each insulator compartment to keep the high voltage insulators clean and dry. The flyash collected in the hoppers is removed by a screw conveyor and rotary air-lock valves.

Located just upstream of the first ESP field is the HII module. It is a two ionizer array with the throats located vertically one above the other. Anode purge air is injected to keep the anode vanes clean. The purge air was heated for this application to prevent any possible SO_3 condensation.

The controls for the mobile pilot are located in a separate control trailer. The pilot is equipped with the capability of changing its configuration to match the main ESP under study. The three ESP fields and the HII field have separate controls (both manual and automatic) which allows for variation in current densities and field strength.

Operating parameters and test conditions for both the pilot unit and the main ESP will be given in a future report to ESEERCO.

The gas is taken from the boiler flue by a slip stream and enters the pilot through an insulated duct. Inline heater con-

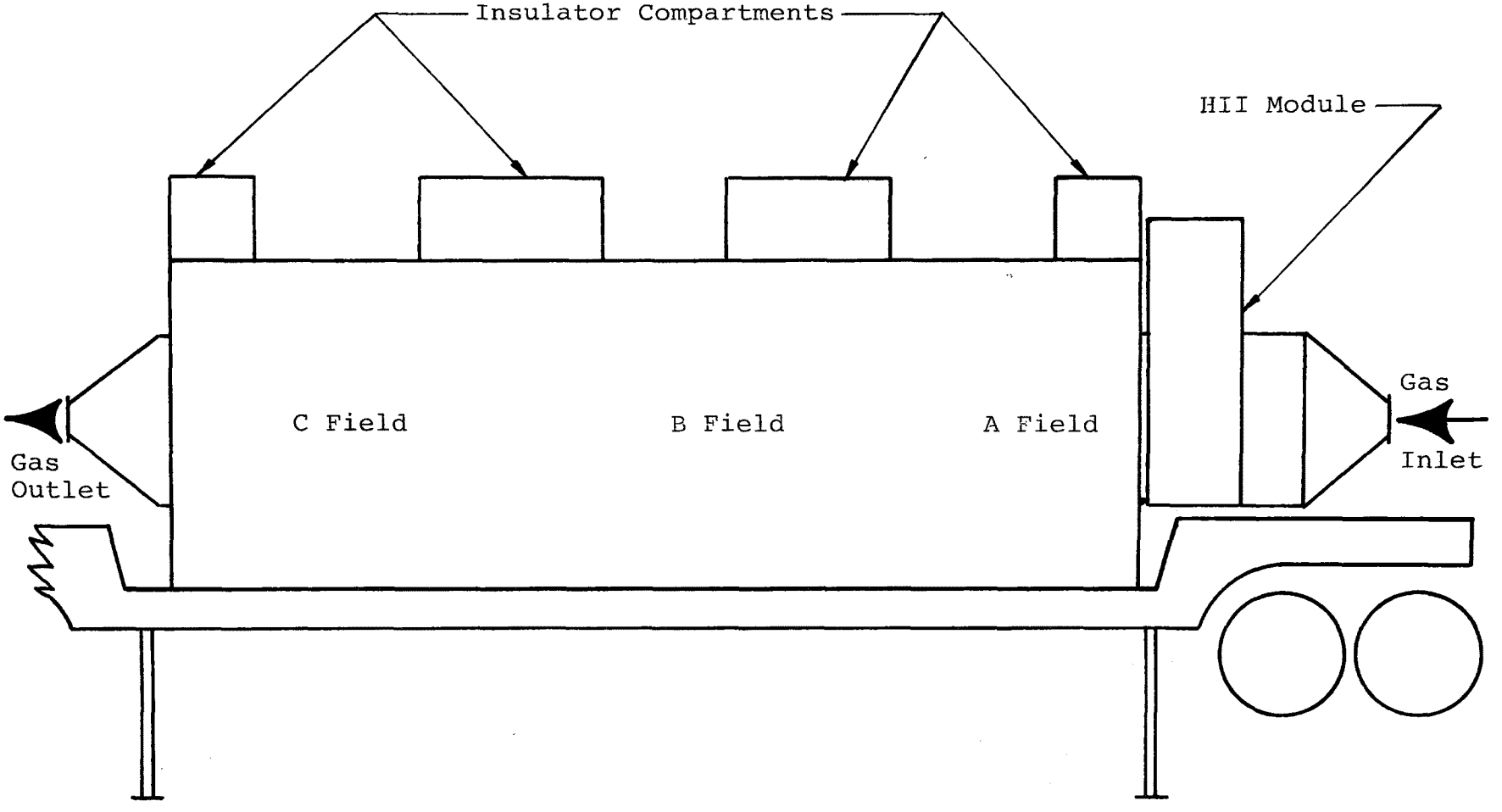

Figure 2 - Mobile Pilot HII/ESP

trols monitor the slip stream temperature and maintain the gas temperature entering the pilot approximately the same as that exiting the boiler flue. At this installation, the slip stream was taken off just upstream of the main ESP south compartment by an isokenetic sampling scoop. The flue gas passed through the pilot and was reinjected into the boiler flue approximately 10 feet downstream of the takeoff location.

The relative location of the pilot unit is illustrated in Figure 3. A detailed description of the Unit #1 at the Northport Power Station will also be included in the later report to ESEERCO.

TEST PROGRAM

Main Precipitator Testing

Performance testing for the main ESP consisted of simultaneous inlet/outlet particulate measurements. Simultaneous EPA Method 17 tests for total mass determination and overall particle collection efficiency were made. Particle size distributions at both the inlet and the outlet were determined by three methods. Low pressure cascade impactors, electrical mobility analyzers and electrical aerosol samplers (scanning electron microscopy) were used to determine the particle size distributions. Particle diameters measured ranged from .05 to 20.0 microns at both the inlet and outlet of the precipitator.

Testing was performed as described above at two boiler load conditions. A baseline sustained load was established at 362 MW to 368 MW. Testing was also done at a reduced load of 128 MW.

Precipitator operating parameters were monitored during the test program. Boiler operating conditions were also monitored with no testing being performed during an upset condition. Stable boiler operation was insured by continuous measurement of O_2, CO and NO_x emissions at the economizer exit. Periodic measurements for SO_x were also performed on both the main ESP and pilot unit using the Goksyor/Ross controlled condensation method.

HII-ESP Pilot Plant Testing

Determination of Pilot Plant Operating Parameters

Establishing the ESP electrical operating parameters first involved characterizing the main precipitator. Voltage and current characteristics were averaged for each electrical field over the period of one month of continuous operation prior to pilot testing. Average current densities and field strengths were calculated. Since the V-I relationship for the main precipitator fields did not exactly match those of the pilot unit, the current densities in the pilot ESP were adjusted to equal those for the main ESP. The field strength at these current densities

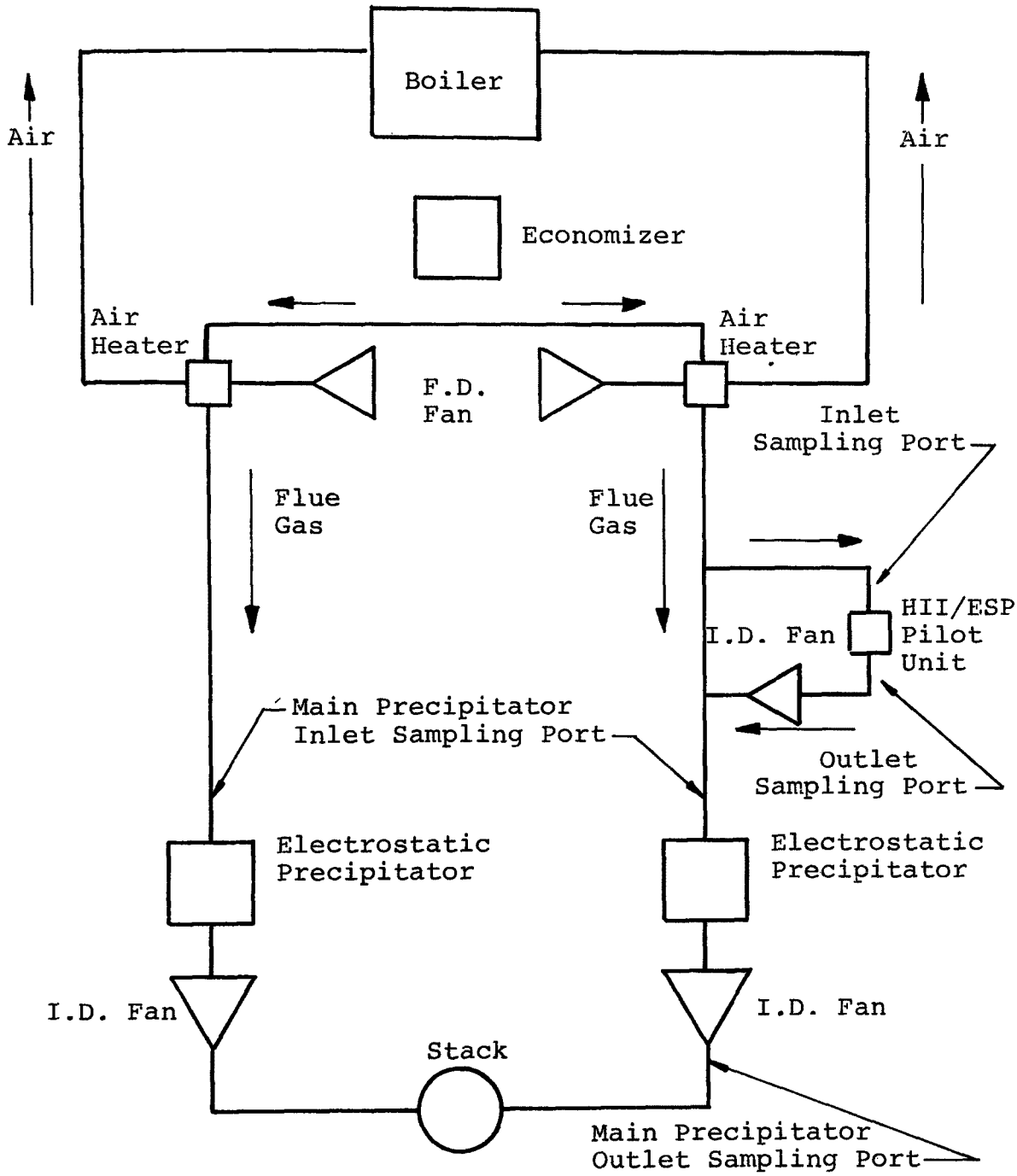

Figure 3 - Overall Schematic

was maintained at both conditions of HII energized and HII de-energized.

Physical characteristics such as wire to plate spacing, total collecting area, and number of lanes were established and set prior to operation of the pilot plant. Such physical parameters were adjusted to simulate the main precipitator as closely as possible.

Testing on the pilot unit was performed at three gas flow rates; low flow, baseline flow and high flow. The baseline flow was established by matching the face velocity in the last field of the pilot ESP with the face velocity at the exit of the main ESP.

Performance Testing

Test methods for evaluation of the pilot plant performance were identical to those used on the main ESP. At each of the three gas flow rate (SCA) conditions, simultaneous inlet/outlet testing was performed with the HII energized and de-energized.

Pilot plant operating parameters and boiler conditions were monitored throughout the testing. The boiler maintained a baseline load condition within a range of 340 MW to 360 MW. A system load limitation towards the end of the testing required some tests to be performed at a slightly lower load condition.

Presentation of Results

A later report to ESEERCO, when released, shall include the results of the testing program. Particle size distributions will be presented for both the main ESP and the pilot plant. Particle collection efficiency and penetration (both overall and fractional) will also be presented. Utilizing this data, the level of reduction in particulate emissions from the main ESP will be predicted with the addition of an HII array.

ENDNOTES

Acknowledgements

This pilot demonstration pilot project was funded by the Empire State Electric Energy Research Corporation under ESEERCO Project EP80-3. Fred Weisz of Long Island Lighting Company's Northport Station was the ESEERCO Project Manager. Special appreciation is given to the LILCO personnel for their cooperation in this program.

References

1. Schwab, J., et.al.(1976), "Development Program for an Ionizer Precipitator Fine Particle Dust Collection System as Applied

to Coal-Fired Utility Steam Generators", final report submitted to EPRI on Project 386-1, by Air Pollution Systems, Inc., Seattle, Washington.

PRIMARY AND SECONDARY IONIZATION IN AN ELECTRON BEAM PRECIPITATOR SYSTEM*

By: W.C. Finney, L.C. Thanh, J.S. Clements, R.H. Davis
Department of Physics
Florida State University
Tallahassee, Florida 32306

ABSTRACT

Recent investigation into the possibility of using energetic electron beams for generating high ion current densities for particle charging in electrostatic precipitators has shown exceptional promise. Copious ion current densities, at least 500 times that in a conventional corona driven precipitator, have been reported earlier. Experimental results, however, have indicated a secondary ionization phenomenon in a parallel plate system which affects the charge density stability.

The results of a study of the onset and extent of secondary ionization are presented here. Ion current vs. voltage experiments were performed using the parallel plate system used in previous ion current density investigations. The electron beam flux delivered to the system was restricted in intensity to determine the transition from primary ionization to the saturation plateau, then the onset and extent of secondary ionization was explored. An analysis of the plate system's variable parameters was made to quantify the conditions for initiation of secondary ionization. This secondary ionization is thought to be the result of the combined effects of plate spacing and plate voltage in the precipitator section.

INTRODUCTION

Electron beam ionization is the process of delivering an electron beam into air, thereby creating a bipolar plasma of charged air molecules or ion pairs, the number of pairs being dependent upon the energy and current of the electron beam. Past experiments using electron beam ionization in coal fly ash precipitator geometries have demonstrated measured ion current densities in excess of two orders of magnitude greater than those generally obtainable in a conventional corona-wire driven electrostatic precipitator (1,2). These experiments showed that the observed ion current vs. applied voltage relationship can be approximated by a straight line using linear scale axes. No saturation current plateau, which marks the total extraction of charge from the ionization zone, was observed.

A preliminary investigation of the factors influencing the onset of ion current saturation was initiated and the results were reported recently (3). Saturation of ion current density was defined as the process whereby the "cloud" of ion pairs produced by the ionizing electron beam is totally extracted from the bipolar interelectrode volume by an electric field strength larger than a certain value. It was found that the ion current vs. voltage characteristics exhibited a well defined ion current saturation plateau which depends on the electrode spacing, the beam energy and current,

and the type of beam collimation device used.

This study will focus on primary and secondary ionization processes by refining and extending the experimental measurements done in the preliminary study (2). Primary ionization is defined in this study as the plasma produced directly by energetic primary electrons from the electron beam which collide with gas molecules. Secondary ionization in a parallel plate system occurs when free electrons created in the primary ionization process gain energy from high collecting plate electric fields and, in conjunction with space charge phenomena, cause further ionization in transit to the electrode.

The effect that separation distance, beam current, and beam geometry have on the saturation plateau and secondary ionization will be addressed. A comparison between the calculated and measured ion current saturation values will be made. A correction for recombination of opposite polarity ions which is caused by incomplete separation and collection of the bipolar plasma between the electrodes is calculated. Finally, a quantitative analysis of the amount and extent of secondary ionization will be made at different plate spacings.

EXPERIMENTAL DETAILS

The 3 MeV Van de Graaff electron accelerator at Florida State University was used to generate an electron beam which was brought out into air from vacuum through a thin aluminum foil window. A movable beam current measurement probe was located downstream from any beam restriction devices present, if any. The probe beam current is referred to as the "actual" beam current, and represents the amount of flux available for ionization. Electron beam energy remained constant but beam current was varied in one of two ways: either by controlling it at the accelerator cathode source or by mechanically restricting the amount of beam allowed to leave the window. In this investigation, the accelerator was operated to deliver a beam of 1.2 MeV (million electron volts) energy and actual beam currents of 10, 20, 50, 100, 200, and 500 nA, and 1.0, 2.0, 4.0, and 10.0 μA. All experiments were run at 25°C, 70% relative humidity, and 760 mm Hg.

A parallel-plate electrostatic precipitator test system incorporating three electrodes each on an upper and lower tier was used to collect the ion current (Figure 1). Plates b, b', d, and d' served as guard electrodes while plates c and c' were ion current measuring electrodes. The distance from the foil window to the center of plates c and c' was 50 cm. All of the plates in the system were biased at the same voltage; the upper set was at positive (anode) and the lower set was at negative (cathode) electric potential. To determine the effect of plate spacing on ion current saturation, separation distances of 2.5, 5, and 10 cm (1, 2, and 4 inches) were used. This laboratory scale system is analogous to a conventional precipitator except that the corona wires which produce an avalanche of unipolar working ions are replaced by an electron beam with bipolar working ions.

Saturation phenomena were studied by mounting thick stopping baffles on the end of the accelerator beam tube. The baffles were 4" x 4" x 1/4" thick aluminum plates each with a different diameter circular aperture drilled in the center. According to the range-energy relation of energetic electrons passing through aluminum (4), all electrons not passing through the aperature

are stopped at the baffle. Diameters (in inches) of the apertures are as follows: 1/16, 1/8, 1/4, 5/16, 3/8, 7/16, 1/2, 1. When no baffle was used, the beam passed unobstructed out of the beam tube, the end of which is 2.0 in. diameter. The purpose of using stopping baffles with apertures was to restrict the ionizing flux entering the test volume between plates c and c' to attempt to achieve ion current saturation. The baffles allowed a relatively disperse region of low intensity ionization to be delivered to the test volume as compared to a tightly collimated beam. To determine what role beam geometry might play, several baffles with different sized apertures were used at one actual beam current.

RESULTS

Electrode Spacing Comparison

Ion current vs. voltage curves for various experimental conditions were plotted and analyzed. Only the negative ion currents are shown since they are approximately equal in magnitude to the companion positive ion currents in every case. The ion current characteristics of three electrode spacings at two electron beam currents, each an order of magnitude apart, were compared. Figures 2 and 3 show ion current and ion current density plotted against electric field at 2.5, 5, and 10 cm plate spacings. The electric field is an average value, i.e., it is the applied voltage divided by the electrode spacing.

At 10 nA beam current (Figure 2), the 2.5 cm curve has a short straight section but levels off above 500 volts/cm as the ion current saturates. The ion current increases at about the same rate from 0.5 to 19 kV/cm with very little upturn at the end indicating secondary ionization. This is in contrast to the 5 cm and 10 cm curves which do exhibit ion current enhancement. The saturation bend on the 5 cm curve is more gradual and the plateau has a greater slope than the 2.5 cm curve but the ion current saturation knee is apparent. Ion current enhancement effects begin at about 11 kV/cm and continue to increase until sparkover. At 10 cm spacing, there is almost no plateau with the saturation knee almost immediately giving way to substantial secondary ionization.

A two order of magnitude increase in electron beam current to 1.0 μA produces a different arrangement as shown in Figure 3. The 2.5 cm curve levels off at 2 kV/cm but a slight upturn between 19 and 21 kV/cm may indicate the onset of secondary processes. A very gradual turnover marks the transition from the linear to the saturation section of the 5 cm curve which is terminated by a secondary ion current rise. An almost linear 10 cm curve does bend slightly but no other features are distinguishable. Secondary processes undoubtedly occur at low electric field and completely obscure any saturation plateau.

The observation that more absolute ion current is collected at any single beam current when the electrode spacing is larger is qualitatively accounted for in several ways. First, the larger volume means that more of the ionizing flux will fall between the electrodes and will be collected. Additionally, fewer energetic electrons still capable of initiating ion formation will be

absorbed by the plates. Volumetric considerations alone, however, are not sufficient to explain the shape differences of the curves. Electrons produced in the primary avalanche must travel farther to reach a widely-spaced electrode and therefore they encounter a greater number of molecules than at smaller separation distances. The additional electron-molecule collisions increase the probability of ion pair production. This explains the reduction in electric field necessary to initiate ion current enhancement when separation distance is increased.

In contrast, the onset of ion current saturation occurs at a higher electric field at larger spacings because more of the primary ionization cone falls within the interelectrode space. Therefore, a higher applied field is required to collect all of the primary ion current. The combination of higher electric field for the onset of saturation and lower electric field for initiation of secondary ionization as plate spacing is widened causes an increase in the saturation plateau slope and a reduction in the absolute size of the plateau. At large spacings saturation is not observed because the rise in copious secondary ionization compensates and then overrides the tapering off of primary ionization. A nearly linear plot makes it difficult to separate the relative contribution of primary and secondary effects.

Electron Beam Current Comparison

Ion current vs. voltage relationships for 5 electron beam currents at a plate spacing of 2.5 cm are shown in Figure 4. The curves are plotted on linear axes to indicate their relative magnitude although the shapes of the lower beam current curves are somewhat indistinct. All 5 curves show the characteristic linear, saturation, and secondary ionization regions. The onset voltage of saturation increases with higher beam current but secondary multiplication begins at the same applied voltage. The magnitude of the saturation ion current increases and the asymptotic approach is more gradual as the electron beam current is increased. Raising the beam current creates more primary ionization, requiring a higher applied electric field to completely separate the bipolar ion flux. Plate spacing does not affect this result for a given primary ionizing current. The combination of a higher onset voltage for saturation and the same onset voltage for secondary amplification results in a smaller and steeper saturation plateau as beam current is raised.

Table 1 shows maximum ion current densities and sparkover voltages for the entire set of experimental conditions. A larger absolute amount of collected ion current was obtained with higher electron beam current because of a more densely populated ionization region. Doubling the plate spacing increases the maximum amount of ion current collected, probably due to higher plate voltages obtainable before sparkover and a larger interelectrode volume. At 10 μA beam current and 10 cm spacing, the highest ion current density obtained was 82.5 mA/m^2. This value is in agreement with previous experimental work (1), and is about 400 times greater than that generally found in conventional corona wire precipitators (5). Electrical breakdown alone limits the maximum ion current value and larger values can be obtained by increasing the separation distance, raising the electron beam energy or current, or restricting the angular dispersion of the beam using collimation.

Each of the experimental ion current vs. voltage curves was extended until cathode-anode sparking halted the measurements (Table 1). When no electron beam was admitted to the test volume no ion current was measured until plate-plate breakdown occurred. An initial abrupt decrease in the sparkover voltage is attributable to ionization in the test volume. Following this drop sparkover voltages remain constant except at high beam currents. Widening the plate spacing increases the voltage required to sustain a breakdown as expected. The effect, however, is non-uniform.

Sparkover voltages measured in this parallel plate electrode system without the electron beam are somewhat lower than other published values at each plate spacing. The electrode perimeters were rounded to suppress edge effects but a strong field exists at the lateral edges of the center electrodes (plates c and c'), which is where sparkover usually takes place. At high beam currents, a large electric field exists near the plates due to space charge effects. A high localized electric field is the major cause of premature sparkover. When the electron beam is admitted to the test volume, primary ionization reduces the effective interelectrode gap by producing a disperse plasma at approximately ground potential between the plates (1). Spark propagation becomes easier as the plasma-electrode distance decreases.

Baffle Aperture Comparison

As described earlier, mechanical electron beam current variation by substituting baffles with different sized apertures also altered the beam geometry, producing a more disperse electron beam as aperture size was enlarged. A comparison of ion current densities using different baffle apertures while keeping electron beam current constant was performed. Figure 5 shows ion current vs. voltage plots at 10 cm plate spacing and 2.0 μA beam current using aperture diameters of $^{1}/_{2}$", 1", and 2" (= no baffle). Although similar in shape, the plotted curves reveal that less ion current is collected as aperture size increases. The curves are characterized by a smooth rolloff of ion current to 35kV followed by a very slight upturn.

For a constant electron beam current, increasing the size of the baffle aperture allows a more diffuse beam and a greater amount of scattering leading to a lower beam density in the test volume. Less delivered beam means a lower ionization rate and therefore a smaller measured ion current.

DISCUSSION

Analysis of a Generalized I-V Curve

The form of the collected ion current vs. applied plate voltage plots reveal the complex nature of the interaction of several ionization phenomena. A generalized I-V curve exhibits three regions (6). From the origin of the plot, the ion current rises linearly with increasing voltage because a larger fraction of the ion flux produced by the electron beam is drawn to the electrodes. As the voltage is increased further the ion current asymptotically approaches a saturation plateau, and at still higher voltages the current increases rapidly until sparkover occurs. Although each of these character-

istic regimes can be discussed separately, at high beam currents or large plate spacings they often overlap, obscuring their precise delineation.

During irradiation of air by an electron beam, both positive and negative ions are produced resulting in a bipolar plasma at nearly ground potential midway between the electrodes. The negative ions are formed by electron attachment to electronegative molecules while positive ions are formed by electron-neutral molecule collisions which strip off other electrons. At zero applied voltage, the ionic charges in the interelectrode volume simply recombine in a continous process of ionization and recombination. When an electric field is imposed, separation of charge occurs and as the electric field increases, the fraction of ions which recombine decreases. The current value that is measured if all of the ions formed between the plates by the electron beam are collected is the saturation current.

The extent of the saturation plateau is limited by the onset of secondary ionization (7). At sufficiently high electric fields an electron gains enough energy in a single mean free path to ionize the next molecule with which it collides. This releases other free electrons so that a rapid multiplication of electrons and ions occurs. This explanation is consistent with the rapid rise of the ion current as the electric field is increased.

An example of the calculations which have been performed with the data is shown below for the experimental conditions of 1.2 MeV electron beam energy and 20 nA beam current. A low value of beam current is used so that the effects of space charge are minimal.

Saturation Currents and Recombination

The actual saturation currents are obtained from the I-V curves using the method of Boag (6):

$$j = (f)j_s = (1 - R)j_s = \left(1 - \frac{(2S^2)maj}{6V^2}\right)j_s \qquad (1)$$

Where: j = measured ion current density (statamps/cm)
j_s = saturation current density (statamps/cm)
f = collection efficiency
R = percentage of charge which recombines
m^2 = 36.7 V^2-sec/esu-cm = a constant characteristic of the gas
a = width of ionization region measured in the direction of the electric field (cm)
V = applied voltage = E(2S)
$2S$ = plate spacing (cm)

A plot of j vs. $\frac{j}{V^2}$ should be a straight line with a slope of $-(1/6)m^2a(2S)^2j_s$ and a Y-intercept equal to j_s. The saturation current can be obtained by extrapolating the line backward to the Y-axis. The saturation current plots for 2S = 2.5, 5, and 10 cm are shown in Fig. 6. The data points were fit with a straight line using equation (8). The best fit line with slope = $(1/6)(36.7)^2(2)(2S)^2$ was used for each value of 2S, and the electron beam was assumed to have an effective diameter of a = 2 cm. Theoretically, the saturation ion currents should be the same for different plate spacings if the ion pair pro-

duction in the test volume remains constant (Eq. 7). As seen in Figure 6, the saturation current increases with increasing plate spacing. Because of the angular dispersion of the primary ionizing flux, the configurations with larger volume receive more electron beam and utilize it more completely, and there is less absorption of energetic electrons by the plates.

The saturation ion current densities (j_S) calculated from Figure 6 are converted to ion currents (I_S) and compared below to the values of the saturation plateau currents found from the I vs. E plot of the data.

2S(cm)	I_S(μA)	Plateau Current(μA)
2.5	1.8	1.8
5	3.2	3.0
10	5.3	?

The amount of recombination for 2S = 5 cm is given by:

$$R = 1 - \frac{I}{I_S} = 1 - \frac{3.0}{3.2} = 6.25\%, \text{ so } 6.25\% \text{ of the ions recombine.} \quad (2)$$

Secondary Ionization

The rapid increase of current at high electric fields can be described using the equation for secondary ionization (8):

$$I \simeq I_o e^{(\alpha-\eta)d} \quad \text{for large } d. \quad (3)$$

where: $I_o = I_S$ = saturation plateau ion current
I = measured ion current during secondary ionization
η = attachment coefficient
α = Townsend's first coefficient
d = average distance primary charge travels to collecting plate = S
$2S$ = plate separation

The primary charge consists of the charge liberated symmetrically about the center of the test volume by the electron beam. The primary charge liberated by the electron beam forms the saturation current. At high electric fields some of the electrons do not attach to the molecules with which they collide but instead ionize the molecules releasing more free electrons. The coefficient $(\alpha-\eta)$ gives the relative degree of multiplication and attachment. The value of $(\alpha-\eta)$ is determined by plotting ln(I) vs. S for a constant electric field, as shown in Figure 7. The coefficient $(\alpha-\eta)$ is given by the slope of the line, which is a function of E/p, where E=energy and p=pressure. The primary ion current (I_o) is given by the value of the Y-intercept.

$$\ln(I) = (\alpha-\eta)S + \ln(I_o) \quad (4)$$

Since the primary currents (saturation currents) were not constant for the different plate spacings, the 2S = 10cm currents (I) were normalized so that I_S(10cm) = I_S(5cm). The following values of $(\alpha-\eta)$ were obtained from the slopes.

E(kV/cm)	$(\alpha-\eta)$	$(\alpha-\eta)/p=760$ mm Hg
8	0.36	0.00047
6	0.236	0.00031
4	0.19	0.00025

The value of the primary ion current from the Y-intercept in Figure 7 is I_o = 3.4 μA. This is consistent with the previous value of I_s for 2S = 5 cm of 3.2 μA. As can be seen in Figure 7, secondary ionization occurs in the region E = 4 to 8 kV/cm. In the absence of an electron beam, the normal range (9, 10) of electric field which produces secondary ionization is E = 20 to 30 kV/cm. The electron beam causes the primary electrons to have a higher average energy; therefore, they are accelerated to the ionization energy of the molecules at lower electric fields.

CONCLUSION

A parallel plate electrostatic precipitator test system using electron beam ionization instead of corona wire energization was employed in a study of primary and secondary ionization and ion current saturation. A series of experiments were conducted to investigate the nature of the ionization present in the interelectrode volume. Large ion current densities of 80 mA/m^2, or 400 times that in conventional precipitators, were found. Sparkover voltages were lowered somewhat when the test volume was irradiated, but high applied electric fields on the plates were still possible.

At lower electron beam current, the ion current vs. voltage curves have linear, saturation plateau, and secondary ionization regions. At higher beam currents, the ion current saturation plateau region is not established before secondary ionization begins. The experimental conditions required for saturation are low beam current or narrow plate spacing. As the electric field and plate separation distance were increased, a greater amount of secondary ionization occurred. Beam geometry, varied using a series of stopping baffles with apertures of different diameters, did not greatly affect the saturation of ion current or secondary ionization.

While the purpose of this study was not to focus on a complete mathematical description of ion current saturation and secondary ionization, many of the mechanisms involved were quantified. For all three plate spacings, the measured saturation currents are in agreement with those calculated from the electron beam intensity and from the recombination equations. Secondary ionization was described using the Townsend equation which yields values for $(\alpha-\eta)$. Secondary ion multiplication occurred at electric fields between 4 and 8 kV/cm which is much lower than the normal range (E = 20 to 30 kV/cm) with no electron beam.

ACKNOWLEDGEMENTS

The authors gratefully acknowledge the assistance of Mr. Kenneth J. Schafer and Mr. R. Mark Whitton in all phases of this study. We also acknow-

ledge Mr. Dempsey Lott and Mr. Walt Phillips for their operation of the 3 MeV electron accelerator.

*Work supported in part by the U. S. Department of Energy, Contract No. DE-A521-78EP11316.

†Present address: Research-Cottrell, Inc., Somerville, New Jersey.

ENDNOTES

1. Finney, W. C., L. C. Thanh, and R. H. Davis. Ion Current Densities Produced by Energetic Electrons in Electrostatic Precipitator Geometries. In: Proc. of the Second Symposium on the Transfer and Utilization of Particulate Control Technology. Volume II, Electrostatic Precipitators. pp. 391-398, EPA-600/9-80-0396, September 1980.

2. Thanh, L. C., W. C. Finney, and R. H. Davis. The Effects of Back Corona Discharge on Ion Current Density in Electron Beam Precipitators. In: Conf. Record of IAS-IEEE Annual Meeting, Cleveland, Ohio, p. 126, October 1979.

3. Thanh, L. C., W. C. Finney, and R. H. Davis. Total Separation of Charges Produced by Electron Beam Ionization in a Precipitator Development System. In: Conf. Record of IAS-IEEE Annual Meeting, Cincinnati, Ohio. pp. 935-940. October 1980.

4. Berger and Seltzer. Tables of Energy Losses and Ranges of Electrons and Positrons. NASA SP 3012. p. 125. c.a. 1960.

5. White, H. J. Industrial Electrostatic Precipitation. Reading, Mass., Addison-Wesley, 1963.

6. Boag, J. W. Ionization Chambers. In: Radiation Dosimetry, Volume II. Attix, F. H. and W. C. Roesch (eds). Academic Press, pp. 11-17, 1966.

7. Loeb, L. B. Basic Processes of Gaseous Electronics. University of California Press, pp. 647-727, 1961.

8. Loeb, L. B. Basic Processes of Gaseous Electronics. University of California Press, p. 712, 1961.

9. Prasad, A. N. and J. P. Craggs. Measurement of Ionization and Attachment Coefficients in Humid Air in Uniform Fields and the Mechanism of Breakdown. In: Proc. Phys. Soc. London. 76:223, 1960.

10. Dutton, J. Electron Swarm Data. J. Phys. Chem. Ref. Data. 4:577, 1975.

TABLE 1. MAXIMUM ION CURRENT DENSITY AND SPARKOVER VOLTAGE FOR VARIOUS BEAM CURRENTS AND PLATE SPACINGS

Electron Beam Current (nA)	Maximum Ion Current Density (mA/m^2)			Sparkover Voltage (plate-to-plate) (kV)		
	2.5 cm	5 cm	10 cm	2.5 cm	5 cm	10 cm
0	-	-	-	56	84	110
10	0.2	0.6	1.0	50	70	82
20	0.4	1.0	1.2	50	70	82
50	0.5	1.5	1.8	50	70	82
100	0.9	2.7	3.3	50	70	82
200	1.2	4.0	7.0	50	70	82
500	3.8	8.5	12.8	50	70	82
1000	5.7	13.0	20.8	50	66	82
2000	12.0	20.3	30.8	50	62	82
4000	19.5	33.3	50.0	50	62	82
10000	36.3	76.3	82.5	50	58	72

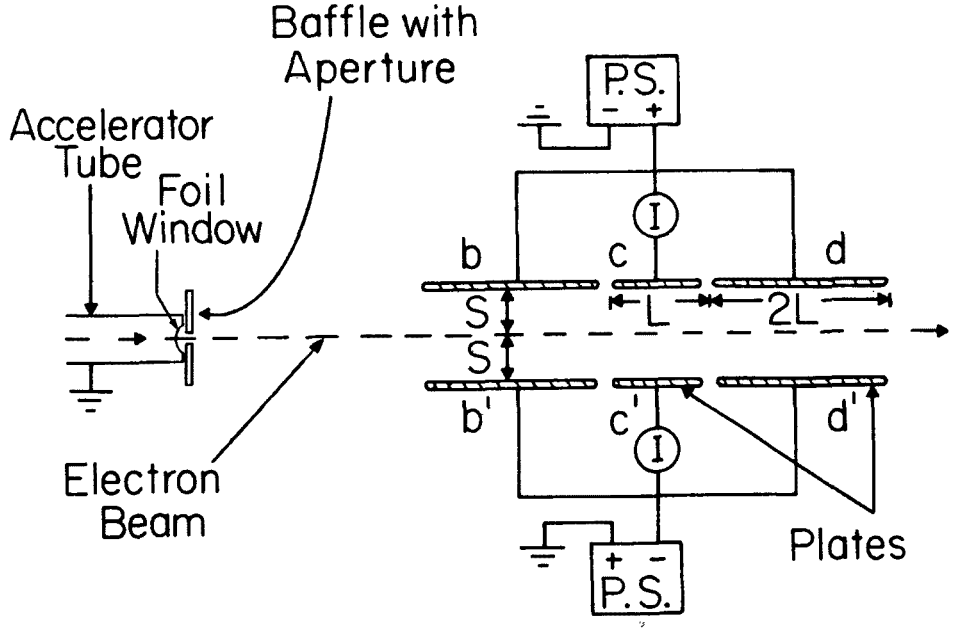

Figure 1. Schematic diagram of the experimental apparatus. The electron beam passes through the baffle aperture and into the interelectrode region. L = 10 cm, foil window to center of plates c,c' = 50 cm. Upper plates are anode, lower plates are cathode.

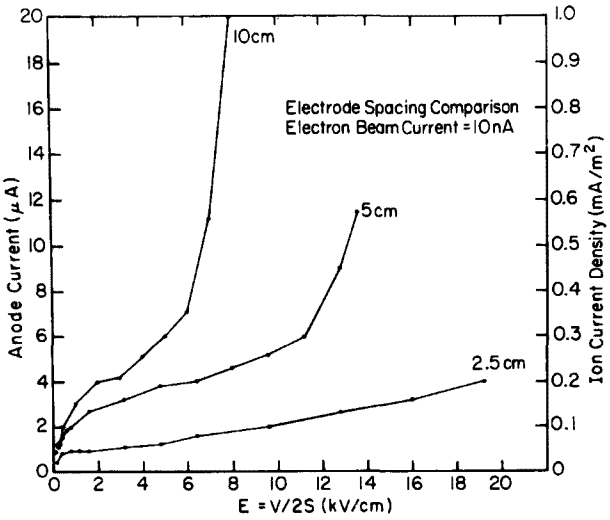

Figure 2. Comparison of ion current vs. applied electric field curves.

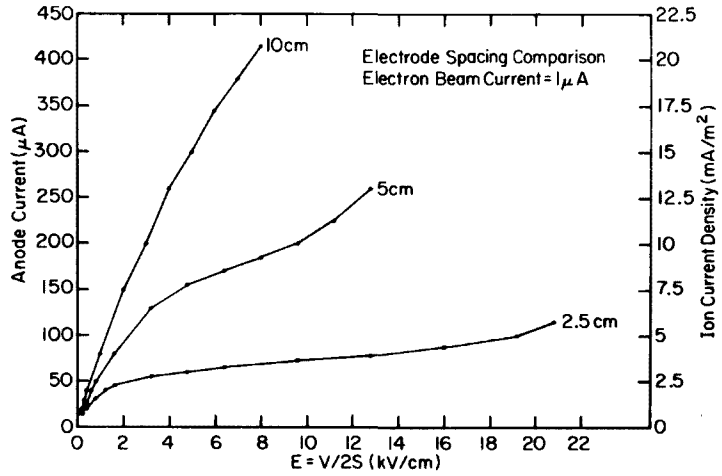

Figure 3. Comparison of ion current vs. applied electric field curves.

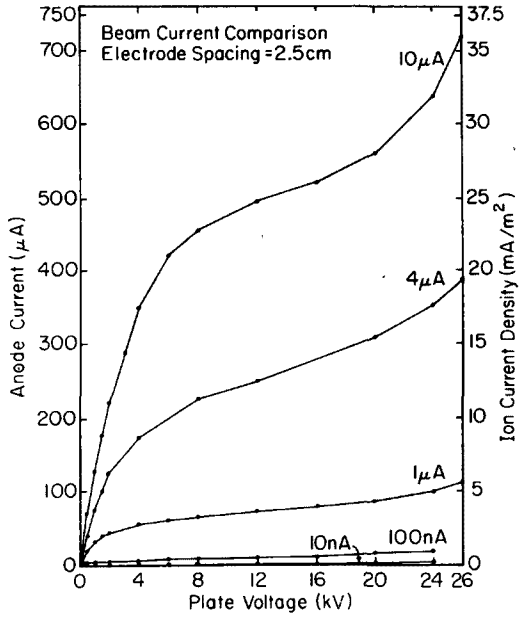

Figure 4. Ion current vs. plate voltage comparison for five electron beam currents.

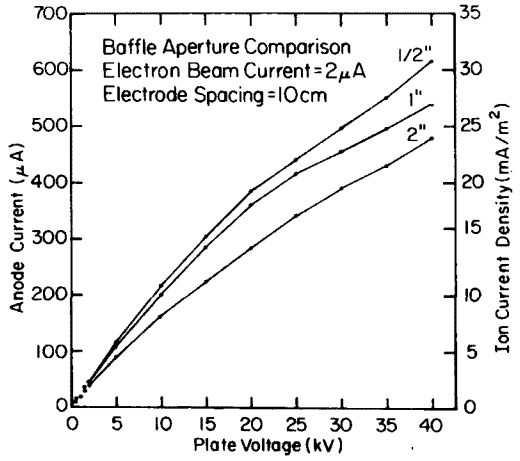

Figure 5. The effects of three different sized baffle apertures on the ion current vs. plate voltage characteristics.

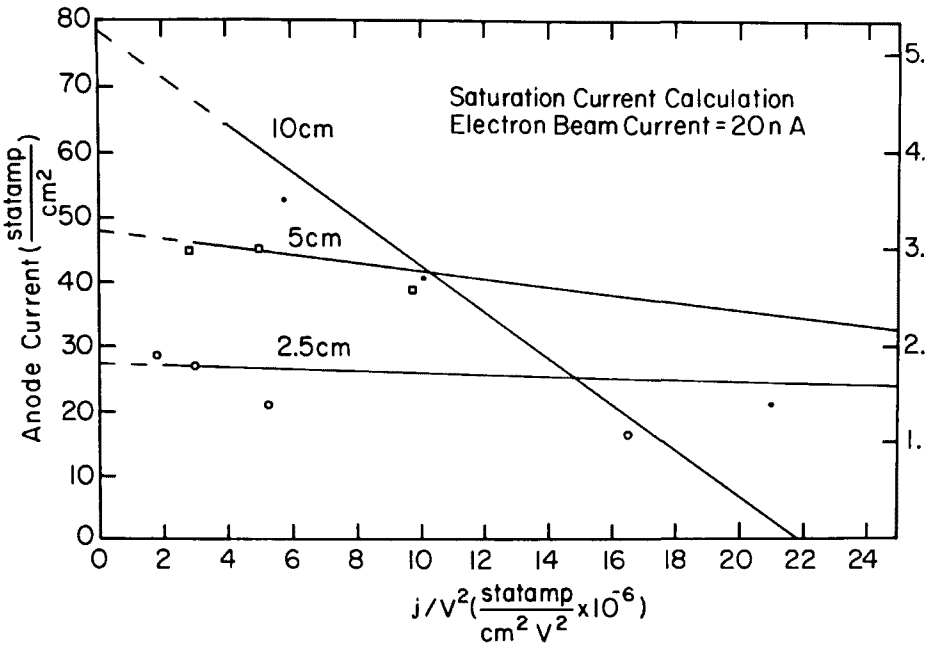

Figure 6. Straight line fits to j vs. j/V^2 plots used to calculate the saturation currents.

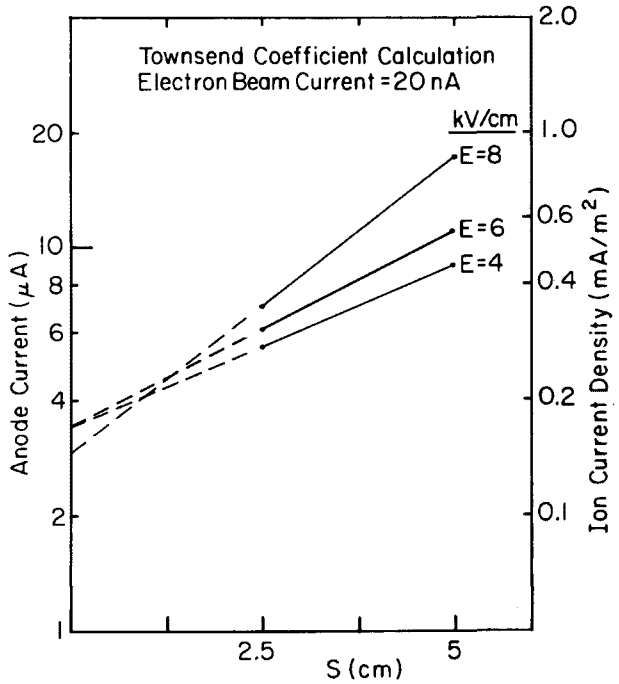

Figure 7. Ion current vs. S comparison used to calculate Townsend's first coefficient.

INFLUENCE ON PARTICLE CHARGING OF ELECTRICAL PARAMETERS AT DC AND PULSE VOLTAGES

By: Hans Joergen Joergensen
Jesper Toexen Kristiansen

High Voltage Laboratory, Building 329,
Technical University of Denmark,
DK-2800 Lyngby, Denmark.

Preben Lausen,
F.L. Smidth & Co. A/S,
Vigerslev Allé 77,
DK-2500 Valby, Copenhagen, Denmark.

ABSTRACT

Enhanced particle charging is considered to be one of the reasons for the improved performance of pulse energized precipitators. For a pulsed condition, the charging levels obtained are influenced by several electrical parameters such as underlying DC voltage, pulse level, and pulse repetition frequency. In the investigation reported, these influencing factors are examined. The measurements are performed by a Faraday cage method on a conducting ball of 3 mm diameter, charged within the interelectrode space of two circular cylindrical electrodes. The investigation includes DC as well as pulse energization. The results of the DC situation are compared with the saturation charges expected from the field charging theory. In the case of pulse energization, a simple model for the field charging under pulsed conditions is suggested and is used for a similar comparison.

INTRODUCTION

For the DC situation, the basic theory of field charging was established by Pauthenier (1), while the pulse situation has been treated by Masuda (2). Masuda's theory covers the case where ionic space charge is present during the pulse as well as in the period between pulses.

This paper deals with the situation where the DC level is kept below corona onset, and the pulse repetition frequency is low enough to allow a complete removal of ionic space charge before application of the following pulse. Both calculations and measurements are performed with negative voltage, but when discussing the results, numerical values are used for convenience.

THE FIELD CHARGING PROCESS

In the DC situation, free electrons are constantly created in the ionization zone near the discharge electrode and attached to electronegative gas molecules to form negative ions just outside this region. Because of the constant flow of ions from the discharge electrode, the electric field strength and the ion density do not vary with time at a fixed position in the interelectrode space. For this quasi-static case, Pauthenier derived the classic equation for the field charging of a spherical conducting particle (1):

$$q(t) = 12\pi\varepsilon_0 Ea^2\left[t/\left(t+\frac{4\varepsilon_0}{\rho b}\right)\right] \qquad (1)$$

where

$q(t)$	: charge of particle as function of time	(C)
E	: electric field strength	(V/m)
a	: radius of spherical particle	(m)
ε_0	: vacuum permittivity	(F/m)
ρ	: ionic space charge density	(C/m^3)
b	: ion mobility	(m^2/Vs)

With pulse energization where short duration pulses are superimposed on a DC voltage, the corona emission is limited to the pulse period if the DC level is below corona onset. If in addition the time between successive pulses exceeds the transit time of the ions, the interelectrode space will be free of ionic space charge when a pulse is applied.

During the negative pulse voltage, electron avalanches are initiated. The avalanches leave a positive space charge behind, and the electrons attach to gas molecules in regions of lower field strength to form negative ions. The positive ions quickly reach the cathode, while the negative ions travel towards the anode and only traverse part of the distance in the pulse period.

A particle situated at a fixed position outside the region close to the discharge electrode thus experiences variations with time in both electric field strength and ion density. In the pulse period, a high field strength is reached, but no ions are present, while later when the negative ions arrive at the position of the particle, the ion density is high but the field strength lower than in the pulse period. As field charging requires the presence of ions the saturation charge of the particle is determined by the maximum field strength during the passage of the space charge cloud.

MATHEMATICAL MODEL OF THE FIELD CHARGING PROCESS

A simplified mathematical model has been established for calculation of the charge attained by a spherical, conducting particle in a pulse energized concentric-cylinder electrode arrangement. The model is based on the following assumptions:

- The corona discharge occurs instantaneously at a certain moment in the pulse period and is uniformly distributed over the emitting electrode.
- The electrons generated in the corona attach to gas molecules and form an ionic space charge cloud limited by two cylindrical surfaces.
- The positive ions immediately travel to the inner electrode.

Temporal Variation of Field Strength and Space Charge Distribution

The spatial and temporal variations of the electric field strength and the space charge distribution are determined by successive calculations of the electric field and the movement of the space charge.

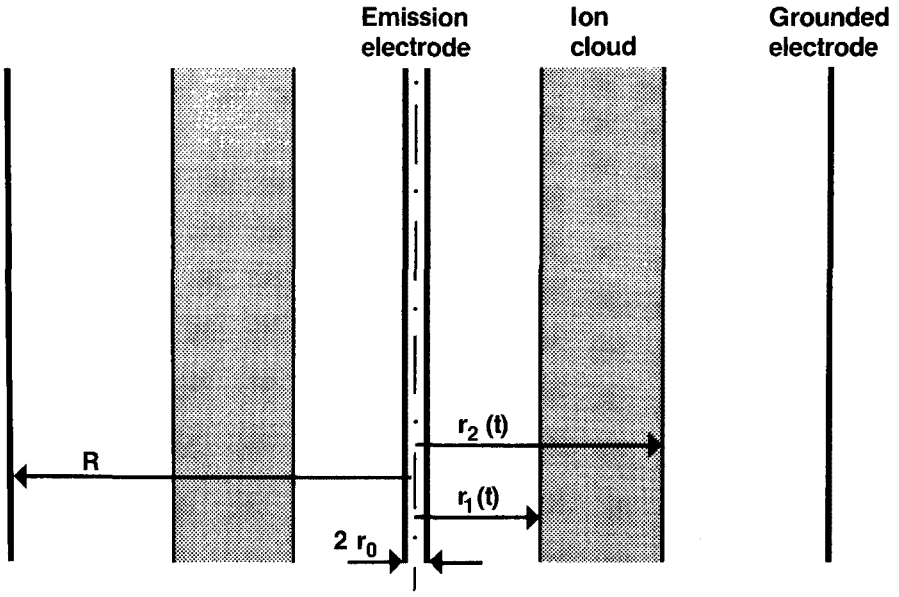

Figure 1. Negative space charge cloud between concentric-cylinder electrodes.

Figure 1 shows the situation at a time t. The radii of the concentric-cylinder electrodes are r_0 and R, respectively, and the negative space charge cloud is situated between $r_1(t)$ and $r_2(t)$. Using the rotational symmetry and Gauss' law, the electric field strength at radius r is given by:

$$E(r,t) = \begin{cases} q_w(t)/2\pi\varepsilon_0 r & \text{for} \quad r_0 \le r \le r_1(t) \\ [q_w(t) + \int_{r_1(t)}^{r} \rho(r,t)\ 2\pi r dr]/2\pi\varepsilon_0 r & \text{for} \quad r_1(t) \le r \le r_2(t) \\ [q_w(t) + \int_{r_1(t)}^{r_2(t)} \rho(r,t)\ 2\pi r dr]/2\pi\varepsilon_0 r & \text{for} \quad r_2(t) \le r < R \end{cases} \qquad (2)$$

where

$E(r,t)$	: electric field strength	(V/m)
$q_w(t)$	: charge per unit length on inner electrode	(C/m)
$r_1(t)$ and $r_2(t)$	: inner and outer radius of ion cloud	(m)
$\rho(r,t)$	: space charge density of the ion cloud	(C/m^3)
ε_0	: vacuum permittivity	(F/m)

The negative space charge per unit length, q_c, is given by the integral:

$$q_c = \int_{r_1(t)}^{r_2(t)} \rho(r,t)\ 2\pi r dr \qquad (3)$$

The mean value of q_c is:

$$q_c = i/f \qquad (4)$$

where i is the average corona current per unit length (A/m) and f is the pulse repetition frequency (s^{-1}). To calculate $E(r,t)$ from equation (2), the space charge distribution $\rho(r,t)$ has to be known. In the model, $\rho(r,t)$ is assumed to

be of the form:

$$\rho(r,t) = q_c/[2\pi r(r_2(t) - r_1(t))] \tag{5}$$

Using equations (3) and (5), E(r,t) becomes:

$$E(r,t) = \begin{cases} q_w(t)/2\pi\varepsilon_0 r & \text{for} \quad r_0 \le r \le r_1(t) \\ [q_w(t) + q_c \dfrac{r-r_1(t)}{r_2(t) - r_1(t)}]/2\pi\varepsilon_0 r & \text{for} \quad r_1(t) \le r \le r_2(t) \\ [q_w(t) + q_c]/2\pi\varepsilon_0 r & \text{for} \quad r_2(t) \le r \le R \end{cases} \tag{6}$$

Integration of equation (6) yields:

$$q_w(t) = \left[2\pi\varepsilon_0 U(t) - q_c\left(1 + \log\left(\frac{R}{r_2(t)}\right) - \frac{r_1(t)}{r_2(t)-r_1(t)} \log\left(\frac{r_2(t)}{r_1(t)}\right)\right)\right]/\log\left(\frac{R}{r_0}\right) \tag{7}$$

where U(t) is the potential of the inner electrode. Hence, if U(t) and the position of the space charge cloud is known, E(r,t) can be calculated using equations (7) and (6).

Subsequently, the movement of the space charge in a small time increment dt is calculated. Only the movements of the boundaries of the space charge cloud are determined, while the distribution of the space charge within the cloud is assumed to maintain the form given in equation (5). The inner radius of the space charge cloud at the end of a small time increment dt is:

$$r_1(t + dt) = r_1(t) - bE(r_1(t),t)dt \tag{8}$$

where b is the mobility of the negative ions. The mobility is taken as a constant. Using equation (8) and a similar expression for $r_2(t + dt)$, the new lo-

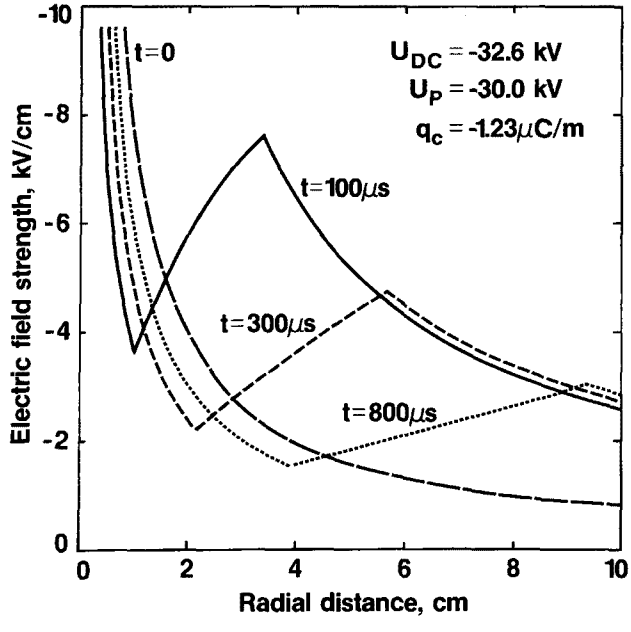

Figure 2. Calculated temporal and spatial variation of electric field strength with concentric cylinder electrodes (r_0 = 1.5 mm, R = 100 mm).

cation of the space charge is found. In the computer program used, the space charge cloud is divided into several parts the movements of which are calculated individually.

A result of such step by step calculations is shown in figure 2. The inner and outer radii of the concentric cylinders are 1.5 mm and 100 mm, respectively. The pulse wave form used is shown in figure 5, and the initial position of the space charge is assumed to be between the inner electrode and a cylindrical surface of radius 20 mm.

Charging of a Spherical, Conducting Particle

The calculation of the charge acquired by a spherical, conducting particle situated at a fixed position in the interelectrode space is performed treating the passing of the ion cloud as a series of quasi-stationary DC states. In a short time interval dt, the electric field strength and the ion density can be taken as constant, and the classic equations of field charging are applied. If the particle of radius a is placed at the radius r_p, the increase in particle charge q(t) in the time interval dt is (1):

$$dq(t) = 3\pi a^2 E(r_p,t)\rho(r_p,t)b\left(1 - \frac{q(t)}{12\pi\varepsilon_0 a^2 E(r_p,t)}\right)^2 dt \qquad (9)$$

Initially, the particle is assumed to be uncharged. As the particle acquires a charge, however, the repelling field from this charge is of sufficient magnitude to prevent ions from reaching the particle during part of the passage of the ion cloud. Thus charging takes place only if the following condition is fulfilled:

$$|E(r_p,t)| > \frac{|q(t)|}{12\pi\varepsilon_0 a^2} \qquad (10)$$

The saturation charge is given by the Pauthenier limit for the maximum field strength in the presence of space charge at the position of the particle:

$$q_{sat} = 12\pi\varepsilon_0 a^2 E(r_p,t)_{max} \qquad (11)$$

The temporal variations of the field strength and the ion density at the particle position are determined using the mathematical model described above. Then the passage of the ion cloud is divided into short time intervals, and the charge flow to the particle in each of these intervals is calculated by means of equation (9) if condition (10) is satisfied. This procedure is repeated to yield the particle charge as a function of the number of applied pulses.

In figure 3, a comparison is made between the calculated charge acquired by a conducting sphere of 3 mm diameter under pulsed and DC conditions, respectively. The DC curve is based on equation (1) using the formulas for the electric field strength in a coaxial cylinder geometry given in (1). The saturation charge is considerably higher with pulse than with DC energization, and despite the slower convergence, the calculated pulse charge exceeds the DC charge at all instants.

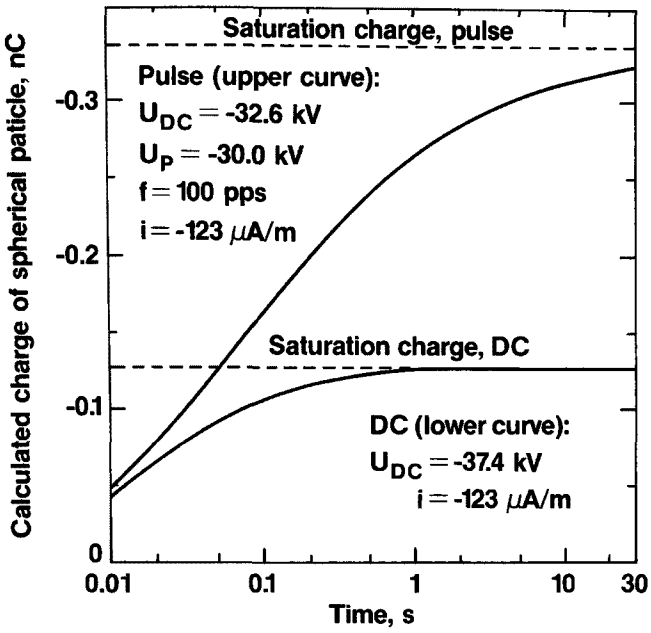

Figure 3. Charging of a conducting sphere (a = 1.5 mm) in a concentric cylinder geometry (r_0 = 1.5 mm, R = 100 mm). Particle position: r_p = 60 mm.

EXPERIMENTAL ARRANGEMENT

The measuring principle is similar to the ones used by Smith (3) and Masuda (4), where a large, spherical particle is suspended in the interelectrode space by means of an insulating string, and the particle charge is measured in a Faraday cage. In this arrangement, however, two Faraday cages are used: one measuring the particle charge plus the charge on the adjacent part of the string,

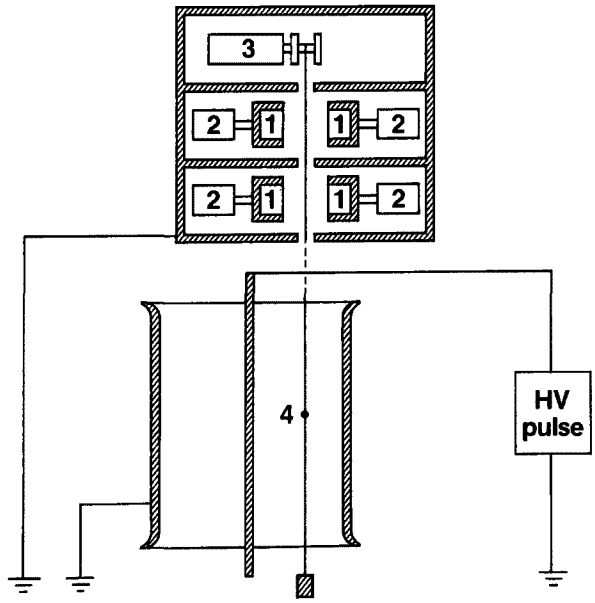

Figure 4. Experimental arrangement. 1: Part of Faraday cage. 2: Pneumatic cylinder. 3: Pneumatic motor. 4: Suspended particle.

the other measuring the charge on part of the string above the particle. The particle charge is found as the difference between these measured values.

The experimental setup is shown in schematic form in figure 4. A grounded metal case containing the two Faraday cages and an air motor is placed above the concentric cylinders. The string to which the 3 mm brass ball is glued is fastened to the pulley of the motor, and is weight loaded to minimize deflection. The cylindrical Faraday cages each consists of two movable parts mounted on the insulated piston rods of two pneumatic cylinders.

The brass ball is charged in the interelectrode space using the pulse wave form shown in figure 5 and moved to the position between the two parts of the lower Faraday cage. The two cages are closed by activation of the pneumatic cylinders, and the charges are measured simultaneously with two electrometers. A contact spring inside the Faraday cage ensures complete charge transfer from the ball to the cage.

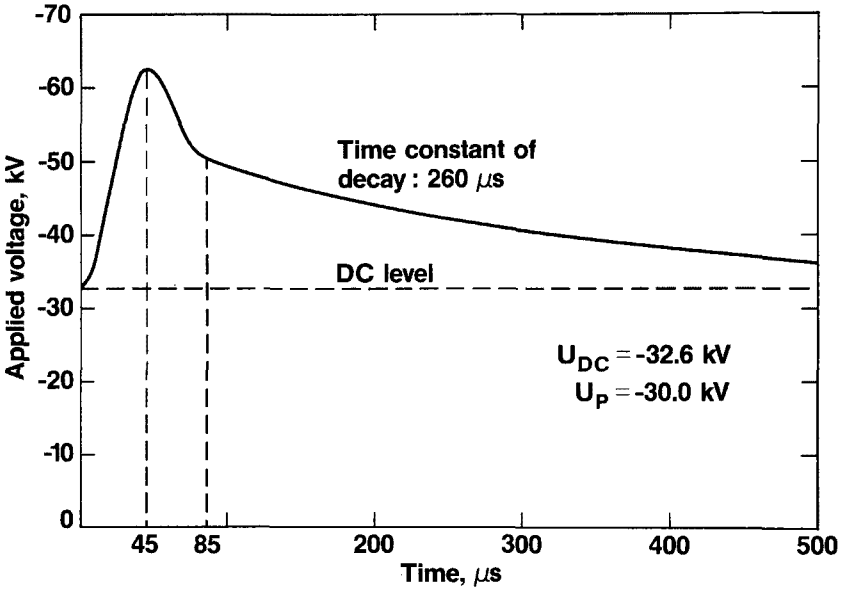

Figure 5. Pulse wave form used in calculations and measurements.

EXPERIMENTAL RESULTS

The 3 mm brass ball was positioned at a distance of 60 mm from the axis of the coaxial cylinder arrangement with radii 1.5 and 100 mm and height 170 mm. The particle was charged by applying approximately 3000 pulses to the electrodes. In each series of measurements, 10 individual measurements were performed, and the mean value and a 95 per cent confidence interval were calculated, assuming the measured values to possess a normal distribution.

Variation of Pulse Voltage

Initially, the performance of the measuring apparatus was checked by carrying out a number of DC measurements and comparing the results to calculated values. A few of these measurements are shown in figure 6 together with the calculated curve. Though deviations from the expected values did occur, the

general agreement was satisfactory.

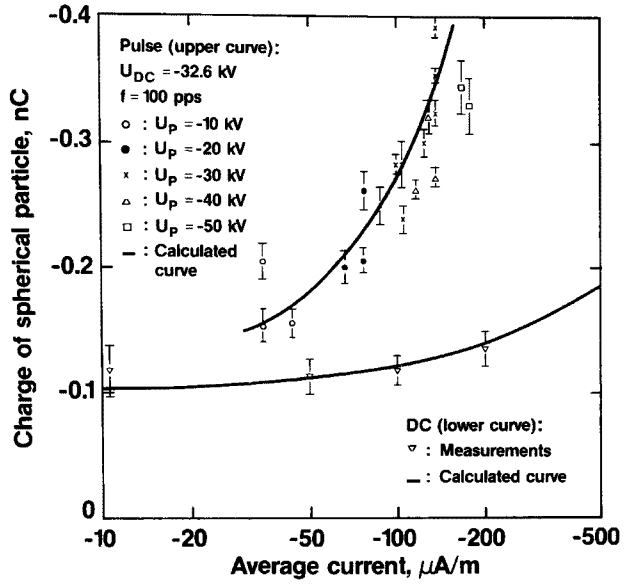

Figure 6. Measurements with DC and with varying pulse voltages.

Measured values of the charge acquired with pulse energization and varying pulse amplitudes are also shown in figure 6. The calculated curve gives the charge obtained after the application of 3000 pulses. This value corresponds to approximately 95 per cent of the saturation charge, cf. figure 3. The particle charge is seen to rise substantially with increased pulse voltage. This is mainly due to an increase in the amount of emitted space charge and hence, a larger field enhancement at the particle position.

Variation of Pulse Repetition Frequency

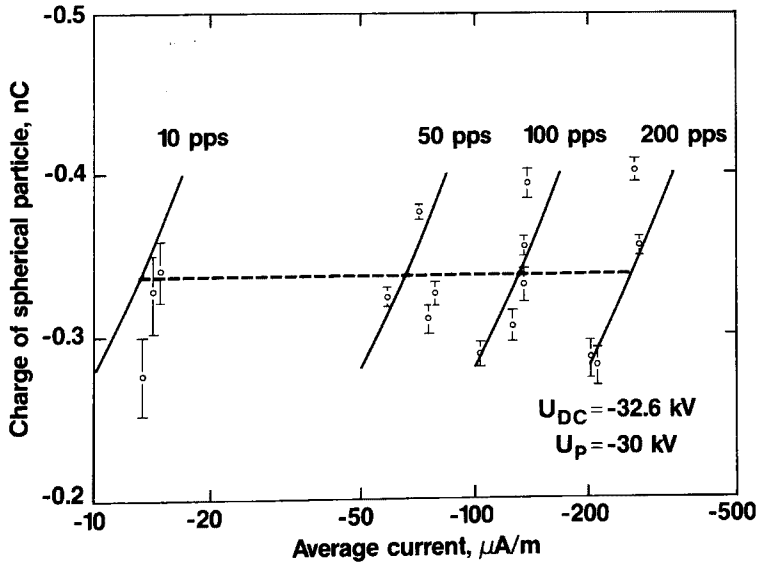

Figure 7. Charge acquired with 3000 pulses at varying repetition frequencies.

As long as the time between consecutive pulses exceeds the transit time of the ions, the average corona current is found to be proportional to the pulse repetition frequency (5), and therefore the mean value of the space charge emitted per pulse is constant, cf. equation (4). Hence, a variation of the repetition frequency should not cause any change in the acquired charge provided that the number of applied pulses is the same at all frequencies. An experimental verification of this is shown in figure 7. The full curves are the calculated values at the four repetition frequencies while the dotted line is the calculated charging level corresponding to the average emitted charge per pulse for all the measurements.

Variation of DC level

In order to determine the influence on the particle charge of the DC voltage, a number of measurements were carried out with varying DC level. The total maximum voltage (U_p+U_{DC}) was kept at -60 kV and the average current therefore fairly constant. The results are shown in figure 8 with calculated values corresponding to the mean value of the corona current for each of the three series. The particle charge is seen to increase with increasing DC level.

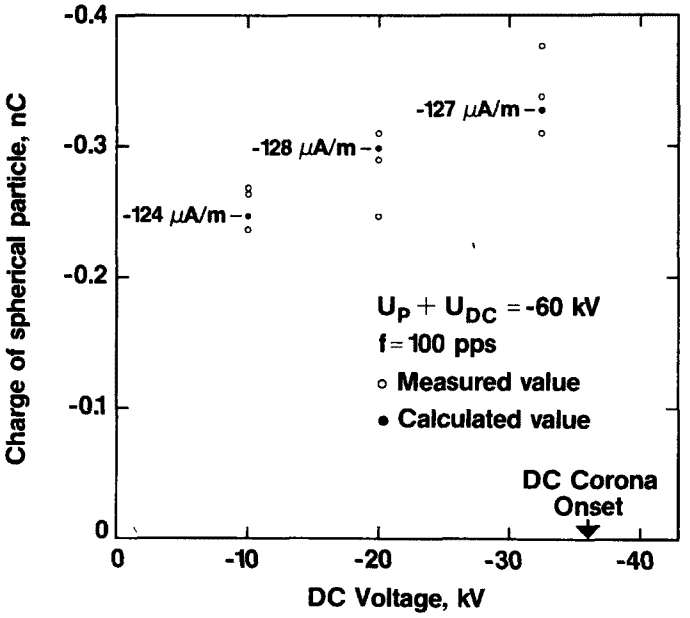

Figure 8. Charge acquired with pulse energization at varying DC levels and constant peak voltage.

CONCLUSION

The simple mathematical model suggested in this paper yields results in good agreement with experimental values. Even though the model is established for concentric cylinders, the concept of an ion cloud traversing the interelectrode space in the time between consecutive pulses is equally valid for more practical electrode configurations and therefore qualitatively similar results would be expected in these configurations.

To obtain a high particle charge, the peak voltage should be as high as possible, as both field strengths and ion densities increase with increasing peak voltage.

A certain peak voltage can be reached using a low DC level and a high pulse voltage or vice versa. In the investigated range of DC levels below corona onset the particle charge increases with increasing DC voltage.

The pulse repetition frequency itself is of no importance to the charge acquired by pulse energization as long as the time between pulses is sufficient for the ions to reach the collecting electrode. The particle charge is only determined by the number of pulses applied.

A comparison between DC and pulse energization with the same average current shows substantial improvement in particle charging by using pulse energization. Furthermore, under pulse conditions a high particle charge can be reached at very low current densities.

REFERENCES

1. Pauthenier, M. and M. Moreau-Hanot. La charge de particules sphériques dans un champ ionisé. Journal de Physique et le Radium, Paris, France, series 7, vol. 3, pp. 590-613, 1932.

2. Masuda, S. and A. Mizuno. Maximum Charge of a Spherical Particle Imparted by Pulse Charging. Proc. 1978 International Workshop on Electric Charges in Dielectrics, Oct. 9-12, 1978, Kyoto, Japan.

3. Smith, P.L. and G.W. Penney. The Charging of Nonspherical Particles in a Corona Discharge. Trans AIEE (Commun. Electron.) Vol. 80 I, p. 340-346, 1961.

4. Masuda, S. and M. Washizu. Corona Charging of a Spherical Particle Having an Extremely High Resistivity. Proc. 1978 International Workshop on Electric Charges in Dielectrics, Oct. 9-12, 1978, Kyoto, Japan.

5. Petersen, H.H. and P. Lausen. Precipitator Energization Utilizing an Energy Conserving Pulse Generator. Presented at the 2nd Symposium on the Transfer and Utilization of Particulate Control Technology, Denver, Colorado, July 1979.

BOXER-CHARGER MARK III AND ITS APPLICATION IN ESP's

By: Senichi MASUDA, Hajime NAKATANI and Akira MIZUNO
Department of Electrical Engineering, Faculty of Engineering, University of Tokyo
7-3-1, Hongo, Bunkyo-ku, Tokyo, Japan 113

ABSTRACT

The latest model of Boxer-Charger denoted by "MARK III" uses for its electrode assemblies the double-helix electrode units and very fast-rising pulse voltages with 40 - 200 ns duration time for their excitation to produce plasma ion source. The helical discharge wires of a double-helix unit are insulated not by the ordinary insulators but by coils which effectively reflect such a fast-rising, short-duration pulse voltage. This is called "inductance-isolation", and contributes much to the ease in construction and lowering of costs of the electrode assemblies. Its charging performance is presented. Then, the effect of pre-charging on the collection performance of a conventional ESP operated with a dc voltage under severe back discharge condition, a pulsed ESP operated with a pulse voltage superimposed to a dc voltage, and a conventional ESP operated under no back discharge condition, is presented and compared to each other. It is shown that the collection performance at dust resistivity of 10^{11} - 10^{12} ohm-cm can be greatly increased to a level equal to that obtainable under no back discharge condition, when the pre-charging is made in front of each collection field repeatedly and the collection field of an ESP energized with dc-plus-pulse voltage.

INTRODUCTION

Boxer-Charger "Mark III", its third generation, is one of the ideal pre-chargers capable of imparting very high level of charge to high resistivity particles within a short time [1]. This allows the exact evaluation of the requirements to be met in the collection fields of an ESP to be located downstream. Since the enhanced charge of the particles from the precharger should be diminished in the collection field subjecting to back discharge, it is considered to be imperative to suppress its effect by using the "back discharge free" collection field, such as the pulsed field or parallel-plate field. In the present paper is reported the results obtained with the pulsed field. It is expected that a slight quantity of ionic current, lower than its threshold to cause back discharge, must be supplied to avoid a severe rapping loss by electrical adhesion force. The pulse charging superimposed to dc voltage can provide the ionic current at any desired level without losing its uniformity in distribution and also the required level of collection field strength. From the same reason the parallel-plane field is considered as vulnerable to rapping loss although free of back discharge. However, its test is to be made soon, and its results will be reported later. It should be added that special precautions are taken in the present tests of pulse charging so as to keep the dc voltage below a critical level of causing spontaneous lateral propagation of back discharge.

1. Experimental Apparatus

1.1 Pulse-Energized Double-Helix Type Boxer-Charger (Mark III)

Figure 1 shows a double-helix electrode assembly to construct the latest model of Boxer-Charger "Mark III" used in the present tests. This configuration has its inherent advantages in (1) maintaining the wire-to-wire gap at a small and constant value without being affected by thermal deformation of its supporting system, (2) avoiding the edge-effect to cause corona discharge in the unexcited period, and (3) ease in its support. The conditions (1) and (2) are highly important to raise the peak value of ac main field between two electrode assemblies so as to increase the particle charge. But a small wire-to-wire gap does not allow the stable coronas to appear uniformly along the wires owing to excessive sparking. This difficulty is solved by using a very short pulse voltage with 40 ns duration time which proceeds along the helix wires in a form of a travelling wave producing very active and uniform streamer coronas as an ideal plasma ion source without causing any sparking at all (see Figure 1(b)). The use of such a short duration pulse voltage makes possible the "inductance-isolation" to be used for electrically insulating the two helix wires from each other (Figure 1(c)). An inductance element, reflecting the wave, can be used instead of an insulator. This contributes much to simplifying the electrode construction and reducing its cost. The general description of Boxer-Charger is given in the references[1-3].

Figure 2 indicates a photograph of Boxer-Charger I of Mark III type installed within the inlet duct of a test ESP. This consists of two parallel electrode assemblies spaced at 10 cm (face-to-face), each electrode assembly consisting of 3 double-helix assembly units arranged on a plane. Its effective length in the gas flow direction is 60 cm, and the residence time 0.040 s at gas velocity of 15 m/s. The theoretical charge at this residence time is 54.1 % of Pauthenier's saturation limit whereas its measured value being 47.4 %. The sparking field strength between two parallel assemblies is 5 kV/cm at 100 deg C, and 4.5 kV/cm is used.

Figure 3 shows a photograph of Boxer-Charger II of Mark III type located inside an inter-field section between the first and second collection fields of the ESP. Six double-helix assembly units are arranged at 10 cm spacing (face-to-face) on a plane perpendicular to the gas flow direction, so that this configuration is especially suitable for being inserted into a narrow space inside an ESP. The gas velocity is 0.82 m/s to provide 0.073 s residence time for an effective length assumed at 6 cm. The theoretical charge for this residence time is 68.2 % of Pauthenier's saturation limit for the charging time constant of 34 ms.

Figure 4 shows a circuit diagram of the power supply providing a main high voltage with 50 Hz to be applied between the electrode assemblies to construct the ac charging field, and two pulse high voltages with 40 ns duration time (Figure 5), each to be applied to one of the two electrode assemblies facing each other between its helical wires at an instant when it takes the negative peak of the main ac voltage. As a result the plasma ion source out of continuous streamers is produced alternately on one of these two electrode assemblies in synchronous to the main ac voltage, and negative ions are extracted from this plasma by the main ac field to produce the alternating current of negative monopolar ions within the charging field. The dust particles are bombarded by these ions from both sides alternately, and charged up very quickly.

1.2 Race-Track System and Model ESP

Figure 6 indicates schematically the laboratory race-track system comprizing a model ESP which has three collection fields in series. Each collection field consists of two parallel ducts having a plate-to-plate spacing of 30 cm, effective height of 70 cm and a length in gas flow direction of 50 cm. The discharge electrodes are wires with 3 mm in diameter arranged on each center plane at 6 cm wire-to-wire spacing. This small spacing is to raise the corona starting voltage, which is adjusted by adding fine-shaped projections along each wire at 5 cm spacing. The voltage-current characteristics of each field collecting high resistivity test fly-ash with 10^{11} - 10^{12} ohm-cm at 100 deg C gas temperature indicates a very distinct hysteresis, owing to the lateral propagation of back discharge initiated at one point. Its corona starting voltage is 42 kV at 100 deg C in air under contaminated condition, whereas the back discharge extinguishing voltage 23 kV. The resistivity of test fly-ash drops under 10^{10} ohm-cm at 20 deg C. The circulating gas is room air, and its temperature is changed by an electric heater up to 200 deg C for varying dust resistivity. The standard test conditions are 100 deg C gas temperature, 1,350 m^3/h gas flow rate (15 m/s at the inlet-duct and 0.82 m/s at collection field), and 10^{11} - 10^{12} ohm-cm dust resistivity, but test is made also at normal temperature to obtain the reference data under no back discharge condition. The mass-loading of dust is measured at both the inlet and outlet of the ESP using two sampling filters and two dust-loading monitors (Konitest). The charge-to-mass ratio of dust is also measured with two suction-type Faraday cages at the inlet and outlet.

2. Experimental Results

The tests are further made under three different operation modes of the ESP with and without the prechargers operated:

i) a dc voltage is applied to each field of ESP under high dust resistivity condition to cause severe back discharge (dc operation mode under back discharge),

ii) a dc voltage not to cause back discharge propagation, ca. -35 kV, is applied to each field as a base-voltage, and a pulse high voltage with a crest voltage of -20 kV, duration time of 1 ms and repetition frequency of 100 Hz is superposed to this base-voltage (dc-plus-pulse operation mode), and

iii) a dc high voltage is applied to each field, but under no back discharge condition at 20 deg C gas temperature for the purpose of reference (dc operation mode without back discharge).

2.1 DC Operation Mode under Back Discharge

The test conditions are: gas temperature T = 100 deg C, dust resistivity = 10^{11} - 10^{12} ohm-cm, inlet dust loading w_i = 6.5 g/Nm^3, applied voltage V = 41 - 43 kV corresponding to average field strength in collection field E = 2.7 - 2.9 kV/cm, and average current density J = 0.3 - 0.9 mA/m^2. A severe back discharge is detected by naked eye and a very distinct hysteresis in voltage-current characteristics. The current rises with increasing dust thickness on the collection electrodes to become maximum just before rapping.

Figure 7 indicates the mass-penetration of dust through the test ESP as a function of the effective length in gas flow direction of the collection field. The effective length is varied by connecting the first, second, and third collection field successively from the upstream side to the high voltage

source, and it is indicated by the number of the connected fields, each being 50 cm in length. The curve A represents the blank case where no precharging is made. The penetration starts from 50 % as a results of purely mechanical collection which is made mostly up to the end of the first field in this particular case. It is interesting to see that the curve A shows an exponential decay following Deutsch equation even under the severe back discharge condition. The curve B is the same result obtained when only the Boxer-Charger I in the inlet-duct is being operated. The curve C is for the case when the Boxer-Charger I and II are being operated. It can be seen that the effect of precharging appears distinctly in its succeeding collection field to raise the apparent migration velocity of dust, w, but its effect is lost from the next field on to make the curves B and C parallel to the curve A from the second and third fields. The enhanced charge decays in the first downstream field due to back discharge down to a saturation level specific to its charge neutralization condition, As is to be reported separately, this condition is specified by the magnitudes of the field strength, E, current densities of positive and negative ions, i_+ and i_-, their ratio i_+/i_-, and the space distribution of these quantities. The higher migration velocity in the first downstream field is evidently resulted by the higher average charge of dust during its decay process down to the new saturation charge. This saturation charge, approximately equal to that in the blank case (curve A), will control the collection process in the succeeding fields to provide a decreased migration velocity close to its value for the curve A.

Figure 8 shows the magnitudes of charge-to-mass ratio of dust measured at the outlet in the same tests as described in Figure 7. The highly charged particles will be rapidly collected in the active field without contributing to the indicated values of charge-to-mass ratio at the outlet, whereas the small particles, hard to collect and to become dominant at the outlet, tend to raise the measured value. This makes a clear interpretation of the curves in Figure 8 difficult. However, it seems that the charge-to-mass ratio enhanced by the first Boxer-Charger I is further raised by the second Boxer-Charger II. It is not clear whether the rise of the curve A with increasing field length represents a time increase in particle charge or the size decrease at the outlet as a result of increasing collection performance.

At any rate it is expected that the penetration will drop exponentially with the field length following the dotted line in Figure 7 when the Boxer-Chargers are used successively in front of each collection field. The migration velocities, w_o and w_1 derived from the curve A and dotted line respectively, are indicated in Table 1. The enhancement factor of collection performance by the successive precharging, expressed in terms of w_1/w_o, is as high as 2.44 in this particular case. It should be added that this enhancement factor is a function of different variables, including the chaging performance of precharger, residence time and back discharge severity in the combined collection field, particle size distribution of dust, etc.

In order to take full advantage of precharging it is imperative to use the proper collection fields which are free of back discharge, such as those consisting of parallel plane electrodes or the pulsed field of twin-electrode or tri-electrode types. The pulsed field is likely to be more suitable in view of avoiding rapping reentrainment with electrical adhesion force. The value of ionic current density in this case should be higher than needed for providing a sufficient electrical adhesion to the dust deposit on the collection electrodes, but lower than the critical level of triggering back discharge.

The successive use of prechargers by inserting into each inter-field section provides a second alternative in the case when the conventional ESP fields can not be altered.

2.2 DC-Plus-Pulse Operation Mode

With the considerations described above in mind the same tests are continued with the pulsed collection fields under the same high resistivity conditions. The dc high voltage of -35 kV (2.3 kV/cm) is applied to the discharge electrodes of each field, and a negative pulse high voltage with a crest value of -20 kV, duration time of 1 ms and repetition frequency of 100 Hz is applied superimposed. All other variables are kept identical to those in the previous section. A noticeable feature of this operation mode is a greatly reduced current density level at J = 0.04 mA/m^2, and no back discharge is detected by naked eyes. The pulsed corona occurs uniformly along the wires, and the uniformity of current over the collecting electrodes is distinctly noticed from the mode of uniform dust deposition.

Figure 9 shows the same results as Figure 7 where the curves A, B, and C are corresponding to the same precharging conditions of A, B, and C in Figure 7. Again in this case the similar tendency appears in the curves A, B, and C with the increased decay rate. It is noted that a substantial improvement is obtained by the pulsed fields only owing to an effective suppression of back discharge, providing the enhancement factor of w_p/w_o = 1.63 as indicated in Table 1.

As expected the effect of precharging becomes much more pronounced in this case, and the enhancement factor derived from the migration velocity for the dotted line, w_{p1}, becomes as high as w_{p1}/w_o = 2.91. This migration velocity, w_{p1}, specific to this particular combination of successive precharging with the pulsed collection field exceeds a level obtainable under an ideal ESP condition where no back discharge is taking place, as described later.

The deviation of curves B and C from the dotted line occuring from the second field on, although greatly reduced in this case, indicates a slight effect of charge neutralization due to back discharge which is still existing even under the pulsed condition. The magnitude of this deviation, which can be expressed by the ratio of the migration velocity for the second branch to that for the first branch, w_{p2}/w_{p1}, provides a good measure of back discharge severity usable for design purpose of this precharger-collector hybrid system.

2.3 DC Operation without Back Discharge

For reference purpose the tests are further performed at room temperature T = 20 deg C where dust resistivity drops under 10^{10}ohm-cm and no back discharge occurs. The magnitude of main voltage applicable to the Boxer-Chargers and collection fields becomes greatly increased. As a result the maximum value of ac main field at the Boxer-Chargers is raised from 4.5 to 5.4 kV/cm, and the dc high voltage applied to the collection fields from 41 - 43 to 51 - 55 kV (from 2.73 - 2.87 to 3.4 - 3.7 kV/cm). This is to compare the advantage of the precharger and its combination with the pulsed fieds to the best possible standard of ESP operated under ideal conditions. The applied voltage in the collection fields is regulated so that a constant current density J = 0.15 mA/m^2 is maintained. The inlet dust loading is kept constant at 8 g/Nm^3.

Figure 10 indicates the results obtained, where the curves A, B, and C represent the operating conditions corresponding to A, B and C in the Figures

7 and 9. The curve A in this case consists of three different branches. The first one corresponds to a lower migration velocity, possibly owing to lower average charge of particles at the first field. Then, the migration velocity rises with increasing charge in the second field. It drops again in the third field, perhaps because of decrease in particle size.

The use of the first Boxer-Charger I acts for raising the migration velocity at the first field, indicating the effect of precharging without which the particle charge must rise from zero and, hence, the time-average of the particle charge becomes lower. Then, the curve B becomes parallel to the curve A in the succeeding fields as in the case in Figures 7 and 9. A striking feature in this case is that the curve C shows very little deviation from the curve B, distinctly indicating no improvement to be obtained by successive precharging. It is considered that, once the particles have been fully charged by either the first Boxer-Charger or corona charging in the first field, the high level of charge will be preserved in this case since no charge reduction by positive ions will take place in this case.

Thus, the effect of precharging in the case of low dust resistivity appears only in the first field, and this only reduces the inlet dust loadings of its succeeding fields. Ths enhancement factor in this case is only w_{b1}/w_{bo} = 1.21 as indicated in Table 1.

3. Conclusions

The following conclusions are obtained from the present experiments:

1) The Boxer-Charger Mark III using double-helix units for its electrode assemblies and very short pulse voltage for plasma excitation indicates a very satisfactory charging performance.
2) The dust mass-loading shows an exponential decay with distance in gas flow direction even under a severe back discharge condition, indicating Deutsch equation to hold also in this case.
3) The use of a precharger provides a great performance improvement in the collection field immediately downstream, but its effect is lost from the succeeding fields in the case when a severe back discharge is occuring. This suggests that the enhanced initial charge of the particles can drop, by charge elimination of back discharge, fairly rapidly to a new saturation level, even within a residence time in this field. This means that the performance improvement obtained in this field by no means corresponds to the level of the enhanced initial charge at its inlet, but to the effective charge averaged over the entire field during its elimination process.
4) The performance improvement can be expressed by "enhancement factor" as the ratio of enhanced migration velocity to its blank value.
5) The repeated precharging is necessary in front of each collection field under back discharge condition in the case when the collection fields can not be altered from a conventional ESP design. This provides the enhancement factor as high as 2.44 in the present experiments.
6) The use of "back discharge free collection fields" is necessary for taking full advantage of precharging. A parallel plane electrode system or pulsed field system of either twin- or tri-electrode type can be used for this purpose. The pulsed field is likely to be more suitable because it can provide an electrical adhesion force to the dust deposit on collecting electrodes so as to avoid rapping reentrainment.
7) The figure of merit of the back discharge free field is given by the deviation of decaying line of dust mass-loading from its initial branch in the

first field, expressed in terms of the ratio of respective migration velocities. This ratio can be used for design of the precharger-ESP hybrid system in general.

8) The combination of repeated precharging with pulsed collection fields of twin-electrode type energized with the dc-plus-pulse operation mode provides an enhancement factor as high as 2.91 at dust resistivity of 10^{11} - 10^{12} ohm-cm. The dust migration velocity in this case becomes slightly higher than that for a reference case of ESP operated at its maximum performance under no back discharge condition.
9) In the case when no back discharge is taking place, only the first precharger provides a distinct effect, but no further improvement can be obtained by the repeated precharging.

The test of parallel plane electrode system as another type of back discharge free collection field is being undertaken. The development of the Boxer-Charger Mark III and its pulse power supply is being performed for application in the large scale ESP's of coal burning boilers. Figure 11 illustrates its conceptual design of frame-supported construction using the inductance-isolation to support each double-helix unit at its both ends, and also at its center point for fixing and rapping.

References

(1) S.Masuda, A.Mizuno, H.Nakatani and H.Kawahara: Application of Boxer-Charger in Pulsed Electrostatic Precipitator, Record of IEEE/IAS 1980 Annual Meeting, pp. 904 - 911 (Sept. 29 - Oct. 3 , 1980 in Cincinnati, Ohio).
(2) S.Masuda, M.Washizu, A.Mizuno and K.Akutsu: Boxer-Charger - A Novel Charging Device for High Resistivity Powders, Record of IEEE/IAS 1978 Annual Meeting, pp. 16 - 22 (Oct. 1978).
(3) S.Masuda, A.Mizuno and H.Nakatani: Application of Boxer-Charger in Electrostatic Precipitators, Record of IEEE/IAS 1979 Annual Meeting, pp. 131 - 138 (Oct. 1979 in Cleveland, Ohio).

TABLE 1 DUST MIGRATION VELOCITY AND ENHANCEMENT FACTOR

Operation Mode of Collection Fields	Tg (°C)	ρd (ohm-cm)	Dust Migration Velocity (cm/s)		Enhancement Factor
			precharging off	precharging on*	
DC Operation Mode under Back Discharge	100	10^{11} - 10^{12}	w_o = 11.7	w_1 = 28.6	w_1/w_o=2.44
DC-Puls-Pulse Operation Mode at high ρd	100	10^{11} - 10^{12}	w_p = 19.1	w_{pl} = 34.1	w_p/w_o=1.63 w_{pl}/w_o=2.91
DC OPeration Mode under No Back Discharge	20	< 10^{10}	w_b = 32.7	w_{bl} = 39.5	w_b/w_o=2.79 w_{bl}/w_b=1.21

Remarks: * ----- Repeated precharging mode,
T_g = gas temperature, ρ_d = dust resistivity

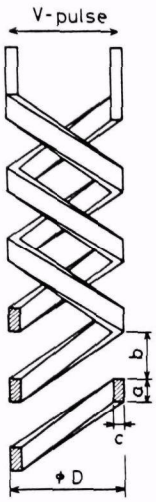

D = 30 mm
a = 3 mm
b = 8 mm
c = 1 mm

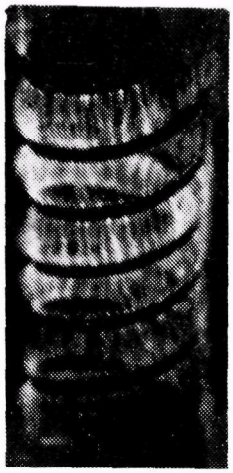

(b) streamers

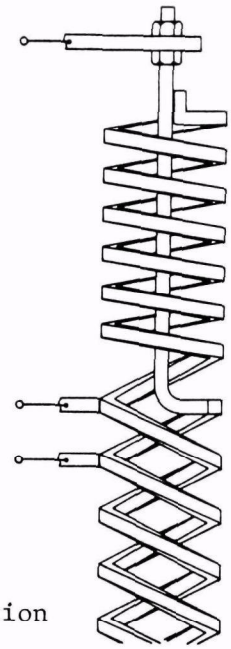

(a) Double-Helix Unit

(c) Inductance-Isolation

Fig. 1 Electrode Assembly Unit of Boxer-Charger Mark III

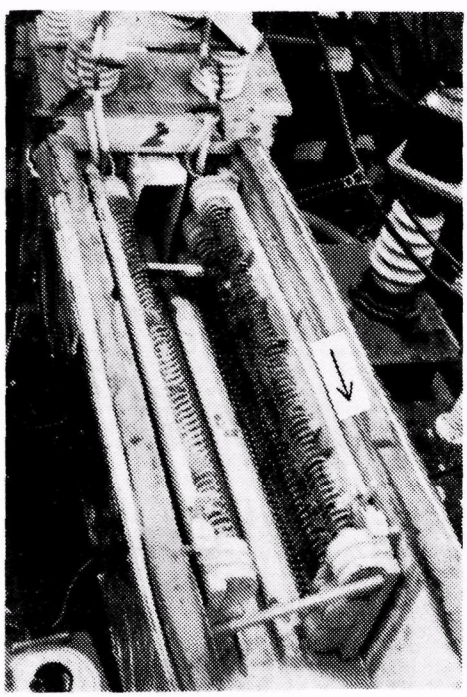

Fig. 2 Boxer-Charger I
(installed in inlet-duct)

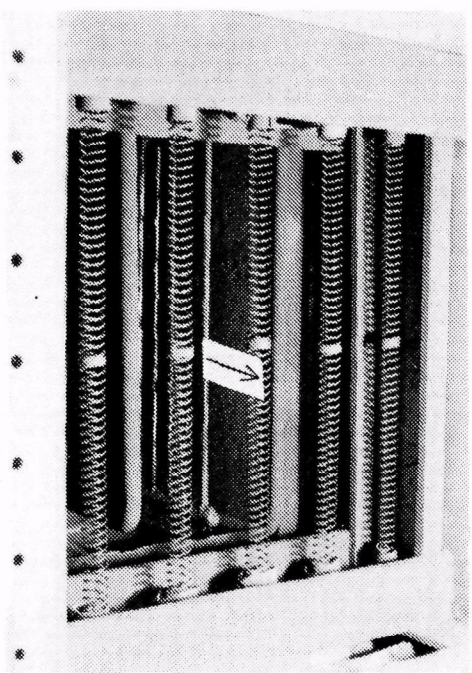

Fig. 3 Boxer-Charger II
(installed in inter-field section)

(↓ : gas flow direction)

Fig.4 Pulse and Main Voltage Supply

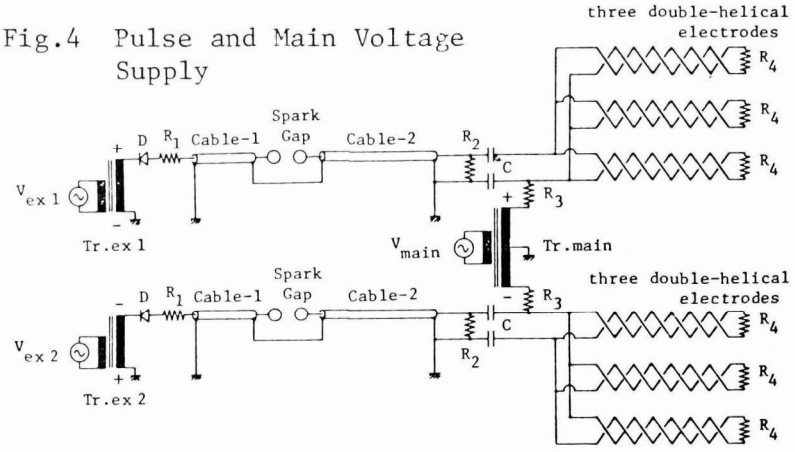

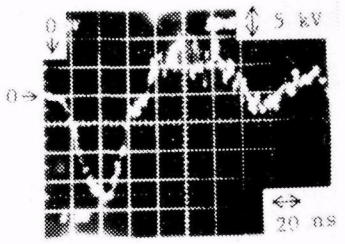

Fig. 5 Pulse Wave Form

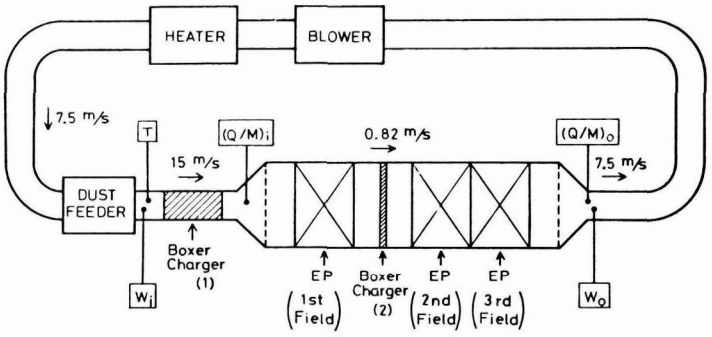

W_i, W_o: dust-loading monitor

$(Q/M)_i$, $(Q/M)_o$: charge-to-mass ratio measurement

T: thermometer

Fig. 6 Race-Track System

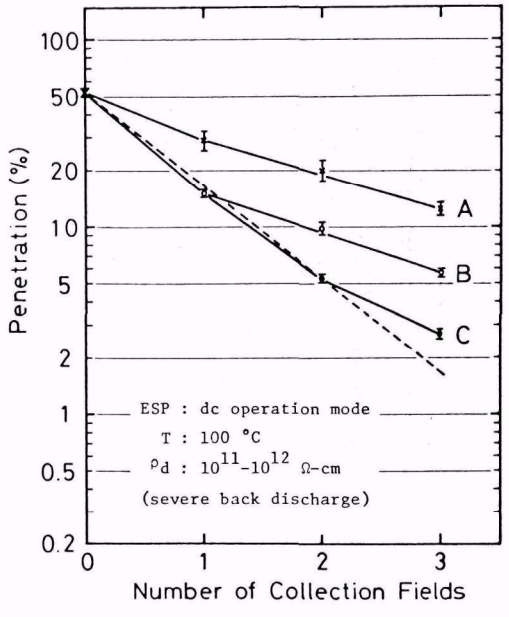

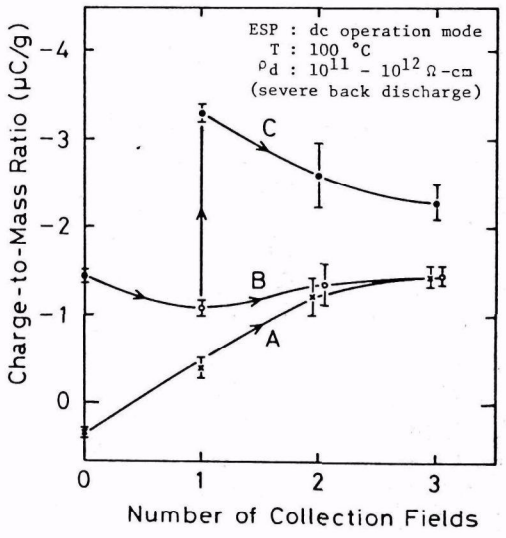

Fig. 8 Charge-to-Mass Ratio (measured at outlet; dc operation mode)

Fig. 7 Dust Penetration vs. Effective Length of Collection Field (dc operation mode under severe back discharge condition)

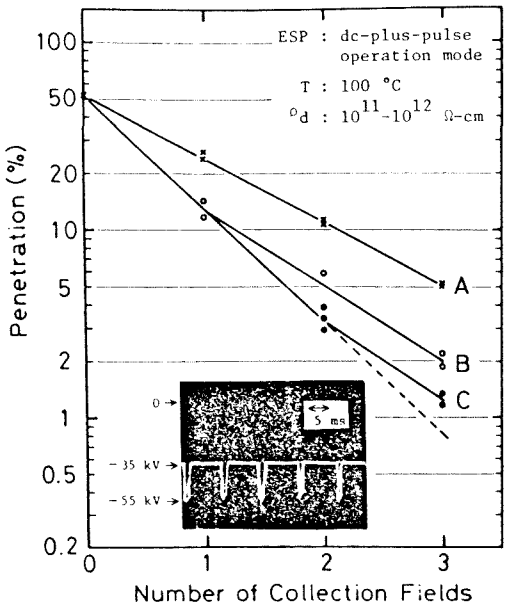

Fig. 9 Dust Penetration vs. Effective Length of Collection Field (dc-plus-pulse operation mode)

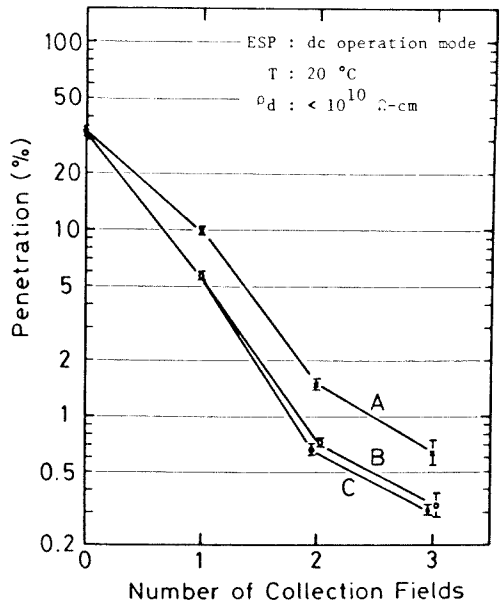

Fig. 10 Dust Penetration vs. Effective Length of Collection Field (dc operation; no back discharge condition)

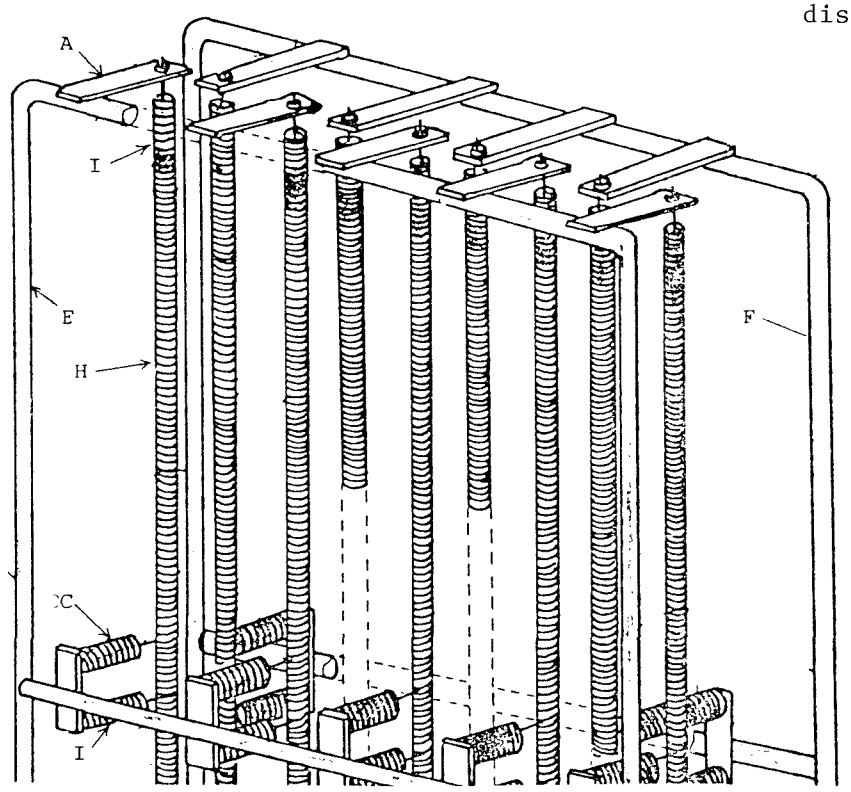

H: double-helix unit

F: frame

A: supporting arm

I: inductance-isolation

C: center supporting arm for rapping with inductance-isolation

Fig. 11 Conceptual Structure of Frame-Supported Boxer-Charger (to be installed in inter-field sections)

THE PERFORMANCE OF AN EXPERIMENTAL PRECIPITATOR WITH AN ALL-PLATE ZONE

By J. Dalmon
Central Electricity Research Laboratories, Leatherhead, England

ABSTRACT

An 'All-Plate' ESP collector zone has been developed by the CEGB and tested in a small research rig at atmospheric temperatures. To provide data more closely related to power station precipitator conditions a programme of tests has been carried out by permission of the Environmental Protection Agency on their experimental electrostatic precipitator facility at Research Triangle Park. This consists of a four zone, single lane unit and for the tests the conventional discharge wires in one zone were replaced by a single charged plate. In all zones the spacing between the earthed plates was 200 mm. The gas velocity was kept constant at 1.6 m/s and the gas temperature ranged from 17°C to 150°C. The test dust was fly ash having a mass median diameter of 6 μm and a resistivity of 1×10^{12} ohm cm.

The performance was evaluated as an 'Effective Migration Velocity' enhancement factor, defined as EMV with plate-plate electrodes/EMV with wire-plate electrodes. The factor averaged 3.1 with all plates in zone three and 2.9 for zone four with a value of 1.4 over the complete precipitator.

The results indicate a clear advantage for a precipitator incorporating an all-plate zone.

INTRODUCTION

As part of a programme of research into methods of improving the dust collecting performance of large power station electrostatic precipitators, the Central Electricity Research Laboratories of the Central Electricity Generating Board carried out a pilot scale investigation in which the discharge wires in the final zone of a three zone precipitator were replaced by negatively charged plates. The work, which was reported by Dalmon (1974)[1] showed that particles entering the final zone were already charged and were collected in the high electric field between the parallel plates without the necessity of a corona discharge. The experiments, carried out under atmospheric conditions using aluminium oxide and perspex test dusts to simulate normal and highly resistive ash respectively, showed clear advantages for the 'All-Plate' final zone with a twofold increase in its effective migration velocity. Inter-electrode spacings of 50 mm and 150 mm were investigated over a rnage of velocities from 0.9 m/s to 2.75 m/s and it was concluded that a spacing of 100 mm would be the practical optimum for full-scale use. These early tests did not include the effects of rapping and further work showed that although the emv fell for both wire-plate and all-plate geometries in the final zone, there was still an emv enhancement by a factor of two.

During 1979, the Industrial Environmental Research Laboratory of the United States Environmental Protection Agency offered the use of their 'hot' experimental precipitator facility at Research Triangle Park for further testing of the All-Plate concept under dust and gas conditions more

representative of power station practice. This led to a programme of tests during 1980 which are reported here.

EXPERIMENTAL FACILITY

The EPA experimental precipitator has been fully described by Lawless, Daniel and Ramsey[2], so only its main features are summarised here. It consists of a single lane with four zones in series. Each zone normally has a pair of flat collecting plates 1.22 m square and a single row of discharge wires, but this was modified as described later. Both the plate spacing and the wire pitch can be readily altered. Rapping of both plates and wires is by pneumatically operated hammers acting vertically and the frequency of operation can be controlled separately for each zone. Ambient air is drawn from outside the laboratory directly into the inlet ducting and may be heated by three propane burners. The gas flow rate is measured by an orifice plate upstream of the ID fan and is variable between wide limits. Dust is injected by two sandblast guns facing into the gas stream and situated $\sim$2 m downstream of the burners and a similar distance from the inlet of the first precipitator zone. Sampling ports are arranged in vertical groups of three at the precipitator inlet, between zones and at the outlet. Each zone is supplied by a manually controlled 100 kV, 10 mA transformer-rectifier. Kilovolts and milliamps are displayed digitally and may be printed out at selected intervals. Voltage-current characteristics may be taken and plotted in real-time on an X-Y plotter. Gas temperatures, orifice differential and dust emission are also displayed and printed with the electrical readings.

MEASUREMENTS AND TECHNIQUES

Mass Burden, Efficiency and Effective Migration Velocity

Mass burden was measured by standard isokinetic sampling techniques using 47 mm dia. GF/F glass fibre filters. The sampling duration varied from 5 to 150 mins according to location and dust burden and either three or four sampling trains were used simultaneously. The middle of the three sampling ports was used as previous EPA investigations had shown this to give representative results. The sampled weights were used to calculate overall and zonal efficiencies and effective migration velocities (emv's) were derived using the well known Deutsch equation.

Particle Size Distribution

This was an in-situ measurement using an MRI seven stage cascade impactor with a 47 mm GF/F back-up filter. Data from the tests was processed by a desk computer using a programme developed by the EPA to give cumulative distribution by mass and, by combining data from various locations overall and zonal size-efficiency relationships were provided.

Particle Charge to Mass Ratio

This was measured by a Faraday cage type probe of EPA design inserted into the sampling ports previously mentioned with the exception that it could not be used at the outlet due to insufficient clearance. Problems with dust by-

passing the inlet nozzle seal prevented any successful measurements at ambient temperatures.

Ash Resistivity

Resistivity was measured at the precipitator inlet using a point-plane probe designed by the Southern Research Institute[3], and on collected samples over a range of temperatures and relative humidities by the Denver Research Institute using a laboratory cell.

Emission Monitoring

The opacity of the emitted flue gas was monitored by an MRI 'Plant Process Visiometer (PPV)[4]. The instrument passes a continuous sample of gas through an optical chamber where opacity is measured by the total light scattered by the particles.

TEST PROGRAMME

Zonal Arrangement

Throughout the test programme the inter-electrode spacing was maintained at 100 mm (i.e. 200 mm between earthed plates) in all four zones. Base-line tests (Tests 1 to 7) were conducted with six 3.2 mm dia. round wires at 200 mm centres in all zones. A single h.t. plate, 1.07 m long by 1.14 m high having radiused corners and edged by a 17.5 mm dia. tube, then replaced the wires in the final zone (Tests 8 to 18). The h.t. plate was then fitted in zone three and the wires refitted in zone four (Tests 19 to 27). Final tests were carried out with wires in all zones (Tests 28 to 31).

Test Conditions

Tests were conducted at ambient temperatures ($\sim 17^{\circ}C$) and within the range $107^{\circ}C$ to $157^{\circ}C$ at a constant gas velocity of 1.6 m/s both with and without rapping. The normal rapping rates are given in Table 1 but higher rates were used on zone four, as indicated in Tables 4 to 7, to accentuate the effects of re-entrainment.

TABLE 1. INTERVAL BETWEEN RAPS

Zone	1	2	3	4
Plate (min)	15	30	60	120
Wire (min)	7.5	15	30	60

NB. (1) Timing arranged so that raps are not coincident.
(2) On certain tests zone 4 was rapped every 10 min.

The test dust was fly ash collected from the hoppers of a Detroit-Edison ESP when Illinois coal was being burned, and its resistivity, as previously measured by the Denver method was 1×10^{11} ohm cm at $150^{\circ}C$. The ash analysis is given in Table 2 and of the rig gas in Table 3. The inlet burden was kept close to 8 g/m^3 NTP throughout.

TABLE 2. ELEMENTAL ANALYSIS OF FLY ASH (%)

Al	Si	Ca	S	K	Ti	Fe
26.44	28.60	1.74	0.27	2.54	0.85	39.56

TABLE 3. TYPICAL GAS ANALYSIS (%)

H_2O	CO_2	CO	O_2	N_2
3.4	6.0	4.0	10.0	78.0

Test Procedure

Following preparation for the base-line tests voltage-current characteristics were taken on all zones under clean electrode and gas conditions at 17°C and 124°C with both static and flowing air.

After overnight cooling fly ash was injected for 3 hrs with voltage of 32 kV applied to all zones and with all the rapping operating as given in Table 1. This allowed dust to build up on the electrodes in a realistic manner. The voltage was then raised to the maximum (Test 1) and when stable conditions were indicated by the PPV mass sampling commenced. Further tests at ambient conditions were made at lower voltages. The plant was then shut down overnight with the residual dust left on the electrodes.

The following morning the gas temperature was raised to 120°C over a period of two hours with nominal electrical settings, V-I characteristics were then taken and dust injection commenced. Further characteristics were taken and the information used to adjust the electrical settings to give minimum emission readings on the PPV before performance testing began. These procedures for temperature raising, performance optimisation, testing and rig shut-down were followed on a daily basis. Priority was given to mass sampling with impactor, charge and resistivity measurements being made less frequently. Some eight to nine hours running were achieved daily.

Electrode changes were accomplished with the minimum electrode cleaning, but dust samples were taken from the all-plate zone for resistivity measurements at Denver.

Tests with each electrode arrangement commenced with measurements at ambient conditions.

RESULTS AND DISCUSSION

Electrical Characteristics

At ambient temperature, ∿17°C, the voltage-current characteristics of the wire-plate zones were normal for electrodes coated with a moderately resistive dust and a typical example is given in Figure 1. The all-plate zone

shows virtually zero current until sparkover occurs. The characteristics were not dissimilar to those taken with clean electrodes. At temperature the characteristics for wire-plate zones exhibited classic back-ionization features of run-away current at low voltage, a depressed sparkover voltage and a very marked hysteresis effect (Figure 2). In contrast, the all-plate zone showed zero current to sparkover and was very little changed from the clean characteristic. Sparkover in this zone triggered some flow of current which was small by comparison with wire-plate zones. The voltage at sparkover for the all-plate zone was always well in excess of the value for other zones at the same time, by as much as 20 kV in some instances. The low moisture content of the flue gas, 3.4% compared with 6% normally encountered, plus the fact that there was no SO_2 may have contributed to the steepness of the V-I curves, although this would have been offset somewhat by the O_2 content which was 10% compared with a usual 6% for power station precipitators.

Observation of the PPV trace indicated that minimum emission was obtained at the onset of back-ionization and this coincided with the point of maximum voltage as shown in Figure 2. This point was selected from the V-I curves taken prior to each test and used as the operational setting for that test. There was considerable daily variation in the characteristics, but this was only to be expected with the severe back-ionization experienced. An attempt was made to obtain more stable conditions by altering the gas temperature and, thus, the dust resistivity. However, the resistivity changed very little over the range of interest and, hence, the effect was minimal.

Resistivity

New measurements at Denver showed that the resistivity of the feed dust had risen from the previous value of 1×10^{11} ohm cm to 1×10^{12} ohm cm at 150°C in an atmosphere containing 5% moisture. As the moisture content of the rig gas was 3.4% a rather higher value would be expected in the rig. Measurements on ash taken from the electrodes of the all-plate zone gave a resistivity of 2×10^{12} ohm cm. The in-situ measurements taken with the SRI probe gave a somewhat lower value of 1×10^{11} ohm cm at 150°C. This order of magnitude difference is no doubt due to the different methods. Never-the-less, the measurements showed that the dust was highly resistive and, thus, must be responsible for the severe back-ionization at temperature.

The Denver resistivity measurements indicated that for temperatures around 17°C the resistivity would be below 10^{10} ohm cm, this would account for the fact that no back-ionization was experienced in low temperature tests.

Examination of Electrodes

Inspection of the electrodes after each test series showed that between 3 mm and 10 mm of flakey dust had accumulated on the collecting plates of wire-plate zones. The all-plate zone had a fairly even coating <2 mm thick on both electrodes when in the final zone and up to 5 mm when in zone three. The discharge wires were coated to <1 mm. The dust thickness on shut-down reflects the immediate rapping history and it is probable that variations in deposit thickness could have caused some of the day-to-day variations in electrical conditions.

The level of deposits observed is quite normal in power station precipitators and this gives confidence that the test conditions were closely representative of full-scale operation.

Charge-to-Mass Ratio

The calculated and measured charge-to-mass ratio plotted in Figure 3 shows that the latter is less by a factor of ∿3 than predicted. This is very probably due to the presence of positive ions under the strongly back-ionizing conditions encountered, which may not only have reduced the charge on the particles but could have resulted in positively charged particles being collected in the probe. This hypothesis could not be checked for non-back-ionizing conditions at ambient temperature because of the problems with the probe mentioned previously. The experimental data in Figure 3 was obtained at various positions along the ESP and it is apparent that the charge is a function of the voltage applied upstream of the measuring point rather than residence time. Examination of the data showed that particles entering the precipitator had a small, but significant charge and the maximum charge was attained in the first zone (Figure 3, Test 27). It was also found that particles escaping from the all-plate zone three had virtually the same charge-to-mass ratio as when they entered the zone (the two experimental points for Test 24).

Performance

The performance, in terms of efficiency and emv, is given for all the tests in Tables 4 to 7, which are grouped into gas temperature bands. It is apparent from Table 4 that at low temperatures, with no back-ionization problems, overall efficiencies are well over 99% and overall emv's were correspondingly high at over 20 cm/s. It is also apparent that both overall and zonal performance varied considerably from day-to-day under similar operating conditions.

There is a marked drop in performance at temperature with back-ionization present (Tables 5 to 7) and, again, there are considerable differences between tests where temperature, rapping and electrical conditions were reasonably similar, (e.g. Tests 6 and 7, 21 and 22, Table 6). There is a weak tendency for the emv to increase with gas temperature over the range 107 to 157°C.

The effects of rapping are far from consistent, e.g. test 10 with rapping has a higher efficiency than tests 11 and 12 with no rapping (Table 6). This also applies to test pairs 17-18 and 26-27 (Table 7), where the last zone has accelerated rapping. In other cases, tests 15-16 (Table 5) for example, the efficiency, as would be expected, is greater without rapping.

In view of these anomalies, which can be partly but not wholly explained by the uncontrolled effects of back-ionization, the results for similar test conditions have been averaged and presented in Tables 8 and 9 as "emv enhancement factors". This is defined as the emv with plate-plate electrodes/the emv with wire-plate electrodes. Table 8 shows the very considerable increase in emv for zones three and four when the plate-plate arrangement replaced the wire-plate geometry. The greatest emv enhancement is for zone three with no back-ionization (a factor of 13). Zone three, however, shows a greater

variability in this factor than zone four which has a value of about three at all temperatures with rapping. Its value without rapping is strangely, less at 1.2. In terms of the overall emv the factor, apart from two cases, varies from 1.2 to 1.6 irrespective of the position of the all-plate zone (Table 9). The exceptions are due to less efficient collection in the wire-plate upstream zones, e.g. in test 29 the combined efficiency of zones one to three was 82.58% (wire-plate in zone four) whereas in test 17 (plate-plate in zone four) it was only 75.29%. Taking all the high temperature tests together gives enhancement factors of 1.4 and 1.3 for zones three and four respectively. Thus, there is without doubt, a clear advantage for the all-plate system.

The reason for the enhanced performance was originally attributed to a combination of a higher and more uniform electric field in the absence of corona and less gas turbulence with the simpler plate arrangement[1]. No turbulence measurements were made during the present trials but a typical plot of emv versus applied voltage (Figure 4) clearly shows the importance of the higher operating point and, hence, the increased field with the all-plate zone.

Particle Size and Grade Efficiency

The average mass geometric mean diameter of the fly ash at the precipitator inlet, as measured by the cascade impactor, was 6 μm. This represents an extremely fine dust and compares with a typical value for a CEGB power station precipitator of 18 μm. The size distribution for test 25 is given in Figure 5 for the inlets to zones one, three and four and the outlet of zone four. The dust becomes progressively finer with distance from the inlet, the mean sizes being 6.7, 5.2, 3.2 and 2.9 μm respectively.

The size data has been used to calculate grade efficiencies and Figure 6 shows this information both for the complete precipitator and for the all-plate zone on test 25. It may be noted that there is a well defined minimum efficiency for the complete precipitator as would be expected from changes in charging mechanisms and this lies at 0.8 μm. There is a less obvious minimum at 0.4 μm for the all-plate zone alone. These results are typical of the limited number of cascade impactor tests but there is insufficient data to draw firm conclusions regarding the size-efficiency characteristics of the all-plate zone except to say that it appears better at collecting the fine particles.

IMPLICATIONS FOR FULL SCALE

The use of an all-plate zone is zeen initially as a method of up-grading an existing precipitator by substitution in, say, the final wire-plate zone. If for example, a precipitator having a measured efficiency of 98.3%, a specific surface of 58.85 $m^2/m^3/s$ and an emv of 6.9 cm/s has its emv enhanced by a factor of 1.2 the efficiency rises to 99.24% and an enhancement of 1.3 gives a predicted efficiency of 99.5%. This corresponds to a reduction in emission of 55% and 71% respectively. A real case, would obviously have to be investigated in depth rather than using this simple approach, before any decision on fitting an all-plate zone were made. However, in anticipation of a retrofit, the CEGB have commissioned engineering rigs at the works of two manufacturers with the object of investigating detail design, electrical and rapping problems. The rigs consist of five, full height plates (three

earthed and two h.t.) and testing is well under way. The designs are proprietary, so no details can be given here.

CONCLUSIONS

Trials of an 'All-Plate' collector zone in the four zone EPA pilot electrostatic precipitator under conditions realistic of power station plant have amply confirmed earlier tests at CERL under atmospheric conditions using artificial dusts. The results have shown that the substitution of an all-plate arrangement for the normal wire-plate configuration enhances the zonal emv by an average factor of 2.9 when used in the final zone and by 3.1 when in the penultimate position. The overall emv was increased by a factor of at least 1.3.

ACKNOWLEDGEMENTS

The author wishes to thank Mr J.H. Abbott and Dr L.E. Sparks of the U.S. Environmental Protection Agency for making this investigation possible. The help of G.H. Ramsey, B.E. Daniel, R. Valentine and R. Ogan with the experimental work is gratefully acknoweldged. The paper is published by permission of the Central Electricity Generating Board.

ENDNOTES

1. Dalmon, J. The Performance of an Experimental Electrostatic Precipitator with a Low Turbulence Zone, Australian Inst. Fuel Symposium, Adelaide, Nov. 1974.

2. Lawless, P.A., Daniel, B.E. and Ramsey, G.H. Characterisation of the EPA/IERL-RTP Pilot-Scale Precipitator, EPA-600/7-79-052, Feb. 1979.

3. Nichols, G.B. and Banks, S.M. Test Methods and Apparatus for Conducting Resistivity Measurements, SORI-EAS-75-090, Sept. 1977.

4. Ensor, D.S., Bevan, L.D. and Markowski, G.R. Application of Nephelometry to the Monitoring of Air Pollution Sources, Paper 74-110, June 1974, A.P.C.A. Meeting, Denver, June.

TABLE 4. PERFORMANCE IN TEMPERATURE RANGE 9°C TO 24°C

Test No.	Rapping	Efficiency (%) Z1	Z2	Z3	Z4	Overall	Emv (cm/s) Z1	Z2	Z3	Z4	Overall
	All Wire-Plate										
1	√	-	-	-	36.11	99.93	-	-	-	5.9	23.8
2	√	-	-	-	55.33	99.81	-	-	-	10.6	20.6
3	√	-	-	-	43.80	99.73	-	-	-	7.6	19.4
	Zone 4 Plate-Plate										
8	√	97.89	82.24	15.38	91.78	99.91	50.6	22.7	2.2	32.8	23.0
9	√	99.22	71.54	28.38	63.64	99.95	63.7	16.5	4.4	13.3	24.9
	Zone 3 Plate-Plate										
19	√	← 99.61	→ 87.5		-	-	← 36.2	→ 27.3		-	-
20	√	← 99.49	→ 99.0		33.33	99.997	← 34.6	→ 60.4		5.3	34.2

TABLE 5. PERFORMANCE AT TEMPERATURE OF 107°C

Test No.	Rapping	Efficiency (%) Z1	Z2	Z3	Z4	Overall	Emv (cm/s) Z1	Z2	Z3	Z4	Overall
	Zone 4 Plate-Plate										
15	×	-	-	-	53.85	85.90	-	-	-	10.2	6.4
16	√	-	-	-	18.09	73.94	-	-	-	2.6	4.4

√ = Normal rapping
× = No rapping.

TABLE 6. PERFORMANCE IN TEMPERATURE RANGE 112-125°C

Test No.	Rapping	Efficiency (%) Z1	Z2	Z3	Z4	Overall	Emv (cm/s) Z1	Z2	Z3	Z4	Overall
	All Wire-Plate										
4	✓	-	-	-	5.87	78.64	-	-	-	0.8	5.1
5	✓	-	-	-	Zero	73.08	-	-	-	Zero	4.3
6	✓	60.70	49.51	23.69	4.30	85.51	12.3	10.0	3.6	0.6	6.3
7	✓	22.02	33.26	27.75	34.35	81.48	3.3	9.0	3.6	5.5	5.3
30	+	← 73.51	→ 35.71		14.45	85.43	← 8.7	→ 5.8		2.1	6.3
31	×	← 72.97	→ 16.29		43.24	87.16	← 8.6	→ 2.3		7.4	6.7
	Zone 4 Plate-Plate										
10	✓	-	-	-	40.62	99.03	-	-	-	6.8	8.7
11	×	57.71	68.39	58.75	60.53	93.23	10.7	15.1	11.6	13.2	8.8
12	×	-	-	-	30.99	91.07	-	-	-	4.9	7.9
	Zone 3 Plate-Plate										
21	✓	← 34.48	→ 36.45		27.86	69.96	← 2.8	→ 6.0		4.3	4.0
22	✓	← 52.92	→ 48.58		27.70	82.50	← 4.9	→ 8.7		4.3	5.7

TABLE 7. PERFORMANCE IN TEMPERATURE RANGE 142°C-157°C

Test No.	Rapping	Efficiency (%) Z1	Z2	Z3	Z4	Overall	Emv (cm/s) Z1	Z2	Z3	Z4	Overall
	All Zones Wire-Plate										
28	+	← 80.74	→ 3.64		35.04	87.94	← 10.8	→ 0.5		5.7	6.9
29	×	← 76.94	→ 24.43		38.89	89.35	← 9.6	→ 3.9		6.5	7.3
	Zone 4 Plate-Plate										
13	✓	69.97	33.30	35.44	70.54	94.93	15.8	5.3	5.7	16.0	9.8
14	✓	68.50	12.45	55.75	83.57	98.09	15.2	1.7	10.7	23.7	13.0
17	×	-	-	-	43.23	85.97	-	-	-	7.4	6.4
18	+	-	-	-	41.27	88.70	-	-	-	7.0	7.2
	Zone 3 Plate-Plate										
23	✓	← 67.83	→ 61.19		54.07	94.27	← 7.4	→ 12.4		10.2	9.4
24	✓	← 73.91	→ 61.37		7.07	90.64	← 8.8	→ 12.5		1.0	7.8
25	✓	← 80.78	→ 71.69		47.26	97.13	← 10.8	→ 16.6		8.4	11.7
26	+	← 61.48	→ 76.71		57.41	96.18	← 6.3	→ 19.1		11.2	10.7
27	×	← 79.47	→ 56.91		47.35	95.34	← 10.4	→ 11.1		8.4	10.1

✓ = Normal rapping
\+ = Zone 4 rapped every 10 mins
× = No rapping.

TABLE 8. EMV ENHANCEMENT FACTOR FOR ZONES FITTED WITH PLATE-PLATE ELECTRODES IN PLACE OF WIRE-PLATE ELECTRODES

Test Conditions	Zone 3	Zone 4
Gas temp. 17°C, with rapping	13.3	3.1
Gas temp. 118°C, with rapping	1.3	3.1×
Gas temp. 149°C, with rapping	4.9	2.8
Gas temp. 118°C, no rapping	-	1.2
Gas temp. 149°C, no rapping	3.0	1.2

TABLE 9. OVERALL EMV ENHANCEMENT FACTOR FOR 4 ZONE PILOT E.S.P. WIRE-PLATE ELECTRODES IN THREE ZONES, PLATE-PLATE ELECTRODES IN ONE ZONE

	Zone 3 Plate-Plate	Zone 4 Plate-Plate
All tests in gas temp. range 107°C to 157°C	1.4	1.3
17°C with rapping	1.6	1.2
118°C with rapping	0.9	1.6
149°C with rapping	1.4	1.4
118°C no rapping	-	1.2
149°C no rapping	1.4	0.9

$$\text{Emv Enhancement Factor} = \frac{\text{Emv with Plate-Plate Electrodes}}{\text{Emv with Wire-Plate Electrodes}}$$

The results are averages of several tests.

Gas temperatures are the averages of the bands in performance tables.

× Ignores test 5 which has zero emv for zone 4.

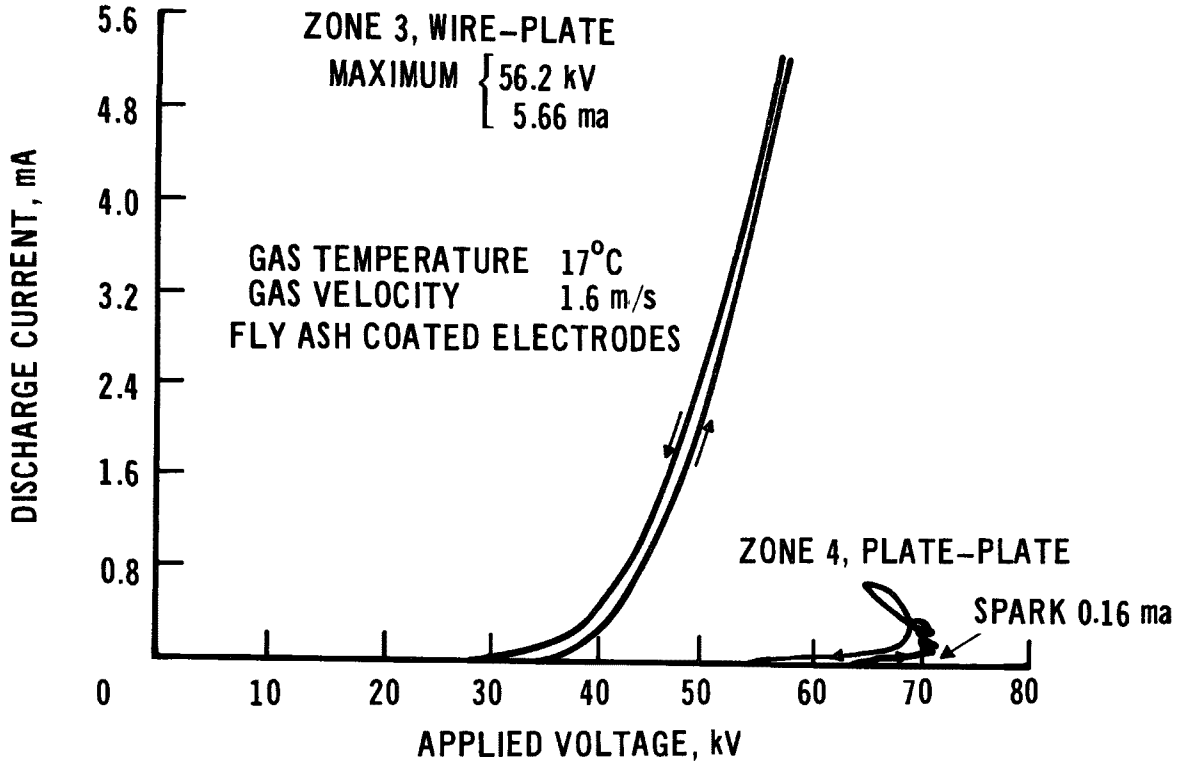

FIG. 1 VOLTAGE CURRENT CHARACTERISTICS OF A WIRE–PLATE ZONE COMPARED WITH A PLATE–PLATE ZONE

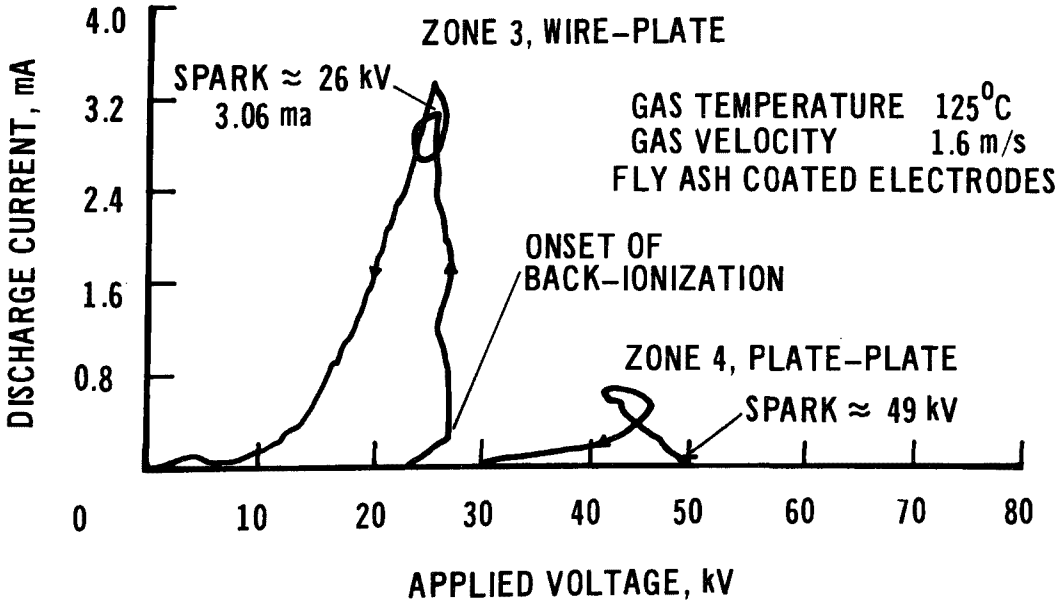

FIG. 2 VOLTAGE CURRENT CHARACTERISTICS OF A WIRE–PLATE ZONE COMPARED WITH A PLATE–PLATE ZONE

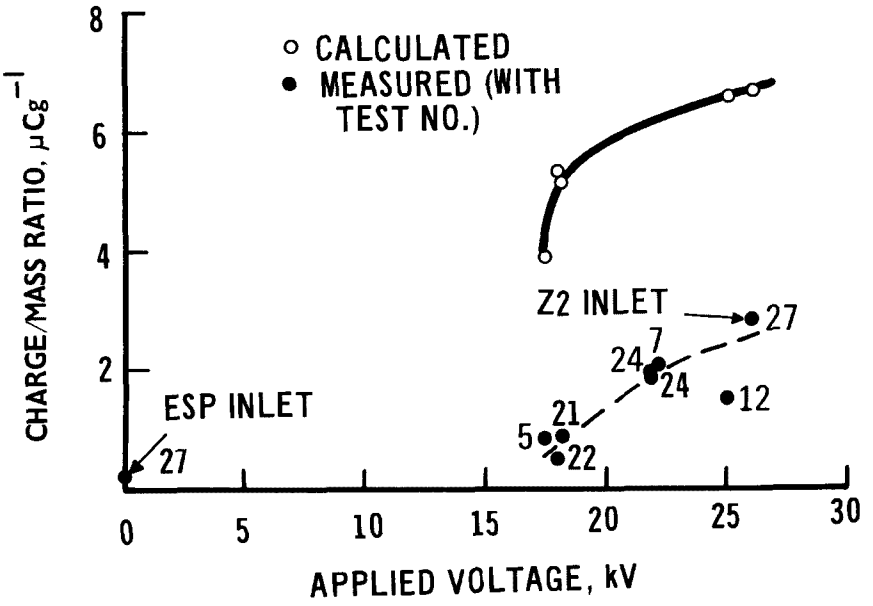

FIG. 3 CALCULATED AND MEASURED CHARGE/MASS RATIO RELATED TO THE VOLTAGE UPSTREAM OF THE MEASURING PLANE.

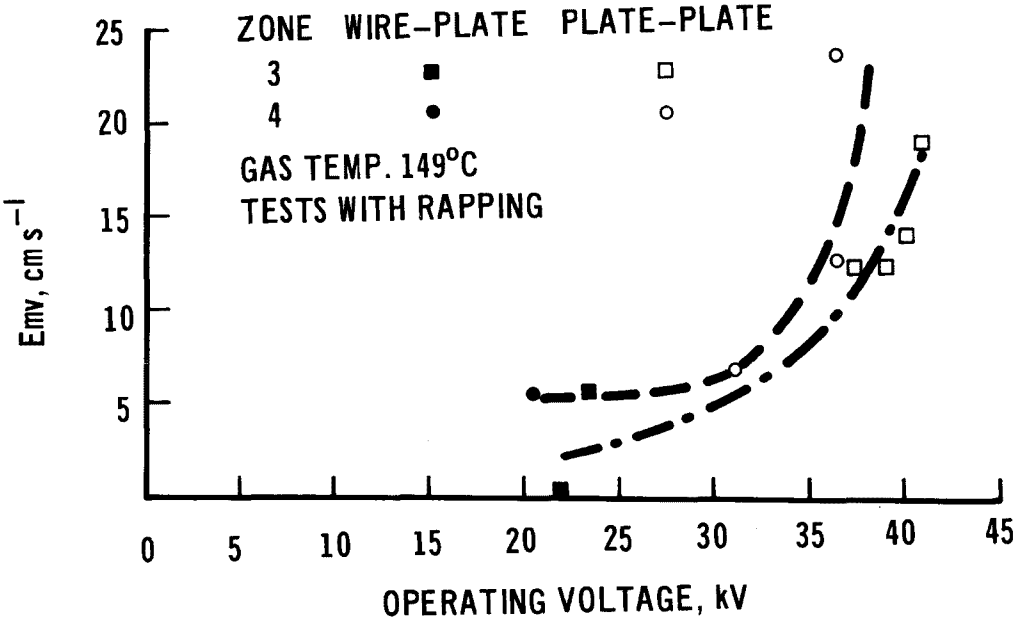

FIG. 4 RELATIONSHIP BETWEEN OPERATING VOLTAGE AND EMV FOR WIRE-PLATE AND PLATE-PLATE ZONES

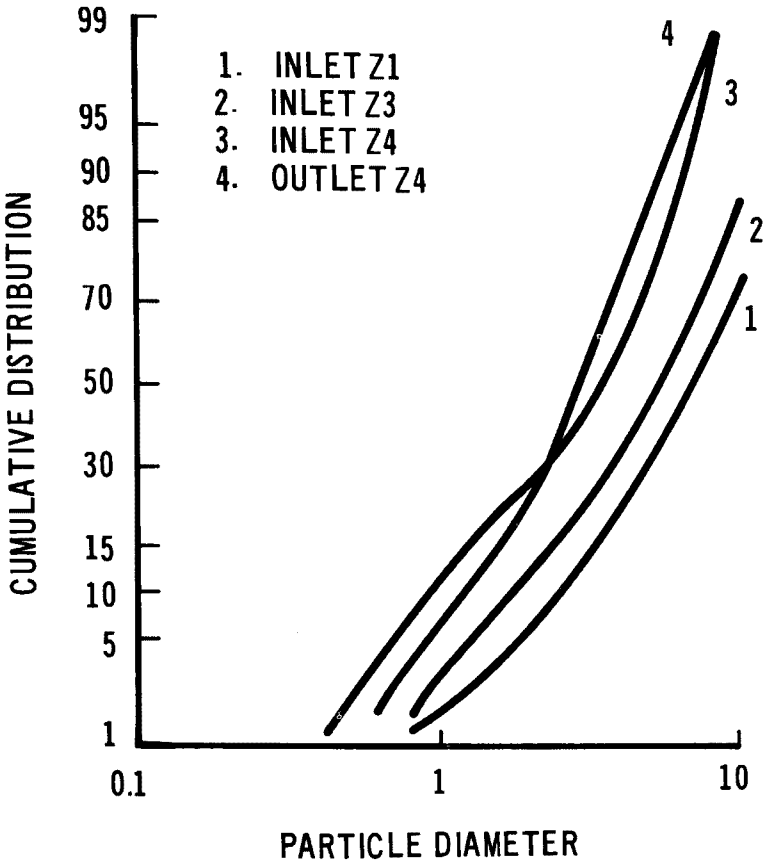

FIG. 5 PARTICLE SIZE DISTRIBUTION TEST 25
H.T. PLATE IN ZONE 3.

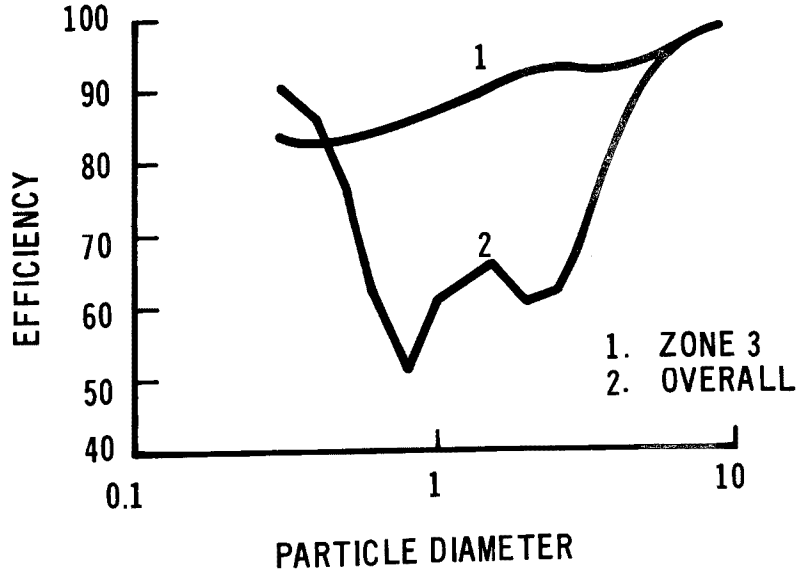

FIG. 6 EFFICIENCY v PARTICLE DIAMETER
H.T. PLATE IN ZONE 3. TEST 25

THE PHYSICS OF PULSE ENERGIZATION OF ELECTROSTATIC PRECIPITATORS

By: Lionel Menegozzi, P.L. Feldman
Research-Cottrell
P.O. Box 1500
Somerville, NJ 08876

ABSTRACT

Analytical/numerical computations for pulser operation are given for a simple geometry. The model describes and calculates the negative ion density produced by corona discharge due to a DC voltage with superimposed pulses. The space charge is then used to estimate wire-quenching effects, and compute the charging and collecting fields. The computer calculations also provide the amplitude and duration of the resultant current pulses. This information is needed for analytical treatment of back-corona suppression with pulse energization. Finally, we obtain the precipitation enhancement factors for both large and small particles. The results indicate that pulser application is a conceptually sound technology that would improve the precipitator performance in power-limited situations such as those arising with high resisitivity dusts. The results also give a deeper insight into the dynamics of pulse energization.

NOTE: Please contact the author for information regarding this paper.

ADVANCED ELECTRODE DESIGN FOR ELECTROSTATIC PRECIPITATORS

By: S. Bernstein, K. Ushimaru, E. W. Geller
Flow Research Company
21414 68th Avenue South
Kent, Washington 98031

ABSTRACT

The subject of this paper is a wavy electrode precipitator which employs a new collecting electrode. The wavy electrode precipitator incorporates a contoured collecting electrode geometry which produces a nearly uniform electric field along the electrode. This feature allows operation with higher average electric field strengths near the electrode than in conventional designs. The wavy electrode provides separated flow zones within its "valleys", which fluid dynamically shield particles from the main stream. The design also provides mechanical rigidity to vertical bending wtihout the sharp flanges normal to the flow commonly found in conventional precipitators. These features permit increased performance for all particle sizes, but especially help in the precipitation of fine particles which are normally the most difficult to collect.

INTRODUCTION

This paper describes the wavy electrtode precipitator and gives an analysis of its performance. This advanced electrode design is based on a unique geometrical configuration of electrodes which is expected to provide significantly improved performance as well as reduced cost over conventional precipitators.

Overall reviews of electrostatic precipitator technology are given by White (1,2), and Robinson (3). A state-of-the-art precipitator configuration is illustrated in Figure 1a. The collecting electrodes are typified by baffles which provide plate stiffness and shield the collected particulate layer from direct scouring by the mainstream, particularly during rapping. The advanced design presented in Figure 1b is typified by a wavy collecting electrode shape which provides the same functions with certain advantages. A brief outline of fundamental collection processes is given here to emphasize the advantages of the latter configuration. These processes are ion generation, particle charging, particle capture, particle removal, particle reentrainment, and sparkover.

Gas ions are obtained from a corona discharge at the anode to provide a source for particle charging by diffusion and by field charging. Diffusion charging dominates the charging process for very small particles (submicron

size); the charge increases as the free ion density increases. High ion density in turn is obtained by high operating voltage and uniform current distribution in the interelectrode space. Field charging occurs when a collision of an ion and a particle takes place. A particle continues to capture ions until the repulsive electric field of the accumulated free ions on the particle balances the attracting electric field of the background. The value of the saturation charge increases linearly with the magnitude of the background electric field, which is determined by the voltage applied to the electrodes and by the electrode configuration.

An electrically charged particle experiences a coulomb force directed toward the collecting electrode and proportional to the charge on the particle and the intensity of the electric field. Since this force increases with particle charge and with the driving electric field intensity, highly charged particles and a high average field intensity along the collecting electrode surface promote efficient collection. The resulting migration accelerations for fine particles are small compared to the accelerations imparted by the turbulent fluctuations present in the flow through the precipitator. However, in regions near the collecting electrode where the flow is separated and relatively protected from the turbulent eddies, the electric field forces are effective in moving the particles to the collector. Thus, one design goal is to increase the sparkover threshold (discussed below), which is the determining factor for the maximum voltage that can be applied. Another goal is to enhance the charging and collecting electric field and current distribution for a given operating voltage which will also increase the charging effectiveness.

It is desirable to maximize both the charging and the collecting field operation at the highest possible voltage. The upper limit for the operating voltage is determined by the sparkover voltage of the given electrode. Thus, peaks in the distribution of electric field intensity along the collecting electrode surface tend to promote early sparkover. Conversely, a uniform distribution delays the onset of sparkover.

Several other phenomena play significant roles in precipitator performance (e.g., chemical composition of the particulate, back corona generation, the conveyance of particulates into the hopper, and particulate removal). We do not intend to minimize the significance of these process, although a full discussion of these topics is beyond the scope of the paper.

THE WAVY ELECTRODE PRECIPITATOR

The wavy electrode precipitator is illustrated in Figure 1b. In terms of electric field and gas flow characteristics, the fundamental improvements over the standard precipitator configuration shown in Figure 1a are: (1) A more uniform electric field which gives a higher average electric field for a specified operating voltage and which allows operation at a higher operating voltage without sparkover. (2) The ability to obtain this condition while maintaining separated flow regions which, for the standard configuration, are created by flanges that are generally detrimental to the electric field. The bulging of the flow channel at each of the wire electrodes provides the more uniform electric field (i.e., voltage gradient) and also provides the pockets

of "dead" air. (3)The wave shape provides structural stiffness for the collector plates so that no stiffeners need be attached during manufacture.

The disadvantages and unknowns associated with the wavy electrode precipitator are the increased cost of manufacturing the wavy shape, the problem of how to design the hanging of plate so as not to promote sparkover, and the fraction of the collector plate area that will be protected from scouring by the mainstream as compared to a standard configuration. The theoretical investigation has provided some quantitative measure of the improvement in collection efficiency that can be expected from the wavy electrode configuration. This work is reported in the next section.

PERFORMANCE ANALYSIS

In order to compare the performance of the advanced wavy electrode with that of the conventional electrode, a detailed analysis of fluid dynamic flow field, electrical characteristics and efficiency was performed. The analysis included the adaptation of a numerical model introduced by Bernstein et al., (4,5) which consists of a system of seven coupled nonlinear partial differential equations: a three-equation fluid dynamics model which describes conservation of mass and momentum for the fluid flow, a two-equation turbulence model, and a two-equation electrostatic model. In order to predict the efficiency of the precipitator for each particle size, a differential form of the classical Deutch efficiency equation is used. The precipitator section is divided into fine elements, and the local electric field is used to compute the charging field and the collecting field. The charging field is assumed to be the average field normal to the electrode surface and the collecting field is the field near the collecting electrode at each point consistent with the Deutch model.

It should be recalled that for the purpose of computing the efficiency, the restrictive assumptions of the Deutch model (see, for example, White(1,2)) are still applicable. These include the assumption that the fluid turbulence is dominant and effective in dispersing the particles to obtain uniform particle concentration in the interelectrode space. Electric field effects are dominant near the collecting electrode. No reentrainment of particulates is allowed, and no particle-particle interactions.

In this section, we describe the basic structure of the model, the boundary conditions, and the techniques of solution which have been employed. The solution in the numerical model employs a finite difference scheme. Since the wavy electrode is not easily represented by a finite difference scheme, a coordinate transformation was employed to map the wavy electrode into a rectangular grid.

Numerical Model

In the present study we have adapted and modified a model for the description of time-averaged fluid motion (4). The model includes fluid transport equations and electrostatic equations.

Transport Equations

For time-averaged flow, the continuity and momentum equations can be written as

$$\frac{\partial \rho U_i}{\partial x_i} = 0 \tag{1}$$

$$\frac{\partial \rho U_i U_j}{\partial x_i} = -\frac{\partial P}{\partial x_i} - \frac{\partial \tau_{ij}}{\partial x_i} + \rho^* E_i \tag{2}$$

where $\rho(x)$ is the time-averaged fluid density at position, U is the averaged velocity, P the pressure, and τ_{ij} the stress tensor. The term $\rho^* E_i$ is the pressure gradient caused by the discharge electric field where ρ^* is the space charge density, and E_i is the electric field intensity. The turbulence kinetic energy equation is written as

$$\frac{\partial \rho U_i k}{\partial x_i} = \frac{\partial}{\partial x_i}\frac{\mu_{eff}}{\sigma_k}\frac{\partial k}{\partial x_i} - \frac{\partial U_i}{\partial x_j}\tau_{ij} - \rho\varepsilon \tag{3}$$

and the turbulence energy dissipation equation as

$$\frac{\partial \rho U_i \varepsilon}{\partial x_i} = \frac{\partial}{\partial x_i}\frac{\mu_{eff}}{\sigma_\varepsilon}\frac{\partial \varepsilon}{\partial x_i} - \frac{\varepsilon}{k}\left(C_{\varepsilon 1}\frac{\partial U_i}{\partial x_j}\tau_{ij} + C_{\varepsilon 2}\,\rho\varepsilon\right) \tag{4}$$

and furthermore

$$\tau_{ij} = -\mu_{eff}\left(\frac{\partial U_i}{\partial x_j} + \frac{\partial U_i}{\partial x_i}\right) + \frac{2}{3}\left(\rho k + \mu_{eff}\frac{\partial U_\ell}{\partial x_\ell}\right)\delta_{ij} \quad . \tag{5}$$

Equations (3) and (4) describe the transport of the turbulent kinetic energy, k, and its rate of dissipation, ε. The effective viscosity are given by

$$\mu_{eff} = C_\mu \rho k^2/\varepsilon \quad . \tag{6}$$

The parameters C_μ, $C_{\varepsilon 1}$, $C_{\varepsilon 2}$, σ_k, and σ_ε are empirical constants.

Electrostatic Equations

The two dependent variables describing the electrostatic field are the voltage and the ion space charge. These dependent variables may be described using Maxwell's electrostatic equation and conservation of current.

Maxwell's Equation

$$\frac{\partial^2}{\partial x_i^2}\phi = -\frac{\rho^*}{\varepsilon_o} \tag{7}$$

Conservation of Current

$$\frac{\partial}{\partial x_i}(\rho^* b E_i) = 0 \tag{8}$$

where ϕ is the electrostatic portential, ε_o is the dielectric constant of the medium, ρ^* is the space charge density as before, and b is the mobility assumed to be constant.

These equations model the interaction between the electrostatics and fluid dynamics. However, the model presently excludes the effects of particle dynamics on fluid field using the following assumptions: (1) The response time of any given particle to adjust itself to the surrounding fluid environ-

ment is sufficiently small to ensure that the particles follow the small-scale fluid motion. (2) In case of low particle loading, the fluid dynamics field exerts little influence on the electric field and, consequently, the correlation between fluid velocity and electric field is neglected.

COMPUTATIONAL MESH GENERATION

The above set of equations is numerically solved using finite differencing techniques. These computational methods for solving physical problems in complex-shaped regions require the generation of an appropriate grid system in the region. A good grid system ensures the economy and accuracy in the computational procedure. This section will discuss the two independent methods of grid generation: one for the conventional precipitator and the other for the wavy electrode precipitator.

Grid System for Conventional Precipitator

A state-of-the-art conventional precipitator is illustrated in Figure 1a. An appropriate grid system conforming to this configuration is the one that models the regions of high gradient (in fluid transport and electrostatics) in detail. For this reason, denser grids were allocated to the regions near the wires and the baffles. Additional constraint is imposed on the field intensity near the discharge electrode. Following the discussion in Cobine (6), a characteristic corona radius is used for the calculations of the field intensity near the wire. The grid system was constructed by taking the first grid node at that characteristic distance away from the wire and gradually increasing the grid size to the center of the precipitator cell. To achieve a better resolution of the velocity gradients near the baffles, a similar method was used in the lateral direction to allocate a denser mesh in those regions. Thus, nonuniform mesh system of 59 x 30 grids was constructed.

Grid System for Wavy Electrode Precipitator

For the wavy electrode precipitator, a boundary-conforming, orthogonal, curvilinear coordinate system was generated. A recent series of papers by Reid et al. (7) and Mobley and Stewart (8) presented a method with flexibility in generating grid systems more appropriate to physical problems. A second transformation is incorporated to stretch and pack the grid as the problem necessitates.

A sample mesh system of 59 x 29 grids for a wavy electrode precipitator was used. The coordinates were packed towards the wire in order to place the first computational grid node at the characteristic wire radius as before. The grids were stretched gradually away from the wire to optimize the number of grid nodes for economical computation.

To utilize the general orthogonal coordinate system, the governing equations were rewritten using the usual rules of coordinate transformation.

RESULTS AND DISCUSSION

The results of numerical modeling for electrostatics are presented in Figure 2. The applied conditions were a wire voltage of -70 kV at a room temperature of 15°C. These conditions were selected for comparisons with laboratory conditions. Obviously, in a full-scale precipitator, the operating temperature will be higher and the maximum allowable operating voltage, as well as the current densities, will be much lower. However, both the conventional and wavy electrodes were considered under the same conditions for our analysis. The test wavy collector was a sine wave with height (from the centerline to the peak of the wave) of 15 cm, wave amplitude (peak-to-valley distance) of 3 cm, and wavelength of 22.5 cm. The solution for the electric potential takes into account the effect of ion space charge, and the boundary conditions along the inlet and outlet are assumed periodic. As can be observed in Figure 2a, there is a strong gradient of potential near the baffles in a conventional precipitator, indicating an imminent sparkover under the given test conditions. The wavy electrode shows, on the other hand, more uniform distribution of potential throughout the precipitator cell, as seen in Figure 2b. This favorable property of the wavy electrode may allow the applied voltage to be increased without promoting a sparkover as discussed earlier.

Figures 3a and b show the fluid dynamic flow field at corresponding applied conditions. The volume flow rate was set at 0.6 m^3/s which translated to the inlet velocities of 0.6 m/s for the conventional precipitator and 0.5 m/s for the wavy electrode precipitator because of varying inlet geometries. As illustrated, the numerical predictions show the dramatic effect of ion motion and ionic wind along the electric field lines.

The influence of the ionic flow is strong enough that just beyond the cell entrance the calculations show a rapid adjustment of the flow to the electric field. The region between the discharge wires experiences a minimum in both the electric field and space charge concentrations; this results in a locally minimum electric pressure gradient $\rho^* E_i$ which allows the fluid a return path to the wire.

The wavy electrode exhibits a different pattern in separation region near the collection plate. The strong interaction between the ion migration and the fluid motion along the wavy-shaped plate promotes a large recirculation zone behind the inlet section. In the conventional precipitator, the recirculation zone extends to about one-quarter of the cell behind the inlet baffles. On the other hand, nearly two-thirds of the collection plate in the wavy precipitator is protected by the recirculation flows.

A comparison of current flux distribution is given in Figure 4. The applied voltage was at -70 kV and at room temperature. The solid line corresponds to a numerical prediction of current density of a wavy electrode, and the broken line corresponds to that of a conventional precipitator electrode. The conventional precipitator has a peak current at the plate exactly opposite to the wire, whereas the wavy electrode shows nearly uniform current density over the collection plate.

This condition is conducive to a higher average migration velocity for the particles being collected. Particularly for fine particles (submicron-diameter particles), the wavy electrode shows favorable trends in improving the particle charging process by two ways: (1) The average charging field over the precipitator cell is higher for the wavy electrode, giving the higher field charging. (2) The average current density in interelectrode space is higher in the wavy electrode, to promote the higher diffusion charging on the fine particles.

The results of these theoretical calculations have been utilized to obtain a qualitative measure of the improvements offered by the wavy design: namely, the increase in particle collection efficiency per unit collector area. Figure 5 shows the efficiency per cell versus particle size using a modified Deutch-Anderson technique. The efficiency predicted in this figure is a relative value and should not be taken as equivalent to the total performance of a given precipitator system. As expected, the submicron particles are most difficult to collect. However, the wavy collector consistently outperforms the conventional collector counterpart. Since the field intensity peaks are not present in the wavy design, sparkover may be delayed and the operating voltage may be increased as schematically illustrated in Figure 5.

CONCLUSIONS

The advanced precipitator electrode with the wavy geometry shows promising improvements over the conventional precipitator electrode. Based on the present analysis, this improved collector design will offer (1) a higher average electric field and (2) a larger flow-shielding region without sharp flanges. A combination of fluid dynamic advantages and improvements in electrostatic properties may become attractive for precipitator optimization once the improvement provided by each technique is proven. The design may also be incorporated with other design innovations, such as the pulse-charging, rigid-frame electrode and multistaging of precipitators.

ENDNOTES

1. White, H.J. Industrial Electrostatic Precipitation. Reading, Massachusetts, Addison-Wesley Publishing Co., Inc., 1963.

2. White, H.J. Electrostatic Precipitation of Fly Ash. Journal of the Air Pollution Control Association, 27(1), January 1977; 27(2), February 1977; 27(3), March 1977; 27(4), April 1977.

3. Robinson, M. Electrostatic Precipitation in Air Pollution Control, Part I., Strauss, W. (ed.). New York, John Wiley & Sons, Inc., 1971.

4. Bernstein, S. and C.T. Crowe. Interaction Between Electrostatics and Fluid Dynamics in Electrostatic Precipitators. (Presented at the 2nd Symposium on the Transfer and Utilization of Particulate Control Technology, Denver, Colorado, July 23-27, 1979.)

5. Butler, G. W., K. Ushimaru, and S. Bernstein. An Investigation of Fluid Dynamics, Electrostatics, and Fine Particle Interaction in Electrostatic Precipitators, Flow Research Note No. 187. Kent, Washington, Flow Research Company, December 1980.

6. Cobine, J.D. Gaseous Conductors. New York, McGraw-Hill, 1941.

7. Reid, R.O., A.C. Vastano, R.E. Whitaker, and J.J. Wanstrath. Experiments in Storm Surge Simulation. In: The Sea, Vol. 6, Chap. 5, Goldberg, E.D. (ed.). New York, John Wiley & Sons, 1977.

8. Mobley, C.D., and R.J. Stewart. On the Numerical Generation of Boundary-Fitted Orthogonal Curvilinear Coordinate Systems. Seattle, Washington, NOAA/ERL Pacific Marine Environmental Laboratory, 1980.

ACKNOWLEDGEMENT

This effort was supported by the U.S. Department of Energy (DOE) under contract DE-AC03-8EV10506. We wish to acknowledge the encouragement for this effort provided by Dr. Fred Witmer of the DOE.

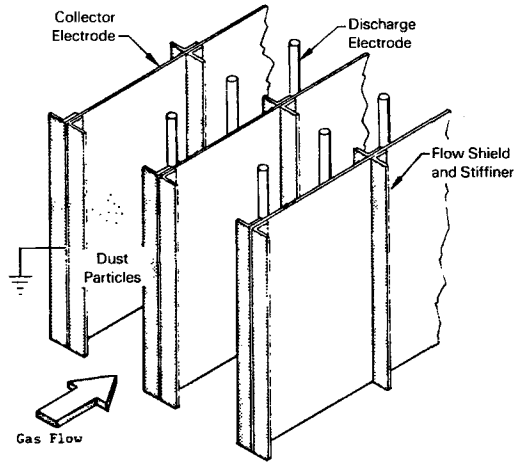

(a) A State-of-the-Art Electrostatic Precipitator

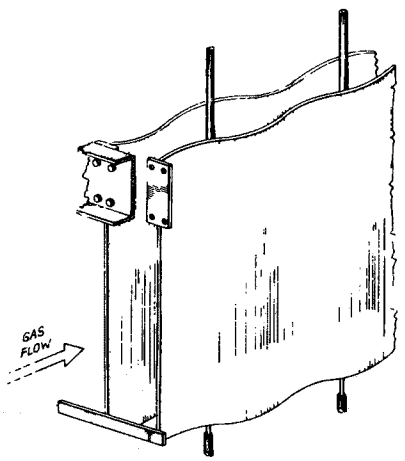

(b) The Wavy Electrode Electrostatic Precipitator

Figure 1. Precipitator Electrode Geometry

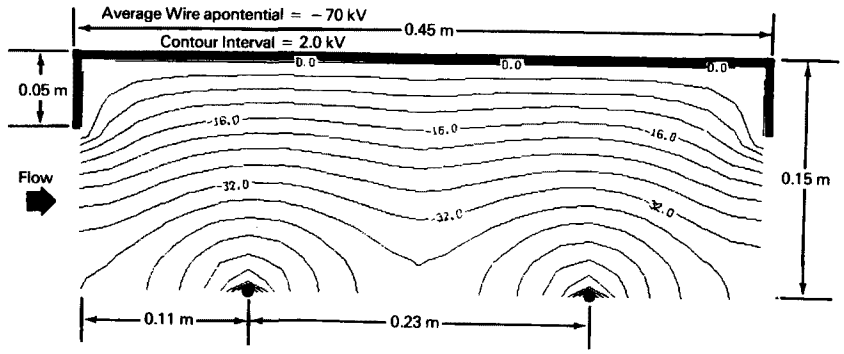

(a) A State-of-the-Art Electostatic Precipitator

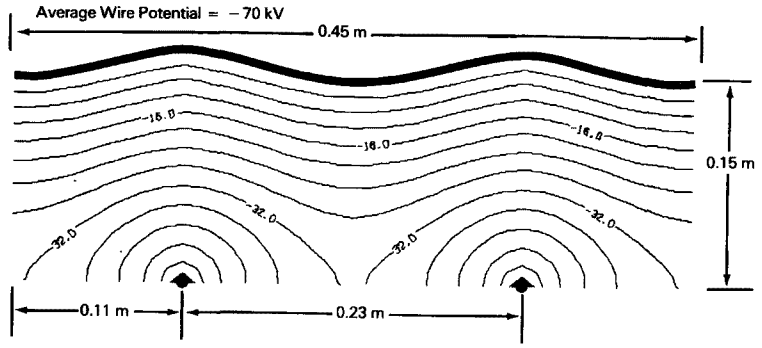

(b) The Wavy Electrode Electrostatic Precipitator

Figure 2. Computed Electrostatic Potential, -70kV

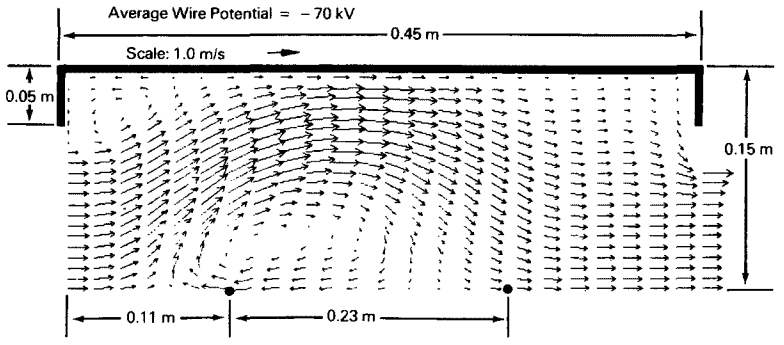

(a) A State-of-the-Art Electrostatic Precipitator

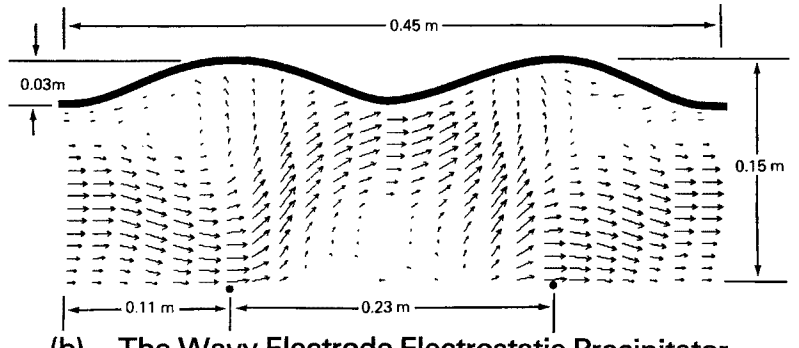

(b) The Wavy Electrode Electrostatic Precipitator

Figure 3. Computed Velocity Field with Average Wire Potential of -70 kV

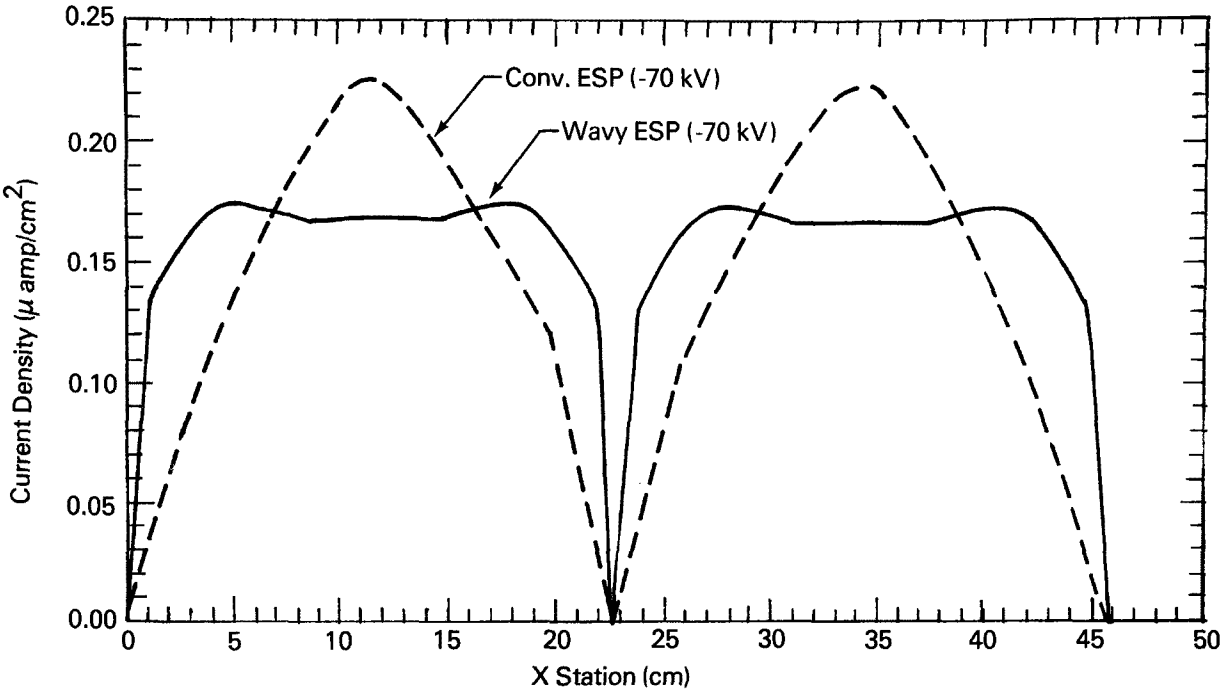

Figure 4. Comparison of Computed Current Density, -70 kV

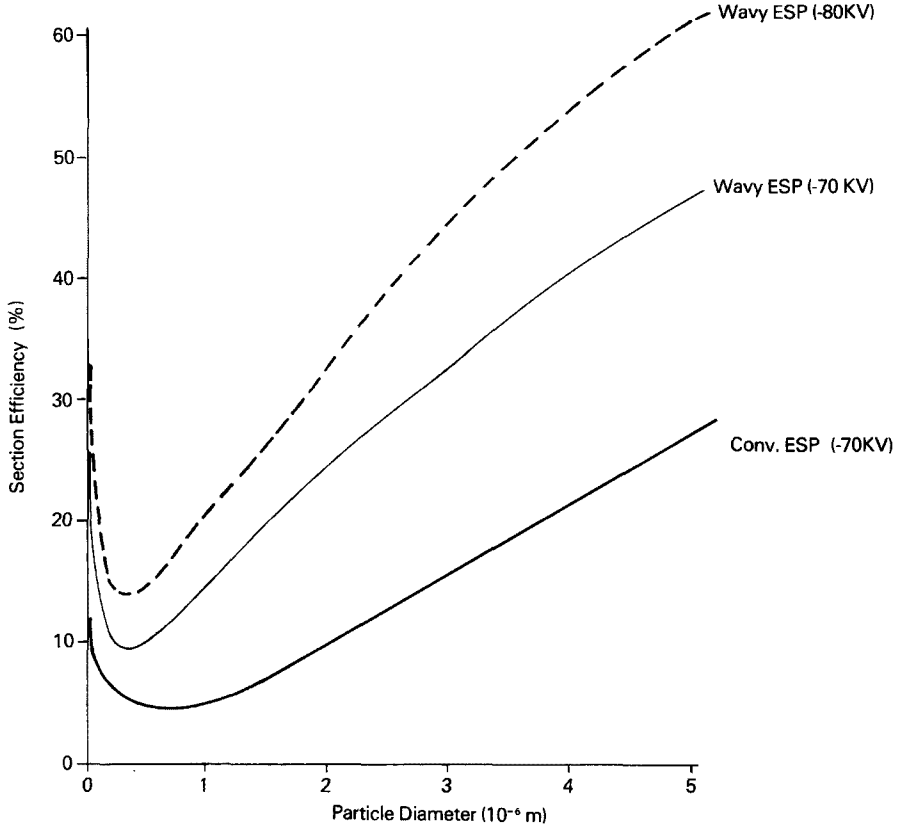

Figure 5. Particle Collection Efficiency as a Function of Particle Size

PROBLEMS IN APPLYING AN ELECTROSTATIC PRECIPITATOR TO A SALVAGE FUEL-FIRED BOILER

BY CHARLES R. THOMPSON
ATLANTIC DIVISION, NAVAL FACILITIES
ENGINEERING COMMAND
NORFOLK, VIRGINIA 23511

ABSTRACT

This paper addresses the problems encountered in applying electrostatic precipitator technology to a trash burning, salvage fuel-fired boiler. The electrostatic precipitators were designed and constructed in a period between 1972 through 1976. Stack emission tests were undertaken after construction was completed and revealed that the emissions were .86 grains/DSCF at 12 percent CO_2. The Virginia Air Emission Standard was .14 grains/DSCF at 12 percent CO_2. Outlined are the steps undertaken to achieve final compliance. Each improvement of electrostatic precipitators such as correction of inlet gas flow patterns, plate and wire alignment, wire improvements, increase in the number of collecting fields and increase in the power to fields, is described and discussed. Also, improvements to the salvage fuel-fired boiler operating modes such as trash feed, over-fired and under-fired air and excess air are outlined. Finally, the design and actual operating parameters for the electrostatic precipitators are presented and compared.

INTRODUCTION

In the early 1960s, the U.S. Navy in Norfolk, Virginia, foresaw a future problem in the disposal of its refuse. An engineering analysis showed the feasibility of burning refuse to produce steam. A salvage fuel-fired boiler plant was constructed and completed in May 1967. The constructed plant consists of two 180 tons-per-day water wall furnaces. The furnaces are capable of producing 50,000 pounds-per-hour of steam each. The facility was the first steam generating water wall furnace to be built in the United States for incinerating refuse. (1)

The plant operation involves the dumping of refuse into a storage pit and lifting the refuse, by crane, into a charging hopper. The refuse is burned in three stages on incline recipitating grates. The grates move the refuse through the combustion chamber with a vertical drop off between each grate stage to tumble the refuse. The tumbling improves refuse distribution and enhances its combustion. Under-fired and over-fired air are provided for combustion. Each furnace also has an auxiliary oil burner used to assist refuse burning and to supplement any equipment breakdown that prevents refuse burning.

The plant was originally constructed with cyclone separators for particulate control. The collectors were made of 24-inch diameter cyclones with 12 cyclones per boiler. The cyclones' operation efficiency was approximately 30 percent. (2) The passage of the Clean Air Act in 1970 and

the State of Virginia Air Pollution Implementation Plans applied more stringent environmental regulations to this facility. The use of these low efficiency cyclones on the incinerators did not meet the new environmental regulations. These regulations required the construction of new and more efficient pollution abatement controls on the incinerators.

Design of electrostatic precipitators for the facility was started in 1972. The design specifications for the electrostatic precipitators called for a single electrostatic precipitator for each incinerator. The design specifications for the precipitators were a performance specification. The only items specified were inlet flue gas parameters, maximum flue gas, velocity through precipitator, a minimum collection efficiency and a final outlet grain loading.

In February 1973, a contract was awarded for the construction of the two precipitators. The precipitators were supplied by Buell Emission Control Division of Envirotech Corporation; each included two transformer-rectifiers rated at 45KVA DC and 550MA DC output, two collection fields, electrode cleaning by vibration and collecting plate cleaning by rappers. Table 1 lists the electrostatic precipitator's parameters as it was originally constructed in 1976.

The salvage fuel-fired boiler exhaust with the completed electrostatic precipitators was stack tested in 1976 to demonstrate final compliance with Environmental Protection Agency new source performance standards and the State of Virginia Air Pollution Regulations. Test results showed emissions to be above the state standard. The emissions varied from a low of .167 grains/DSCF corrected to 12 percent CO_2 up to .6 grains/DSCF corrected to 12 percent CO_2. During this operating time visible emissions ranged from 20 percent opacity to 60 percent opacity with a normal average of around 40 percent. After the results of the stack acceptance test were reviewed, a program was undertaken to correct the electrostatic precipitators' operation and to meet the State Air Pollution Standards.

ANALYSIS OF THE ELECTROSTATIC PRECIPITATORS

Investigation

The Atlantic Division, Naval Facilities Engineering Command, the Navy Public Works Center, Norfolk, and a consultant investigated the poor electrostatic precipitator performance. The evaluation revealed that the precipitator had performed at a collecting efficiency between 89 and 96 percent. But the current operating efficiency of the precipitator had decreased to approximately 88 percent and had not operated near 96 percent since initial completion of the precipitators. This efficiency decrease was consistent with the power decrease in the Corona power input. It was also found that the original equipment design was among the least conservative of municipal incinerator percipitators already constructed. (3)

Stack test data taken during the acceptance test showed low CO_2 readings which continually dropped to an average of eight percent at the stack. The excess air had increased to 200 percent. Temperatures of the

flue gas stream were between 600° and 700°F.

The assessment of the electrical performance of the precipitator revealed very low voltage and current with heavy sparking, particularly in the inlet section of the unit. This, in effect, caused 40 percent of the precipitator collection fields not to be operational. A suspected cause was poor combustion in the furnace which caused large carbon flakes to be entrained in the gas stream and enter the precipitator. The hopper of the precipitator also had a problem filling up with ash and possibly shorting out the bottom of the HT frame and weights. The anti-sway insulators and top support insulators were evaluated and a high build up of ash was found on them. This situation fostered tracking across the insulators and eventual cracking of them. The anti-sway insulators in particular had a continuing problem of cracking and breaking requiring continuous replacement. All the air load electrical data taken during the investigation and past operating performance showed lower than expected readings. In addition to cracked insulators contributing to poor electrical readings, poor electrode alignment evolved, caused by large expansion from high flue gas temperatures of 600 to 700°F. Also, at that temperature range, the carbon content of the ash would yield very low effective resistivity.

A check was made of the resistivity of the ash. The results showed a range of 5×10^6 to 3×10^5 ohms - centimeters; consistent with expectations and with results from other incinerators. At this resistivity, it would take a high Corona power input, low average gas velocity of three to four feet per second and good gas distribution for this percipitator to achieve high performance.

The refuse characteristics that were estimated for the U.S. Navy refuse are in line with the expectations of refuse in general. It must be noted, however, that observations of the refuse by the author showed a large quantity of metals and large wood pieces entering the furnace. The test results showed that the incinerator was operating at excess air far above what was considered good practice. (Good practice would dictate excess air of approximately 70 to 80 percent.) Nevertheless, the operators at this facility had always maintained a high flow of under fire conbustion air and no over fire air. The non use of the over fire air was to keep any low melt point metals from melting down. Any melting metals have caused the grates to freeze up and the entire boiler to be shut down.

A final and important area investigated was the flow distribution into the precipitator. A model study was accomplished during the precipitator design using a 30 percent, open perforated plate at the inlet to the precipitator. The precipitator was constructed using vertical channels at that location. The vertical channels do not offer any control of flow vectors in the up or down direction.

These vectors in the up or down direction would cause leaking under or over the treatment zones and lead to poor collecting efficiency of the precipitator. The data from the model study showed gas distribution quality in the model to be only marginally acceptable with maximum gas flow 40

percent above average velocities in several areas and a standard deviation of 28 percent. The Industrial Gas Cleaning Institute Standard mandates no reading above a maximum gas flow of 40 percent and a standard deviation of 25 percent.

Deficiencies

The investigation revealed numerous deficiencies in the facility. The deficiencies could be categorized into two areas: boiler combustion and electrostatic precipitator deficencies.

The boiler deficiencies found were type of refuse, classified material and combustion air. The refuse fed to the boiler was a mixture of industrial wastes with some municipal refuse. The industrial refuse included large items of metal and wood, such as pallets, sheets of plywood and four by four boards. These items caused pockets of poor burning. The low melting point metals would melt down and solidify on the grates. It was also found that the trash feed included, many times during the day, large quantities of classified material. This material was shredded and manifesting a tendency to burn at a very high temperature causing sudden boiler operation changes and upsets. Another deficiency found on the boiler was that the over-fired air was not being used to assist the combustion. This was due to the fact that in the past when over fired air was used, the grates tended to freeze up and break.

The electrostatic precipitator had numerous deficiencies in its design and operation. It was found that the air leakage into the precipitator, both from the boiler and the expansion joints, was highly excessive. The gas distribution into the precipitator was found to be very suspect due to a 90 degree turn immediately in front of the precipitator and a rapid expansion in all four directions at the inlet transition. The discharge electrodes were found to be highly corroded and a large build up of ash was found in many locations. Ash build up was also found along the support insulators at the top of the precipitator and the anti-sway insulators at the bottom of the precipitator. A check of the plate and wire alignment showed some possible poor alignment but nothing extreme. From the design perspective, it was found that the aspect ratio (the length-to-height of the precipitator) was poor, .536, and that the power applied to each field and the amount of collection areas should have been increased.

After the above deficiencies had been identified, steps were undertaken to correct each one. The items were listed in order of those which would merit the most impact in meeting the air pollution regulations in the least amount of time. Essentially, this led to a first attempt in bringing the precipitator into compliance with Virginia State Air Standards. These efforts did not have the results that was originally intended and subsequently compliance with the Virginia Air Emission Regulations did not meet or exceed projected goals. A second attempt was undertaken to collectively correct most of the above deficiencies to assure that final compliance would be obtained by the July 1979 deadline the U.S. Navy had agreed upon with the State of Virginia Air Pollution Control Board.

CORRECTIVE ACTIONS

First Corrective Implementation

The first major corrective action involved moving the anti-sway insulators outside the precipitator shell and blowing hot purge air over them. It was thought that this correction would eliminate the low voltage levels and numerous electrical trip-outs that were occurring regularly. The top support insulators were also manifesting a problem of dust build up and tracking across them. The purge air system to these insulators was slightly modified. The modification involved the way in which the purge air was being directed across the insulators.

Stack emissions were tested after correction of the above items. The results of the tests revealed that there was essentially no change in the particulate or visible emissions from the facility. The particular emissions were still averaging .86 grains/DSCF corrected to 12 percent CO_2. Visible emissions averaged greater than 20 percent opacity most of the time. The performance of the electrostatic precipitator had not improved. The number of electrical trip-outs and the power level to the fields were the same as before the corrected items were attempted. Consequently, it became apparent that improving the precipitator performance with piece-meal corrective actions would not bring the precipitator into compliance with State of Virginia air pollution standard by July 1979.

Second Corrective Implementation

The second phase of corrective action was a simultaneous effort attacking all the other deficiencies previously noted. These deficiencies were grouped in five primary areas: the insulator's purge air system, precipitator alignment and internals, inlet flow distribution, total power available to the collection fields and, finally, boiler operation problems.

Continued investigation into the purge air systems and the dust build up and tracking across the insulators led to measuring the volumetric flow in this system. The measurements found that the purge air flow was very low and that many insulators were obtaining no purge air at all. To correct the situation the total volume of purge air for both the top support and the anti-sway insulators was doubled. This was done by adding additional fans and separating duct work to the insulators. This effort led to a dramatic decrease in the amount of dust being deposited upon the insulator and essentially eliminated any tracking problems across them.

The electrode and collecting plate alignment were rechecked for tolerances. This check found a few minor alignment problems which were immediately corrected. The biggest deficiency found was the fact that the existing electrodes were shroudless wires, and that some necking down was taking place where the wires pass the top and bottom stiffeners of the plates. To correct this deficiency new electrodes were procured and installed with shrouds. The shrouds were one-half inch in diameter and extended approximately eight inches past the plate stiffeners. It was found that immediately after installating the new electrodes there was a

significant increase in current to the collecting plates and less sparking. But heavy sparking was still taking place in the inlet field.

The third area of correction was the flow distribution. Flow readings were taken at the inlet flow transition approximately three to four feet before the precipitator. The results showed high flows in the center and top of the electrostatic precipitator and some reverse flow on one side (4). It was also expected that much of the flow was dividing into vectors heading to the top and bottom of the precipitator. These flow vectors could cause the gas steam to channel itself to the top and/or bottom of the precipitator. To correct this possibility, the existing vertical channels were replaced with a 50 percent open perforated plate. On the inlet transition side of the plate, eight inch wide horizontal shelving was placed at approximately 1.5 feet intervals. It was expected that these shelves would assist in minimizing the upward and downward flow vectors. Also, the existing flow straighteners at the 90 degree bend before the transition were extended 15 inches.

The fourth area corrected involved increasing the total power within the precipitator. The original design of the precipitator called for the construction of two collection fields. But the precipitator was constructed with the ability to divide into a five-field precipitator, each field being three feet in length. A new third transformer-rectifier set was added to each precipitator to modify the precipitator into a three-field precipitator. The new transformer-rectifier was attached to the first three foot field of the precipitator; with the second and third collecting field each being six foot in length using the existing transformer rectifiers. This set up allowed the isolation of any continued heavy sparking and fostered low power levels to only the first three feet of the precipitator. Hence, the second and third fields could operate at a much higher power level and improve the overall collection efficiency of the precipitator. After energizing the precipitator with this set up, the above intended impact did occur.

The final deficiency area corrected was boiler operations. This involved resealing all possible air inleakage spots such as furnace observation and entrance door seals and grate access door seals. Also the electrostatic precipitator extension joints were rebuilt. As previously discussed the over-fired air had been used very rarely due to the freezing up of the grates. To allow greater use of the over-fired air the under-fired air was more evenly redistributed throughout the furnace combustion zone instead of being isolated in one primary grate area. Also damper controls were installed on over-fired air fans. An evaluation of combustion activity in the modified furnace revealed an increase in the recirculation of air over the flame zone with much better combustion and less large unburned particulate matter leaving the furnace area. When all of the above work was accomplished there was a decrease in gas flow volume from the precipitator of approximately 30 percent.

RESULTS

Completion of the corrective work on the furnace and electrostatic

precipitators brought visible emissions down to 10 percent opacity or less. A stack emission test was then run for particulate emissions with the results showing a significant decrease from the previous testing. However, compliance with the State standards was still not met. The results were for particulate matter .244 grains/DSCF corrected to 12 percent CO_2 and visibile emission of approximately three percent opacity.

A review of the situation revealed that the electrostatic precipitator was performing competently with the Corona power level as expected. A review supported that all corrective items discussed had been completed. The stack emission testing crew reviewed their testing procedure and the collected sample. It was then discovered that approximately six times more of the particulate catch was in the wash than on the filter. This meant that a substantial amount of the particles emitted from the stack were very large. Consequently, since large particulate matter would not emerge through the precipitator the reason for failure of the stack test was probably due to reintrainment of particulate matter after the precipitator.

A maintenance review of the downstream breaching and stack was undertaken. This examination found large rust flakes continually peeling off breaching walls and an ash build up in the bottom of the stack all the way up to the point where the breeching enters the stack. A thorough cleaning of the duct work and stack area was undertaken and new stack emission tests run. Results of the tests showed that both the particulate and visible emissions were in compliance with Virginia Air Pollution Regulations. The particulate results were .052 grains/DSCF corrected to 12 percent CO_2 and opacity at seven percent.

COMPARISON OF OPERATING PARAMETERS

A comparison of the final operating parameters to the original design warranty is shown in Table 2. A review of the table shows that it took a 50 percent decrease in the flue gas volume for particulate emissions to comply with the required design emission. After the first corrective action, the flue gas volumetric flow and temperature met design specifications; therefore, the other design parameters were met. But as previously stated, the outlet particulate concentration exceeds the air standards. I believe this again documents the fact that the original precipitator design is not conservative

An additional parameter that has changed but can not be shown on the table is the manner in which refuse is fed to the boilers. Before the last stack emission tests all refuse was presorted on the tipping floor. This sorting eliminated large metal and wood items. The change meant a more complete and consistent burn of the refuse. This presorting had a large impact on lowering the gas flow, flue gas temperature and inlet concentration.

ENDNOTES

1. Collins, John P., Refuse: The Urban Ord. U.S. Navy. (Presented at American Defense Preparedness Association, Energy/Environment Conference, Kansas City, Missouri, March 27-31 19771) p.3-4.

2. Bibbens, Richard N., Air Pollution Source Emissions Test of Salvage Fuel Boiler (technical report YF 38.534.003.01.001 for Navy Public Works Center, Norfolk, Virginia).

3. Hall, H. J., Electrostatic Precipitator Operations, Problems and Solutions in Refuse Incinerator Applications (Presented at American Society Mechanical Engineers, Solid Waste Processing Division Meeting, New York, New York, January 16, 1980)

4. Buhmann, K. A., Technical Report 651:KAB (Technical Report for Department of Navy, Atlantic Division, Naval Facilities Engineering Command).

TABLE 1 SUMMARY PARAMETERS FOR ELECTROSTATIC PRECIPITATORS ON SALVAGE FUEL-FIRED BOILERS NAVAL STATION, NORFOLK, VIRGINIA

Item	Parameter
1. Particulate Perf. Reqm't	
Federal Emission Reqm't	0.08 gr/SCF @ 12% CO_2
State of VA. emission reqm't	0.14 gr/SCFD @ 12% CO^2
2. Fuel fired	Solid waste material & fuel oil
3. H_2O, % vol in gas	13-15
4. Δ P across PPTR, Max "H_2O	0.5
5. Airtight seals	Max drop 0.25% CO_2 inlet to outlet
6. Design gas flow	76,000 ACFM @ 690F
7. Guar. Eff., % wgt	96
8. Inlet Conc., gr/ACFM	0.92
9. Gas vel., ft/sec	3.35
10. Chambers, cells	1 each
11. No. of Fields	2 (9' + 6')
12. No. of Ducts	18, 9" width
13. Plate Height, ft.	28
14. Coll. Plate Length, ft.	15
15. Coll. Area, ft^2	15120 inlet 9072 outlet 6048
16. SCA, ft^2/1000 ACFM	199
17. Design w, ft/sec	0.27
18. Aspect Ratio, l/h	0.536
19. Area/rapper, ft^2	3024 Impulse (5)
20. Discharge wire	0.105" dia. Hi C steel - 25# wgt
21. Effect wire length, ft	10080
22. Ft. of wire/rapper	2016
23. No. Rect. Sets, Si	2 - 35KVA ea. 45KVDC, 550 MA
24. Total Installed I_{av}, MA	1100
25. Avg J, ma/100 ft^2	58 inlet J = 48.5 outlet J = 73
26. Automatic Control	Ana Comp II
27. Hopper heat	yes one hopper/PPTR
28. Disch. wire spacing, in	8
29. Gas Distribution	Vertical channel + Perf. PL. on inlet/ Perf. plate on outlet

TABLE 2 PERFORMANCE DATA FOR ELECTROSTATIC PRECIPITATORS ON SALVAGE FUEL-FIRED BOILERS NAVAL STATION, NORFOLK, VIRINIA

	Parameter	Design	November 1979
1.	Gas 1000 ACFM inlet	76	34.0
2.	Inlet gas temperature, ^{o}F	690-725	573
3.	SCA, ft^2/1000 ACFM	199	444.7
4.	Eff. % wgt*	96	97.0
5.	w, ft/sec	0.27	.0079
6.	Avg v, ft/sec	3.35	1.49
7.	Outlet gr/SCFD @ 12% CO_2	0.08	0.052
8.	Avg inlet CO_2%		7.2
9.	Avg outlet CO_2%		6.9
	EA %		161
10.	Max drop in CO_2 inlet to outlet	.25%	.3%
11.	Inlet conc lb/hr, avg	600	12.04
12.	Outlet conc lb/hr, avg	24	5.39

*Calculated using gr/SCFD measurements

THE APPLICATION OF ELECTROSTATIC PRECIPITATORS TO BOILERS FIRING MULTIPLE FUELS

By: Robert L. Bump, Technical Manager
Industrial Precipitators
Research-Cottrell, Inc.
Somerville, New Jersey

ABSTRACT

Recent years have seen a swing to boiler designs which afford versatility in the fuel fired. This is, of course, a result of the economics and availability of conventional fuels. Many process industries are using their own waste products as a principle fuel source. The varying conditions imposed on the air pollution control device as a result of this practice will be discussed in this paper. Case histories will be presented as well as a discussion of some of the operational considerations which must be recognized. Since the pulp and paper industry has been a forerunner in this activity, the majority of the data presented will derive from this application.

INTRODUCTION

The theoretical aspects of electrostatic precipitator application and behavior are well known and need little commentary. The original Deutsch-Anderson equation has given way to more sophisticated methods of establishing precipitator size for a given duty which involve computer programs that take into account the many process and fuel variables which affect design. Figure 1 indicates the various inputs required to derive the proper specific collecting area. The division of responsibility for the input data between the engineer/user segment and the supplier is also indicated. The complexity is caused primarily by the fuel types and sources, ash analysis and their resultant impacts on design. Coupled with the increasing stringency of legislation and demand for a very high level of reliability we have a ball game which if not new is certainly different. To make the problem more challenging, we have the added ingredient of most industrial power boilers being designed for multiple firing of coal, waste and oil. This is, of course, a result of the uncertainty of adequate fuel supplies, the attendant costs and the nebulous state of SO_2 legislation for industrial power boilers.

Application Considerations

How does this situation affect the engineer specifying air pollution control equipment and his counterpart applying it?

There are fundamental data, usually furnished by the boiler manufacturer, which are basic to the application process. Figure 2 outlines this information. It is obvious that in the case of multiple fuel usage this information is required for each operating mode. Figures 3 to 8 are from a typical specification and indicate fuel analysis and operating data for a boiler designed to burn coal, wood waste and oil in various combinations. The most important conditions to be considered in sizing the precipitator for the specified efficiency are the gas volume for each operating mode, particulate loading, temperature and ash analysis as affecting the precipitability (resistivity) for each fuel or combination. In the example cited, the gas volume and the particulate loading for the coal-wood combination is greater than the 100% coal or oil-wood combination. The frontal area of the precipitator is, then, set by the highest gas volume and the maximum gas velocity permitted by the suppliers design or the specification. In this case the specification set 3.5 feet per second as maximum. The resistivity of the coal ash was found to be approximately one order of magnitude greater than the other fuel combinations necessitating the highest specific collecting area for the specified efficiency. In summary, we have a situation where the coal-wood gas volume set the cross sectional area and the coal ash resistivity set the length of the precipitator. It is not unusual for the "best to worst" conditions on a multiple fuel application to involve as much as 50% spread in the sizing requirements. Figure 9 demonstrates this point.

Mechanical & Electrical Design Considerations

Multiple firing conditions also require additional care in several mechanical and electrical design areas. Since power density varies with changes in gas and particulate composition, it is necessary for the designer to be aware of these ramifications in order to make proper selection of the transformer-rectifiers. In our example because the ash from wood waste is of a lower resistivity and the moisture content of the gas about 20% higher than the coal fired mode it controlled the applied power density. Probably the most important area of design care on multiple fuel applications is versatility in the collecting surface rapping system. It is understood that most losses (of particulate) in a precipitator occur as a result of reentrainment during rapping. It is also understood that the energy required to remove high resistivity ash from collecting surfaces can be as much as six times that needed to dislodge a highly carbonaceous, conductive material. A rapping system must, therefore, have a very high degree of intensity and cycle adjustment which may be readily made in order to cope with fuel variations. A microcomputer based control permits keyboard adjustment of each rapper as well as the cycle time. All operational parameters should be displayed at the controls via digital readout devices.

The last area where design care is of utmost importance is the dust removal system. A large percentage of precipitator operational and maintenance problems stem from improper ash removal design or operation. The topic is too involved to treat here, however, suffice to say the system must be sized properly, preferably of the continuous removal type, with sufficient auxiliaries (hopper heat, vibrators, level detectors, etc.) to do the job. This is particularly true with multiple fuels since much of the particulate has a high combustible content and the danger of fires exists if the ash is allowed to accumulate in the hoppers. There has been good experience with trough type hoppers and continuous removal by the use of screw conveyors. Reference 1 treats this subject in considerable detail.

Operational Considerations

The final consideration in applying precipitators to multiple fuel operations is the variations in operating characteristics. Each firing mode and fuel results in gas composition and particulate chemistry which is different and the precipitator reacts operationally to these variations. It is, therefore, essential that not only the rapping system have the versatility described but that the precipitator power control system design affords fast, effective reactions to the process changes. Modern digital and analog controls accomplish this in milliseconds. Figure 10 demonstrates the operation of an effective precipitator control circuit. Other control areas which are important have to do with the combustion process. As an example, take a boiler firing wood waste and coal. The wood waste is typically fired on a grate, requires considerably more air to burn than coal, and the resultant particulate may be as high as 40-50% combustible. Care must be taken to minimize fire hazard. Oxygen monitors interlocked with the precipitator power supplies are advisable. Periodic checks to insure a "tight" system should be made since O_2 inleakage at doors, expansion joints, dust valves, etc. can cause hazardous conditions. The importance of a proper dust removal system and auxiliaries has already been emphasized. Thorough operator training on the effects of fuel variations not only at the firing end but in the entire process is a necessity.

Conclusion

The technology for the application of electrostatic precipitators to multiple fuel fired boilers has been demonstrated. Care and accuracy in specifying the conditions for the various firing modes is essential from the user end. The supplier must recognize the effects of the variables on equipment application and design.

Reference 1 - "Design and Operation of Reliable Central Station Flyash Hopper Evacuation Systems" by Joint Technical Committee of American Boiler Manufacturers Association and Industrial Gas Cleaning Institute, Inc. Presented at American Power Conference, April 21-23, 1980, Chicago, Illinois.

PRECIPITATOR SIZING DATA

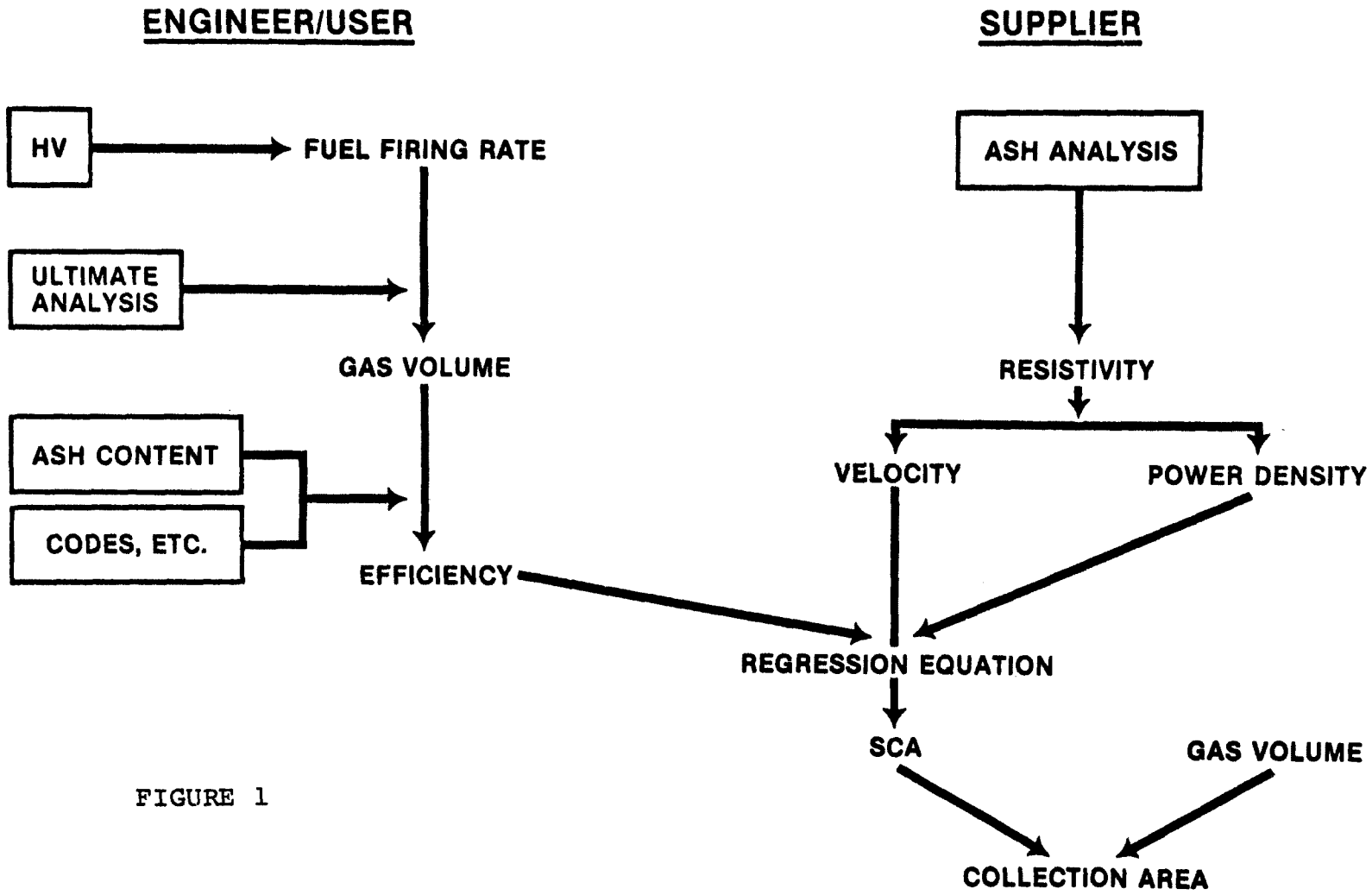

FIGURE 1

Basic Specification Information

Gas volume, acfm, normal and peak

Temperature, normal and peak

Pressure, normal and design

Dust loading, grains per acf or scfd

Efficiency required

Type of boiler (P.C. stoker, etc.)

Type of fuel(s)

Fuel analysis

Particle size

Figure 2

Coal Analysis (Identify State and Mine)

Ultimate (percent by weight)	Performance	Range
Carbon	73.50	65.0-85.0
Hydrogen	4.80	4.5- 5.5
Sulfur	0.70	0.5- 1.1
Nitrogen	1.20	1.0- 2.1
Oxygen	5.60	4.0- 8.0
Moisture	7.00	3.0-15.0
Ash	7.20	2.0-16.0

Figure 3

Ash Analysis (Percent by weight)

P_2O_5	0.15
SiO_3	29.79
Fe_2O_3	38.07
Al_2O_4	20.13
TiO_2	0.81
CaO	4.27
MgO	0.91
SO_3	4.45
K_2O	1.01
Na_2O	0.41
Misc.	1.31

Figure 4

Analysis of Wood Waste and Bark (Percent by weight)

Type	3/8" max. size
Carbon	24.0
Hydrogen	2.5
Sulfur	----
Nitrogen	----
Oxygen	18.5
Moisture	45.0 - 65.0
Ash	5.0
Sand	29.0 (of the ash as SiO_2)
HHV	4300 BTU/lb.

Figure 5

Analysis of No. 6 Fuel Oil	(Percent by weight)
Sulfur	0.70
Hydrogen	10.33
Carbon	88.33
Nitrogen	0.14 (0.3 max.)
Oxygen	0.50
Heating Value	18,400 BTU/lb.

Figure 6

Particulate Size Leaving Air Heater

Size	Coal	Coal/Wood	Oil	Oil/Wood
% less than 30 microns	83	83/50	53	53/50
% less than 20 microns	65	65/36	34	34/36
% less than 10 microns	44	44/27	27	20/27

Figure 7

Precipitator Design Criteria

	100% Coal	50% Coal 50% Wood	50% Oil 50% Wood
Gas Flow, acfm	335,000	435,000	348,000
Temperature, ^{o}F	273 ±20	335 ±20	318 ±20
Heat Input to Boiler, BTU/hr. x 10^6	1055	1055	1055
Fly ash, inlet, lbs./hr.	13,950	19,500	17,500
Fly ash, outlet, lbs./10^6 Btu	0.075	0.075	0.075
Ground Elevation, ft.	14'-6"	14'-6"	14'-6"
Hopper Storage, hrs.	12	12	12
Minimum Aspect Ratio	1.0	1.0	1.0
Maximum Plate Height, ft.	32	32	32
Maximum Pressure Loss, "Wg.	0.5	0.5	0.5
Maximum Gas velocity, ft./sec.	3.5	3.5	3.5
Efficiency, %	99.5	99.5	99.5
Opacity, %	20	20	20

Figure 8

Precipitator Sizing Example

Design Conditions	Wood Waste	Coal
Gas volume, acfm	288,360	246,040
Inlet loading, gr/scfd	6.5	1.47
Outlet loading, gr/scfd	0.02	0.02
Efficiency, %	98.97	98.57

Note: Coal to be worst Eastern Bituminous

Sizing Parameters		
Velocity, fps	4.2	3.64
Treatment time, secs.	X	1.4X
Aspect ratio	1.5	1.8
Resistivity, ohms/cm.	3.5 x 10^7	6.3 x 10^{12}

Figure 9

FIGURE 10

TYPICAL POWERTRAC™ CONTROL OPERATION DURING UNSTABLE PROCESS CONDITIONS

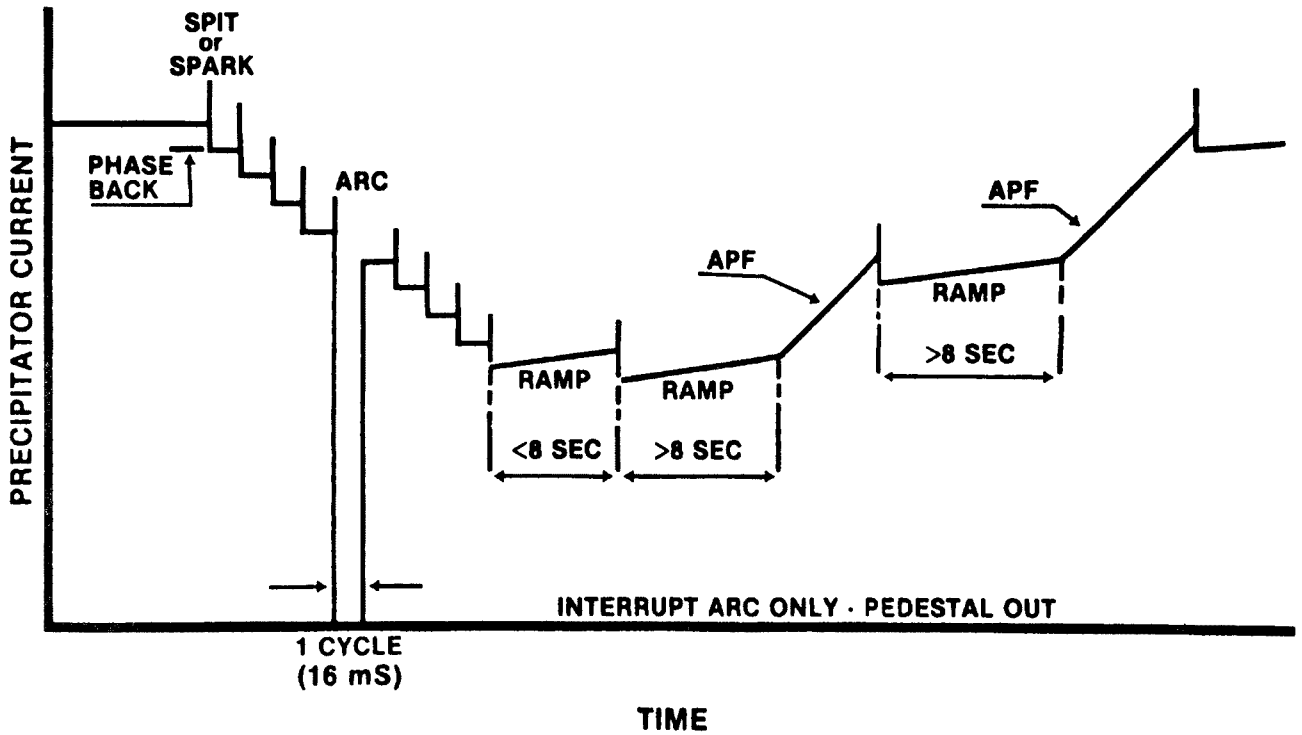

AUTHOR INDEX

AUTHOR NAME	PAGE
Albrecht, P.R.	IV-116
Anderson, M.H.	II-334
Arce-Medina, E.	II-76
Ariman, T.	III-290
Armstrong, J.A.	IV-188, IV-252
Bakke, E.	I-236
Balfour, W.D.	III-119
Bamberger, J.A.	III-398
Bergmann, L.	I-323
Berlant, M.J.	II-218
Bernstein, S.	II-405
Beutner, H.P.	III-71, III-228
Bickelhaupt, R.E.	I-165
Boericke, R.R.	III-353
Bohn, R.	IV-344
Borenstein, M.	III-90
Brookman, E.T.	IV-125
Bump, R.L.	II-425
Bush, P.V.	I-157
Calvert, S.	III-1, III-10, IV-156
Carnes, D.	IV-135
Carr, R.C.	I-118
Chamberlain, H.L.	IV-406

AUTHOR INDEX (cont.)

AUTHOR NAME	PAGE
Chambers, R.	I-45
Chiang, T.	III-250, III-261
Chou, K.H.	IV-73
Cowen, S.J.	IV-264
Crippen, L.K.	I-148
Crowson, F.	III-438
Crynack, R.R.	II-242
Czuchra, P.A.	IV-55
Dalmon, J.	II-390
Demski, R.J.	I-341
Dennis, R.	I-1, III-140
Dietz, P.W.	III-449, III-459
Donovan, R.P.	I-11
Drehmel, D.C.	III-341, IV-210
DuBard, J.L.	IV-383
Durham, M.	II-54, IV-285
Ensor, D.S.	I-176, IV-242
Eskinazi, D.	III-238
Faulkner, M.G.	II-199, IV-395
Feldman, P.L.	IV-3
Ferrigan III, J.J.	I-197
Finney, W.C.	II-358
Fjeld, R.A.	II-179
Fortune, O.F.	I-82

AUTHOR INDEX (cont.)

AUTHOR NAME	PAGE
Frazier, W.F.	III-171
Gardner, R.P.	III-128
Gaunt, R.H.	I-216
Gehri, D.C.	I-333
Gentry, J.W.	III-406
Giles, W.B.	III-468
Hardison, L.C.	III-33
Harmon, D.L.	IV-317
Hawks, R.L.	III-221
Helfritch, D.	I-75
Henry, F.	III-301
Henry, R.F.	IV-63
Hesketh, H.E.	IV-222
Hoenig, S.A.	III-382
Hovis, L.S.	I-23
Hyde, R.C.	I-129
Iionya, K.	III-181, III-321
Jaworowski, R.J.	I-185
Jensen, R.M.	I-138
Joergensen, H.J.	II-370
Johnson, C.A.	I-352
Kalinowski, T.W.	III-311
Kanaoka, C.	III-280
Kirstein, B.E.	III-373

AUTHOR INDEX (cont.)

AUTHOR NAME	PAGE
Kolnsberg, H.J.	IV-179
Krishnamurthy, N.	IV-232
Ladd, K.	I-55, I-65
Lagarias, J.S.	I-272
Landham, Jr., E.C.	I-237
Langan, W.T.	III-211
Lawless, P.A.	II-25, II-35, II-44
Leith, D.	III-270
Leonard, G.L.	II-120
Maartmann, S.	II-130
Mahoney, D.F.	I-206
Mappes, T.E.	III-150
Martin, D.	IV-145
Masuda, S.	II-189, II-380
Mathai, C.V.	IV-200
Mazumder, M.K.	II-160, II-169
McCrillis, R.C.	IV-306
McElroy, M.W.	I-94
McLean, K.J.	I-265, II-304
Menegozzi, L.	II-404
Menoher, C.	III-111
Mitchner, M.	II-97
Moore, W.E.	IV-105
Mormile, D.	IV-363

AUTHOR INDEX (cont.)

AUTHOR NAME	PAGE
Moslehi, G.B.	II-109
Mosley, R.B.	II-1, II-13
Musgrove, J.G.	III-193, III-201
Noonan, F.M.	IV-326
Oglesby, H.S.	III-80
Ostop, R.L.	I-107
Parker, R.	III-51, IV-2
Parquet, D.	III-363
Parsons, Jr., E.L.	I-303
Patton, J.D.	III-160
Pearson, G.L.	I-120
Pedersen, G.C.	III-60
Petersen, H.H.	I-291
Piulle, W.	I-253
Potokar, R.W.	III-417
Prem, A.	III-21
Presser, A.M.	IV-26
Pyle, B.E.	II-66
Raemhild, G.A.	II-349
Reardon, F.X.	III-102
Rimberg, D.B.	II-262
Rinaldi, G.M.	IV-95
Rinard, G.	II-283, II-295
Rubow, L.N.	IV-83

AUTHOR INDEX (cont.)

AUTHOR NAME	PAGE
Rugg, D.	II-273
Samuel, E.A.	II-149
Schliesser, S.P.	II-252
Semrau, K.T.	III-43
Shilling, N.Z.	II-230
Smith, W.B.	I-96
Snaddon, R.W.L.	IV-74
Sparks, L.E.	II-314, II-326
Spawn, P.D.	IV-335
Starke, J.	III-428
Stevens, N.J.	I-313
Sullivan, K.M.	II-141
Tatsch, C.E.	IV-353
Teller, A.J.	III-393
Thompson, C.R.	II-415
Urone, P.	IV-275
VanOsdell, D.W.	I-35
Viner, A.S.	IV-168
Wakabayashi, A.	III-332
Wang, H.H.	IV-36
Wang, J.C.F.	IV-373
Wegrzyn, J.	IV-46
Weyers, L.L.	I-226
Wilks, W.H.	IV-15

AUTHOR INDEX (cont.)

AUTHOR NAME	PAGE
Williamson, A.D.	IV-297
Yamamoto, T.	II-87
Yung, S.	IV-1, IV-155
Zarfoss, J.R.	II-208

☆USGPO: 1982 — 559-092/0430